COMPRESSIVE BEHAVIOR OF REFRACTORY CERAMICS AT ELEVATED TEMPERATURES

by

Fouad George Tamer

Bachelor of Engineering
American University of Beirut
(1983)

Master of Science
Massachusetts Institute of Technology
(1985)

SUBMITTED TO THE DEPARTMENT OF CIVIL
ENGINEERING IN PARTIAL FULFILLMENT OF THE
REQUIREMENTS FOR THE DEGREE OF

DOCTOR OF PHILOSOPHY

at the

MASSACHUSETTS INSTITUTE OF TECHNOLOGY

October 1988

Signature of Author _____
Department of Civil Engineering
October 25, 1988

Certified by _____
Professor Oral Buyukozturk
Thesis Supervisor

Accepted by _____
Professor Ole S. Madsen
Chairman, Departmental Committee on Graduate Students

ABSTRACT

Analysis and design of refractory linings for high temperature process vessels is complex. Previous research at the Massachusetts Institute of Technology in that area concentrated on developing constitutive models of the material behavior, implementing them into finite element codes and performing parameter studies to obtain design recommendations. There was a need to generate a fundamental understanding and characterization of the behavior of different refractory material systems manufactured by various processes in slagging coal gasifier environments. The objective of this work is to characterize the short—term compressive behavior of refractory ceramic oxides at elevated temperatures, with a focus on candidate materials for slagging coal gasifier linings.

The materials studied were alumina—chromia and chromia—magnesia refractories manufactured by cold—pressing and sintering, hot—pressing or fusion—casting. A high temperature testing facility was designed and built. Recommended specimen preparation procedures are established and utilized. The variation of the material properties within a refractory brick, between bricks within the same production batch and between bricks from different production batches is established. The macroscopic fracture and deformation behavior of the candidate materials are characterized under monotonic, cyclic and creep uniaxial compressive loads, and constant and increasing temperatures. The effects of reducing atmospheres, slag—impregnation and different chemical compositions on the deformation and fracture behavior of the hot—pressed alumina—chromia systems are assessed. The microstructure of virgin and tested, as—manufactured and slag—impregnated materials is characterized by using stereoscopic and Nomarski optical microscopy, scanning electron microscopy, X—ray diffraction, mercury porosimeter tests, and bulk density measurements. The microstructural characteristics are related to the observed deformation and fracture behavior. Finally, a material database of thermomechanical and thermophysical properties is assembled, which may be useful to the manufacturers and users of the refractory materials.

A transition temperature (roughly equal to $T_m/2$, where T_m is the melting temperature of the material) is observed. In monotonic tests at temperatures below transition, linear elastic deformations are observed with brittle final fracture. For temperatures above transition a temperature dependent transition strain rate is observed. Linear inelastic deformations with brittle fracture are observed for strain rates higher than transition, non—linear inelastic deformations with unstable fracture propagation are observed for strain rates around transition, and non—linear inelastic deformations with stable fracture propagation are observed for strain rates slower than transition. Constant load tests at constant temperature indicate that creep is a major factor in non—linear deformations above the transition temperature. Deformation maps characterizing the creep behavior are constructed. The constant load increasing temperature tests provide a way to measure the transient thermal strain.

In monotonic tests at temperatures below transition, narrow cavities with orientations between 15 to 60 degrees (to the applied load direction) seem to be the major factor affecting the deformation mechanism, while at temperatures above transition, large pores with no specific orientation are predominant. Observing specimens tested under creep loads, it seems that creep cavitation is a major deformation mechanism at temperatures above transition. Significant transgranular cavitation and grain growth are also observed for temperatures in that range.

Under cyclic loads at temperatures below transition, the first loading cycles and the last cycle before final fracture exhibit larger deformations than intermediate ones, while at temperatures above transition the deformation of all cycles is similar.

Three–dimensional failure surfaces are produced to show the number of cycles at failure for different temperature and stress levels.

The effect of environmental factors was studied for cold–pressed sintered materials only. At temperatures below transition, slag–impregnated materials exhibit higher strength and stiffness than as–manufactured ones. At temperatures above transition slag–impregnated materials show higher rate of decrease of strength with temperature and at 2400F the slag–impregnated materials strength is lower than the one for as–manufactured materials. The results of X–ray diffraction and open porosity measurements indicate that open porosity is a major factor in slag– impregnation. Reducing atmospheres do not adversely affect the behavior of the candidate materials for temperatures below transition. Reducing atmospheres do not seem to affect the behavior of the alumina–chromia, but decrease the strength of the slag–impregnated chromia–magnesia refractory.

For the same material system going from cold–pressed sintered to fused–cast to hot–pressed refractories, the grain size decreases, the homogeneity of the microstructure increases, the strength increases (but the rate of decrease in strength with temperature also increases), the creep strain rates decrease at same load level, the cracking patterns are more defined, and the cost of the material is higher. The alumina–chromia may be preferred to the chromia–magnesia for its thermomechanical properties, and the chromia–magnesia may be preferred for its smaller degree of slag–impregnation. An increase in the chromia content in the hot–pressed alumina–chromia seems to produce better thermomechanical properties. As–received fused picrochromite grains are found to be precracked prior to their use in processing the cold–pressed sintered chromia–magnesia system. Tabular alumina grains in the cold–pressed sintered alumina–chromia do not exhibit cracks prior to testing. The reduction of open porosity is desirable in order to reduce the extent of slag impregnation.

Thesis Supervisor: Oral Buyukozturk
Title: Professor of Civil Engineering

ACKNOWLEDGEMENTS

TABLE OF CONTENTS

CHAPTER 1
INTRODUCTION

1.1   PROBLEM DESCRIPTION

The general application area is high temperature and pressure containment vessels. High temperature containment vessels are important components used in many industrial facilities such as fossil power plants, coal gasification plants (Bakker et al., 1984; Bakker and Stringer, 1981; Chen and Buyukozturk, 1984; Kennedy, 1979), petroleum refinery units (Crowley, 1984; Crowley and Johnson, 1972; Gilchrist, 1977; Wygant and Bulkley, 1954), blast furnaces (ISI, 1968), steel convertors, metal smelting and refining industry (Hugget, 1966; McGannon, 1964), boilers, petrochemical plants, steam—raising plants, ammonia plants, incinerators, and cement kilns. These vessels are usually composed of an outside steel shell and layers of refractories. Refractory linings protect the steel shell from high temperatures, and attack by gases and process by—products. The linings are usually composed of a dense layer next to the hot face and a layer of insulating material next to the steel shell. The linings can be either monolithic or composed of bricks that are jointed together using a mortar material. Cooling systems can be used to keep the shell temperature at certain predetermined levels.

In most of these applications the refractory linings used to protect the steel shell are subjected to the action of extremely severe process environments. The operating conditions include a combination of elevated temperatures, high pressures, cyclic mechanical and thermal loads, corrosive gases, and molten by—products that run down the walls of the gasifiers. These severe environments lead to the failure of

the refractory linings. The cost of maintenance and repair of the refractory linings, combined with the cost of down—time of the facility justify a more thorough research aimed at producing better linings.

The conducted research concentrates on a specific application, which is slagging coal gasifiers with brick linings. The gasification process is aimed at converting coal into a suitable and economic gaseous fuel. In slagging gasifiers the refractory layers are composed of dense bricks next to the hot—face and of insulating material next to the steel shell. The dense refractory layer, which is in direct contact with the process environment, is provided to resist high temperature, corrosion, and erosion. The insulating refractory layer, which has a relatively low coefficient of thermal expansion, reduces the shell temperature and increases the thermal efficiency of the system. The bricks are usually joined together using mortar material.

The analysis and design of refractory linings is complicated primarily due to the complexity in modeling the material behavior. Such an analysis should consider the refractory material behavior with respect to the effects of monotonic and cyclic mechanical loads, elevated temperatures and thermal cycling, environmental interaction such as slags and process gases, and history of thermomechanical loadings. Thermomechanical data on the behavior of the refractory materials in the process environment is unavailable or incomplete.

There is a need for fundamental research to:

o   achieve a basic understanding of the refractory material behavior in the process environment;

o   assess the role of different manufacturing processes on the thermomechanical properties of the materials;

o   relate phenomenologically the behavioral trends at the macroscopic

level to the microstructural characteristics of the material; and

o   assemble a database of thermomechanical and thermophysical properties of different refractory materials to be used by designers and manufacturers of these vessels.

The research conducted in the present project at MIT, and reported here is directed towards satisfying these needs.

1.2   SUMMARY OF PREVIOUS MIT WORK

Over the past several years, comprehensive analytical and experimental studies have been undertaken at the Massachusetts Institute of Technology (MIT) dealing with the behavior of monolithic refractory concrete and refractory brick linings. Numerous publications have resulted from these research efforts (Buyukozturk, 1977, 1981, 1982; Buyukozturk and Connor, 1979; Pike et al., 1980; Buyukozturk and Tseng, 1982, 1983; Tseng and Buyukozturk, 1982, 1983; Bremser and Buyukozturk, 1982; Buyukozturk and Shareef, 1983, 1984; Chen and Buyukozturk, 1985a, 1985b, 1985c; Zisman, 1979; Chehayeb, 1985; Hens, 1986; Hens et al., 1986a, 1986b; Ameur–Moussa, 1987; Tseng, 82; Chen, 84).

For the monolithic refractory concrete linings, constitutive models were developed for both dense and insulating refractory concretes applicable to coal gasification vessel linings. For the development, experiments were performed on refractory concrete plate specimens subjected to biaxial compression at various temperatures. Based on the test results, a general hypoelastic model was developed for refractory concretes. A temperature dependent creep model based on the concept of thermorheologically simple material was also developed. For accurate predictions of temperature distribution through the vessel walls a transient heat transfer analysis

capability was developed with the adoption of a finite difference solution. The developed material models and the heat transfer analysis capability were implemented in a finite element program for three dimensional non linear analysis of refractory linings or heat–up and cool–down cycles. This analysis package was used to define optimum design parameters of these complex systems.

The research on brick linings focused on the behaviorial understanding and the determination of the optimal design and operational parameters applicable to high temperature slagging gasifiers. Data was collected from the literature on the thermomechanical and thermophysical properties of high alumina and high–chromia refractories. Temperature dependent material models were developed to represent the material behavior. Emphasis was on the development of a time–independent constitutive model to predict the material response to multiaxial, non–proportional and cyclic loads. The temperature effect is introduced by scaling the stress–strain curves at different levels, with respect to the peak stress and the associated axial peak strain. A power law creep model, a conductivity model for cracked media, and polynomial representations of the thermophysical properties were also proposed. The different models were incorporated in a finite element program. A predictive corrosion model was proposed to study the long–term corrosion process of lining systems. Based on this model, sensitivity studies were performed to identify the important factors characterizing the long term behavior of the linings. Using the finite element program, the thermomechanical behavior of linings with various material combinations, lining geometries, and heating schemes was studied. Based on the findings from the thermomechanical and corrosion analyses, tentative recommendations were made for the design and operation of lining systems.

1.3 INTERACTION WITH OTHER DOE PROJECTS

The research conducted at MIT was sponsored by the Advanced Research and Technology Development (AR&TD) office of the U.S. Department of Energy (DOE). "The objective of the AR&TD Fossil Energy Materials Program is to conduct research and development on materials for fossil energy applications with a focus on the longer—term and generic needs of the various fossil fuel technologies". The program aims "toward a better understanding of materials behavior in fossil energy environments and the development of new materials capable of substantial enhancement of plant operations and reliability" (Judkins and Carlson, 1987).

In this context the current research at the Massachusetts Institute of Technology (by O. Buyukozturk and F.G. Tamer) focused on the characterization of refractory materials for linings of slagging gasifiers. This combined very appropriately with other related DOE programs which studied similar materials for various applications. The other programs concurrently conducted with the MIT program were:

o   High temperature creep behavior of refractory bricks at Iowa State University: (by Thomas D. McGee);

o   Effect of slag penetration on the mechanical properties of refractories at the National Bureau of Standards: (by S.M. Wiederhorn and R.F. Krause, Jr.);

o   Thermodynamic Properties and Phase Relations for Refractory—Slag Reactions in Slagging Coal Gasifiers at the Pennsylvania State University: (by A. Muan); and

o   Alkali attack of coal gasifier refractory linings at Virginia Polytechnic Institute and State University: (by J.J. Brown).

This led to interaction of the MIT researchers with the other researchers, and integration of the work within the materials program. As a specific example of this integration, the MIT program combined some of its high temperature creep data with results obtained at ISU to develop deformation maps, and compared some of its results on slag–impregnated materials with NBS data.

1.4 RESEARCH OBJECTIVES

The general objectives of the work performed at MIT are to:

1. characterize the compressive behavior of refractory ceramics at high temperatures in coal gasifier environments;

2. relate the macroscopic deformation and fracture behavior to the microstructural properties; and

3. develop a comprehensive material database, to be used in studying the thermomechanical behavior of brick–mortar lining systems.

1.5 RESEARCH APPROACH

The approach used to conduct this research may be summarized in the following steps:

1. Review existing material properties and relevant material models. Review standard testing methods and specimen preparation procedures. Establish materials to be tested and thermomechanical testing program.

2. a. Design and develop a high temperature testing facility under controlled gas environment. Establish specific procedures to be followed in high–temperature testing.

      b.   Establish standard specimen preparation procedures, characterize brick properties, and study material variability.

3.   a.   Perform short–term uniaxial monotonic compression tests at constant room and elevated temperatures in air, on as–manufactured and slag–impregnated cold–pressed sintered high–alumina and high–chromia refractories, and as–manufactured hot–pressed and fused–cast high–alumina and high–chromia refractories. Study the strain rate effects on the material behavior under these loading conditions.

      b.   Perform short–term uniaxial monotonic compression tests at constant room and elevated temperatures in controlled reducing gas atmospheres, on as–manufactured and slag–impregnated cold–pressed sintered high–alumina and high–chromia refractories.

      c.   Perform short–term uniaxial cyclic compression tests at constant room and elevated temperatures in air, on as–manufactured cold–pressed sintered high–alumina and high–chromia refractories.

      d.   Perform short–term uniaxial creep compression tests at constant room and elevated temperatures in air, on as–manufactured cold–pressed sintered, hot–pressed, and fused–cast high–alumina and high–chromia refractories.

      e.   Perform short–term uniaxial constant compression tests at increasing temperatures at different heating rates in air, on as–manufactured cold–pressed sintered high–alumina

refractories.

    f.   Summarize the deformation and fracture behavior of the studied refractory ceramics under the specific loading and environmental conditions listed in 3a. to 3e.

4.   a.   Observe microstructural characteristics of virgin and tested materials (such as the size, distribution, orientation, type, and interaction of cavities, and phase distributions) using stereoscopic and Nomarski optical microscopes and a scanning electron microscope.

    b.   Study the chemical composition of slag–impregnated cold–pressed sintered high–alumina and compare it to the as–manufactured material, and study the chemical composition of as–manufactured fused–cast high chromia refractory using X–ray diffraction.

    c.   Characterize the open porosity of virgin and tested materials by mercury porosimeter tests.

    d.   Measure the dry bulk density of refractory specimens before and after testing.

    e.   Summarize the microscopic descriptions of the studied refractory ceramics from tasks 4a. to 4d., and relate these observations to the macroscopic properties.

5.   Collect the thermomechanical data from the above–mentioned tests. Collect modulus of rupture data at room and elevated temperatures, and thermophysical data from the literature. Assemble the acquired data in a material database as graphs, tables, or functions, in a form to

be used by designers and manufacturers of high temperature vessels.

6.   Discuss the obtained results for the different loading and environmental conditions studied. Compare the behavior of refractory ceramics manufactured by different processing techniques. Relate the macroscopic properties to the observed microscopic characteristics.

1.6   DOCUMENT ORGANIZATION

A literature review of previous work on linings and materials is given in Chapter 2 with emphasis on coal gasification vessels. The system behavior of high temperature containment vessels is reviewed first. The behavior of brittle materials in compression and at high temperatures is reviewed next, as well as the interaction of slags and reducing atmospheres with refractory materials. Finally, testing and related considerations are discussed.

Chapter 3 describes the equipment built for high temperature testing under controlled gas environments, the equipment used for microstructural observations, and the testing procedures. Chapter 4 presents the materials tested, and the scope of the testing program.

The results from the thermomechanical tests and microstructural characterization and the discussion of behavioral trends are presented in Chapters 5, 6, and 7 for cold–pressed sintered, hot–pressed, and fused–cast refractories, respectively. The tests carried out for specimen preparation, block characterization, and the variability study are also described. Results of compression tests at elevated temperatures include monotonic, cyclic, and creep short–term uniaxial compression tests, at constant or increasing temperatures, in air or reducing atmospheres.

In the case of cold–pressed sintered materials, the effects of slag–impregnation and varying strain rates in monotonic tests are examined as well. In the case of hot–pressed materials, different chemical compositions are studied for the alumina–chromia refractories. The microstructural observations of virgin and tested materials under different loading and environmental conditions are reported at the end of each chapter.

For Chapters 2 through 7, except Chapter 4, an indicative synopsis and an informative summary are included for clarity. Chapter 4 only contains a synopsis. The synopsis is a shorter qualitative description of what is presented in the chapter. The summary is more quantitative, and presents major conclusions from the chapter.

Chapter 8 includes a description of the assembled material database.

Chapter 9 presents the summary, conclusions, and contributions from the present research, as well as suggestions for future work.

The references, list of figures and list of tables are included after Chapter 9.

The material database is presented in Appendices A and B. Details about the microstructure observations are summarized in Appendix C. Additional information on the design of the retort system is presented in Appendix D. Finally, selected results from the variability study are included in Appendix E.

CHAPTER 2
REVIEW OF PREVIOUS WORK ON
LININGS AND MATERIALS

2.1   SYNOPSIS

This chapter is a review of previous work on linings and materials, with an emphasis on the material behavior. The system behavior is reviewed first in Section 2.2, with a focus on slagging coal gasifiers. The system configuration (Section 2.2.1) and causes of lining failures (Section 2.2.4) are similar to other high temperature vessels. However, the operating conditions (Section 2.2.2) and candidate materials (Section 2.2.3) are dependent on the different application. The refractory materials used in high temperature vessels are brittle materials. It is relevant to our work to review the previous work on the behavior of other brittle materials under conditions similar to the ones in our testing program. It appears that there are similarities in the behavior of ceramics, rocks, and concretes in compressive loading at high temperatures. The behavior of brittle materials in compression and at elevated temperatures is reviewed in Sections 2.3.1 and 2.3.2 respectively. Our test program also examines the effect of slag–impregnation and reducing atmospheres on the thermomechanical behavior of refractory materials. Previous work in this area (Section 2.4) concentrated on the chemical interaction between the environment and the materials), and not as much on the effect of the environment on the thermomechanical properties. The test procedures and interpretation of results are important for the assessment of the mechanical properties of brittle materials, and

are reviewed in Section 2.5. Finally, the relation of present research to previous work is presented in Section 2.6.

2.2 SYSTEM BEHAVIOR OF HIGH TEMPERATURE CONTAINMENT VESSELS

2.2.1   System Configuration

Gasification vessels, in which coal is converted to combustible gas, are usually cylindrical in shape, from 100 to 250 feet in height, and 15 to 60 feet in diameter. The vessels are usually composed of an outside steel shell and refractory linings. The main purposes of the refractory linings are to maintain and improve the thermal efficiency of the system, and to protect the steel shell from high temperatures, and severe environments. The linings are either made of monolithic refractory castables (Fig. 2.1), or from refractory bricks jointed together using a mortar material (Fig. 2.2). The refractory linings are usually composed of a dense layer next to the hot face and of insulating material next to the steel shell. The dense refractory layer, which is in direct contact with the ' process environment, is provided to resist high temperature, corrosion, erosion and abrasion. The dense refractory layer usually has high thermal conductivity and better thermomechanical properties and thermal shock resistance. The insulating refractory layer, which has a relatively low coefficient of thermal expansion and a low heat capacity, reduces the shell temperature and increases the thermal efficiency of the system. In the case of monolithic linings, steel anchors extending from the steel shell into the refractory linings are usually used to enhance the integrity of the system. In the case of brick linings, the bricks are joined together using mortar material. The bricks are in the form of trapezoidal blocks with either a straight edge (Fig. 2.3a), or a circular edge (Fig. 2.3b). They may sometimes
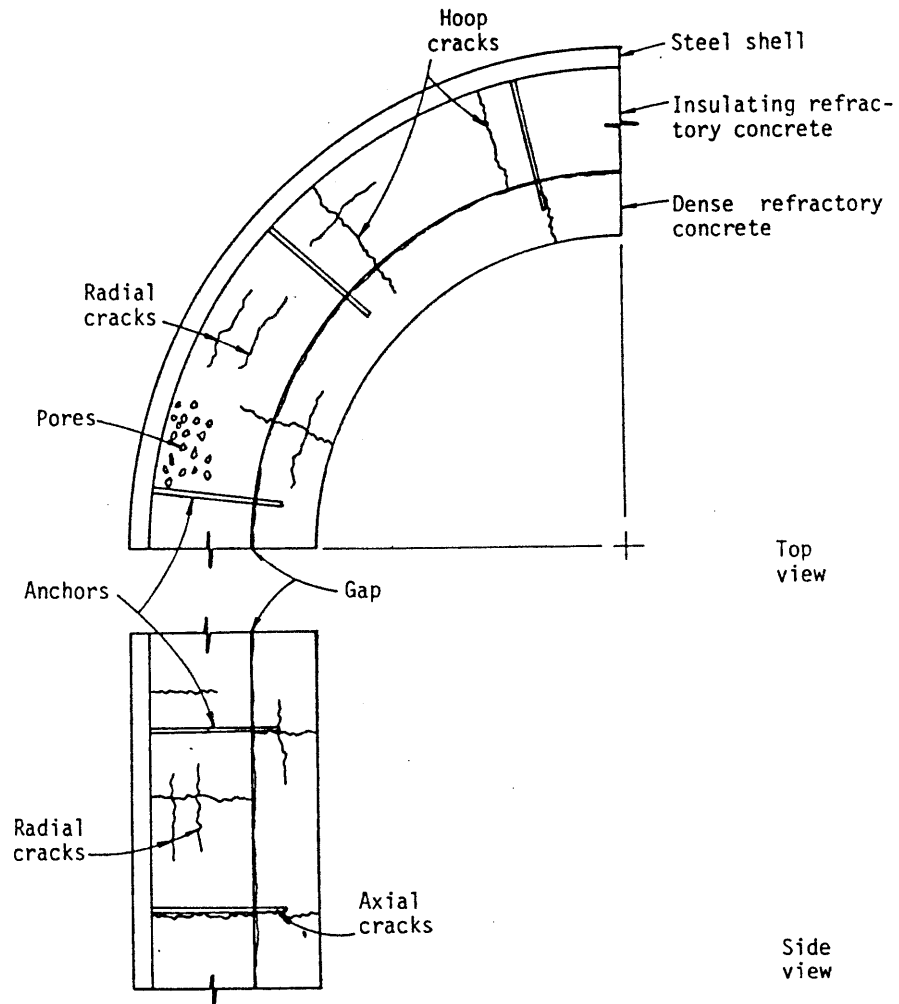
Figure 2.1   High temperature monolithic linings (Tseng, 1982)
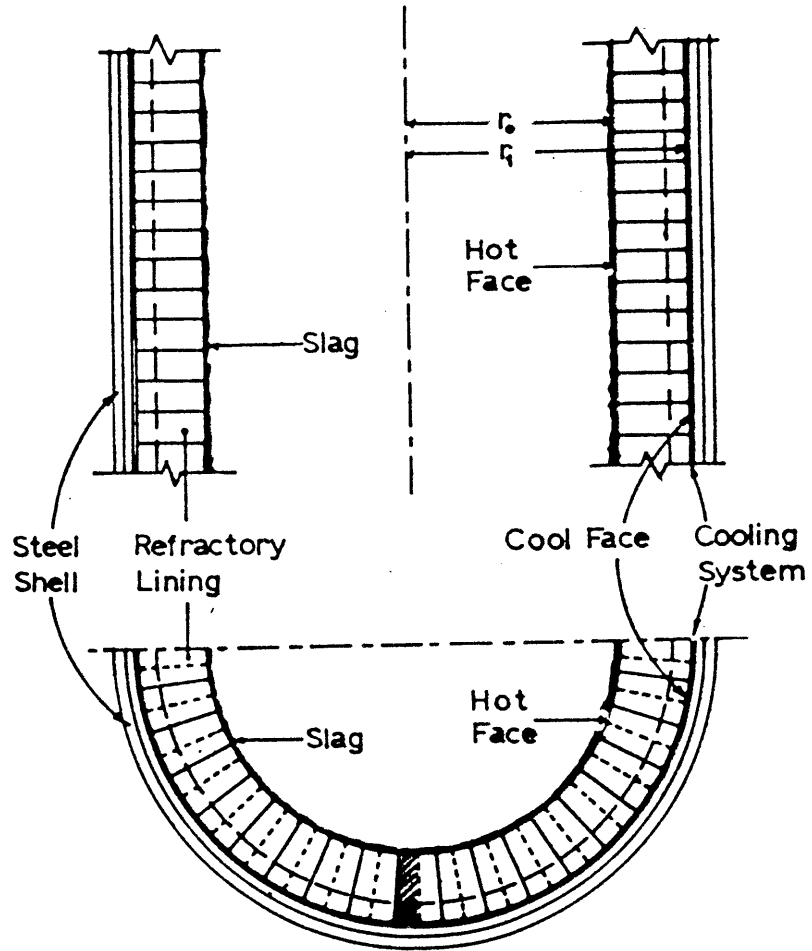
Figure 2.2   High temperature brick linings (Chen, 1984)
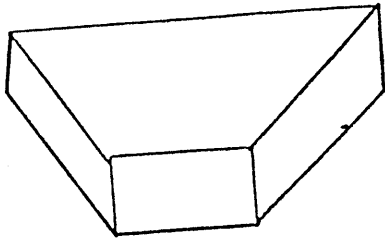
(a) straight edge brick
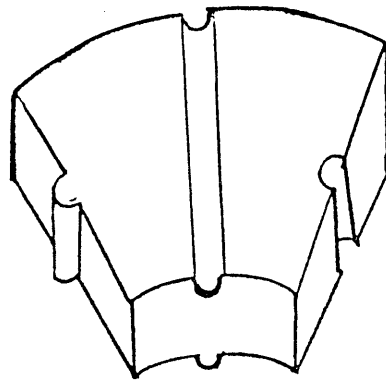
(b) circular edge brick
with grooves and keys

Figure 2.3   Typical refractory bricks

be keyed together for mechanically interlocking them anticipating an improvement in the system integrity (Fig. 2.3b). Cooling systems are frequently used to keep the shell temperature at certain predetermined levels. A compressible material layer can be used between the steel shell and the refractory linings to relieve some of the stresses caused by the linings expansion at elevated temperatures.

2.2.2   Operating Conditions

In slagging coal gasifiers the operating conditions are extreme (Cooper and Ellingson, 1984; Bakker and Stringer, 1981; Crowley, 1975). Generally, the range of operating temperatures in slagging gasifiers is $2400^{\circ}F - 3300^{\circ}F$ ($1315^{\circ}C - 1816^{\circ}C$). Ash is generally present as molten slag that runs down the walls of the gasifiers, and is corrosive to the linings. Gas pressures in the gasifiers usually range from atmospheric to 1000 psi (6.9 MPa). Gases present consist of H_2O (steam), H_2, CO, CO_2 and small amounts of CH_2, N_2, NH_3 and H_2S. These gases are usually reducing in nature, and a typical value of the partial oxygen pressure during operation is 10^{-8}atm. (10^{-3}Pa).

In representing the gasifier environment in the laboratory, two essential parameters are: the partial oxygen pressure (P_{O_2}) and the slag.

The gas environment is important because it can directly affect the material thermomechanical and thermophysical properties, and also affect the interaction between the molten products in the process environment and the refractory materials. Different researchers use different gas mixtures to simulate coal gasification atmospheres. Different methods are used by Robins and Mauer (1981), Washburn (1982), Muan (1983 and 1987), McGee (1984), Bakker et. al. (1984), Easler (1985), Greenberg and Peoppel (1985), and Wiederhorn and Krause (1986). Some of these

are summarized in Table 2.1.

Coal–Ash slags are complex multicomponent silicates that are mainly composed of SiO_2, CaO, Al_2O_3, FeO and Fe_2O_3. Two quantities are usually used to characterize the slag: their base–to–acid ratio and their ferritic content (Kennedy, 1980; Washburn, 1982). The P_{O_2} of the atmosphere can be back calculated from the ferritic content of the slag (Washburn, 1982).

2.2.3   Candidate Materials

The candidate materials for high temperature applications are refractories. Refractoriness is usually defined as the capability of maintaining a desired degree of chemical and physical identity at high temperatures and in the environment and conditions of use (Budnikov, 1964). The main types of refractory materials are: refractory castables, plastic refractories, ceramic refractories, refractory fibers, and refractory metals (Crowley, 1984). The uses of refractory materials are numerous (ACI, 1982; AFML, 1963; Duffy, 1980; Norton, 1968; Shaw, 1972; Wygant and Crowley, 1964).

In general two types of refractory materials have been used in slagging gasifiers: high–alumina and high–chromia refractories (Bakker and Stringer, 1981; Sweeney and Cross, 1982; McGee, 1984). The high–alumina refractories are known for their good resistance to thermal shock (Bandyopahyay et al., 1983), while high–chromia refractories are known for their good corrosion resistance (Bakker et al., 1984; Bonar et al., 1980; Kennedy, 1980; Washburn, 1982).

2.2.4   Causes of Linings Failure

Different modes of failure of the brick–mortar lining systems have been

Researcher	Gas Mixture Used	Aim	Achieved P_{O_2}
Muan, 87	CO_2, H_2	Maintain P_{O_2} typical of slagging coal gasifiers	10^{-8} atm. @ $1400^{\circ}C$
McGee, 84	CO, CO_2	Control P_{O_2}	10^{-6} - 10^{-18} atm.
Easler, 85	Medium-Btu Coal Gas 30%H_2, 44%CO, 10%CO_2, 1.4%N_2 0.6%H_2S, 14%H_2O	Control P_{O_2}	P_{O_2} < 10^{-12} atm.
Greenberg et.al., 1985		Represent slagging coal gasifier environment	10^{-8} - 10^{-9} atm.
Robins and Mauer 1981	20%CO, 15%CO_2 25%H_2, 40%H_2O	Coal gasification environment	
Washburn, 1982	NH_3, N_2	Control P_{O_2}	10^{-6} - 10^{-9} atm.
Wiederhorn and Krause, 1986	N_2	Suppress Distillation of Cr_2O_3	10^{-4} atm.

Table 2.1   Gas atmospheres used by different researchers to simulate coal gasifier environments

observed and studied. Failure can occur by degradation of the mechanical properties of refractories at elevated temperatures, through cracking, crushing, and spalling of the refractory materials under thermomechanical loadings, by creep rupture, by joint failure of the brick–mortar system, by disintegration of the refractories under gas attack, and by corrosion or erosion due to slag attack.

2.3 REVIEW OF BRITTLE MATERIALS BEHAVIOR

2.3.1 Behavior of Brittle Materials in Compression

The fracture of brittle solids in tension appears to be well understood. On the other hand the fracture of brittle solids in compression has been less studied, but is as important (NMAB, 1983). The fracture of brittle solids in compression is a tensile phenomenon at the atomic scale. Fracture originates from pre–existing cavities or from the nucleation of cavities next to stress concentrations at grain boundaries, aggregate interfaces, and triple junctions. Under triaxial compressive applied loads unequal compressive forces are produced and result in shear stresses along the pre–existing or nucleated cavities. These cavities are usually differentiated in two different classes: cracks and pores. The criteria that is sometimes used to differentiate between cracks and pores is the aspect ratio of the cavity. The interactions between different cracks, and between cracks and pores have been studied previously.

Griffith (1924) was the first one to study the fracture of brittle solids in compression. He postulated that the strength of solids is smaller than the theoretical strength due to small cracks formed during manufacturing or treatment. The Griffith criterion indicated a compressive strength equal to eight times the tensile strength independently of triaxiality effects. Orowan (1949) re–interpreted the work of

Griffith, and showed that the cracks can produce a stress concentration that reaches the theoretical material strength, for an applied stress that is much lower. Later on, McClintock and Walsh (1962) modified the Griffith criterion, by taking into consideration that cracks may close under a certain combination of triaxial stresses, thus allowing normal and frictional stresses to be carried across the surfaces of the crack. For the crack to close the applied stress has to be larger than a critical value σ_c. Closed cracks can carry an effective normal stress on the surface equal to the value of the applied stress less the critical stress σ_c, and can also carry shear stresses. The frictional shear stress for the crack to grow is equal to a friction coefficient times the effective normal stress. This theory gives the compressive strength under confining pressure with respect to the uniaxial compressive strength. Nemat Nasser and Horii (1982) studied the problem further by studying analytically the problem of kinked extension of an initially closed crack under far–field compression, which may undergo frictional slip. According to the study the kinks first grow gradually under increasing axial compression in a stable growth manner, but after the kinks reach a certain length the rate of growth increases dramatically, and the kinks grow in an unstable manner at the final stages of loading.

According to a recent NMAB report (1983) these theories are based on overall fracture developing mainly by splitting due a single crack, which has dimensions comparable to the size of the specimen. This mode of failure in compression involves the extension of a single crack in a direction parallel to the maximum principal stress direction (Figure 2.4), and is termed extrinsic (NMAB, 1983). However, when the existing microcracks are small compared to the size of the specimen, they may link up and form a local region of increased shear compliance. This region develops further under increasing compression to produce a shear fault instability that will lead to
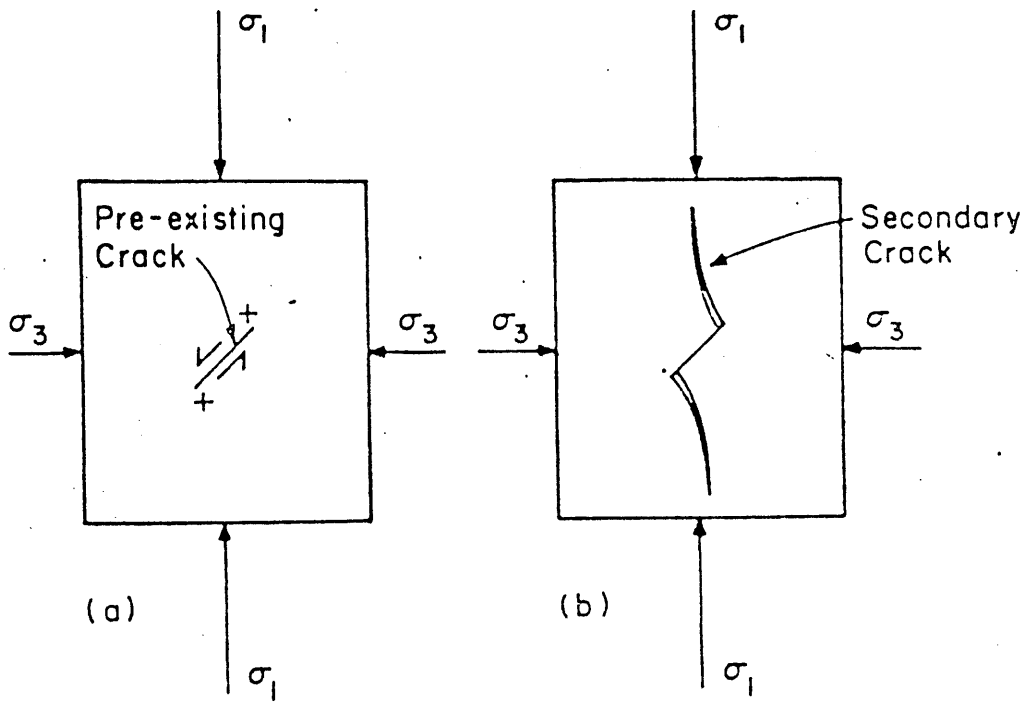
Figure 2.4   Extrinsic fracture behavior (NMAB, 1983)

failure in a direction inclined to the principal stress direction (Figure 2.5). This second mode of failure is termed intrinsic (NMAB, 1983). The intrinsic mode is usually observed in tougher materials. The extrinsic mode of fracture is a mode I. In the intrinsic mode of fracture, however, experimental evidence suggests that fracture might be obeying a mode II in—plane shear behavior (NMAB, 1983). Both of these modes of failure have been observed in brittle materials.

The behavior of rocks and concrete in compressive loading at room temperature is used as an illustration. There seem to be indication that for rocks subjected to compressive deviatoric stresses, fracture is not the result of a single "Griffith Crack" (Kranz, 1979). Rocks in their natural state have already existing crack—like cavities. Criteria have been suggested to differentiate between the cracks caused by applied stresses and the existing cavities (Spunt and Brace, 1974; Tapponnier and Brace, 1976). These studies show that stress induced cracks are easily differentiated from natural ones mainly by their shape. At loads below 75% of the peak stress, the nature of cracking is mostly intergranular and healed transgranular. At loads above 75% of the peak stress, a majority of transgranular cracks is observed. Close to the peak stress, linking of the cracks starts to be a major mechanism. There is evidence that pores did nucleate and grow during loading. Fractures form from the intersection or coalescence of microcavities. One main difference between tension and compression behavior, is that in tension the tensile stress concentration increases with crack length, while in compression the crack extension force is maximum during initial propagation and reduces after that, so that the crack in compression reaches a stable position. Thus, previous researchers have concluded that a macroscopic fault under compression cannot be the result of a single crack, but the coalescence of crack branches, given boundaries, and pores. The
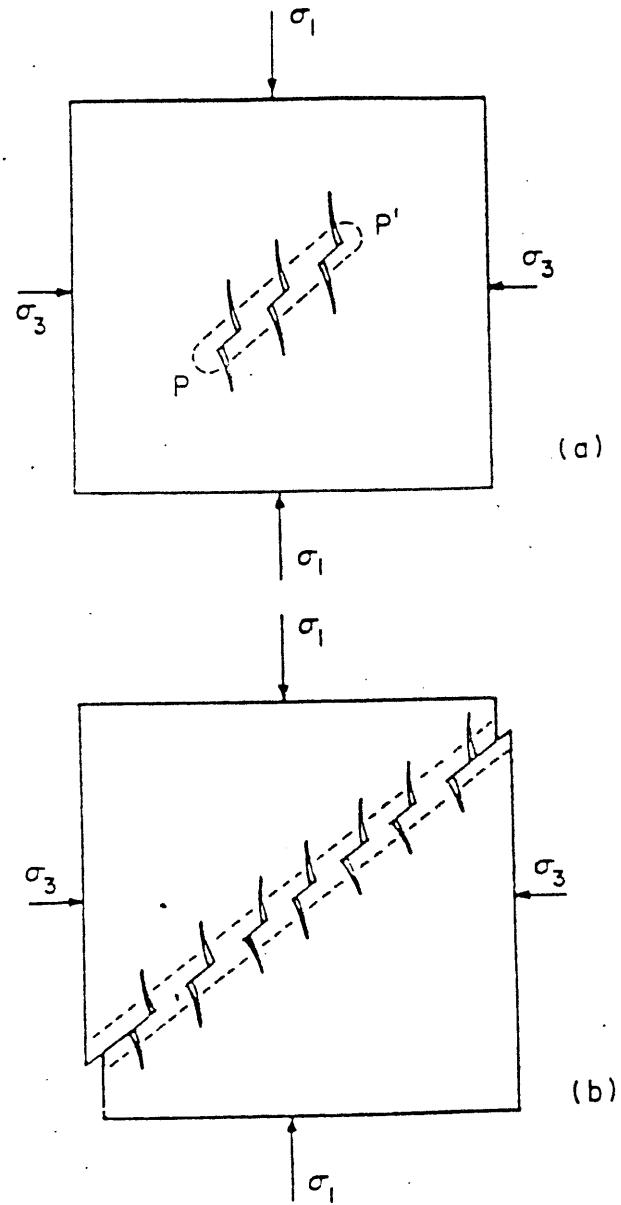
Figure 2.5   Intrinsic fracture behavior (NMAB, 1983)

interaction between these cracks have been studied extensively (Brace & Bombolakis, 63; Hoek & Bieniawski, 65; Lange, 68; Swain & Hagan, 78; Kranz, 79; Fonseka et. al., 1985). "En echelon" cracks (Figure 2.6) were found to link either parallel to the applied stress, or in a shear linkage. "En passant" interaction (Figure 2.7) occurs when cracks approach each other on different planes, and at first shear stresses deflect the crack paths away (K_{II}/K_I is positive), and then toward each other (K_{II}/K_I is negative). The linkage occurs when the tip of one crack runs in the side of the other. The interaction of pore and a crack is more complex. Cracks can be deflected from their preferred path by the region of a high stress concentration next to a void. The hole concentrates Mode I stresses, and if large Mode II stresses are present, K_{II}/K_I can be large enough to deflect the crack into the hole. Kranz (1979) observed cracks running into pores at orientations varying from $10^\circ - 20^\circ$ of the principal stress directions up to 90° of the principal stress direction. A microcrack model of rock inelasticity was developed by Kachanov (1982a, 1982b) that helps explain the basic features of the macroscopic behavior. The model assumes that frictional sliding on microcracks is the major mode of inelasticity at moderate compressive stresses. This represents the first stage of inelasticity. At higher stresses, kinking and propagation of microcracks is considered to be a major mechanism. A comprehensive testing program followed by microstructural analysis was conducted by Wong (1982a) for Westerly Granite, in compression under different conditions of pressure and temperature. Samples retrieved prior to failure showed a lot of transgranular cracks at low angles ($<15^\circ$) to the maximum compression direction, as well as many high angle ($>15^\circ$) transgranular cracks. In the post–failure samples, most cracks were inclined at 15° to 45° to the maximum compression direction. Outside this localized region of deformation, bands of axial cracks were observed. The inclined cracks join

Applied
Load ↓

Stage 1　　　Stage 2　　　Stage 3

Applied ↑
Load
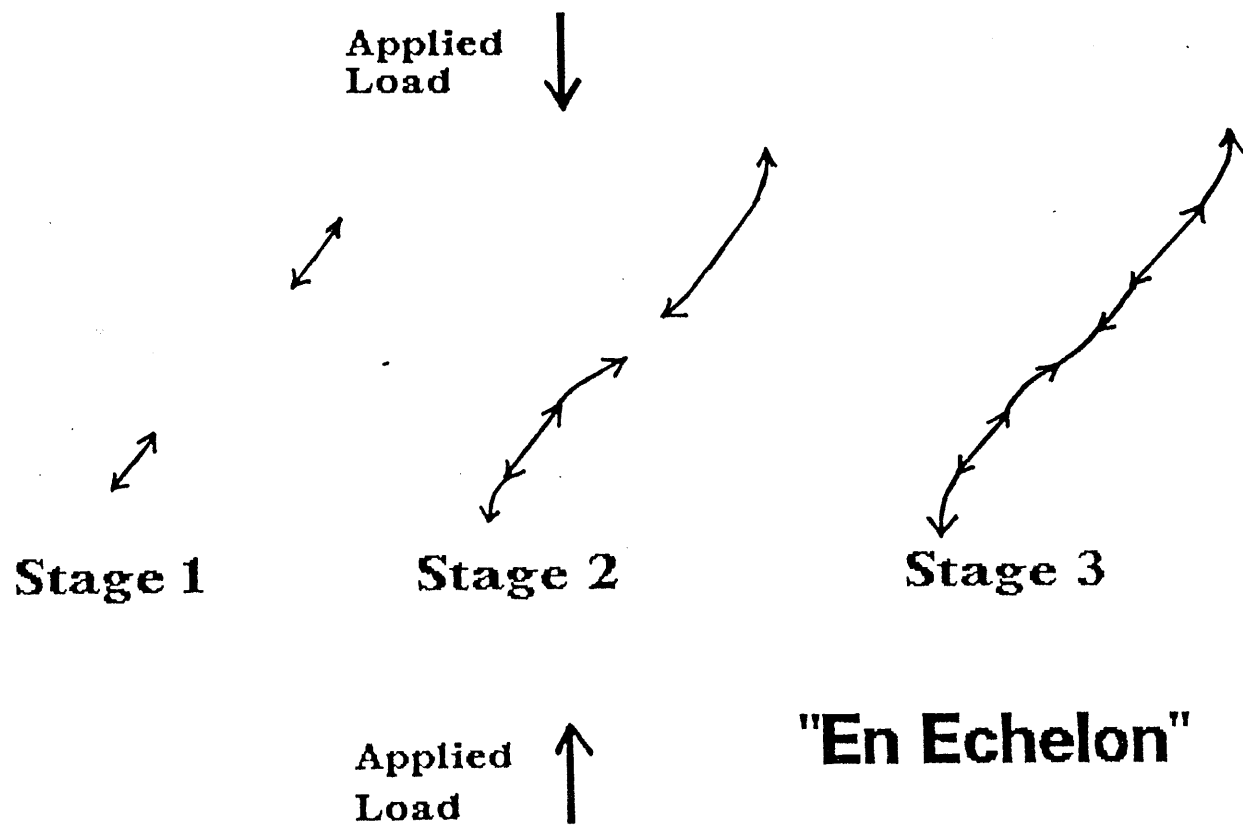
"En Echelon"

Figure 2.6　　　　"En Echelon" crack interaction
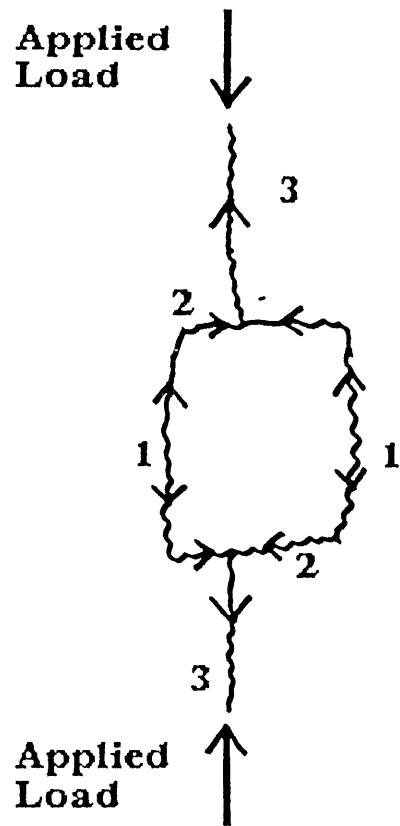
"En Passant"

Figure 2.7   "En Passant" crack interaction

up to form a shear zone, and eventually overcome the resistance formed by other crack arrays to form a shear fault. Some microcracks were also observed perpendicular to the applied principal stress direction. The explanation was that unloading can result in tension cracks that are oriented as such (Boland and Hobbs, 73; Wong, 82a). Samples deformed at higher pressure or temperatures showed a higher crack density.

Similar studies have been conducted on concrete. Concrete contains bond cracks before it is loaded (Krishnaswamy, 1971). During initial loading in compression some pre—existing microcracks might close, and no propagation of microcracks is observed until about 30% of the peak strength. With increasing loads up to 70% of the peak strength the density of the bond cracks increases. As the load reaches about 90% of the ultimate load, bond cracks are joined by mortar cracks, preferentially on large aggregates instead of small aggregates (Shah and Slate, 1965). At peak stress crack networks are present, and in the post peak region spalling of the concrete occurs. The bond cracks occurring at the aggregate—mortar interface may be caused by tensile or shear stress or a combination of both. The mechanism of cracking may include sliding and/or separation at these interfaces (Buyukozturk et al., 1972). Local tensile failure seems to be the dominant mode of fracture of concrete in compression (Raju, 1970). At lower load levels, the cracks are parallel to the applied load but near the ultimate load these vertical cracks connect in what appears to be a shear failure (Robinson, 1965). The mechanism of crack extension in a brittle solid is tensile splitting at the atomic level (Shrive and El—Rahman, 1985; Soon, 87). However with the load approaching the ultimate, shear cracks are observed as well (Soon, 87).

Concrete has also been tested extensively in cyclic compression. (Award and Hilsdorf, 1972; Tepfers, 1982; Raithby, 1979; Hsu, 1981; Sparks, 1982; Holmen, 1982; Bresler, 1976; Soon, 1987). It is interesting to briefly review existing behavioral trends, since our tests involve cyclic loading. The uniaxial monotonic stress—strain curve is an envelope curve to the cyclic stress—strain response. The intersection between the unloading branch with the next loading branch is called a common point. If the maximum cyclic stress is above the common point envelope, non—recoverable strain is produced and failure will occur after only a limited number of cycles. On the other hand, if the maximum cycle stress is below the common point envelope, failure will occur after a large number of cycles. At certain stress levels hysterisis loops are obtained. The intersection point of the stabilized hysterisis loop are called stability points. If the maximum cyclic stress is below the stability points envelope, identical hysterisis loops are produced, and failure of concrete under cyclic stresses is unlikely. The common and stability points envelope were found to be at about 80% and 75% of the monotonic strength of concrete respectively (Lam, 1980), and independent of the minimum load levels. Microcracking of concrete in cyclic compression appears to be more progressive (Raju, 1970; Shah and Chandra, 1970; Stroeven, 1979). The density of bond cracks is 15% more than the one observed for monotonic compression tests. The mortar cracks were more prominent than bond cracks. The low cycle (high stress) fatigue life of concrete in compression was observed to be very sensitive to the maximum cyclic stress, but the minimum cyclic stress did not appear to have a great influence (Soon, 87). The low cycle fatigue life was divided into three major zones: the first one was composed of initial cycles with large deformations, the intermediate range was characterized by uniform hysterisis loops, and just before failure, the deformations picked up again (Soon, 87).

A large variety of constitutive models have been proposed for concrete. They can be classified as: elasticity–based, plasticity–based, endochronic, plastic–fracturing, strain space models, damage–type, and bounding surface models. The first type of models developed and later on improved is based on failure surfaces. A failure surface is defined as the focus in the principal stress space of all peak stresses. These models include: Bresler and Pister (1958), Ottosen (1977), William and Warnke (1974), and Lade (1982). The elasticity models include the hyperelastic models (Chen, 1982; ASCE report, 1982) which express the stresses as a function of a strain energy function, and the hypoelastic models (Chen, 1982; Buyukozturk and Shareef, 1984; Elwi and Murray, 1979) that express the incremental stresses as a linear function of the incremental strains. The elastoplastic strain–hardening models (Chen, 1982; Buyukozturk and Shareef, 1984; Buyukozturk, 1977; Chen and Chen, 1975; Han and Chen, 1985) postulate the existence of a loading surface in stress space which expands from the yield surface to the failure surface as a function of plastic deformation. The plastic strain increments are obtained by an associated flow rule. Most of these previously mentioned models are for proportional loading, and their accuracy decreases with deviation from proportional loading. Bazant and Tsubaki (1980) have proposed a model that take into consideration path dependency. Endochromic models (Bazant and Bhat, 1976,; Bazant and Shieh, 1980) obtain inelastic strains from the variation of an intrinsic time which increases whenever deformation takes place. The concept of fracturing loading surface has been used (Bazant and Kim, 1979) to extend the elastoplastic models to the strain softening range. The concept of bounding surfaces has been used more extensively recently (Fardis et al., 1983; Yang et al., 1985; Chen and Buyukozturk, 1985a; Ameur Moussa, 1987; Dafalias, 1986). In these models a mapping rule associates an image stress

point on the bounding surface with any stress point within the surface. Although this type of model is widely used, disagreement between different researchers still exist on the type of damage parameters to be used.

2.3.2 Behavior of Brittle Materials at Elevated Temperatures

The behavior of ceramics, concretes, and rocks at elevated temperatures is briefly reviewed in this section with emphasis on compressive loading.

The behavior of ceramics at elevated temperatures has been categorized in three different regions (Evans and Langdon, 1976). In the first region, at relatively low temperatures, the behavior of the material is brittle and only a small decrease in strength is observed with temperature. The second behavioral region at intermediate temperatures exhibits a "deformation assisted brittle fracture" (Evans and Langdon, 1976), where the material strength decreases faster with temperature. At elevated temperatures in the third behavioral region a ductile behavior is observed. The different behavioral regions have also been observed for an alumina ceramic, where at $2300^{\circ}F$ the failure is by fracture and at $2318^{\circ}F$ an upper yield stress and a lower yield plateau are observed (Kingery et. al., 1976). The effect of slower strain rates has been compared to the effect of higher temperatures for alumina ceramics (Kingery et. al., 1976). The decrease in strength with temperature is usually monotonic. However some exceptions have been observed. Tests on alumina–silica (Miller and Davies, 1966) showed a small decrease in MOR from room temperature to about $1500^{\circ}F$. Then, from $1500^{\circ}F$ to about $2000^{\circ}F$ an increase in MOR with temperature was observed. A 90% dense alumina exhibit a MOR of about 2500 psi at $1500^{\circ}F$ compared to 3500 psi at $2000^{\circ}F$. This increase in strength has been observed by other researchers as well (Hunt and Bradley, 1941; Folk and Bohling, 1968). This

phenomenon does not occur in all ceramics systems, but is observed in systems containing more than one mineralogical phase. The increase in strength at intermediate temperature is more pronounced for systems containing both crystalline and glassy phases. This effect was less important in systems containing two different crystalline phases, but no glassy phases. At temperatures higher than $2000^{\circ}F$ a rapid drop in MOR with temperature is observed. A super–duty fireclay shows a drop from a MOR of about 2200 psi at $2000^{\circ}F$, to a MOR of 200 psi at $2500^{\circ}F$ (Miller and Davies, 1966). Similar results have also been observed for hot–pressed silicon nitride (Clarke, 1983) where the flexural strength shows no degradation up to temperatures of about $900^{\circ}C$ and then decreases monotonically at a rapid rate for higher temperatures.

The behavior of concrete at elevated temperatures was studied by different researchers (Thelandersson, 1974; Anderberg and Thelandersson, 1976; Khoury et. al., 1985). The compressive strength was observed to decrease slowly with temperature from $25^{\circ}C$ up to $400^{\circ}C$, and rapidly from $400^{\circ}C$ to $800^{\circ}C$ at which it is reduced to 25% of its original room temperature value. The static elastic modulus at $400^{\circ}C$ is about 50% and at $800^{\circ}C$ is about 15% of its room temperature value. It is shown by Anderberg and Thelandersson (1976) to compare well with the dynamic modulus obtained by Cruz (1966). The material behavior is initially linear elastic from room temperature up to $400^{\circ}C$. The constitutive model of the material is based on a representation of strain as the sum of four different strain components:

1. a thermal strain component including shrinkage, measured on unstressed specimens under variable temperature, and depending only on temperature;

2. an instantaneous stress–related strain, obtained by loading at constant

temperatures, and depending on stress, stress history, and temperature;

3. a time—dependent creep strain measured under constant stress at constant temperature, and depending on stress, stress history, temperature, and time; and

4. a transient strain measured from the constant stress increasing temperature tests, and depending on stress and temperature.

The high temperature behavior of refractory concrete is similar to the high temperature behavior of ceramics. A review by McCullough and Rigby (1972) reported two kinds of variation of strength with temperature for alumina refractory concretes: (1) a decrease in strength, levelling off over the range of 400–1000°C, followed by an increase in strength with temperatures above 1100°C, and (2) an increase in strength at temperatures around 200°C followed by a decrease in strength to a minimum value at about 1200°C, followed by a further increase in strength at temperatures above 1300°C. The increase in strength of refractory concrete at high temperatures is similar to the one observed for certain ceramics, as discussed at the beginning of this section. In the case of the refractory concrete the increase in strength was attributed to the formation of a ceramic bond which began to form at about 1125°C. However, the variation of static modulus with temperature reported by McCullough and Rigby (1972) was not similar to the one seen in ceramics. They observed an increase in the values of E until a flat maximum occurred at temperature of about 900 to 1100°C. The values of E started decreasing sharply at temperatures above 1200°C. Heindl and Post (1954) not only reported an increase in compressive strength in the temperature range 1100°C − 1200°C, but an increase in tensile strength as well. An increase in compressive strength for both dense and insulating

refractory concretes for temperatures in the range 1100°F $-$ 1500°F was also reported (Tseng and Buyukozturk, 1981).

As for the case of brittle solids in compression, the behavior of rocks under compressive loads at high temperatures is the best understood. Griggs et al. (1960) established that in the brittle regime the failure stress is relatively insensitive to temperature. This was confirmed by other studies (Handin and Hager, 1958; Raleigh and Paterson, 1963). Failure and post failure behavior of Westerly granite at pressures up to 400 mPa and temperatures up to 700°C, showed that for dry samples the effects of temperature and strain rate on the failure stress are not significant relative to that of pressure (Wong, 1982b). The independence of strength on strain rate in the brittle regime has also been reported by Brace and Martin (1968) who observed a strength increase of only 10% over three orders increase in strain rate. The failure stress is expected to increase with pressure, and its pressure dependence to decrease with temperature. But this does not always agree with the reported data (Griggs et al., 1960). For the same pressure the reduction in strength is about 20% from room temperature to 500°C for Westerly granite, but at temperatures above 500°C an accelerated downward trend is observed (Wong, 1982b). In post—failure samples clear cut faults were observed, and the localized zones grew wider at higher temperatures. Both temperature and pressure tend to stabilize the post—failure behavior. The transition temperature for stable failure in Westerly granite was observed to be at 660°C at 80 MPa, 450°C $-$ 550°C at 250 MPa, and $350 - 420^\circ$C at 400 MPa (Wong, 1982b), and at $25 - 300^\circ$C at 500 MPa (Griggs et al., 1960). The extent of thermal cracking at a given pressure was found to increase with increasing temperatures (Wong and Brace, 1979). But based on the data of Wong (1982b) thermal cracking is not responsible for the decrease in strength with temperature,

because the failure stress does not show a sharper decrease with temperature at lower pressures. The review of the post failure behavior of rocks at high temperature was reviewed extensively by Paterson (1978). The microstructure of Westerly granite at different loading combinations of temperature and pressure were also examined by Wong (1982b), and a large number of high—angle cleavage cracks, and shear cracks at 45° were observed. Cracks nucleation was also observed next to the pre—existing pores in the material. The proportion of high—angle cracks was observed to increase with an increase in pressure and temperature. The sequence of failure suggested by Wong (1982b) is by first extension of the high angle (15–45°) cracks to full length, and any further slip can occur by overcoming the frictional resistance in the pre—failure region. The axial cracks networks act as barrier to linking up of the coplanar shear cracks. The failure starts by collapse of these barriers, and transfer of the localized stresses to the next barrier. This is followed by linking between the barrier and the inclined shear crack. This results in a reduced frictional resistance along the incipient fault, until the residual stress level is reached along the entire fault spanning the sample. A ·thorough review of mechanical, physical and thermal properties of granite rocks has been done by Heuze (1983). His data shows decrease in modulus with temperature to about 10% of its room temperature value at 600^oC for Stripa and British granites, and a decrease to about 5% of its room temperature value at 1200^oC for Salisbury granite. Dry granite melts at about 1050^oC. The Brazilian tensile strength for Westerly and Charcoal granites was found to decrease from about 14 MPa at room temperature to about 10 MPa at 500^oC, but then decrease much faster to almost zero at 1000^oC. The qualitative decrease of compressive strength with temperature was similar to the tensile strength variation for dry Westerly granite. However, the compressive strength of charcoal granodiorite

follows a different trend. For long testing times and high temperatures, the steady—state creep component was found to overshadow the transient creep component. The steady state creep strain rate, $\dot{\epsilon}$,

was related to the deviatoric stress by:

$$\dot{\epsilon} = A\, \sigma^n \exp\left(-Q/RT\right) = \sigma\mu$$

where μ is an inverse viscosity which can be a function of stress and temperature (non—Newtonian flow), or only a function of temperature (Newtonian flow), A and R are gas constants, T is the absolute temperature, and Q is the creep activation energy. Tests on Indiana limestone showed no significant change in the compressive strength for temperature up to $300^{\circ}C$ (Karfakis, 1985). In the same range of temperatures, the Brazilian tensile strength decreases by about 25%.

The thermal shock properties of the materials used at high temperatures are very important as well. Some researchers examined the relationship between the thermal shock and the thermomechanical properties (Hasselman, 1963; Bandyopadhyay, 1983). Ceramic materials subjected to thermal shock generally fail in tension, and there is thus a relationship between the thermal shock resistance and the maximum tensile stress. In general the maximum radiation to which a body can be subjected to is proportional to (Hasselman, 63)

$$\frac{S_{ts}\ (1-\nu)^{1/4}}{\alpha\, E\, \epsilon}\ ,$$

where S_{ts} is the tensile strength, ν is the Poisson's ratio, k is the thermal conductivity, α is the coefficient of thermal expansion, E is the modulus of elasticity, and ϵ is the surface emissivity. Materials with strongly temperature dependent strength properties could fail in thermal shock in compression, because heating parts of the specimen will be softening more. Bandyopaadhyay et al. (1983) studied the thermal shock of refractories used in coal gasifiers. A thermal shock study was

conducted on eight different refractories, including six dense high—chromia refractories. Specimens heated up to $1000^\circ C$ ($1830^\circ F$) were quenched in 1 second to $100^\circ C$ ($212^\circ F$). For all the materials tested, $500^\circ C$ was the minimum temperature differential to initiate cracking. Some refractories exhibited sudden drops in their tensile strength properties, showing an unstable crack propagation behavior. The stability of crack propagation was closely related to microstructural characteristics such as porosity, grain size, second phases, or glassy phases present at the grain boundary. For the case of a single quench from $1000^\circ C$ to $100^\circ C$, Bandyopadhyay et al. (1983) found that the refractories with the highest initial strength showed the biggest loss in strength. The high—alumina refractories, with an alumina—chromia solid solution bond were the best for thermal shock resistance. The chromia spinels with high contents of magnesia (from 18.0% to 25.5%) and a direct bond, retained amounts of strength comparable to the high—alumina materials. However, the high—chromia materials, with larger percentages of alumina (from 6.0% to 20.0%) and smaller percentages of magnesia (from 0.1% to 8.1%) showed a tremendous drop in strength.

2.4   REVIEW OF THE ENVIRONMENTAL EFFECTS ON THE BEHAVIOR OF REFRACTORY MATERIALS

The environmental effects are very important in evaluating the behavior of the refractory materials at high temperatures. The main two environmental effects of interest in gasifiers are gas and slag attack. These will be reviewed in this section.

2.4.1 Effect of the Gas Environment on the Behavior of Refractory

Materials

In slagging gasifiers, the refractories interact with natural gas. The main components that were found to affect the refractory behavior are hydrogen (H_2) and carbon monoxide (CO). A hydrogen rich atmosphere was found to raise significantly the thermal conductivity of porous refractories. This effect was even more pronounced at high pressures (Wygant and Crowley, 1958). A significant number of studies were conducted to measure the CO disintegration, and the gaseous corrosion resistance of refractories for coal gasifiers (Brown, N.R., 83; Brown, J.J., 83). It was found that the effects of steam dominate the effects of CO (Brown, N.R., 83), and that in high–Btu gas atmospheres at $500^{\circ}C$, and 1000 psi, conditions exist such that CO decomposition may occur. Iron (Fe) was found to be an active catalyst for CO decomposition, and on the other hand the introduction of H_2S suppresses carbon formation in refractories. Similar conclusions were arrived at by J.J. Brown (1983). It was also found that lightweight castables are prone to CO disintegration. Fiber reinforcement was found to decrease CO resistance, and a primary restriction on the use of fiber reinforcement was that the fibers must not be oxidized. In order to use fiber reinforcements, low CO contents and the presence of H_2S is needed in gasifier atmospheres.

Refractory failure can also happen by akali attack. In coal gasification vessels the alkalies are present from the coal. Alkali corrosion may degrade the refractory material or cause premature failure (Gentile et. al., 1987). The alkali attack can result in incipient melting of the hot face due to alkali fluxing, and surface washout by dissolution of alkali compounds. For refractories made from the $Al_2O_3 - SiO_2 - CaO$ system, alkali attack is inevitable. In order to retard the alkali attack, one

suggestion was to maximize the maturity of the bonding phase to develop a strong ceramic bond. This can be achieved by pre–firing the refractory materials in an alkali–free atmosphere.

A representative measure of the gas environment is the partial oxygen pressure P_{O_2}, and is used by many authors in controlling their test atmospheres. It is mainly used when the effect or oxidizing of reducing gas environments on the system behavior needs to be assessed. The conditions used by different researchers were summarized briefly in Table 2.1. Muan (1987) uses gas mixtures of CO_2 and H_2 in controlled proportions (usually in ratio 10:1) to maintain oxygen pressures typical of slagging coal gasifiers, at 10^{-8} atm. at $1400^{o}C$. McGee (1984) uses gas mixtures consisting of controlled proportions of CO and CO_2, to achieve partial oxygen pressures ranging from 10^{-6} atm. to 10^{-18} atm. Easler (1985) uses a medium–Btu coal gas (30% H_2, 4% CO, 10% CO_2, 1.4% N_2, 0.6% H_2S and 14% H_2O) which results in partial oxygen pressures not exceeding 10^{-12} atm. In assessing the effect of corrosion by slags, the partial oxygen pressure is one of the main parameters of the study. Greenberg and Peoppel (1985), and Vorres et al. (1985) report using a partial oxygen pressure of about $10^{-8} - 10^{-9}$ atm. which is representative of slagging coal gasifier environment in their slag corrosion tests. Some other researchers conducted tests by circulating a gas representative of the process environment, and the partial oxygen pressure was not monitored. Robins and Mauer (1981) simulate coal gasification environment by circulating a gas at $850^{o}C$ and 7 mPa with the following composition: 20% CO, 15% H_2, and 40% H_2O (steam). It should be noted that the mixtures consisting of CO and CO_2 are toxic, and the mixtures consisting of H_2 are flammable. An approach that is preferable is to control the partial oxygen pressure by using mixtures of NH_3 and N_2. Washburn (1982) used mixtures of NH_3 and N_2

as its gas atmosphere, and measured the partial oxygen pressures from the ferritic content of the slag after the end of the experiments. His partial oxygen pressures were in the range of 10^{-6} atm. to 10^{-9} atm. The partial oxygen pressure changes with temperature and this should be taken into account (Muan, 83). Bakker et al. (1984) describe the reducing atmosphere of coal gasifiers as consisting mainly of CO and H_2 with minor amounts of CO_2 and H_2O. Ratios of $CO:CO_2$ are typically about 3 to 4, and ratios of $H_2:H_2O$ are typically 2 to 3. Minor quantities of H_2S, NH_3 and N_2 are also present. A different approach in controlling the test atmosphere was taken by Wiederhorn and Krause (1986). Instead of representing the cool gasifier atmosphere, they used a nitrogen atmosphere to suppress distillation of Cr_2O_3. This gives oxygen partial pressures of about 10^{-4} atm..

Recently, more interest was shown in potential applications of structural ceramic materials in coal gasifiers, such as in high–temperature heat exchangers. The influence of oxidizing and reducing environments on the corrosion behavior and mechanical properties of silicon carbide ceramics was examined (Easler, 85; Easler et al., 85). At low partial oxygen pressures, an active oxidation behavior is observed, where SiC reacts with oxygen to form SiO_2 and CO. At higher partial oxygen pressures, the SiC reacts with oxygen to form SiO_2 and CO in a passive oxidation behavior. For specimens not exposed to slags, an average weight increase of only 0.02 x 10^{-5} g/cm^{2}h is observed at 115°C and 0.04 x 10^{-5} g/cm^{2}h at 125°C in simulated coal gasifier environment. However the same silicon carbide material shows a weight increase of 1.7 x 10^{-5} g/cm^{2}h in air atmosphere at 1250°C.

The gas environment is not only important because it can directly affect the material thermomechanical and thermophysical properties, but it can also affect the interaction between the molten products from the process environment and the

refractory materials. In the case of slagging coal gasifiers, the partial oxygen pressure is important in determining the interaction between the slag and the refractories. The interaction between the coal slag and the refractory materials in air and coal gasifier environment is reviewed next.

2.4.2 Interaction of Refractory Materials with Slags

Coal–ash slags are complex multicomponent silicates that are mainly composed of CaO, Al_2O_3, SiO_2, FeO, and Fe_2O_3. The interaction between the slag and the refractories can be by erosion or corrosion. Erosion is defined as wearing away of refractory surfaces by the washing action of moving liquids. Corrosion is the destruction of refractory surfaces by the chemical action of external agencies. Corrosion can be further characterized by two mechanisms: dissolution of the refractories or penetration of the slag in the refractories.

Two different kind of tests have been carried in the past to characterize refractory performance in slagging environments. Most of the research conducted concentrated on studying the corrosion rate of the refractory materials under no load (Kennedy, 1980, 1981a, 1981b; Bonar et. al., 1980; Cooper, 1981; Washburn, 1982, 1983; Muan, 1983; Bandyopadhyay et. al., 1983; Greenberg et. al., 1984; Bakker et. al., 1984; Chen and Buyukozturk, 1985c; Greenberg and Peoppel, 1985; Vorres et. al., 1985). The second kind of approach was to directly study the effect of slag impregnation on the thermomechanical properties of the candidate material. Very few researchers have attempted this, and one recent research studied the properties of slag–impregnated silicon carbide (Easler, 1985). The results of these two kind of study are briefly summarized in what follows.

Two main properties used to characterize a slag are its base to acid ratio (B/A) and ferritic content (Kennedy, 1980; Washburn, 1982). The P_{O_2} of the atmosphere can be back calculated from the ferritic content of the slag. Based on their B/A ratio the slags are classified as basic, acidic, or neutral. An acidic slag will attack basic refractories, and a basic slag will attack acid refractories. Acid refractories are based on SiO_2, and usually contain important fractions of Al_2O_3; fireclay bricks belong to this category. Basic refractories include magnesite, dolomite, chrome magnesite, magnesite chrome, and alumina bricks.

The early studies of corrosion by slags examined static slag attack (Endell et. al., 1939), the corrosion rate of bricks during service (Berry et al., 1950), or bricks produced in the laboratory (Rigby and Hutton, 1962). Kennedy (1980) examined the compatibility of eleven different water–cooled refractories with a basic coal–ash slag at $1500^{\circ}C$. The tests were conducted at a partial oxygen pressure of about 10^{-8} atm. (10^{-3} Pa), and the monitoring of the P_{O_2} was carried out by taking gas samples from the furnace and carrying chemical analyses. The slag composition changed with exposure time, and at one hour after starting the test the chemical composition was as follows: 39.2% CaO, 25.1 SiO_2, 15.3% Al_2O_3, 8.3% Feo, 5.5.% MgO, 4.3% Fe_2O_3, 1.0% Fe, 1.0% TiO_2, and less than 0.1% of Na_2O and K_2O. The B/A ratio and ferritic content of the slag were 1.4 and 29% respectively after one hour of exposure, and were monitored during testing. The highest corrosion resistance was exhibited by a fused–cast chrome–spinel refractory (80% Cr_2O_3, 8% MgO, 6% Fe_2O_3, 5% Al_2O_3, 1% SiO_2). The mechanism of corrosion was by enrichment of the spinel with aluminum oxide followed by slow dissolution. Alumina refractories showed poor resistance, and reacted with slag to produce primarily calcium hexaluminate ($CaO.6Al_2O_3$). The addition of Cr_2O_3 (from 16% to 32%) caused a

(Mg, Fe)O.(Al,Cr,Fe)$_2$O$_3$ spinel to form instead, and the corrosion rate to decrease. The density and the Cr$_2$O$_3$ content were thus found to be the most important factors in resisting corrosion by slags. Other studies (Bonar et al., 1980; Kennedy, 1981a) under basic and acidic slags, also showed that fused–cast chrome–spinels exhibited excellent corrosion resistance under both acidic and basic slags. The interaction between the refractory and the slag resulted in the formation of a band of recrystallized chrome–rich spinel, which seemed to protect the brick from further attack. Under acidic slags containing about 10% (MgO+Fe) a fused–cast alumina–chromia refractory was superior to alumina and magnesia–chrome refractories. Under basic slags high alumina refractories dissolved very fast. Kennedy (1981b) summarizes the tests performed on about 60 different refractories, in order to characterize the dissolution and penetration mechanisms. The erosion mechanism is not addressed. The partial oxygen pressure in the gasifier will affect corrosion through both viscosity of slag and the precise nature of corrosion products (Kennedy, 1981b). This is confirmed by Muan (1983) who found that the solubility of Cr$_2$O$_3$ in siliceous systems increases significantly as the P$_{O_2}$ decreases below 10^{-5} Pa. Kennedy (1981b) advises the use of a cooling system to form a frozen slag layer at the hot face, that will minimize corrosion. The disadvantage is that considerable heat losses will occur. The equilibrium thickness of the brick depends on the thermal conductivity of the refractory material and on the lowest temperature (T$_c$) at which reactions between the slag and the refractory will take place. Cooper (1981) noted that corrosion of oxides occurs not by dissolution or evaporation of the oxide, but by the penetration of the solid by some or all of the species from the fluid. The capillary forces can pull the liquid into the open porosity of the solid, and the diffusion of species from the liquid can occur along the grain boundaries or into the bulk of the

solid. Deterioration will then occur by surrounding of a volume of the solid by a fluid phase, expansion or contraction of the solid with associated stress development, or introduction of foreign species into the solid. Another approach to study corrosion was used by Washburn (1982, 1983), in a comparative rotating sample slag test. It is used to compare two refractory samples under controlled conditions. Rotational speed is at 60 RPM, and the oxygen partial pressure ranges from 10^{-5} to 10^{-9} atm. A significant decrease in the slag viscosity was found as P_{O_2} decreased from 10^{-6} to 10^{-9} atm. A magnesium chromite refractory (80% Cr_2O_3, 20% MgO) had a low level of attack and consistent performance for different slags and test conditions. A chrome–alumina refractory (10% Cr_2O_3, 90% Al_2O_3) showed greater dissolution rates and greater glass penetration. It was noted, that although there appears to be a relationship between corrosion attack and chromia content, one has to consider the total system and the effect of the second phases. The dissolution rate was found to be controlled by a boundary layer in the slag adjacent to the refractory. This rate is proportional to the concentration gradient in the layer, inversely proportional to the layer thickness, and proportional to the square root of the rotating speed in the rotating slag test. A different approach to the problem is adopted by Muan (1983). He studied the stability relations among oxide and silicate phases of importance in slagging coal gasifiers, and expressed the equilibrium relations between the main coal–ash slag components and the refractory components as phase diagrams. Bandyopadhay et al. (1983) studied the thermal shock resistance of several refractories, and compared it to their corrosion resistance. Greenberg et al. (1984) adopted a similar approach to Washburn (1982) to study the corrosion of ceramic refractories exposed to synthetic coal slags, using the rotating cyclinder technique. The test temperature was varied from $1480^{\circ}C$ to $1600^{\circ}C$, the partial oxygen pressure

was maintained constant between 10^{-8} to 10^{-10} atm., and the speed of rotation was varied between 50 to 200 RPM. Refractories containing 60–80% chromia showed negligible corrosion at 1500°C. At 1600°C, due to subtle mineralogical differences, various high–chromia refractories of similar composition showed different corrosion rates, especially at high rotational speeds. Low chromia refractories (10% Cr_2O_3) showed greatly accelerated corrosion rates in comparison with the high chromia refractories. A thorough review of the factors affecting refractory life is given by Bakker et al. (1984). They concentrate on studying the wear of refractories by coal slags. It appears that the gasifier operating temperature is probably the most important factor affecting refractory performance. It is above the melting point of the ash that refractory wear rapidly increases with increasing temperature, and only at temperatures above 1500°C–1600°C (2732°F to 2912°F) that refractory wear becomes excessive. The effect of gas composition on refractory wear is generally small. However, reducing conditions lower the slag viscosity. The effect of slag velocity on wear rates is quite pronounced. A two–fold increase in slag velocity caused a ten–fold increase in wear rate of a chromia–alumina refractory. Bakker et al. (1984) proposed two different wear mechanisms for lab tests and in service conditions. For lab tests the following wear mechanism was proposed: the slag penetrates the pore system, and dissolves the bonds between the crystalline phases; shear forces at the surface remove isolated grains and accelerate corrosion by removal of dissolved material from the surface. For in service conditions, higher wear rates are observed, and the factors that could have been overlooked are: slag velocity, refractory spalling, and mechanically and thermally induced stresses. The cracking at the hot face is attributed to creep, and is ascribed to creep cavitation. The cracking mechanism proposed by Bakker et al. (1984) for cracking in service is as follows: high

compressive hoop stresses form due to thermal expansion of the hot face brick accompanied by creep deformation in the direction of the hot face; this causes creep tensile stresses in the radial direction, and microcracking parallel to the hot face; the different microcracks will join to form a large crack, and result in the spalling of the hot–face. Bakker et al. (1984) propose that slag penetration dissolves the bond between refractory grains and lower the hot strength, thus, allowing cracking to develop due to degraded material properties. A mathematical model to predict the long–term corrosion behavior of refractory linings for slagging gasifiers, taking into consideration the effects of dissolution and penetration was proposed (Chen and Buyukozturk, 1985c). The interaction between temperature variation, corrosion rate, and spalling of the lining is considered.

The previously reported works did not address the change in thermomechanical properties of slag–impregnated materials. Structural ceramics were studied for their behavior in slagging environment, and the effect of slag on the thermomechanical properties of siliconized silicon carbide was studied by Easler (1985), and the corrosion of silicon carbide ceramics was studied by Easler et al. (1985). This was motivated by the possibility of using structural ceramics, such as silicon nitride or silicon carbide, in components such as heat exchangers, or valve components. At the gasifier chamber exit, the P_{O_2} is about 10^{-12} atm. and has a high stream content and contains sulfur–bearing gases. Easler (1985) studied the effect of gaseous exposure without slag, and the effect of exposure to both acidic and basic slags on the silicon carbide mechanical properties. After exposure of 200 hours at different conditions, the retained strength was measured at room temperature. The report of Easler (1985) does not state if the fracture stress was in tension, compression, or flexure. After exposure to gases only, acidic slags, and basic slags,

the retained strength of the slip cast silicon carbide was reported to be 64%, 70%, and 71% of the original strength respectively. It should be noticed that specimens exposed to slag exhibit a higher strength retention than specimens which were not exposed to slags. For extruded silicon carbide, the strength retentions were 112%, 105%, and 95% for specimens subjected to gases only, acidic slag, or basic slag respectively. It should be noted that a strength increase is observed for specimens not subjected to slag or subjected to acidic slag. In another study, Easler et al. (1985) also observe a retained strength with exposure to air, acidic slag and basic slag at $1250^{\circ}C$ of 127%, 124%, and 100% respectively. In the case of exposure to coal gasification environment, the retained strength is 108%, 106% and 86% of the original one for exposure to gas only, acidic slag or basic slag respectively. To explain the strength increase, Easler et al. (1985) suggested oxidation blunting of the sharp crack tips. Analysis of fracture surfaces indicated that the failure origins were most commonly associated with an internal pore near the specimen surface. In the case of specimens with decreased strengths, origin of failure was associated with a corrosion pit, produced by degradation 'due to slag, that was larger than any pre—existing microstructural features. Other researchers studied the high—temperature environmental degradation of hot pressed silicon nitride (Clarke, 1983) in coal gasification environments.

The behavior of monolithic refractories under corrosive environment is also of importance. The chemical degradation of castable refractories was studied by Robbins and Mauer (1981). A high purity $CaO-Al_2O_3$ castable with alumina aggregate (93.7 wt.pct. Al_2O_3, 5.6 wt.pct. CaO) and a $CaO-Al_2O_3-SiO_2$ with kaolinite aggregate (55% Al_2O_3, 36% SiO_2, 5% CaO) were studied. The former system at high temperatures and in the presence of steam was subjected to frequent

changes in bonding phases, and to intervals in which the main bonding phase is in a transition state; it also reacted with the alkalis and silica present in the steam due to impurities from the coal. The latter showed an increase in flexural strength with exposure to pilot plant atmospheres. This was attributed to the formation of stabler compounds over large temperature ranges.

2.5   TEST PROCEDURES AND INTERPRETATION OF RESULTS IN ASSESSING MECHANICAL PROPERTIES OF BRITTLE MATERIALS

The need for materials that can retain high strength at elevated temperatures has increased significantly in recent years. This has motivated the use of brittle materials as structural components. Brittle materials exhibit an inherent variation in their properties. There is a need for experimental work to carefully assess the effect of the specific test method and the specimen preparation procedure used on the obtained material properties. It should be ensured that the test results represent the real material behavior and not just the behavior of the laboratory specimens, and that any variability in the results is an inherent material property. There is also a need in the design and analysis of large structures using these materials to take into consideration the inherent variability in the material properties obtained from laboratory specimens, and infer the probability of failure under more complex stress states encountered in service. The variability in the flexural (Ritter and Davidge, 1984) and thermal shock (Brockenbrough et. al, 1986) properties of alumina, and compressive properties of a silica glass (Kschinka et. al, 1986) illustrates the growing concern of designers to use statistical properties, and to assign a failure probability to structural components.

A study of the properties of refractory bricks at elevated temperatures showed a high variability in these properties (Eusner and Kappmeyer, 1962). For the high–duty brick included in the study the study, the MOR varied from 360 to 2920 psi, and the spalling resistance varied from 0.0% to 39.1%. At $2640^{o}F$ the measured deformation under load in certain cases was as high as 15.0%.

The effect of specimen preparation techniques on the properties have been studied by different researchers. The size effect on the material properties has been studied extensively. Smaller size specimens were reported to give higher strength for rocks (Einstein et. al, 1970; Baecher and Einstein, 1981) and concrete (Neville, 1959). This can be explained by the "weakest link" theory (Weibull, 1939) where the risk of rupture is proportional to the volume. However, lower strength was also reported for concrete cylinders with a smaller size (Campbell and Tobin, 1967). One should keep in mind the restriction imposed by a minimum specimen diameter with respect to the maximum grain size (ASTM, 1986). In order to verify laboratory data, large scale testing is sometimes conducted. In the case of rocks, in situ tests on large specimens were found to be an invaluable aid in engineering design (Bieniawski and Van Heerden, 1975). The size of the specimen was also found to be related to the end effects in compression testing (Kotsovos, 1983). The effect of machining of the specimen is also important, and is illustrated by studies of residual stresses in grinded ceramic surfaces (Johnson–Walls and Evans, 1986). Finally, the materials used are usually loaded in multiaxial stress state conditions, and the anisotropy and inhomogeneity of the properties under these conditions should be taken into consideration (Stout and Petrovic, 1984).

The testing procedures of ceramics in compression have been reviewed (Bortz and Burton, 1969; Sines and Adams, 1978). New testing methods have been proposed

by different researchers for compression tests on ceramic materials at room (Sedlacek, 1968; Langford, 1977) and elevated temperatures (Tracy, 1987). It appears that a common problem in testing brittle materials is the difficulty of observing the post—peak behavior. However, a careful selection of the test control variable may allow the assessment of the post—peak behavior (Obuko and Nishimatsu, 1985).

Different statistical theories have been proposed to account for the material variability in analysis and design. Weibull (1939) was the first to introduce statistical analysis. Since then, different statistical approaches have been developed for different loading conditions such as fatigue testing (McClintock, 1955a, 1955b, 1956), and fracture under multiaxial stresses (Batdorf and Crose, 1974; Batdorf and Heinisch, 1978; Evans, 1978). These theories predict the initiation and propagation of microcracks, and their localization to form macrocracks, based on different factors such as the fracture stress distribution, and the specimen size (McClintock and Mayson, 1976; McClintock and Zaverl, 1979). Recently, statistical methods have also been used to predict the corrosion rate of various refractories (Chen and Buyukozturk, 1985c).

2.6   RELATION OF PRESENT RESEARCH TO PREVIOUS WORK

The present research focuses on the macroscopic and microscopic material characterization of refractory ceramics used for the linings of high temperature vessels, with special emphasis on coal gasification vessels. An understanding of the system configuration, operating conditions, candidate materials and causes of linings failure, presented in Section 2.2, is essential in defining the test program and the requirements needed for the testing facility. The critical protective layer in coal

gasification vessels is usually the layer of dense refractory bricks at the hot face. The candidate materials are either high–alumina or high–chromia bricks. This motivated the choice of high–alumina and high–chromia dense refractory ceramic bricks as materials to be tested. The operating conditions in slagging gasifiers combine high temperatures, different mechanical loading combinations, reducing atmospheres, and corrosive slags. These operating conditions dictated the testing program and the requirements needed from the testing system.

The main emphasis of the present study is to generate an understanding of the compressive behavior of refractory ceramic oxides at elevated temperatures. These refractory ceramics are brittle materials, and the review of previous research on brittle material behavior under compressive loads and elevated temperatures in Section 2.4 ties in nicely with the current study. Extrinsic and intrinsic behavior under monotonic compressive loads, different observed modes of crack–crack and crack–pore interactions, location and type of microcracks, behavior under cyclic loads, and modeling considerations reviewed in Section 2.4.1 for rocks, concrete, and brittle materials in general will be referred to later in the course of this study. Similarly, past research on the high temperature behavior of ceramics, concrete and rocks reviewed in Section 2.4.2 show similar behavior between these three classes of material. The variation of strength, and initial stiffness under monotonic loading, and the high temperature creep behavior is similar for these materials. There is a need for a more thorough evaluation of the high temperature deformations, combined strain rate and temperature effects, thermal cycling, and mechanical cycling at elevated temperatures for brittle materials. At the same time the review of the past research on the thermomechanical behavior of refractory ceramics indicate a concentration of the research on the high temperature behavior under small creep

loads, and a lack of information on the behavior of these material under other loading histories. The current study addresses this need and tries to fill this gap.

Past research on the environmental effect on the behavior of refractory ceramics indicated that a large number of corrosion studies had been conducted, phase diagrams established, and the chemical interaction of the refractory materials with different gas environments evaluated. However, there is a lack of understanding of the material behavior under a combination of thermomechanical loads and environmental factors. This study addresses this issue by attempting to characterize the behavior of the refractory materials under the combined effect of loads and aggressive environments.

Finally, in order to get consistent and reliable results the specimen preparation phase is critical. The test program for the current specimen preparation procedures was established following suggestions from past research summarized in Section 2.5.

The current study attempts to integrate past research with the obtained results. In many cases the correlation between past and present research is beneficial.

CHAPTER 3
TEST EQUIPMENT AND TESTING PROCEDURES

3.1 SYNOPSIS

This Chapter describes the equipment designed and built for compressive or flexural testing of materials under elevated temperatures and controlled gas atmospheres. The system was built keeping in mind the requirements needed to simulate slagging coal gasifier environments. Section 3.2 describes the developed thermomechanical test equipment, and Section 3.3 presents the procedures used for compressive testing at high temperatures under controlled gas atmospheres. The equipment used for microstructural characterization is described in Section 3.4.

3.2 EQUIPMENT FOR HIGH TEMPERATURE TESTING

The design and fabrication stages involved extensive changes of plans in close cooperation with the equipment's manufacturer, Applied Test Systems (ATS), Butler, PA. This section describes the successful equipment selected and built, and addresses the design problems in general. The details of the design process, and the iterations that preceded the final plans are not discussed in this report.

The first step in the design process was to determine the functions to be performed by the system, and the requirements that it had to satisfy. The system was built to test materials, under compressive or flexural, monotonic, constant or cyclic mechanical loads, in room or elevated temperatures, in air or controlled gas environments. The first foreseen application was thermomechanical testing of refractory ceramic oxides for coal gasification vessels, under controlled partial oxygen

pressure (P_{O_2}) environment. This led to the following requirements:

o   application of prescribed monotonic and cyclic compressive load histories at selected constant temperature levels;

o   temperatures ranging from room temperature up to $2800^{\circ}F$, with an accuracy of $\pm 5^{\circ}F$ at $2800^{\circ}F$;

o   maximum mechanical load capacity of 50,000 lbs., with noise (i.e., percentage error) levels not to exceed 0.3%;

o   achieving P_{O_2} values in the range of $10^{-7} - 10^{-8}$ atm.;

o   loading rams and heating elements able to resist action of corrosive gases, and melting products; and

o   automated data acquisition and control.

The major system components, identified in Fig. 3.1a, are a 110 kips—mechanical loading frame (from Manufactured Test Systems, MTS), a $2800^{\circ}F$ high temperature furnace (from ATS) with a microprocessor (from LFE Corporation, Clinton, MA) based temperature controller, a muffle tube and retort assembly to apply mechanical loads at high temperatures under controlled gas environment, and a data acquisition (IBM XT and Fluke 2400B) and control (PDP–11) system. A picture of the overall testing system is shown in Fig. 3.1b. The various components are briefly described in the following sections.

3.2.1 Furnace and Temperature Controller

Main c nsiderations in the choice of the high temperature furnace included the dimensions and the shape of the heat zone, temperature uniformity around the specimen, heating elements that would be inert to the specified gas environment and maximum testing temperature. The temperature controller had to be accurate and
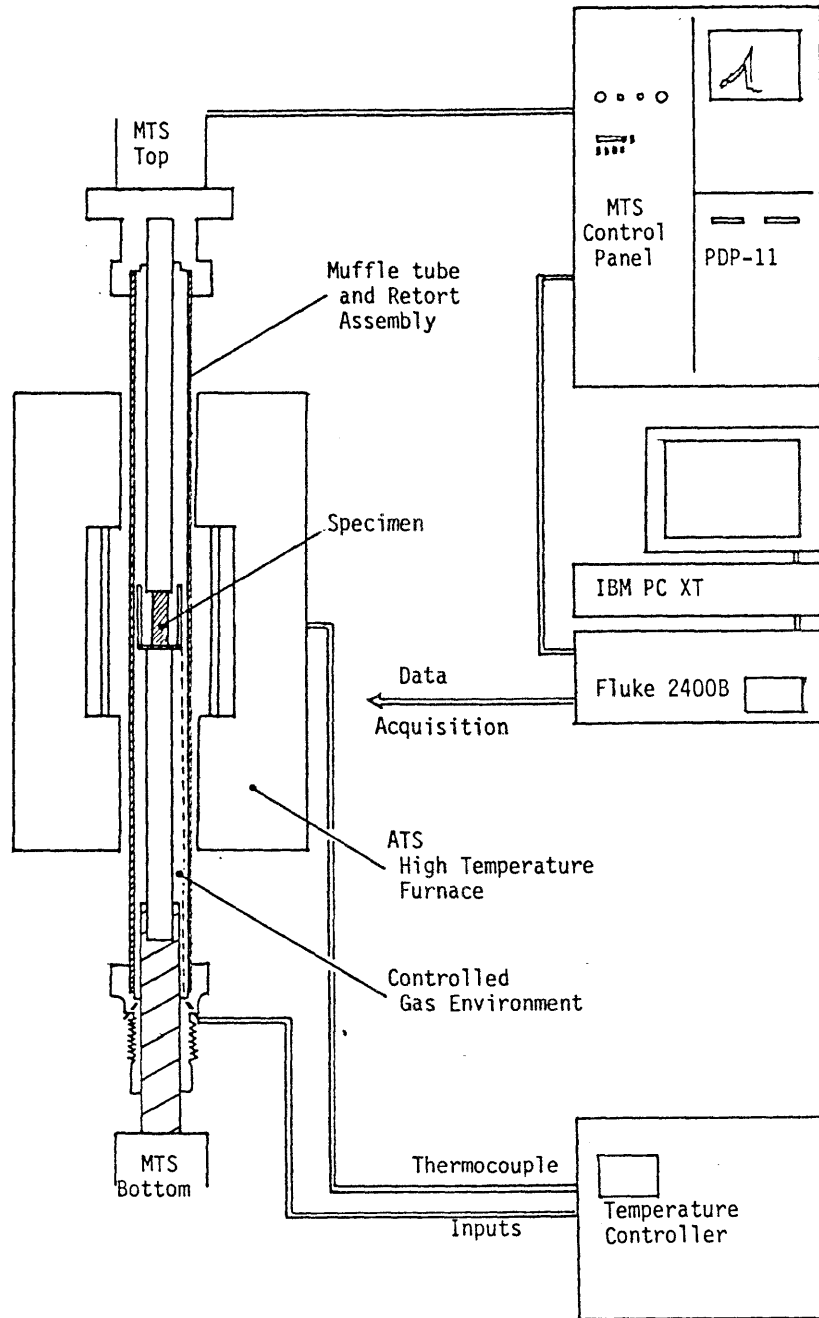
Figure 3.1a   Sketch of the major components of the thermomechanical testing system
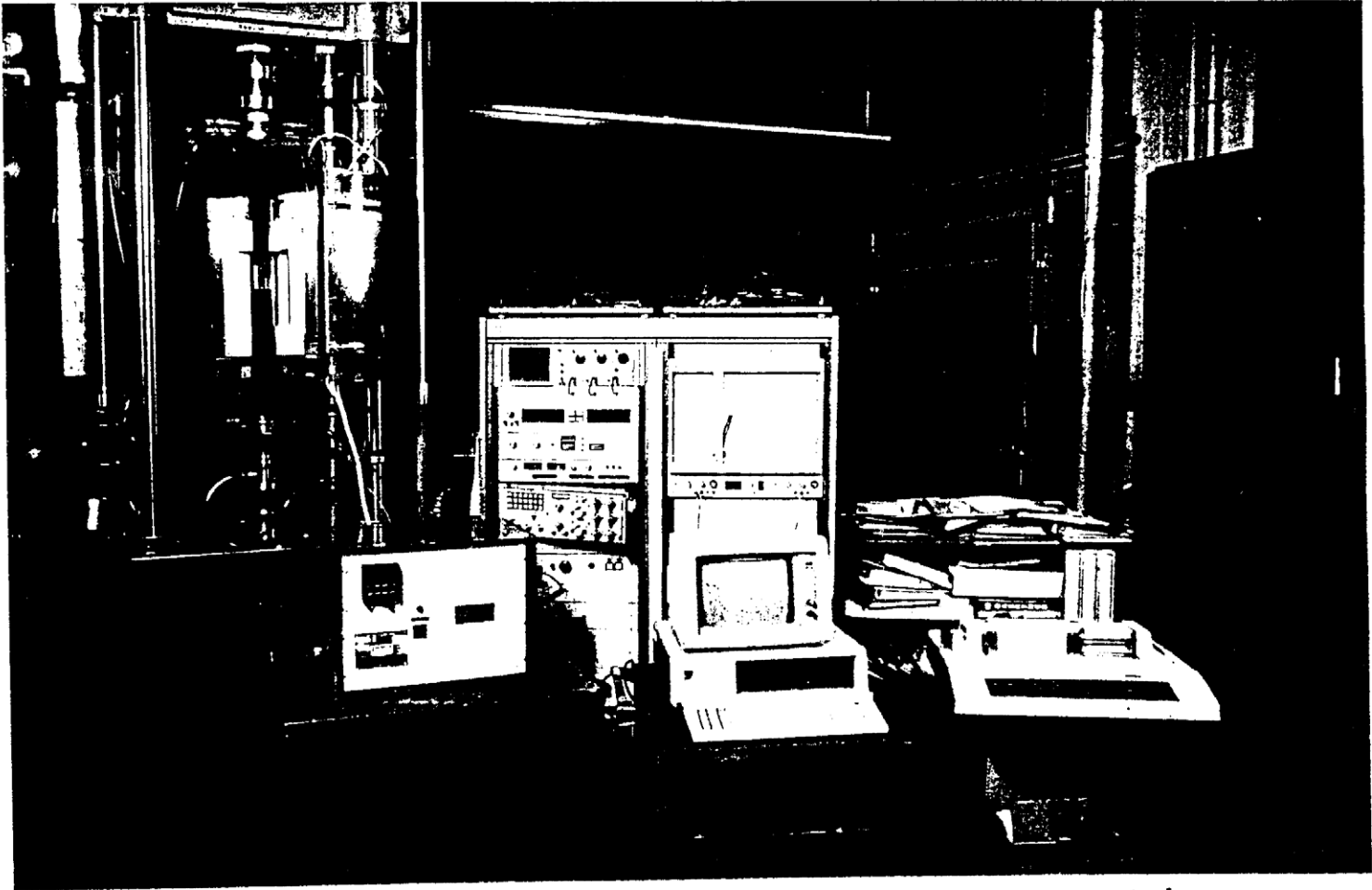
Figure 3.1b   Picture of the major components of the thermomechanical testing system

flexible enough to prescribe different temperature histories.

Different systems were studied to achieve the above—mentioned requirements, keeping in mind the restrictions imposed by the need for a controlled gas environment. The considered alternatives included high temperature furnaces (such as radiant heat chambers, box furnaces, and split furnaces) with muffle tube, and custom made furnaces with leak—free environment.

The selected furnace is a split—type furnace with Silicon Carbide (SiC) resistance heating elements and a maximum operating temperature of 2800°F. It is shown schematically in Fig. 3.2. It is cylindrical with a 16" outsider diameter and a 24" height. The shell length is 16" long, and is protected by one layer of insulation. The heat zone is circular with an 8" diameter and a 10" height. The heat zone shape and dimensions were chosen in order to insure temperature uniformity around a cylindrical specimen that is 2" in diameter and 6" long (these dimensions represent the maximum size specimen for which the system was designed). In order to check for temperature uniformity, three thermocouple ports were provided at the furnace's center, and at 1.5" from the center on either side. An actual check for temperature uniformity was performed during testing, and showed a maximum discrepancy of 3°F between the middle and top thermocouple readings. This result was considered to be very satisfactory. Heating elements are made of Silicon Carbide and are arranged in a circular manner around the furnace's center. The heating elements are connected in series by cables outside the furnace's shell. Both ends of the furnace have 4" bore holes to allow access for the muffle tube and retort loading assembly.

The selected temperature control system can prescribe variable heat—up and cool—down rates, and different soak periods. It is capable of achieving constant temperature levels between room temperature and 2800°F with an accuracy of $\pm 1^\circ$F,
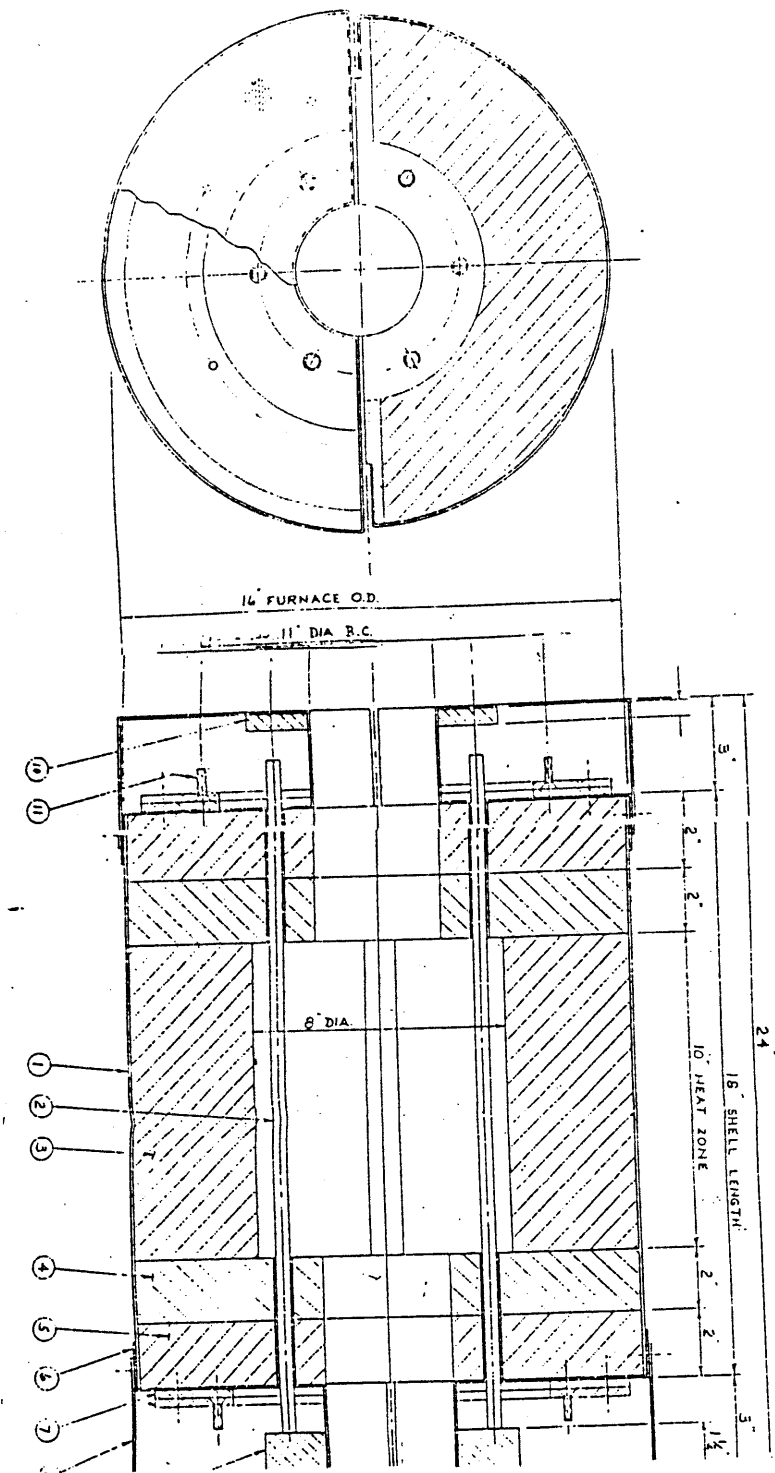
Figure 3.2   High temperature furnace

if tuned properly. In most tests an accuracy of $\pm 2^{\circ}$F was actually achieved. The microprocessor has built–in capabilities for thermal cycling, up to 252 cycles, with up to 8 different ramp and soak periods per cycle. The temperature controller is connected to a Chromel–Alumel (Nickel–Chromium vs. Nickel–Aluminum) type K thermocouple for temperatures below 2000°F, and to a Platinum–Rhodium (Platinum – 6% Rhodium vs. Platinum – 30% Rhodium) type B thermocouple for temperatures above 2000°F. The temperature controller is linked to the data acquisition system, described in Section 3.2.5, to register the prescribed temperature history.

3.2.2 Muffle and Retort Assembly

The muffle and retort assembly was designed to apply up to 50 kips at 2800°F under a controlled P_{O_2} in the range of 10^{-7} atm to 10^{-8} atm. It had to meet the following requirements:

o   all compression rams and load–bearing parts inside the furnace to withstand 50 kips maximum load at 2800°F maximum temperature; all load–bearing items subjected to temperatures above room temperature and are outside the furnace to resist 50 kips of load at a specified maximum temperature; all other load–bearing parts to resist 50 kips load only;

o   any part inside the furnace to resist a maximum temperature of 2800°F;

o   seals at both ends of the muffle tube to be leak–proof at 2800°F; and

o   the length of the system not to exceed 56" (maximum height between crosshead and loading piston on load frame) when fully assembled.

Several iterations were necessary before adopting the final retort assembly shown in Fig. 3.3. The selected mechanical load frame has a 110 kips load capacity. It has a 5" electronically controlled hydraulic piston mounted vertically at the bottom center of a four—post frame. A manually controlled crosshead with a 5" diameter head slides along this frame. The crosshead can be locked at any position up to 56" above the lower actuator. Monotonic, cyclic, and constant mechanical loads can be applied. The maximum tested strain rate is 0.3 $\sec^{-1}$. The actuator's movement can be load, displacement, or strain controlled. The load train inside the furnace consists of recystallized silicon carbide (SiC) tubes (Crystar from Norton Company, Worcester, MA) ended by alpha SiC caps (from Sohio Engineered Materials Company, Niagara Falls, NY). The lower SiC tube has a 2.75" outside diameter (OD) and a 0.25" wall thickness, and frames into a water cooled stainless steel grade 347 loading rod. The upper SiC tube has a 2" O.D. and a 0.25" wall thickness, and frames into a water cooled stainless steel cap. The water cooled stainless steel ram has a bottom diameter of 2.25" up to a diameter of 2.875" where it frames with the SiC ram. The specimen is loaded inside the furnace between the two SiC rams. There is an alumina protective cup around the specimen to protect the rest of the system (and especially the muffle tube) from debris due to brittle fracture, or from melting slags. An alumina muffle tube (from McDanel Refractory Company, Beaver Falls, PA) slides around the loading rams and is connected at the top and bottom to gas—tight water cooled caps. The gas environment inside the muffle tube is monitored during testing. Bellows assembly, around the lower stainless steel ram, provides a moving seal to allow for piston movement. Material selection and sizing of the retort's components had to meet with different specifications.
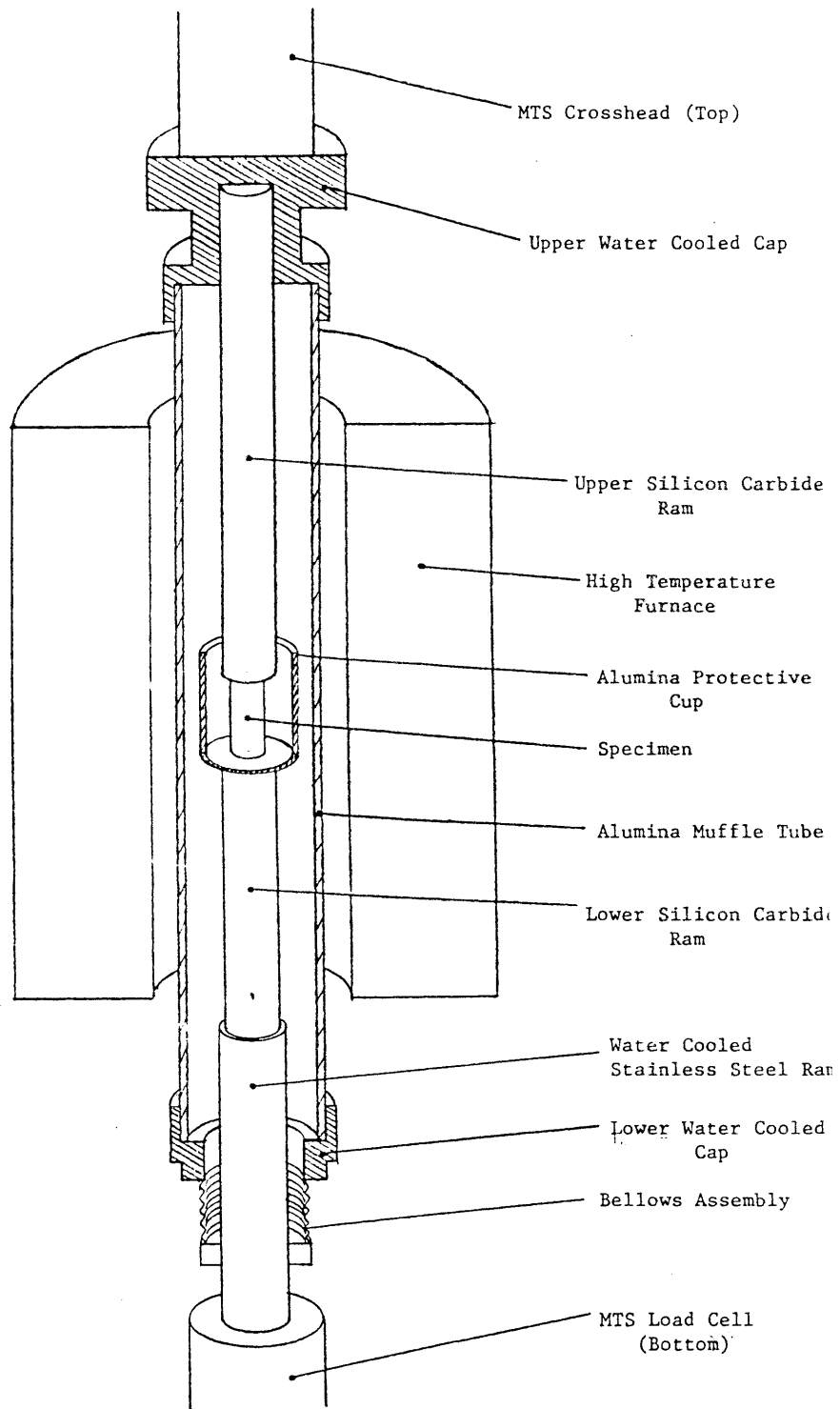
Figure 3.3   Retort assembly for application of compressive loads at high temperatures under controlled gas environments

The material selection was based on the following material properties:

o   thermal conductivity;

o   coefficient of thermal expansion;

o   variation of the initial modulus of elasticity with temperature;

o   variation of the compressive strength with temperature; and

o   resistance to corrosive gases.

The different considerations that were taken into account to determine the size of the retort's components were as follows:

Considerations in designing for mechanical loading

o   buckling (especially for the lower assembly of 27 and 1/8" length, considering change in cross section and in material);

o   crushing of SiC tubes;

o   yielding of stainless steel rods;

o   crushing of SiC cap;

o   punching shear failure of SiC cap; and

o   concentric uniform load on specimen.

Considerations in designing for thermal loading

o   O—rings should not melt; their temperature should be kept below 150^OF when possible (high temperature O—rings);

o   water cooling of stainless steel rods and seals;

o   temperature uniformity around the specimen; and

o   expansion problems:

        —   between stainless steel rods and SiC tube;

— between SiC tube and stainless steel seat;

— between SiC tube and SiC cap;

— between stainless steel rod and stainless steel seat;

— of the different components inside the muffle tube; and

— between the muffle tube and its seals.

An important consideration in the design of the retort system was the attachment between the different components. The problems solved were as follows:

o attachments between the system and the loading frame's actuator and crosshead;

o connection of the top SiC tube to the top water–cooled stainless steel cap;

o connection between the lower SiC tube and the lower water–cooled stainless steel ram;

o attachment between the lower stainless steel ram and the moving piston; and

o connections between the muffle tube's ends and the water–cooled gas–tight chambers.

The whole retort system is designed to be assembled outside the loading machine, then, rotated into position on clamps. The clamp design as well as the auxilliary systems, such as water cooling and gas connections are discussed in Section 3.2.4.

The final design of the retort system is shown in Fig. 3.4a with all the final dimensions. Pictures of the furnace and retort system with and without the muffle tube are shown in Figs. 3.4b and 3.4c respectively.

Figure 3.5 depicts the final design of the water cooled stainless steel push rod.
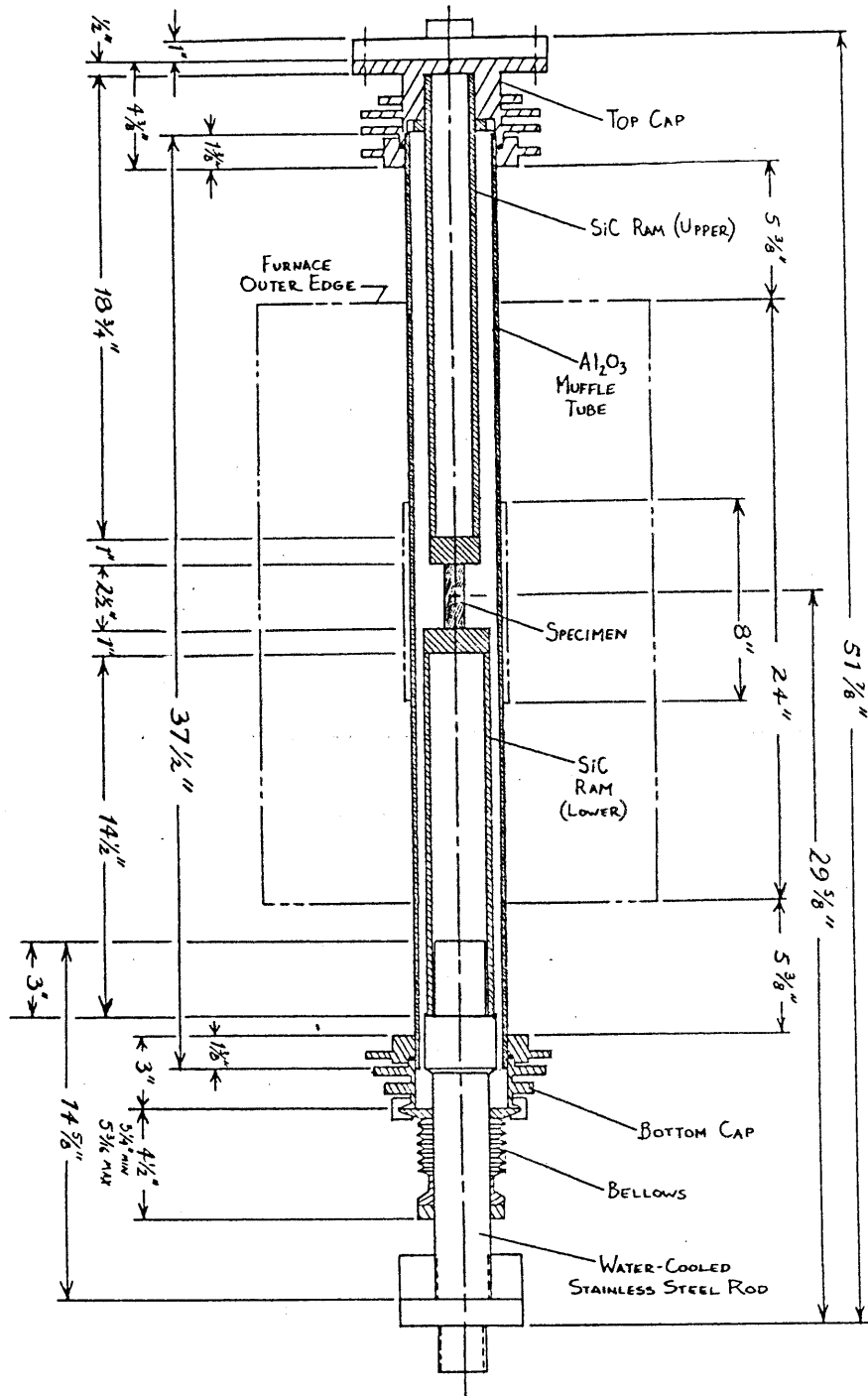
Figure 3.4a   Sketch of the final design of the retort system
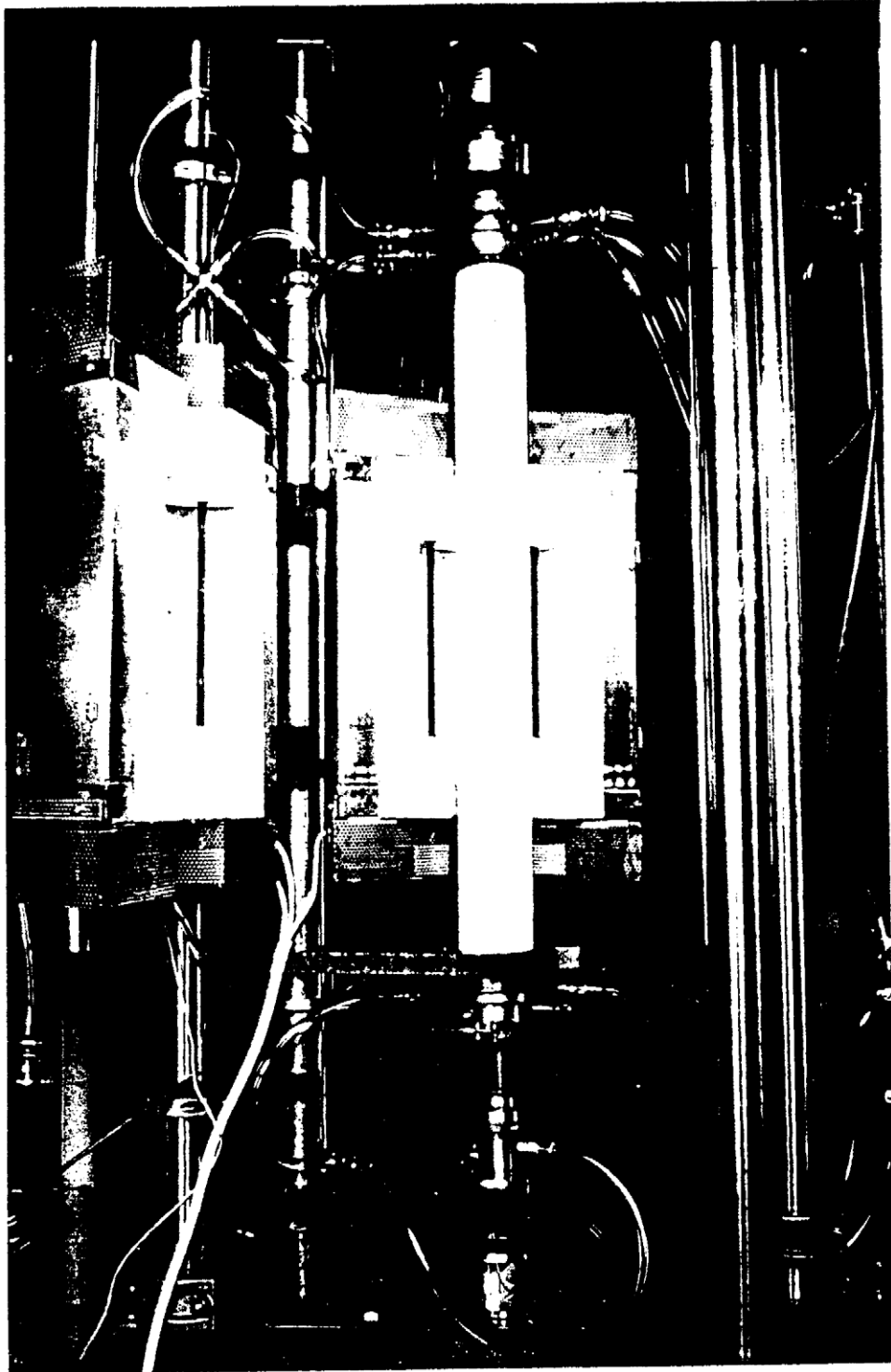
Figure 3.4b   Picture of the the furnace and retort system with the alumina muffle tube
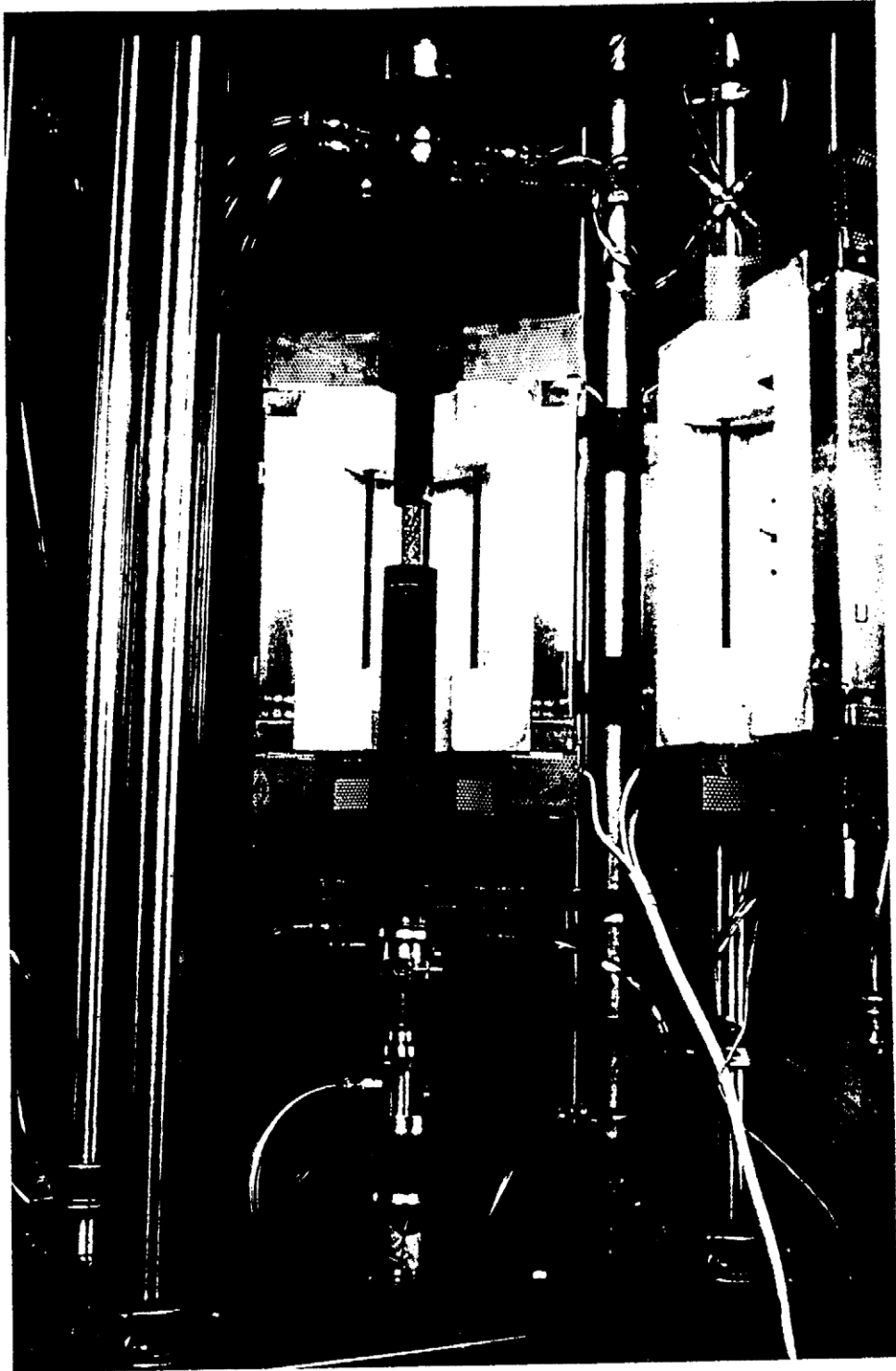
Figure 3.4c   Picture of the the furnace and retort system without the alumina muffle tube
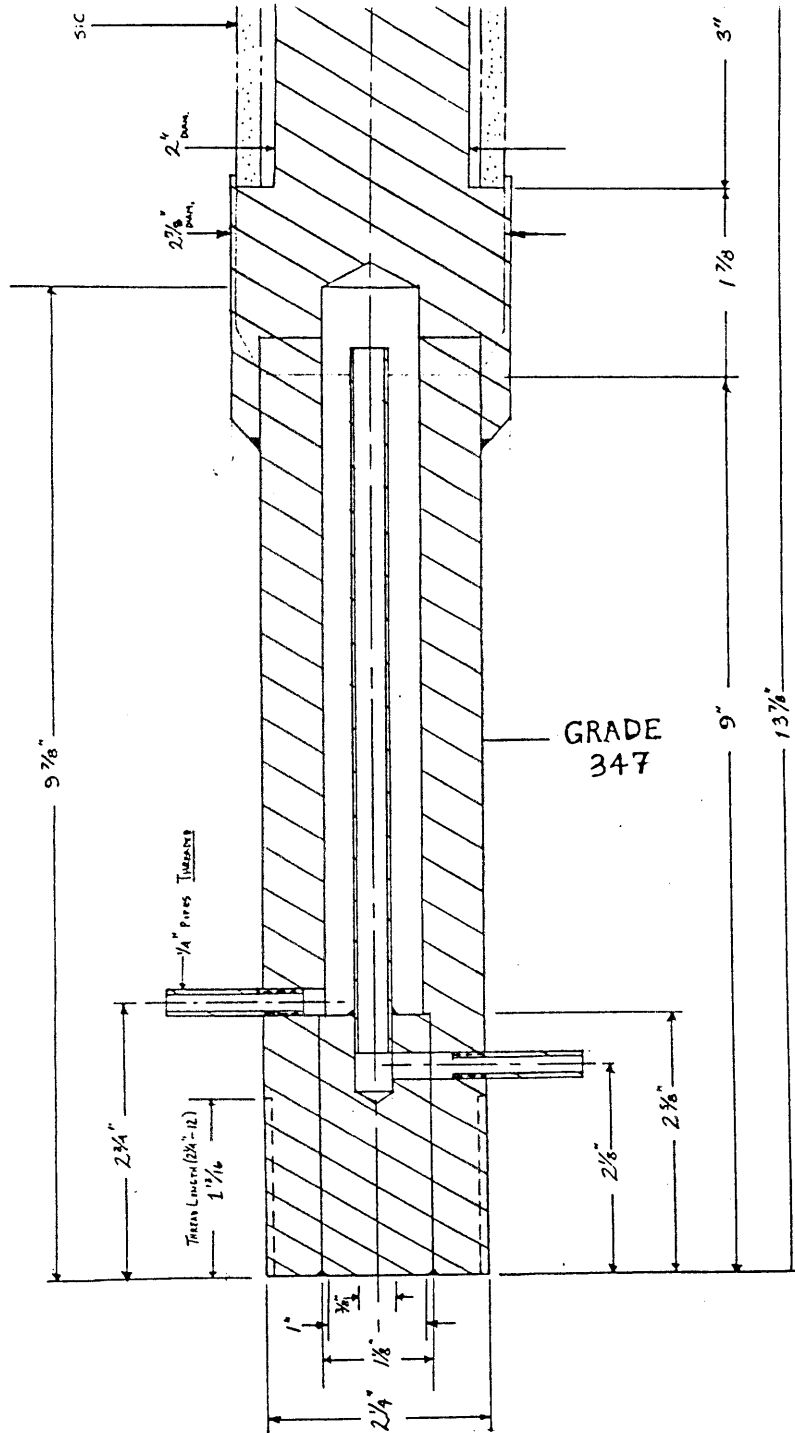
Figure 3.5   Final design of the water cooled stainless steel push rod

All the elements except the water inlet and outlet pipes are welded in position. The inlet and outlet ports are staggered to permit easier construction as well as unobstructed flow in and out. The lip and ledge connection arrangement between the rod and the SiC ram has an alignment cylinder added to ease assembly. As can be seen from this figure, the SiC ram is slightly larger in diameter than the stainless steel rod. To transfer the force from one element to another, the rod widens to accommodate the larger ram. To decrease the cost of machining, the rod is divided into lower and upper sections. The rod is constructed of AISI grade 347 stainless steel, since that material exhibits better strength properties at high temperatures as well as very good resistance to corrosion by gas or water.

Figure 3.6 depicts the lower end cap assembly. Like the preceding parts, all elements not shown bolted are welded together. The bellows assembly and the water—cooled end flange are held together by a standard clamp made necessary by the specification of the bellows. This bellows assembly has the largest interior diameter that could be obtained. This bellows assembly allows over an inch of displacement between the positions corresponding to maximum compression and full extension. Four couplings are provided around the barrel of the end cap, one of which is used for gas exhaust, while the other three are used for thermocouple inputs. Stainless steel of AISI grade 316 is used, since high temperature strength is not important.

Figures 3.7 and 3.8 show the top cap assembly. Again, all parts are welded unless they are shown bolted. Provisions are made for clamps beneath the upper mating plate and the lower O—ring jaw. Three water—cooling cavities can be clearly seen: the largest, near the end of the SiC ram; the smallest, near the end of the alumina muffle tube; and the final chamber in the lower O—ring jaw. AISI stainless steel 316 is used since high temperature performance is not as critical. However, good
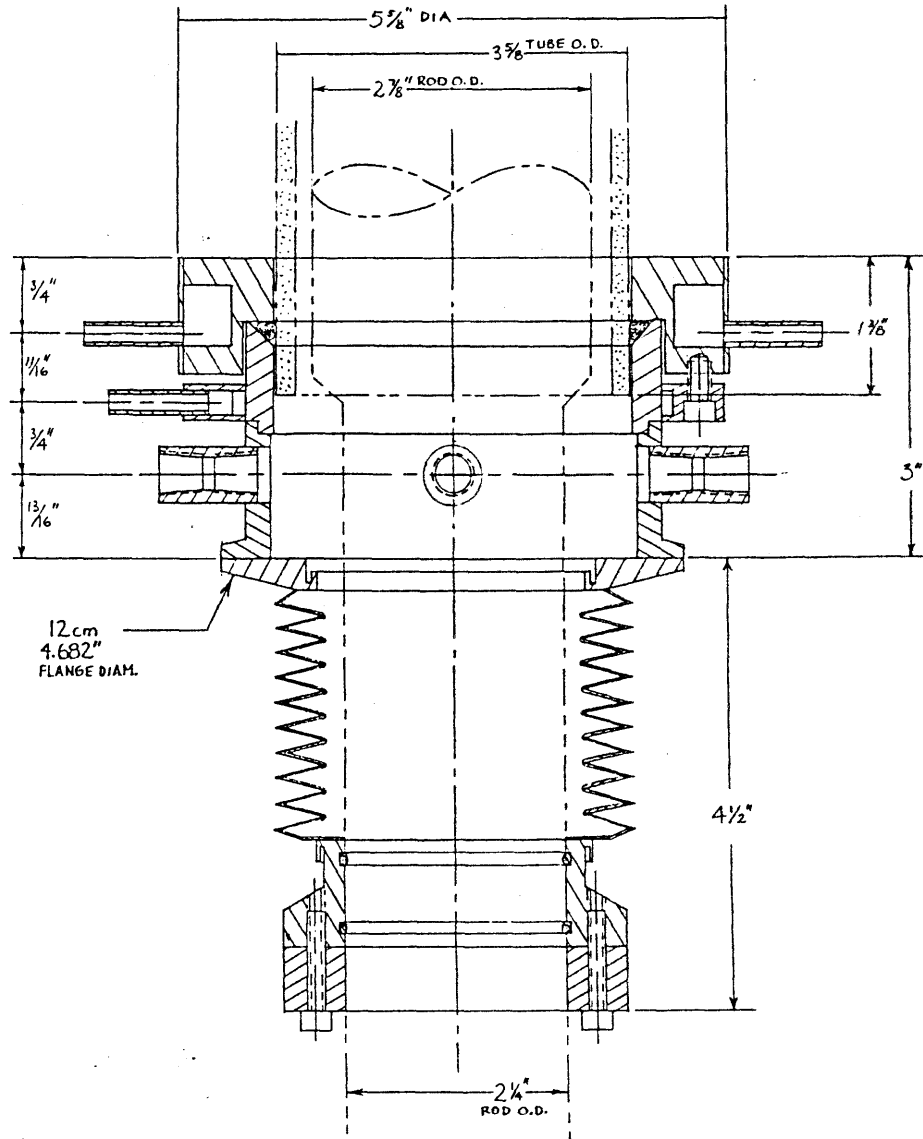
Figure 3.6   Final design of the lower end cap assembly
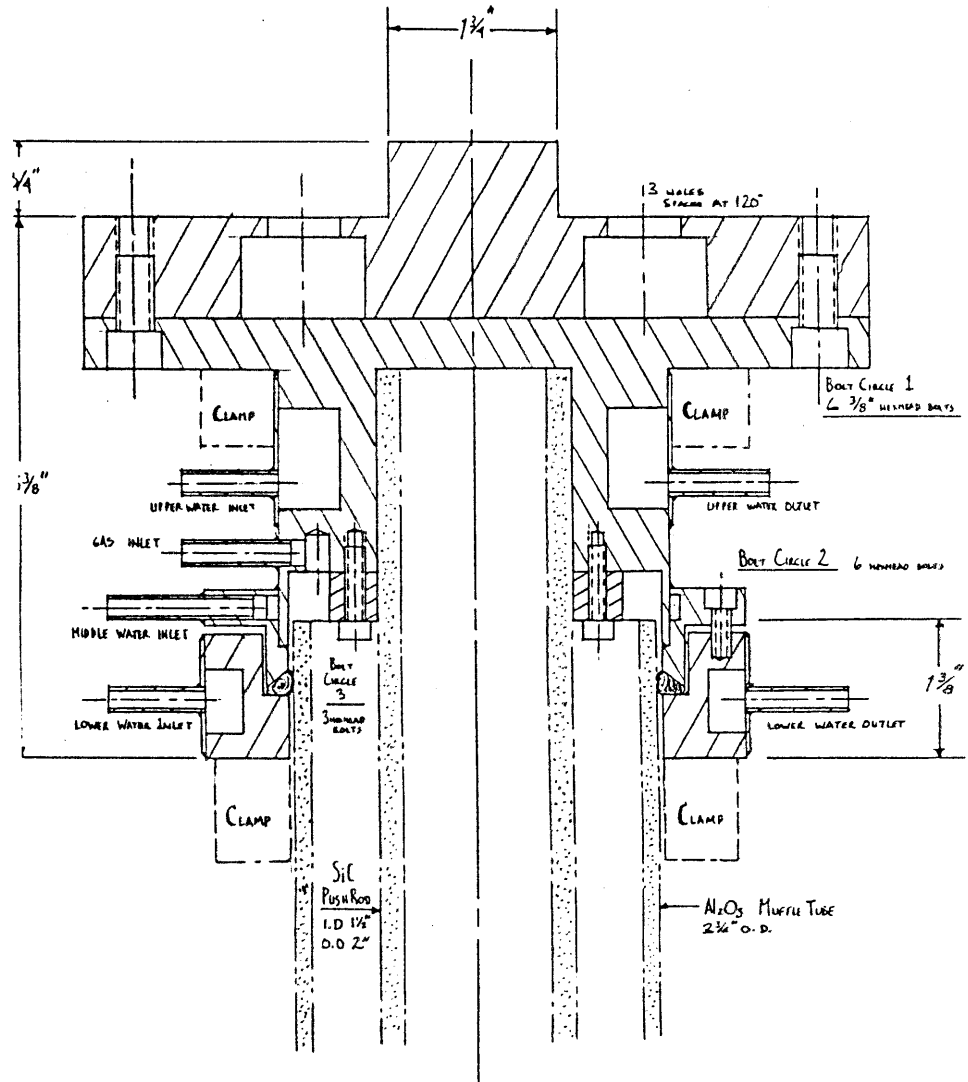
Figure 3.7   Final design of the top cap assembly — cross section

WATER
OUTLETS
1&2

WATER
OUTLET 3

BOLT CIRCLE
R= 1¼"

GAS INLET HOLE

GAS INLET

BOLT CIRCLE
R= 2½"

WATER INLETS
1&2

SiC RAM

Al_2O_3 MUFFLE TUBE

WATER INLET 3
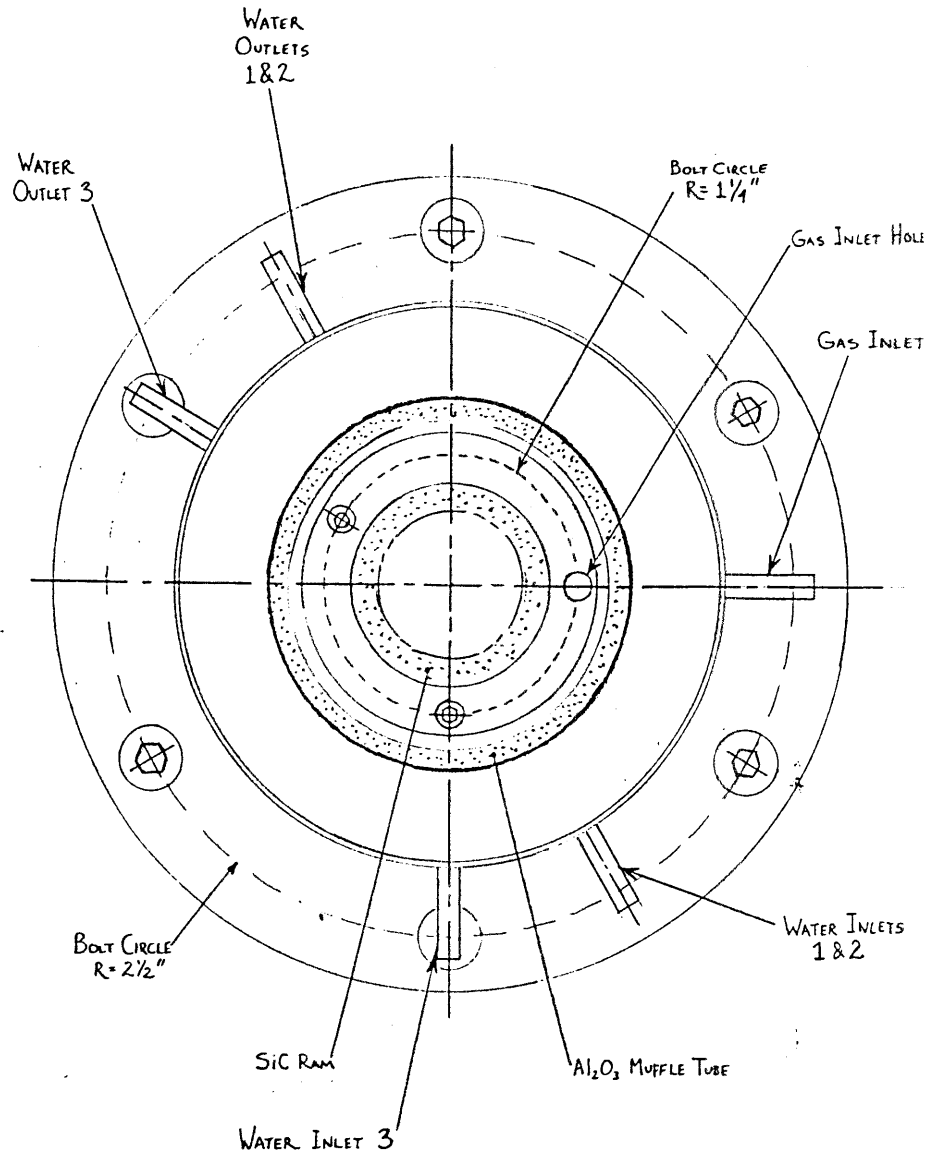
Figure 3.8   Final design of the top cap assembly — plan view

resistance to corrosion by gas or water is still important, and grade 316 has these properties.

The muffle tube is 37.5" long and 3.625" O.D.. Both muffle tube and the protective cup around the specimen are made of high—alumina (99.8% Al_2O_3) ceramic. This material has a good resistance to elevated temperatures, and is impervious to gases.

This concludes the description of the retort assembly. The next section is focused on describing the items needed for controlling the gas environment.

3.2.3 Gas Control System

A schematic of the water—cooling and gas control system is shown in Fig. 3.9. The purpose of the muffle tube and gas system is to control the gas environment during testing. For the present project the coal gasifier environment is simulated. Typical gases in coal gasifier units have low partial oxygen pressures (P_{O_2}) in the range of 10^{-7} to 10^{-8} atm. To achieve this P_{O_2} level a 5% NH_3/N_2 (i.e., 5% NH_3 + 95% N_2) mixture was selected, based on efficiency in attaining the selected P_{O_2}, cost, and toxicity (CO/CO_2 mixtures were used successfully by other researchers, but were judged too toxic for use in our lab environment). The muffle tube around the specimen provides a leak—proof environment up to $2800^{\circ}F$. The muffle tube is sealed at top and bottom by O—rings that are more than 7" (this distance was determined to be critical in order to keep the O—rings at reasonable temperatures) away from each end of the furnace. The O—rings are inside water—cooled chambers in order to keep their temperature down. The muffle tube is designed to withstand only small positive pressures. Therefore, the gas inside the muffle tube has to be kept at
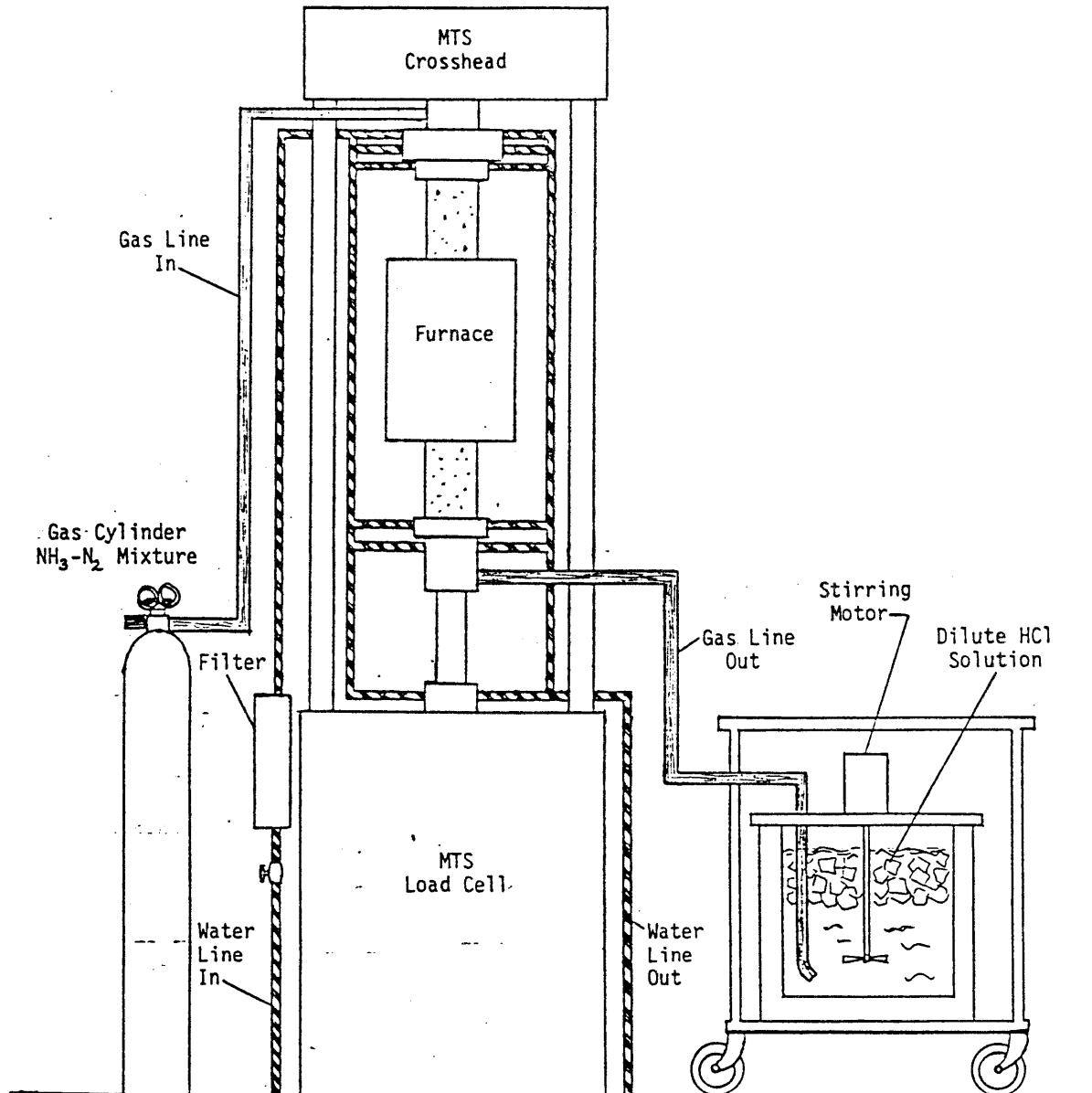
Figure 3.9   Schematic of water–cooling and gas control system

atmospheric pressure (i.e., 1 atm. or 14.7 psi). Two pressure relief valves are positioned at the gas inlet and outlet on each side of the muffle tube, and are set at 20 psi. This allows a small positive pressure build–up inside the muffle tube. The selected gas mixture exits from a high–pressure tank into a rotameter–type flowmeter which controls the flow rate. It, then, passes through the first pressure relief valve into the muffle tube, and exits the system from the bottom into the second pressure relief valve. These different components are shown in Fig. 3.10. Since the selected gas mixture (i.e., 5% NH_3/N_2) is toxic, the ammonia (NH_3) has to be filtered out during testing. An acid bubbler assembly was designed to achieve this purpose. The bubbler consists of a tank filled with a dilute solution of hydrochloric acid (HC1) in water, in which the outlet gas flows. The solution is stirred continuously, allowing an ammonium chloride salt (NH_4Cl) to form, and releasing nitrogen (N_2) into the atmosphere. Since the reaction is exothermic, ice was added to the bubbler. In order to protect the muffle tube from any reverse acid flow, a check valve is used before the acid bubbler. A suction pump was used in the early stages of testing in order to overcome the small pressure caused by the water in the acid bubbler. During production testing, however, a small positive pressure was maintained in the muffle tube to produce the same effect. The elements of the complete gas system are shown in Fig. 3.10. Brass and copper fittings and pipes are used, since they are resistant to corrosion by ammonia.

The gas system had to be tested, and the flow rate calibrated for achieving a P_{O_2} in the range of 10^{-7} to 10^{-8} atm. During testing the muffle tube is, first, filled with a 99.995% Helim (He) gas mixture, to drive most of the oxygen out from the system. Then, a mixture of 95% N_2 and 5% NH_3 (certified to one part per million) is circulated to produce reducing atmospheres according to the following reaction:

Pressure Relief
Valve

Flowmeter

Gas Mixture
N_2-NH_3
at
High Pressure

System
at
1 Atm

Stirring Motor

N_2 Out

Check Valve

Suction Pump

Ice

Acid Bubbler
Assembly

Dilute HCl Acid Solution

Pressure Relief
Valve
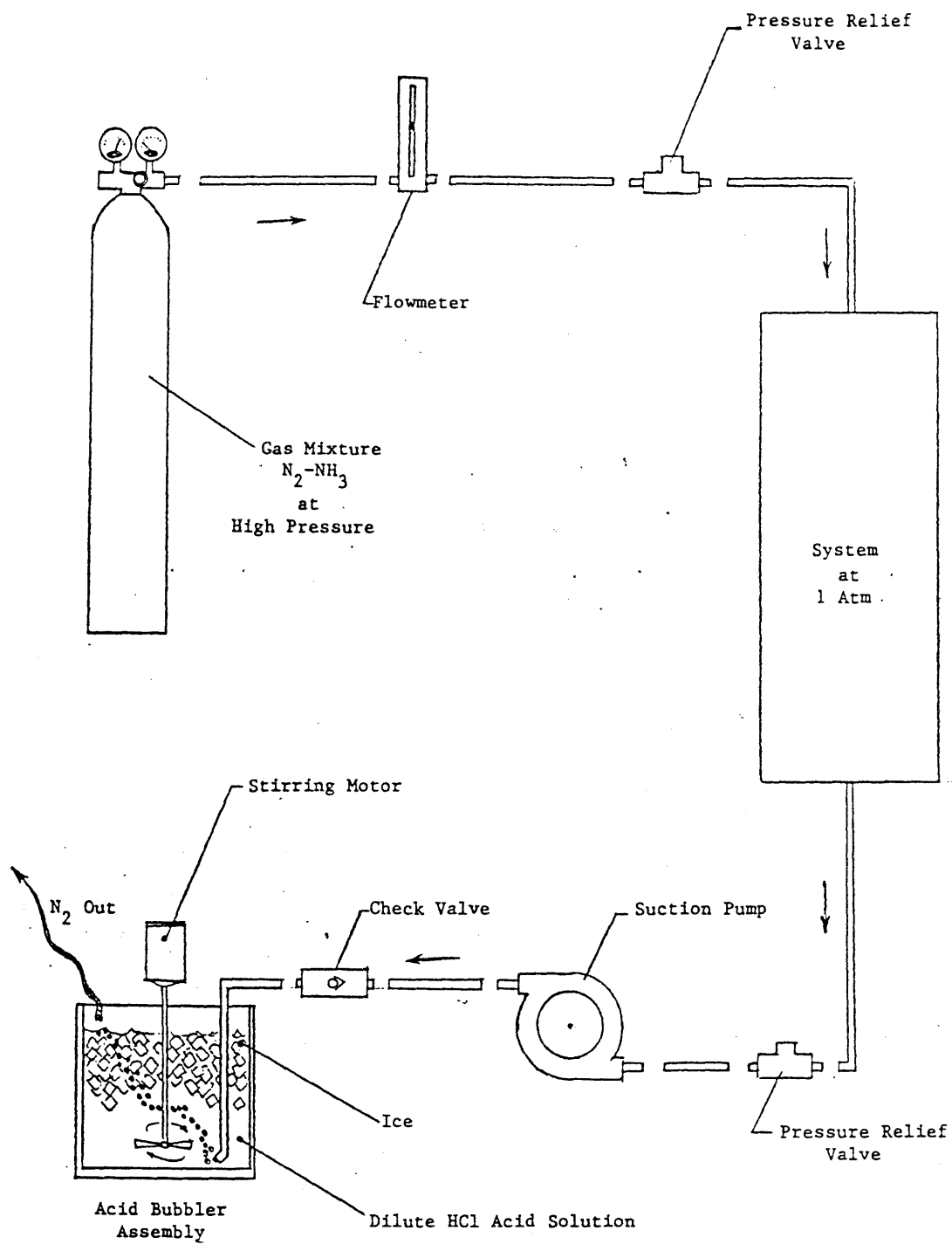
Figure 3.10   Components of the gas control system

$$2NH_3 + \frac{3}{2} O_2 \rightarrow 3 H_2O + N_2 \qquad\qquad (3.1)$$

This NH_3/N_2 mixture is harder to control than a CO/CO_2 mixture, but is less toxic and gives adequate P_{O_2} levels. To check for the actual P_{O_2} level in the muffle tube the gas was passed into a zirconia cell at elevated temperatures, and the voltage drop (between the walls of the zirconia cell in selected gas and air atmospheres) was used to calculate the achieved P_{O_2}. The setup is shown in Fig. 3.11. The zirconia cell is inside the furnace. The temperature of its heated end is constantly monitored by a thermocouple. The inside of the zirconia cell is in contact with the selected gas, while its outside is in air. The voltage drop between both sides is measured. Assuming that the zirconia (ZrO_2) is an ionic conductor and an electronic insulator, and that chemical reactions are fast, the P_{O_2} of the tested gas can be obtained from the following equation (Hein and Best, 1980):

$$(P_{O_2}) = (P_{O_2})_{ref} \exp(-4fV/RT) \qquad\qquad (3.2)$$

where T is the temperature, $(P_{O_2})_{ref}$ is about 0.2 atm. for air, V is the measured voltage, and R and f are constants. After testing the helium gas (99.995% pure) a P_{O_2} of 1.75×10^{-6} atm. was achieved after 14 minutes and stabilized around this value. After the P_{O_2} was stabilized for the helium the 5% NH_3/N_2 mixture was flushed into the system. A P_{O_2} as low as 1×10^{-13} atm. was attained. The desired P_{O_2} of 5×10^{-8} atm. is attained in about 20 minutes.

The auxiliary systems such as water cooling and attachments to the loading machine are discussed in the next section.
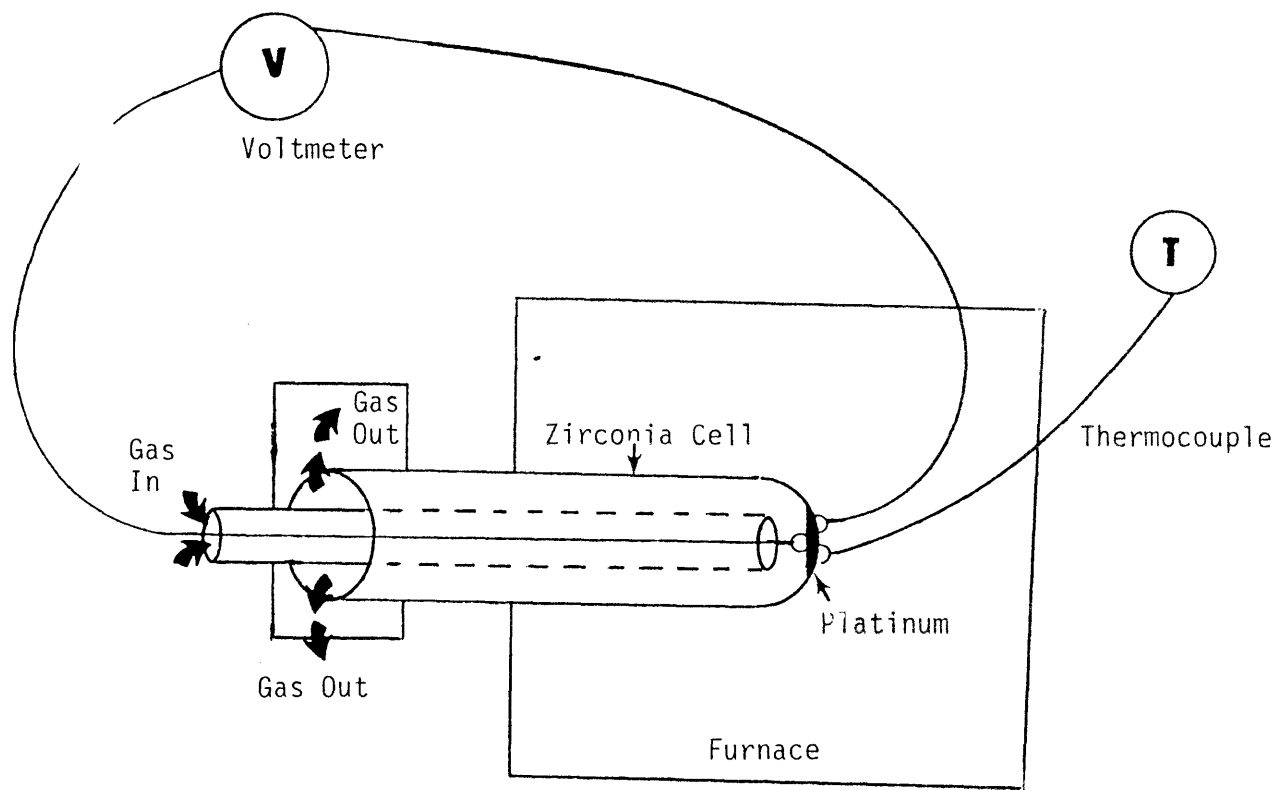
Figure 3.11   Set—up to calibrate partial oxygen pressure

3.2.4 Auxiliary Systems to the Retort Assembly

The water cooling system is efficient, and maintains temperatures in the stainless steel elements much below what was predicted. The water is filtered before entering the six separate cooling chambers. Cooling is done in parallel, which means that each element is cooled down separately. The water cooling piping is shown in Fig. 3.9. Water cooling of the stainless steel push rod, and the lower muffle tube chamber and the lower O—ring seat are shown in Figs. 3.5 and 3.6 respectively. The water cooling of the upper muffle tube chamber, the upper O—ring seat, and the top SiC connection are shown in Figs. 3.7 and 3.8. The dimensions, spacings, and locations of these chambers were modified throughout the whole design process to obtain the most efficient cooling, and the easiest assembly.

The last consideration to be addressed in the design of the thermomechanical system was its attachment to the loading frame. Figures 3.12 and 3.13 show a top view of the furnace clamps, and a side view of the complete clamping system. The furnace, retort assembly, and muffle tube are all clamped to a support rod which is anchored at the top and bottom to the loading frame. The support rod as shown in Fig. 3.12 is 10" away from the center of the loading piston, and 5.5" away from one of the columns of the loading machine. The support rod is fixed to the loading machine by assembly clamps. Four retort clamps and two furnace clamps allow the rotation of the whole system, and its assembly outside the loading frame table.

3.2.5 Data Acquisition and Control System

The components of the data acquisition and control system are shown in Fig. 3.1. The MTS loading frame can be operated manually using the control panel, or computer controlled using a PDP—11 computer with a dual disk drive. Programs are
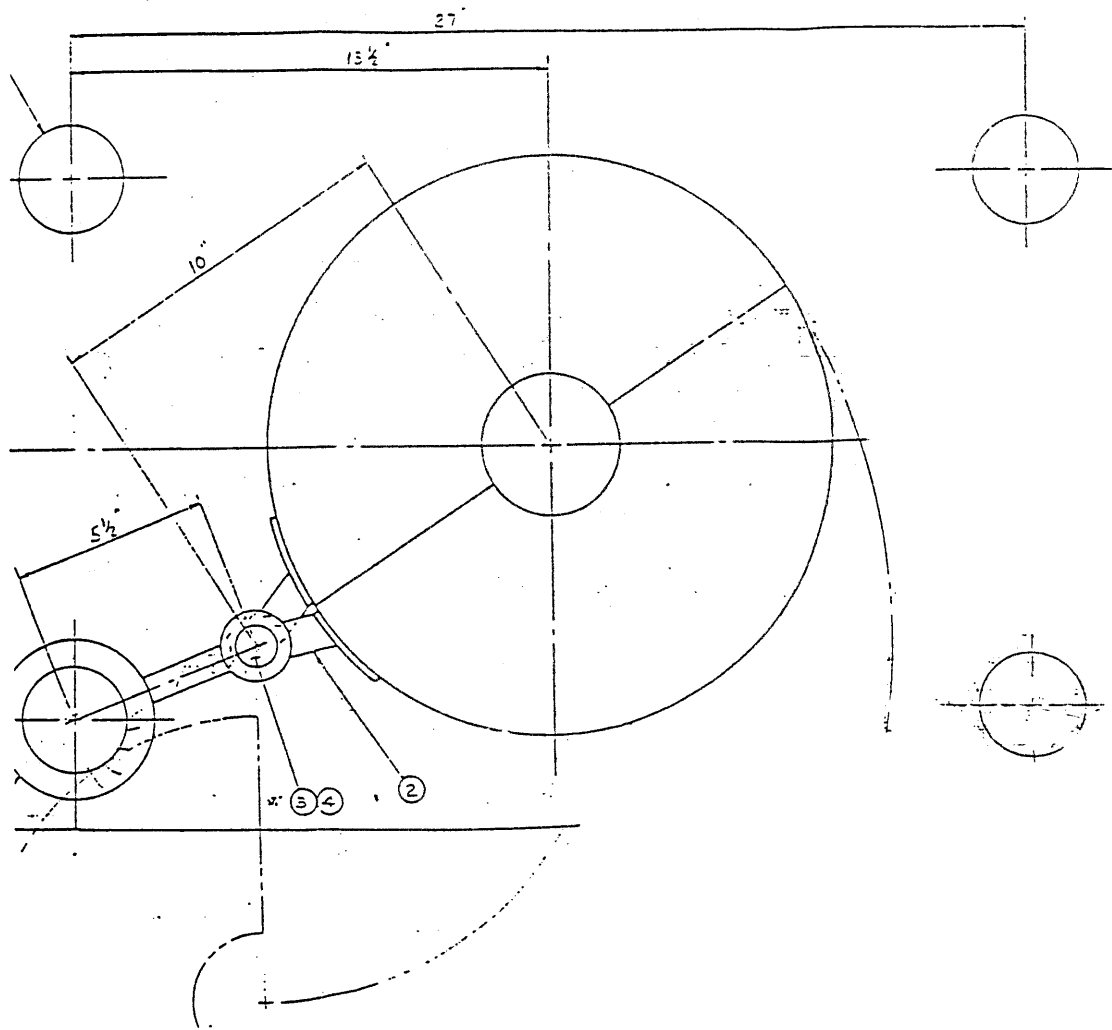
Figure 3.12   Furnace clamping system
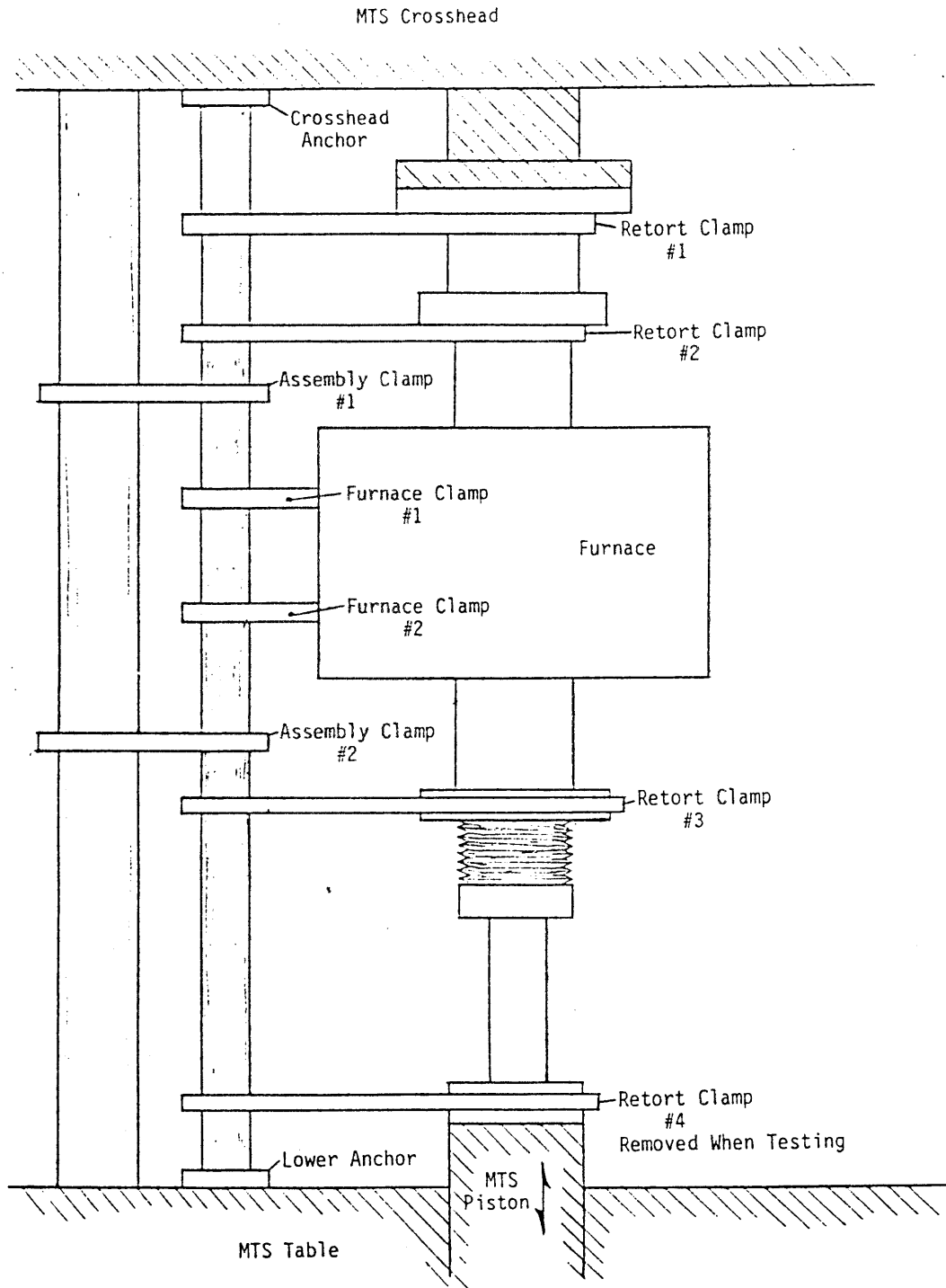
Figure 3.13   Complete clamping system — side view

fully developed for monotonic and cyclic loadings at elevated temperatures. The user can specify the displacement rate in monotonic displacement control test. For cyclic mechanical loads, the user can prescribe cycling between two fixed load levels. Cycling between two displacement levels, or cycling with a fixed load increment per cycle, has to be done manually. Constant load tests can also be carried out. The furnace temperature is controlled by a LFE 2010 microprocessor that can be operated manually or by inputting a program. The program accepts up to 8 different periods of heat up, soak, or cool down, that constitute a cycle. Cycling can be repeated up to 252 times. An accuracy of $\pm 1^{O}F$ on the soak temperature was achieved by proper calibration. The microprocessor should be recalibrated if any of the heating elements is changed, or if the test uses a different kind of thermocouple. Standard calibration has been established for Type B and Type K thermocouples. The PDP–11 computer is mainly used for control. It is fast and reliable. A Fluke 2400B intelligent front end linked to an IBM XT with one floppy disk drive, and a 20 megabytes hard disk provides accurate readings of test data. The disadvantage of the Fluke 2400B is its slower speed. The fastest time to acquire data is once per second. But it is more accurate, and provides easier access to spread sheets and curve fitting programs through the IBM PC software. User–friendly software has been developed for the Fluke–IBM XT data acquisition system. Results can also be displayed on XY recorders.

Additional information about the testing system can be found in Appendix D.

3.3 TESTING PROCEDURES UNDER SHORT—TERM COMPRESSIVE LOADS AT ELEVATED TEMPERATURES AND CONTROLLED GAS ENVIRONMENTS

The testing process consists of the following tasks:

o   material selection;

o   specimen preparation;

o   assembly of test equipment;

o   carrying actual tests; and

o   converting the test data to meaningful information.

For the purpose of this research, the selected testing materials are candidate refractory ceramics for coal gasifier linings. Standard specimen preparation procedures were developed for refractory ceramics extracted from a block. Specimen preparation procedures and block characterization tests are described at the beggining of Chapters 5, 6 and 7, for cold—pressed sintered, hot—pressed and fused—cast materials respectively. The assembly of the test equipment, the actual testing, and the conversion of the test data to useful information is similar for all materials, and is described in this section. The assembly of the test system is a time—consuming task. Care should be taken in both the specimen preparation and the system assembly stages in order to obtain relevant and useful results. Actual testing is a difficult and even physically demanding task. The system is usually heated—up and cooled—down at rates not exceeding $100^{\circ}F/hr.$ for the system with the muffle tube, and $250^{\circ}F/hr.$ for the system without the muffle tube. The temperature is maintained constant for two and one—half hours before applying a load in constant temperature tests, to insure temperature uniformity around the specimen. As a result, each test may be extending over a long period of time. In order to cut down on testing time, it is advisable to set up the system and carry a few tests before disassembling it.

Common problems that delay the testing process are water leaks (including pipe water bursting resulting in overheating and water flood); failure of ceramic loading rams (tubes or caps) under thermal or mechanical loads, or due to fatigue under repeated loads; failure of SiC heating elements; misuse or faulty calibration of control equipment; overheating of the hydraulic; electrical problems; chipping of the diamond corehead due to faulty handling; and wear of the diamond blade used to saw the test specimens. Maintenance of the equipment is important and include duties such as: replacing water filters, making sure ceramic parts are kept clean and not chipped, and cleaning core equipment and diamond blades after specimen preparation. During have to be carefully monitored to avoid any problems.

Five types of short–term compressive load tests are carried out on as–manufactured and slag–impregnated materials:

A — constant temperature, monotonically increasing load tests, in air atmosphere;

B — constant temperature, monotonically increasing load tests in reducing (low P_{O_2}) atmosphere;

C — constant temperature, cyclically varying load tests in air atmosphere;

D — constant load, constant temperature tests in air atmosphere; and

E — constant load, monotonically increasing temperature tests in air atmosphere.

Testing procedures for these test categories are described below:

A — <u>Short—term uniaxial monotonic compressive load tests at constant temperature in air atmosphere:</u> In these tests, the temperature was first raised to a predetermined constant level at a constant heating rate of 250°F/hour (121°C/hour) under no load, and maintained at that level for 2.5 hours before load application. Then the piston displacement was monotonically increased linearly with time until final fracture occurred. The applied load was measured. The specimen displacement was obtained by subtracting the system displacement from the measured piston displacement. The total displacement (system displacement and specimen displacement) rate is constant during the test. However, due to a non—linear variation of the system displacement and to a faster specimen displacement rate (compared to the system displacement) in the final stages of loading, the specimen displacement rate is not truly constant during the test. The data is sampled at small time intervals, such as every four seconds. The engineering strain is calculated from the specimen displacement, and the strain rate between each sampled data is obtained. The strain rate is also not constant during the test, but the variation is not large. An average strain rate from start to end of test is taken as a measure of the test. The discussion of strain rate effects uses this average strain rate. Tests were conducted at the following constant temperature levels: 75°F (24°C), 500°F (260°C), 1000°F (538°C), 2000°F (1093°C), 2200°F (1204°C) and 2400°F (1316°C). Different displacement rates were used in order to assess rate effects: 1.444×10^{-5} in/sec (3.667×10^{-4} mm/sec), 7.218×10^{-5} in/sec (18.33×10^{-4} mm/sec), and $21.65 \times$

10^{-5} in/sec (55×10^{-4} mm/sec). In a typical test failure was obtained in approximately 10 minutes from start of the loading. After failure of the specimen, the constant temperature is maintained for 5 more minutes before the temperature is cooled down to the level of room temperature at a cooling rate of 250°F/hour.

B — Short—term uniaxial monotonically increased compressive load tests at constant temperature in controlled reducing (low P_{O_2}) atmospheres: In these tests, the temperature was first raised at a heating rate of 100°F/hour (38°C/hour) with no load, and maintained constant for 2.5 hours before load application. The system was first flushed with a 99.995% pure helium gas for 14 minutes, then a 5% NH_3–95% N_2 mixture was circulated for 18 minutes. A P_{O_2} of 10^{-8} atm. was reached. The mechanical load application was similar to the one described in Category A.

C — Short—term uniaxial compressive cyclic load tests at constant temperature in air: In these tests, the temperature application was similar to that in Category A. The load was then varied between zero and a constant load level following a preset haversine pattern, at frequencies in the range of 10^{-3} to 10^{-4} Hz. The constant load level used in testing was in the range of 70% to 95% of the strength obtained from monotonic loading tests. In preliminary tests at room temperature, two other types of mechanical load applications were tried: cycling with a fixed load increment per cycle under load control, and cycling between two fixed displacement levels in displacement control.

D — <u>Short—term uniaxial constant compressive load tests (short—term creep) at constant temperature in air</u>: In these tests, the temperature application was similar to that in Category A. A constant temperature level was achieved first. Then, the load was monotonically increased to a constant load level in the range from 50% to 75% of the material strength in monotonic testing, and kept constant at this level. The tests were conducted at constant predetermined temperature levels. Four constant temperature levels were used: $73^{\circ}F$ $(23^{\circ}C)$, $1500^{\circ}F$ $(816^{\circ}C)$, $2000^{\circ}F$ $(1093^{\circ}C)$, and $2400^{\circ}F$ $(1316^{\circ}C)$. Strain variation with time during the application of the constant load was obtained. Duration of these short—term creep tests was less than 5 hours.

E — <u>Short—term uniaxial constant compressive load tests (short—term creep) at increasing temperatures in air</u>: With these tests the load was first applied following the same procedure described for the test in Category D. The temperature was then increased from room temperature to $2400^{\circ}F$ $(1316^{\circ}C)$ at heating rates from $100^{\circ}F/hour$ $(38^{\circ}C/hour)$ to $250^{\circ}F/hour$ $(121^{\circ}C/hour)$. The strain rate variation with time was monitored during the duration of each test.

3.4 EQUIPMENT FOR MICROSTRUCTURAL CHARACTERIZATION

In this section the equipment used for microstructural characterization of the virgin and tested refractories is described. The different types of microscope that were used are described in Section 3.4.1; these include the stereoscopic and Nomarski optical microscopes and the scanning electron microscope along with the X—ray diffraction capability. The mercury porosimeter is described in Section 3.4.2, and the

method for dry bulk density measurements is described in Section 3.4.3.

3.4.1 Optical and Scanning Electron Microscopes

Two different optical microscopes were used for this study: a regular stereoscopic microscope and a Nomarski microscope. The principles of operation of light microscopes is well—known and will not be discussed here. The stereoscopic microscope uses reflected light, while the Nomarski microscope uses polarized light. In the Nomarski microscope the beam of light is split in two producing a differential interface contrast (DIC) that allows to observe the surface details much better. The Nomarski microscope allows magnifications up to 1500X. The operation and principles of the scanning electron microscope are described in more detail.

The first commercial scanning electron microscope (SEM), the Cambridge Stereoscan MK1, was introduced in 1964 [Watt, 85]. Nowadays, the SEM is currently being used in a wide range of applications. These include [Newbury et al, 1986]:

1. The electronics industry which is one of the principal user of SEMs, with nearly half of all new SEMs being used for semiconductor applications; the SEM is especially popular because it allows the operation of switches, transistors, and integrated circuits to be observed under conditions close to the operating ones;

2. Structural materials; recent SEMs allow the observation of the microstructural characteristics during the application of small mechanical loads on the material;

3. Characterization of biological and organic samples; this is a relatively new and rapidly evolving field; and

4. Cyromicroscopy where the materials are examined at temperatures below $O^{O}C$ ($273^{O}K$); this presents several advantages in the preparation, examination, and analysis of organic samples.

Theoretical Basis of SEM

In SEM, a fine probe of electrons, with a diameter of 7 to 10 nm, and energies up to 35 KeV is focused on the surface of the specimen. The probe scans the surface in a series of parallel lines (raster). Under electron impact, secondary electrons with energies of a few tens of eV are emitted, and high energy backscattered electrons are reflected from the primary beam. The intensity of emission is sensitive to the angle at which the electrons hit the surface. This allows for detection of topographical features. The electrons are then collected, the resulting signal is amplified, and the variations in intensity of the signal are used to vary the brightness of the trace on a cathode ray tube.

Different kinds of interactions are generated when the primary electron beam with energies up to 35 KeV strikes the specimen surface. These are:

1. Secondary Electrons which have a low energy, tens of eV, and originate from the collision of the high energy electrons with the specimen atoms;

2. Backscattered Electrons that have high energy ranging from the primary beam energy to the secondary electrons energy level, and are reflected from the specimen surface;

3. X–ray Photons with wavelength and energy characteristics of the elements in the specimen, are emitted under electron bombardment;

4. Transmitted Electrons which go through the specimen if it is thin enough, and are deflected from the main beam direction and have lost energy due to collisions;

5.   <u>Auger Electrons</u> that have energies up to 1 to 2 KeV, and are characteristic of the surface elements;

6.   <u>Cathodoluminescence</u> which is due to the emission of light from the specimen; and

7.   <u>Absorbed Current</u> which is generated by the electrons remaining in the specimen.

For the purpose of this study, the first three types of interactions are the ones that are particularly interesting. The secondary and backscattered electrons are used to show surface features and qualitative compositional information. The X—ray photons are used for qualitative and quantitative analysis of the specimen's elemental composition.

The JEOL SEM

A JEOL scanning electron microscope at Harvard University was used for this study. The SEM column consists of the following:

1.   A high voltage cable;

2.   An electron gun with a tungsten (W) filament. The W—filament usually lasts 100 hours, and is heated up to $2800^{\circ}K$. The accelerated electrons have an energy of 35 KeV for surface characterization and of 25 KeV for X—ray microanalysis;

3.   The anode;

4.   A magnetic shield;

5.   Deflection coils that are used for axis alignment;

6.   A valve that serves as an airlock for the anode chamber;

7.   The condenser lens;

8.   The objective lens;

9.   The objective lens aperture;

10.   A scanning coil that tilts the electron probe. The tilting takes place about a point in the plane of the final aperture;

11.   A deflection coil for image correction;

12.   A stigmator coil and an astigmatism monitor coil for correcting astigmatism;

13.   The secondary electron detector to the right of the specimen;

14.   Two backscattered electron detectors above the specimen; and

15.   The specimen on its stage.

The working distance and magnification for the SEM are as follow:

o   Working distance: The JEOL can operate at two working distances: 15mm and 39mm. The advantage of each will be discussed later; and

o   Magnification: It is the ratio of a dimension, d, on the specimen to the same dimension shown as D on the CRT. The JEOL has magnifications from 10X to 90,000X at a working distance of 39 mm, and magnifications from 20X to 180,000X at a working distance of 15 mm.

The JEOL SEM can be operated in two modes: secondary electron or backscattered electron detection. In the backscattered electron detection mode, the two detectors above the specimen are used. If the signals from both detectors are added the signal is proportional to the composition of the specimen, while if the two signals are subtracted the signal is proportional to the topography of the specimen.

A comparison between the SEM and the light microscope is given next.

Comparison of SEM with Light Microscopes

The advantage of the stereoscopic microscope compared to the Nomarski and SEM is that colors can be observed, allowing for easy differentiation between phases. In our case this was helpful; for example it allowed us to differentiate between chromia grains that have a pink color, alumina grains that have a white color, and the alumina—chromia solid solution that has a brown color.

In the Nomarski it is more difficult to obtain a sharp contrast between different phases due to the polarized light. In the SEM, the different phases can be differentiated using backscattered electrons in the compositional mode.

The advantage of both stereoscopic and Nomarski microscopes compared to the SEM, is that a microstructural study can be performed in a smaller amount of time. It was found helpful to have started the microstructural characterization on the light microscopes first, because it gives a feel for the results. It would be advisable, whenever possible, to conduct a preliminary study on the Nomarski before going to SEM. This would result in saving both time and money.

The advantages of the SEM over light microscopes are numerous:

1. Higher magnifications (180,000X at a working distance of 15mm on SEM, compared to 1,500X on Nomarski);

2. Smaller wavelengths can be obtained in SEM that give higher resolution. The wavelength is determined by the voltage.

3. The beam probe size can be made smaller to improve the resolution as well. The probe size is dependent on the strength of the condenser lens.

4. At the same magnification, the SEM has a larger depth of focus than the light microscopes. This results in easier focusing on SEM.

5. The depth of field is also larger on SEM.

6. On the SEM, it is possible to obtain qualitative and quantitative information of elemental composition by using X—ray microanalysis.

7. By combining secondary electron and backscattered electron detection using compositional and topographical mode, the same area of the specimen can be fully characterized for different features. This is not possible on the same light microscope. However, by combining the stereoscopic and Nomarski light microscopes, the same information can be obtained.

8. The stereoscopic light microscope lenses have to be corrected for chromatic abberation.

Lessons Learned from SEM Experience

Based on the experience gained from using the SEM in the context of this project the following observations were made:

1. It is easier to focus at smaller apertures. This is because at smaller apertures the depth of focus is larger;

2. It is easier to focus at the 39mm working distance than at the 15mm working distance. This is also explained by the fact that the depth of focus is larger at 39mm working distance; however, at 15mm working distance, the magnifications are larger.

3. Use lower condenser lens strength at lower voltages to increase the probe size in order to obtain a clear image.

4. Choose sharp corners or round pores to adjust SEI brightness and contrast.

5. The signal to noise ratio should be at least higher than 2. In observing

the pore structure of a slag–impregnated ceramic at the second object aperture (240μm) the S/N ratio was very small, and the picture was not clear. In order to get a clear picture, the objective aperture was changed to the largest one (600μm). This resulted in more electrons being collected, a greatly improved S/N ratio, and a much clearer picture.

6.   There is a limit of magnification for each objective aperture. For the largest objective aperture (600μm), specimens cannot be observed at magnifications higher than 10,000X, even if the condenser lens is reduced a lot.

7.   In X–ray microanalysis, there is a need to correct for overlapping peaks. For example, in the material studied the 'K$_\alpha$' peaks for Al and Si, overlapped with the 'M' peak for Au.

3.4.2 Mercury Porosimeter

The mercury porosimeter is used to characterize the material's open porosity which is representative of the pores that are connected together. Although the open porosity does not give an information about the total porosity, it is useful since it allows a qualitative understanding of the variation of the open pores before and after testing under different testing conditions. The specimen is inserted in a chamber under vacuum that is filled with mercury (Hg). Then, the inner pressure in the chamber is linearly increased, and the volume change is recorded. This volume change is equal to the amount of mercury that penetrated inside the material pores. The pressure can be related to the pore radius, in order to obtain a relation between pore radius and intruded volume. Assuming that the pores are cylindrical with

circular entrances, and that the surface tension and contact angle do not vary with pressure, the following equation can be used:

$$P\,r\,=\,2\,\gamma\,|\cos\theta| \qquad (3.3)$$

where P is the mercury pressure, r is the pore radius, γ is the surface tension, and θ is the contact angle. This shows that for the imposed linear variation of mercury pressure with time a corresponding non–linear variation in the radius of intruded pores is expected. For interpreting the test results, 480 dyne cm^{-1} was used for γ, and 140° was used for the wetting angle (roughly correct for most materials). The first result from the tests is a cumulative distribution curve of pore radius versus volume intruded. The different information that can be obtained from the curve are the total amount of open porosity, the mean pore radius, and the pore size distribution. Other information can also be obtained from the porosimeter tests such as the surface area which is given by:

$$S = \frac{1}{\gamma\,\cos\theta} \int_{0}^{V} P\,dV \qquad (3.4)$$

It can be noted that Eq. (3.4) represents the area above the intrusion curve. During depressurization some mercury stays entraped in the pores, and as a result the depressurization curve is not the same as the pressurization curve. The deprussurization curve does not have a practical use.

3.4.3 Density Measurements

As a last step in the material characterization process, the density of the specimen before and after testing is measured. A setup to measure the specimen dry bulk density was used. The dry weight, W, of the specimen is first measured. Then the specimen is dipped into molten parafin, and taken out with a "wax skin" around it. Its weight with the wax around it, W_1, is noted. Finally it is immersed in water,

and the immersed weight, W_2, is measured. The bulk density of the specimen is:

$$\rho_{specimen} = \frac{W}{\dfrac{W - W_2}{\rho_{water}} - \dfrac{W_1 - W}{\rho_{parafin}}} \tag{3.5}$$

For the parafin used, and all the weights expressed in gm/cc, this gives:

$$specimen\ density = \frac{W}{1.1236\ W - (0.1236\ W_1 + W_2)} \tag{3.6}$$

3.5 SUMMARY

A testing system was designed and built for compressive loading up to 50,000 lbs, at high temperatures up to 2800°F, under controlled gas environments down to measured P_{O_2} of 10^{-13} atm. The loading rams and heating elements can resist the action of corrosive gases, and the loading rams can resist the attack of molten slags. Various combinations of temperature and mechanical load histories can be applied. The achieved temperature of the microprocessor controlled furnace is within ±1°F of the setpoint, and the observed temperature discrepancy between the top and middle of a 3" specimen is 3°F. The retort system was designed to achieve a leak–proof environment inside an alumina muffle tube at 2800°F, and allow more than 1" of deformation in the specimen using a bellows assembly. The gas control system includes safety fixtures and an acid bubbler for toxic gases. Water cooling of the different parts is done in parallel for efficiency. Loading clamps were designed to assemble the 52" long retort system (with a maximum unassembled height of 75") outside the 56" height loading platform, and swing it in place. The data acquisition and control system consists of an intelligent front end linked to a personal computer,

and of a minicomputer. The testing procedures under compressive loading, high temperatures, and controlled gas environments were standardized.

For microstructural observations an optical stereoscopic microscope, a Nomarski optical microscope, and a scanning electron microscope were used with practical maximum magnifications of 40X, 1500X, and 180,000X. The optical stereoscopic microscope was preferred to observe color features. The Nomarski optical microscope was used to conduct a characterization of the surface features for cold—pressed sintered materials and a rough characterization of the surface features of the hot—pressed and fused—cast materials. The use of the Nomarski microscope is advised to cut the time spent using the scanning electron microscope. The scanning electron microscope was used for a better resolution of surface details and for the observation of finer microstructures. X—ray diffraction was used to characterize the interaction of cold—pressed sintered materials with slags, and the chemical composition of other materials. Setups to measure the open porosity and the dry bulk density of the specimens before and after testing were also used.

CHAPTER 4
MATERIALS AND TESTING PROGRAM

4.1 SYNOPSIS

The materials used for testing, and the testing program are described in this Chapter. The materials tested are refractory ceramic oxides that are being used, or are possible candidates for use, in high temperature refractory brick–mortar linings. These materials are described in Section 4.2. The test program for specimen preparation, block characterization, and high temperature testing is described in Section 4.3. The tests carried out for microstructural charcterization of virgin and tested materials are summarized in Section 4.4.

4.2 MATERIALS TESTED

The materials tested are high–alumina and high–chromia refractory ceramic oxides. The high–alumina materials were chosen for their good resistance to thermal shock (Bandyopahyay et al., 1983). The high–chromia materials were chosen for their known resistance to corrosion by slags (Bakker et al., 1984; Bonar et al., 1980; Kennedy, 1980; Washburn, 1982). They are low–silica containing refractories to resist hydrogen attack, and carbon monoxide disintegration. The materials were received as refractory blocks from the various manufacturers, and the specimens were extracted for testing. The materials tested were either as–manufactured or slag–impregnated. Fourteen different materials were acquired for testing. Seven of these were only used for specimen preparation and block characterization at room temperature. The other seven were used for both block characterization and

high–temperature testing. The materials that were used for specimen preparation, block characterization and thermomechanical testing are shown in Table 4.1, while the materials that were used only for block characterization are shown in Table 4.2. All of the fourteen different materials shown are refractory ceramic oxides used for different high–temperature applications. These materials are possible candidates for use in slagging coal gasifiers. The materials are manufactured using three different manufacturing processes: cold–pressing and sintering, hot–pressing, and fusion–casting. The first manufacturing process, cold–pressing followed by sintering, involves room temperature pressing of a powder and then firing it to high temperatures. The sintering process is carried out at temperatures that vary from 50% to 80% of the melting temperature (T_m). The hot–pressing method involves higher pressures and lower temperatures than the sintering process. In the hot–pressing method the powder is compacted under high pressure while being fired. In the third process, fusion–casting, the powder is melted and then poured into a mold where it solidifies during cooling. These three different manufacturing processes are used to produce a large range of bricks for high temperature applications. The cold–pressed sintered, hot–pressed, and fused–cast materials are referred to as CPS, HP, and FC respectively. Three oxides in the chemical composition are used to differentiate the different materials: Al_2O_3, Cr_2O_3 and MgO are referred to by A, C and M respectively, preceded by the oxide's percentage in the chemical composition. For example, a hot–pressed alumina–chromia containing 90% Al_2O_3 and 10% Cr_2O_3 in the chemical composition is referred to by HP–90A–10C. Tables 4.1 and 4.2 show the different materials used, their chemical composition, the manufacturing process used to produce them, their apparent porosity, open or closed pores, and their density.

Material Classifi-	Chemical Composition	Manufacturing Process	Testing of Slag Impregnated	%Apparent Porosity	Closed Pores	Density (g/cc)
CPS-90A-10C	$90\%Al_2O_3.10\%Cr_2O_3$	Cold Pressing and Sintering	Yes	17	No	3.30
CPS-82C-18M	$82\%Cr_2O_3.18\%MgO$	Cold Pressing and Sintering	Yes	12	No	3.80
HP-90A-10C	$90\%Al_2O_3.10\%Cr_2O_3$		No			
HP-50A-50C	$50\%Al_2O_3.50\%Cr_2O_3$	Hot-Pressing	No	4	Yes	
HP-25A-75C	$25\%Al_2O_3.75\%Cr_2O_3$		No			
HP-80C-20M	$80\%Cr_2O_3.20\%MgO$	Hot-Pressing	No	8	Yes	
FC-8A-78C	$78\%Cr_2O_3.8\%Al_2O_3$	Fusion-Casting	No	5	Yes	

Table 4.1 Materials for Thermomechanical Testing

Material Classifi-	Chemical Composition	Manufacturing Process	%Apparent Porosity	Closed Pores	Density (g/cc)
CPS-16A-62C	$62\%Cr_2O_3$, $16\%Al_2O_3$ $12\%ZrO_2$, $7\%SiO_2$	Cold-Pressing and Sintering	13	No	3.75
CPS-9A-81C	$81\%Cr_2O_3$, $9\%Al_2O_3$ $6\%ZrO_2$, $2.5\%SiO_2$	Cold-Pressing and Sintering	13	No	4.00
CPS-23A-75C	$75\%Cr_2O_3$, $23\%Al_2O_3$	Cold-Pressing and Sintering	15.9	No	4.00
CPS-80C-18.5M	$80\%Cr_2O_3$, $18.5\%MgO$	Cold-Pressing and Sintering	13	No	3.85
CPS-79C-19.5M	$79\%Cr_2O_3$, $19.5\%MgO$	Cold-Pressing and Sintering	14-18	No	3.7-3.9
FC-15A-83C	$83\%Cr_2O_3$, $15\%Al_2O_3$	Fusion-Casting	5	Yes	
FC-50A-28C	$28\%Cr_2O_3$, $50\%Al_2O_3$	Fusion-Casting	4	Yes	

Table 4.2 Materials for Block Characterization Only

The main emphasis of thermomechanical testing concentrates on the materials shown in Table 4.1: Materials CPS–90A–10C, CPS–82C–18M, HP–90A–10, HP–50A–50C, HP–25A–75C, HP–80C–20M, and FC–78A–8C.

Material CPS–90A–10C is produced by cold–pressing and sintering, and is composed of 90% Al_2O_3 and 10% Cr_2O_3, forming a solid solution with 17% open pores. It has some lattice structure. There is no free Al_2O_3 or Cr_2O_3 present. There are two minor phases present: coarse Al_2O_3 penetrated by Cr_2O_3 exhibiting a white color, and finer Cr_2O_3 grains penetrated by Al_2O_3 exhibiting a pink color. Minor impurities consist of small percentages of SiO_2, Fe_2O_3, K_2O and Na_2O. Its average bulk density is 206 lbs. per cubic foot (3300 kilogram per cubic metre). The manufacturer's suggested maximum use temperature is 3450^OF. The phase diagram for the α–Al_2O_3–Cr_2O_3 system is shown in Fig. 4.1 (Bunting, 1931). For a 90%Al_2O_3–10%Cr_2O_3 system, no change is observed for temperatures below roughly 3730^OF (2055^OC).

Material CPS–82C–18M is produced by cold–pressing and sintering and is composed of 82% Cr_2O_3 and 18% MgO. It has 12% open pores. It is mostly picrochromite (MgO.Cr_2O_3), and free Cr_2O_3 exists as a second phase. Impurities consist of Al_2O_3, Fe_2O_3, SiO_2, CaO and TiO_2. It has a spinel structure. Its average bulk density is 235 lbs. per cubic foot (3800 kilogram per cubic metre). The manufacturer's suggested maximum use temperature is 3272^OF. The phase diagram for the MgO–MgCr$_2$O$_4$ system is shown in Fig. 4.2 (Alper et. al., 1964). In the case of CPS–82C–18M no free MgO is found in the product because of the excess chromia.

Three hot–pressed alumina–chromia materials are tested: HP–90A–10C, HP–50A–50C, and HP–25A–75C, composed of 90% Al_2O_3, 50% Al_2O_3, and 25% Al_2O_3, with the balance of Cr_2O_3 respectively. They have 4% closed pores. They
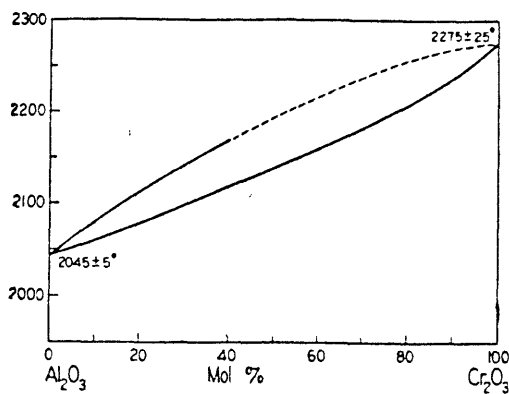
Figure 4.1   Phase diagram for the α–Al_2O_3 – Cr_2O_3 system (Bunting, 1931)
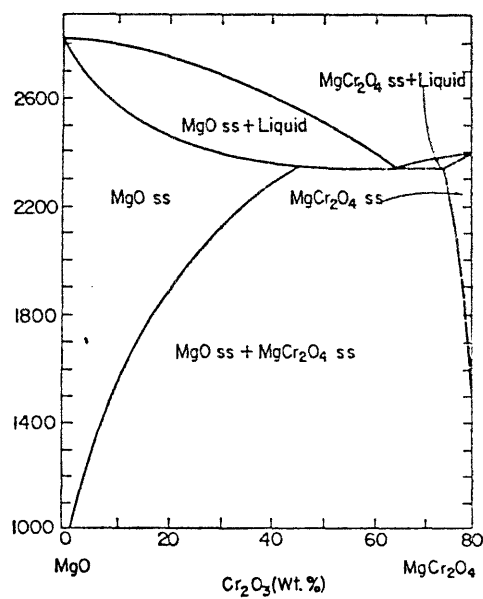
Figure 4.2   Phase diagram for the MgO – $MgCr_2O_4$ system (Alper et al, 1964)

are constituted of a solid solution of alumina–chromia with no second phase.

A hot–pressed chromia–magnesia refractory with 80% Cr_2O_3 and 20% MgO, and 8% closed pores is tested as well.

Finally a fused cast high–chromia (78% Cr_2O_3, 8% Al_2O_3) with 5% apparent porosity is also used.

4.3 THERMOMECHANICAL TESTING PROGRAM

The thermomechanical testing program focuses on uniaxial compressive load tests at high temperatures under controlled gas environments. The testing program is divided into two parts. The first part of the testing program is constituted of preliminary tests carried out for specimen preparation and block characterization. These tests were used to establish standard procedures for preparing refractories extracted from a block, for use in compressive short–term tests under elevated temperatures and controlled gas environments. The second part of the testing program is carried out on specimens prepared according to the standard specimen preparation procedures developed from the preliminary testing. The tests performed are short–term uniaxial compressive load tests at room and elevated temperatures in controlled gas environments.

In this section the testing program for short–term uniaxial compression tests at elevated temperatures on the selected refractory materials shown in Table 4.1 is discussed. These tests represent final tests. Preliminary tests that were carried out to standardize specimen preparation procedures and to characterize refractory blocks behavior are discussed at the beginning of Chapters 5, 6 and 7 for cold–pressed sintered, hot–pressed, and fused–cast refractories respectively and are not included in the following summary.

All tests are short term uniaxial compression tests and they fall into five different categories:

Category A   Increasing mechanical loads to failure, in displacement control mode, under constant pre–selected temperatures in the range of 70°F to 2500°F, in air atmosphere;

Category B   Increasing mechanical loads to failure, in displacement control mode, under constant pre–selected temperatures in the range of 70°F to 2400°F, in reducing gas atmosphere (P_{O_2} in the range of 10^{-7} atm. to 10^{-8} atm.).

Category C   Cyclic mechanical load tests between two fixed load levels, in load control mode, under constant pre–selected temperatures in the range of 70°F to 2400°F, in air atmosphere.

Category D   Constant load between 70% of f_p (where f_p is the strength in monotonic tests) to 95% of f_p, under constant pre–selected temperatures in the range of 70°F to 2400°F, in air atmosphere; and

Category E   Constant mechanical load between 70% of f_p to 95% of f_p, under increasing temperature at different heating rates, in air atmosphere.

Each test category represents several cases, that are summarized in Table 4.3. Each test has been performed between one to four times, to confirm the results. A detailed description of the test conditions follows.

Category A: Controlled Monotonically Increasing Displacement Tests,
   in Air Atmosphere

1.   Material CPS–90A–10C As–Manufactured

   (a)   Displacement rate = 0.00183 mm/sec.
      Temperature levels = 75°F, 500°F, 1000°F, 1500°F,
      2000°F, 2200°F, 2440°F

Short-Term Uniaxial Compression Tests				
Displacement Control. Linear variation with time	Load Control. Haversine variation with time		Load Control. Fixed constant level with time	
Average $\dot{\epsilon}$ is in the range $10^{-4}\,\text{sec}^{-1}$ to $10^{-6}\,\text{sec}^{-1}$	f in the range 10^{-3} - 10^{-4} Hz	$\dot{\epsilon}$ is a test result	Heating rates: 100 to 250°F/hr	
Constant T in the range 70°F to 2500°F			Increasing T from 70° to 2400°F	
Monotonic P to failure	Cyclic P up to 75% f_p to 90% f_p		Constant P between 55% f_p to 85% f_p	
Air	$P_{O_2} = 10^{-8}$ atm.	Air	Air	
CATEGORY	A	B	C	D	E
Mat. CPS-90A-10C As-Manufactured	X	X	X	X	X
Mat. CPS-90A-10C Slag-Impregnated	X	X			
Mat. CPS-82C-18M As-Manufactured	X	X	X	X	
Mat. CPS-82C-18M Slag-Impregnated	X	X			
Materials HP-90A-10C HP-50A-50C HP-25A-75C As-Manufactured	X X X			X	
Material HP-80C-20M As-Manufactured	X				
Material FC-78C-8A As-Manufactured	X			X	

$\dot{\epsilon}$ – strain rate
P – mechanical load
P_{O_2} – partial oxygen pressure

f – cyclic test frequency
T – temperature
f_p – monotonic material strength

Table 4.3   Thermomechanical Test Program Under Current Project

(b)   Displacement rate = 0.000367 mm/sec.

Temperature levels = 1500°F

(c)   Displacement rate = 0.0055 mm/sec.

Temperature levels = 2440°F

2.   Material CPS–90A–10C Slag–Impregnated

Displacement rate = 0.00183 mm/sec.

Temperature levels = 75°F, 1000°F, 1500°F, 2000°F, 2200°F, 2400°F

3.   Material CPS–82C–18M As–Manufactured

(a)   Displacement rate = 0.00183 mm/sec.

Temperature levels = 75°F, 500°F, 1000°F, 1500°F, 2000°F,

2275°F, 2400°F

(b)   Displacement rate = 0.000367 mm/sec.

Temperature levels = 2000°F, 2275°F

(c)   Displacement rate = 0.0055 mm/sec.

Temperature levels = 2275°F

4.   Material CPS–82C–18M Slag–Impregnated

Displacement rate = 0.00183 mm/sec.

Temperature levels = 75°F, 1200°F, 1500°F, 2200°F

5.   Material HP–90A–10C As–Manufactured

Displacement rate = 0.00183 mm/sec.

Temperature levels = 75°F, 1500°F, 2000°F, 2340°F

6.   Material HP–50A–50C As–Manufactured

Displacement rate = 0.00183 mm/sec.

Temperature levels = 75°F, 1500°F, 2000°F

7.   Material HP–25A–75C As–Manufactured

Displacement rate = 0.00183 mm/sec.

Temperature levels = 75°F, 1500°F, 2000°F, 2400°F

8. Material HP–80C–20M As–Manufactured

Displacement rate = 0.00183 mm/sec.

Temperature levels = 75°F, 1000°F, 1500°F, 2350°F

9. Material FC–8A–78C As–Manufactured

Displacement rate = 0.00183 mm/sec.

Temperature levels = 75°F, 1500°F, 2000°F, 2270°F, 2390°F

Category B: Controlled Monotonically Increasing Displacement Tests
in Reducing Atmosphere ($P_{O_2} \approx 10^{-8}$ atm.)

1. Material CPS–90A–10C As–Manufactured

Displacement rate = 0.00183 mm/sec.

Temperature levels = 75°F, 1000°F, 1500°F, 2000°F

2. Material CPS–90A–10C Slag–Impregnated

Displacement rate = 0/.00183 mm/sec.

Temperature levels = 1000°F, 1500°F, 2200°F

3. Material CPS–82C–18M As–Manufactured

Displacement rate = 0.00183 mm/sec.

Temperature levels = 75°F, 1000°F, 1500°F, 2000°F

4. Material CPS–82C–18M Slag–Impregnated

Displacement rate = 0.00183 mm/sec.

Temperature levels = 1200°F, 1500°F, 2200°F

Category C: Controlled Cyclically Varying Load Tests, in Air

         Atmosphere

1.   Material CPS–90A–10C As–Manufactured

    (a)   Temperature level: 75^OF

        Maximum cyclic load levels: 75% f_p, 80% f_p, 90% f_p

        Frequency: 10^{-3} Hz

    (b)   Temperature level: 1500^OF

        Maximum cyclic load levels: 75% f_p, 80% f_p, 90% f_p

        Frequency: 10^{-3} Hz

    (c)   Temperature level: 2400^OF

        Maximum cyclic load levels: 75% f_p, 90% f_p

        Frequency: 10^{-3} Hz

2.   Material CPS–82C–18M As–Manufactured

    Temperature level: 75^OF

    Maximum cyclic load levels: 73% f_p, 77% f_p, 88% f_p, 92% f_p, 95% f_p

    Frequency: 10^{-3} Hz

Category D: Constant Load, Constant Temperature Tests in Air

         Atmosphere

1.   Material CPS–90A–10C As–Manufactured

    Constant load level: 50% to 70% f_p (different load histories)

    Temperature levels: 75^OF, 1500^OF, 2000^OF, 2400^OF

2.   Material CPS–82C–18M As–Manufactured

    Constant load level: 55% to 85% f_p

    Temperature levels: 75^OF, 1500^OF, 2300^OF

3. Material HP–90A–10C As–Manufactured

Constant load level: 55% to 85% f_p

Temperature levels: 75^OF, 1500^OF, 2400^OF

4. Material FC–8A–78C As–Manufactured

Constant load level: 60% to 70% f_p

Temperature levels: 75^OF, 2000^OF

Category E: Constant Load, Increasing Temperature Tests in Air

Atmosphere

1. Material CPS–90A–10C As–Manufactured

Constant load level: 60% to 70% f_p

Heating rates: 100^OF/hr., 250^OF/hr.

In addition, a limited amount of tests was carried out to determine the effect of thermal cycling on the material behavior.

The total testing program represents over 300 tests. Over 150 test were carried out to standardize specimen preparation procedures, and study characteristics of refractory blocks. About '150 other tests were performed to characterize the thermomechanical behavior of standard specimens extracted from the block. Most test cases in each category contain two or three tests carried out to confirm the results.

4.4 MICROSTRUCTURAL CHARACTERIZATION TEST PROGRAM

This Section summarizes the tests performed for the microstructural characterization. The different tasks performed include:

o Observation of the surface features of polished specimens using a stereoscopic, a Nomarski and a scanning electron microscopes;

o   Characterization of the chemical composition using X—ray diffraction;

o   Characterization of the open porosity using a mercury porosimeter; and

o   Measurements of the dry density of specimens prior to and after thermomechanical testing.

These tasks were performed for selected materials and chosen test conditions. In some cases the selection process was limited by the remainings of the specimens after testing, since some specimens were reduced to very small pieces after the final explosive fracture. The selected materials and testing conditions are shown in Table 4.4. Two types of test were used: monotonically increasing and constant short term compressive load tests at constant temperatures in air atmosphere. Specimens were examined prior to and after testing at different temperature levels. As—manufactured and slag—impregnated materials were included, as well as the three different manufacturing processes: cold—pressing and sintering, hot—pressing, and fusion—casting. It should be noted that the stereoscopic light microscope has only been used for cold—pressed sintered refractories, since its magnification range is too small for the observation of the surface features of hot—pressed and fused—cast materials. On the other hand it is possible to use the Nomarski for all materials. The composition of slag—impregnated cold—pressed sintered and of as—manufactured fused—cast refractories were the only ones studied using X—ray diffraction. Table 4.5 shows the different kind of tests used along with the appropriate candidate material. The six summarized tests are microscopic observations using stereoscopic, Nomarski, and scanning electron microscopes, X—ray diffraction, mercury porosimeter, and bulk density measurements.

In what follows, a detailed outline of the tests and materials used is given. At

	Monotonically Increasing Compressive Loads, Constant T, Air Atmosphere Category A in Table 4.3	Constant Compressive Loads, Constant T, Air Atmosphere Category D, Table 4.3
Cold-Pressed Sintered 90% Al_2O_3 - 10% Cr_2O_3 As-Manufactured	Not tested $1500^{\circ}F$, $2400^{\circ}F$	$1500^{\circ}F$ $2400^{\circ}F$
Cold-Pressed Sintered 90% Al_2O_3 - 10% Cr_2O_3 Slag-Impregnated	$75^{\circ}F$ $2400^{\circ}F$	
Cold-Pressed Sintered 82% Cr_2O_3 - 18% MgO As-Manufactured	Not tested $1500^{\circ}F$, $2400^{\circ}F$	
Cold-Pressed Sintered 82% Cr_2O_3 - 18% MgO Slag-Impregnated	$75^{\circ}F$	
Hot-Pressed 90% Al_2O_3 - 10% Cr_2O_3 As-Manufactured	Not tested $2000^{\circ}F$	
Fused-Cast 78% Cr_2O_3 - 8% Al_2O_3 As-Manufactured	Not Tested $2300^{\circ}F$	

Table 4.4   Microstructural characterization testing program

Stereoscopic Optical Microscope	Nomarski Optical Microscope	Scanning Electron Microscope	X-ray Diffraction Microanalysis	Mercury Porosimeter Tests	Bulk Density Measurements
CPS-90A-10C SI-90A-10C CPS-82C-18M SI-82C-18M	CPS-90A-10C SI-90A-10C CPS-82C-18M SI-82C-18M HP-90A-10C FC-7A-78C	SI-90A-10C HP-90A-10C FC-7A-78C	SI-90A-10C FC-7A-78C	CPS-90A-10C SI-90A-10C CPS-82C-18M SI-82C-18M	CPS-90A-10C CPS-82C-18M

<u>Table 4.5</u>

<u>Note:</u> For convenience SI-90A-10C has been used to represent slag-impregnated CPS-90A-10C and SI-82C-18M has been used to represent slag-impregnated CPS-82C-18M.

first the characterization of the materials before testing and after testing under monotonically increasing compressive loads to failure in air atmosphere are discussed:

Observation of Surface Features Using a Stereoscopic Optical Microscope

1. As–manufactured CPS–90A–10C: not tested, tested at 1500^OF and tested at 2400^OF;

2. Slag–impregnated CPS–90A–10C: tested at 75^OF;

3. As–manufactured CPS–82C–18M: not tested; and

4. Slag–impregnated CPS–82C–18M: tested at 75^OF.

Observation of Surface Features Using a Nomarski Optical Microscope

1. As–manufactured CPS–90A–10C: not tested, tested at 1500^OF and tested at 2400^OF;

2. Slag–impregnated CPS–90A–10C: tested at 75^OF and tested at 2400^OF;

3. As–manufactured CPS–82C–18M: not tested, tested at 1500^OF and tested at 2400^OF;

4. Slag–impregnated CPS–82C–18M: tested at 75^OF;

5. As–manufactured HP–90A–10C: not tested and tested at 2000^OF; and

6. As–manufactured FC–7A–78C–8M: not tested and tested at 2300^OF.

Observations of Surface Features Using a Scanning Electron Microscope

1. Slag–impregnated CPS–90A–10C: tested at 75^OF and tested at 2400^OF;

2. As–manufactured HP–90A–10C: not tested and tested at 2000^OF; and

3. As–manufactured FC–7A–78C–8M: not tested and tested at 2300^OF.

Characterization of Chemical Composition Using X–Ray Diffraction

1. Slag–impregnated CPS–90A–10C: tested at 75^OF; and

2. As–manufactured FC–7A–78C–8M: not tested.

Characterization of Open Porosity Using Mercury Porosimeter

1. As–manufactured CPS–90A–10C: not tested, tested at 1500^OF and tested at 2400^OF;

2. Slag–impregnated CPS–90A–10C: tested at 75^OF;

3. As–manufactured CPS–82C–18M: not tested, tested at 1500^OF and tested at 2400^OF; and

4. Slag–impregnated CPS–82C–18M: tested at 75^OF.

Dry Density Measurements

1. As–manufactured CPS–90A–10C: not tested, tested at 1000^OF, tested at 1500^OF, tested at 2000^OF, and tested at 2400^OF; and

2. As–manufactured CPS–82C–18M: not tested, tested at 1000^OF, tested at 1500^OF, tested at 2000^OF, and tested at 2275^OF.

The surface features of as–manufactured CPS–90A–10C tested at 1500^OF and 2400^OF under constant compressive loads in air atmosphere were also examined using the Nomarski optical microscope.

CHAPTER 5

COLD–PRESSED SINTERED HIGH–ALUMINA AND HIGH–CHROMIA MATERIALS

5.1 SYNOPSIS

This Chapter is the first of three presenting and discussing the results of compression tests at elevated temperatures under controlled gas atmospheres as well as the microstructural characterization of virgin and tested candidate refractory ceramics for slagging coal gasifiers. In this Chapter the behavior of cold–pressed sintered high–alumina CPS–90A–10C and high–chromia CPS–82C–18M is examined. The specimen preparation methods used for compression tests at high temperatures are examined in Section 5.2 Using the determined specimen preparation procedures, a study of the variation of the material properties within a refractory brick, between bricks within the same production batch, and between different production batches is presented in Section 5.3. Based on these different studies, criteria for standard specimens are defined, and used for further thermomechanical testing. The behavior of as–manufactured refractories is studied first in Section 5.4, under different combinations of: (1) monotonically increasing, constant, or cyclically varying short–term compressive uniaxial mechanical loads, (2) constant, increasing, or cyclic (limited to one thermal cycle) temperature histories, and (3) air or reducing atmospheres. Strain rate effects are also studied in the monotonic compression tests at constant temperature. The behavior of slag–impregnated materials is studied in Section 5.5. The microstructural characterization of virgin and tested, as–manufactured and slag–impregnated

materials is presented in Section 5.6. Microstructural observations made with a stereoscopic and Nomarski optical microscopes, a scanning electron microscope as well as X—ray diffraction microanalysis, mercury porosimeter tests, and bulk density measurements are reported. An informative summary presenting the major conclusions from the Chapter is presented in Section 5.7.

5.2 SPECIMEN PREPARATION

The isostatically—pressed sintered materials were received as bricks from different manufacturers. The bricks are in the form of rectangular bricks with either a rectangular cross—section (Fig. 5.1a) or a trapezoidal cross section (Fig. 5.1b), trapezoidal bricks with either a straight edge (Fig. 5.1c) or a circular edge (Figs. 5.1d and 5.1e), or circular bricks (Fig. 5.1f). The bricks may have keys and grooves for mechanically interlocking them anticipating an improvement in the system integrity (Figs. 5.1e and 5.1f). The bricks have various dimensions, and typical sizes are shown in Fig. 5.1.

Specimen preparation techniques were refined using materials CPS—90A—10C and CPS—82C—18M. The specimens were cored out of the bricks, and the end surfaces were prepared for testing. Some specimens were further slag—impregnated. The factors affecting the specimen preparation are: (1) specimen's shape and dimensions; (2) the coring speed; (3) the end—surface preparation; (4) the skill of the operator; and (5) the slag—impregnation procedure.

The main considerations in choosing the specimen shape are:

1.   Obtaining load uniformity over the cross—section;

2.   Minimizing end effects; and

(a)

(b)

(c)

(d)

(e)

(f)
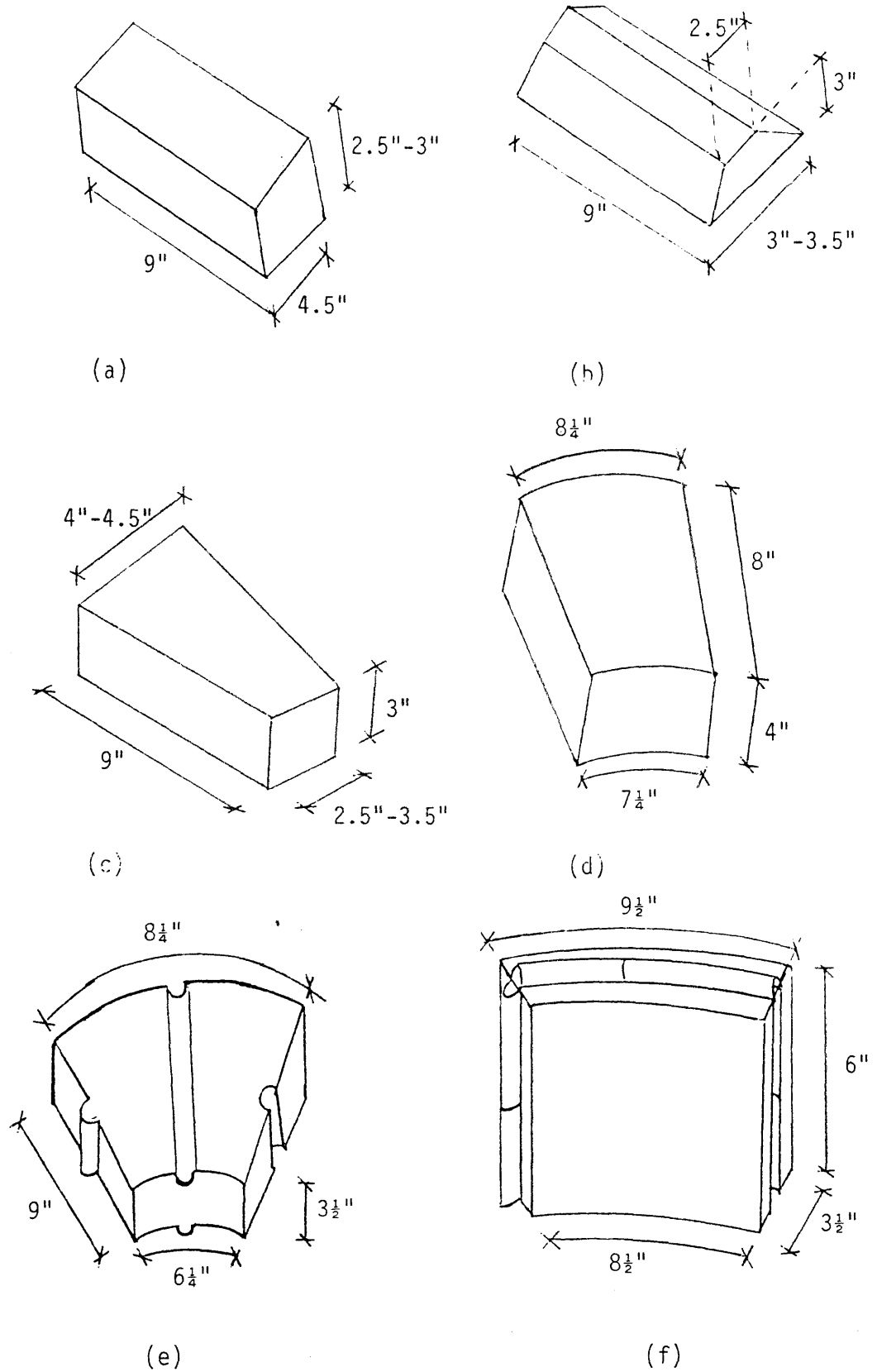
Figure 5.1   Typical shapes and sizes of as—received as—manufactured cold—pressed sintered bricks

3.   Obtaining temperature uniformity around the specimen for high temperature testing using a circular heat zone.

Although the rectangular cross sections are easier to be produced than the circular ones, a cylindrical shaped specimen was preferred over a rectangular one to ensure the conditions specified above.

In choosing the dimensions of the specimen, the size of the largest aggregate is important. For the CPS–90A–10C the largest aggregates are fused grains of alumina that are about 1/3" long.   For the CPS–82C–18M the largest aggregates are picochromite grains that are about 1/4" long. A one–inch diameter was chosen to comply with the minimum required size imposed by ASTM, which is 3 to 4 times the size of the largest aggregate. A diameter study was conducted to assess the effect of specimen's diameter on the material behavior. Figure 5.2 shows the strength (defined as the peak stress on the stress–strain curve) variation with specimen's diameter for Material CPS–90A–10C from preliminary tests. A diameter of 0.875" leads to a consistently lower strength than that of a diameter of 1.0". the largest size aggregate being one–third of an inch for Material CPS–90A–10C, one notices that the 0.875" diameter does not comply with the ASTM requirement.

The height of the specimen was chosen based on strength and strain considerations. For strength consideration, it has been determined empirically that H/D $\geq$ 1.7 (H is the specimen height and D is its diameter) is desired (Kotsovos, 1983). Based on strain considerations, the height of the specimen is determined in such a way that a central zone of near–uniform uniaxial compressive stress exists. As shown in Fig. 5.3, in a specimen under compressive loading, two end zones of a height

$\sqrt{3 / 2}$ x D and a central zone of H/3 exist. In the end zone, the interaction between the specimen ends and the loading device creates a complex state of stress imposed by

As Manufactured CPS–90A–10C
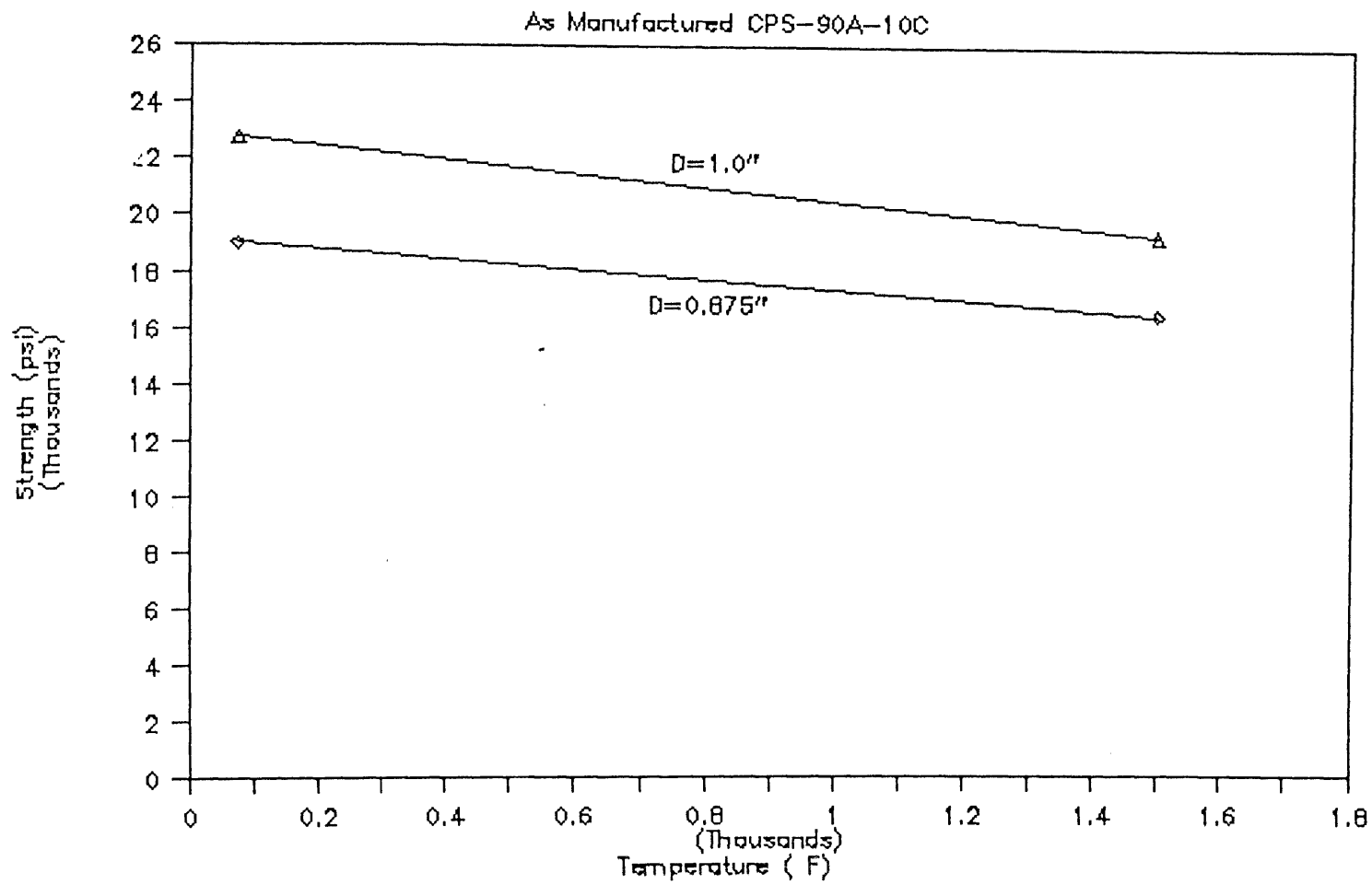
Figure 5.2   Strength variation with diameter for CPS–90A–10C
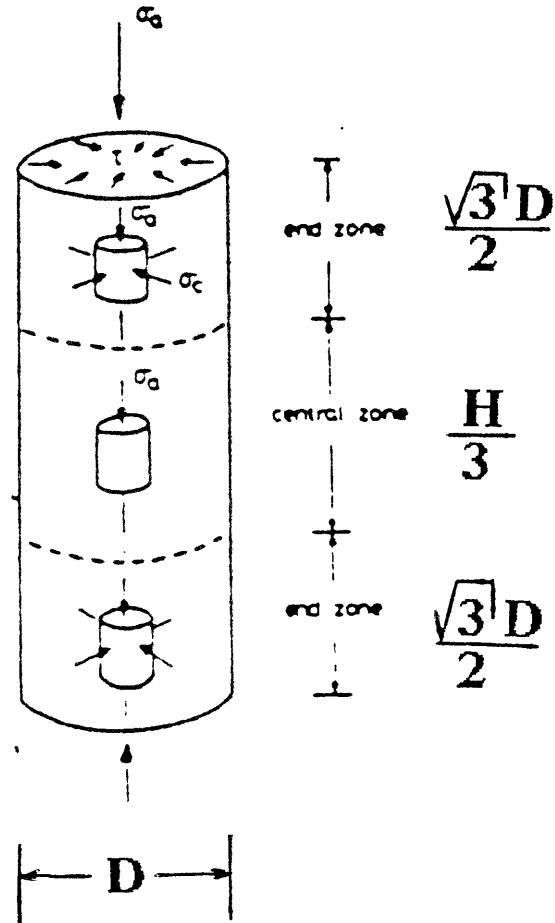
Figure 5.3   Height to diameter ratio consideration for a cylindrical specimen (Kotsovos, 83)

frictional restraints. By imposing a central zone height of H/3, the height of the specimen is determined to be such that H/D $\geq$ 2.6. Due to these different considerations cylindrical specimens of one inch diameter and 2.5 inches to 3 inches height were adopted as standard for testing.

To extract the cylindrical specimen from the brick, coring and surface preparation are needed. Minimizing the damage due to these operations is an important step in specimen preparation. A coring speed study was conducted on Material CPS–82C–18M at 375 RPM, 525 RPM, 1000 RPM and 1400 RPM. The results of the study are shown in Fig. 5.4. The strength values at 375 RPM and 525 RPM are almost equal and the damage due to coring appears to be negligible at 375 RPM. A similar conclusion can be arrived at by comparing the stress strain curves in Fig. 5.5 for specimens cored at different coring speeds. The speed of 375 RPM was, thus, adopted as a standard for specimen preparation.

As far as preparing the end surfaces for testing, sawing of the end surfaces is preferred to high–temperature capping, and grinding, and adopted as a standard for preparation. Since the specimen deformation is obtained by subtracting the system deformation from the total deformation, high–temperature capping is not desirable. The reason is that high–temperature capping may deform under load and temperature and thus introducing errors in the system calibration. Grinding of the specimen end surfaces is not used either, because it produces chipping of the specimen edges. Sawing of the specimen ends to produce parallel and smooth surfaces for testing was adopted as a standard. The sawing was done on an automatic slow–speed diamond saw, at a constant feed rate.

In coring the specimen out of the brick and sawing its end surfaces, the skill of the operator was found to be very important. Table 5.1 gives average strengths for
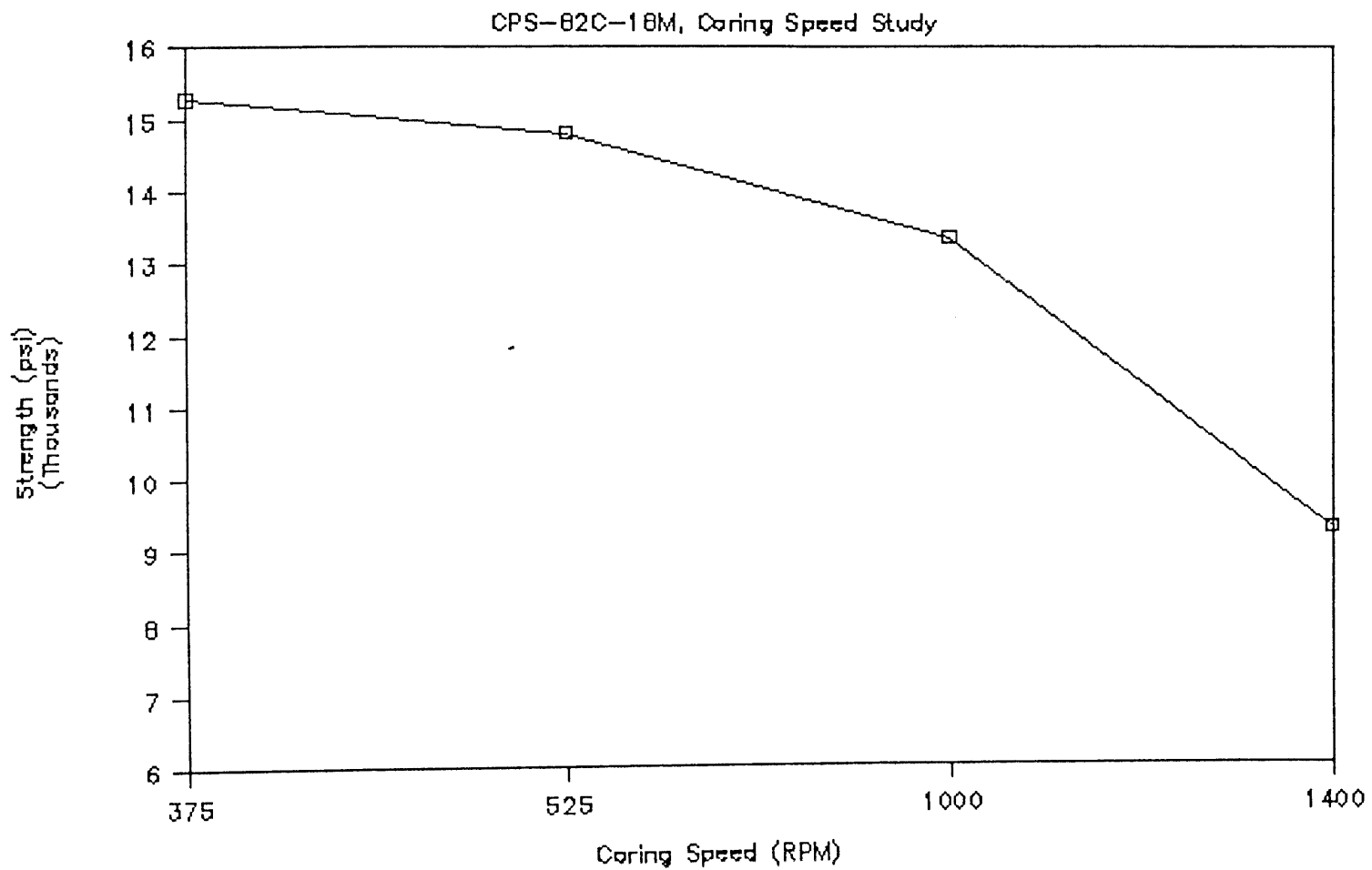
Figure 5.4   Strength values at different coring speeds for CPS–82C–18M
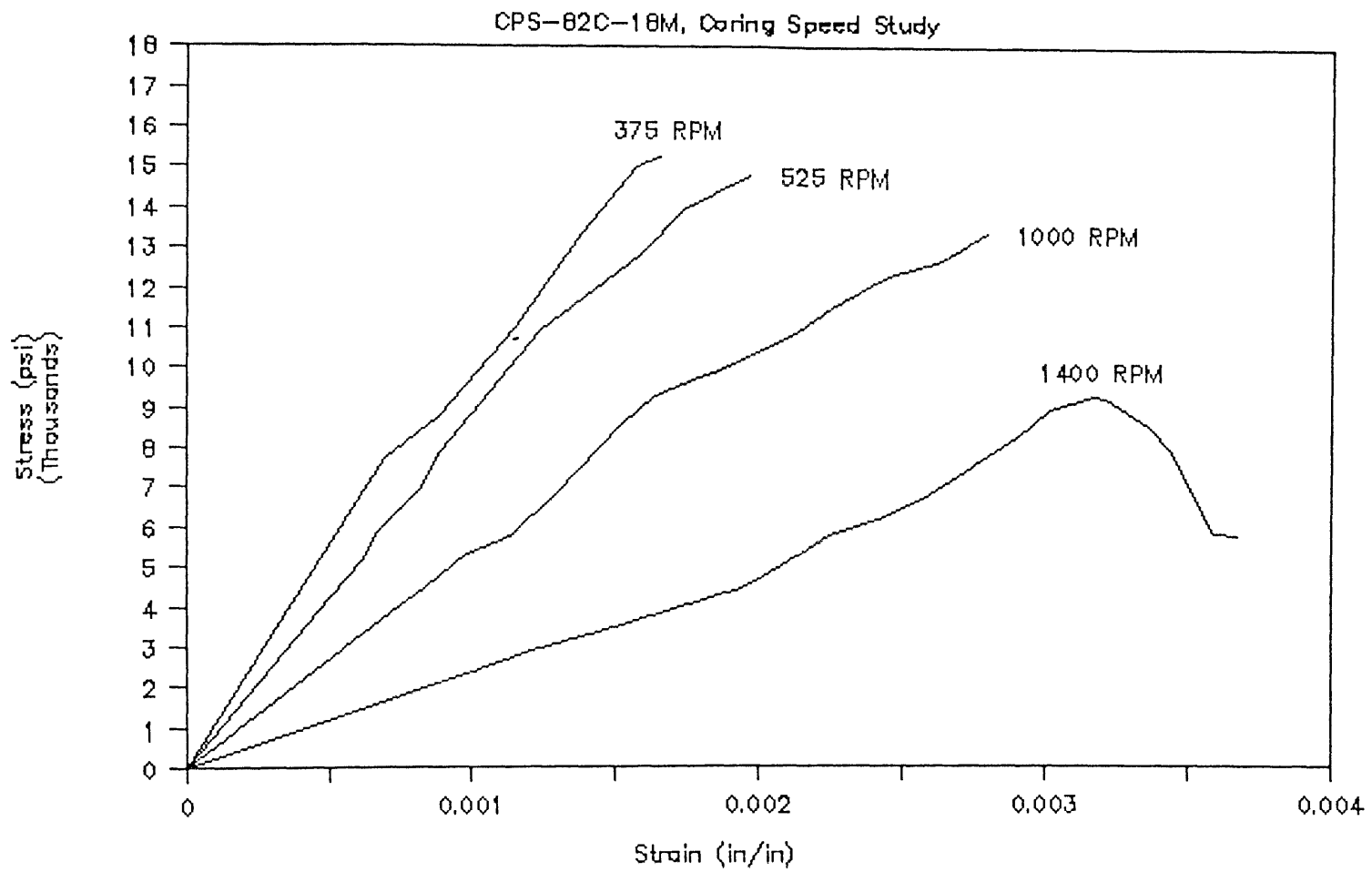
Figure 5.5　　　Stress strain curves at different coring speeds for CPS–82C–18M

		Grinding Process	
		Experienced Operator	Inexperienced Operator
Coring Process	Experienced Operator	19050 psi*	18150 psi*
	Inexperienced Operator	12490 psi*	

Table 5.1 – Average Strength Values for
Cores with a Diameter of 7/8"

*   Average of three specimens

specimens prepared by experienced and inexperienced operators for the drill press and the saw. The strength values shown in Table 5.1 show the importance of experience in the machining process, especially for the coring operation. All standard specimens used for mechanical testing at elevated temperatures are cored and sawed by the same experienced machinists.

To study the effect of slag–impregnation, specimens were impregnated with a western–acid slag (Table 5.2) of the following composition: 52.4% SiO_2, 22.5% Al_2O_3, 10.1% CaO, 6.0% Fe_2O_3, 2.0% C, 1.9% Na_2O, 1.8% MgO, 1.1% TiO_2, 0.5% K_2O, and less than 0.5% of other constituents. The specimens were packed in an alumina crucible with slag powder. The specimens were kept for 10 hours in slag at $2822^{\circ}F$ ($1550^{\circ}C$) under an atmosphere of N_2 and NH_3, with an estimated P_{O_2} of 10^{-3} to 10^{-4} atm. Material CPS–90A–10C was slag–saturated, while Material CPS–82C–18M was slag–impregnated but not saturated. Two positions of the specimens were tried in the crucible: a horizontal position that resulted in uniform impregnation over the length of the specimen but with distorted cross sections (Fig. 5.6), and a vertical position that produced a uniform impregnation over its cross sections (Fig. 5.7). The horizontal position resulted in an average strength of 11150 psi for chromia specimens at room temperature, compared to an average strength of 21900 psi for specimens impregnated in the vertical position. The method of horizontal impregnation was not used for further testing. Test results from vertically slag–impregnated specimens were consistent.

The standard specimen preparation methods for specimens extracted from an cold–pressed sintered refractory brick are as follows:

1. specimen shape: circular;

2. specimen size: diameter = 1", height = 2.5 − 3.0";

Constituent	Percentage
SiO_2	52.4
Al_2O_3	22.5
CaO	10.1
Fe_2O_3	6.0
C	2.0
Na_2O	1.9
TiO_2	1.8
K_2O	0.5
others	< 0.5 for each

Table 5.2 - Western Acid Slag Composition
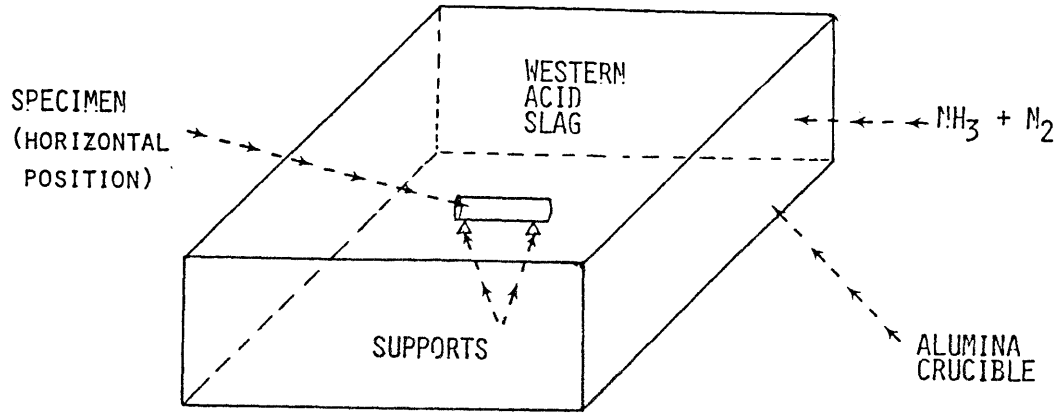
Figure 5.6   Horizontal specimen position for slag–impregnation resulting in length uniformity
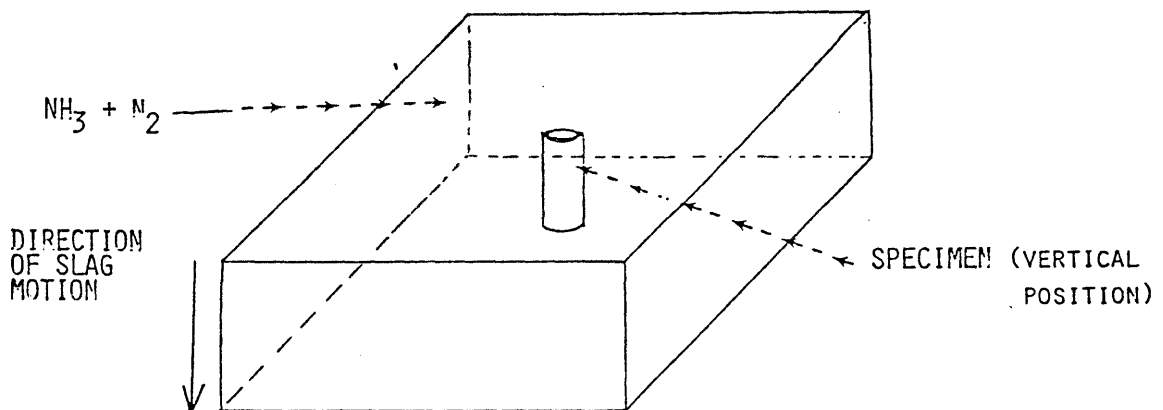
Figure 5.7   Vertical specimen position for slag impregnation resulting in cross section uniformity.

3. coring speed: 375 RPM;

4. automatic slow—speed sawing of end surfaces;

5. coring and sawing processes performed by same skilled operators; and

6. vertical position of specimen during slag impregnation.

In order to verify the adequacy of these specimen preparation methods, as—received as—manufactured refractory bricks were tested, and this behavior was compared to lab specimens extracted from these bricks. The results show a good correlation between the strength of the brick and the specimen extracted from it. The difference in strength is within 15%.

The developed standard specimen preparation procedures are used to obtain specimens for brick characterization and elevated temperature testing.

The preparation of sections for microstructural characterization was carefully done. The cylindrical specimen was first sliced along its length, and a section was extracted from its middle as shown in Fig. 5.8. Before being viewed in optical microscopes, the section was first mounted on a base support, then polished with decreasing grit size wheels by 'specialists at a commercial facility. For specimens to be viewed in the SEM, the section was further gold—coated under vacuum and silverpaint was used to join the surface of the viewed section to a copper specimen holder.

5.3 BRICK CHARACTERIZATION AND VARIABILITY STUDY

Brick characterization is needed to study the variation of material properties within a brick, between bricks within the same production batch, and between bricks produced at different times and belonging to different batches. The factors studied for brick characterization are: (1) the direction of coring from the brick; (2) the

location on the brick from which the specimen is taken; and (3) the variability of the mechanical properties between different batches of bricks, and within bricks obtained from the same batch.

The first parameter examined was the direction of coring from the brick. The brick behavior was found to be anisotropic, with distinct material properties for specimens cored out parallel to the pressing direction and specimens cored out perpendicular to the pressing direction. An average uniaxial compressive strength of 20,700 psi was found for specimens cored out along the pressing direction (Fig. 5.9). The specimens cored in the direction perpendicular to the pressing direction exhibited an average strength of 17,470 psi (about 15% reduction) and a greater ductility. The anisotropic material behavior is attributed to the nature of the pressing process. To limit the number of tests, and for consistency within the present test program as well as the tests conducted by other researchers in the field it was decided to examine only specimens cored out with their axis parallel to the pressing direction.

Next the location on the brick from where the specimen is extracted was examined. The bricks were found to exhibit an inhomogeneous material behavior. Figure 5.10 shows typical stress–strain curves for specimens cored out from the corner and interior of Material CPS–82C–18M bricks. The corner specimens exhibit a weaker strength of 19100 psi (about 8% reduction) than the specimens cored out from the interior of the brick. This is probably related to the sintering process, and may be explained by the fact that more friction develops at the corners of the mold, thus creating a less dense material next to the corners. Figure 5.9 shows average strengths for the specimens from different directions and locations of coring from a Material CPS–82C–18M brick. The brick is thus anisotropic and inhomogeneous.

P : Compressive Uniaxial Load
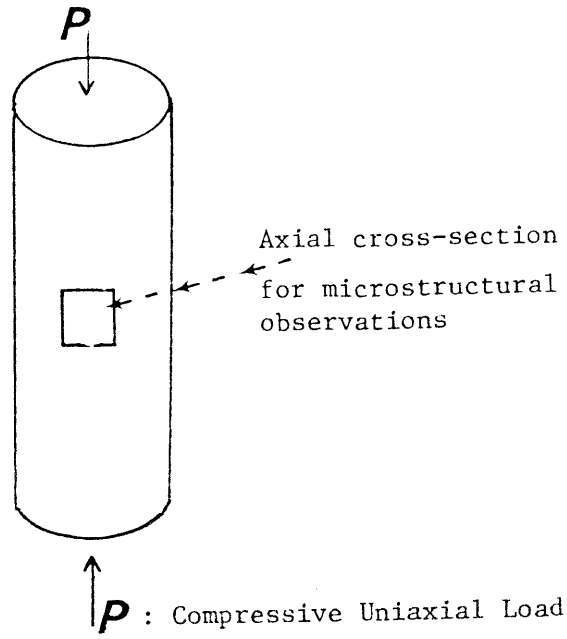
Figure 5.8   Section for microstructural observations
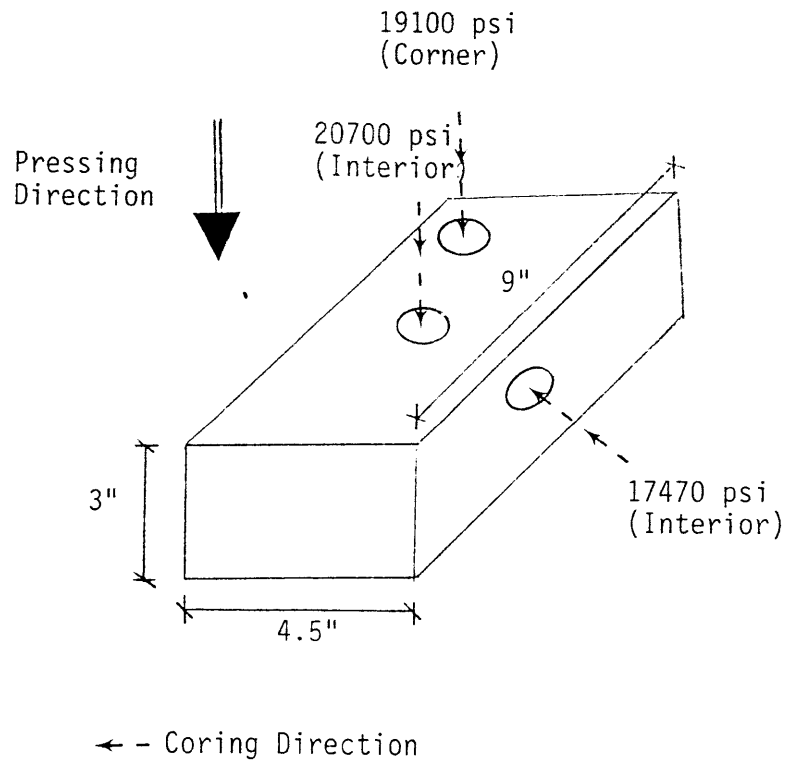
- - Coring Direction

Figure 5.9   Strength variation with location and direction of coring in
                    CPS-82C-18M
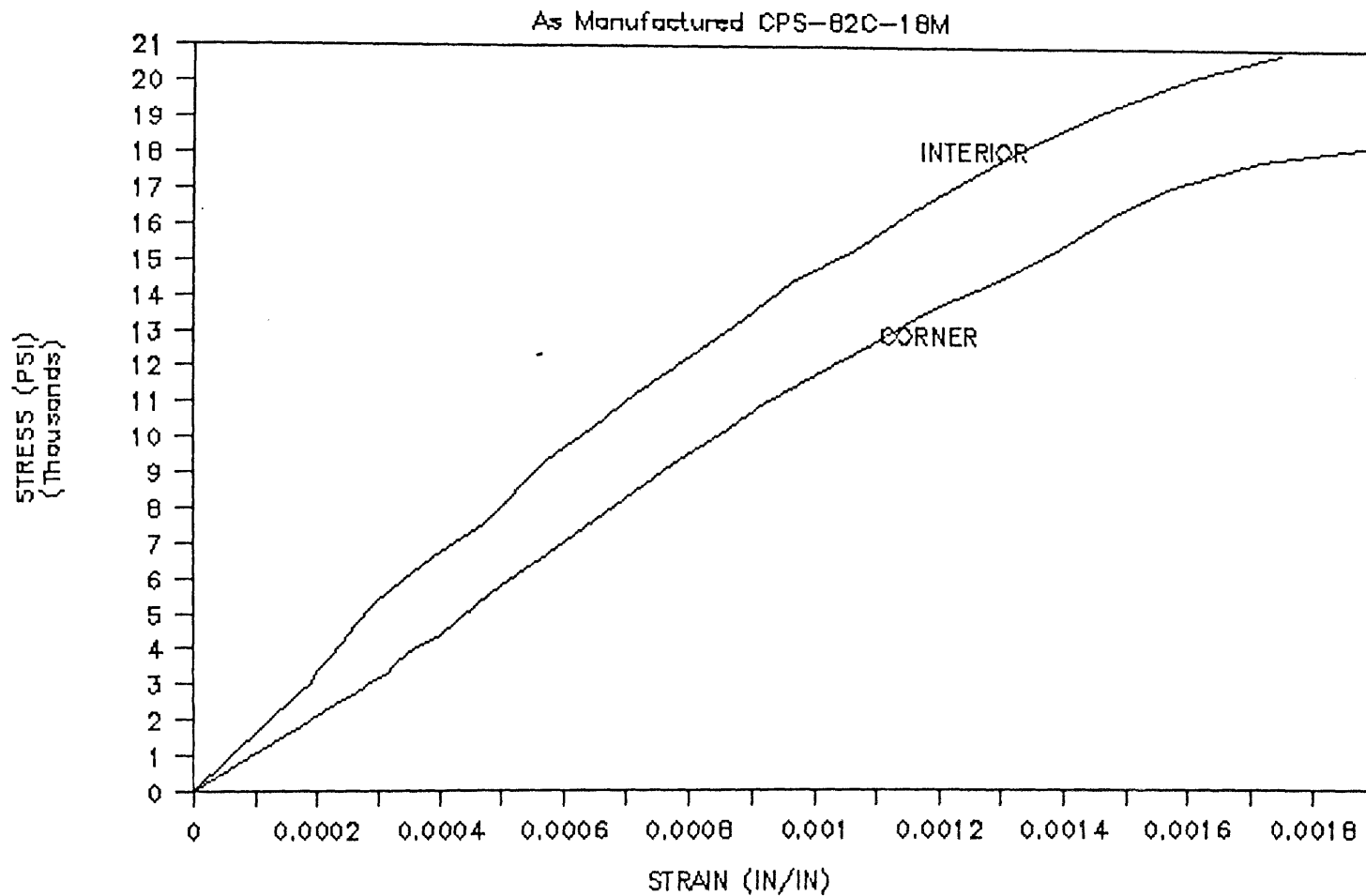
Figure 5.10   Effect of coring location on stress strain curves of
                     CPS–82C–18M

Interior specimens cored out with their axis parallel to the pressing direction were adopted as a standard for further testing.

The production line of a high–alumina and a high–chromia refractory materials was studied over a period of one year. Bricks were taken at random from the production line and specimens extracted from these bricks were tested under short–term compressive uniaxial monotonic loads at room temperature. The specimens used were prepared using the standard procedures described in Section 5.2. The variation in properties of bricks obtained from different production batches was found to be twice as large as that for bricks from the same batch. All standard specimens used for further high–temperature testing were taken from the same batch of bricks, to reduce the variability. More details about this variability study are given in Appendix E.

As a result of the brick characterization and variability study, specimens used for elevated temperature testing were taken from the same batch of bricks, and extracted from the interior of the brick in a direction parallel to the pressing direction.

5.4 ELEVATED TEMPERATURE BEHAVIOR OF AS–MANUFACTURED MATERIALS UNDER UNIAXIAL SHORT–TERM COMPRESSIVE LOADS

5.4.1 Behavior Under Monotonic Compressive Loads at Constant Temperature in Air Atmosphere

The effect of temperature on the behavior of materials CPS–82C–18M and CPS–90A–10C under loading with constant displacement rate is studied first. Stress strain curves for different temperature levels, and a constant displacement rate of 1.83×10^{-3} mm/sec (corresponding to an average strain rate of about 1×10^{-5}sec^{-1} at room temperature and an average strain rate of 2×10^{-5} sec^{-1} at 2400°F (1316°C),

are shown in Figs. 5.11 and 5.12, for materials CPS–82C–18M and CPS–90A–10C respectively. For both of these materials, two distinct deformation and fracture behavioral regions are identified with respect to temperature. There appears to be a transition temperature that separates these behavioral regions, and this transition temperature is found to correspond to about one–half the melting point of the material. The two distinct behavioral trends are:

1. For temperature levels below roughly $1/2$ T_m (where T_m is the melting temperature of the material), the deformation behavior is linear elastic with a brittle fracture. A sudden fracture of the specimen was observed at a load level corresponding to the peak stress on the stress–strain curve, and thus, no post–peak behavior was obtained.

2. At temperature levels between 0.5 T_m and 0.7 T_m (tests were limited to a maximum temperature level of 0.7 T_m for these cases), the deformation behavior of the material is initially linear, but exhibits significant non–linearities at stress levels close to the peak strength. In the post–peak region, the observed non–linear deformations are even more pronounced.

The strain rate effect at temperatures below $T_m/2$ was studied for CPS–90A–10C at 1500°F (816°C) at three different average strain rates of 2×10^{-6} sec^{-1}, 7×10^{-6} sec^{-1}, and 15×10^{-6} sec^{-1} as shown in Fig. 5.13. The three stress strain behaviors exhibited a similar linear variation with a brittle fracture at an approximately equal final strength. A slight difference between the stiffnesses was observed. Similar results have been obtained for CPS–82C–18M as shown from the stress strain curves at 2000°F in Fig. 5.14. For all practical purposes, it appears that the material behavior at temperatures below $T_m/2$ is essentially strain rate
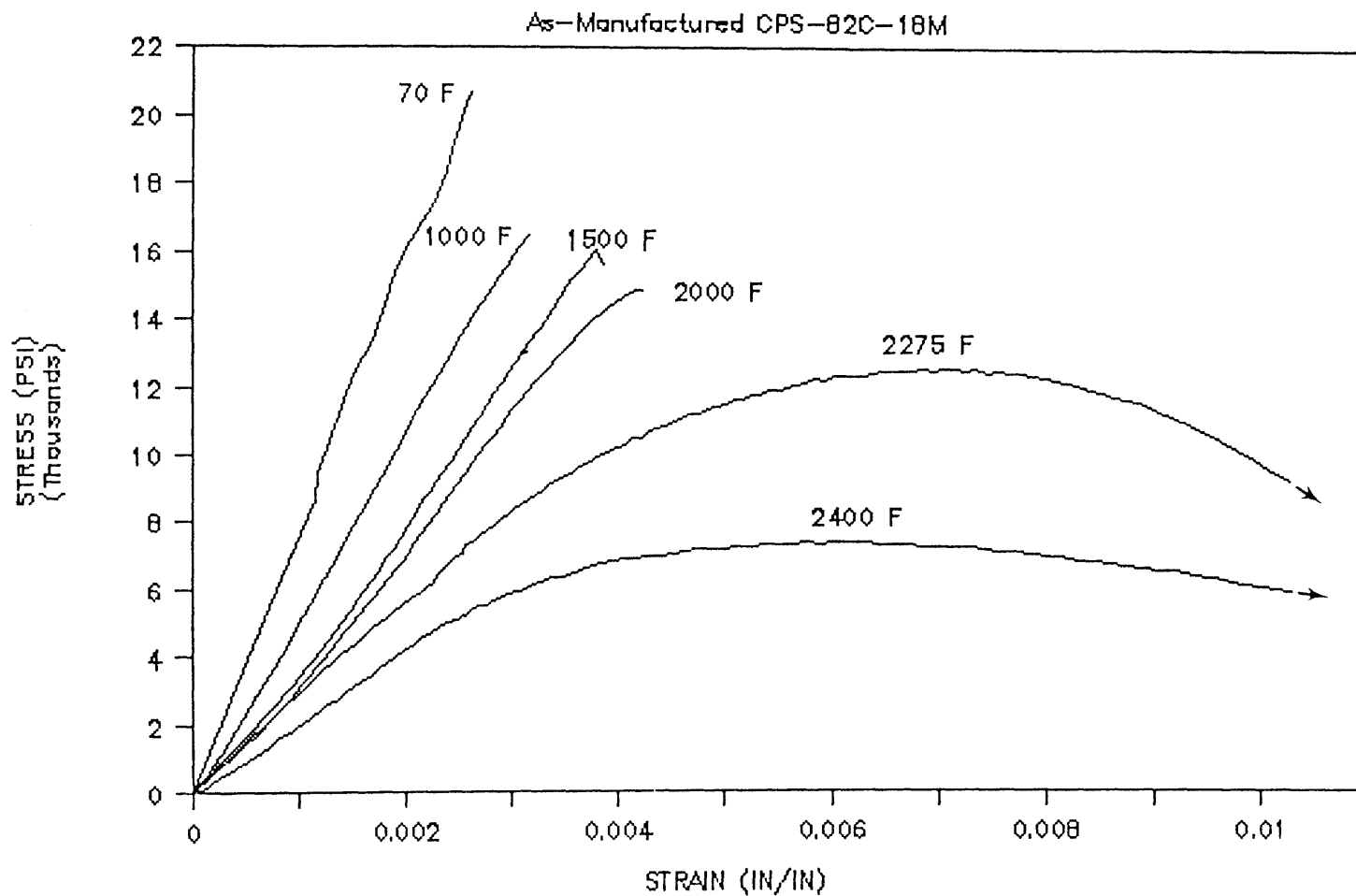
Figure 5.11   Stress strain curves for CPS–82C–18M at different temperature levels and a constant displacement rate of 7.218 x 10^{-5} in/sec

As—Manufactured CPS—90A—10C
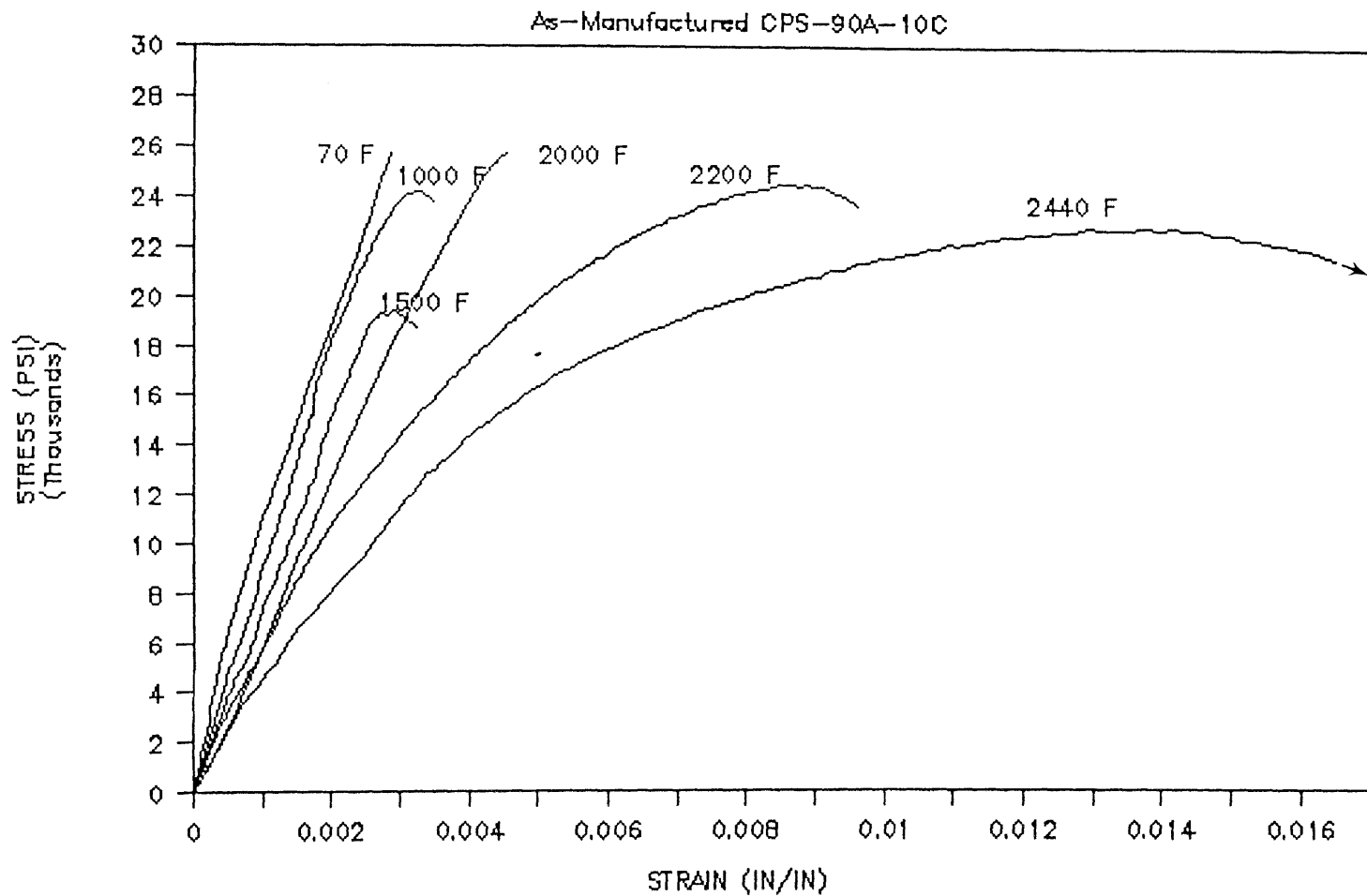
Figure 5.12   Stress strain curves for CPS—90A—10C at different
temperature levels and a constant displacement rate of 7.218
x 10^{-5} in/sec

As Manufactured CPS-90A-10C

STRESS (Thousands)

1500 F, 7E-6/sec

1500 F, 2E-6/sec

STRAIN (IN/IN)
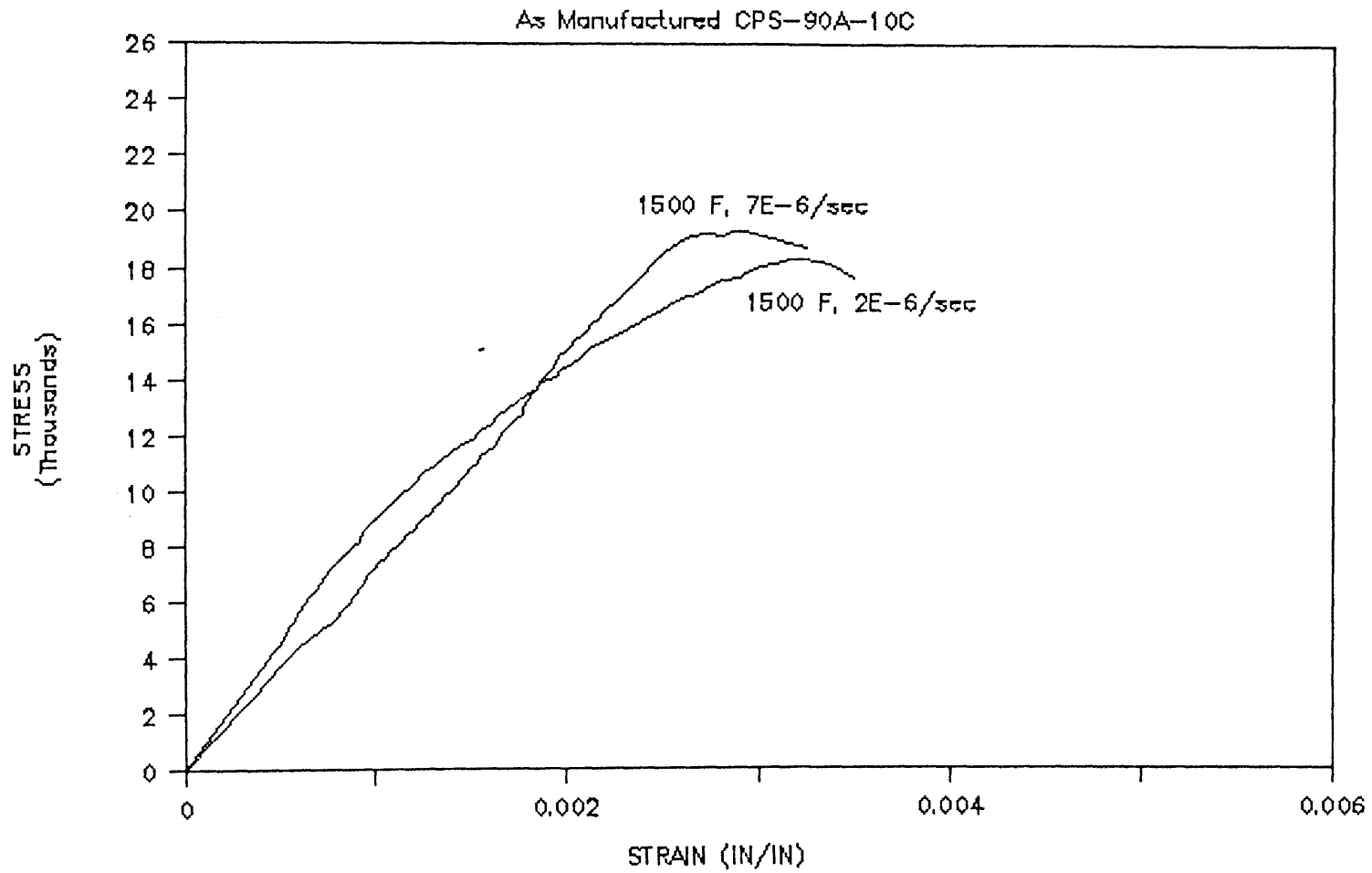
Figure 5.13   Stress strain curves for CPS–90A–10C at 1500°F and two different average strain rates
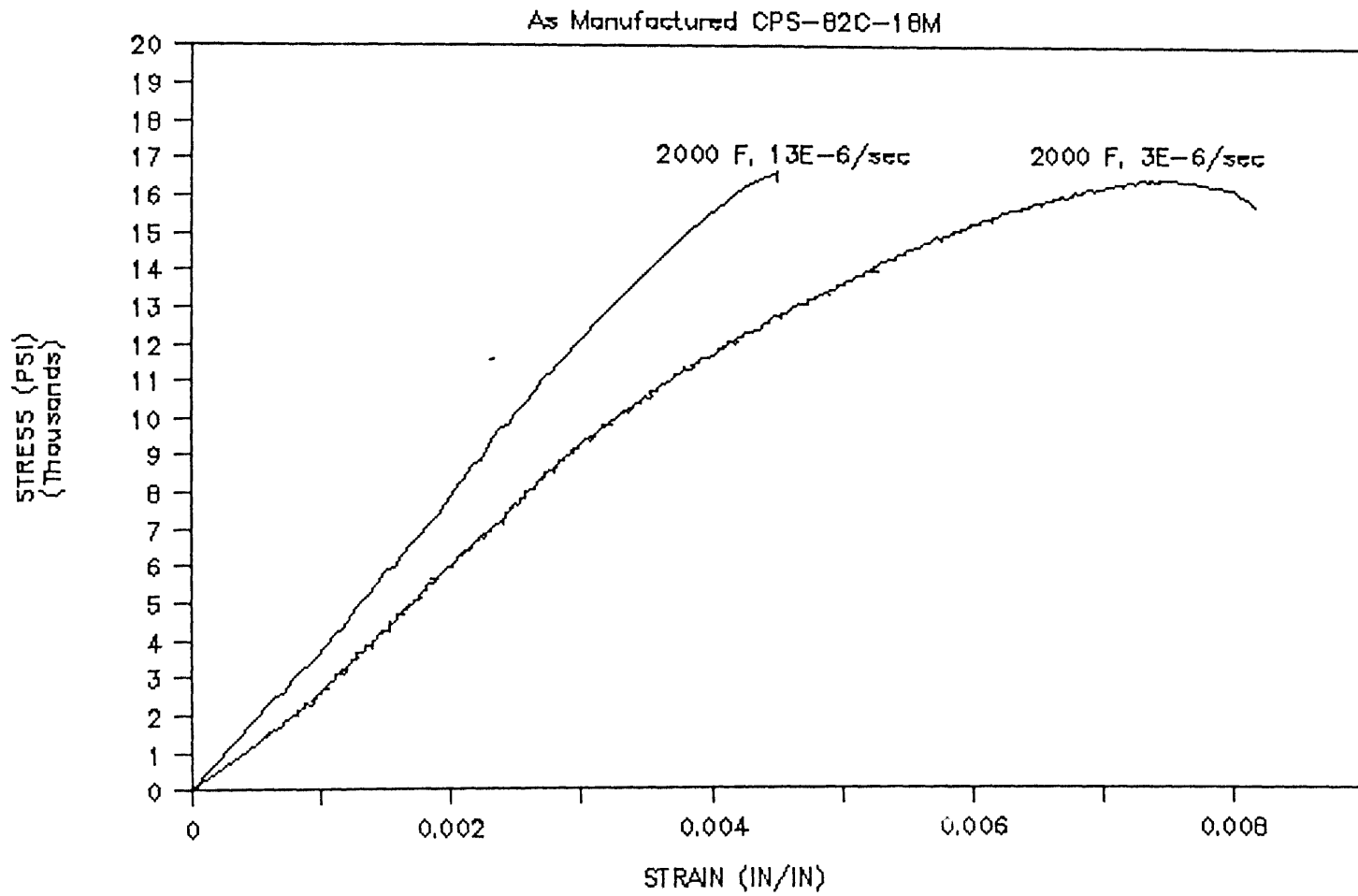
Figure 5.14   Stress strain curves for CPS–82C–18M at 2000°F and two different average strain rates

independent for strain rates in the range from 10^{-4} to 10^{-6} sec^{-1}.

The strain rate effect at temperatures above $T_m/2$ is illustrated by the three stress strain curves in Fig. 5.15 for CPS–82C–18M at 2275°F (1246°C) and average strain rates of $4\text{x}10^{-6}$ sec^{-1}, $20\text{x}10^{-6}$ sec^{-1}, and $40\text{x}10^{-6}$ sec^{-1}. The following observations are made:

1. At the strain rate of $40\text{x}10^{-6}$ sec^{-1} linear deformations are observed with a brittle final fracture. This is similar to the material behavior exhibited for temperatures below 0.5 T_m.

2. For a strain rate of $20\text{x}10^{-6}$ sec^{-1} the material deformation was initially linear with some inelastic deformation, and exhibited significant non–linearities prior to the peak stress. Significant inelastic deformations are found in the post–peak region. This post–peak deformation is characteristic of an unstable fracture propagation behavior, and the deformation rate in the post–peak region is much faster than the one prior to the peak. The final fracture occurs at a stress level slightly lower than the peak stress.

3. For a strain rate of $4\text{x}10^{-6}$ sec^{-1} the deformation behavior prior to the peak is similar to the one for a strain rate of $20\text{x}10^{-6}$ sec^{-1}. However, in the post–peak region the deformation is characteristic of a stable fracture propagation, and the deformation in the post–peak region is in the same order of magnitude as the one prior to the peak. Final fracture occurs at very small loads. The post–peak deformation is more significant than the one prior to the peak.

The different deformation and fracture mechanisms are summarized in Fig. 5.16 in the range of temperatures from room temperature to 0.7 T_m, and for strain
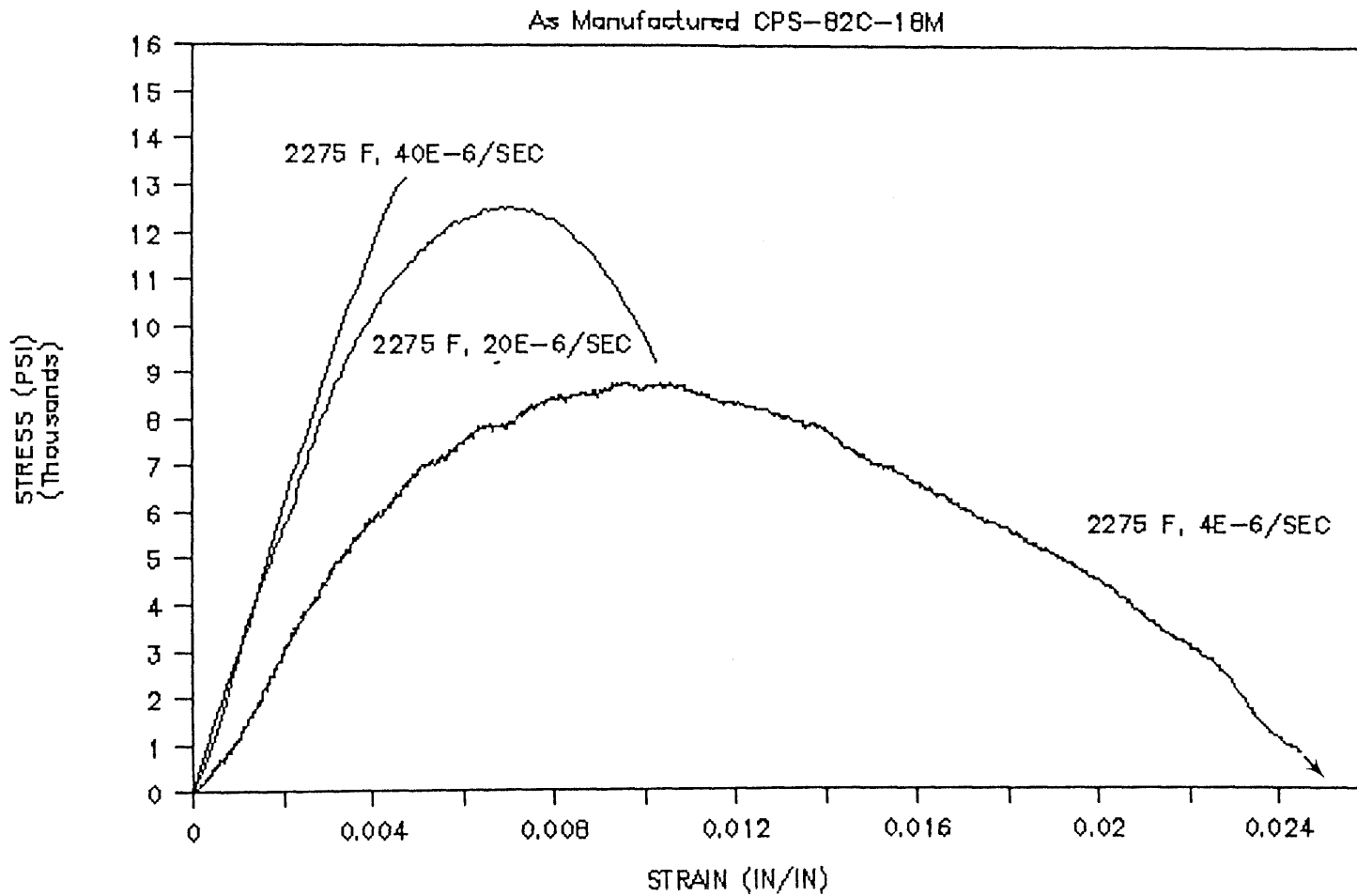
Figure 5.15   Stress strain curves for CPS–82C–18M at $2275^\circ F$ and three different average strain rates
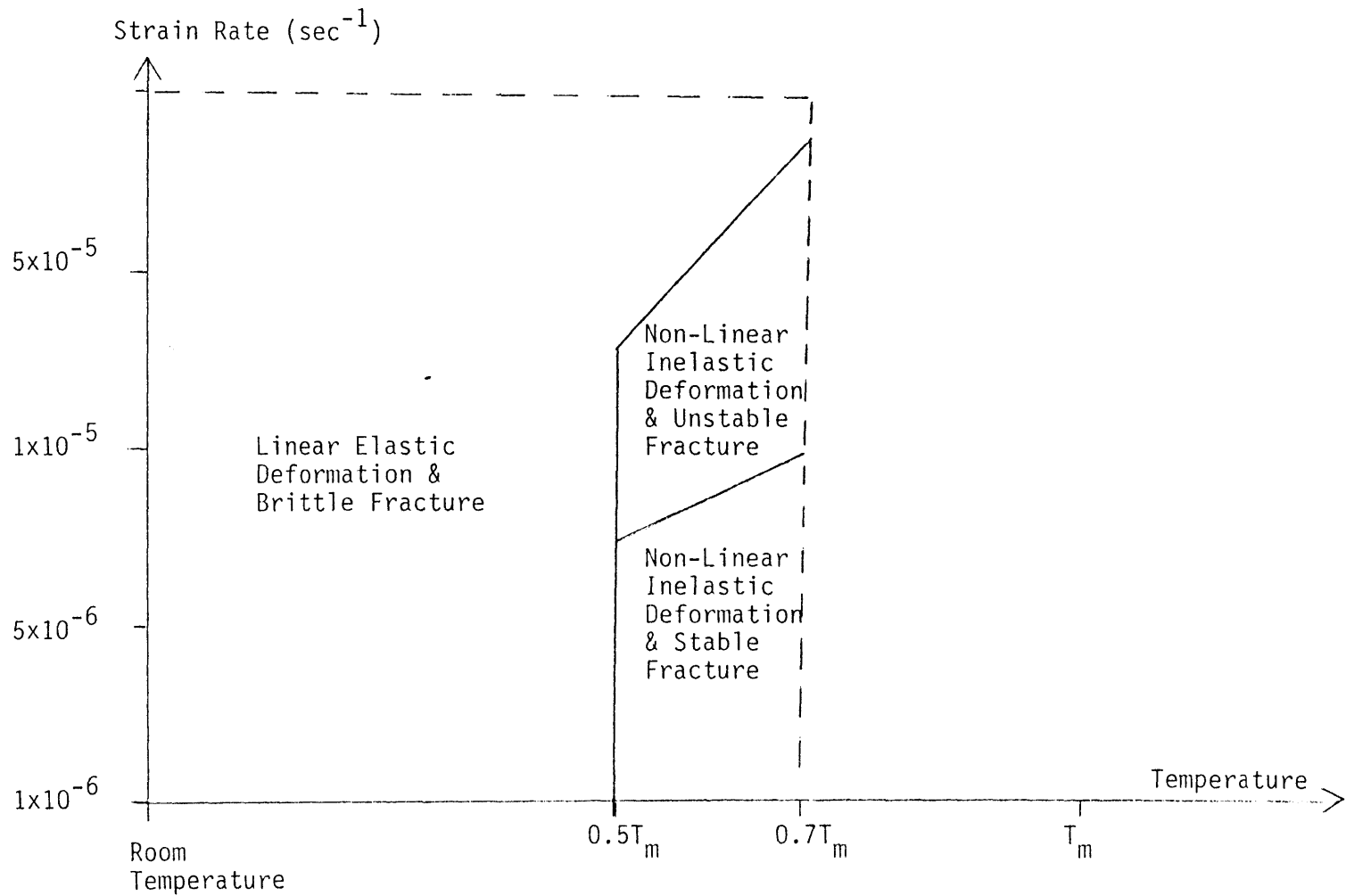
Figure 5.16   Deformation and fracture mechanisms from room
temperature to 0.7 T_m, and for average strain rates from
10^{-4} to 10^{-6} sec^{-1}

rates in the range of 10^{-4} to 10^{-6} sec^{-1}. The diagram gives mainly a qualitative understanding.

In order to study the nature of the non—linear deformation, short—term creep tests were performed on both CPS—90A—10C and CPS—82C—18M. These will be described in the next section.

In what follows some specific material characteristics, namely, the strength, the initial slope of the stress—strain curve, the associated peak strain, the equivalent toughness defined as the area under the stress—strain curve and the cracking patterns are studied.

The strength of the material CPS—82C—18M seemed to follow two different mechanisms as shown in Fig. 5.17: a slight decrease in strength with temperature was observed for temperatures below 0.5 T_m, followed by an increased rate of decrease in strength for temperatures above 0.5 T_m.

Strength degradation for temperature levels below 0.5 T_m was found to be proportional to the square root of T, and may be expressed by the following equation:

$$S = \hat{\tau}\,[1 - (T/T_0)^{1/2}] \tag{5.1}$$

where S is the strength of the material, and T_0 and $\hat{\tau}$ are fitting parameters. $\hat{\tau}$ is linked by some researchers to inherent material properties (Megusar et al., 1979), and represents the ideal strength of the material at $0^{\circ}K$. T_0 is the temperature at which the strength is reduced to zero. This strength variation is found to be independent of strain rates in the range from 10^{-4} to 10^{-6} sec^{-1} for temperatures below 0.5 T_m. This is shown in Fig. 5.17 for temperature levels below $2000^{\circ}F$ ($1093^{\circ}C$).

For temperatures in the range of 0.5 T_m to 0.7 T_m, the strength degradation is proportional to T, and may be expressed as:

As—Manufactured CPS—82C—18M
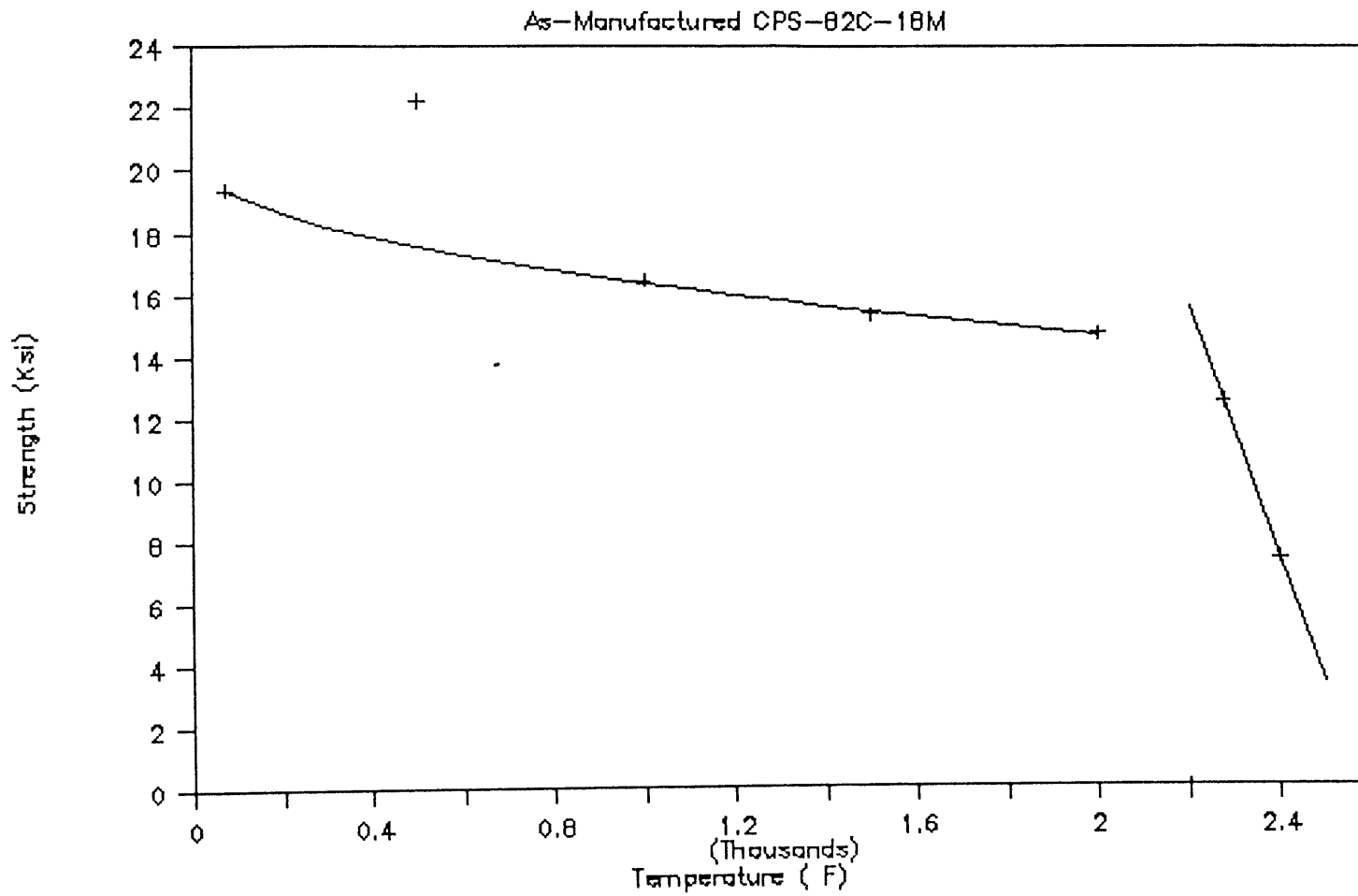
Figure 5.17   Strength variation with temperature for CPS—82C—18M

$$S = S(T_m/2) \frac{T_o \; (\dot{\epsilon}) \; - \; T}{T_o \; (\dot{\epsilon}) \; - \; T_m/2} \qquad (5.2a)$$

where $S(T_m/2)$ is the strength of the material at 0.5 T_m, and T_o is the same as for Eq. (5.1) except that it is a function of the strain rate $\dot{\epsilon}$. Equation (5.2a) can also be written as:

$$S = \hat{\tau} \, (\dot{\epsilon}) \; \{1 - [T/T_o(\dot{\epsilon})]\} \qquad (5.2b)$$

where both $\hat{\tau}$ and T_o are a function of the strain rate $\dot{\epsilon}$. This behavior is shown in Fig. 5.17 for material CPS–82C–18M at temperatures above 2000^oF (1093^oC).

The transition temperature, which separates linear deformation behavior with brittle fracture from a ductile behavior has also been observed for alumina ceramic (Kingery et al., 1976) for which at 2300^oF (1260^oC) the failure is by fracture, and at 2318^oF (1270^oC) an upper yield stress and a lower yield plateau are observed. A similar strength variation has been reported for ceramics in general (Evans and Langdon, 1976) where the fracture stress decreases slowly at low temperatures, controlled by a simple crack propagation. At intermediate to high temperatures, the fracture stress decreases much faster, governed by a so–called deformation assisted brittle fracture (Evans and Langdon, 1976). And finally, there is a third region, where ductile fracture occurs at higher temperatures. Our tests appear to represent the first two behaviorial regions for refractory ceramics. The temperature level of $T_m/2$ (which represents the transition temperature in our tests) is usually taken as the lower limit for the initiation of diffusional processes.

For the material CPS–90A–10C, an increase in strength is observed between 1500^oF (816^oC) and 2000^oF (1093^oC), and the material strength at 2000^oF is higher than the room temperature strength (Fig. 5.18). Strength decrease in the temperature range from 73^oF (23^oC) to 1500^oF (816^oC) seems to be governed by

As—Manufactured CPS—90A—10C
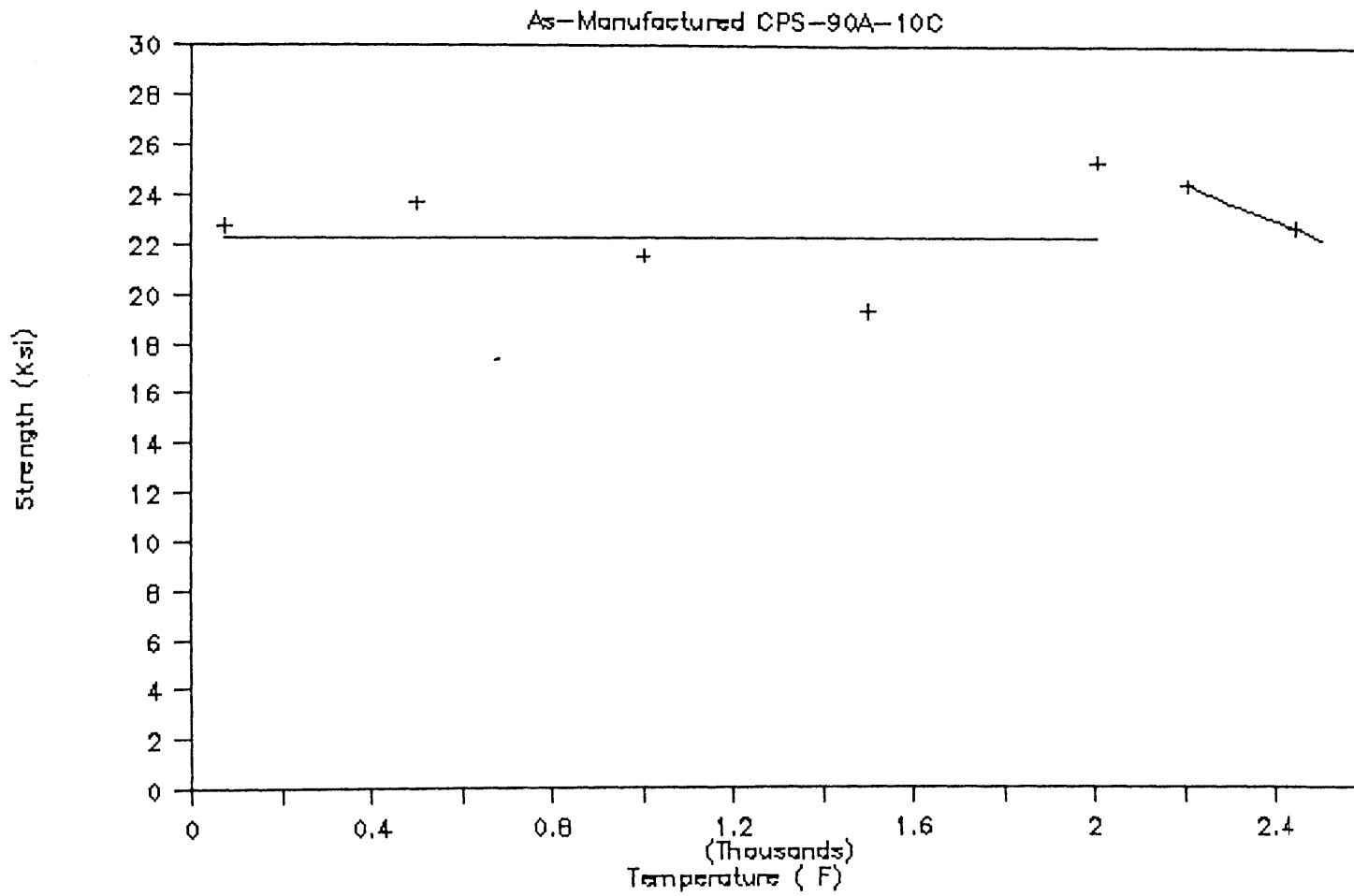
Figure 5.18   Strength variation with temperature for CPS—90A—10C

Equation (5.1) and the strength variation from $2000^{\circ}F$ ($1093^{\circ}C$) to $2440^{\circ}F$ ($1338^{\circ}C$) by Equation (5.2). The strength increase at $2000^{\circ}F$ represents a 25% increase with respect to the strength at $1500^{\circ}F$. This has been confirmed by 4 tests per case. This increase in strength for intermediate temperatures has been observed for alumina–silica bricks (Miller and Davis, 1966), alumina–cement refractory concrete (Heindl and Post, 1954), low carbon steels (MacGregor and Fisher, 1946), and other mixed refractory oxides (Hunt and Bradley, 1941; Foek and Bohling, 1968; McCullough and Rigby, 1971). This phenomenon is usually observed in systems containing more than one mineralogical phase. The peak at intermediate temperatures is even more pronounced for systems containing both crystalline and glassy phases.

The initial slope of the stress strain curve decreases sharply with increased temperatures. This is shown in Fig. 5.19 for material CPS–82C–18M. A similar behavior is observed for material CPS–90A–10C as shown in Fig. 5.20. It is difficult to measure true modulus at high temperatures, because of creep contributions as the temperature is raised. In this case the measured modulus is effectively a relaxed modulus. The obtained data is similar to those by other researchers for brittle solids, such as the obtained variation of temperature for Portland Cement concrete (Anderberg and Thelandersson, 1976; Cruz, 1966), and granite rocks (Heuze, 1983). It is found that the ratio of the material's strength to the cubic root of the initial modulus is about constant for temperatures below 0.5 T_m. This is shown in Fig. 5.21 for the material CPS–82C–18M

The variation with temperature of the peak strain values associated with the peak stress, for the material CPS–90A–10C, is shown in Fig. 5.22. The rate of increase in the peak strain is lower for temperatures below 0.5 T_m than those above

As–Manufactured CPS–82C–18M
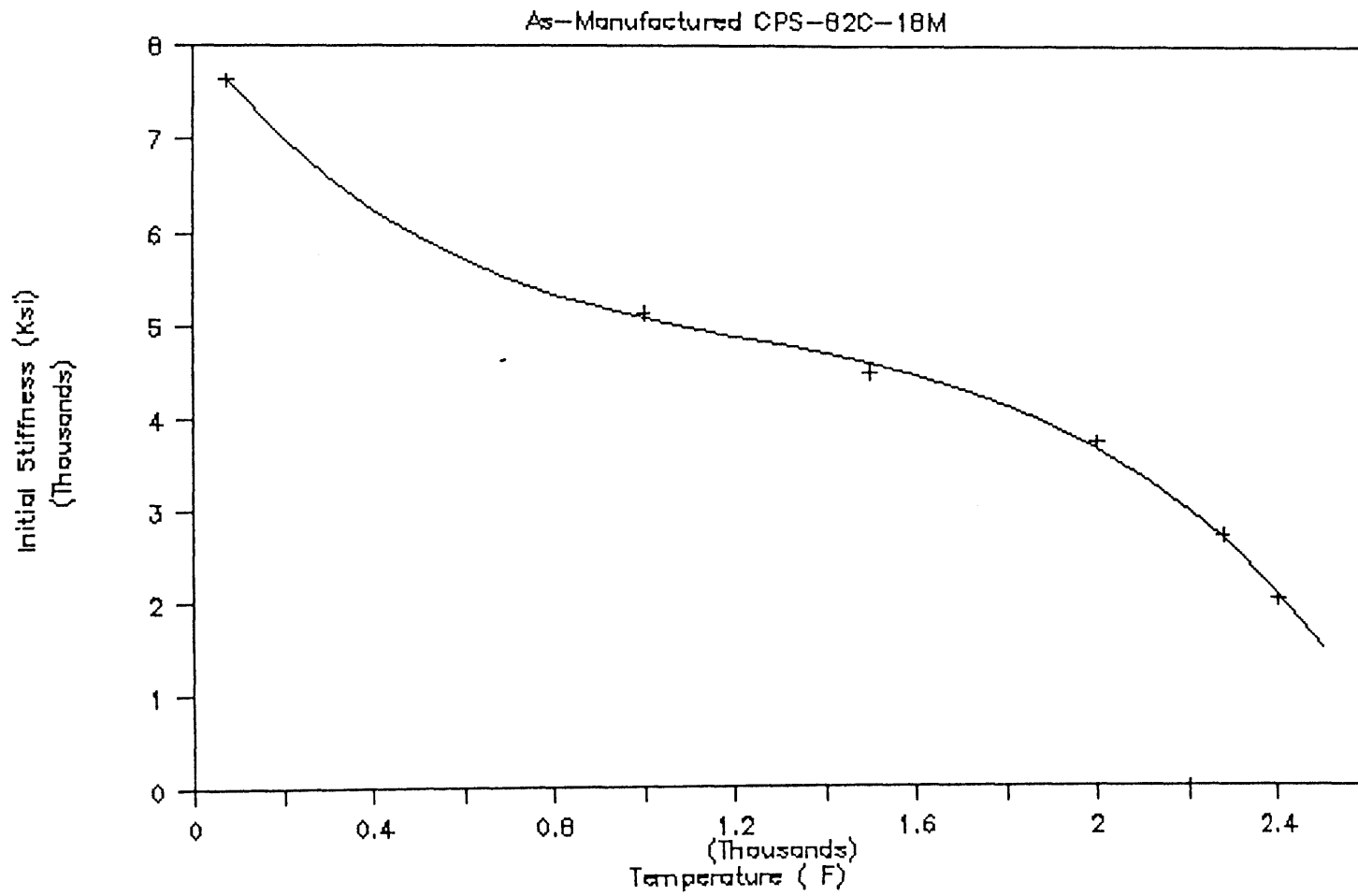
Figure 5.19   Initial stiffness variation with temperature for
CPS–82C–18M

As-Manufactured CPS-90A-10C
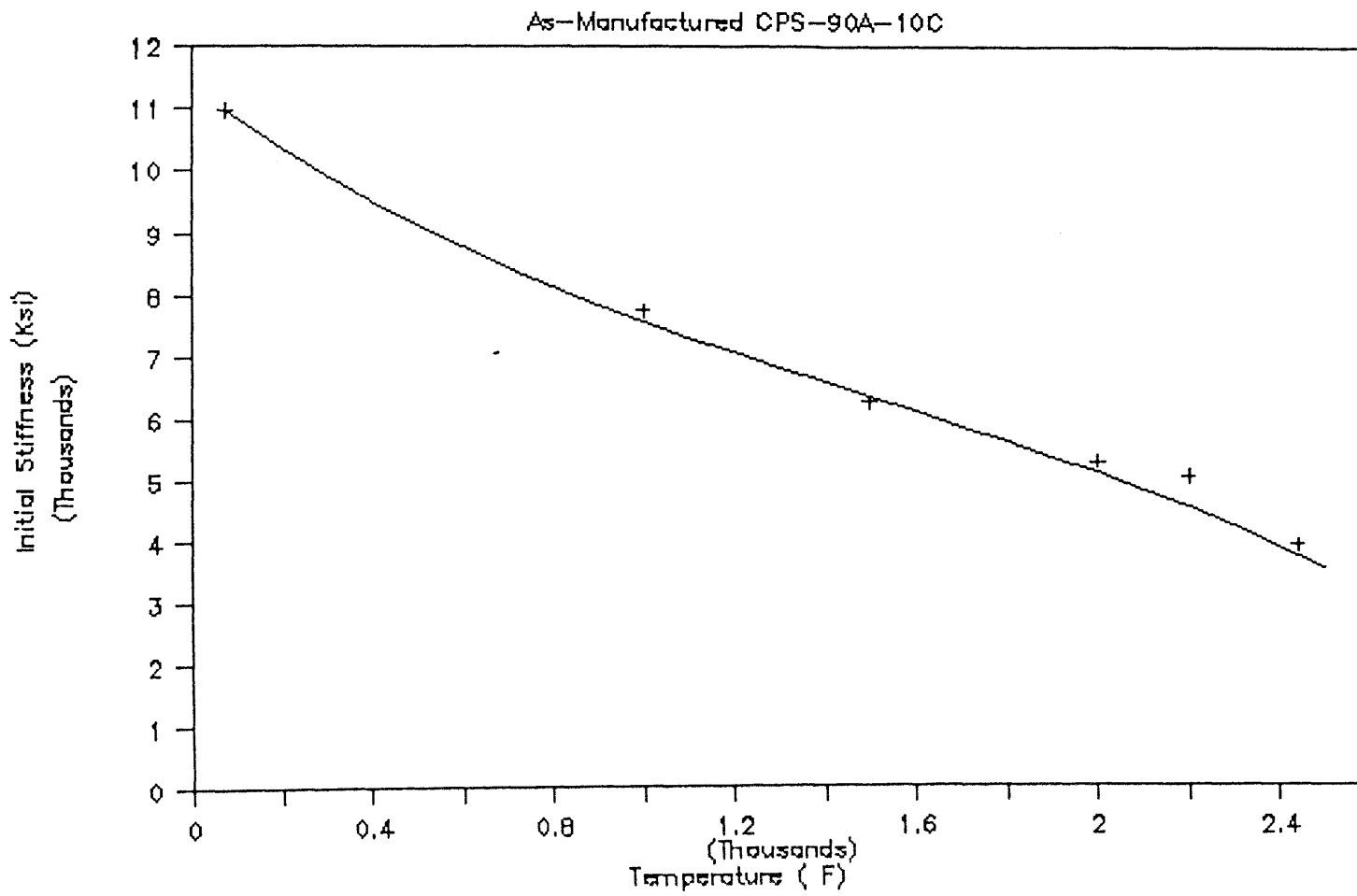
Figure 5.20   Initial stiffness variation with temperature for CPS-90A-10C
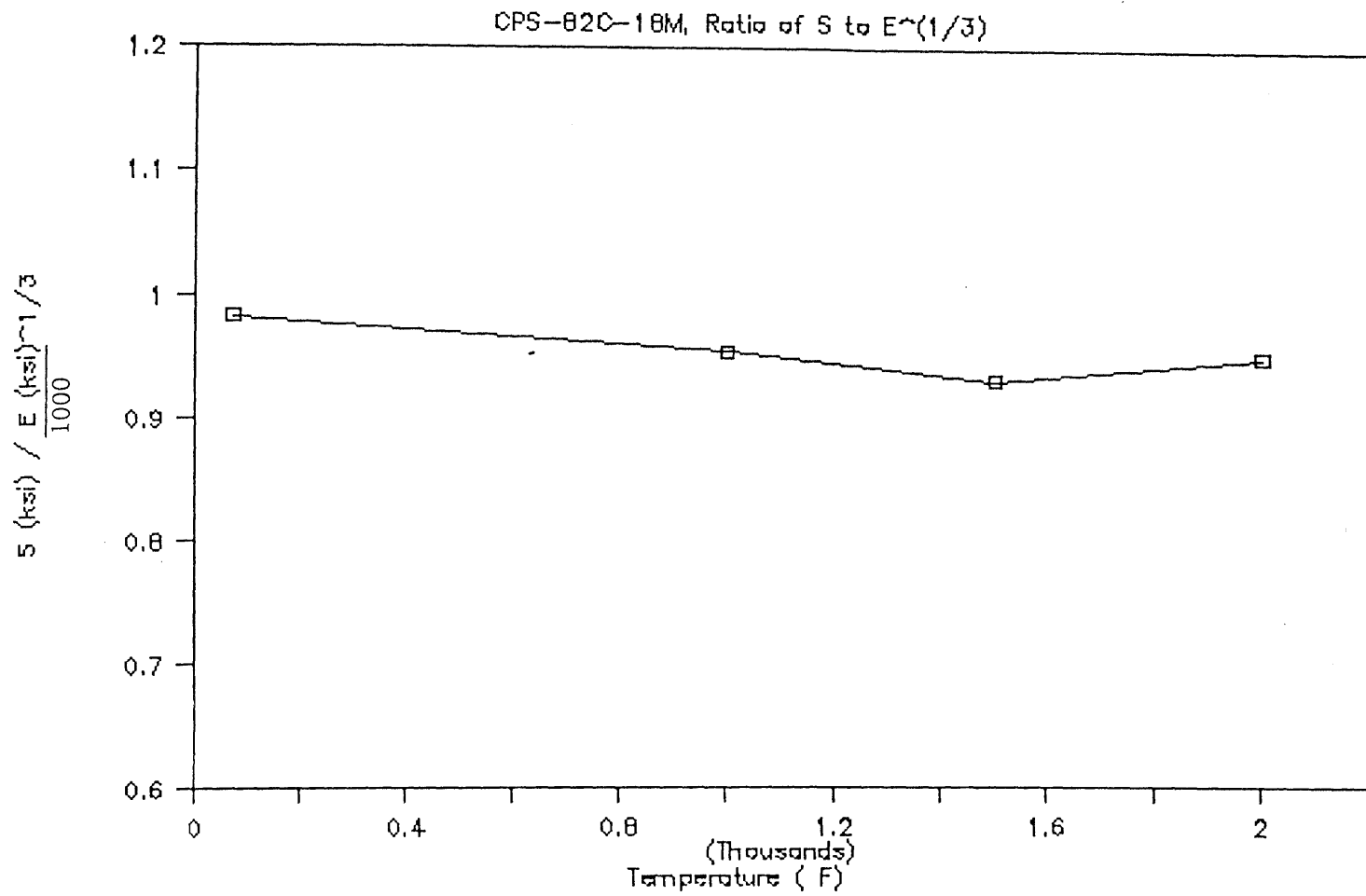
Figure 5.21   Ratio of the strength to the cubic root of the initial modulus
for CPS–82C–18M

As—Manufactured CPS—90A—10C
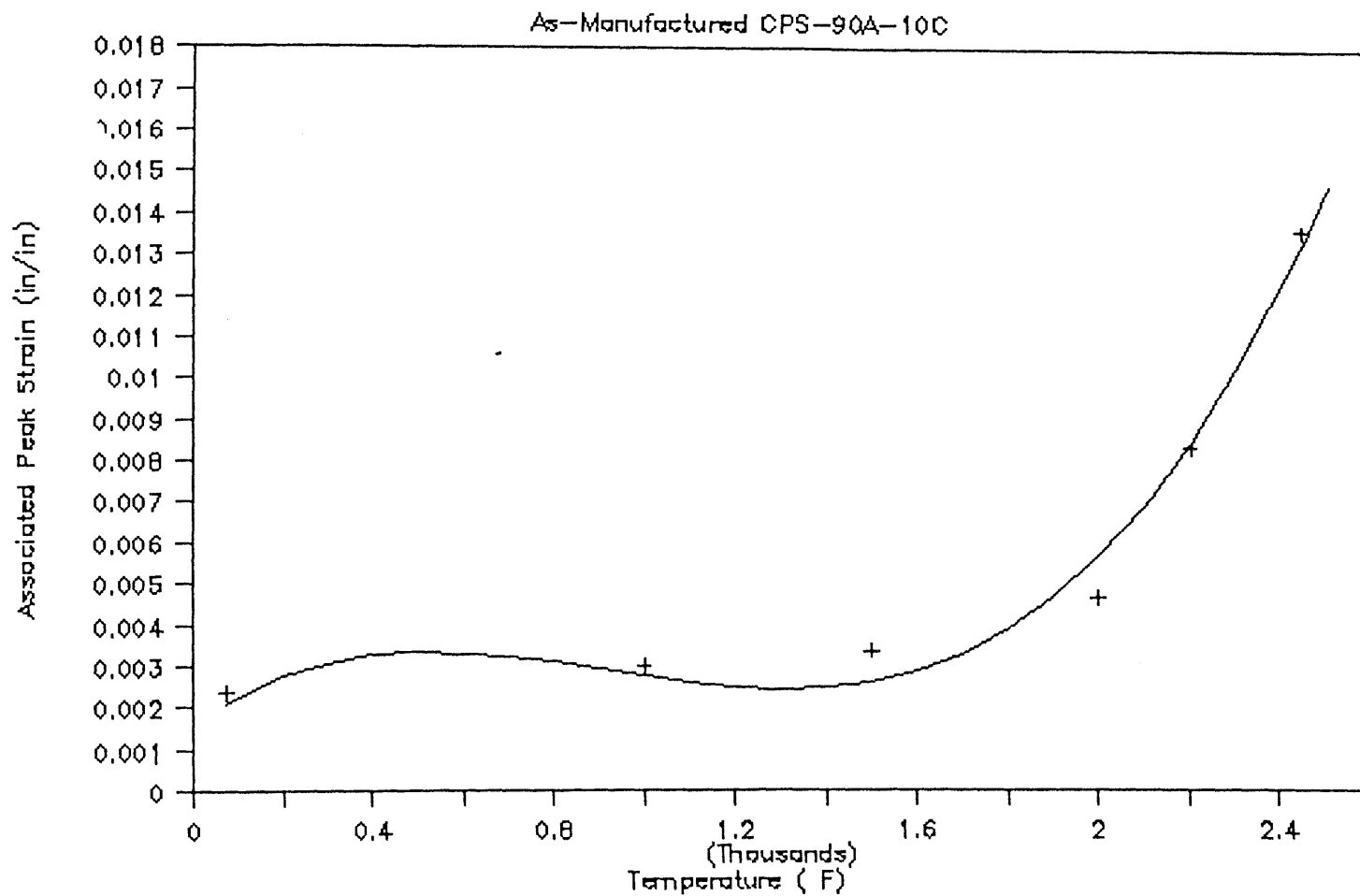
Figure 5.22   Associated peak strain variation with temperature for CPS—90A—10C

$0.5\ T_m$. A similar behavior is observed for material CPS–82C–18M as shown in Fig. 5.23.

Below $0.5\ T_m$ the specimen fails in a brittle mode, and the fracture strain is fitted by the following expression:

$$\epsilon_f = C_1 \exp\left(\frac{-C_2\ S\ (1 - (S/\hat{\tau})^2}{T}\right)$$ (5.3)

where S is the material strength given by Equation (1), and C_1 and C_2 are constants. In materials such as metallic glasses (Megusar et al., 1979) Equation (3) applies for temperatures below $0.6\ T_g$ (T_g defined as the glass transition temperature)

For the temperatures below $0.5\ T_m$ the associated peak strain and the final fracture strain are equal. For temperatures above $0.5\ T_m$, the final fracture strain is significantly larger than the associated peak strain due to significant non–linear deformations in the post peak region.

The equivalent toughness (defined as the area under the stress strain curve) variation with temperature is shown in Fig. 5.24 for material CPS–82C–18M. The equivalent toughness is approximately constant for temperatures below $0.5\ T_m$, and increases sharply for temperatures above $0.5\ T_m$. The reason for this increase may be that although the material strength decreases with higher temperatures, the associated peak strain and the final fracture strain are increasing faster. In the brittle fracture region it is reasonable to assume that the strength is proportional to the equivalent toughness. The slow decrease in strength for temperatures below $0.5\ T_m$, although the equivalent toughness is about constant, can be attributed to the decrease in the initial stiffness of the stress–strain curve. Similar considerations have been studied for material CPS–90A–10C as shown in Fig. 5.25.

It appears that the variation in the previously discussed properties is larger at room temperature than at high temperatures. The standard deviation, expressed as a

As—Manufactured CPS—82C—18M
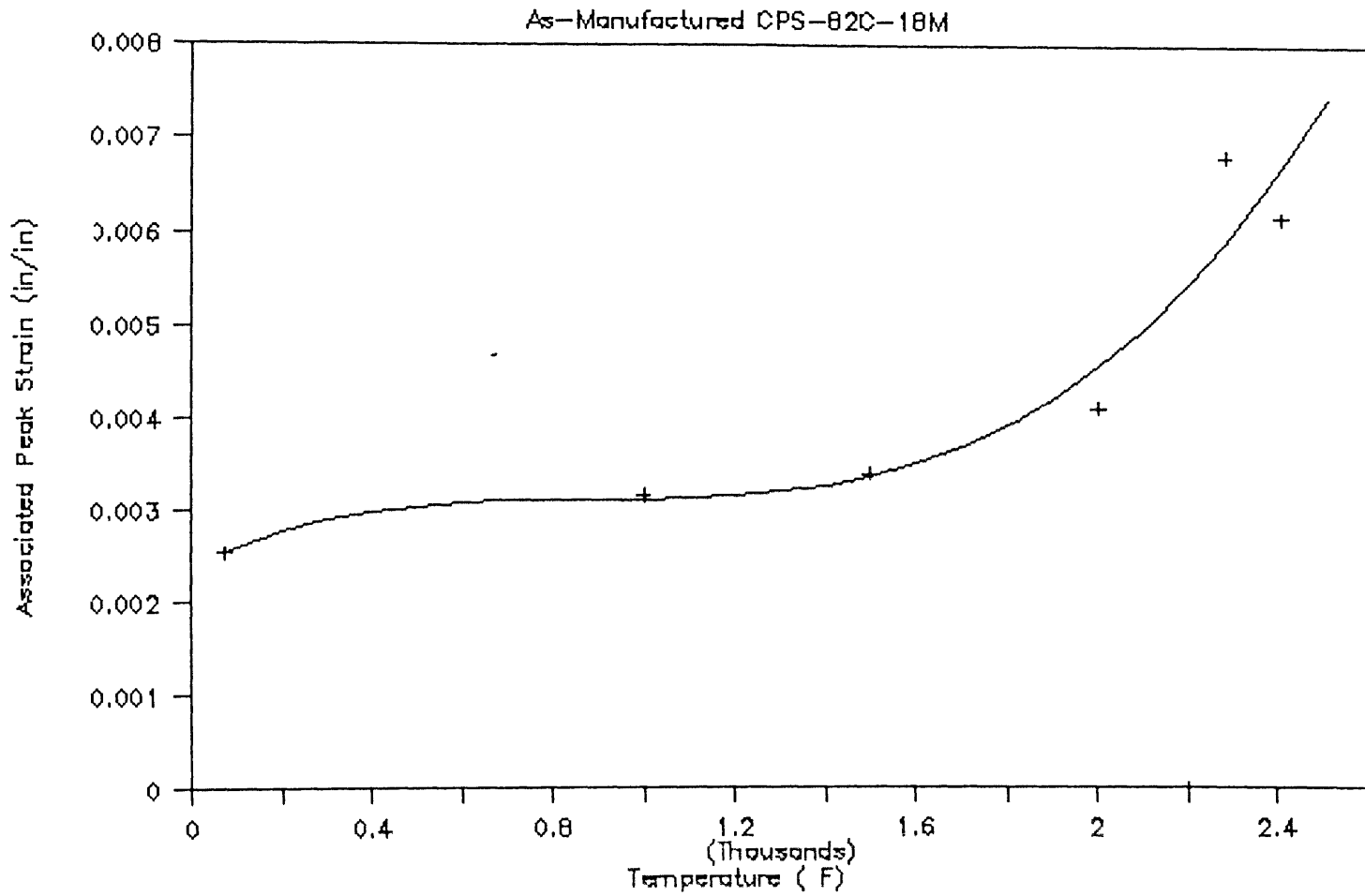
Figure 5.23   Associated peak strain variation with temperature for
                     CPS—82C—18M
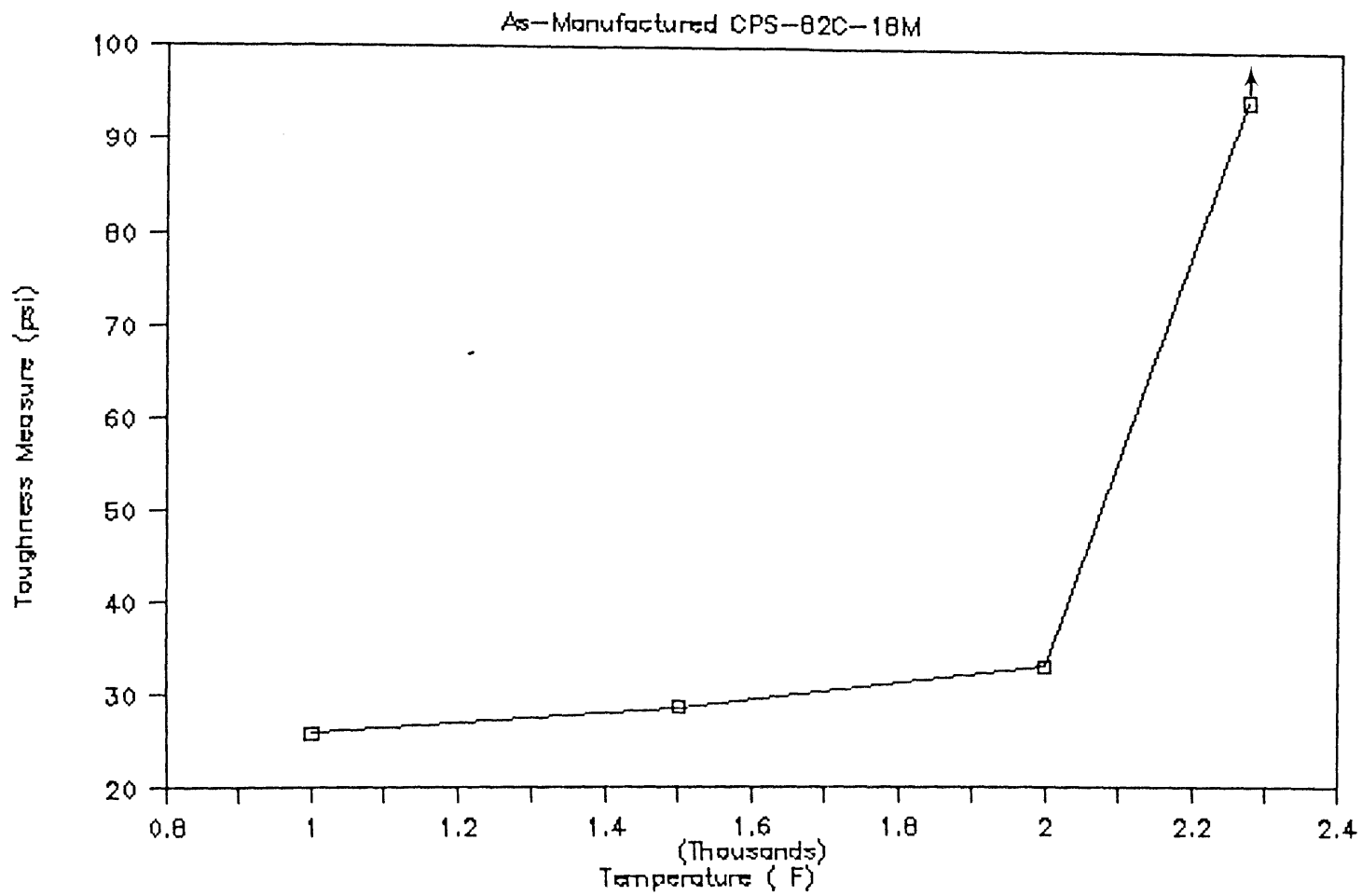
Figure 5.24   Toughness measure variation with temperature for CPS–82C–18M
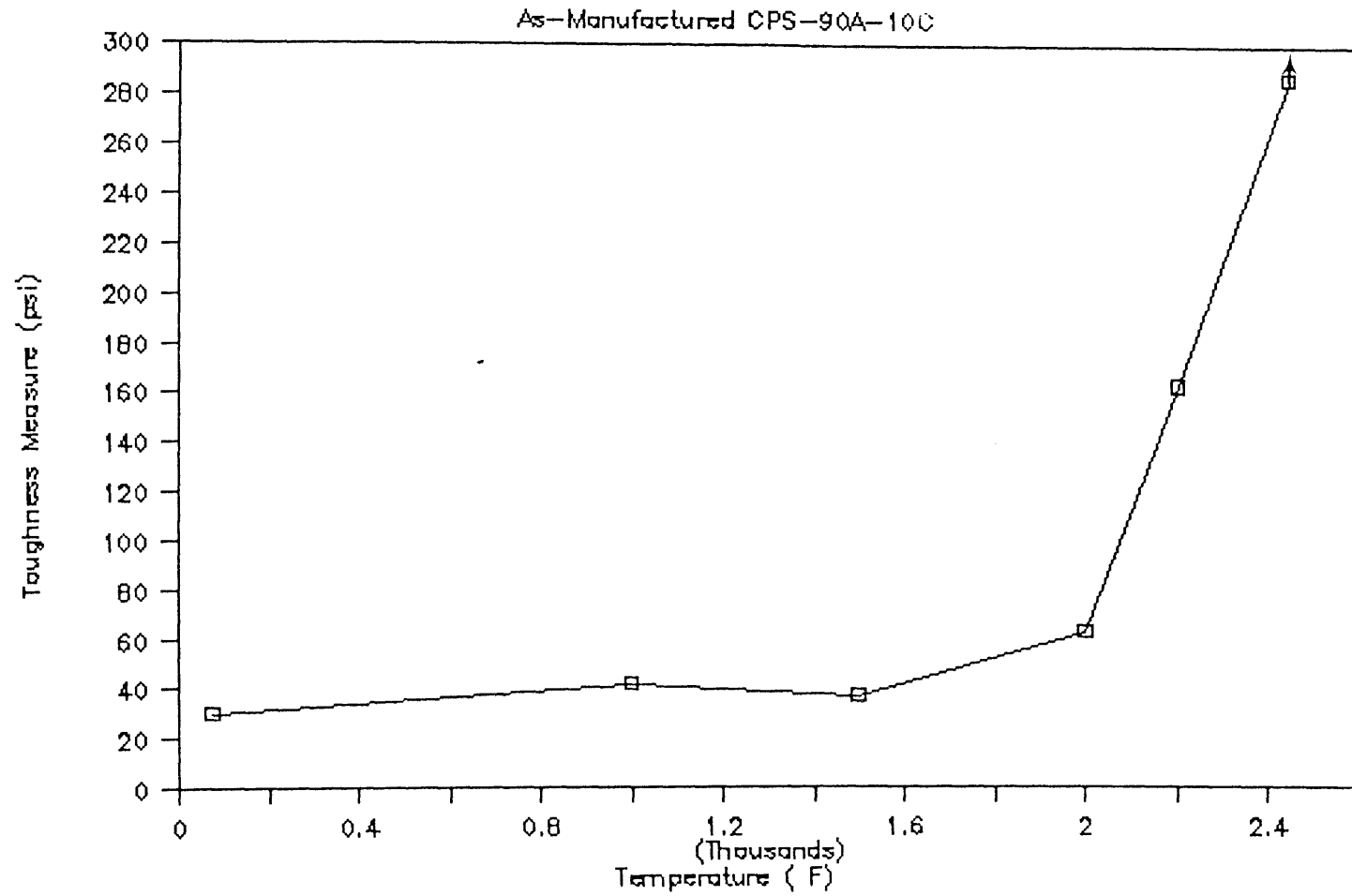
Figure 5.25   Toughness measure variation with temperature for
CPS-90A-10C

% of the mean, varies from room temperature to $2000^{\circ}F$ ($1093^{\circ}C$) for material CPS–90A–10C as follows:

- from 10% to 1.2% for strength values;

- from 19% to 6% for associated peak strains; and

- from 30% to 3% for the area under the stress strain curve

  which is termed equivalent toughness.

This is observed consistently for material CPS–82C–18M as well, and is explained by the less brittle behavior of the refractory oxides at higher temperatures.

In the brittle regime final fracture occurs in an explosive manner, and it is often hard to deduce the mode of cracking from the remaining pieces. Two observed modes of cracking of the cylindrical specimens at room temperature are shown in Figs 5.26a and 5.26b. Observed variations of these modes of cracking that may be due to end effects are shown in Fig. 5.27. At elevated temperatures most specimens exhibit the mode of cracking shown in Fig. 5.26a. The mode of fracture observed in Fig. 5.26a is an intrinsic fracture behavior. This kind of intrinsic fracture is usually expected in tougher materials (NMAB, 1983). At elevated temperatures the equivalent measure of toughness, that is the area under the stress strain curve, increases rapidly. This may be the reason for observing most modes of cracking to be of the intrinsic nature at elevated temperatures. The stress fields are inhomogeneous, due to the different grain sizes and different phases. This might explain the shear fault growing in a stable manner, such as the fracture observed for material CPS–82C–18M at $1246^{\circ}C$ ($2275^{\circ}F$) and $4 \times 10^{-6} \ sec^{-1}$ in Fig. 5.15. However in the brittle regime, and for strain rates above the transition strain rate the shear faults lead to unstable fracture. This mechanism of shear faulting have been observed in rocks and studied in detail at the macroscopic and microscopic levels (Kranz, 1979;
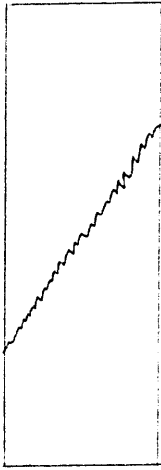
5.26a - Observed modes of fracture
        at room and elevated
        temperatures
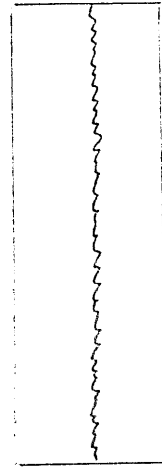
5.26b - Observed modes of fracture
        at room temperature

Figure 5.26   Most observed Modes of failure for CPS—90A—10C and
                     CPS—82C—18M
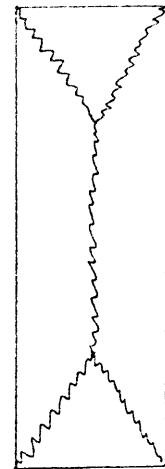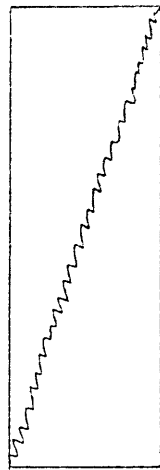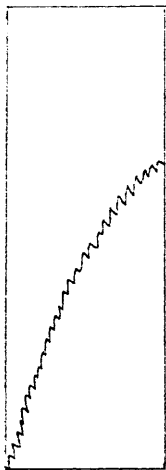
Figure 5.27   Other Modes of Failure for CPS—90A—10C and
                     CPS—82C—18M

Wong, 1982a, 1982b; Kachanov, 1982a, 1982b). Shear faults at 45° orientation, leading to shear failure in the specimens, have also been observed by McGee and Konrady (1983/3 and 1983/4) for cold–pressed sintered high–chromia refractories tested under long–term creep at elevated temperatures. The materials used by McGee and Konrady are similar to the ones used in this study.

5.4.2 Behavior Under Constant Compressive Loads At Constant Temperature In Air Atmosphere

The purpose of the constant compressive load tests at constant temperature was to study the nature of the non–linear deformations in monotonic load tests, and to quantitatively characterize the high temperature material behavior under high constant loads (up to 85 % of the monotonic strength). Longer term creep tests carried out by other researchers, characterize the behavior of similar materials for constant load levels generally below 15% of the monotonic strength (McGee and Konrady, 83–87).

Figure 5.28 shows the variation of the creep strain rate for CPS–90A–10C at temperature levels of 1500°F (816°C), 2000°F (1093°C), and 2400°F (1316°C), under 68%, 66%, and 68% of the uniaxial monotonic strength respectively. For the tests at 2000°F and 1500°F, the contribution of the short–term creep deformation (during the 10 minute duration of monotonic tests) to the total deformation appears to be negligible. However at 2400°F the contribution of the creep deformation to the total deformation of monotonic tests seems to be significant. The creep strain rate $(\dot{\epsilon}_{creep})$ initially decreases at a fast rate with time, but its variation is slower afterwards. This is shown in Fig. 5.29 where the results are plotted as log $(\dot{\epsilon}_{creep} \times 10^{8})$ vs. time for different temperature levels. A steady state creep strain rate is not always reached during the two to three hours duration of these short–term creep tests. The

As—Manufactured CPS—90A—10C

Creep Strain (in/in)

2400 F, 74% S

2400 F, 57% S

2000 F, 55%S

1500 F, 66%S

(Thousands)
Time (sec)
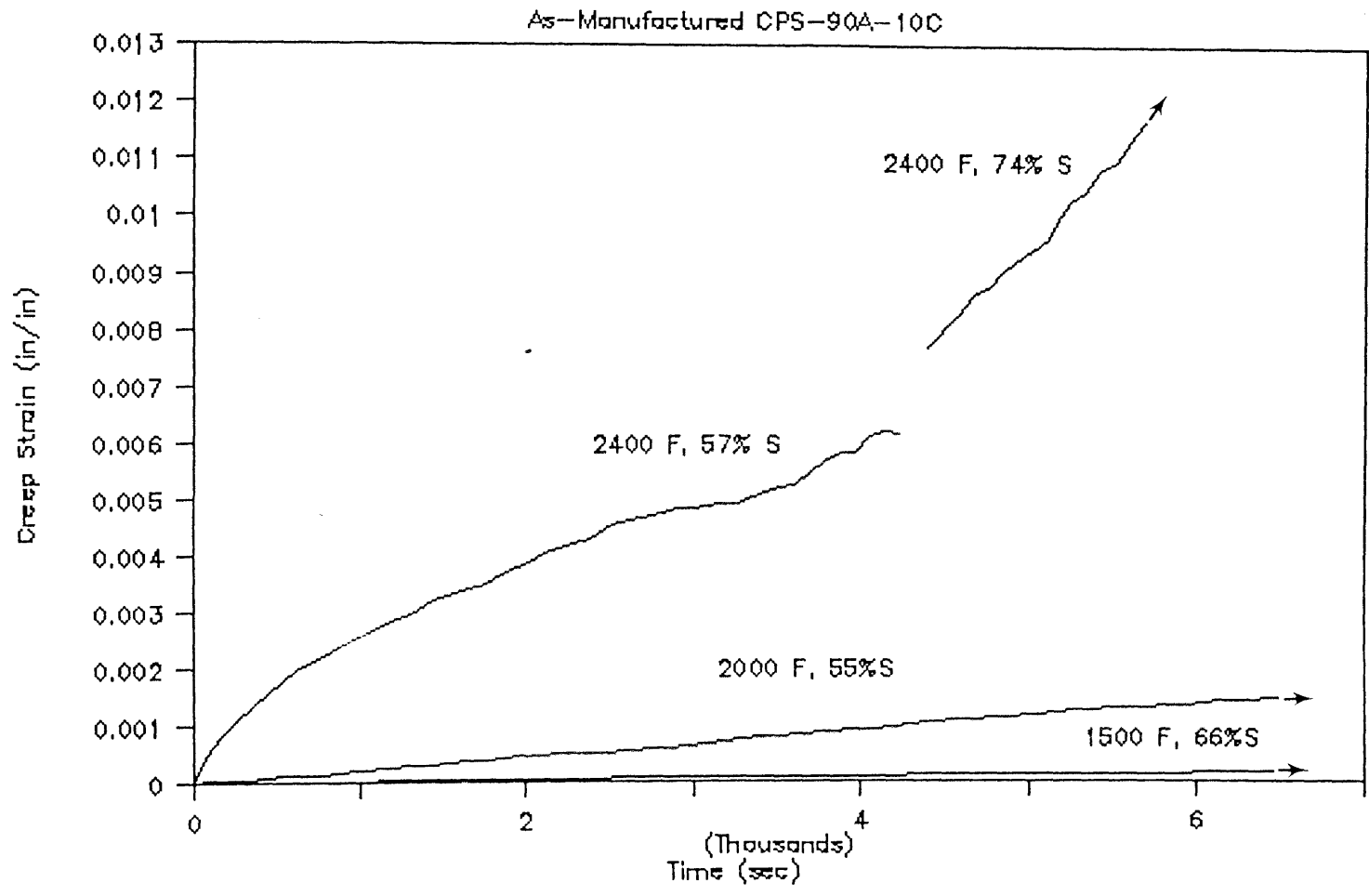
Figure 5.28   Creep strains for CPS—90A—10C at different temperature and load levels
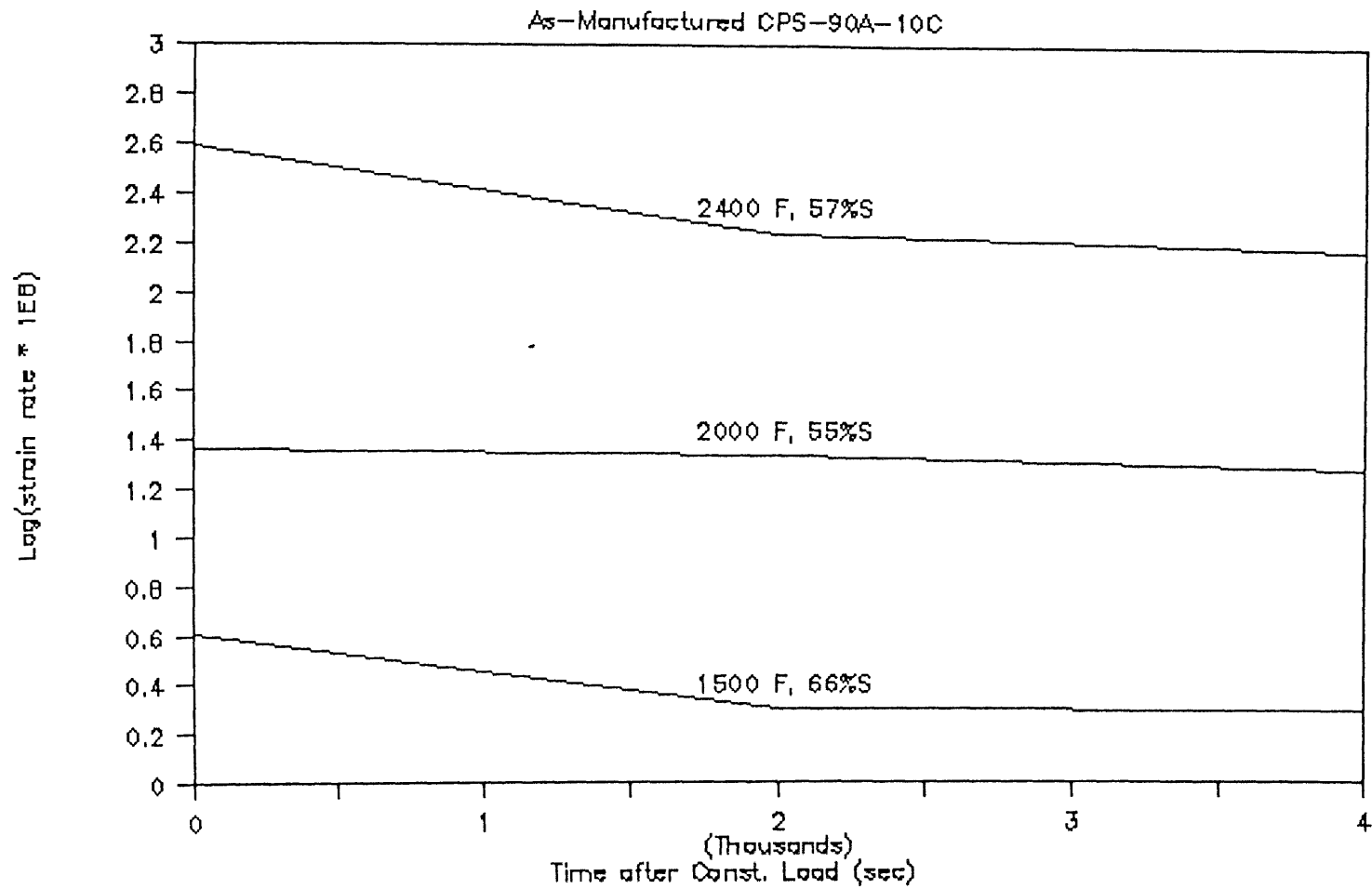
Figure 5.29   Variation of the log of the creep strain rate at different temperature and load levels for CPS–90A–10C

results of the short term creep tests on material CPS–82C–18M, are similar to the ones on CPS–90A–10C as shown in Figs. 5.30 and 5.31. It is noted that CPS–82C–18M exhibits higher deformation rates than CPS–90A–10C under short–term creep.

The effect of load histories on the results of short term creep tests is studied as well. Two specimens of CPS–90A–10C were both tested at 2400°F (1316°C). The first one was subjected to a constant load level of 52% of the monotonic strength for 4000 sec, before the load level was raised to 68%, and kept at 68% for 2000 sec. The second specimen was loaded directly to 68% of the monotonic strength, and failed after 3000 sec. The creep strain variation for both specimens is shown in Fig. 5.32. This shows the importance of load histories on the material behavior. The first load appears to have consolidated the material, before the second load was applied.

A useful way to represent the deformation behavior of the material with respect to temperature is by the use of deformation mechanism maps (Frost and Ashby, 1982). These maps highlight different behaviorial regions on a map with $T/_{TM}$ as its X–axis and $\tau/\hat{\tau}$ as its Y–axis, where τ is the shear strength and $\hat{\tau}$ is the ideal shear strength of the material. The strain rate effect is incorporated into the map as well. In this paper, deformation maps are used in two ways. First, comparison of the tests data with available deformation mechanism maps is carried out and next deformation maps combining the results of our short–term tests, with published long–term creep tests (McGee and Konrady, 1983–1987; Wiederhorn and Krause, 1986) are constructed.

A stress–temperature map for Cr_2O_3 with a grain size of 10 μm is extracted from Frost & Ashby (1982), and the features relevant to the present discussion are shown in Fig. 5.33. It is interesting to study, using this map, the behavior of tested

As Manufactured CPS—82C—18M

Creep Strain (in/in)

2400 F, 68%S

2400 F, 55%S

1500 F, 84%S

(Thousands)
Time (sec)
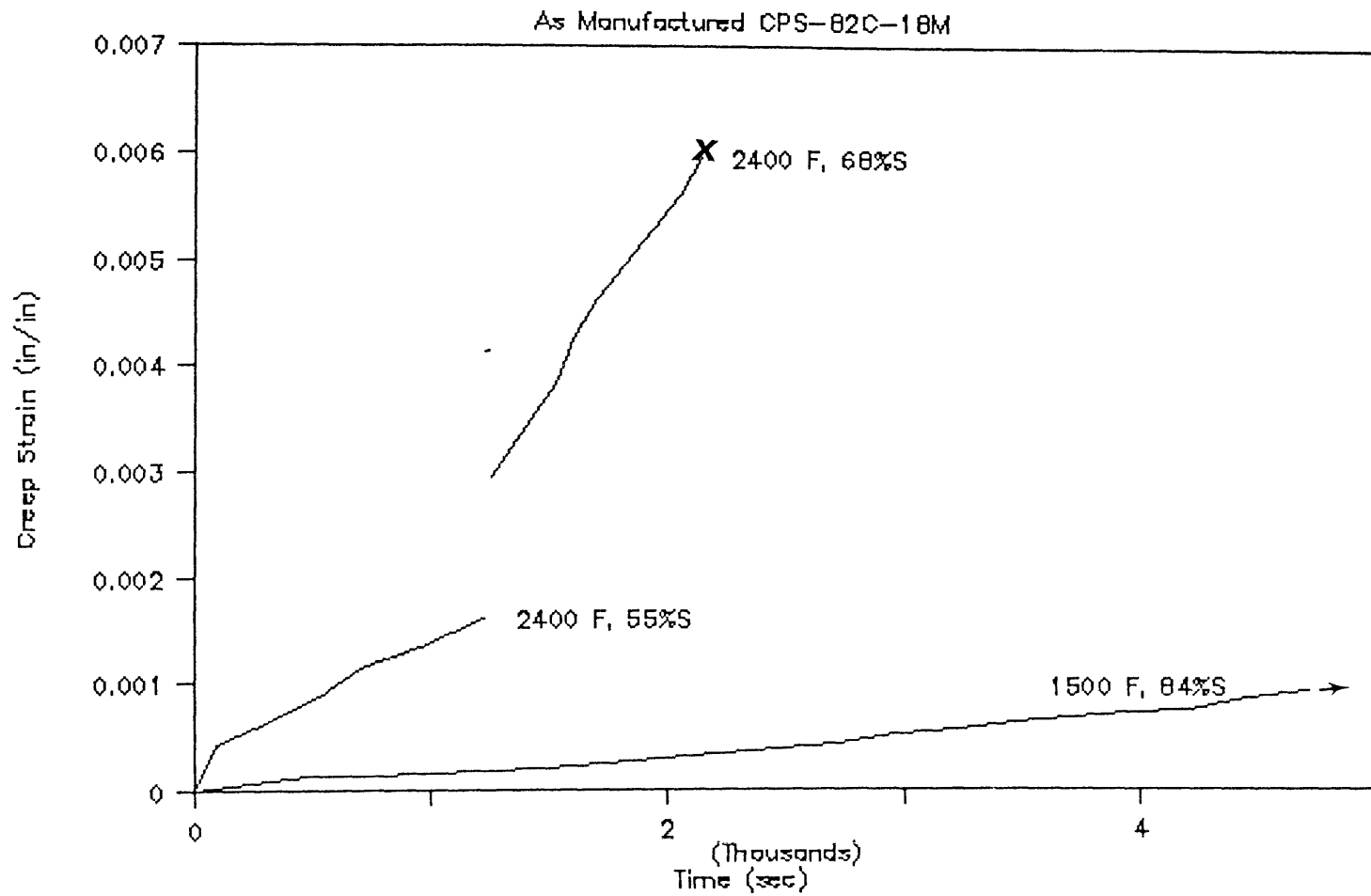
Figure 5.30   Creep strains for CPS—82C—18M at different temperature
                   and load levels
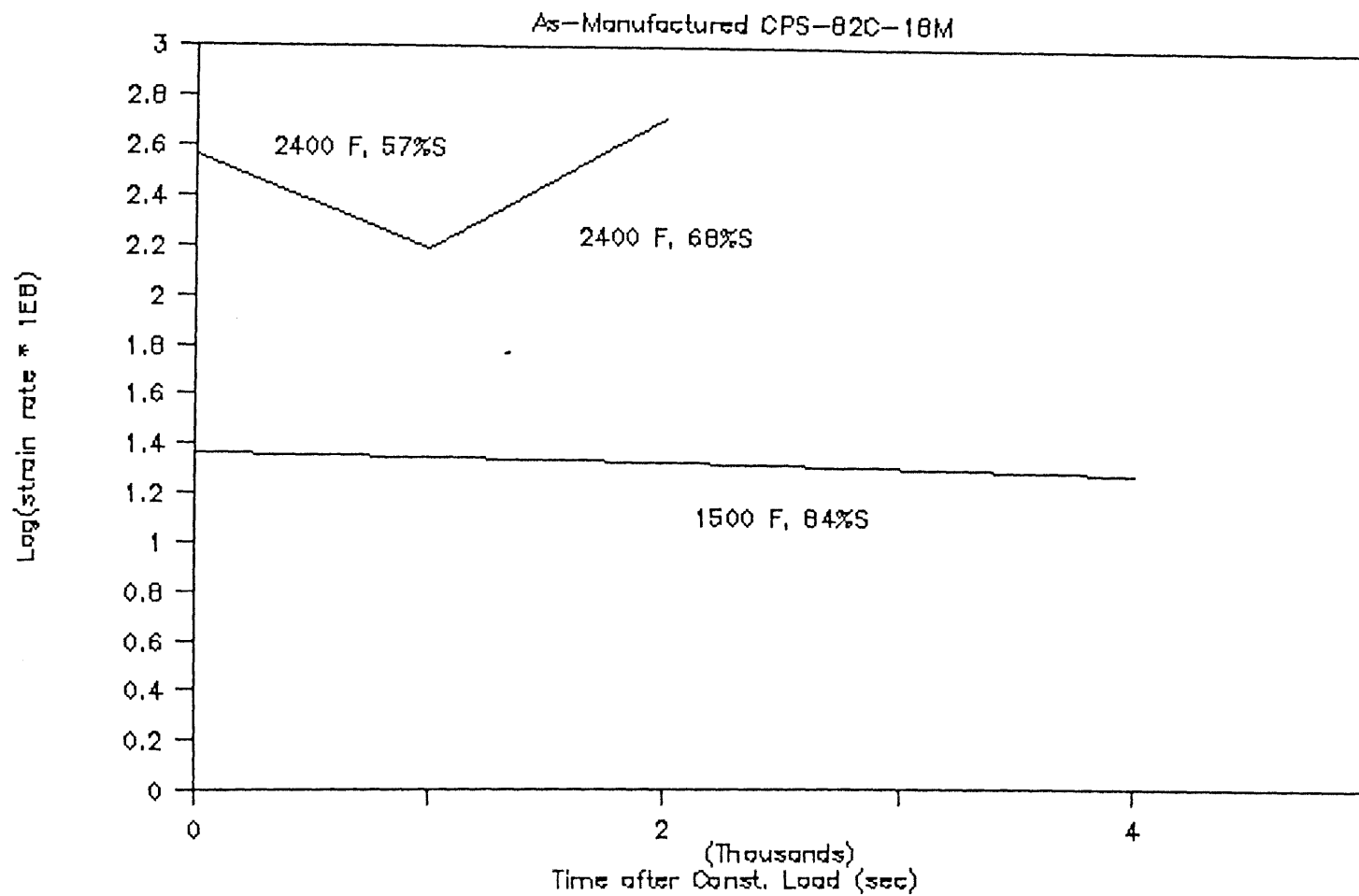
Figure 5.31   Variation of the log of the creep strain rate at different temperature and load levels for CPS–82C–18M
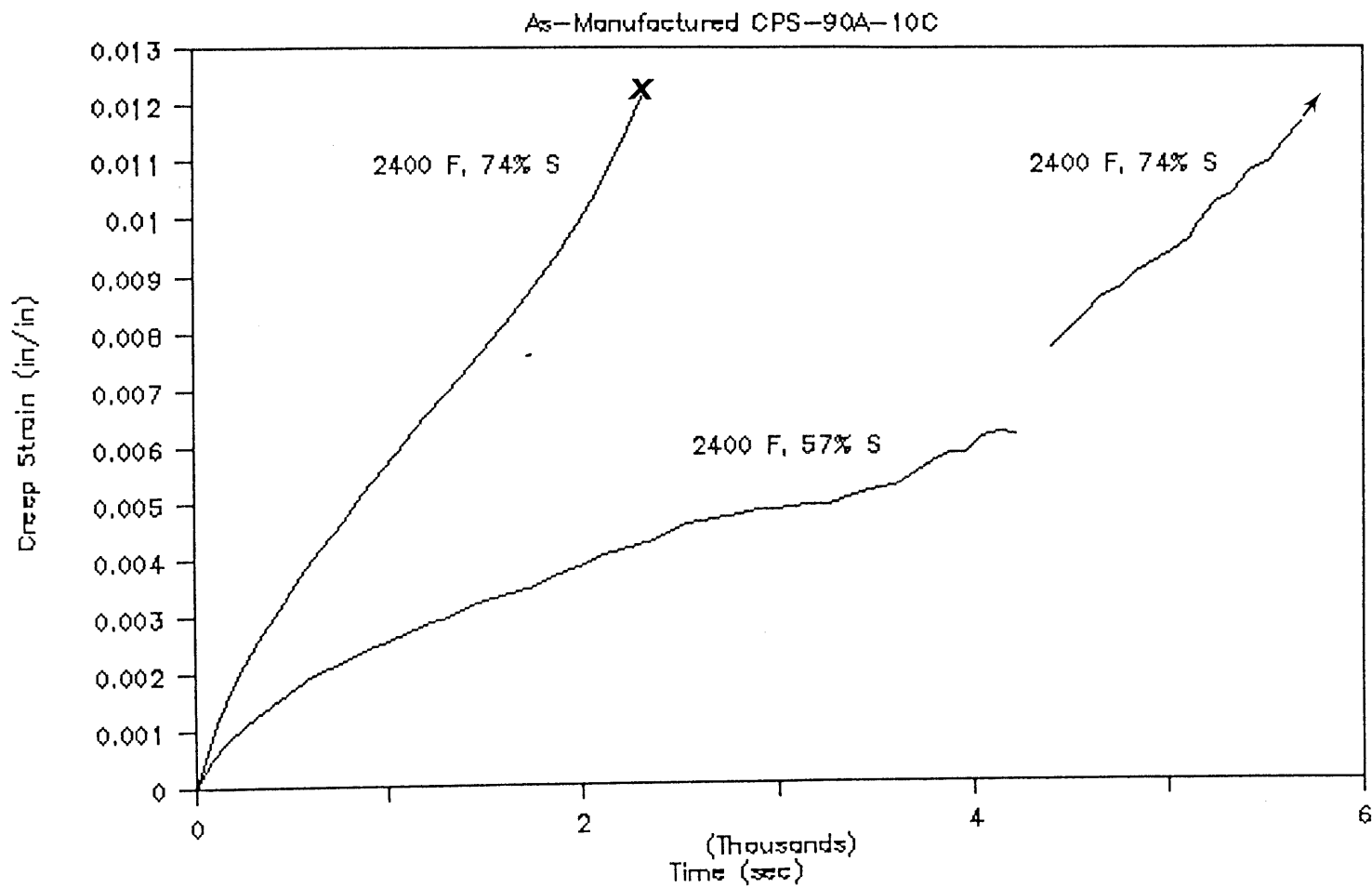
Figure 5.32   Creep strains for CPS–90A–10C at the same temperature and final load level, but different load histories

high–chromia (CPS–82C–18M), keeping in mind that there is 18% MgO in the Material CPS–82–18M, and that the grain size and porosity are different. Two points are used to define the brittle fracture line on the map, and they are: point I at room temperature: 73°F (23°C) and a strength of 19300 psi (133 Mpa) and point II at 1000°F (538°C) and a strength of 16461 psi (113 Mpa). Point III is then added to the map, at 2400°F (1316°C), and a strength of 6500 psi (45 Mpa). Points I and II clearly are outside the creep regime, while point III falls in the power law creep region, below the brittle fracture line defined by points I and II. The stress–temperature map predicts a strain rate of 10^{-5} sec^{-1}. The average test strain rates were 1.1 x 10^{-5} sec^{-1} for 1000°F, and 2.1 x 10^{-5} sec^{-1} for 2400°F which represents a good agreement.

The data obtained from our short term creep and monotonic tests have been combined with data obtained by McGee and Konrady (1983–87) to produce deformation maps for the materials under consideration. The results are shown in Figs. 5.34 and 5.35 for CPS–90A–10C and CPS–82C–18M respectively. For both CPS–90A–10C and CPS–82C–18M the results of the short–term creep tests (total test time about two to three hours, and constant load values ranging from 50% to 85% of the monotonic strength) conducted under the current project correlate nicely with the results of the long–term creep tests from McGee and Konrady (total test time exceeding 100 hours, and constant load values less than 10% of the material monotonic strength). The deformation maps facilitate the comparison of deformation rates between different materials. The deformation rates of CPS–82C–18M are about an order of magnitude greater than the ones for CPS–90A–10C (as an example, from Figs. 5.34 and 5.35, at 2000°F and 1000 psi the maps predict deformation rates of about 5x10^{-7}/sec for CPS–90A–10C and about 5x10^{-6}/sec for CPS–82C–18M).
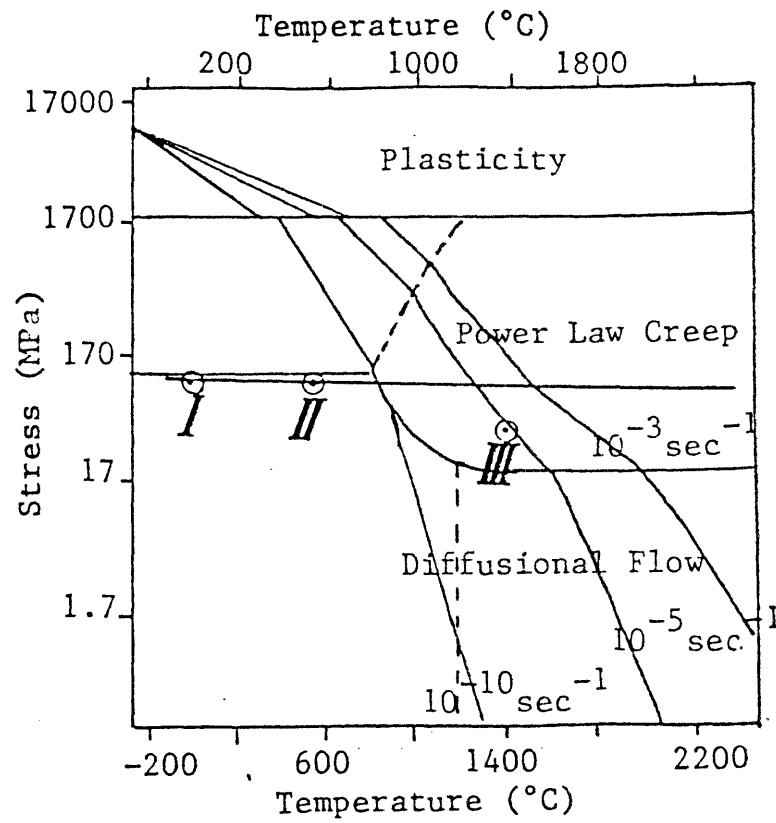
Figure 5.33   Comparison of the results obtained in monotonic tests for CPS–82C–18M with a stress temperature map for Cr_2O_3 from Frost and Ashby (1982)
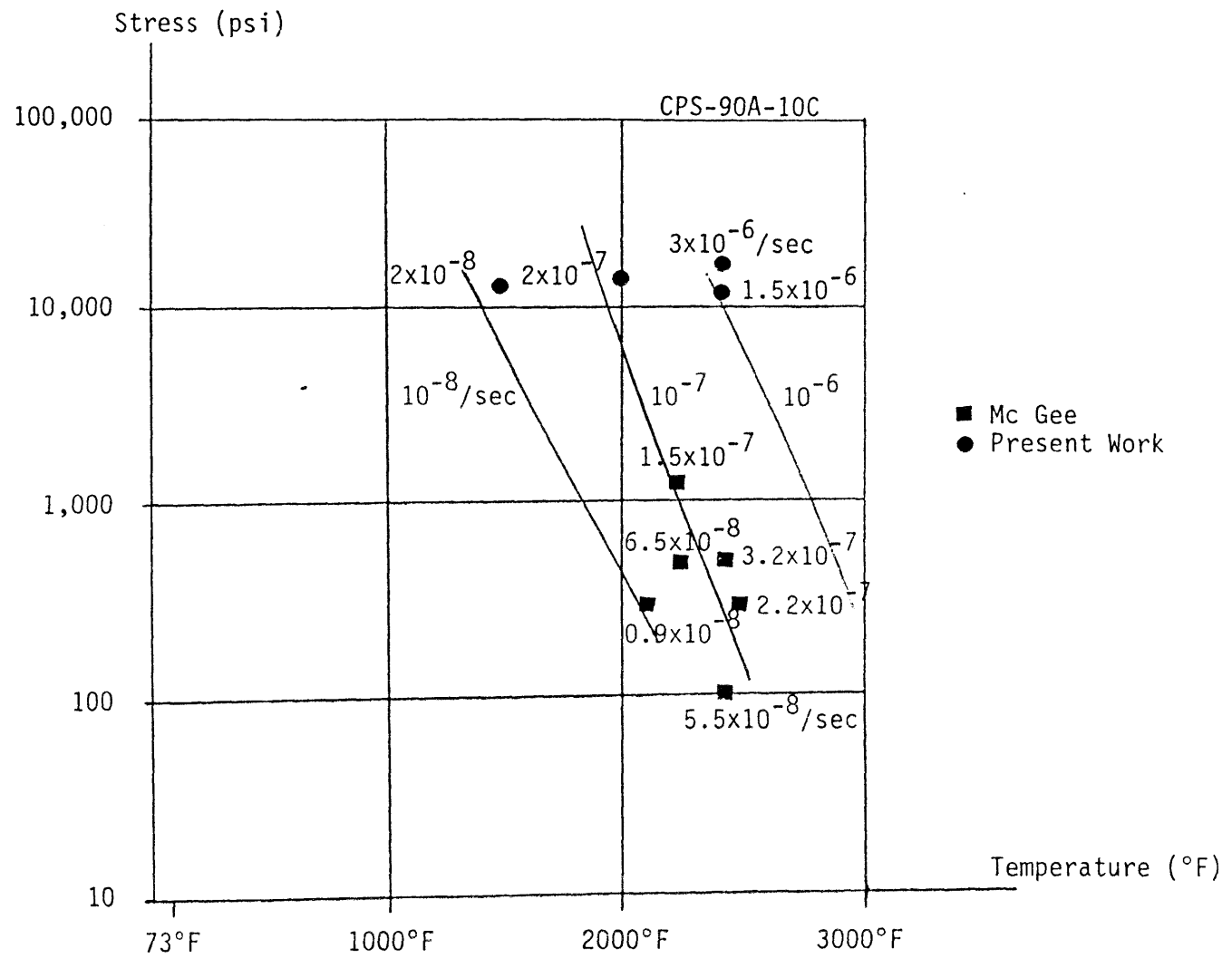
Figure 5.34   Deformation map for CPS–90A–10C
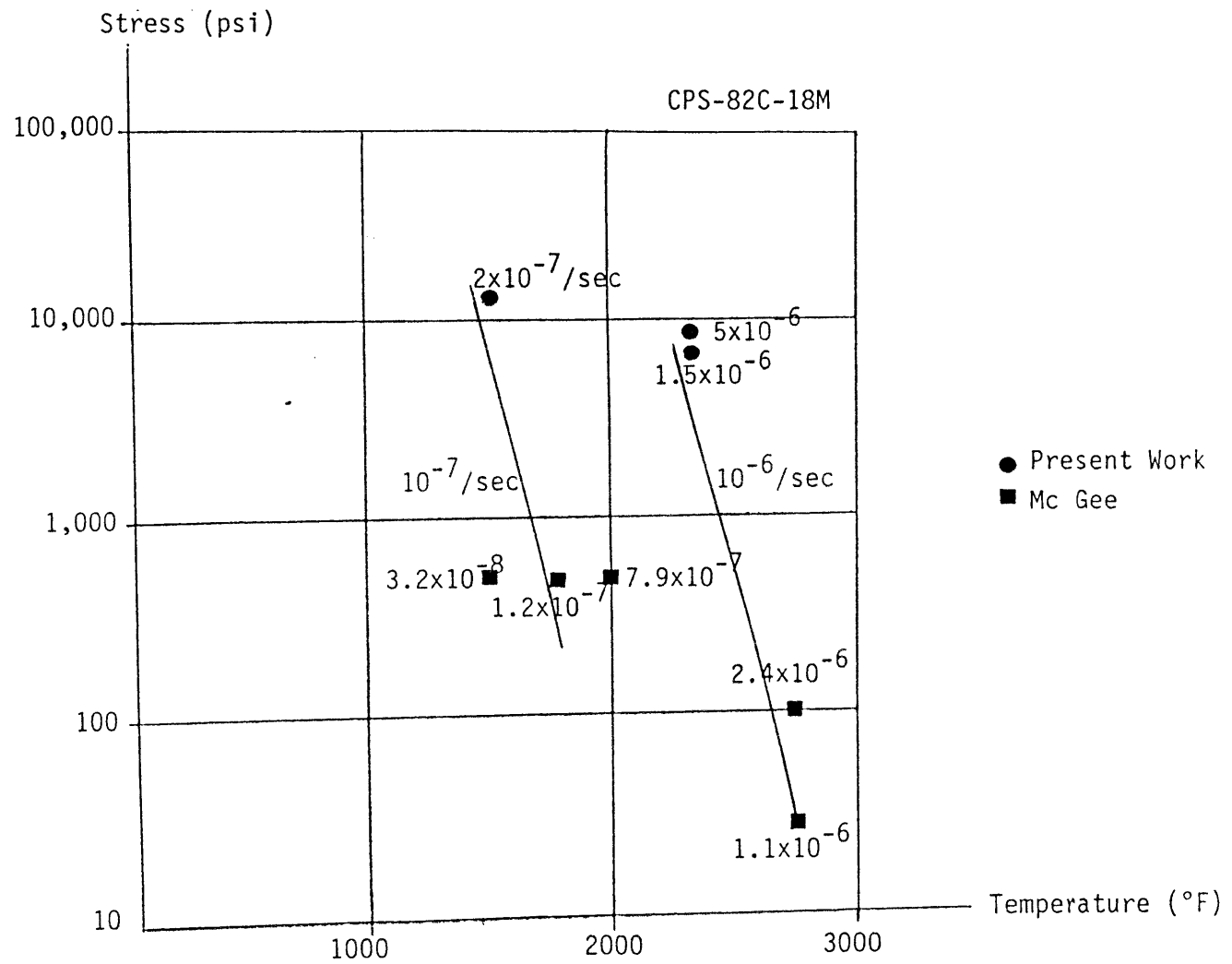
Figure 5.35　　　　Deformation map for CPS–82C–18M

These deformation maps are also useful in showing the whole spectrum of loading conditions generally encountered in high temperature containment vessels.

The deformation map of Fig. 5.34 for CPS–90A–10C is redrawn on a semi–$\log_{10}$ plot with scaled axes: σ/E (where σ is the stress and E is the initial stiffness) and T/T_m (where T is the temperature and T_m the melting temperature) in Fig. 5.36. The purpose was to compare it with a fracture mechanism map for alumina from Ghandi and Ashby (1979) which includes results from monotonic load tests as well as creep tests; the normalized tensile stress is used as y–axis, and compression data are included after dividing the stress by eight. Most tests shown on our map fall within two regions on Ghandi and Ashby's map: brittle intergranular fracture and intergranular creep fracture. Their description of the mechanisms of deformation and fracture in the brittle intergranular fracture region is that for temperatures above about 0.5 T_m (1000°C), alumina starts to creep and the fracture strain increases with temperature. Slip or grain boundary sliding concentrate stress, nucleating boundary cracks, until one of them propagates to give the brittle intergranular fracture. At' higher temperatures and lower stresses, in the intergranular creep fracture region, failure is by void growth. They also report that the rate of loading has a pronounced effect in these ranges. This correlates well with the results obtained in our own testing program and also with the results of our microstructural characterization discussed in Section 5.6.

The mechanisms of deformation above half the melting point of the material are different from those at low temperatures, due to the effect of atomic diffusion which is important in deformation at elevated temperatures and is not present at low temperatures (Takeuchi and Argon, 1976). Different creep mechanisms prevail at
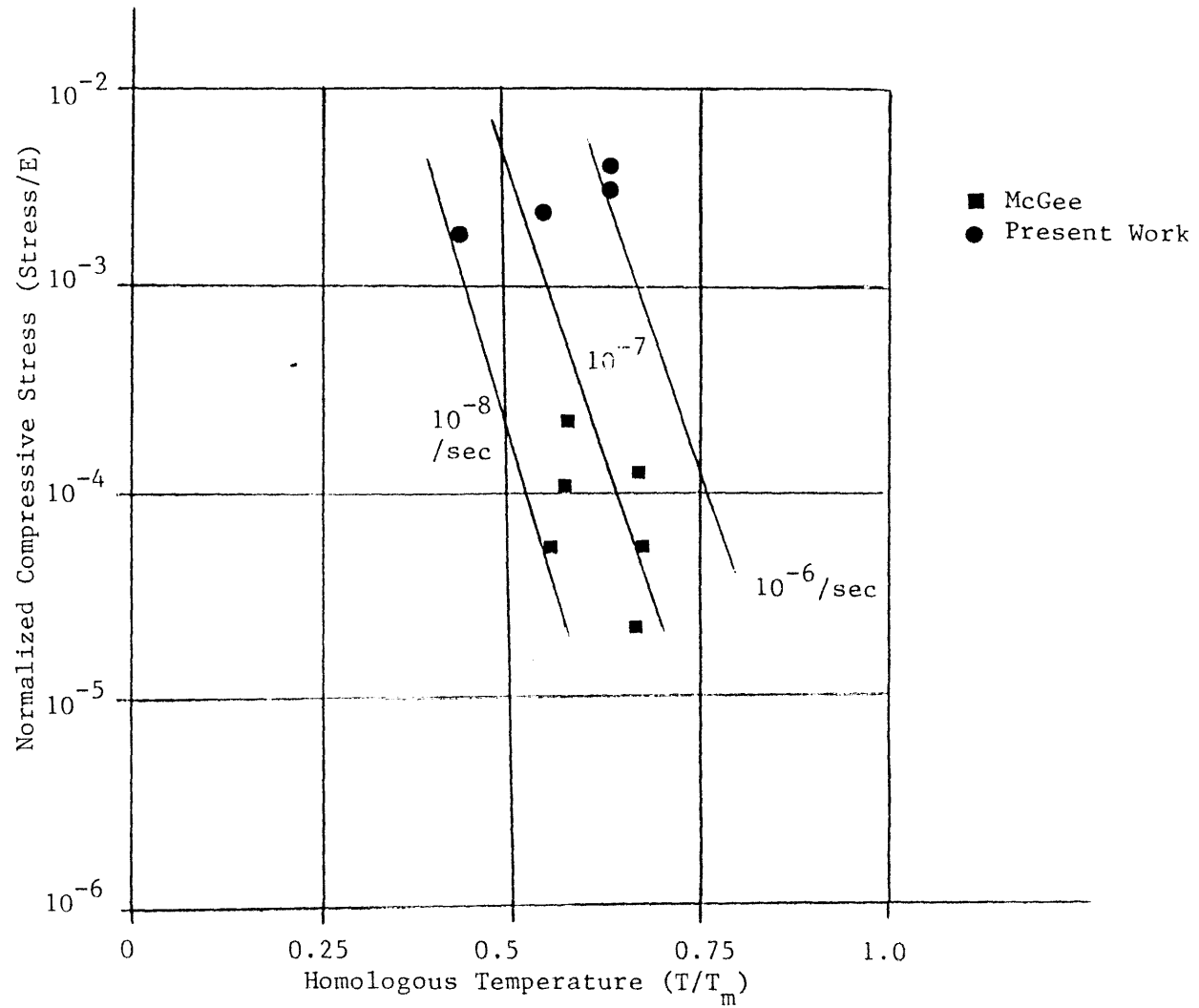
Figure 5.36   Deformation mechanism map for CPS–90A–10C using normalized axis

different temperature levels: (1) dislocation gliding at low temperatures and (2) dislocation climbing and gliding, grain boundary sliding, grain boundary migration and direct diffusion at higher temperatures (Ashby, 1973; McClintock and Argon, 1966). Diffusion can occur along the grain boundaries: Coble creep (Coble, 1963), or within the grains: Nabarro–Herring creep (Herring, 1950). For ceramic materials dislocations do not play an important role. For refractory ceramics, many factors make their creep behavior extremely difficult to analyze (Kingery e. al., 1976), such as the presence of many inhomogeneous angular phases, particularly glass phases and incompletely reacted phases.

The creep results often are analyzed using the following equation:

$$\dot{\epsilon}_{creep} = A \, \sigma^n \exp(-Q/RT) \qquad (5.4)$$

where A is a constant, σ is the stress raised to a stress exponent n, Q is the activation energy, R is the molar gas constant and T is the absolute temperature. The stress exponent, n, can be obtained from a plot of ln $\dot{\epsilon}$ versus ln σ at constant temperature. For self diffusion the activation energy is the sum of the energies of formation and of motion of vacancies (McClintock and Argon, 1966). The activation energy can be obtained from an Arrhenius temperature–dependence plot of ln $\dot{\epsilon}$ versus reciprocal temperature 1/T at constant stress. A least–squares fit of the data obtained for the short–term creep tests on CPS–90A–10C gave:

1. an activation energy of 185 kJ/mole from the slope of the Arrhenius plot shown in Fig. 5.37a (for temperatures from 1089°K (1500°F) to 1589°K (2400°F), at 90 MPa (13ksi)); and

2. a stress exponent of 1.83 from the slope of the ln $\dot{\epsilon}$ versus ln σ plot shown in Fig. 5.37b (for stresses from 90 MPa (13 ksi) to 120 MPa (17.4 ksi), at 1589°K (2400°F)).
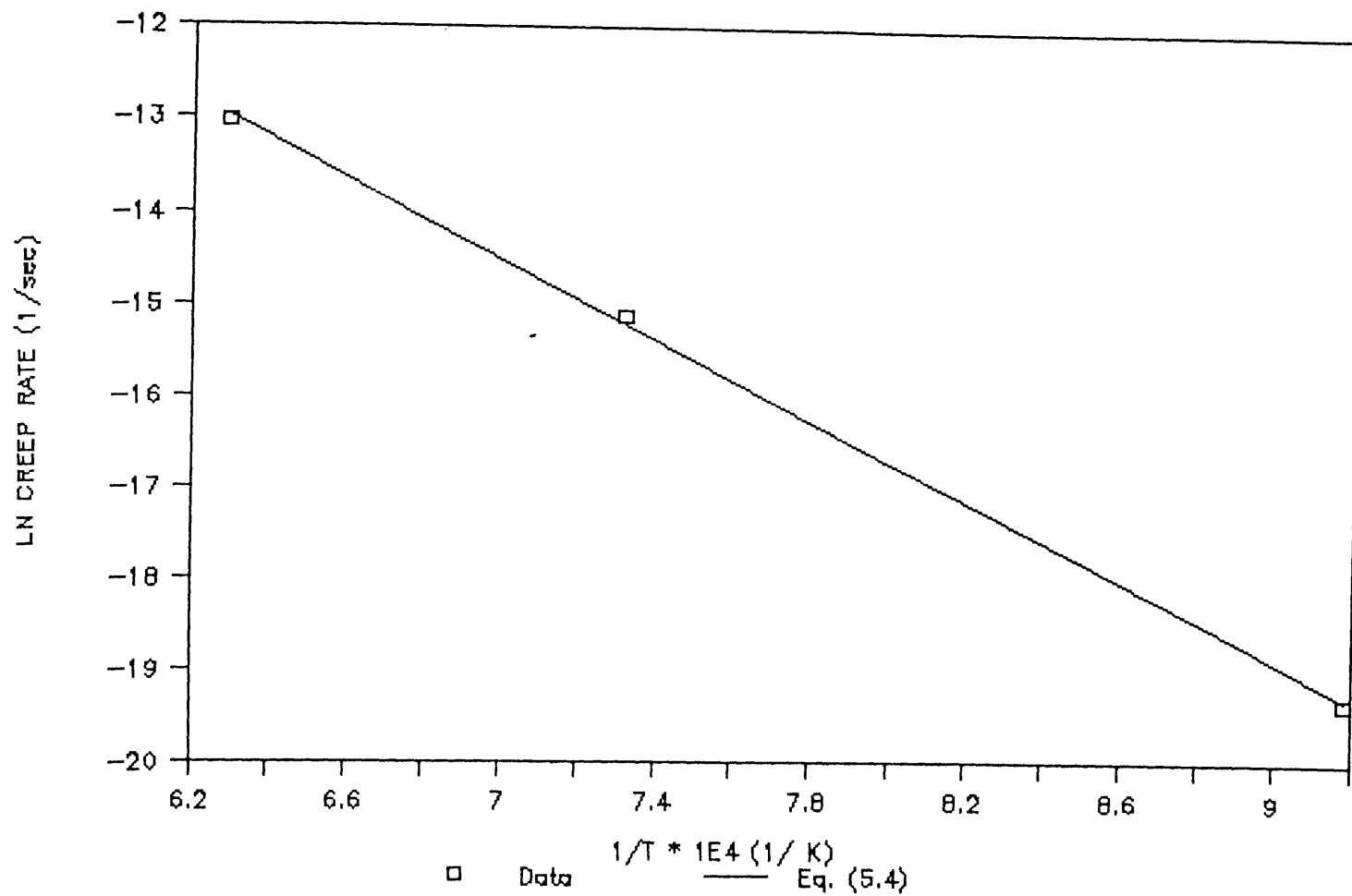
Figure 5.37a   Arrhenius plot of ln ε̇ vs. 1/T for CPS–90A–10C used to obtain the activation energy
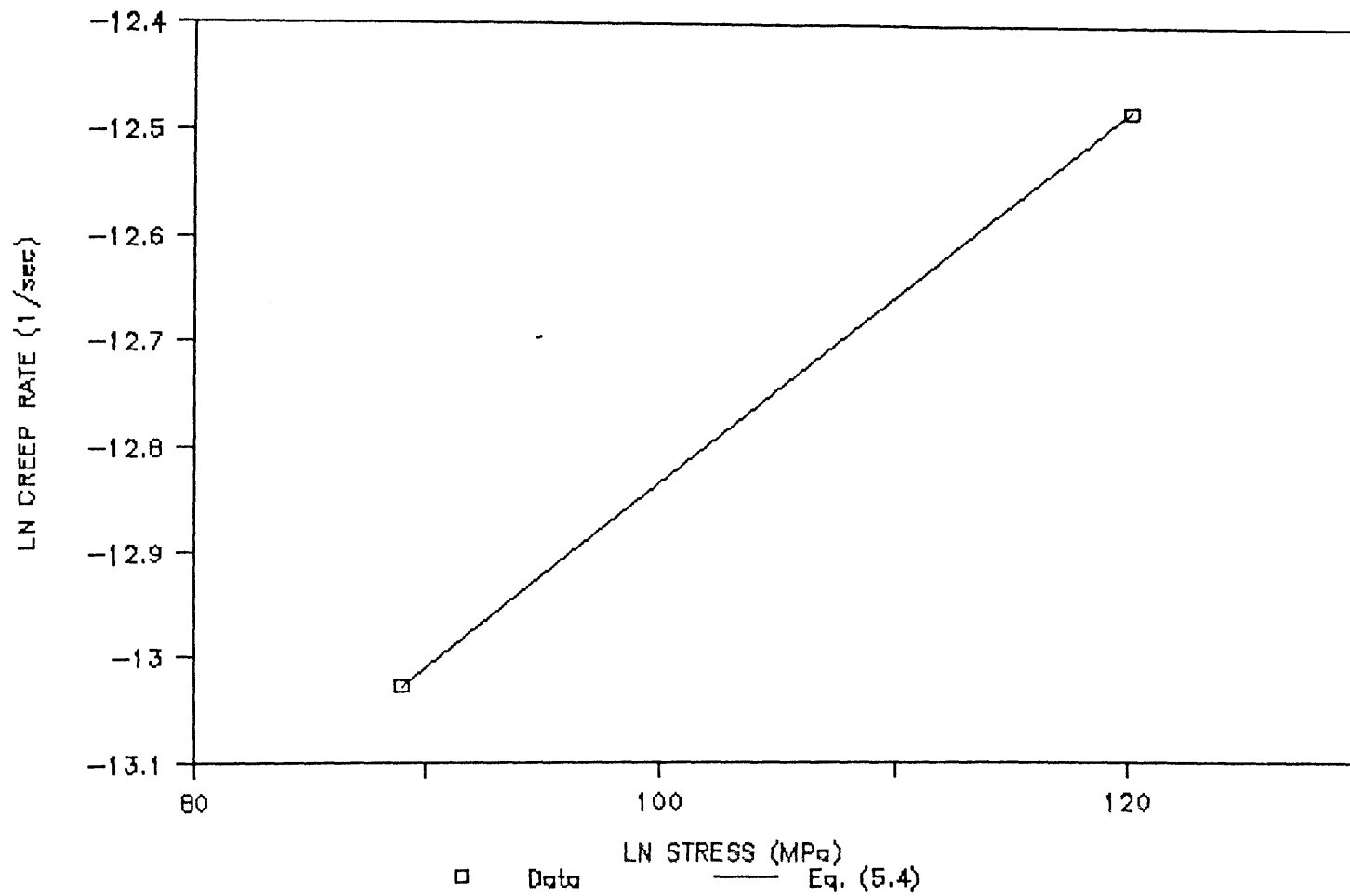
Figure 5.37b   Plot of ln $\dot{\varepsilon}$ vs ln σ used to obtain stress exponent

For refractory materials, results of longer term creep tests (specimens under creep from 10 to 40 hours) at small loads (up to 700 psi) on fused high-chromia refractories (from 73% to 80% chromia) showed activation energies from 160 kJ/mole to 240 kJ/mole, and stress exponents of 0.41 to 1.27 (McGee and Wiedemeier, 1985a); no explanations were given for the stress exponents smaller than one. In another report an activation energy of 518 kJ/mole was found by McGee and Wiedemeier (1985b) for a sintered 80%-chromia refractory. Wiederhorn et. al. (1986) found an activation energy of 926 kJ/mole with a stress exponent of 4.85 for vitreous bonded 96%-alumina material; it was noted that the activation energy value was high, and grain boundary devitrification was given as an explanation of this result.

For other ceramics such as magnesium oxide, the activation energies for vacancy diffusion and grain boundary diffusion were reported to be 261 kJ/mole and 230 kJ/mole respectively (Cambridge University Class Notes). For metals the reported activation energies for self-diffusion (193 kJ/mole for Cu, 178 kJ/mole for Au) are equal to the sum of the reported activation energies for the formation of vacancies (124 kJ/mole for Cu and 92 kJ/mole for AU) and for the motion of vacancies (68 kJ/mole for Cu and 82 kJ/mole for Au) (2.301 Class Notes MIT). It is interesting to note that the activation enrgy for vacancy formation is about 30% of the activation energy for sublimation (341 kJ/mole for Cu and 378 kJ/mole for Au).

In view of these different reported values, the obtained activation energy for CPS-90A-10C seems to be low, however, it is in the correct order of magnitude. It compares well with some of McGee and Wiedemeier (1985a) results.

An interesting correlation made by Dorn in 1956 showed that for pure metals above half their melting point, the activation energies found from creep tests are close to the ones for self-diffusion from studies of electrical resistivity; these activation

energies were also related to the melting point of the material (McClintock and Argon, 1966). For both cold—pressed sintered high—chromia and high—alumina considered in this study melting temperatures of 4000°F to 4200°F are reported (2480°K to 2590°K). Dorn's plot of melting temperatures versus activation energies predicts activation energies of about 300 kJ/mole. This is again of the same order of magnitude as the numbers found.

5.4.3 Behavior Under Constant Compressive Loads and Increasing Temperatures In Air Atmosphere

Constant load, increasing temperature tests were also conducted on cold—pressed sintered refractories. The purpose of this series of tests is to measure the transient strain. Figure 5.38 shows the strain after application of the load, vs. time, for Material CPS—90A—10C, under 75% of the monotonic strength, and heat—up rates of 250°F/hour (121°C/hour), and 100°F/hour (38°C/hour). It appears that the creep strain rate at low temperatures reduces with time until a transition temperature level. At high temperatures, above this new transition temperature (determined to be 1330°F for this combination of load and heat—up rate), the creep strain rate reaches a steady state value. This is an interesting result, and could prove useful in the design of refractory linings. This transition temperature seems independent of the heating rate. From the results shown in Fig. 5.38, it also appears that slower heating rates produce higher final strains. This might be due to the increased creep strain because of the longer load application time.

Use of Described Tests in Modeling Strain Response

Figure 5.39 shows typical temperature and pressure histories for a process vessel. These complex loading histories give rise to four different strain components:
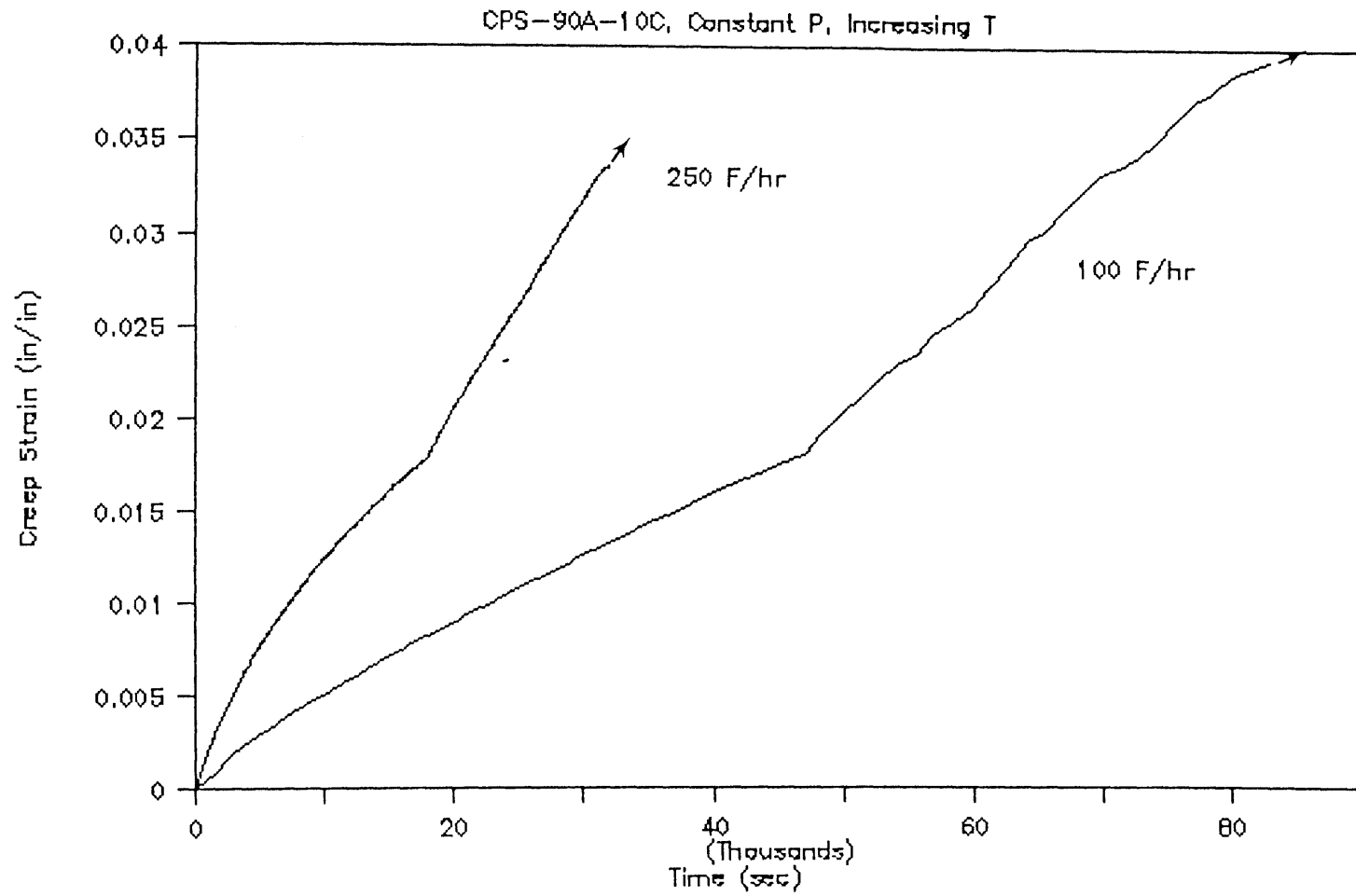
Figure 5.38   Strain variation under 75% of the monotonic strength, and different heat up rates for CPS–90A–10C
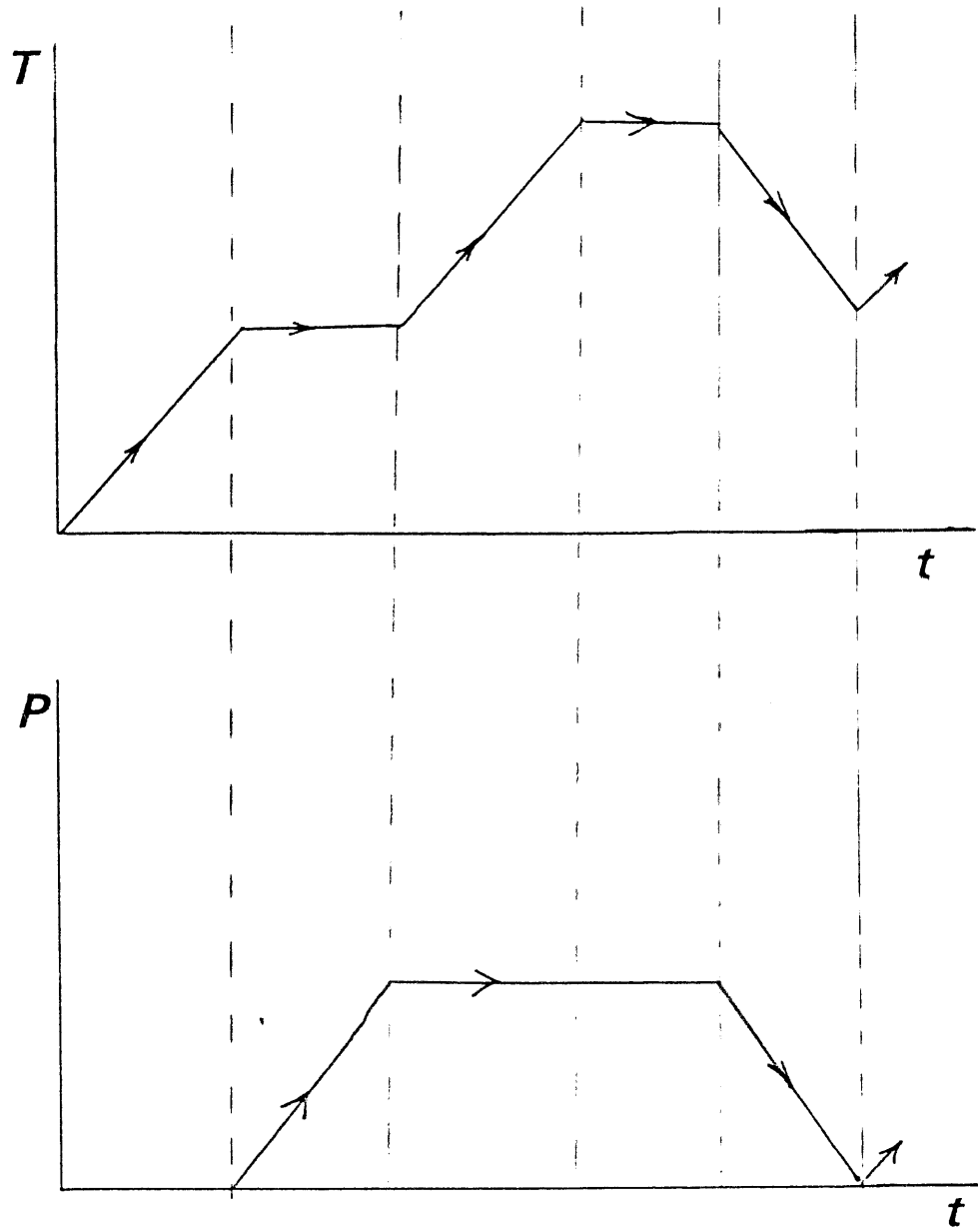
Figure 5.39   Complex load and temperature histories in process vessels

thermal, stress–induced, creep and thermal transient. These strains are usually hard to separate. A model predicting the strain behavior of the material could be expressed as the sum of elastic, plastic and creep components. The former two components would dominate at temperatures below transition and the latter one would dominate at temperatures above transition. The three kind of tests described so far, namely, monotonic loads contant temperature, constant load constant temperature and constant load increasing temperature are all needed to validate the model under different load and temperature histories.

5.4.4 Behavior Under Cyclic Compressive Loads at Constant Temperatures in Air Atmosphere

The purpose of the cyclic tests was to study the short–term material behavior under low–cycles high–stress conditions. In the preliminary testing stage, two types of tests were conducted: cycling between two fixed load levels as shown in Fig. 5.40a, and cycling with a fixed load increment per cycle as shown in Fig. 5.40b. Only low–cycle high–stress cyclic tests between zero and fixed load levels (in the range of 70% to 95% of the monotonic strength) were carried out on standard specimens. In cyclic tests at room temperature and $816^{O}C$ (below $T_m/2$) the initial cycles accumulated significant amount of inelastic strain, and later cycles accumulated relatively less inelastic strains. Large amount of accumulated inelastic strains were observed immediately before final failure. This is shown in Fig. 5.41 for material CPS–90A–10C cycled at 75% of its monotonic strength at $1500^{O}F$. However at temperatures above $1/2$ T_m the material behavior is different. Figure 5.42 shows a specimen cycled at 75% of its monotonic strength at $2400^{O}F$ ($1316^{O}C$), for CPS–90A–10C. All of the cycles (initial, intermediate, or final cycles) accumulate about the same amount of inelastic strain. This may be due to the relaxation of the
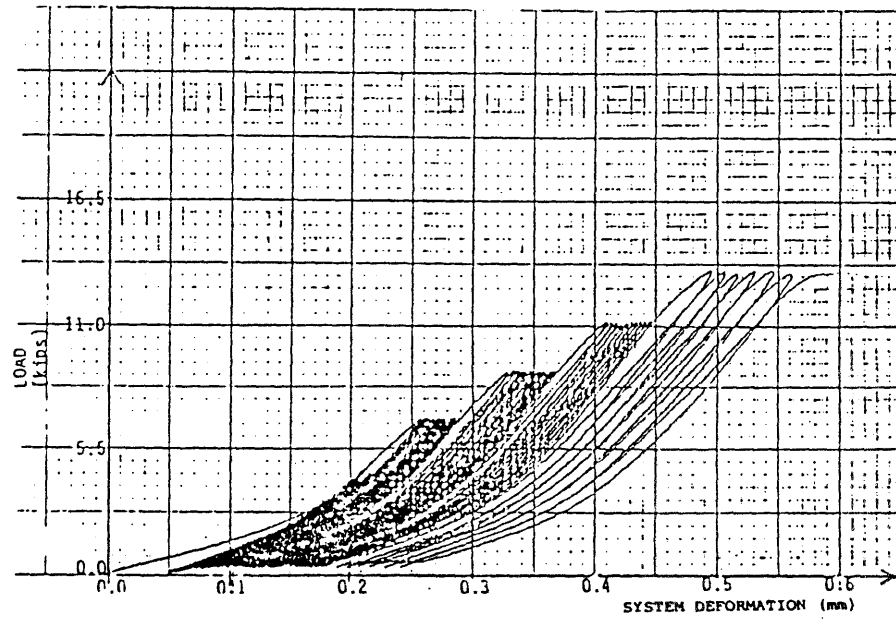
Figure 5.40a   Cyclic tests between two fixed load levels
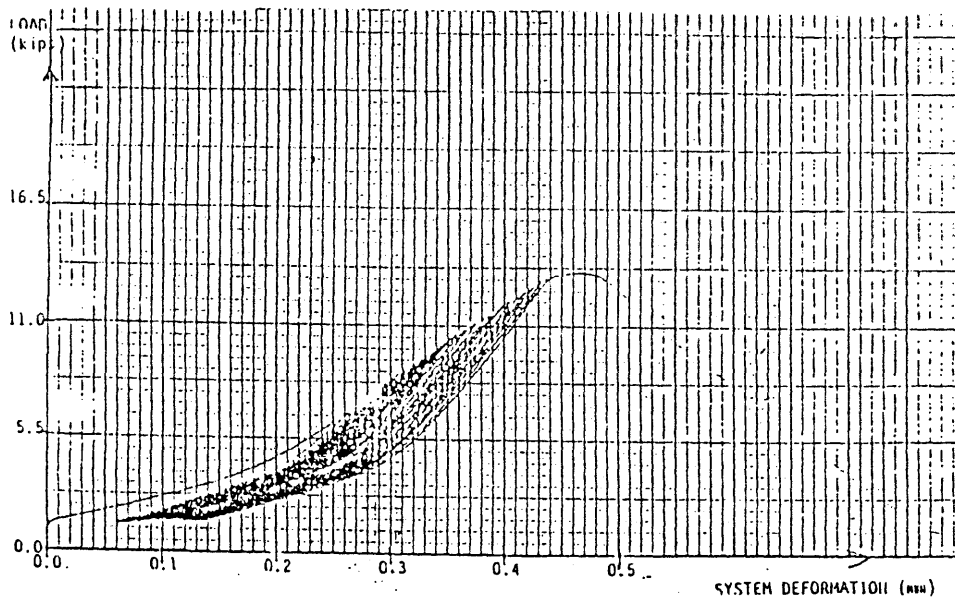
Figure 5.40b   Cyclic tests with a fixed load increment per cycle

CPS-90A-10C, Cyclic, 1500F, 75%S
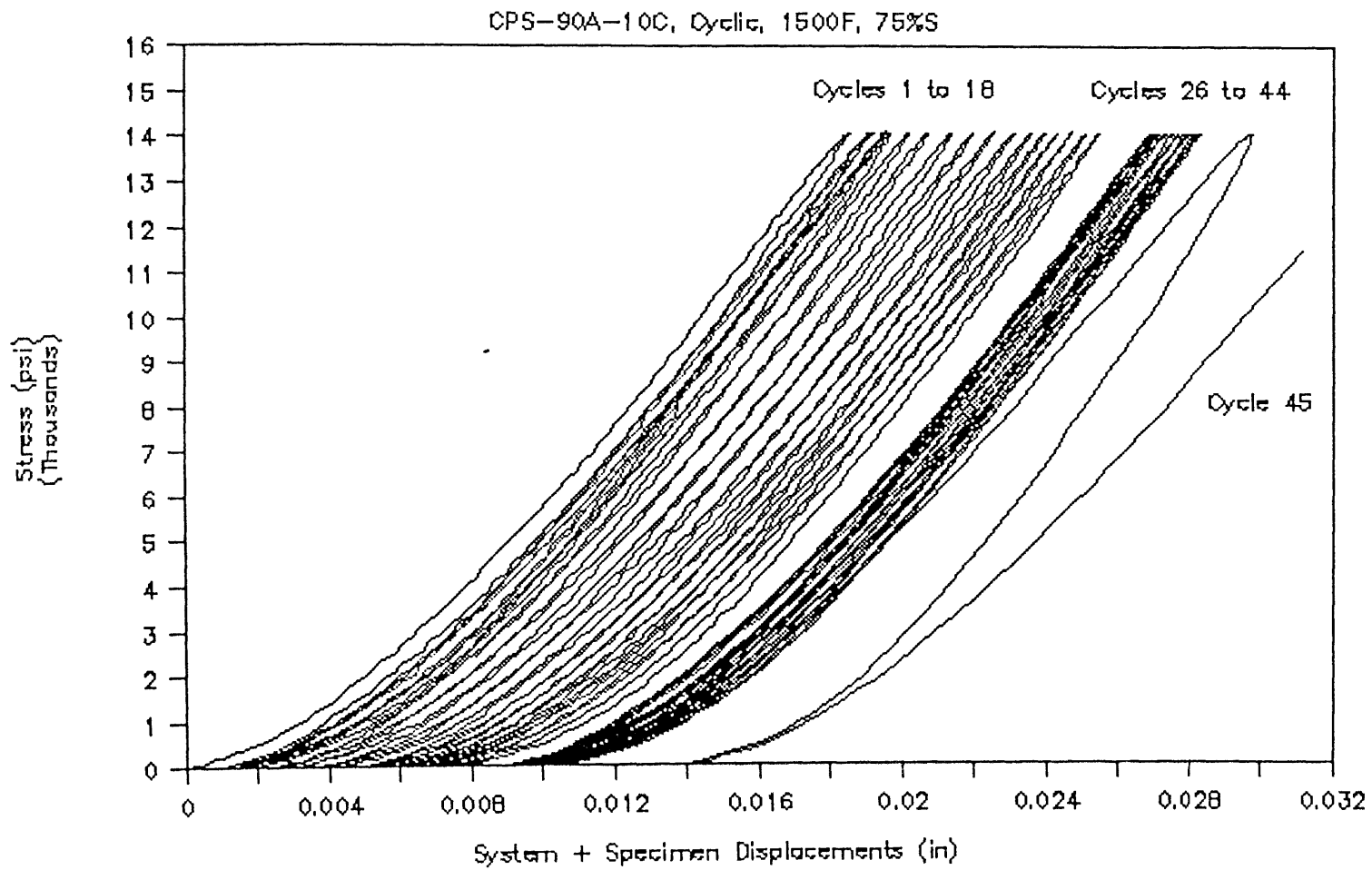
Figure 5.41   Typical cyclic test at 1500°F for CPS–90A–10C
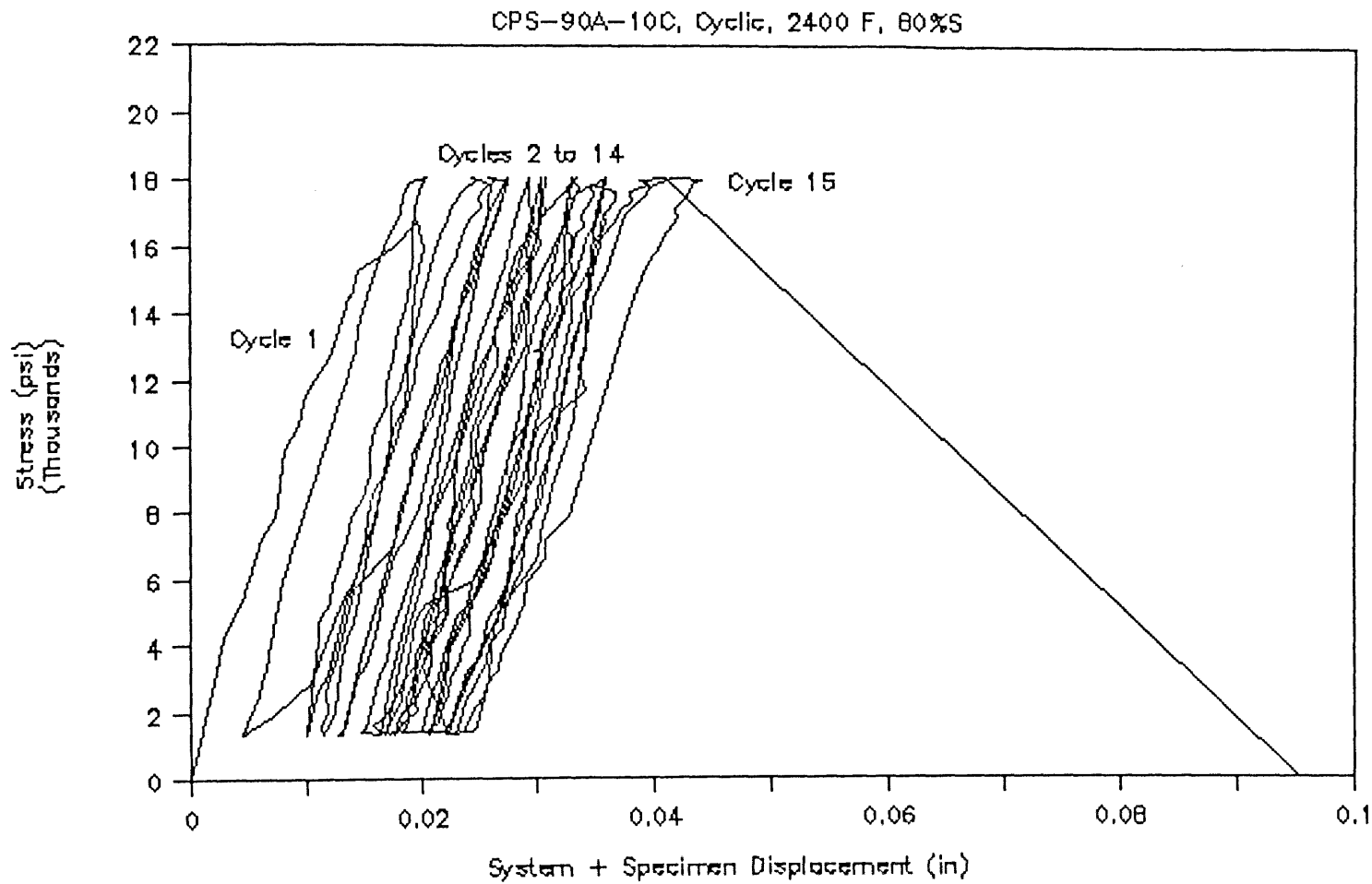
Figure 5.42   Typical cyclic test at 2400°F for CPS–90A–10C

material during unloading at high temperatures. Observed final fractures were brittle.

The variation of number of cycles to failure for CPS–90A–10C with the maximum cyclic load level is shown in Figs. 5.43a, 5.43b and 5.43c for tests at room temperature, $1500^{\circ}F$, and $2400^{\circ}F$ respectively. These results can be combined in a three dimensional "temperature − % of monotonic strength − number of cycles to failure (N)" chart, as shown in Fig. 5.44. This is useful to the designer in predicting N, by knowing the two other parameters.

The behavior of CPS–82C–18M has been studied at room temperature, and the variation of number of cycles to failure with load level is shown in Fig. 5.45. It should be noted that due to the variability in the material behavior, the characterization of the response under cyclic loads is difficult. Similarly to the results of monotonic tests, the variability in material properties is smaller at elevated temperatures. As an example the standard deviation in the number of cycles to failure varies from 25% of the mean at room temperature to 12% at $1500^{\circ}F$ ($816^{\circ}C$). This scatter in number of cycles to failure has been studied by other researchers (McClintock, 1955a, 1955b, 1956).

5.4.5 Behavior Under Monotonic Compressive Loads at Constant Temperature in Reducing Atmosphere

In this section, the effect of partial oxygen pressure on the behavior of as–manufactured materials is examined. During testing a P_{O_2} value of 10^{-8} atm. (10^{-3} Pa) representative of the gasifiers environment (Washburn, 1982; Greenberg and Peoppel, 1985) was used. The initial elastic modulus in low P_{O_2} environment was compared to the one in air. The low P_{O_2} atmosphere used was found not to

CPS—90A—10C, Room Temperature
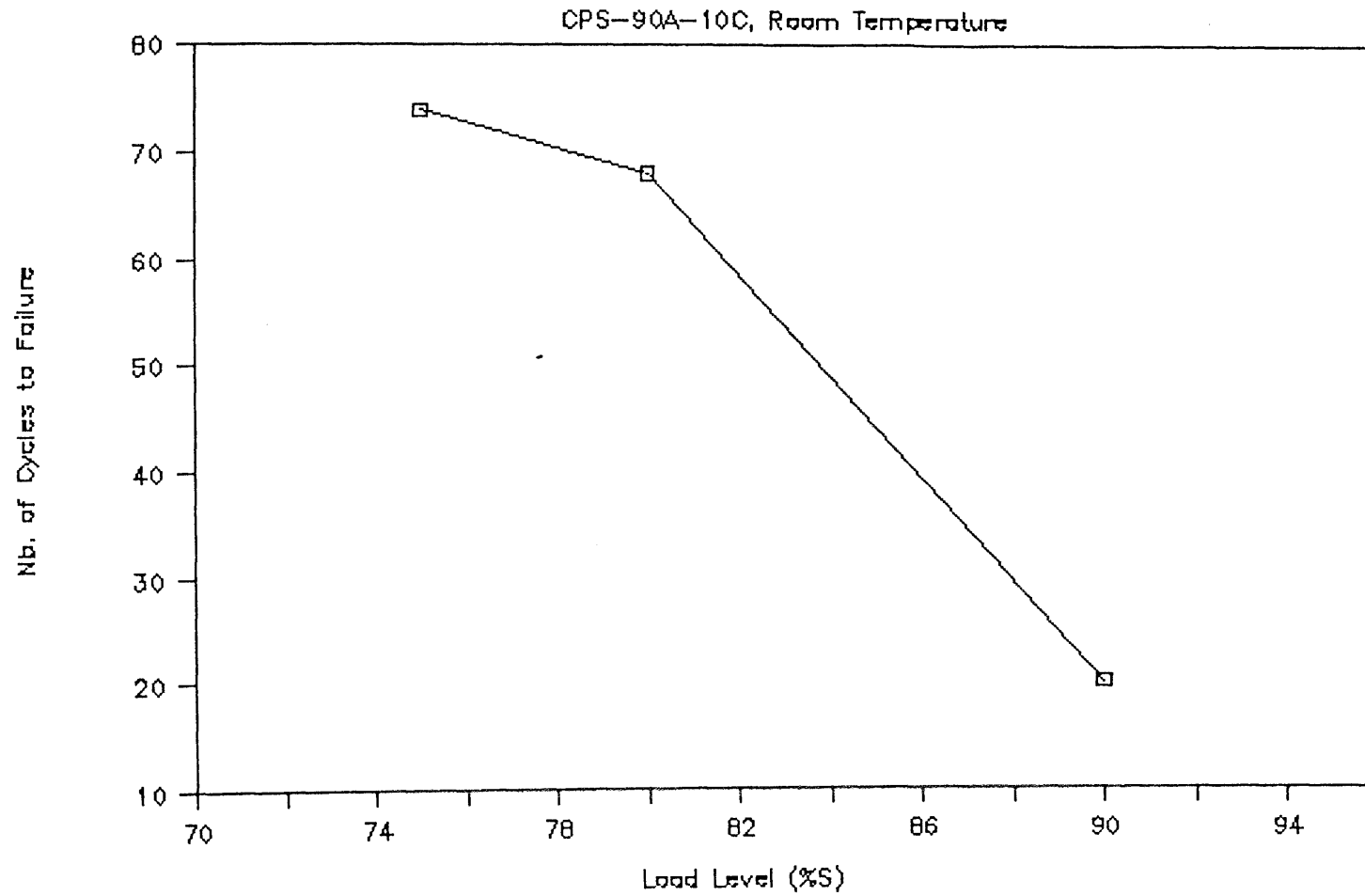
Figure 5.43a   Variation of the average number of cycles to failure with the load level for CPS—90A—10C at room temperature
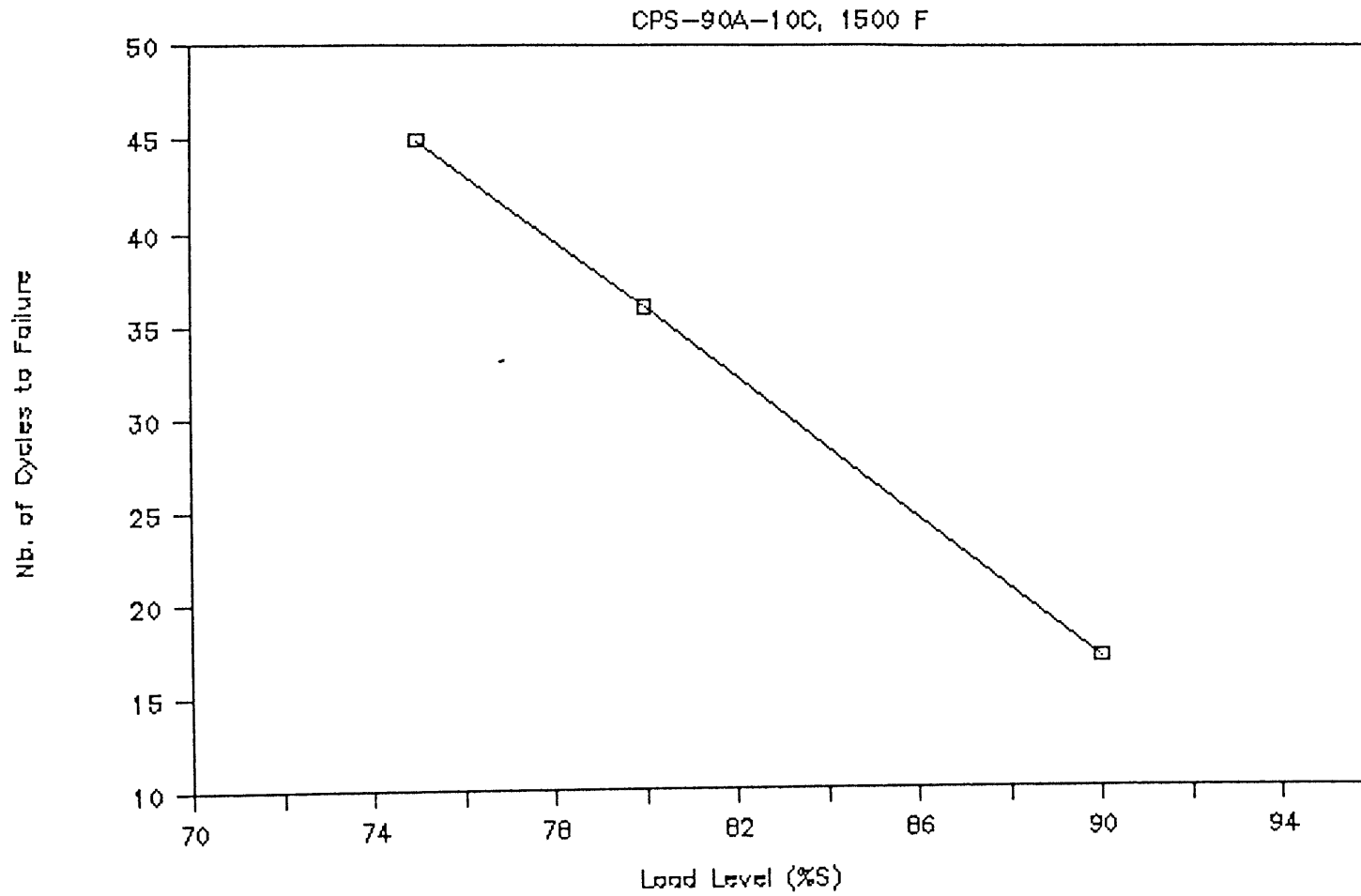
CPS—90A—10C, 1500 F

Figure 5.43b   Variation of the average number of cycles to failure with the load level for CPS—90A—10C at 1500°F
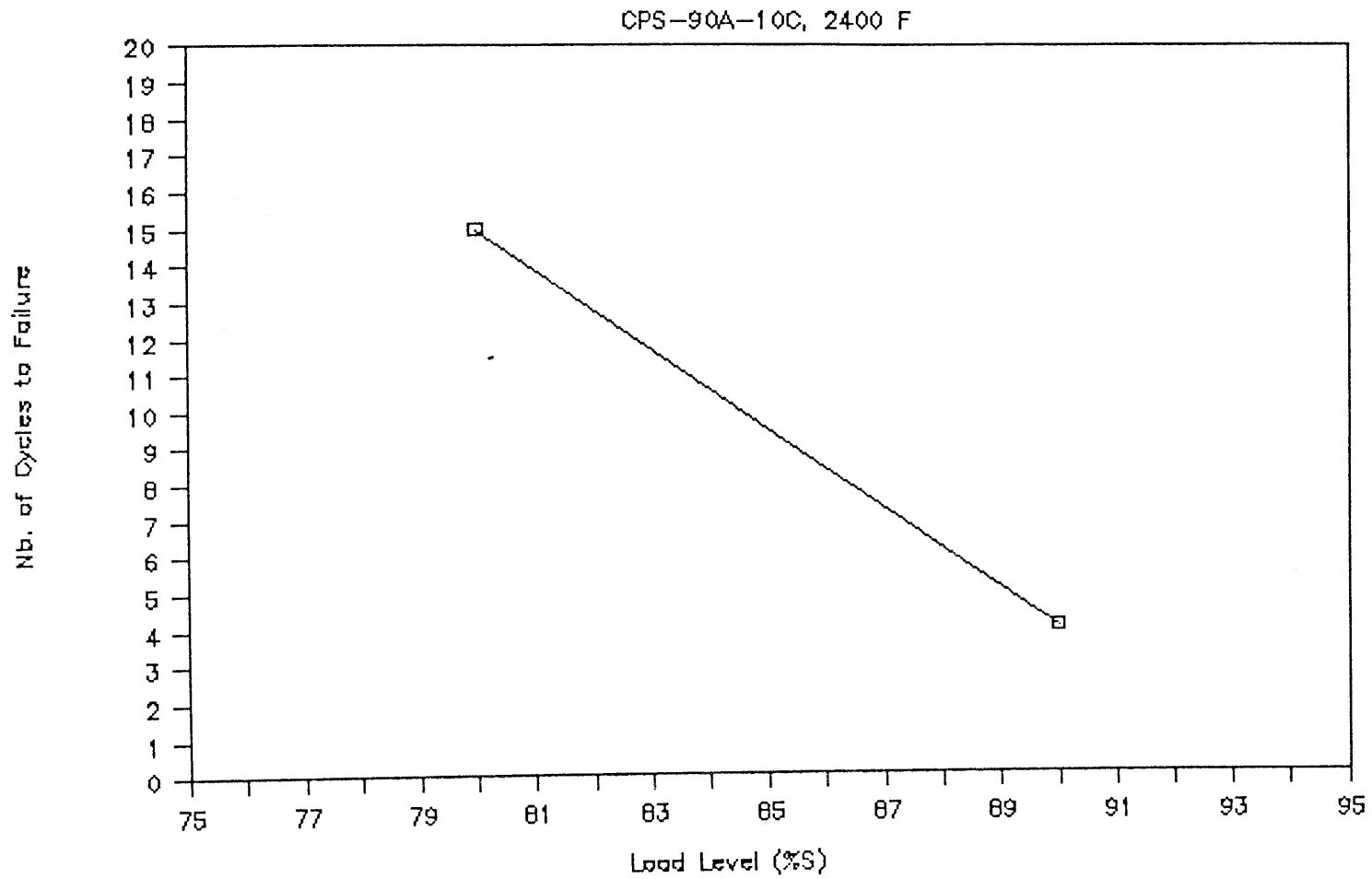
CPS—90A—10C, 2400 F

Figure 5.43c   Variation of the average number of cycles to failure with the load level for CPS–90A–10C at 2400°F
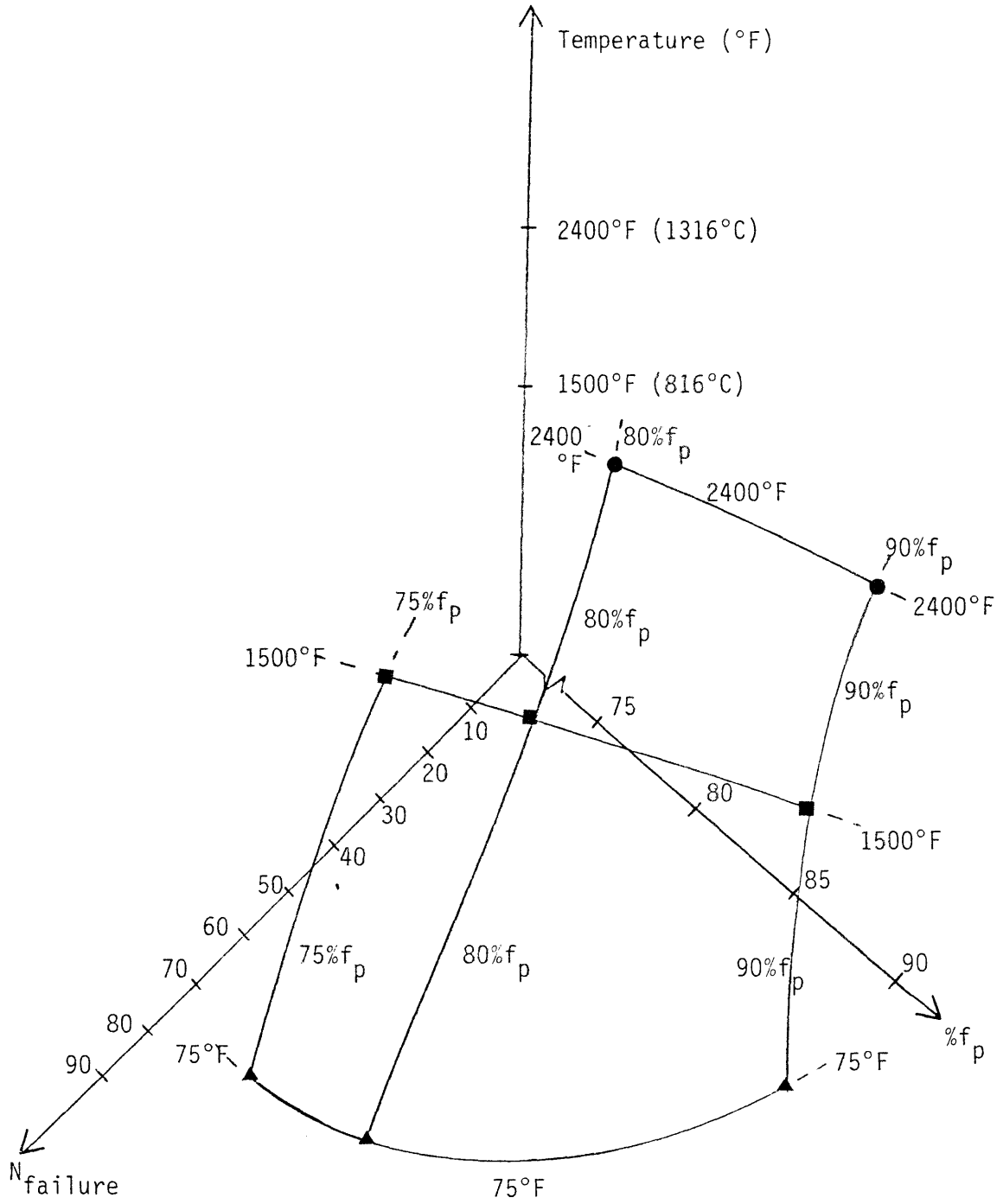
Figure 5.43   "Number of cycles − temperature − load level" failure surface for CPS−90A−10C
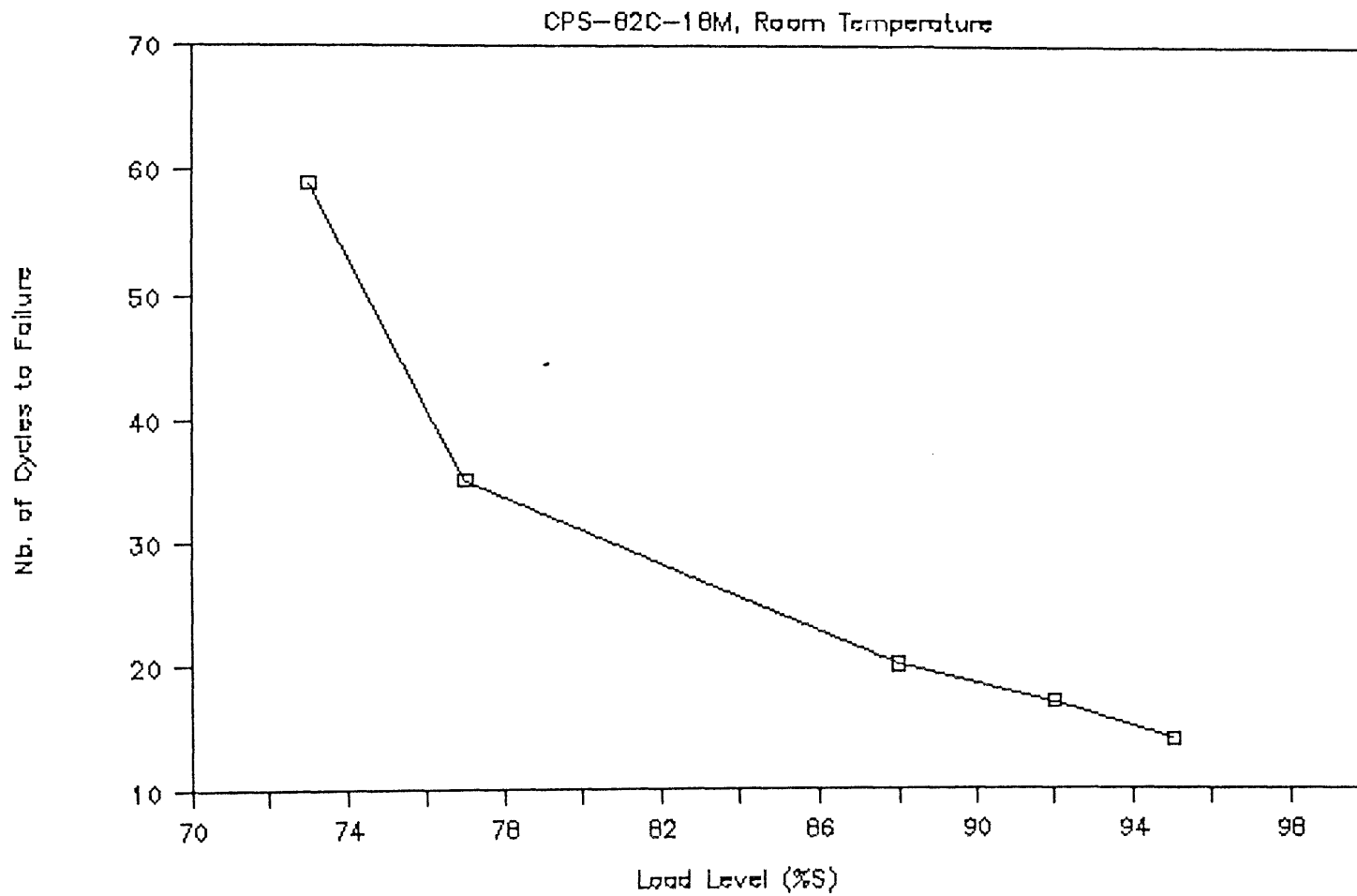
Figure 5.45   Variation of the average number of cycles to failure with the
                load level for CPS–82C–18M at room temperature

adversely affect the behavior of CPS–90A–10C and CPS–82C–18M. The effect on CPS–90A–10C is not conclusive as shown in Fig. 5.46. For material CPS–82C–18M at temperatures below 0.5 T_m the low P_{O_2} atmosphere does not have any effect. But at $1204^\circ C$ ($2200^\circ F$), under a P_{O_2} of 10^{-3} Pa (10^{-8} atm.), a 36% increase in stiffness is consistently observed for Material CPS–82C–18M. This is shown in Fig. 5.47. This might suggest that at high temperatures, under reducing atmosphere, a subtle change of phase of Material CPS–82C–18M is occurring. It was difficult to observe the change of phase, since it is expected to reverse when the specimen is brought back to air (i.e., more oxidizing atmosphere).

5.4.6   Effect of Limited Thermal History on the Material Behavior

The effect of limited thermal cycling on the behavior of as manufactured CPS–90A–10C has been studied. Specimens were subjected to one temperature cycle under no load. The thermal cycle consisted of: a ramp from room temperature to $2200^\circ F$ at $100^\circ F$/hour, a soak period at $2200^\circ F$ for 2.5 hours, and cooling from $2200^\circ F$ to room temperature at $100^\circ F$/hour. Then, the specimens were tested at room temperature and the stiffness was compared to the one obtained without thermal cycling. In air atmosphere an average stiffness reduction of 6.2% was observed after one thermal cycle, and in reducing atmosphere ($P_{O_2}=10^{-8}$ atm) a stiffness reduction of 3.5% was observed. This is shown in Fig. 5.48. This reduction is not significant, however, it would be interesting to study the effect of longer exposures to thermal cycling.

As-Manufactured CPS-90A-10C
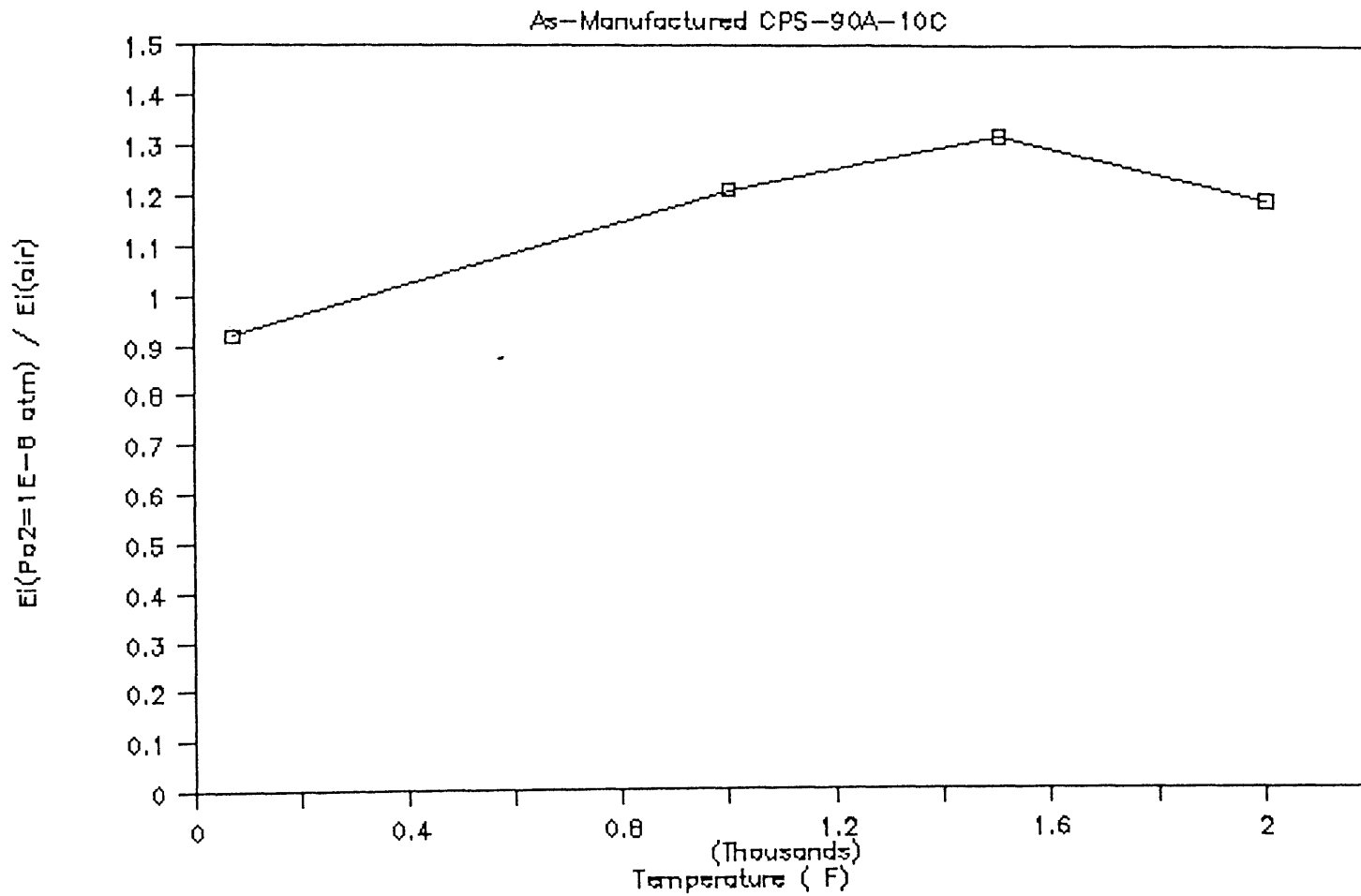
Figure 5.46   Effect of a P_{O_2} of 10^{-8} atm. on the stiffness of
CPS-90A-10C

As–Manufactured CPS–82C–18M
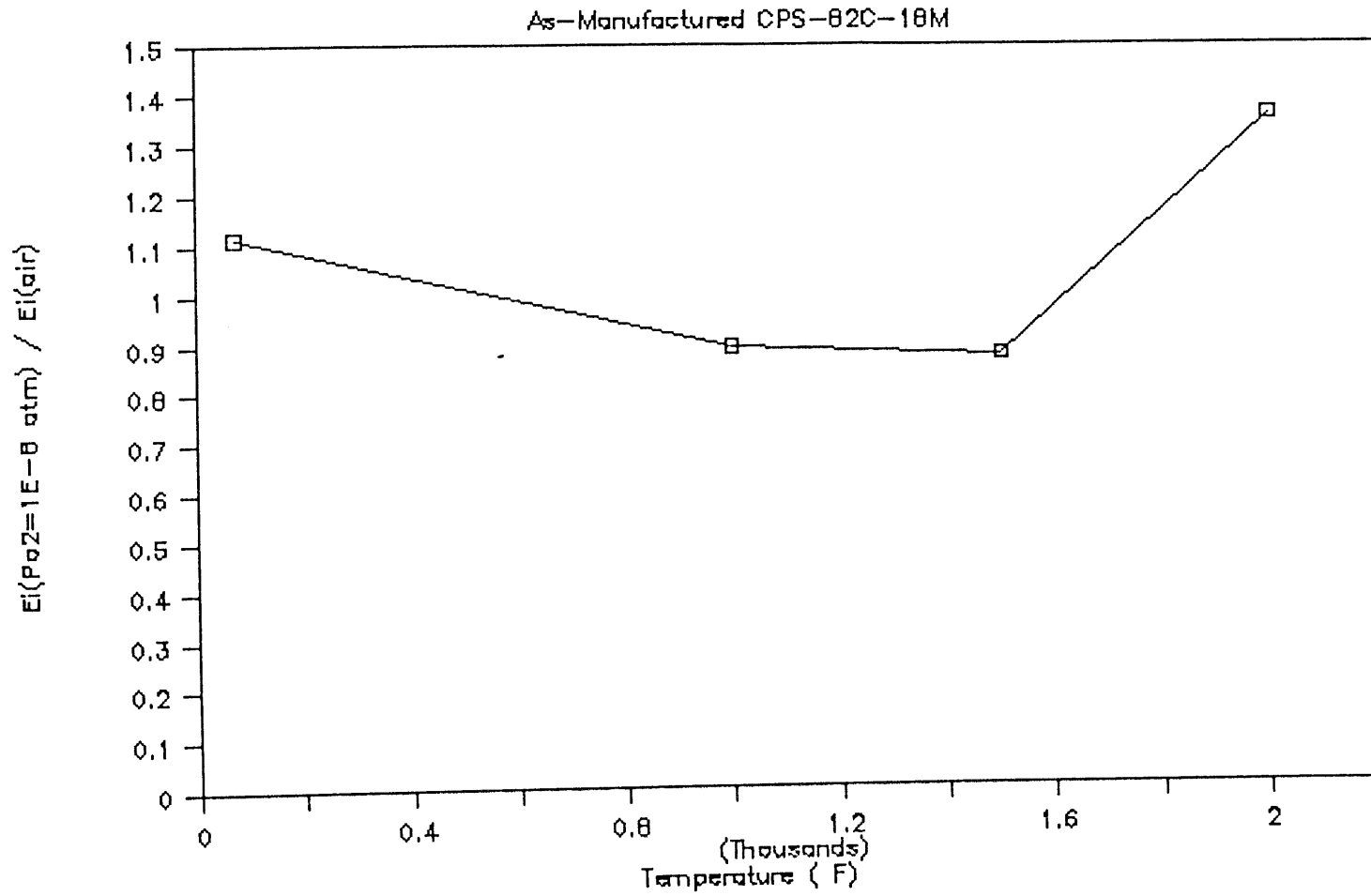
Figure 5.47   Effect of a P_{O_2} of 10^{-8} atm. on the stiffness of CPS–82C–18M

As—Manufactured CPS—82C—18M
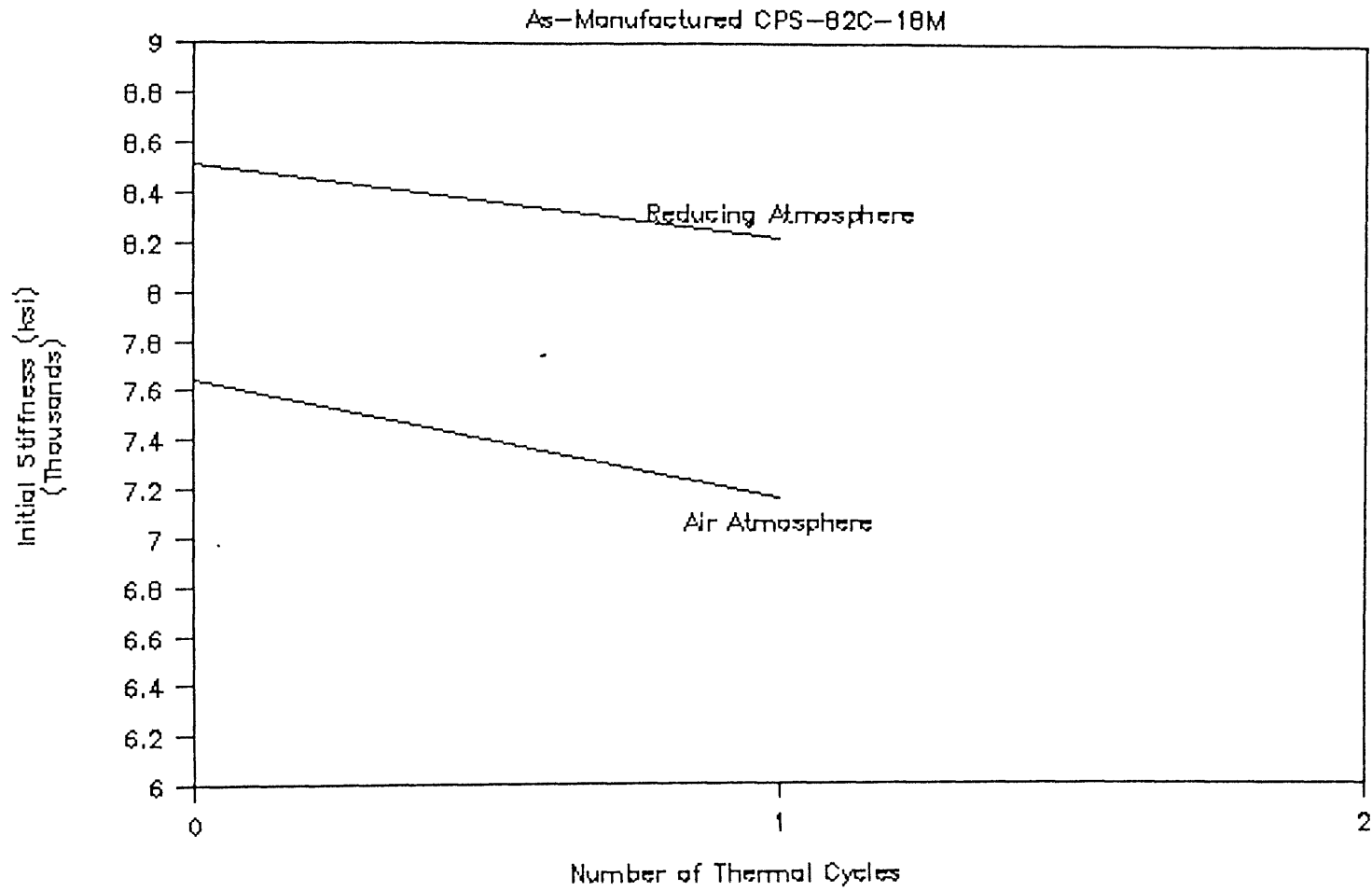
Figure 5.48   Effect of one thermal cycle on stiffness of CPS—82C—18M in air and a reducing atmosphere ($P_{O_2} = 10^{-8}$ atm.)

5.5 ELEVATED TEMPERATURE BEHAVIOR OF SLAG—IMPREGNATED MATERIALS UNDER UNIAXIAL SHORT—TERM COMPRESSIVE LOADS

In this section the high—temperature behavior of slag—impregnated high—alumina and high—chromia under short—term compressive monotonic loads is studied, in air and reducing atmospheres.

5.5.1. Behavior Under Monotonic Compressive Loads at Constant Temperature in Air Atmosphere

Slag—impregnated specimens were tested under both air and low P_{O_2} atmospheres. The purpose of duplicating the same thermomechanical loading conditions, in two different gas environments, was to be able to separate the slag effect from the P_{O_2} effect. This section describes testing of slag—impregnated specimens in air.

The behavior of as—manufactured and slag—impregnated CPS—90A—10C at room temperature and 2400°F are compared in Fig. 5.49. The room temperature behavior of the materials with and without slag—impregnation is linear elastic up to the maximum stress on the stress—strain curve, where brittle fracture occurs with negligible amounts of inelastic strains. The strength of slag—impregnated specimens was higher than those of as—manufactured specimens at room temperature. This was attributed to the slag penetrating into the pores, solidifying at room temperature, and acting as a glassy bond. The slag—impregnated material was, thus, less porous with stronger bond between its grains. The room temperature behavior of as—manufactured and slag—impregnated CPS—82C—18M is shown in Fig. 5.50. Material CPS—90A—10C exhibited a larger increase in strength with slag—impregnation than Material CPS—82C—18M. This is attributed to the fact that
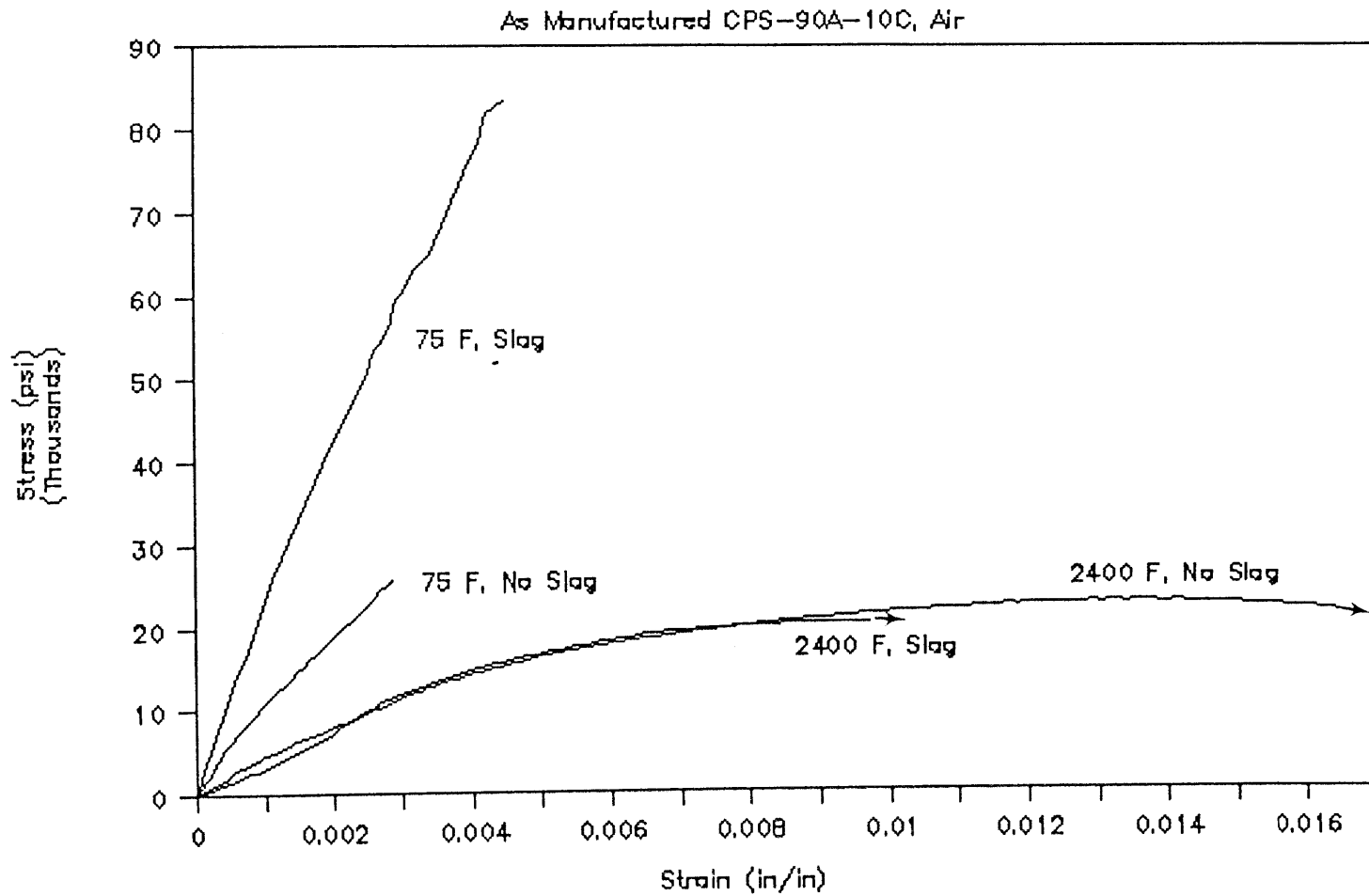
Figure 5.49   Stress strain behavior of as–manufactured and slag–impregnated CPS–90A–10C at room temperature and $2400^{O}F$ in air atmosphere
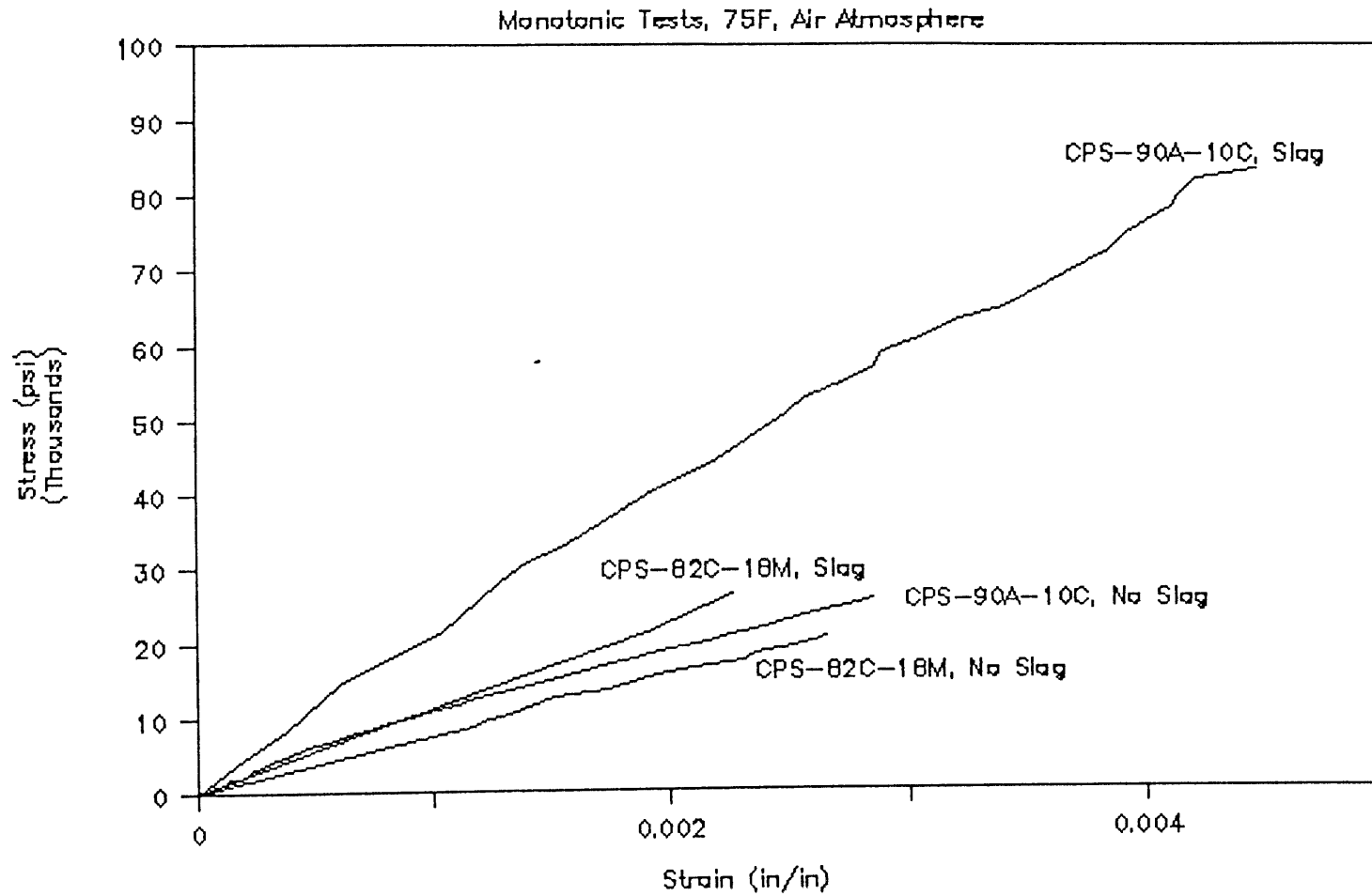
Figure 5.50   Comparison of the behavior of as—manufactured and
slag—impregnated CPS—90A—10C and CPS—82C—18M at
room temperature

Material CPS–90A–10C was impregnated to a higher degree than Material CPS–82C–18M, thus having less empty pores after slag–impregnation. At high temperatures the strength of slag–impregnated materials drops at a faster rate than the as–manufactured strength. The strength of slag–impregnated CPS–90A–10C at 2400^OF is just below the strength of as–manufactured CPS–90A–10C. The variations of strength and associated peak strain with temperature for slag–impregnated CPS–90A–10C are shown in Figs. 5.51 and 5.52 respectively. As temperature increases, a ductile post–peak behavior is observed, for slag–impregnated materials, similar to the one previously discussed for as–manufactured materials. As–manufactured specimens exhibit a linear–elastic behavior initially for temperatures below $T_m/2$ while slag–impregnated specimens deviate from the initial elastic behavior at high temperatures. Figure 5.53 shows the variation of initial stiffness with temperature for as–manufactured materials and slag–impregnated material CPS–90A–10C. The decrease of initial stiffness is faster for slag–impregnated CPS–90A–10C than for as–manufactured CPS–90A–10C and at 2400^OF (1316^OC) the stiffness of slag–impregnated CPS–90A–10C is smaller than that of as–manufactured CPS–90A–10C. This may suggest that corrosion of the CPS–90A–10C refractory is more important at temperatures above 2400^OF (1316^OC). Similar results have been obtained for slag impregnated silicon carbide (Easler, 1985) showing an increase in strength with slag–impregnation. This is also consistent with the results obtained for higher corrosion rates at high temperatures (Bakker, et. al., 1984). Similar work has been completed on slag–impregnated CPS–82C–18M in air atmosphere. The behavior of slag–impregnated CPS–82C–18M is similar to that of slag–impregnated material CPS–90A–10C. The variation of the initial slope of the

Slag—Impregnated CPS—90A—10C

Strength (Ksi)

80

70

60

50

40

30

20

10

0

0   0.4   0.8   1.2   1.6   2   2.4
(Thousands)
Temperature (F)
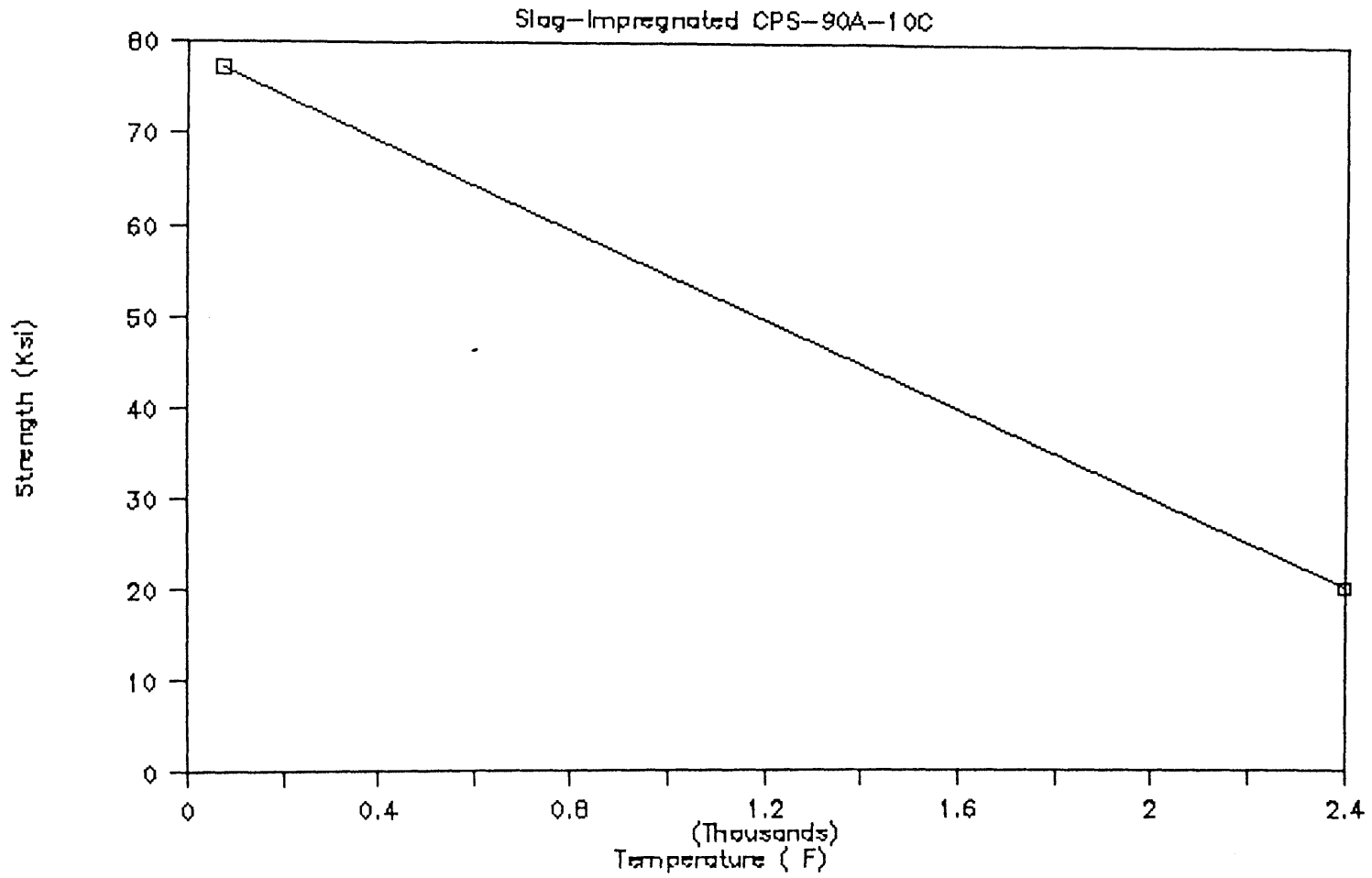
Figure 5.51   Variation of strength with temperature for slag—impregnated
                   CPS—90A—10C in air atmosphere
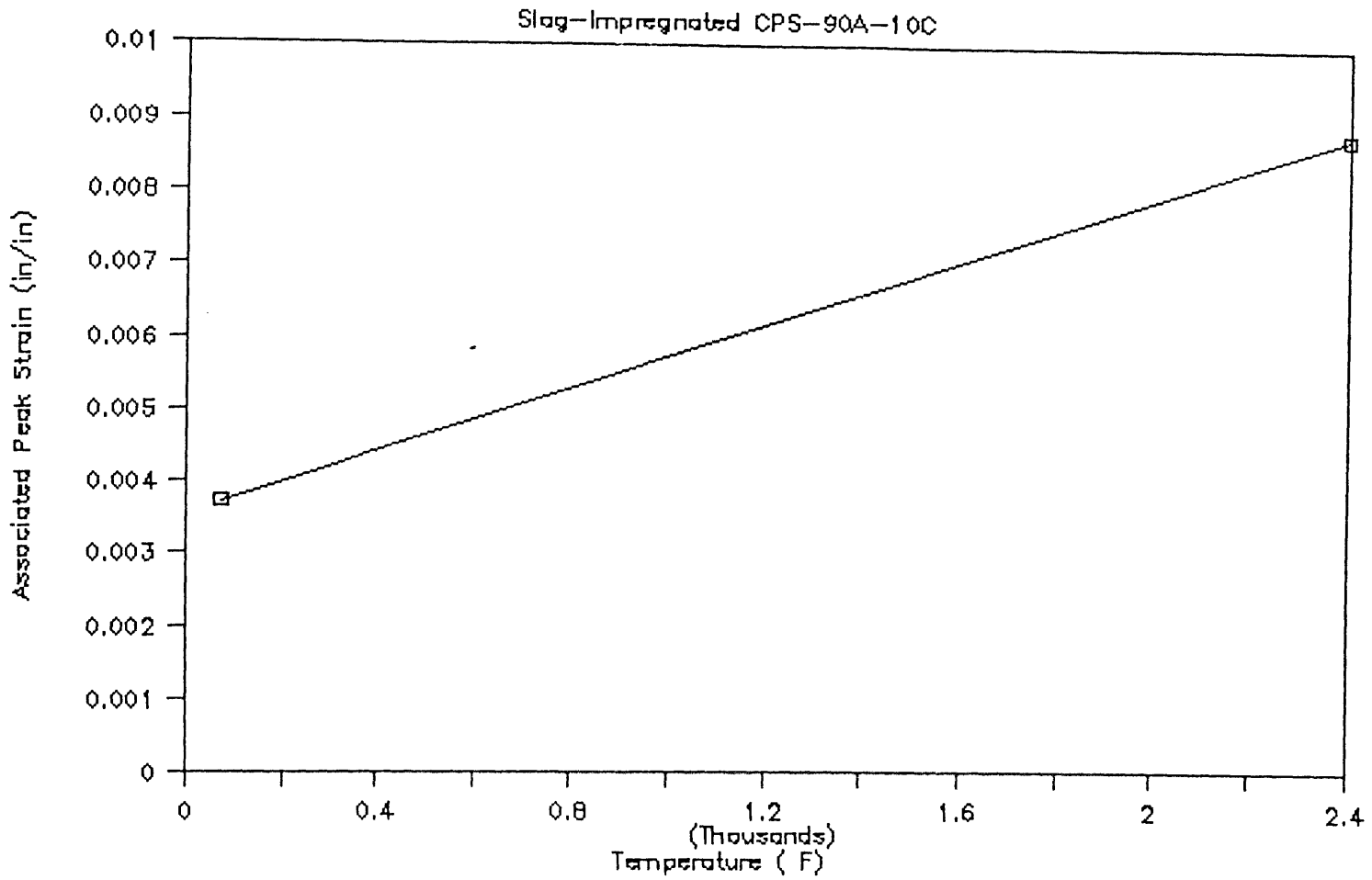
Figure 5.52   Variation of associated peak strain with temperature for
slag—impregnated CPS—90A—10C in air atmosphere
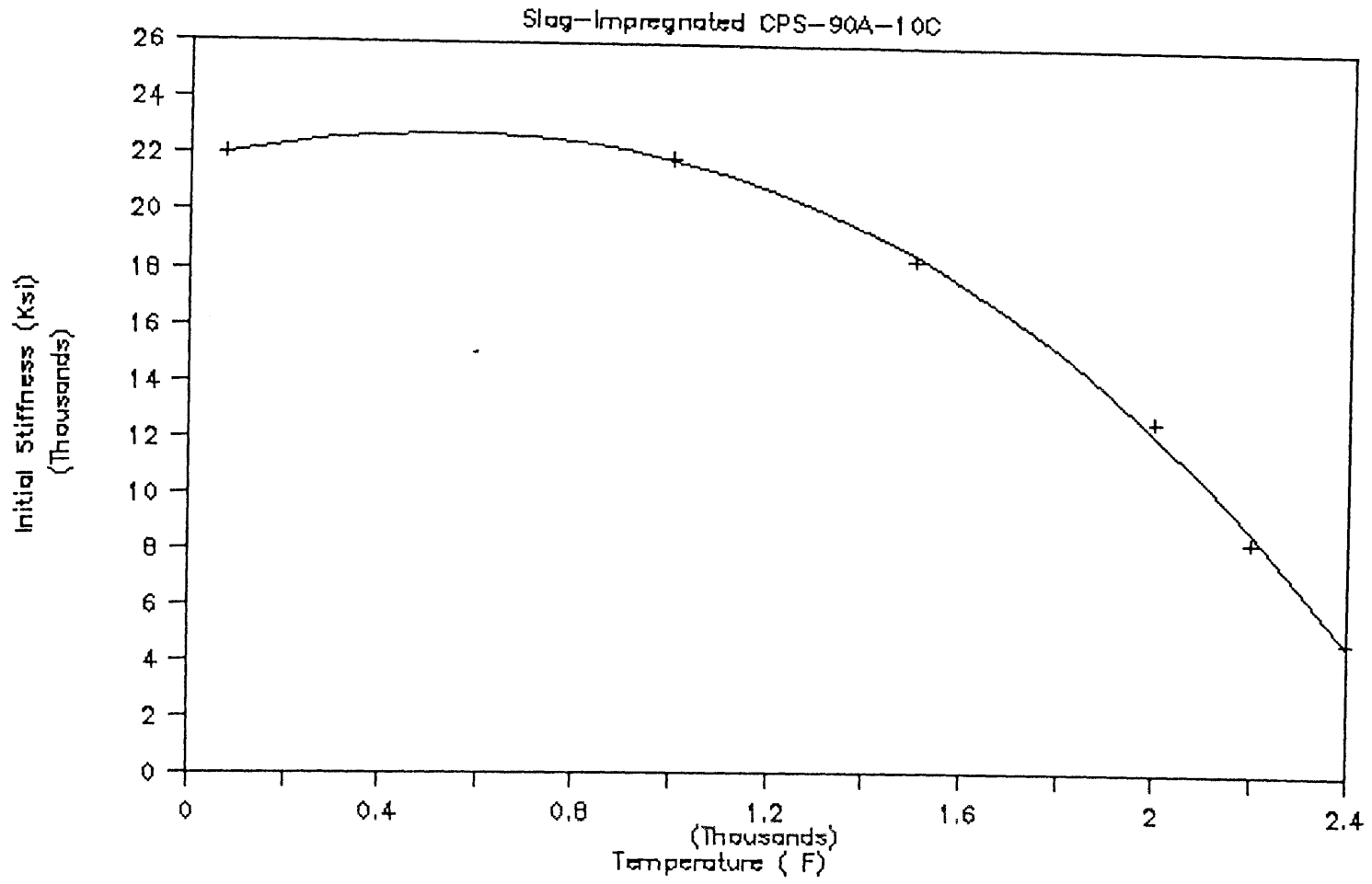
Figure 5.53   Variation of initial stiffness with temperature for
slag–impregnated CPS–90A–10C in air atmosphere

stress strain curve with temperature for slag–impregnated CPS–82C–18M is shown in Fig. 5.54.

5.5.2   Behavior Under Monotonic Compressive Loads at Constant Temperature in Reducing Atmosphere

Slag–impregnated materials tested under controlled P_{O_2} atmosphere were studied. The low P_{O_2} atmosphere did not have much effect on the behavior of slag–impregnated Material CPS–90A–10C as shown by the stiffness variation in Fig. 5.55. As in the case of as–manufactured specimens, the low P_{O_2} atmosphere had an effect on Material CPS–82C–18M at high temperature. A substantial strength decrease is observed for slag–impregnated Material CPS–82C–18M at $2200^{O}F$ and a P_{O_2} of 10^{-3} Pa (10^{-8}atm.). Figure 5.56 shows the stress strain curves for slag–impregnated CPS–82C–18M at room temperature in air and at $2200^{O}F$ in reducing atmosphere. The variation of the initial slope of the stress strain curve with temperature for slag–impregnated CPS–82C–18M is shown in Fig. 5.57.

5.6   MICROSTRUCTURAL   CHARACTERIZATION   OF   VIRGIN   AND TESTED MATERIALS

5.6.1 Microscope Observations

In this section the microstructure of as–manufactured and slag–impregnated cold–pressed sintered high–alumina and high–chromia refractories is studied using microscope observations. The stereoscopic optical microscope is used first to get color pictures that show the different phases and the rough topography of the material. The Nomarski microscope is used next to extract more detailed
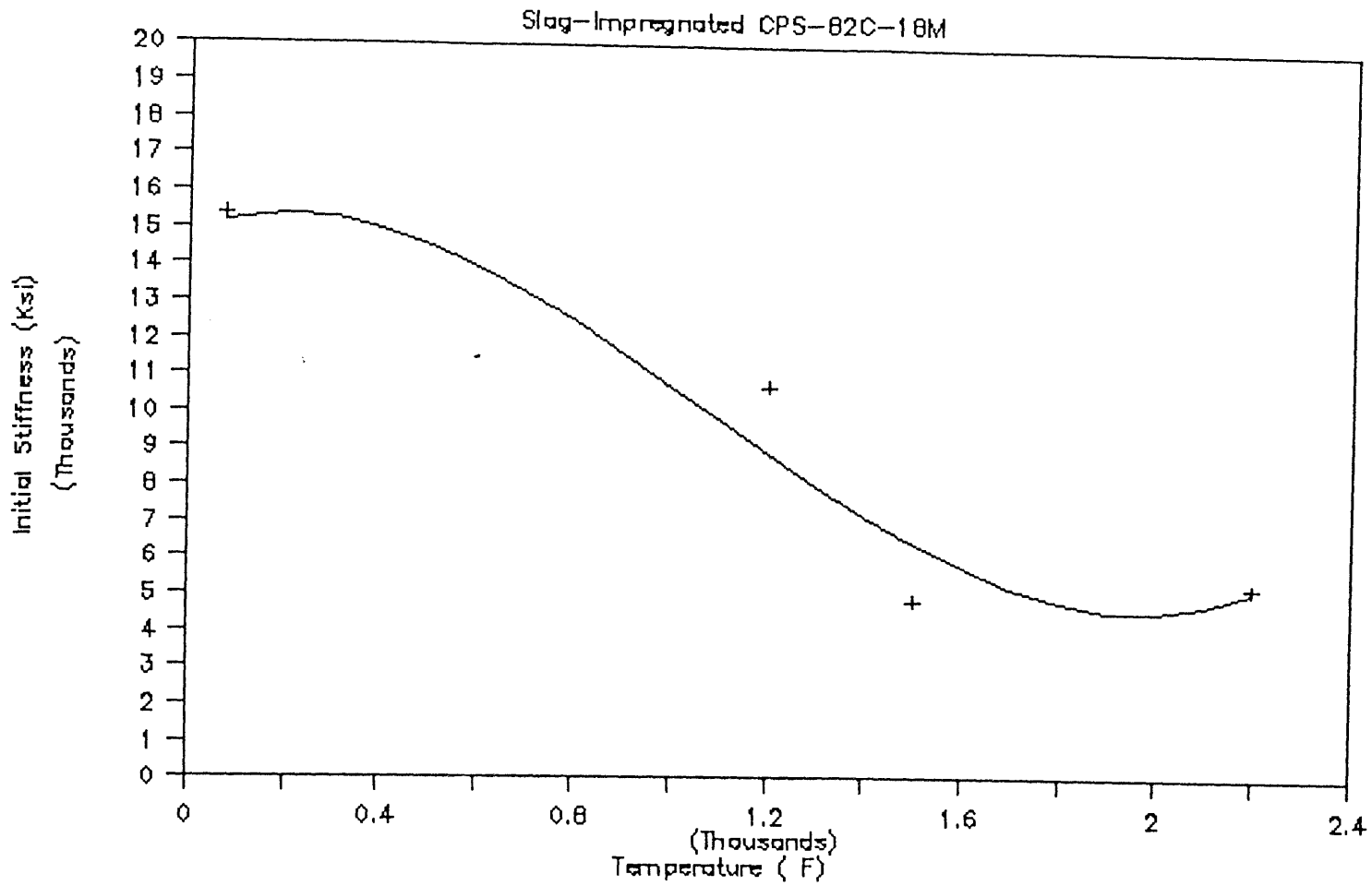
Figure 5.54   Variation of initial stiffness with temperature for
                     slag—impregnated CPS—82C—18M in air atmosphere
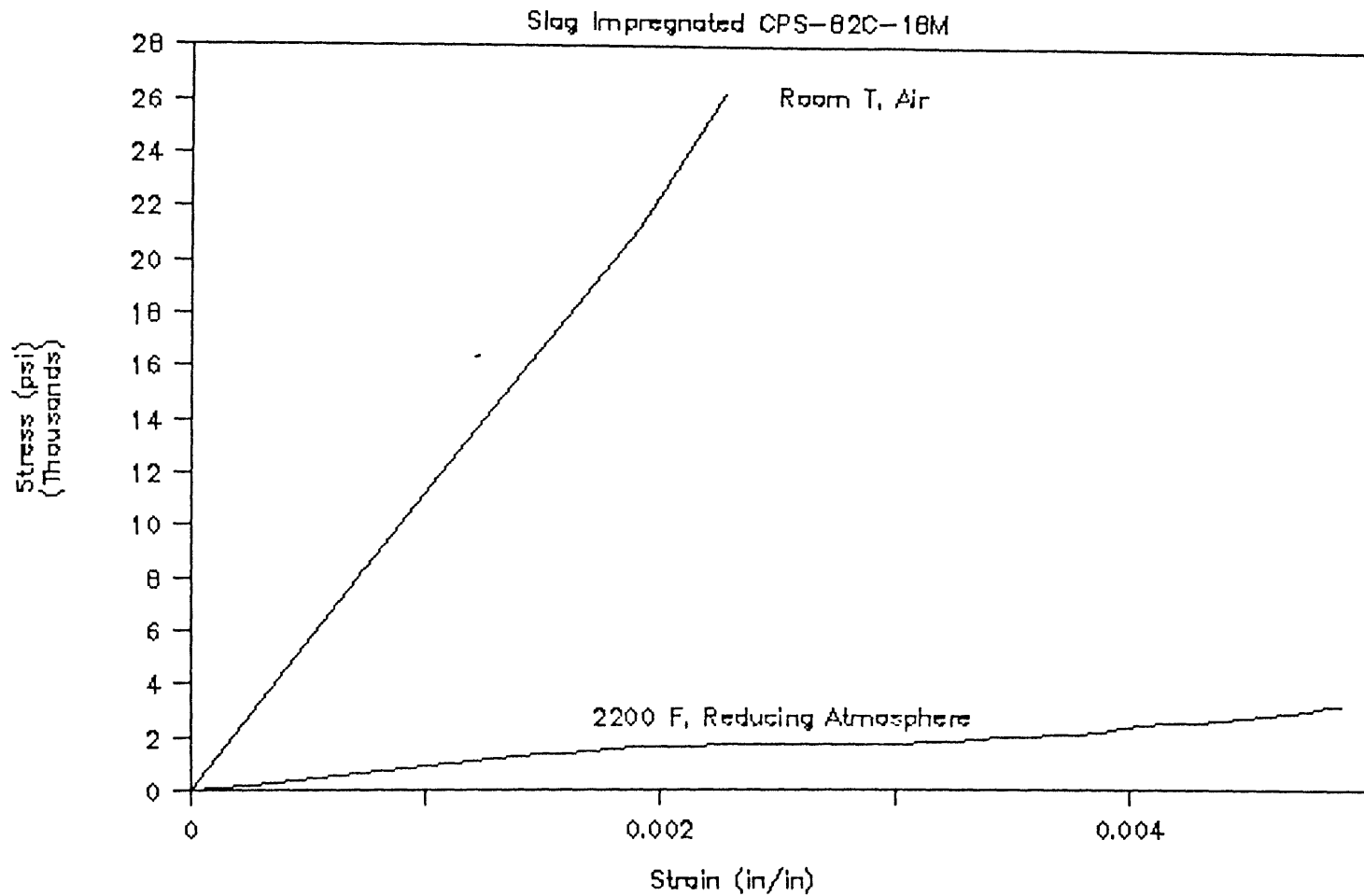
Figure 5.55   Stress strain curves for slag—impregnated CPS–82C–18M at room temperature in air, and at $2200^{\circ}F$ in air atmosphere with a P_{O_2} of 10^{-8} atm.
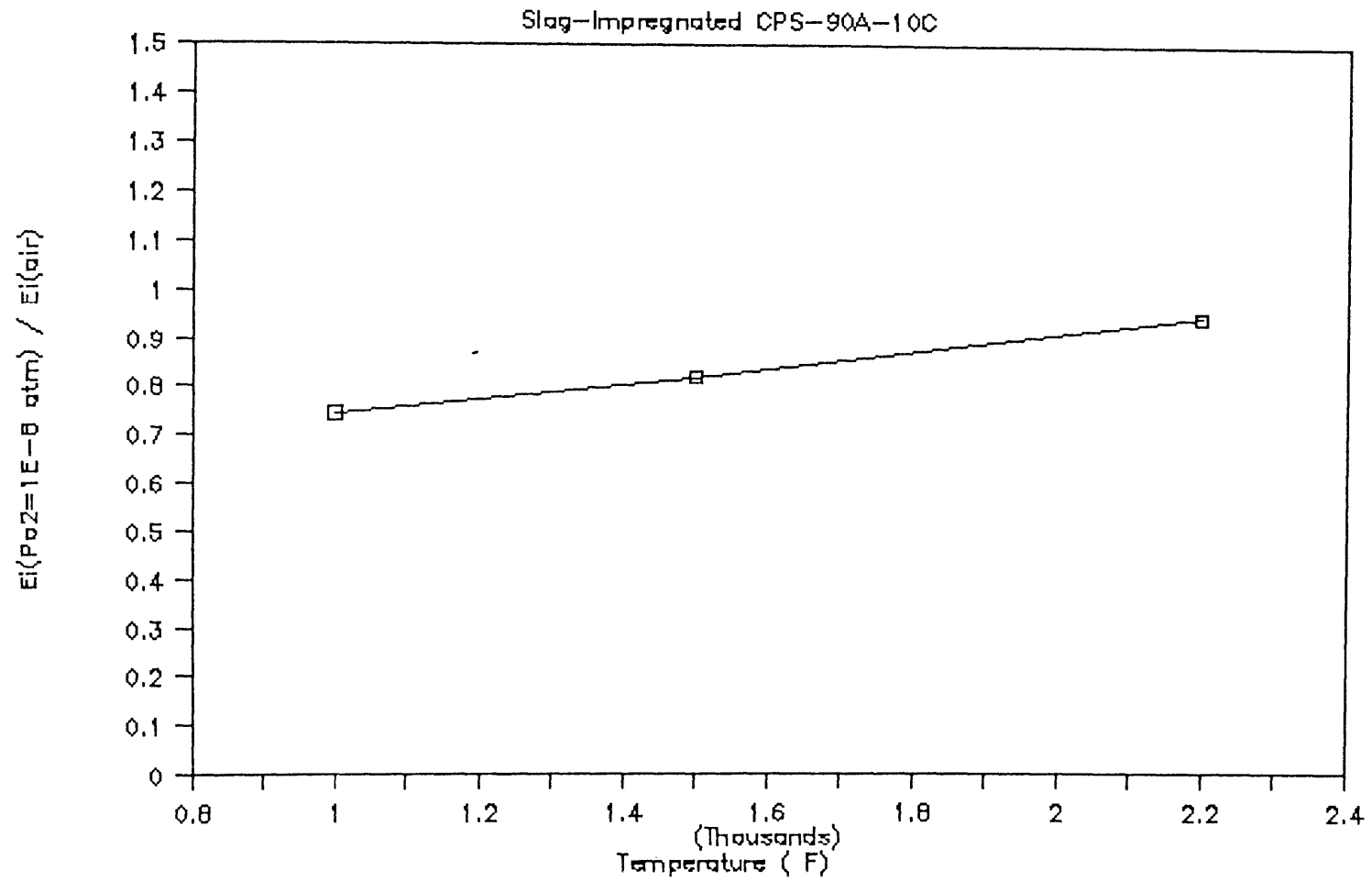
Figure 5.56   Ratio of initial stiffness in air to initial stiffness in a reducing

atmosphere $(P_{O_2} = 10^{-8}$ atm.) for slag–impregnated

CPS–90A–10C

Slag-Impregnated CPS-82C-18M
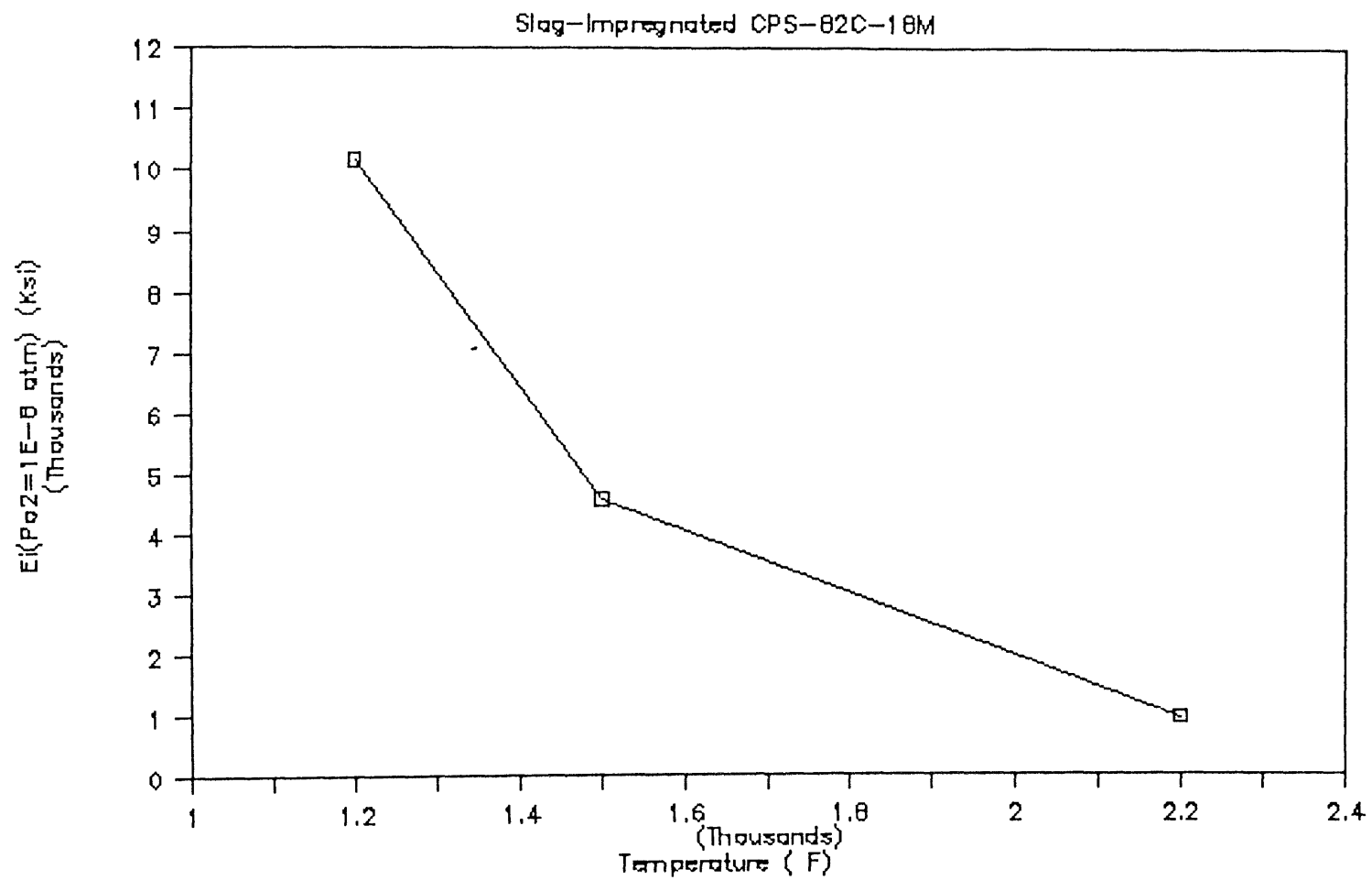
Figure 5.57   Ratio of initial stiffness in air to initial stiffness in a reducing atmosphere ($P_{O_2} = 10^{-8}$ atm.) for slag–impregnated CPS–82C–18M

microstructural characteristics, and finally the scanning electron microscope is used to obtain the fine details.

<u>As–Manufactured CPS–90A–10C Tested Under Monotonic Loads</u>

The microstructure of the non–tested as–manufactured CPS–90A–10C consists of a solid solution of alumina–chromia that binds tabular alumina grains together. The alumina grains are white and the solid solution is brown. Alumina grains penetrated by chromia exhibit different degrees of color, ranging from pink to light brown. A picture of the non–tested CPS–90A–10C taken using the Nomarski is shown in Fig. 5.58. It can be seen that small cavities exist in the tabular alumina grains that might have been formed during sintering of the tabular alumina grains. The different phases, however, do not appear on the Nomarski picture. The Nomarski picture also reveals the finer microstructure of the solid solution showing a conglomerate of sub–micron grains. The advantage of using the stereoscopic microscope is that color can be used to quickly identify the various phases. A CPS–90A–10C specimen tested at 1500^OF is shown in Fig. 5.59 in a Nomarski picture at 16X. This can be compared to Fig. 5.58 for a non–tested specimen to show a decrease of the large grains and the formation of smaller cavities in the matrix. As the test temperature is increased to 2400^OF, the intragranular cavities increase significantly. This increase may be attributed to the separation of the individual sintered grains in the tabular alumina at 2400^OF. Figure 5.60 shows an area of the test specimen at 2400^OF, taken at 12.8X. By comparing it to Figs. 5.58 and 5.59 the overall increase in the number and volume of cavities can be appreciated. It appears that the growth and coalescence of interface and matrix cavities is an important factor in the deformation process. Figure 5.61 shows a tabular alumina grain in the specimen tested at 2400^OF with major intra–granular cavity growth. The strength of

Figure 5.58   Nomarski microscope picture of virgin CPS–90A–10C at 16X showing more detailed surface features

Figure 5.59   Nomarski microscope picture of CPS–90A–10C at 16X tested
                   to failure under monotonic compression at 1500°F
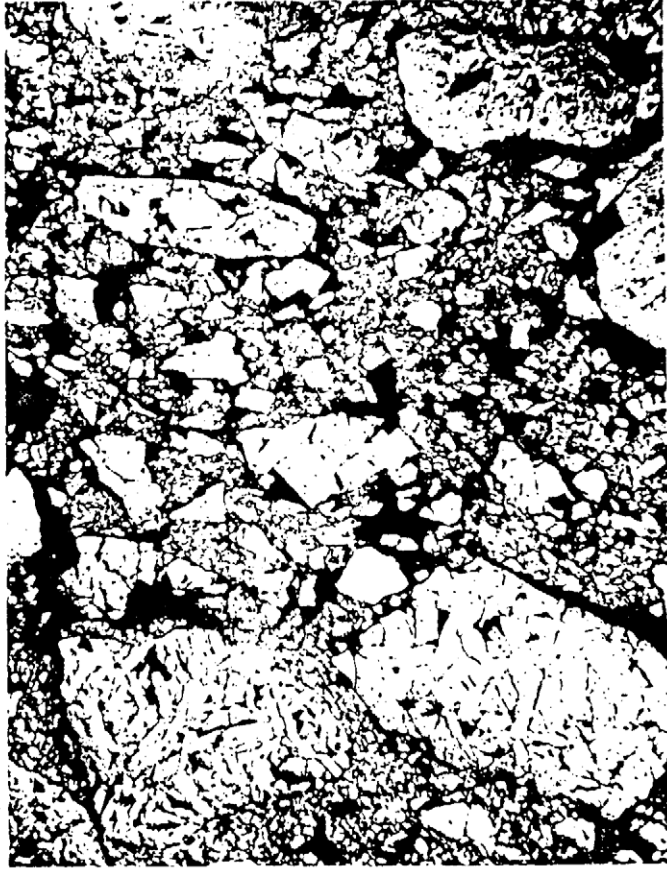
Figure 5.60   Nomarski microscope picture of CPS–90A–10C at 12.8X
tested to failure under monotonic compression at 2400°F
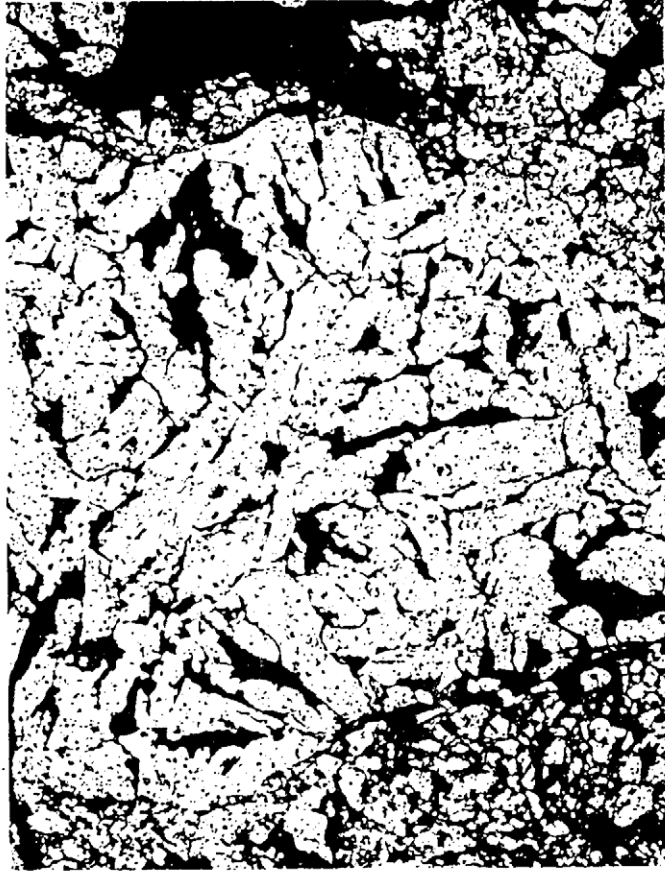
Figure 5.61   Nomarski microscope picture of CPS—90A—10C at 40X tested to failure under monotonic compression at 2400°F showing the growth of the intra—granular cavities inside an alumina grain

fused and tabular alumina grains has been studied by Bertrand, et al (1988) who found the strengths of the tabular alumina grains to be higher than the strengths of fused alumina grains. This will be discussed again in the context of the fused grains in CPS–82C–18M.

The width, length, orientation, and type of cavities have been characterized for the as–manufactured CPS–90A–10C in the non–tested condition as well as after testing under monotonic loading at $1500^{O}F$ and $2400^{O}F$. In what follows a discussion of the observed trends is given. More quantitative details can be found in Appendix C. The cavity characteristics will be discussed based on observations made on a cross–section taken from the specimen, such as cavity % area and number of cavities per unit area. The cavity % area is equal to the cavity % volume. However, the number of cavities per unit volume N_v is larger than the number of cavities per unit area N_a. A more exact discussion using N_v is preferable. N_v could be calculated from N_a by using stereology (DeHoeff and Rhines, 1968), but this treatment is beyond the scope of this work.

The first parameter to be investigated is the distribution of the cavities with respect to their width to length ratio. A criteria for distinguishing pores from cracks has been suggested by Brace; he characterized cracks as being cavities with a width to length ratio smaller than 0.10. In this study rather than making such a distinction, the cavity characteristics are always discussed keeping in mind the various width to length ratios. The classification of these cavities can be made, based on the number of cavities per unit area or on the area of these cavities as a percentage of the total area studied. The cumulative distribution of the number of cavities for different width to length (w/l) ratios is shown in Fig. 5.62; this cumulative number does not include the intra–granular cavities with both dimensions smaller than 6 μm. The
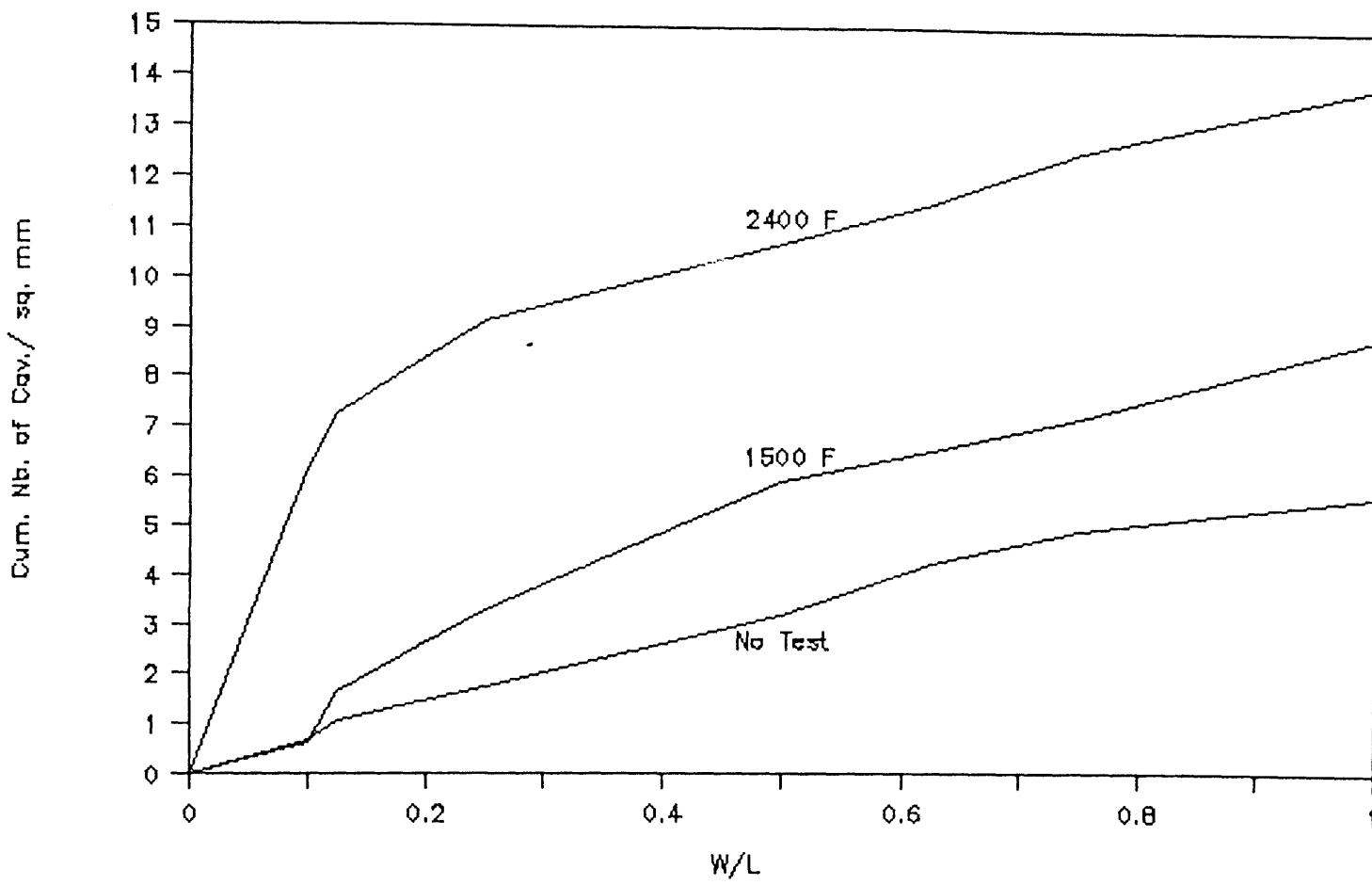
Figure 5.62 Cumulative distribution of number of cavities per mm^2 with respect to width to length ratio, for as—manufactured CPS—90A—10C under different conditions

variation of the intra–granular cavities with both dimensions less than 6 μm is discussed later. For the non–tested material CPS–90A–10C, the cumulative distribution of the number of cavities per mm^2 is almost linear for w/l ratios smaller than 0.75. The increase in the number of cavities for w/l ratios larger than 0.75 is smaller. For CPS–90A–10C tested at 1500°F an increased number of cavities is found with w/l ratios between 0.1 and 0.5. The distribution for CPS–90A–10C tested at 2400°F shows the largest number of cavities with w/l smaller than 0.125. This seems to indicate the prevalence of cavities with smaller aspect ratios (w/l < 1/8) at higher test temperatures. The three curves shown in Fig. 5.62 exhibit a similar variation for large w/l (w/l larger than 0.75). The three curves also show an increase in the total number of cavities per unit area with test temperature (total number of cavities of 5.62/mm^2, 8.86/mm^2 and 13.92/mm^2 for the CPS–90A–10C non–tested, tested at 1500°F and tested at 2400°F respectively). This increase seems to suggest that nucleation of cavities occurs as the test temperature is increased. The information contained in Fig. 5.62 is not self–sufficient. In order to be able to interpret the data correctly, one needs to observe the cumulative distribution of the percentage cavity area with respect to w/l as shown in Fig. 5.63. For CPS–90A–10C in the non–tested condition the contribution of the cavities with various w/l to the total % cavity area is almost the same. For CPS–90A–10C tested at 1500°F larger percentages of the total cavity area seem to be made up by cavities with smaller w/l. On the contrary, for CPS–90A–10C tested at 2400°F most of the cavity area is composed of cavities with w/l ratios larger than 0.75. These large pores in the materials tested at 2400°F are the most noticeable characteristics and will be observed as well in CPS–82C–18M and in materials tested under short–term creep, as will be discussed later. The development of these large pores seems to be linked to
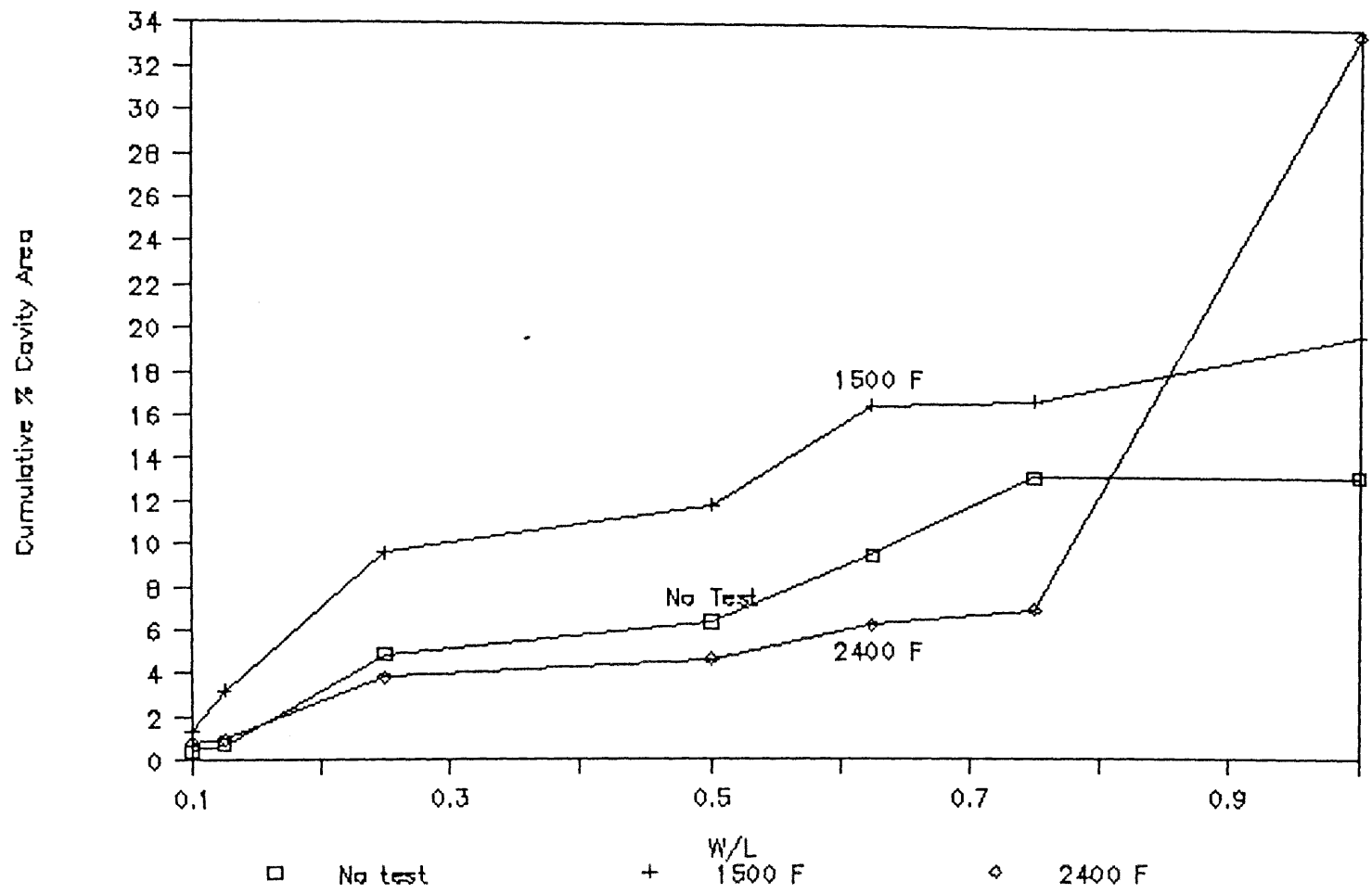
Figure 5.63 Cumulative distribution of percent cavity area with respect to width to length ratio, for as–manufactured CI'S–90A–10C under different conditions

the large non—linear deformations observed in the post—peak of the stress strain curves for the monotonic tests at temperatures above $T_m/2$. The increase of the total cavity % area with respect to higher test temperature is also significant (13.20% total cavity area for the non—tested CPS—90A—10C, compared to 19.82% and 33.75% for CPS—90A—10C tested at 1500^OF and 2400^OF respectively).

The discussion so far excluded the intra—granular cavities with both dimensions smaller than 6 μm (referred to as GC for the rest of the discussion). The GC are numerous but do not constitute a large percentage of the total cavity area. For CPS—90A—10C tested at elevated temperatures the number of GC per mm^2 was 47.58 and 189.06 for tests at 1500^OF and 2400^OF respectively. This is a relatively large number compared to the total number excluding GC (13.92/mm^2 for tests at 2400^OF). The total cavity area of the GC is relatively small, amounting to only 0.08% and 0.18% for CPS—90A—10C tested at 1500^OF and 2400^OF respectively.

The variations of the average length and width of the various cavities was found not to follow any special trend. The average width of all cavities varied from about 67 μm for non—tested CPS—90A—10C, to 41 μm and 68 μm for CPS—90A—10C tested at 1500^OF and 2400^OF respectively. The average length of these cavities varied from about 203 μm to 165 μm and 255 μm under the same conditions. These number do not appear to be meaningful because they represent the lumped averages for the intra—granular, interface and matrix cavities without any further division according to w/l ratios. A more in—depth study of the types of cavities is given later.

Next the orientation of the cavities with respect to the cold—pressing direction in the non—tested material and with respect to the direction of the uniaxially applied compression load in the tested materials is studied. It is noted that the axis of the cylindrical specimens is parallel to both the cold—pressing direction and the direction

of the applied compression force. Since both directions are the same, they will be referred to as direction of load application for the rest of the discussion. The orientations of the different cavities are grouped into two low—angle (0°–15°, and 15°–30°), two medium angle (30°–45°, and 45°–60°) and two high angle (60°–75°, and 75°–90°) categories. The circular pores with no specific orientation are classified in a N/A (non applicable) category. As in the case of classification with respect to different w/l both the number and area of cavities are important. Figure 5.64a shows the cumulative distribution of the number of cavities per mm^2 with respect to orientation. In the non—tested condition, the number of cavities in the low and medium angle categories are similar; however, less cavities are observed in the high angle category. For CPS—90A—10C tested at 1500°F the number of cavities in the low and medium angle categories increases by about 50% compared to the non—tested CPS—90A—10C, while the number of cavities in the high angle category is about the same. As the test temperature is increased to 2400°F, a similar trend is observed, where the number of cavities in the low angle category increases by about 150% compared to CPS—90A—10C tested at 1500°F, while the increase in the number of cavities in the medium and high angle categories is not as steep. The cumulative distribution of the cavity percentage area, shown in Fig. 5.64b, shows a complementary view. In the non—tested CPS—90A—10C the cavities in the 30°–45° category constitute the biggest part of the total cavity area (8.01% out of a total of 13.21%), while in the CPS—90A—10C tested at 1500°F the 15°–30° and 45°–60° angle categories represent most of the total area (5.11% and 7.22% respectively for a total of 19.82%). In the CPS—90A—10C tested at 2400°F the large circular pores with no particular orientation (N/A) constitute about 80% of the total cavity area (26.83% out of a total of 33.74%). Thus, the number of cavities with a low angle
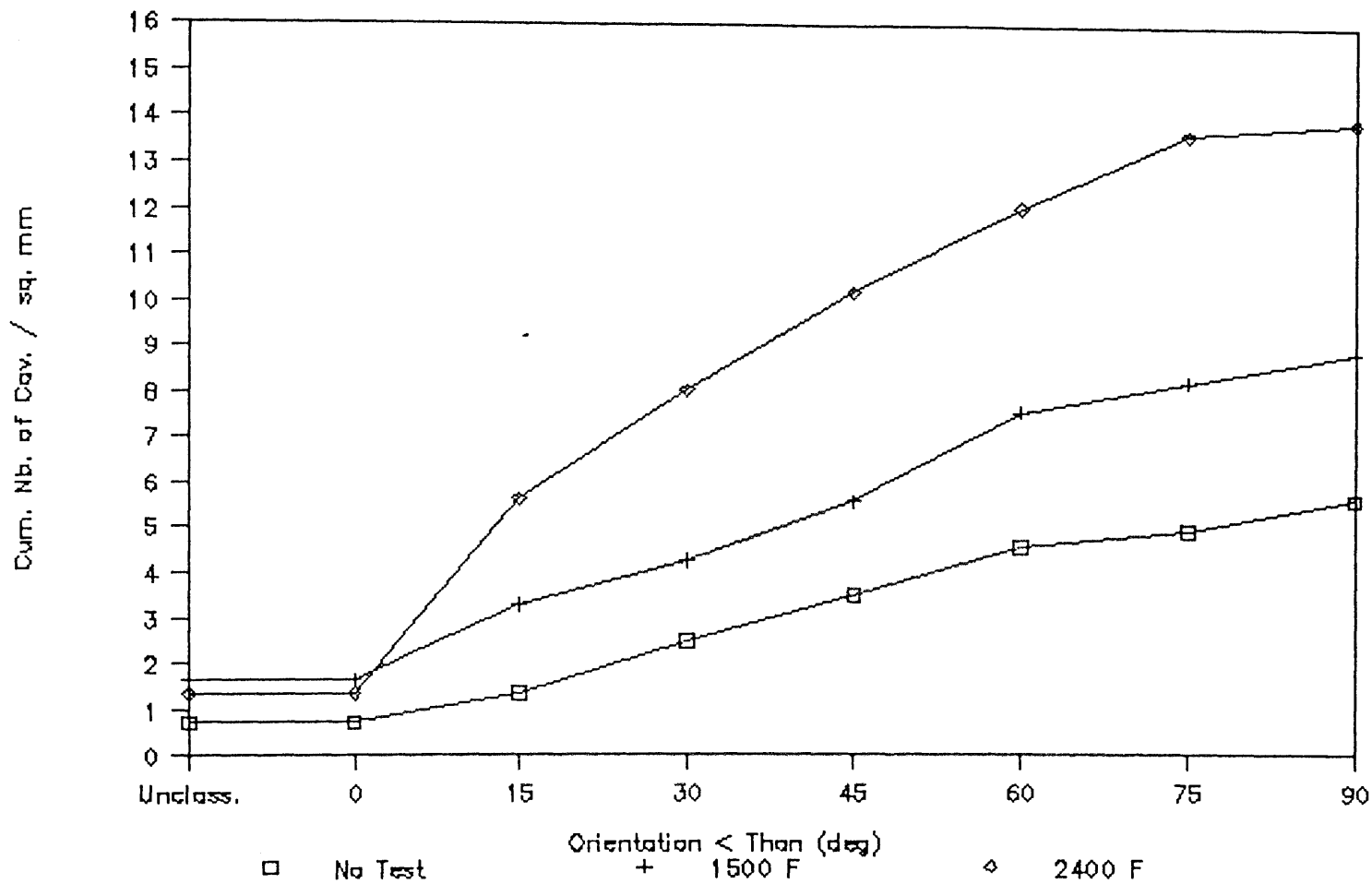
Figure 5.64a   Cumulative distribution of number of cavities per mm^2 with respect to orientation (relative to applied uniaxial compression or cold–pressing direction), for as–manufactured CPS–90A–10C under different conditions
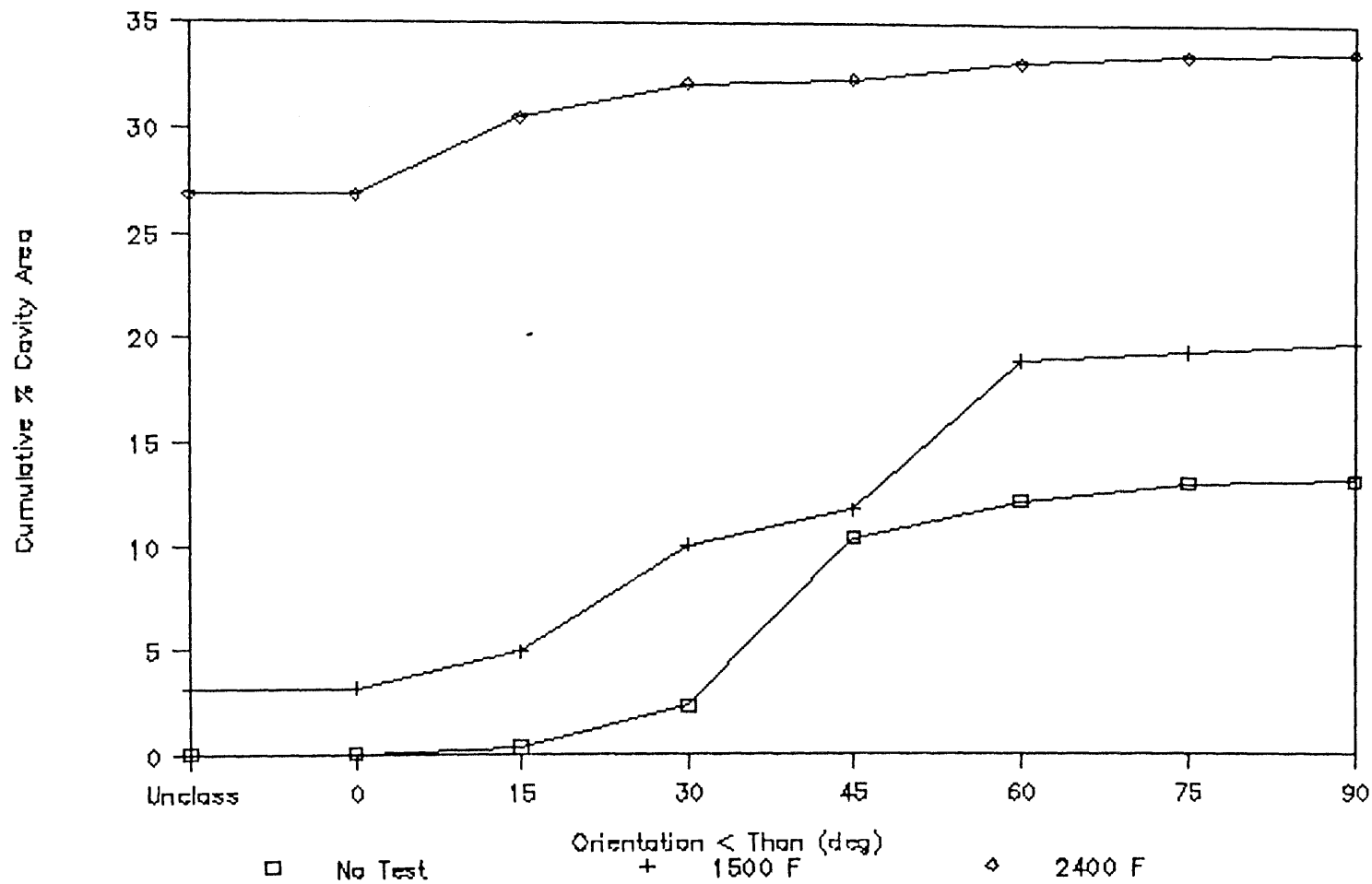
Figure 5.64b   Cumulative distribution of percent cavity area with respect to orientation (relative to applied uniaxial compression or cold–pressing direction), for as–manufactured CPS–90A–10C under different conditions

orientation ($<15^{\circ}$) increases significantly for materials tested at higher temperatures; on the other hand, most of the cavity area at high temperatures is made up from large circular pores with no particular orientation.

Finally, the type of these cavities is examined. The cavities have been classified as interface, aggregate or matrix. The aggregate cavities are the intra—granular cavities that develop in the tabular alumina grains due to load application or separation of the sintered individual grains. The interface cavities occur between the tabular alumina grains and the alumina—chromia solid solution. The matrix cavities nucleate and grow in the alumina—chromia solid solution. Circular and elliptical pores that exist in the matrix, border the alumina grains and also enclose part of the alumina grains are difficult to classify. It is more difficult to categorize the various cavities at higher temperature, especially at 2400°F, where big pores enclose large regions of the specimen. To resolve this problem the unclassified cavities were included in a class of their own. Furthermore, the best way to represent the different categories of cavities according to their type was found to be using pie charts. On these charts the different cavities are classified as 'A' (aggregate), 'B' (bond or interface), 'M' (matrix), and 'P,U' (pores or unclassified). Figures 5.65a, 5.65b and 5.65c show the number of cavities per mm^2 for CPS—90A—10C non—tested, tested at 1500°F and tested at 2400°F respectively. In the non—tested condition, most cavities (46.7%) are circular and elliptical pores that are difficult to classify. A non negligible amount of interface cavities is also observed (29.8%). At 1500°F the number of matrix cavities increases sharply (33.3%) and the number of interface cavities is the largest (37.0%). At 2400°F the number of aggregate cavities and the number of interface cavities is the largest (57.7%). Again, the area of these cavities is needed to be able to make any conclusion. The

Total Nb. of Cvaities / mm2 = 5.63

A (9.4%)

P,U (46.7%)

B (29.8%)

M (14.0%)
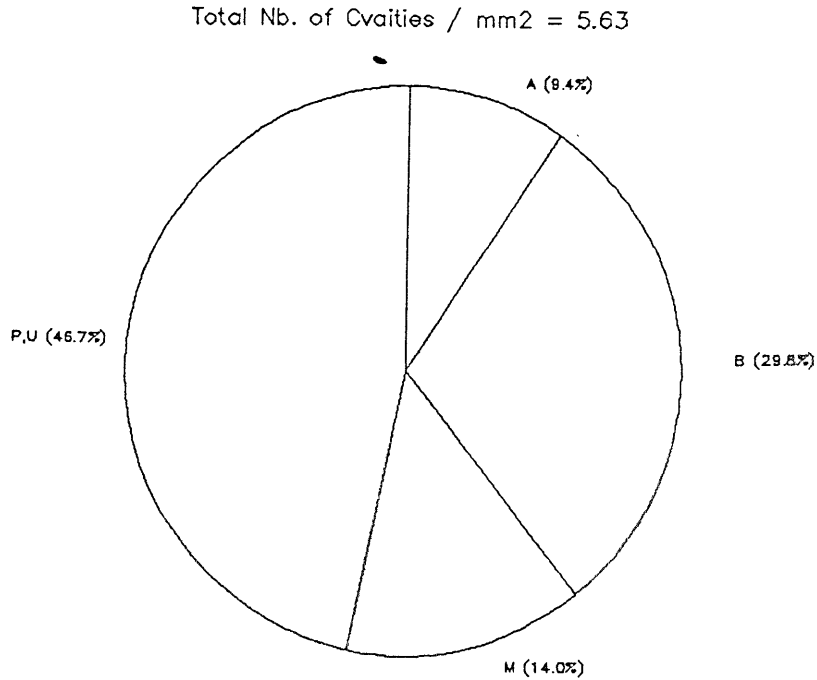
Figure 5.65a   Distribution of number of cavities per mm^2 with respect to cavity type for as—manufactured non—tested CPS—90A—10C

Total Nb. of Cavities / mm2 =8.88

P,U (7.4%)

A (22.2%)

M (33.3%)

B (37.0%)
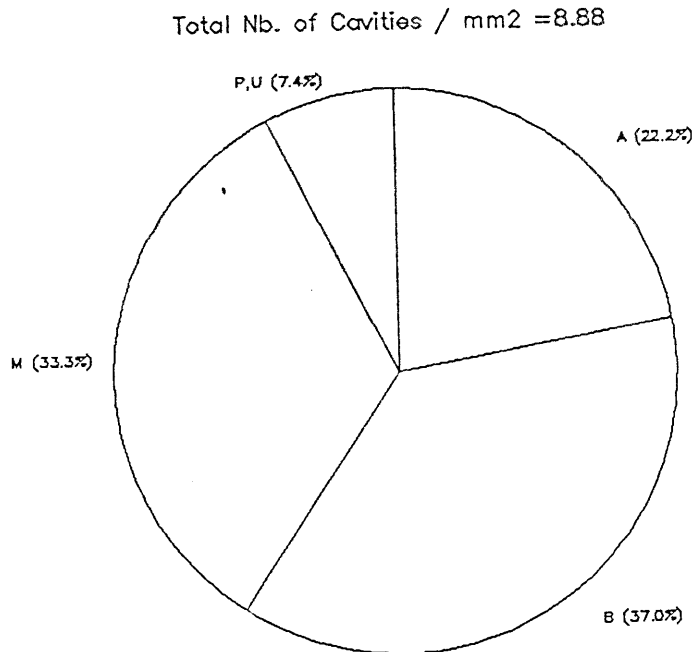
Figure 5.65b   Distribution of number of cavities per mm^2 with respect to cavity type for as—manufactured CPS—90A—10C tested at 1500°F

distribution of the cavity % area is shown in Figs. 5.65d, 5.65e, and 5.65f for CPS–90A–10C non–tested, tested at 1500°F and tested at 2400°F respectively. In both the non–tested CPS–90A–10C, and the one tested at 1500°F the areas of the interface cavities are the most significant (41.3% and 57.1% respectively). In the case of the CPS–90A–10C tested at 2400°F, the area of the unclassified large pores represent the biggest category (79.1%). These results correlate well with the previously observed pictures. It seems that at 1500°F networks of matrix and interface cracks lead to final fracture, while at 2400°F the large pores are the main cause of final fracture.

As–Manufactured CPS–90A–10C Tested Under Creep Loads

The microstructure of the specimens tested under creep loads at high temperatures is similar to the one of the specimens tested under monotonic loads. Figures 5.66 and 5.67 show Nomarski pictures of material CPS–90A–10C specimens tested under creep loads at 1500°F and 2400°F respectively. The specimen at 1500°F shows insignificant cavity growth compared to the non–tested material. This correlates well with the negligible amounts of creep deformatin observed at temperatures below $T_m/2$ at the macroscopic level. The specimen at 2400°F shows large pores and tabular alumina grains with large amounts of intra–granular cavities. This seems to suggest that creep cavitation is a mjor deformation mechanism at elevated temperatures.

As–Manufactured CPS–82C–18M Tested Under Monotonic Loads

Similar observations have been made for as–manufactured material CPS–82C–18M which consists of a grayish picrochromite ($MgCr_2O_4$) spinel matrix

Total Nb. of Cavities / mm2 = 13.92

P,U (9.6%)

M (11.6%)

A (57.7%)

B (21.1%)
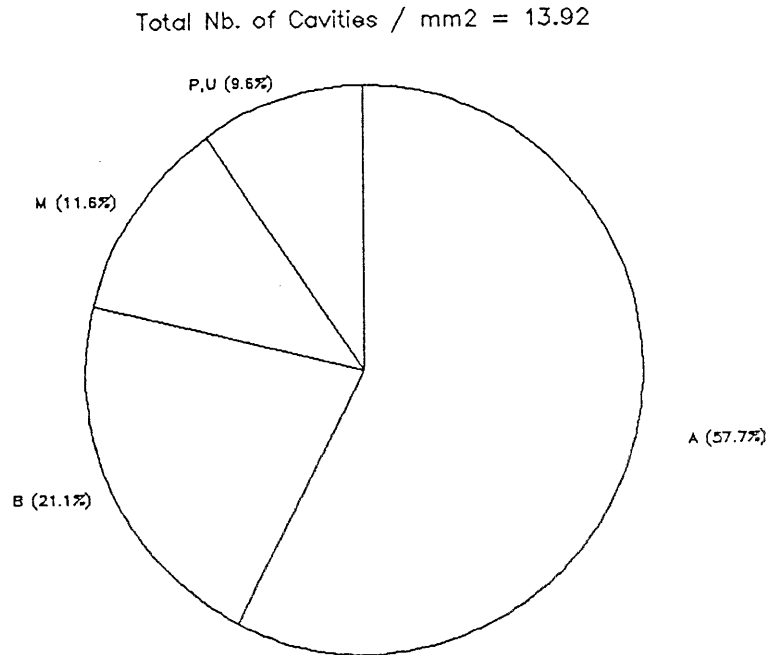
Figure 5.65c

Distribution of number of cavities per mm^2 with respect to cavity type for as–manufactured CPS–90A–10C tested at $2400^{O}F$

Total % Cavity Area = 13.21

A (0.4%)

P,U (29.8%)

B (41.3%)

M (28.5%)
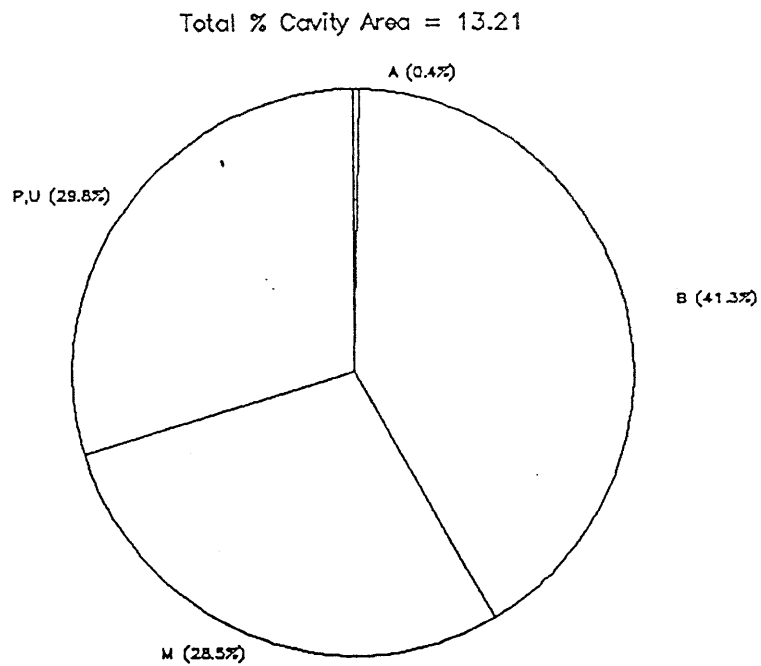
Figure 5.65d

Distribution of percent cavity area with respect to cavity type for as–manufactured non–tested CPS–90A–10C

Total % Cavity Area = 19.82

P,U (1.5%)   A (9.5%)

M (31.7%)

B (57.1%)
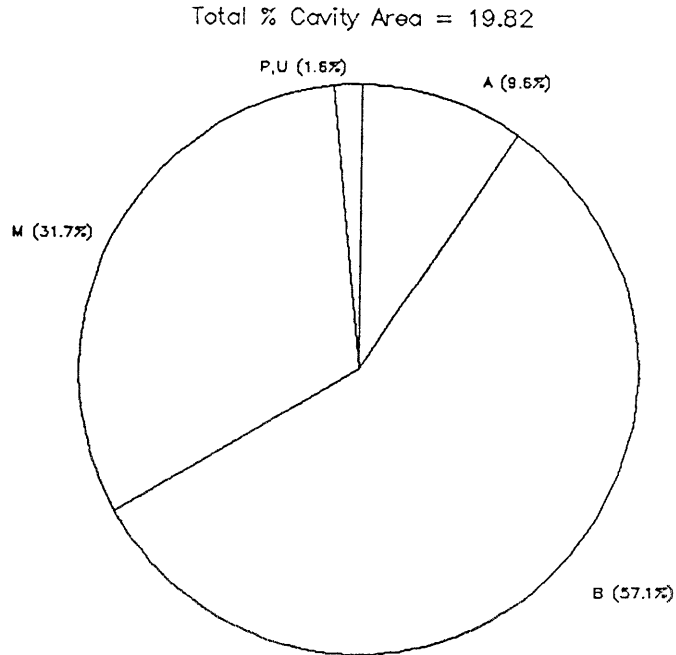
Figure 5.65e   Distribution of percent cavity area with respect to cavity
type for as—manufactured CPS—90A—10C tested at 1500°F

Total % Cavity Area = 33.76

A (5.5%)

B (14.5%)

M (0.9%)

P,U (79.1%)
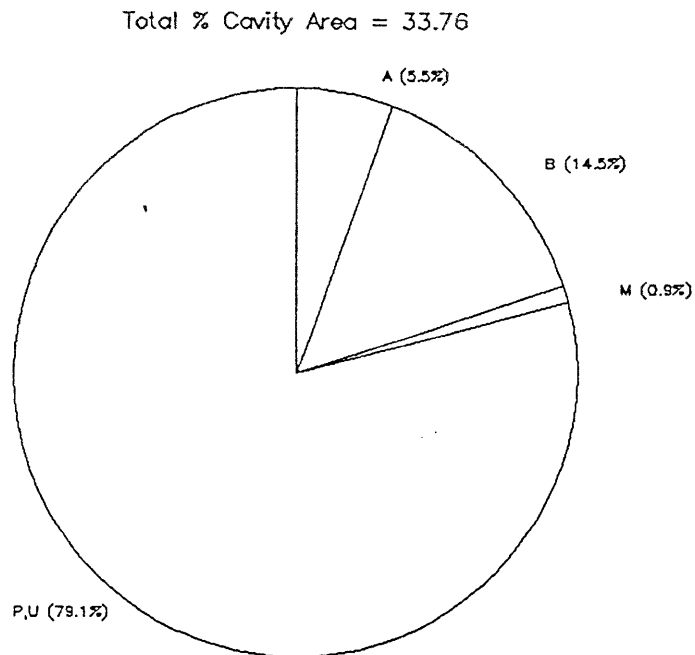
Figure 5.65f   Distribution of percent cavity area with respect to cavity
type for as—manufactured CPS—90A—10C tested at 2400°F

Figure 5.66   Nomarski microscope picture of CPS—90A—10C at 12.8X
                tested under a creep load of 66% of the monotonic strength at
                $1500^{O}F$

Figure 5.67   Nomarski microscope picture of CPS–90A–10C at 12.8X
                     tested under a creep load of 57% raised to 74% of the

                     monotonic strength at $2400^{O}F$

which binds black picrochromite fused grains. Figure 5.68 shows a Nomarski picture of non—tested CPS—82C—18M. Cracks are observed in the fused picrochromite grains. This is a major difference with material CPS—90A—10C which had no cavities in the as—received tabular grains. Observations made on the as—manufactured fused grains before they were used to produce material CPS—82C—18M showed the existence of these cracks as well. These cracks are thus originating from the production of the fused grains and not from the production of material CPS—82C—18M. Two major differences between materials CPS—82C—18M and CPS—90A—10C are recognized:

1. CPS—82C—18M has the same phase composition for both the matrix and the grains while CPS—90A—10C has different ones; and

2. Material CPS—82C—18M has fused pre—cracked grains while material CPS—90A—10C has tabular grains that only show negligible amounts of pre—existing cavities.

Figures 5.69 and 5.70 show Nomarski pictures of specimens tested at $1500^{O}F$ and $2400^{O}F$ under monotonic compression. Similarly to material CPS—90A—10C, CPS—82C—18M tested at $2400^{O}F$ exhibits large pores. The area of the large pores is bigger than the one observed for material CPS—90A—10C, and this seems to be correlate with the higher creep rates observed in CPS—82C—18M. This also tends to confirm that cavitation is a major factor in creep deformations.

Slag—Impregnated CPS—90A—10C Tested Under Monotonic Loads

The microstructure of material CPS—90A—10C after slag—impregnation is much more homogeneous. The slag penetration into different constituents of the material is studied by X—ray diffraction and is discussed in Section 5.5.2. In this
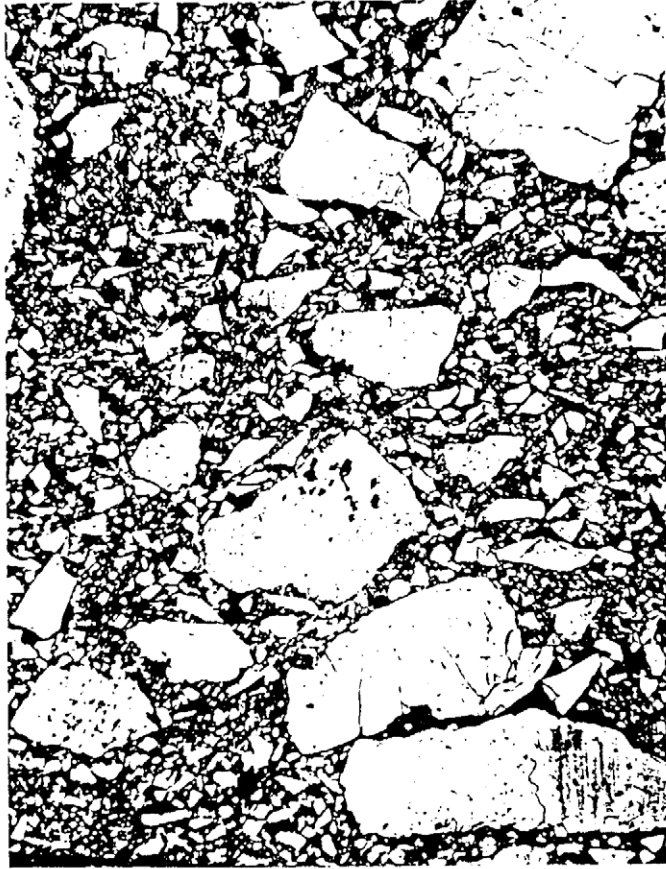
Figure 5.68   Nomarski microscope picture of virgin CPS–82C–18M at
12.8X

Figure 5.69   Nomarski microscope picture of CPS–82C–18M at 12.8X
tested to failure under monotonic compression at 1500°F
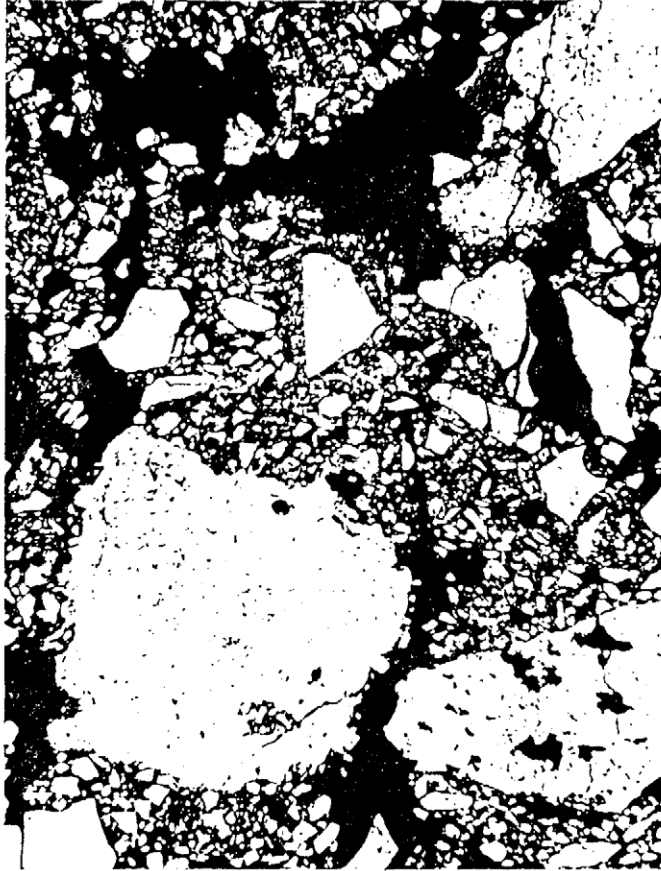
Figure 5.70   Nomarski microscope picture of CPS–82C–18M at 12.8X
tested to failure under monotonic compression at $2400^{O}F$

section the observations made by using a stereoscopic, Nomarski and scanning electron microscopes are reported. The microstructure of slag–impregnated CPS–90A–10C is much more homogeneous than the one of the as–manufactured CPS–90A–10C. Figure 5.71 shows a large crack that runs parallel to the principal stress direction that was the major cause of final fracture of slag–impregnated CPS–90A–10C tested at $2400^{\circ}F$. This kind of clear fracture path was not observed in the as–manufactured cold–pressed sintered materials. This may suggest that the cracking pattern depends on the homogeneity of the microstructure. Various new phases are observed in slag–impregnated CPS–90A–10C. Figure 5.72 is a Nomarski picture of slag–impregnated CPS–90A–10C showing penetration of the slag into the alumina grains and grain growth in the alumina–chromia solid solution. Similar grain growth has been observed by Wiederhorn et al (1988) for a slag–impregnated high–chromia refractory. Different kinds of microcracks interaction have been observed by scanning electron microscopy in the slag–impregnated CPS–90A–10C: "en passant" and "en echelon interaction". In the observed "en passant" interaction two parallel microcracks join along a line perpendicular to their axis before propagating further, as shown in Figs. 5.73a and 5.73b. In the case of the "en echelon" interaction, isolated microcracks first develop kinks parallel to the principal stress direction and then join to form longer crack formations, as shown in Figs. 5.74a and 5.74b. These en echelon formations may be inclined with respect to the principal stress direction to form a shear fault developing into a failure plane.

Slag–Impregnated CPS–82C–18M Tested Under Monotonic Loads

Slag–impregnated CPS–82C–18M has been penetrated by the western acid slag but has not been saturated by it as in the case of slag–impregnated

Figure 5.71   Nomarski microscope picture of slag–impregnated
CPS–90A–10C at 64X tested to failure under monotonic
compression at 2400°F showing a single macro crack parallel
to the principal stress direction
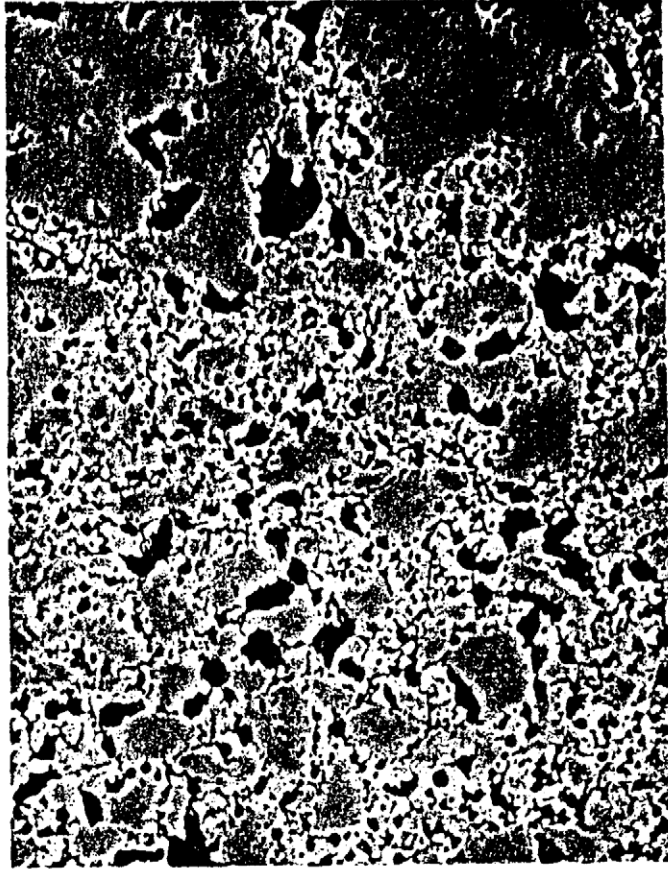
Figure 5.72   Nomarski microscope picture of slag–impregnated
                     CPS–90A–10C at 32X showing grain growth in the regions
                     between longer aggregates
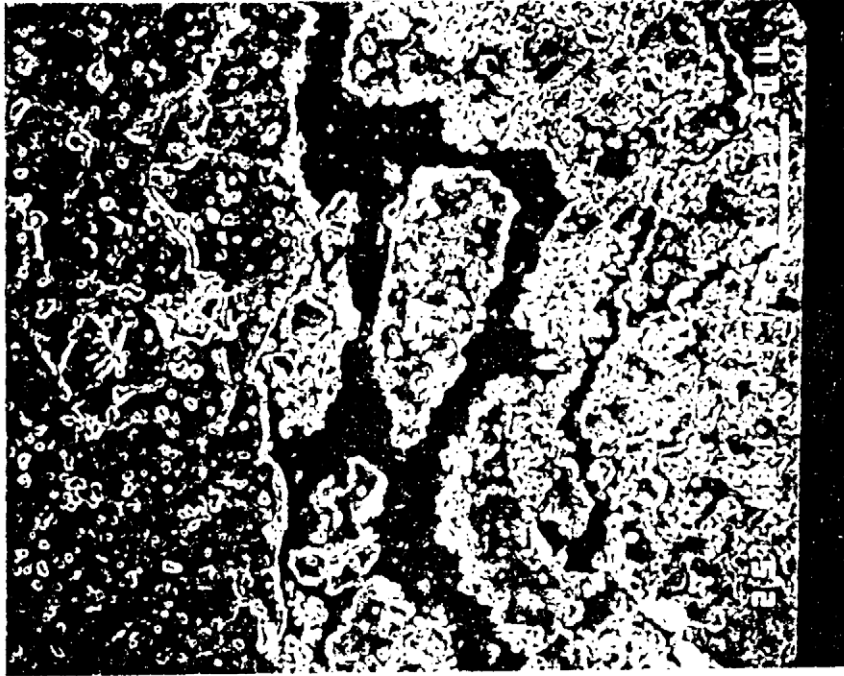
Figure 5.73a   An "en—passant" formation observed using SEM at 180X
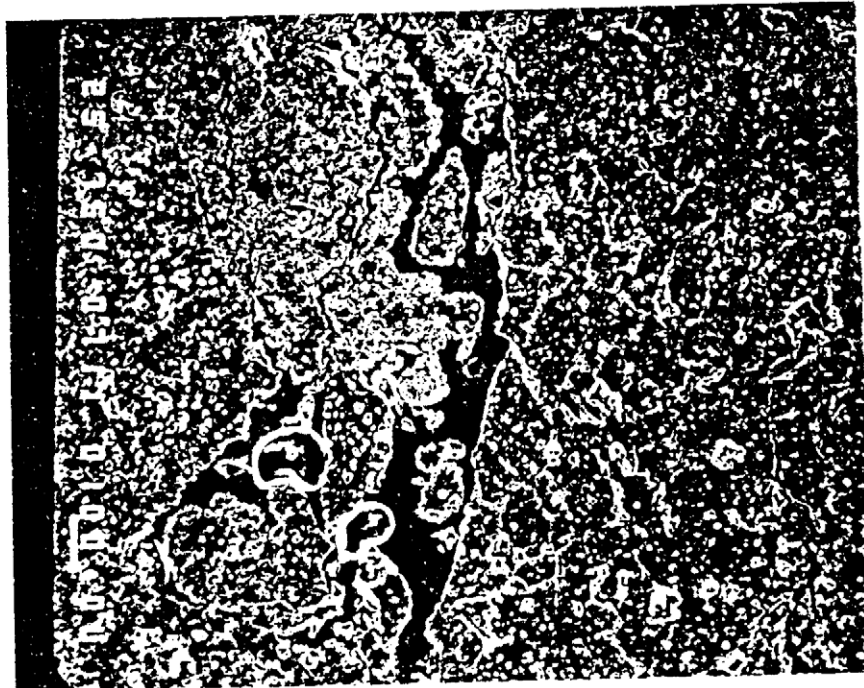
Figure 5.73b   Two "en—passant" formations joining parallel to the principal
stress direction observed using SEM at 75X

Figure 5.74a   An "en—echelon" formation observed using SEM at 200X
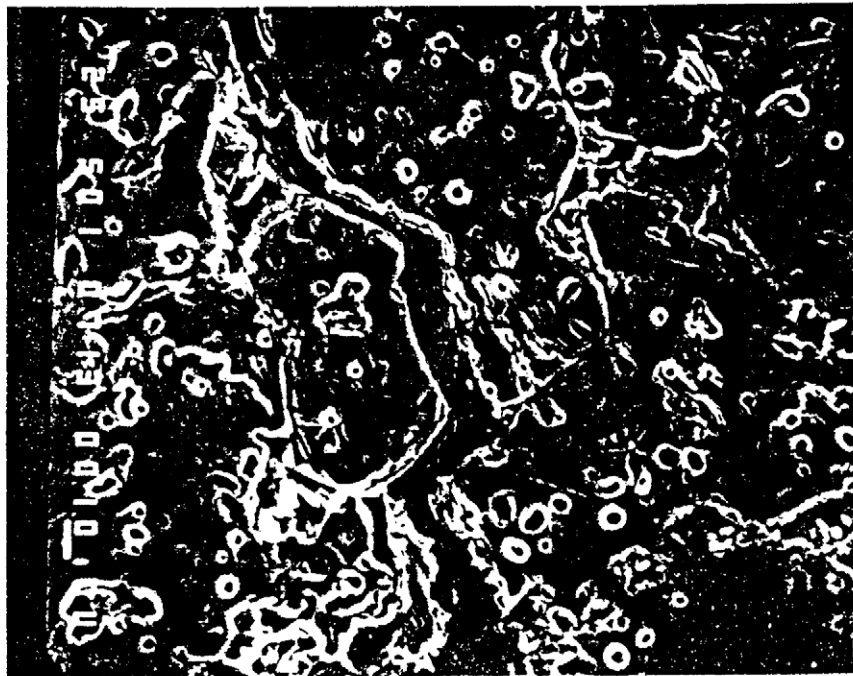
Figure 5.74b   Two "en—echelon" formations joining parallel to the principal stress direction observed using SEM at 500X

CPS–90A–10C. Grain growth is observed. The picrochromite grains do not appear to be penetrated to the same extent as the tabular alumina grains. The different phases that have appeared due to slag impregnation are better noticed using the Nomarski microscope. The cracking pattern in the slag–impregnated CPS–82C–18M tested at room temperature is not as clear as in the slag–impregnated CPS–90A–10C, and this may be due to the less homogeneous microstructure of the slag–impregnated CPS–82C–18M resulting from a smaller degree of impregnation.

5.6.2 X–ray Microanalysis

The slag degrades the refractory ceramic by two mechanisms: corrosion and erosion. The corrosion mechanism is usually characterized by dissolution and penetration. The aim of this specific examination was to study the penetration mechanism.

The as–manufactured CPS–90A–10C has an open connected–pores structure. The elemental composition was quantified by X–ray microanalysis. Three different positions were examined on the specimen:

1. Material composition in a region with no pores;

2. Material composition in a region next to the pores; and

3. Material composition inside a pore.

A semi–quantitative analysis was carried out using the program SSQ (Standardless Semi Quantitative). Two cases were examined for each of the three regions. The results of the semi–quantitative analysis are shown in Table 5.3. The %Al, %Si, %Ca, %Fe, %Na, and %Ti are shown. It is noticed that the Si, Ca and Fe are increasing consistently, and the Al is decreasing, as one moves from a "no–pore" region to an "inside the pore" region. In the "inside pore" region one notices an

	%Al	%Cr	%Si	%Ca	%Fe	%Na	%Ti
Original Mat'l	87.45	12.55	-	-	-	-	-
Matrix	87.62	7.58	4.59	0.19	0.03	-	-
Next to Pore	73.88	10.58	10.34	3.38	1.82	-	-
In Pore	40.35	8.34	22.79	9.55	11.66	6.26	1.06

Note: Results are the average of two runs

Table 5.3

X-ray Microanalysis of Slag-Impregnated CPS-90A-10C
in Matrix, Next to Pore, and Inside Pore

increase in the Ti and Na contents that were insignificant in the other two regions. The %Cr variation is not consistent. These results show an interesting conclusion. The matrix composition was not affected by the slag–impregnation. However, the slag was present in the pores and next to the pores. This seems to suggest that:

1.   The slag penetration into a 90% Al_2O_3, 10% Cr_2O_3 matrix is not significant;

2.   Open porosity is a major factor for slag penetration; this result is consistent with corrosion tests on hot–pressed materials (Washburn, 1985) that showed little penetration of the slag into the hot–pressed materials. It is noted that the hot–pressed materials do not have any open porosity.

5.6.3   Results of Porosimeter Tests

The open porosity of as–manufactured and slag–impregnated CPS–90A–10C and CPS–82C–18M has been studied using mercury porosimeter. Figure 5.75 shows the cumulative open porosity distribution for different pore radii. The as–manufactured materials in the non–tested condition as well as tested at 1500^OF and 2400^OF show a similar open porosity. A small decrease in the total open porosity is observed from 16.5% in the non–tested condition to 16.2% for the test at 1500^OF and 15.3% for the test at 2400^OF. The mean pore radius variation with test condition for as–manufactured material CPS–90A–10C is not very conclusive going from 0.8μm in the non–tested condition to 0.6μm for the test at 1500^OF to 0.8μm for the test at 2400^OF. The distribution of open pores in the slag–impregnated CPS–90A–10C is very different showing a total of only 2.7% in the non–tested condition. This is as expected. Similar observations are made for material CPS–82C–18M and are

Cumulative Open Porosity (%)

Radius (microns)

Legend:
- As-Man. Not tested
- As-Man. Tested 1500F
- As-man. Tested 2400F
- Slag-Imp. Tested 75F
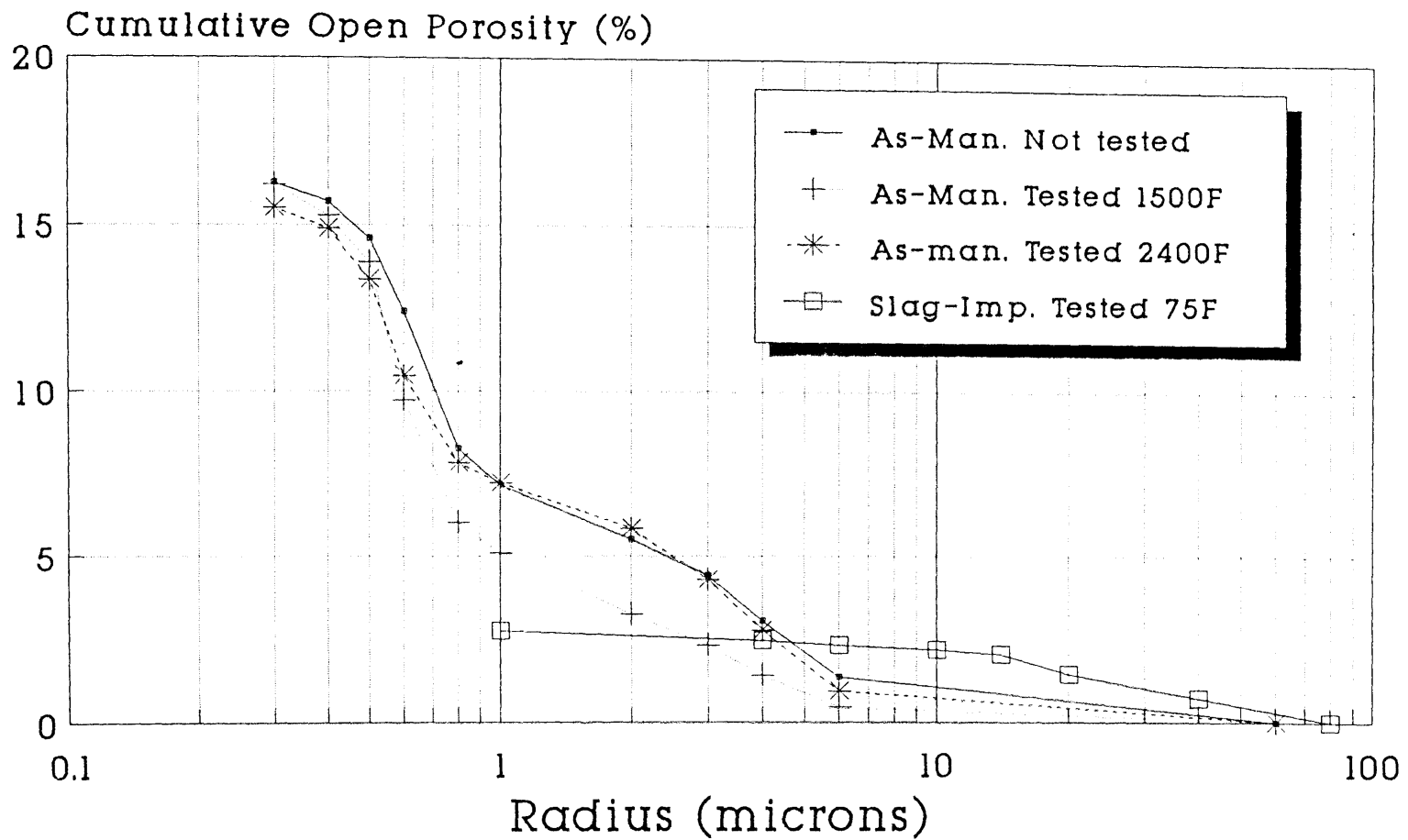
Figure 5.75   Cumulative open porosity (expressed as % of total area) variation with pore radius for CPS–90A–10C under different conditions

summarized in Table 5.4. The decrease in open porosity of the slag–impregnated material combined with the results of the X–ray microanalysis seems to suggest two conclusions:

1. The open porosity is a main factor in controlling the extent of the slag penetration into the refractory; and

2. The slag does fill the pores explaining the increased strengths observed in the monotonic compression test at room temperature.

5.6.4 Dry Density Measurements

The dry bulk densities of as–received and tested as–manufactured materials were measured. For as–manufactured CPS–90A–10C the results were conclusive and a decrease of the density with test temperature is observed. This indicates larger amounts of microcracking at higher test temperatures and is consistent with the results obtained for microscopic observations. A relation between the density after testing and the final fracture strain is established and is represented in Fig. 5.76. This relationship is valid for temperatures below $T_m/2$ and does not apply for temperatures above that.

Additional information about the microstructural characterization of CPS–90A–10C and CPS–82C–18M can be found in Appendix C.

5.7 SUMMARY

As a result of the specimen preparation and brick characterization studies, the following guidelines were adopted for standard specimens used in thermomechanical testing:

1. Circular cylinders with 1" diameter and 2.5" to 3.0" height;

<u>Open Porosity (%)</u>

Condition	Material Open Porosity (%)			
	CPS-90A-10C As-Man.	CPS-90A-10C Slag-Imp.	CPS-82C-18M As-Man.	CPS-82C-18M Slag-Imp.
Not Tested	16.53	2.74	15.20	4.36
Tested 1500°F	16.17	-	14.09	-
Tested 2400°F	15.37	-	13.23	-

<u>Mean Pore Radius (μm)</u>

	CPS-90A-10C	CPS-82C-18M
Not Tested	0.8	2.0
Tested 1500°F	0.64	1.4
Tested 2400°F	0.8	1.92

Table 5.4   Open porosity and mean pore radius obtained from porosimeter tests for CPS—90A—10C and CPS—82C—18M

$$\varepsilon_f = (1 + (\Delta\rho)^{3/2})\, \varepsilon_{room}$$

$\varepsilon_f \neq \varepsilon_{peak}$

$\Delta\rho = -1.195\%$
$2000^{\circ}F$

$\Delta\rho = -0.518\%$
$1000^{\circ}F$

$\Delta\rho = 0\%$
$75^{\circ}F$

$\Delta\rho = -0.549\%$
$1500^{\circ}F$

$T_{Transition}$

(Thousands)
Temperature ($^{\circ}$F)

□ data   ——— model

Peak Strain/Room T Peak Strain
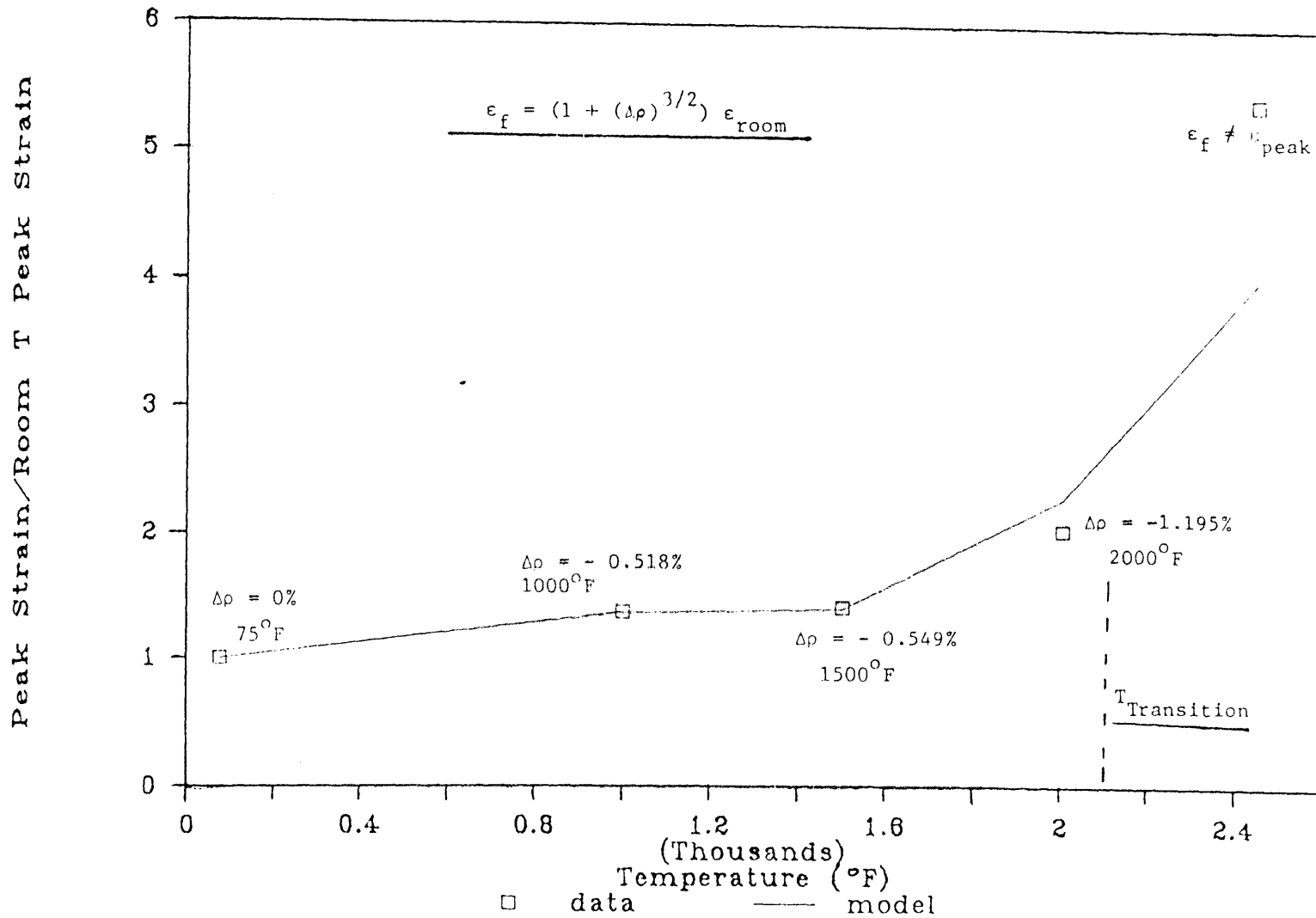
Figure 5.76   Relationship between density after testing, test temperature
                  and peak strain for CPS—90A—10C

2.   Coring speed of 375 rpm;

3.   Slow speed sawing of end surfaces;

4.   Vertical position of specimen during slag–impregnation;

5.   Specimen preparation performed by the same skilled operators;

6.   Coring parallel to the cold–pressing direction;

7.   Specimens extracted from the interior of the brick; and

8.   Specimens taken from the same batch of bricks.

The following results were observed for tests in monotonic compression. For both CPS–90A–10C and CPS–82C–18M, two distinct behavioral trends are observed with respect to temperature under compressive loads. For temperatures below a transition temperature approximately equal to $T_m/2$ the material behavior is linear elastic with a brittle fracture. For temperature levels above $T_m/2$, significant non–linear deformations are observed. Furthermore, for temperatures below $T_m/2$, the material behavior is essentially strain rate independent for strain rates in the range from 10^{-4} to 10^{-6} sec^{-1}. For temperatures above $T_m/2$, if the strain rate is high enough (40×10^{-6} sec^{-1} at $2275^\circ F$ for CPS–82C–18M), linear deformations are observed with brittle final fracture; for intermediate strain rate values (20×10^{-6} sec^{-1} at $2275^\circ F$ for CPS–82C–18M) non–linear deformations with an unstable fracture propagation are observed; and for lower strain rate values (4×10^{-6} sec^{-1} at $2275^\circ F$ for CPS–82C–18M) non linear deformations with a stable fracture propagation are observed.

The strength of CPS–82C–18M in monotonic compression was observed to decrease slightly with temperature (proportional to $T^{1/2}$) for temperatures below $T_m/2$. The rate of strength decrease for temperatures above $T_m/2$ is faster (proportional to T). The strength variation of CPS–90A–10C with temperature is

different from that of CPS–82C–18M, but similar to other mixed mode systems containing alumina. The strength variation of CPS–90A–10C reaches a peak at 2000^OF, and the strength decrease with temperature is slower than the one of CPS–82C–18M. (Varying from 19.4 ksi at room temperature to 14.7 ksi at 2000^OF to 7.4 ksi at 2400^OF for CPS–82C–18M; and from 22.8 ksi at room temperature to 25.4 ksi at 2000^OF to 22.7 ksi at 2440^OF for CPS–90A–10C; for controlled displacement rates of 7.218 x 10^{-15} in/sec).

The variations with temperature of the associated peak strain, the equivalent measure of toughness and the observed macroscopic modes of failure are similar for both CPS–90A–10C and CPS–82C–18M. The associated peak strain increases slowly from room temperature to $T_m/2$, and increases faster for temperatures above $T_m/2$. (Varying from 0.24% at room temperature to 0.48% at 2000^OF to 1.36% at 2440^OF for CPS–90A–10C, and varying from 0.25% at room temperature to 0.41% at 2000^OF to 0.62% at 2400^OF for CPS–82C–18M; for controlled constant displacement rates of 7.218 x 10^{-5} in/sec). The measure of toughness (taken to be the area under the stress strain curve) does not vary much with temperature, for temperatures below $T_m/2$ for both CPS–82C–18M and CPS–90A–10C. However, for temperatures above $T_m/2$ the increase in the toughness measure is significant (from 25.1 psi at room temperature to 33.0 at 2000^OF to more than 95 psi at 2275^OF for CPS–82C–18M and from 30.2 psi at room temperature to 63.0 psi at 2000^OF to more than 287.2 psi at 2440^OF). For both materials the variability in the material properties is smaller at elevated temperatures (standard deviation of 10% in strength values at room temperature compared to 1.2% at 2000^OF). At room temperature, both vertical and inclined macrocracks seem to form. At elevated temperatures, the inclined macrocracks seem to be predominant.

Constant load tests at constant temperature were carried out to study the nature of non–linear deformations at elevated temperatures. The tests were short term tests (about 2 hours) under high constant loads (in the range of 55% to 85% of the monotonic strength). It was found out that at temperatures below $T_m/2$, the contribution of the short term creep deformation appears to be negligible compared to the total deformation under monotonic compression. However, for temperatures above $T_m/2$ the short–term creep deformations are significant. Comparison of monotonic test results for CPS–82C–18M with established deformation mechanism maps from Frost and Ashby (1982) for Cr_2O_3 was satisfactory. The high–load short–term creep tests were combined with the results of the low loads (less than 15% of the monotonic strength) long–term creep tests by McGee and Konrady (1983–87) to form deformation maps. The agreement with the long term creep data is satisfactory. Material CPS–82C–18M was found to have higher creep rates than material CPS–90A–10C. An activation energy of 185 kJ/mole was found for CPS–90A–10C; it is lower than the expected value of about 300 kJ/mole, but compares mell with some other researchers data. A stress exponent of 1.83 shows the occurence of diffusion mechanisms. Comparison of the deformation map for CPS–90A–10C for creep plotted on scaled σ/E and T/T_m with a deformation map from Gandhi and Ashby (1983) for alumina seems to suggest two major fracture mechanisms: brittle intergranular fracture and intergranular creep fracture.

In order to measure the transient thermal strain, constant loads increasing temperature tests were conducted. Slower heating rates were observed to produce higher final strains.

The short–term cyclic behavior in compression was studied. For temperatures below $T_m/2$ the initial cycles accumulate significant amounts of inelastic strains, and

later cycles accumulated relatively less inelastic strains. Large amounts of accumulated inelastic strains were observed immediately before final failure. For temperatures above $T_m/2$ all the cycles accumulate about the same amount of inelastic strains. Three dimensional "temperature — % of monotonic strength — numbers of cycles to failure" failure surfaces were constructed.

Limited thermal cycling showed a 6.2% reduction in stiffness when the material was subjected to one thermal cycle from $75^\circ F$ to $2200^\circ F$.

The effect of a reducing atmosphere (P_{0_2} of 10^{-8} atm) on the as—manufactured material behavior is not as clear. The reducing atmosphere seems to reduce the initial stiffness of as—manufactured CPS—90A—10C at room temperature, and to increase it at higher temperatures. However, no particular trend is observed. For CPS—82C—18M at temperatures below $T_m/2$, the reducing atmosphere does not seem to affect the material behavior. However, at $2000^\circ F$, a 36% increase in initial stiffness is observed.

At room temperature, in air atmosphere the strength of slag—impregnated materials is higher than that of as—manufactured materials, due to the slag solidifying into the pores and acting as a glassy bond. Material CPS—90A—10C is penetrated by slag to a higher degree than material CPS—82C—18M resulting in higher increase in strength for the slag—impregnated CPS—90A—10C than CPS—82C—18M (strength values of 77.3 ksi and 22.8 ksi for slag—impregnated and as—manufactured CPS—90A—10C respectively, compared to 21.9 ksi and 19.4 ksi for slag—impregnated and as—manufactured CPS—82C—18M respectively). The rate of decrease in initial stiffness with temperature is faster for slag—impregnated materials than as—manufactured ones. As a result at $2400^\circ F$, the stiffness of as—manufactured and slag—impregnated CPS—90A—10C are about the same, and the strength of

slag–impregnated CPS–90A–10C is lower than the one of the as–manufactured one (strength of 22.74 ksi for as–manufactured CPS–90A–10C compared to 20.19 ksi for slag–impregnated CPS–90A–10C). This would seem to suggest that at temperature levels above 2400°F, the strength of slag–impregnated materials would always be smaller, and this would be expected to accelerate the corrosion process above 2400°F. This is consistent with the results of corrosion tests (Bakker et al, 1984) that show higher corrosion rates at higher temperatures.

Reducing atmospheres do not seem to have a significant affect on the behavior of slag–impregnated CPS–90A–10C below 2200°F, and on the behavior of CPS–82C–18M below 1500°F. However, at 2200°F reducing atmospheres seems to significantly reduce the strength and stiffness of slag–impregnated CPS–82C–18M.

Microscopic observations showed the structure of as–manufactured CPS–90A–10C to consist of white tabular alumina grains in a brown chromia–alumina solid solution (brown color). Alumina grains penetrated at different degrees by chromia exhibited colors ranging from pink to light brown. The solid solution consists of a conglomerate of sub–micron grains. As test temperature increases the total number of microcavities in CPS–90A–10C increases significantly ($5.62/\text{mm}^2$, $8.86/\text{mm}^2$ and $13.92/\text{mm}^2$ for CPS–90A–10C non–tested, and tested at 1500°F and 2400°F respectively), as well as the total % cavity area (13.20%, 19.82% and 33.75% for non–tested, and for tests at 1500°F and 2400°F respectively). The number of microcavities with width to length ratio (W/L) smaller than 0.1 increases sharply also ($0.66/\text{mm}^2$ for test at 1500°F compared to $6.16/\text{mm}^2$ for test at 2400°F). However, the area of the cavities with small W/L is smaller at higher test temperatures (3.23% at 1500°F compared to 0.95% at 2400°F). At temperatures above $T_m/2$, most of the cavity area is made up by large pores (at 2400°F large pores

constitute 26.7% cavity area compared to 33.75% total cavity area). At temperatures below $T_m/2$ most of the cavity area is made up by smaller W/L cavities at the interface between the grains and the matrix or in the matrix itself. In the high–alumina tested at 1500°F, the orientations of most cavities with respect to the applied uniaxial compressive load are in the 15°–30° and 45°–60° angle categories. At 2400°F, although the number of cavities with an orientation in the 0°–30° category increases significantly, 80% of the total cavity area is made up by large pores with no specific orientation. The number of intra–granular cavities with both dimensions smaller than 6 μm increases significantly at high temperatures in the tabular alumina grains ($189.06/mm^2$ at 2400°F); however, their area is insignificant (0.18% at 2400°F).

Microscopic observations show that material CPS–82C–18M in the non–tested state consists of a picrochromite spinel matrix (gray color) enclosing fused picrochromite grains (black color). The as–received picrochromite grains (before manufacturing of CPS–82C–18M) show a higher number of pre–existing microcracks than the tabular alumina grains. As test temperature increases, less intragranular cavities but larger pores develop in CPS–82C–18M compared to CPS–90A–10C. This seems to be consistent with the higher creep rates observed in CPS–82C–18M in short–term creep tests.

The microstructural characteristics of CPS–90A–10C specimens tested under short–term creep loads is similar to the one of the specimens tested under monotonic loads.

The microstructure of slag–impregnated materials is more homogeneous. Slag is observed to saturate material CPS–90A–10C, and to partially penetrate material CPS–82C–18M. Grain growth is observed in the alumina–chromia solid solution in

slag–impregnated CPS–90A–10C and in the picrochromite spinel in slag–impregnated CPS–82C–18M. The cracking pattern in slag–impregnated materials is also more homogeneous. Final fracture appears to be due to a single crack running parallel to the applied stress direction (or an array of microcracks joining together to form a vertical network parallel to the applied compression direction).

The two main observed types of microcracks interaction are "en echelon" and "en passant" interactions. This is similar to the ones observed in other brittle materials such as rocks.

X–ray microanalysis of the slag–impregnated CPS–90A–10C seems to suggest that the slag penetration into regions of the material with no porosity is not significant. However, the pores are shown to be filled with slag, and the regions next to the pores are penetrated to higher degree than the matrix. Open porosity seems to be a major factor for slag penetration.

The role of open porosity seems to be confirmed by the mercury porosimeter test results. These tests show a decrease of open porosity from 16.53% in the as–manufactured CPS–90A–10C to 2.74% in the slag–impregnated CPS–90A–10C. Porosimeter tests also show a decrease of open porosity for higher test temperatures (16.17% and 15.37% for as–manufactured CPS–90A–10C tested at 1500^OF and 2400^OF respectively).

Bulk density measurements indicated a density decrease in the tested specimens for higher test temperatures which correlates with the increased microcracking. The density decrease can be related to the final fracture strain in as–manufactured CPS–90A–10C for test temperatures smaller than $T_m/2$.

CHAPTER 6
HOT–PRESSED HIGH–ALUMINA AND HIGH CHROMIA MATERIALS

6.1 SYNOPSIS

In this chapter the deformation and fracture behavior of hot–pressed high–alumina and high–chromia materials is examined under short–term uniaxial monotonically increasing and constant loads (Sections 6.3.1 and 6.3.2 respectively) at elevated temperatures in air atmosphere. In the monotonic load tests three different chemical compositions are studied using the alumina–chromia refractories HP–90A–10C, HP–50A–50C and HP–25A–75C. One chromia–magnesia refractory is examined: HP–80C–20M. The microstructural characteristics of virgin and tested HP–90A–10C are described in Section 6.4.

6.2 SPECIMEN PREPARATION

Hot–pressed materials have a smaller maximum grain size than cold–pressed sintered materials (0.001" for HP–90A–10C compared to 0.25" for CPS–90A–10C) allowing a choice of smaller specimens for testing. Furthermore, since hot–pressed materials are expensive and difficult to get in large brick size for coring, prismatic specimens had to be used instead of cylindrical ones. Specimens with 0.3" by 0.3" cross–section and a height of 0.9" (giving a height to side ratio of 3) were chosen. The end surfaces were sawed smooth and parallel for testing.

6.3 ELEVATED TEMPERATURE BEHAVIOR OF AS–MANUFACTURED MATERIALS UNDER UNIAXIAL SHORT–TERM COMPRESSIVE LOADS IN AIR ATMOSPHERE

6.3.1 Behavior Under Monotonic Compressive Loads at Constant Temperature

The high temperature uniaxial compressive behavior under short–term monotonic loads of the three hot–pressed alumina–chromia refractories: HP–90A–10C, HP–50A–50C and HP–25A–75C is discussed first, and the one of the hot–pressed chromia–magnesia: HP–80C–20M is discussed next. Comparison between the behavior of CPS–90A–10C and HP–90A–10C, and the behavior of CPS–82C–18M and HP–80C–20M is carried out. Material HP–90A–10C has the same chemical composition as CPS–90A–10C; material HP–90A–10C is an alumina–chromia solid solution with no second phase, while material CPS–90A–10C consists of a solid solution of alumina–chromia as a matrix, with fused–cast alumina grains that are penetrated by chromia to different extent as a second phase. Material HP–80C–20M has about the same chemical composition as CPS–82C–18M; both chromia–magnesia materials have a spinel structure with picrochromite grains in a picrochromite matrix.

Stress strain curves 'for different temperature levels, and a constant displacement rate of 1.83×10^{-3} mm/sec are shown in Figs. 6.1, 6.2 and 6.3, for materials HP–90A–10C, HP–50A–50C and HP–25A–75C respectively. Similarly to cold–pressed sintered materials, the three alumina–chromia hot–pressed materials, exhibit two distinct deformation and fracture behavioral regions with respect to temperature. There appears to be a transition temperature that separates these behavioral regions, and this transition temperature is found to correspond to about one–half the melting point of the material. The two distinct behavioral trends are:

1. For temperature levels below roughly $1/2$ T_m (where T_m is the melting temperature of the material), the deformation behavior is linear elastic
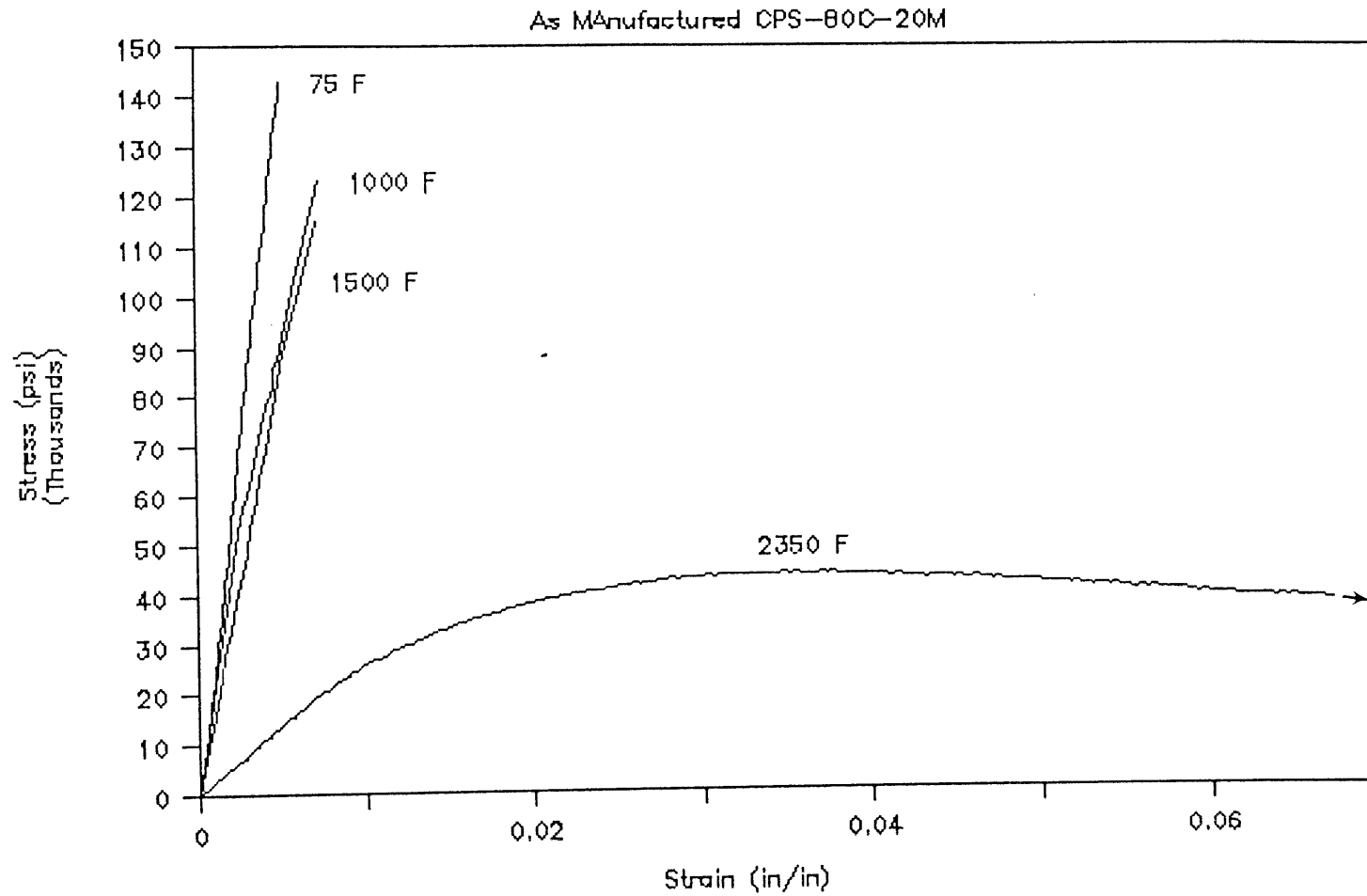
As Manufactured HP—90A—10C
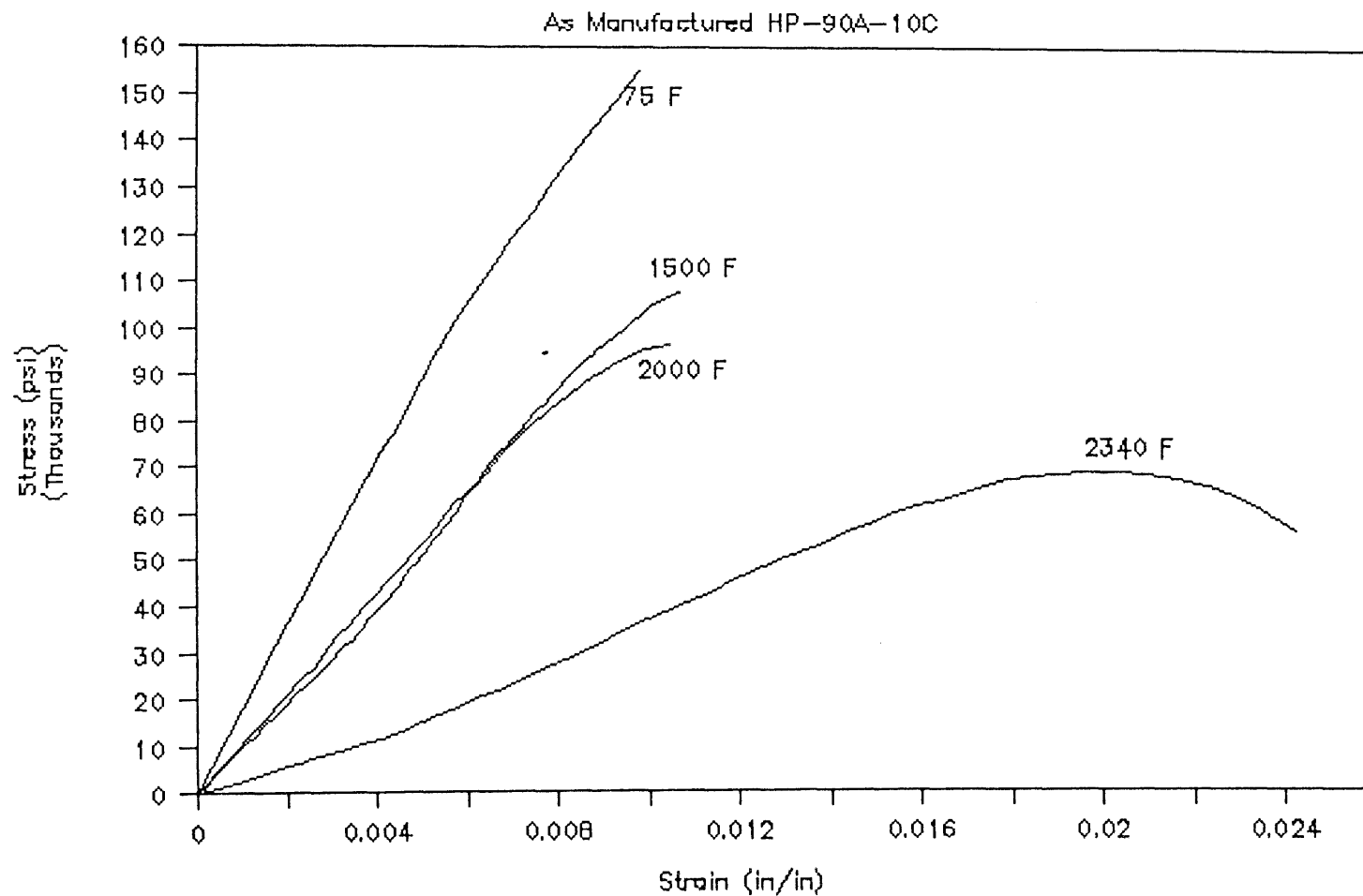
Figure 6.1   Stress strain curves for HP—90A—10C at different temperature levels and a constant piston displacement rate of 7.218×10^{-5} in/sec
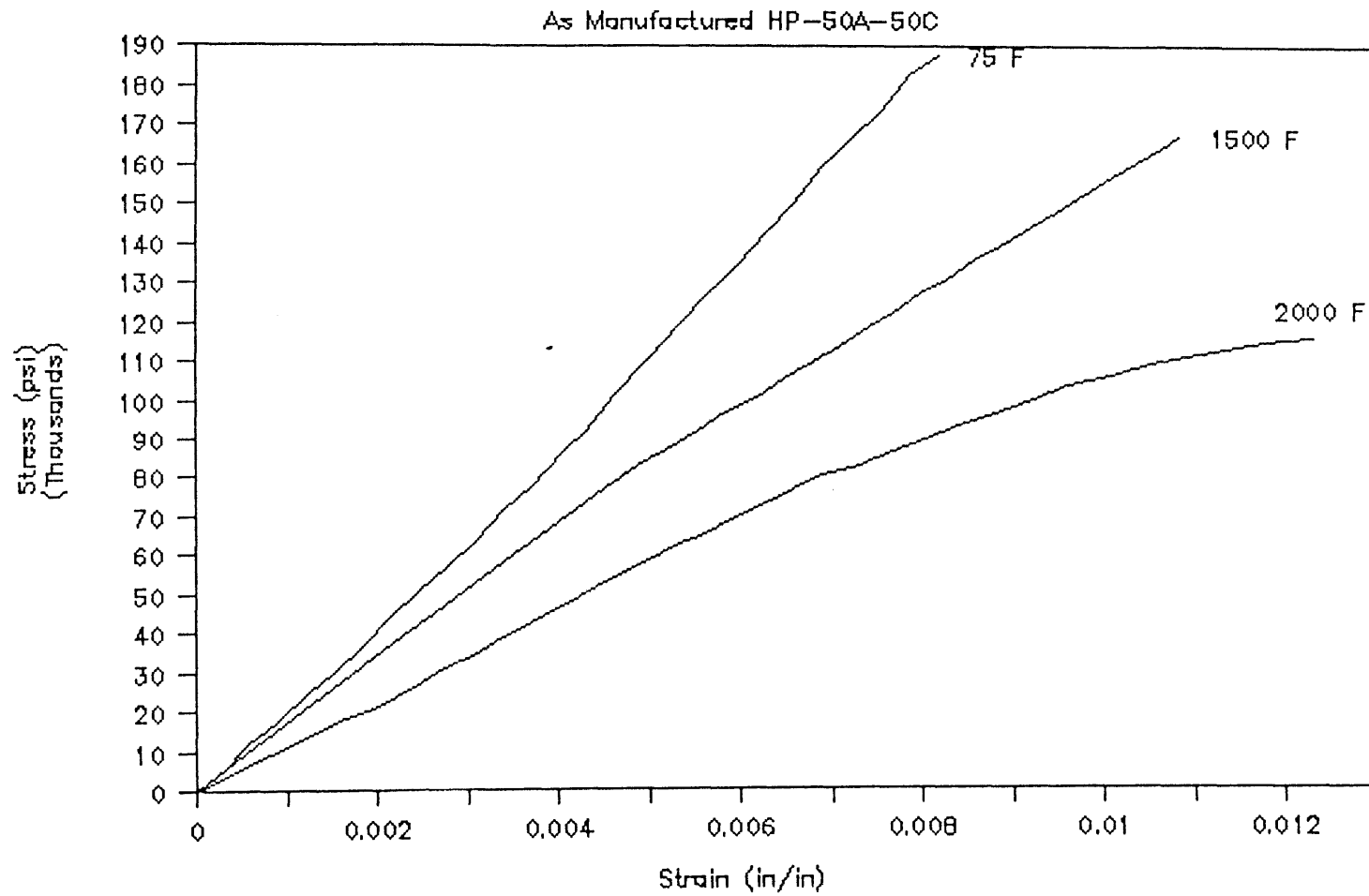
Figure 6.2   Stress strain curves for HP–50A–50C at different temperature levels and a constant piston displacement rate of 7.218×10^{-5} in/sec
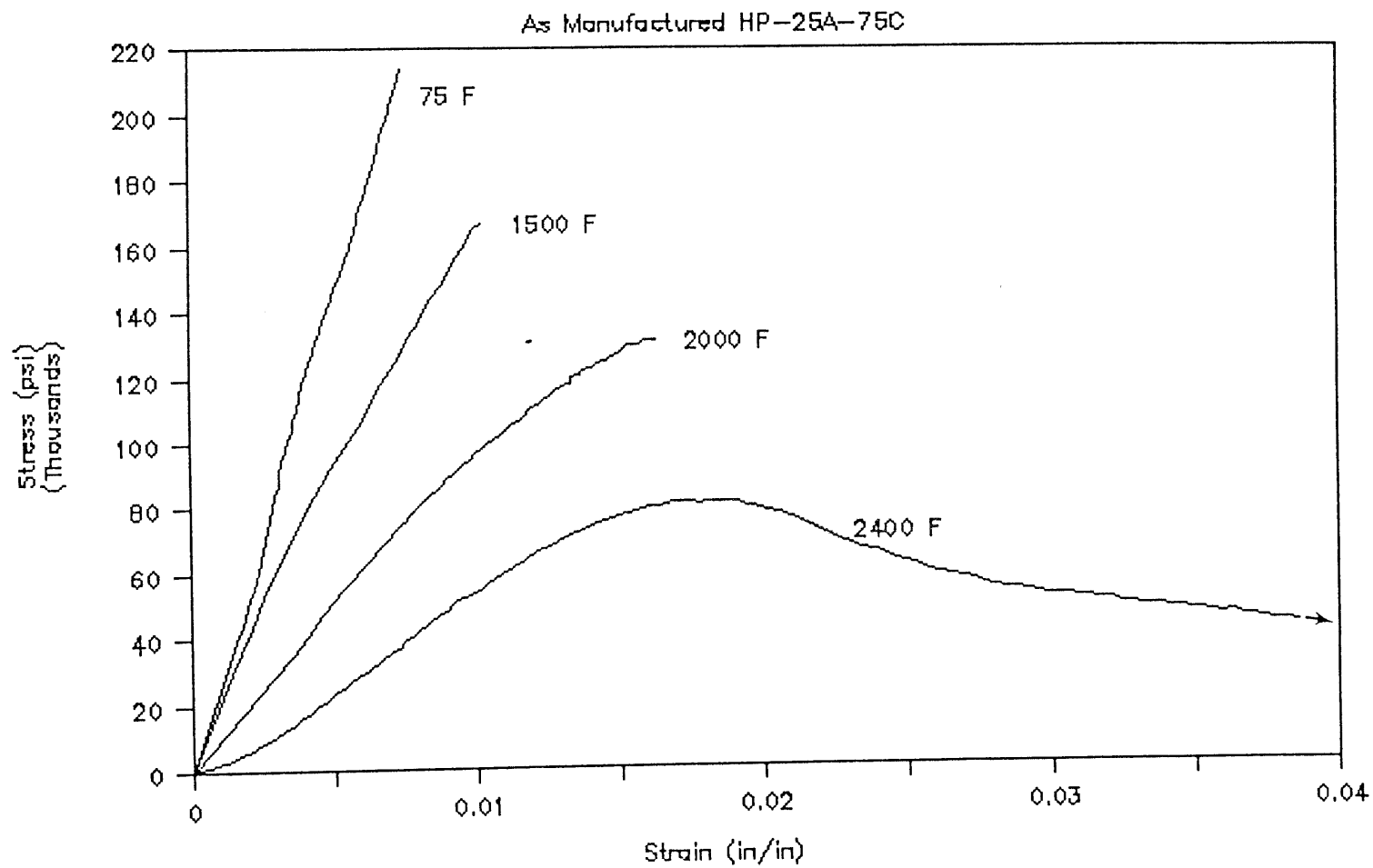
Figure 6.3   Stress strain curves for HP–25A–75C at different temperature levels and a constant piston displacement rate of 7.218×10^{-5} in/sec

with a brittle fracture. A sudden fracture of the specimen was observed at a load level corresponding to the peak stress on the stress–strain curve, and thus, no post–peak behavior was obtained.

2. At temperatures above 0.5 T_m the deformation behavior of the material is initially linear, but exhibits significant non–linearities at stress levels close to the peak strength. In the post–peak region, the observed non–linear deformations are even more pronounced.

In order to investigate the non linear deformations at elevated temperatures short term creep tests were carried out on material HP–90A–10C, and are discussed in the next section.

In what follows some specific material characteristics, namely, the strength, the initial slope of the stress–strain curve, the associated peak strain, and the equivalent toughness defined as the area under the stress–strain curve are studied.

The strength of the material CPS–90A–10C seemed to follow two different mechanisms as shown in Fig. 6.4: a slight decrease in strength with temperature was observed for temperatures below 0.5 T_m, followed by an increased rate of decrease in strength for temperatures above 0.5 T_m.

Strength degradation for temperature levels below 0.5 T_m was found to be proportional to the square root of T, and may be expressed by Eq. (5.1) similar to the cold–pressed sintered materials. For temperatures in the range of 0.5 T_m to 0.7 T_m, the strength degradation is proportional to T, and may be expressed using Eq. (5.2). The variation of the ratio of the strength of HP–90A–10C to CPS–90A–10C with temperature is shown in Fig. 6.5. The hot–pressed material exhibits a significantly higher strength than the cold–pressed sintered material as expected. The ratio of the strengths does not seem to exhibit any specific trend. The explanation may be that
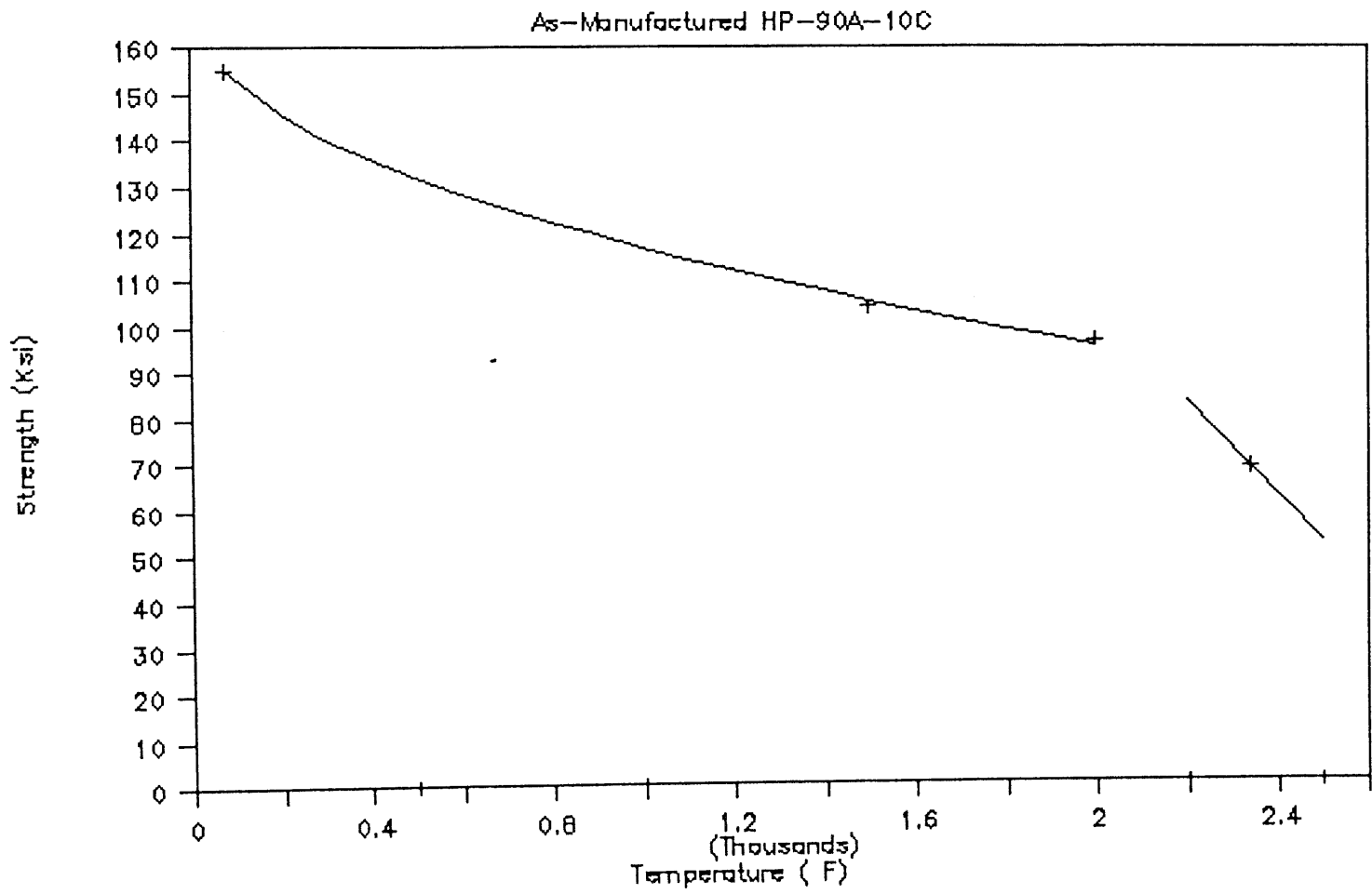
Figure 6.4   Strength variation with temperature for HP—90A—10C
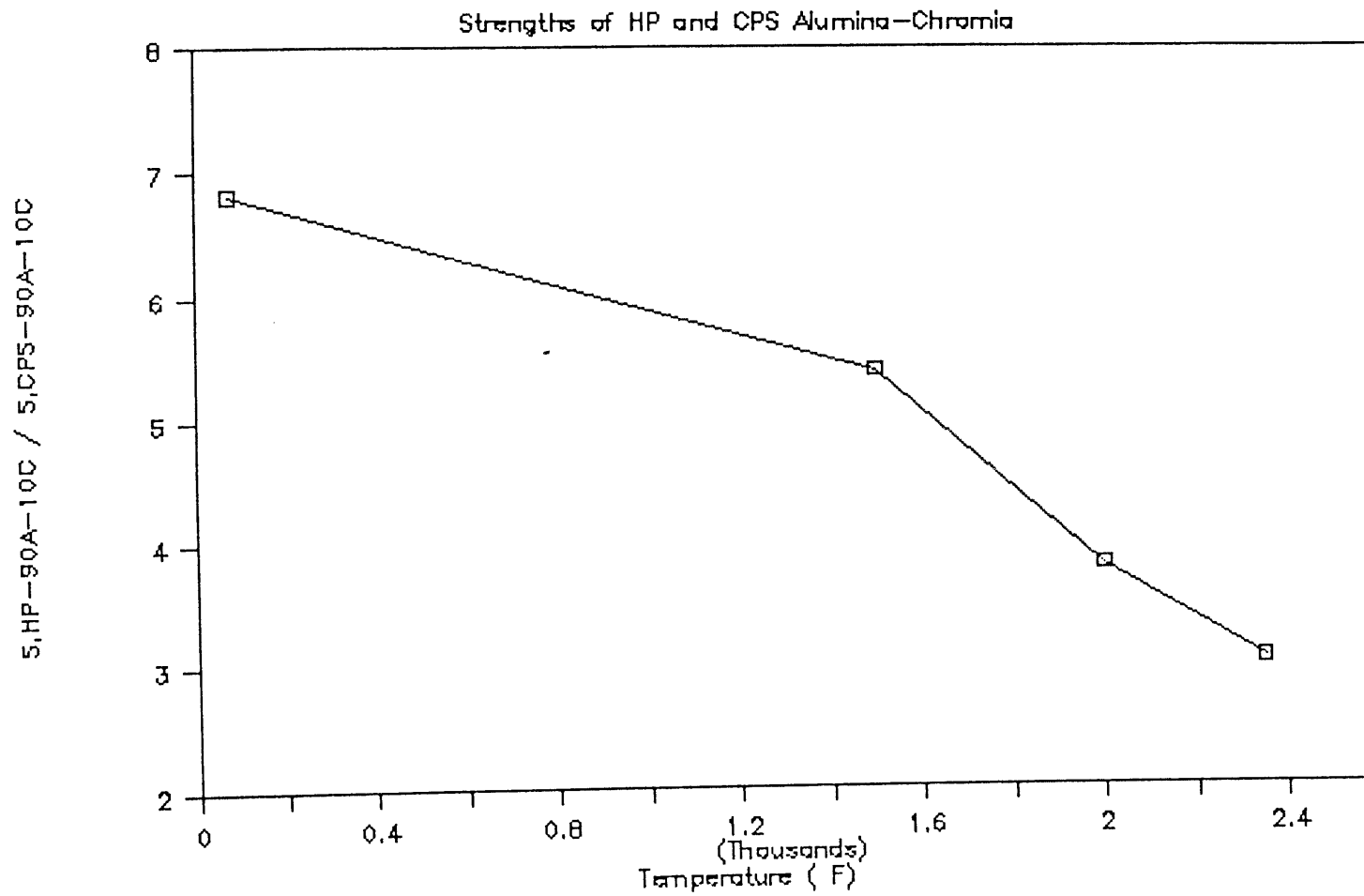
Figure 6.5   Ratio of strength of HP–90A–10C to CPS–90A–10C

although the two materials have the same chemical composition, it is difficult to correlate their behavior because the hot–pressed HP–90A–10C has a more homogeneous structure consisting of only a solid solution with no second phase, while the cold–pressed sintered CPS–90A–10C has a more inhomogeneous structure with a solid solution as a matrix and second phase particles as grains. The grain size distribution is also different for both HP–90A–10C and CPS–90A–10C. This will be different for the chromia–magnesia materials as will be discussed later. The rate of decrease in strength for the hot–pressed HP–90A–10C is larger than the one for the cold–pressed sintered CPS–90A–10C. The ratio of strengths varies from about 7 at room temperature to about 3 at 2400^OF.

Similar results have been obtained for HP–50A–50C and HP–25A–75C, as shown in Fig. 6.6 for HP–25A–75C. For brievity the results for HP–50A–50C are not shown separately, but can be found in the material database in Chapter 8. The strength variations with temperature of the three hot–pressed alumina–chromia materials are compared in Fig. 6.7. Material HP–25A–75C exhibits the larger strength among the three studied alumina–chromia refractories. At first one might conclude that the strength increases monotonically with the chromia content. However, it is possible that a peak in strength might exist for chromia contents between 50% and 75%. In order to check this assumption tests need to be carried out for an intermediary chromia content such as a 62% Cr_2O_3 and 38% Al_2O_3 hot–pressed material.

The variations with temperature of the peak strain values associated with the peak stress, for materials HP–90A–10C, and HP–25A–75C are shown in Figs. 6.8, and 6.9 respectively. For both materials, the rate of increase in the peak strain is lower for temperatures below 0.5 T_m than those above 0.5 T_m. For the temperatures below 0.5
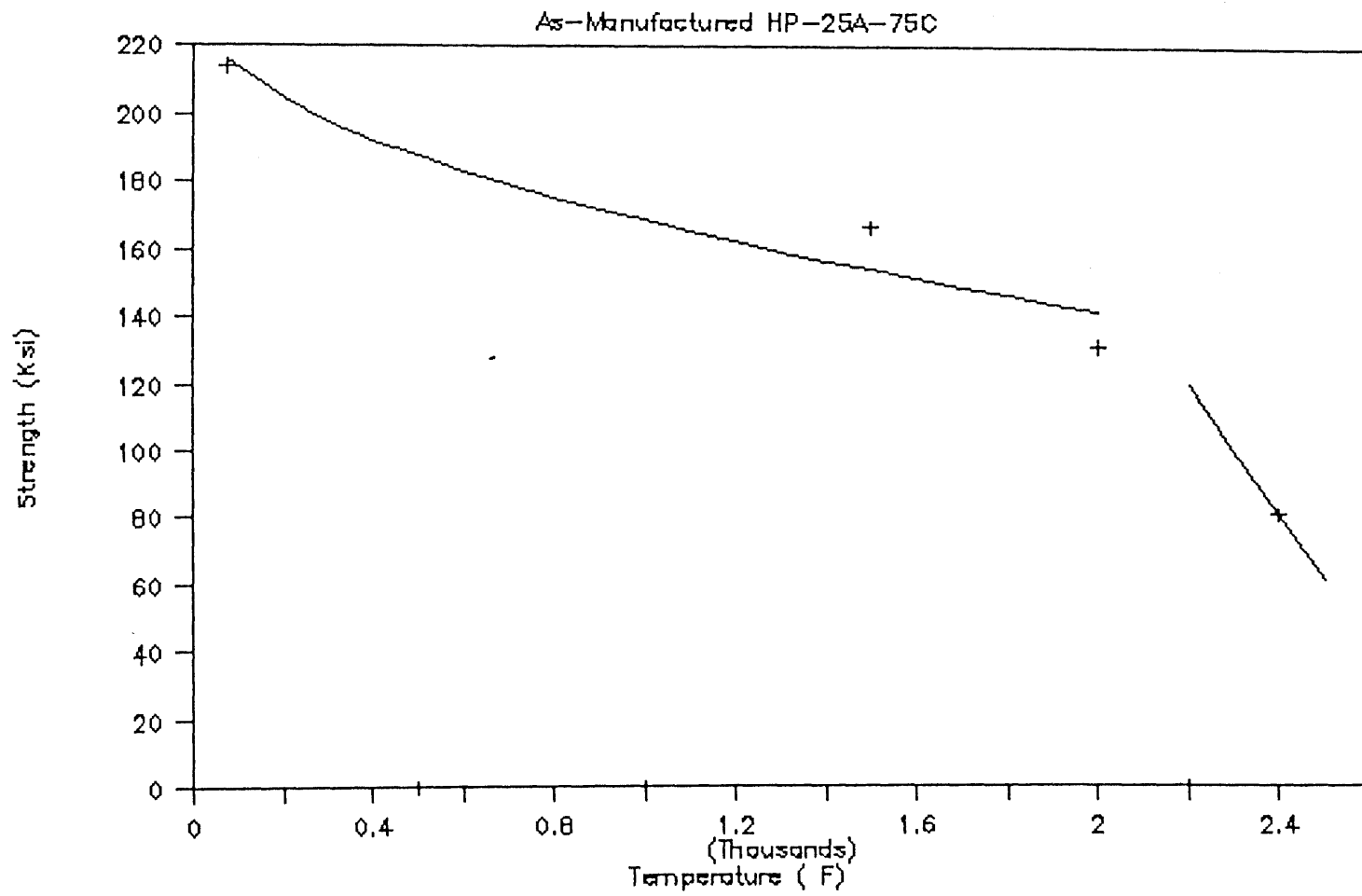
Figure 6.6   Strength variation with temperature for HP–25A–75C

As Manuf. Hot—Pressed Alumina—Chromia
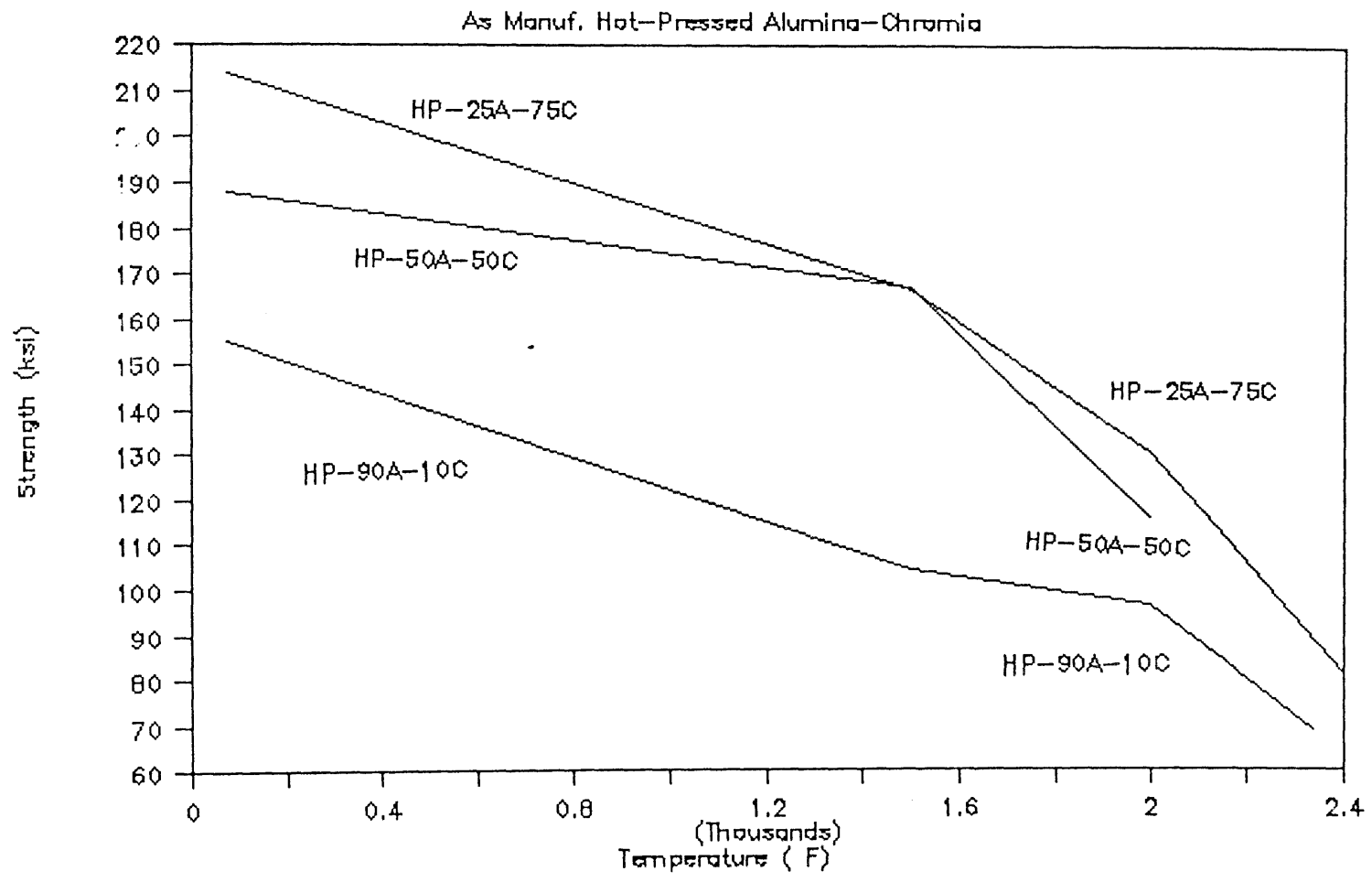
Figure 6.7   Comparison of strengths of the three hot—pressed
alumina— chromia HP—90A—10C, HP—50A—50C and
HP—25A—75C
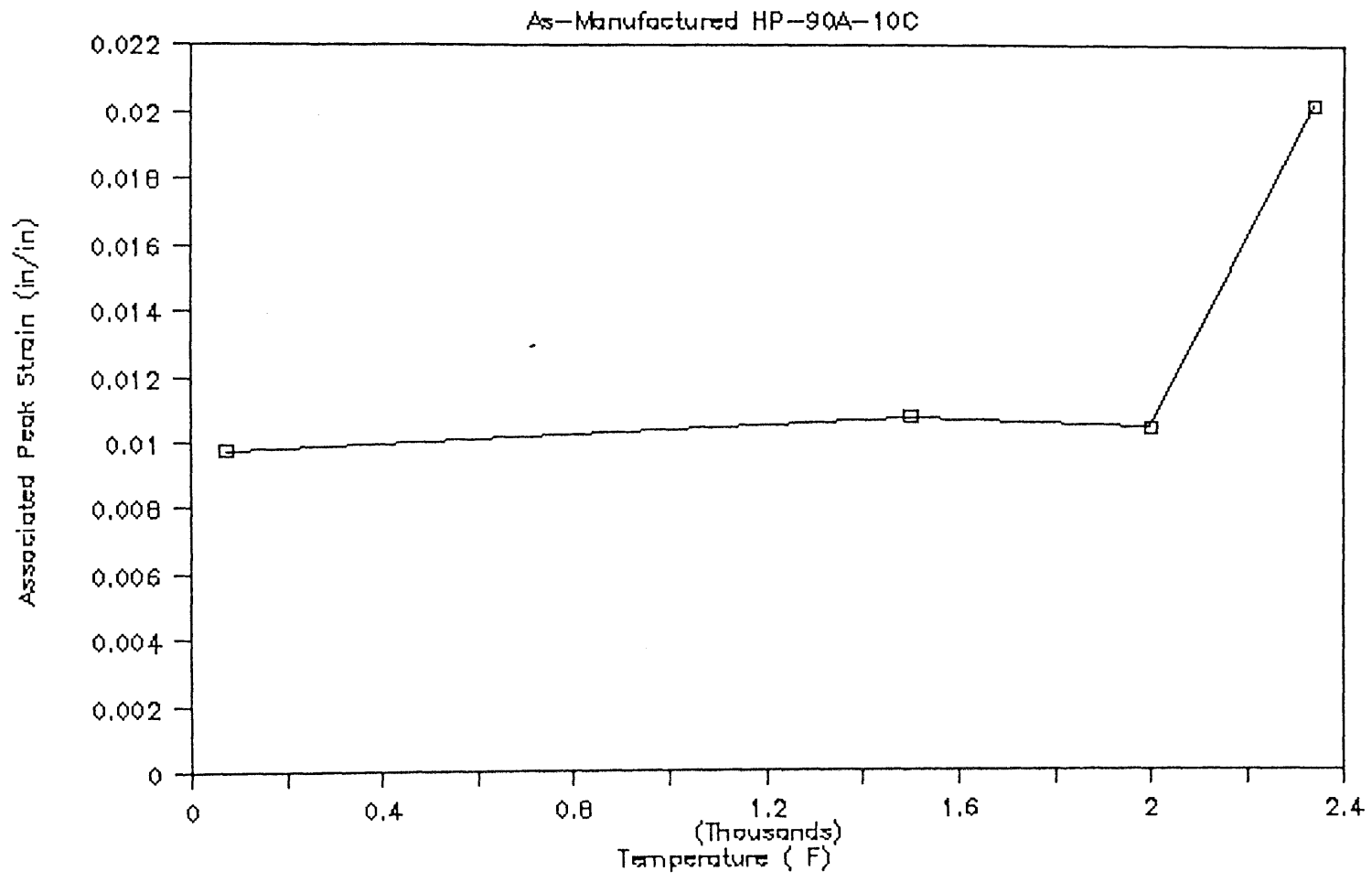
Figure 6.8   Associated peak strain variation with temperature for
                    HP—90A—10C
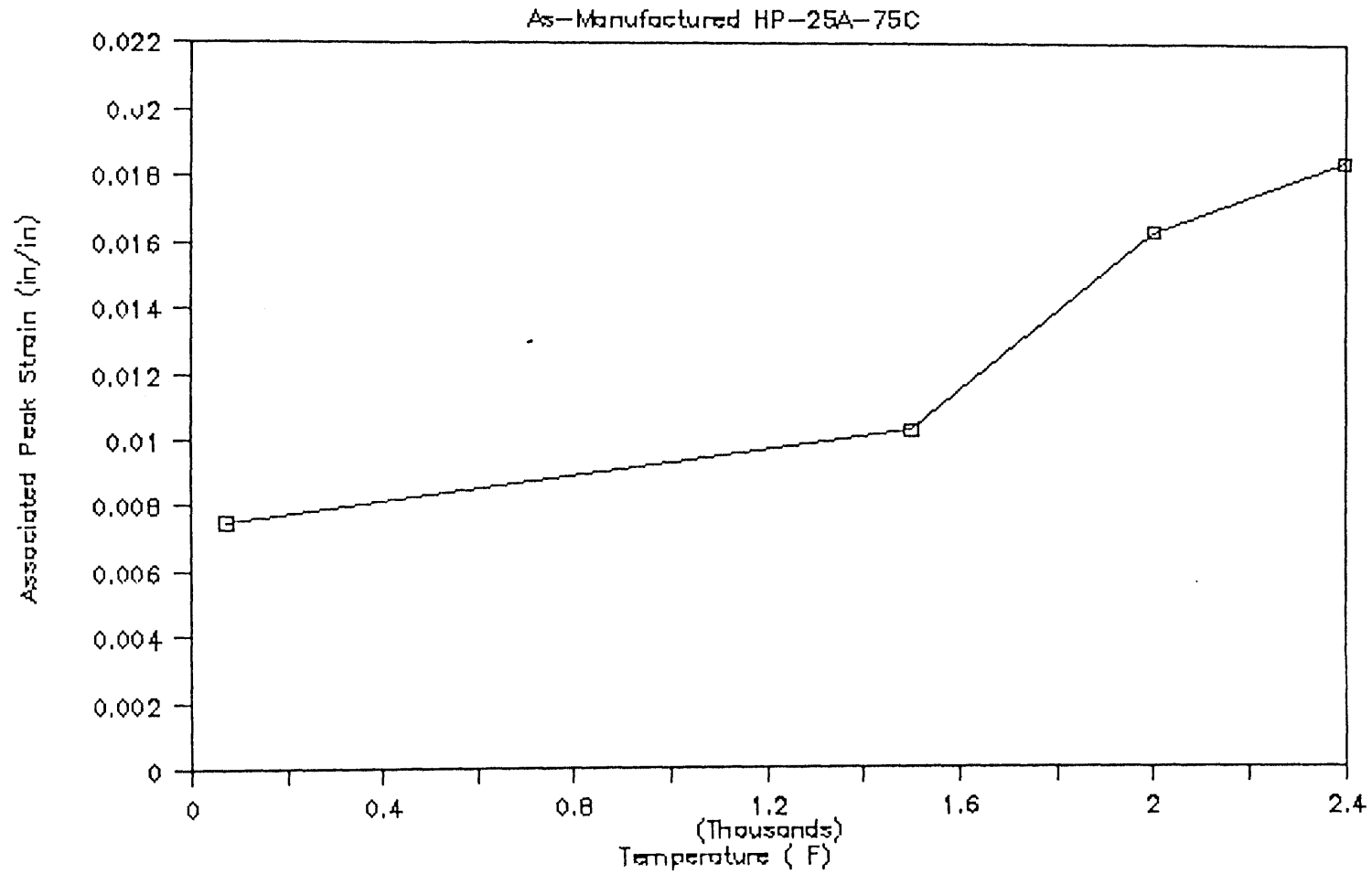
Figure 6.9   Associated peak strain variation with temperature for HP—25A—75C

T_m the associated peak strain and the final fracture strain are equal. For temperatures above 0.5 T_m, the final fracture strain is significantly larger than the associated peak strain due to significant non—linear deformations in the post peak region. Similar results are obtained for HP—50A—50C. The associated peak strains for the three hot—pressed alumina—chromia are compared in Fig. 6.10. It is noticed that the associated peak strains for the three hot—pressed alumina—chromia are larger than the ones for the cold—pressed sintered alumina—chromia. The increase in associated peak strain with temperature is faster for CPS—90A—10C than for HP—90A—10C. The associated peak strains vary from about 0.0024 at 75°F to 0.0136 at 2400°F for CPS—90A—10C, compared to a variation from 0.0097 at 75°F to 0.0202 at 2340°F for HP—90A—10C. The associated peak strains for the three hot—pressed alumina—chromia are in the same order of magnitude except at 2000°F (about $T_m/2$) where the peak strain for HP—25A—75C is larger.

The initial slope of the stress strain curve decreases sharply with increasing temperatures. This is shown for HP—90A—10C, HP—25A—75C, and for the three hot—pressed alumina—chromia in Figs. 6.11, 6.12 and 6.13 respectively. For HP—90A—10C an increase in stiffness is observed at temperatures at about 2000°F, followed by an increased rate of decrease with increasing temperatures. The reason for the increase in stiffness may be due to the nature of the mixed system. In the brittle regime, the strength of HP—25A—75C is larger among the hot—pressed alumina—chromia, followed by HP—50A—50C and HP—90A—10C. The associated peak strains being about equal, results in higher stiffness for HP—25A—75C. At temperatures above $T_m/2$, the rate of decrease in strength for HP—25A—75C is higher than the rate of decrease in strength for HP—90A—10C. This correlates with initial stiffness being about equal for both HP—90A—10C and HP—25A—75C.
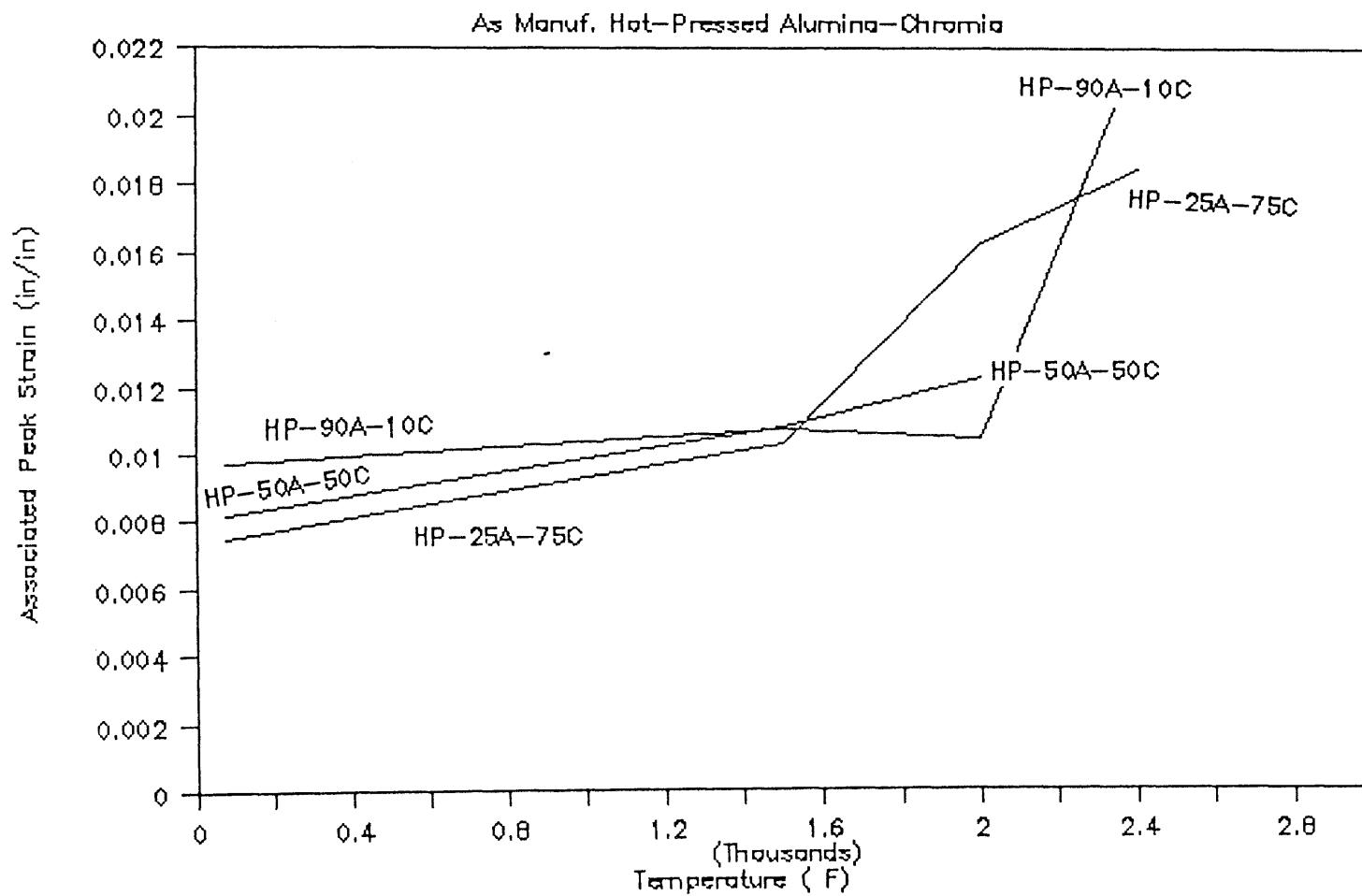
Figure 6.10   Comparison of associated peak strains of the three
hot— pressed alumina—chromia HP—90A—10C, HP—50A—50C
and HP—25A—75C
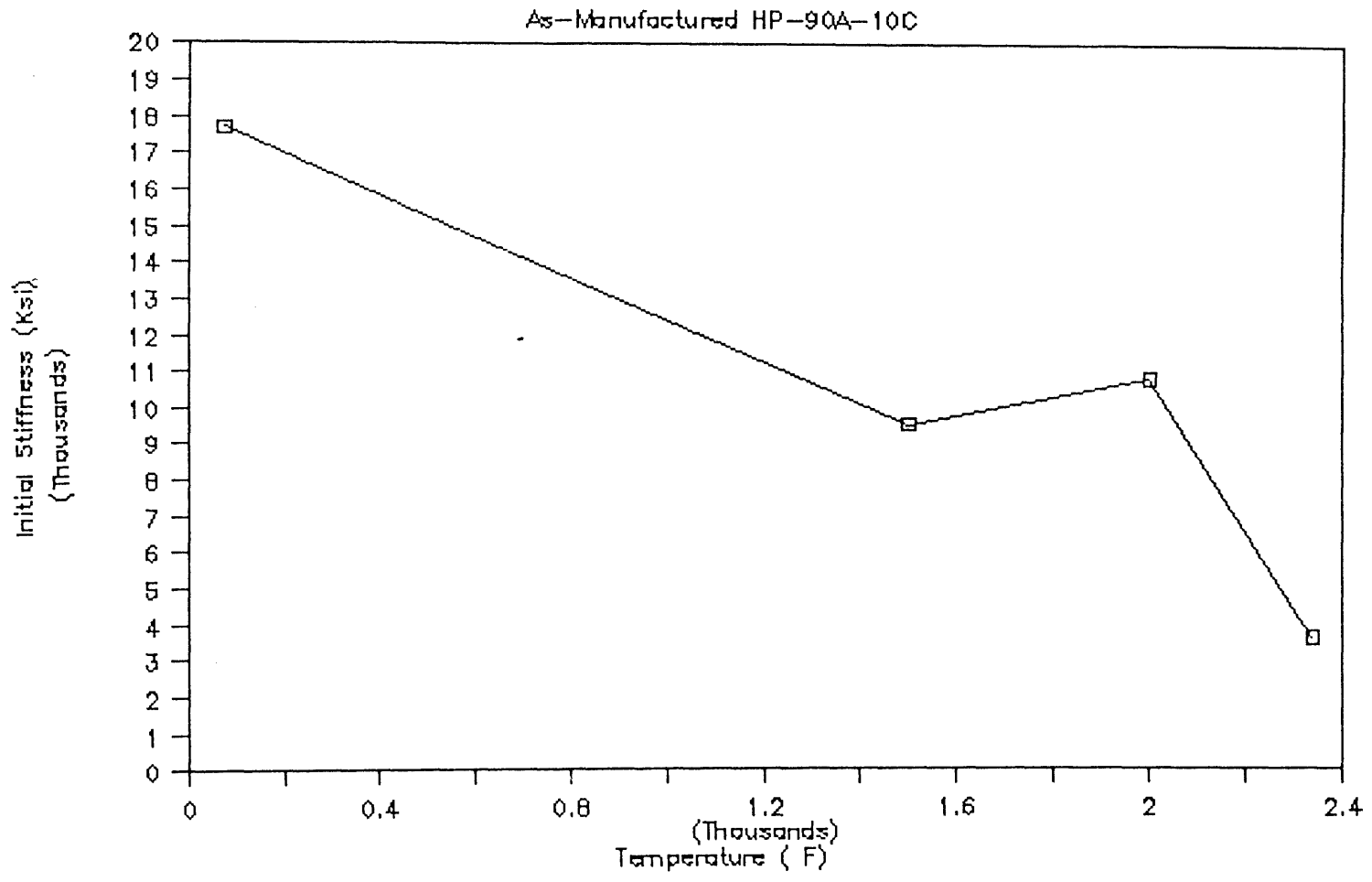
Figure 6.11   Initial stiffness variation with temperature for HP–90A–10C
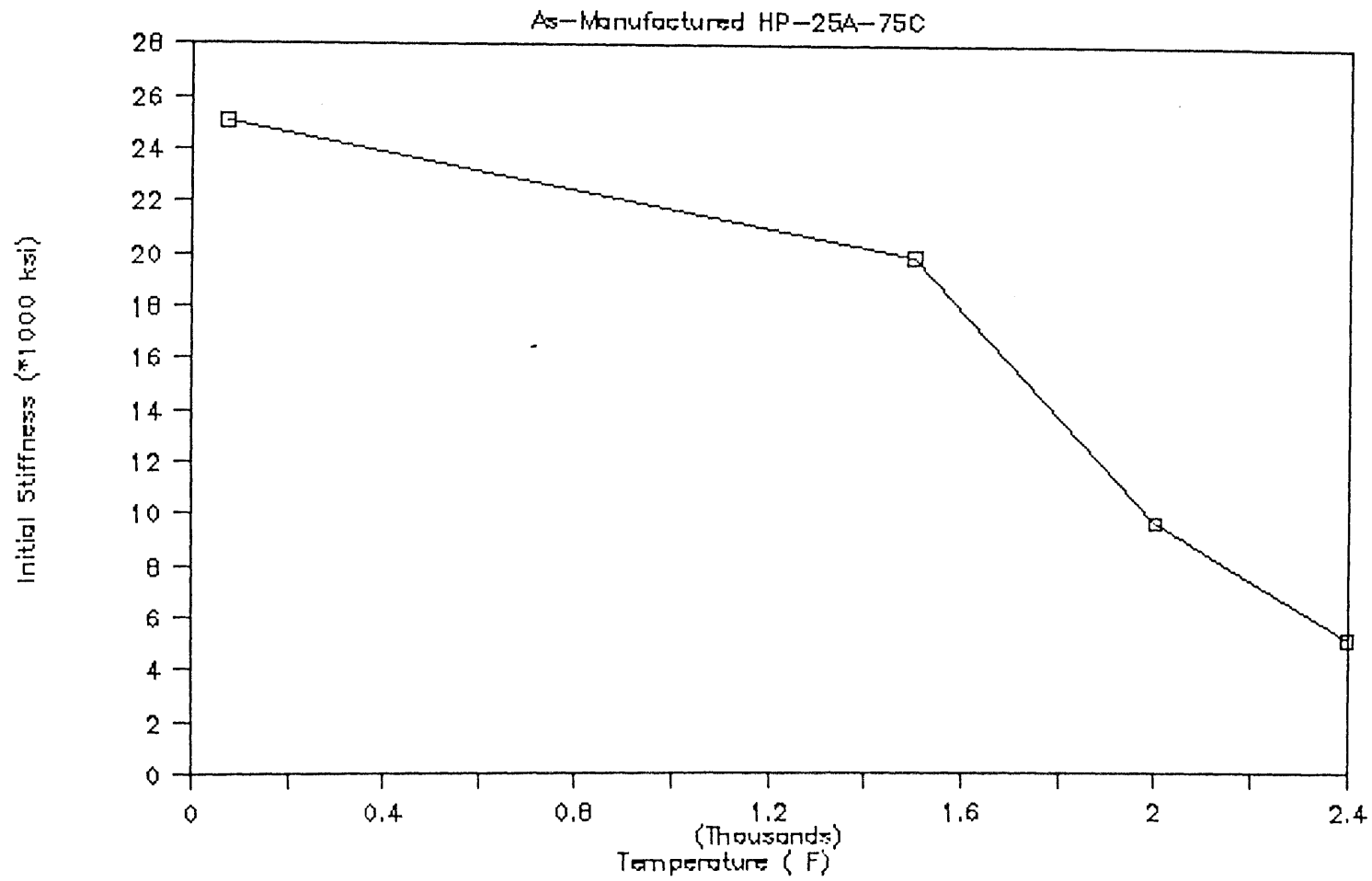
Figure 6.12   Initial stiffness variation with temperature for HP–25A–75C

As Manuf. Hot—Pressed Alumina—Chromia
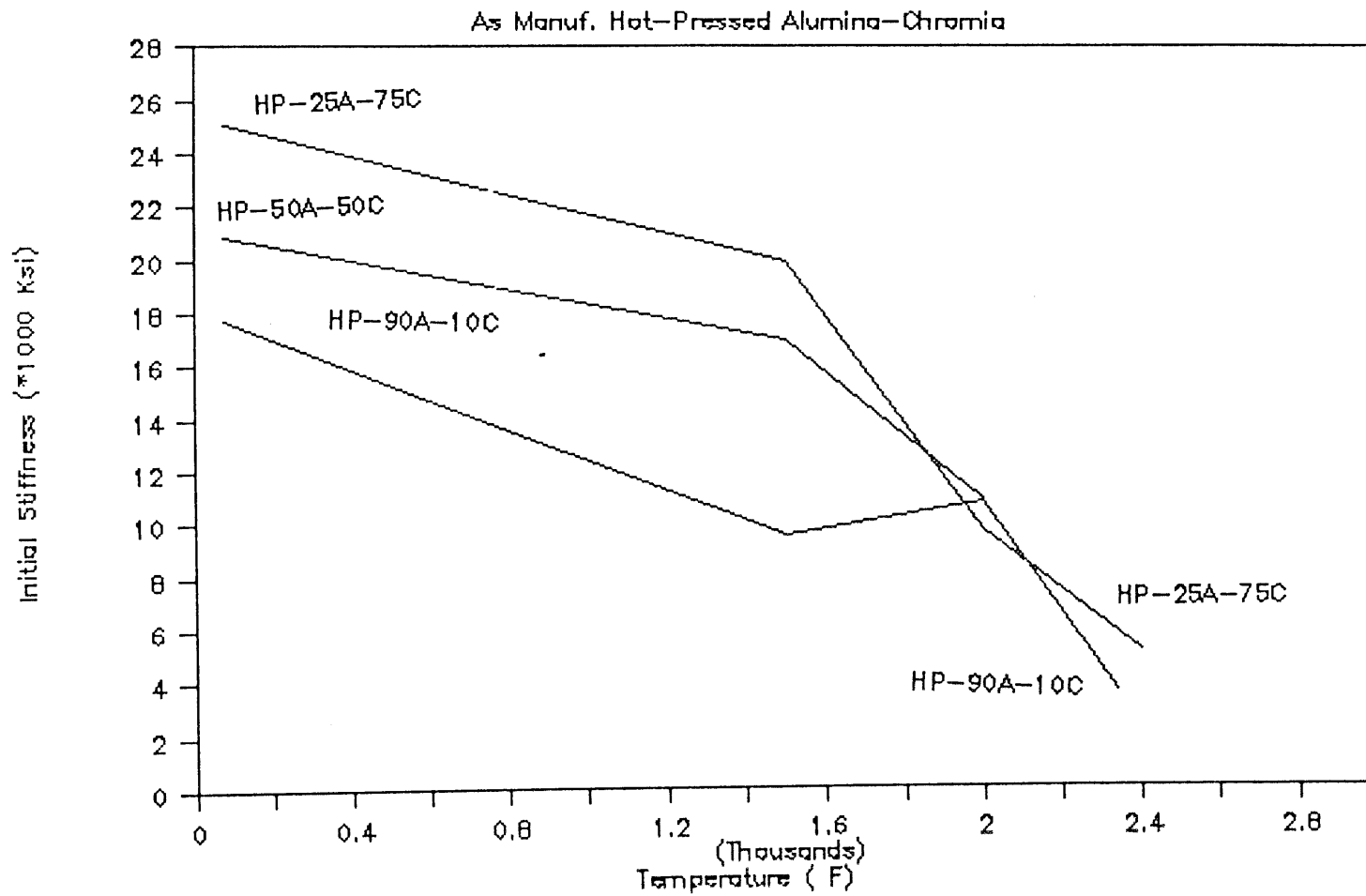
Figure 6.13   Comparison of initial stiffness for the three hot—pressed alumina—chromia HP—90A—10C, HP—50A—50C and HP—25A—75C

The toughness measure (defined as the area under the stress strain curve) variation with temperature is shown for HP–90A–10C, HP–25A–75C, and for the three hot–pressed alumina–chromia in Figs. 6.14, 6.15 and 6.16 respectively. The three hot–presaed alumina–chromia have about the same toughness measure at room temperature. However, the toughness measure for HP–25A–75C increases at a much faster rate, and at $2400^{O}F$ the toughness measure for HP–25A–75C is larger than twice the toughness measure for HP–90A–10C. The toughness measure variation with temperature for HP–25A–75C exhibits a similar trend to the one of CPS–90A–10C.

As a summary, material HP–25A–75C exhibits larger strength, about the same associated peak strain, and larger initial stiffness and toughness measure than HP–90A–10C and HP–50A–50C. Material HP–25A–75C also exhibits a larger increase in toughness than HP–90A–10C, and HP–50A–50C. For these reasons, HP–25A–75C appears to be a better candidate material for use under monotonic compression loading at high temperatures. However, it is to be noted that in the same temperature range, HP–25A–75C has a larger rate of decrease in strength than HP–90A–10C.

Stress strain curves for different temperature levels, and a constant displacement rate of 1.83 x 10^{-3}mm/sec are shown in Fig. 6.17 for material HP–80C–20M. The behavior of the hot–pressed chromia–magnesia is similar to the behavior of the cold–pressed sintered materials and the hot–pressed alumina–chromia materials. A transition temperature is observed with linear deformations and brittle fracture for temperature levels below it, and significant non linear deformations for temperature levels above it.

The strength variation with temperature for HP–80C–20M is shown in Fig. 6.18. The behavior is similar to that found for the sintered materials, and the strength
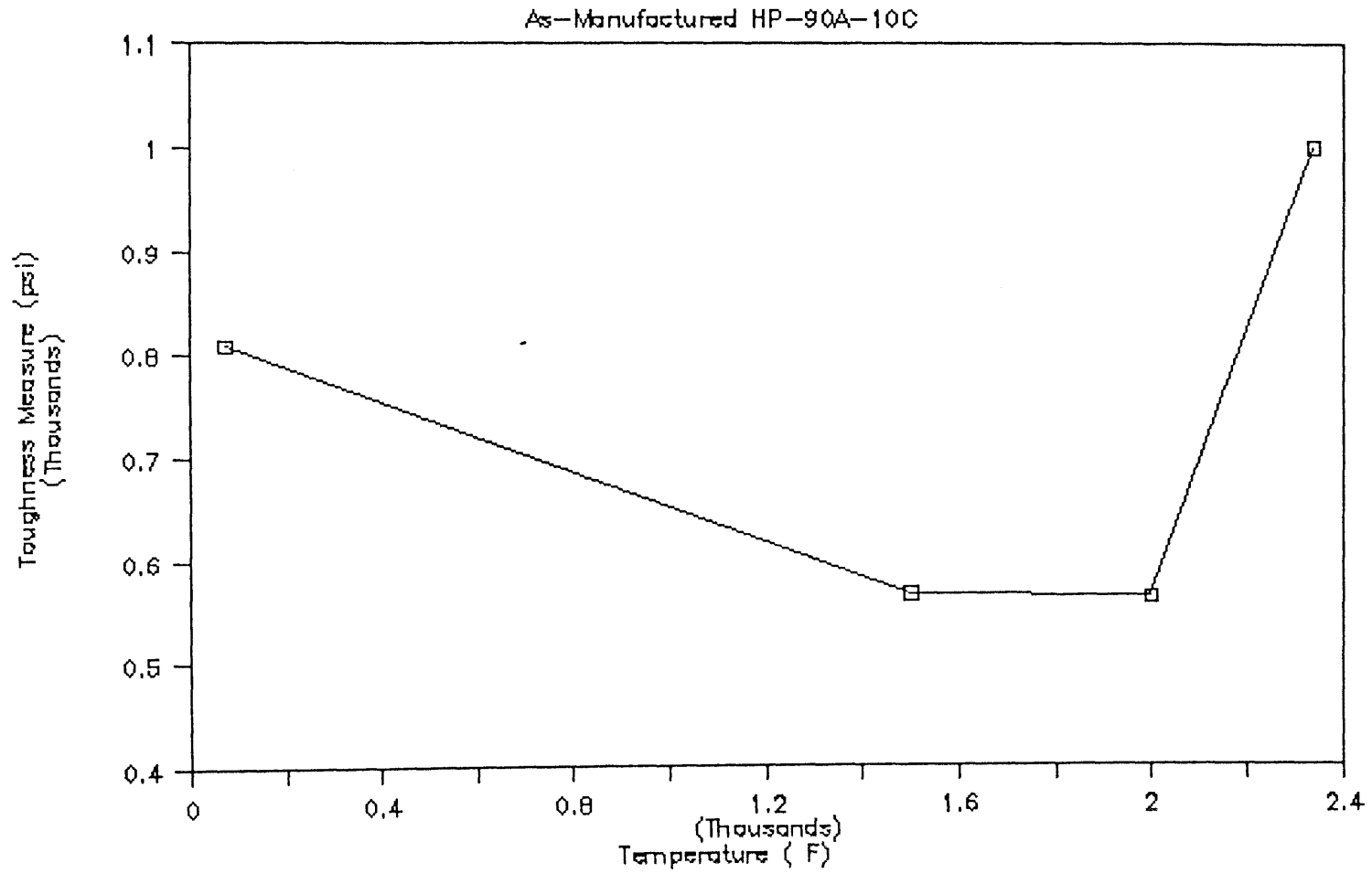
Figure 6.14   Toughness measure variation with temperature for HP—90A—10C
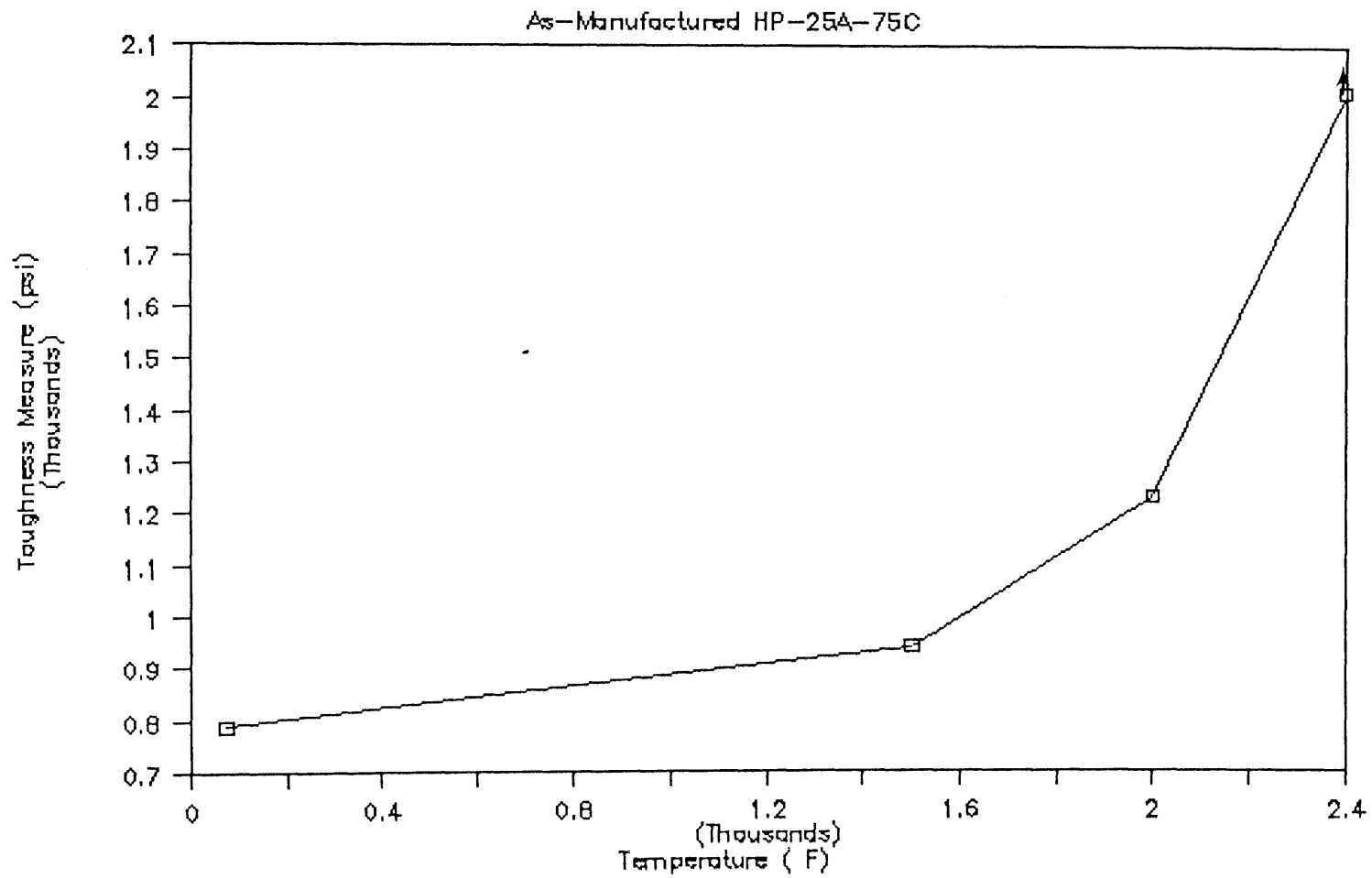
Figure 6.15   Toughness measure variation with temperature for
HP–25A–75C

As Manuf. Hot-Pressed Alumina-Chromia
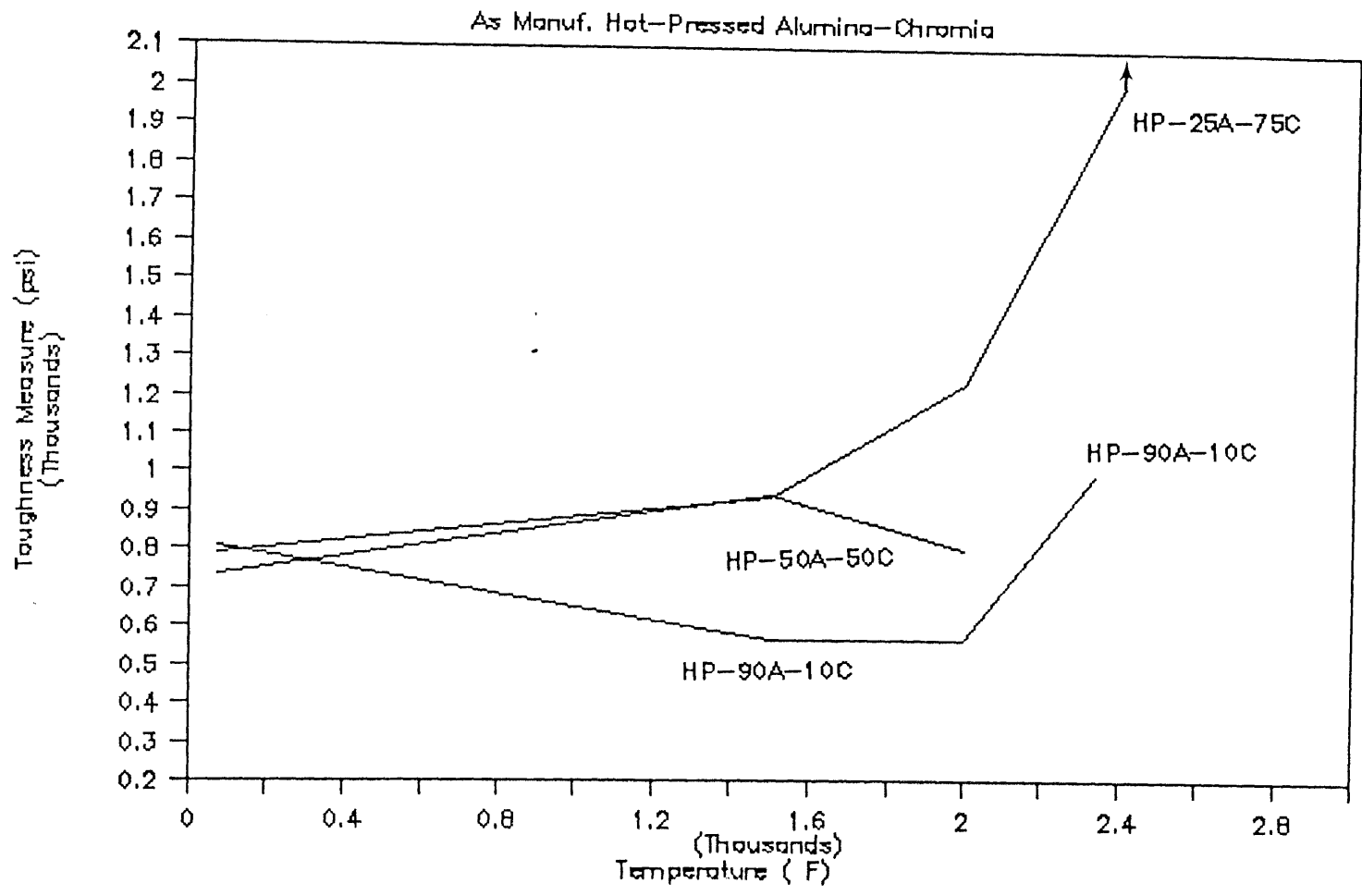
Figure 6.16   Comparison of the equivalent toughness for the three
hot-pressed alumina-chromia HP-90A-10C, HP-50A-50C
and HP25A-75C

As MAnufactured CPS–80C–20M

Figure 6.17   Stress strain curves for HP–80C–20M at different temperature levels and a constant piston displacement rate of 7.218 x 10^{-5} in/sec
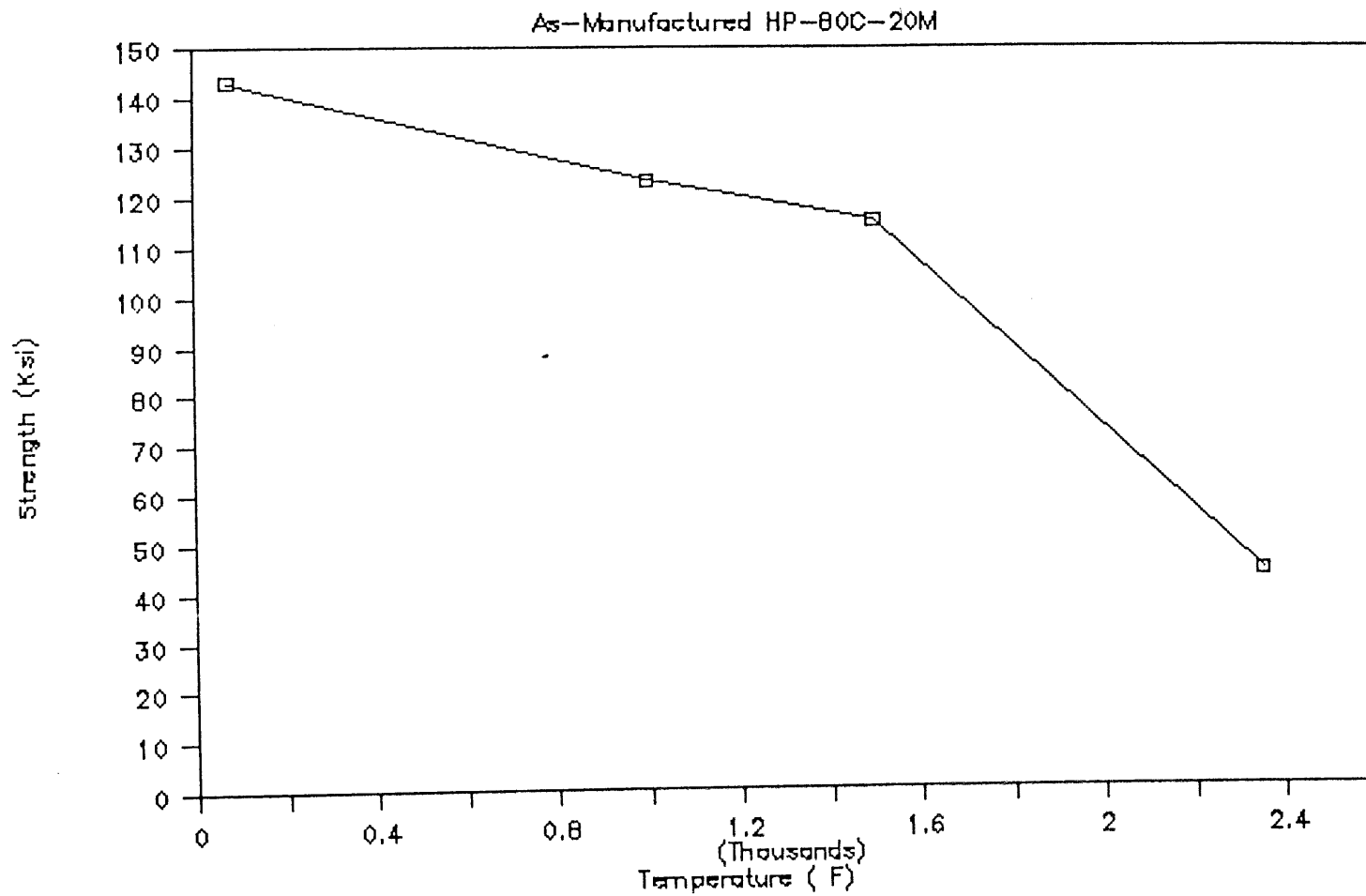
Figure 6.18   Strength variation with temperature for HP–80C–20M

is governed by Eq. (5.1) for temperature levels below $T_m/2$. In the same temperature range below $T_m/2$, the ratio of the strength (S) of hot–pressed high–chromia HP–80C–20M to sintered high–chromia CPS–82C–18M is a constant, whichis equal to the ratio of the maximum grain sizes (d_{max}) of the two materials to the 3/8 power. This is given by:

$$\frac{S_{HP-80C-20M}}{S_{CPS-82C-18M}} \approx \left[\frac{d_{max\ CPS-82C-18M}}{d_{max\ HP-80C-20M}}\right]^{3/8} \qquad (6.1a)$$

which could also be written for HP–80C–20M and CPS–82C–18M as:

$$S\ d_{max}^{3/8} \approx \text{constant} \qquad (6.1b)$$

where S is the strength of the material, and d_{max} is the maximum grain size. This is shown in Fig. 6.19. Assuming that below the transition temperature weak grain boundaries act as initial flaws, one can assume that: 2c=d, where 2c is the crack length, and d the grain size. Assuming that below the transition temperature fracture is governed by a constant fracture toughness criterion the following expression can be obtained:

$$S\ d^{1/2} = \text{constant}. \qquad (6.2)$$

The discrepancy between Eqs. (6.1b) and (6.2) may be explained by the fact that the tested sintered high chromia does not have uniform grain sizes, but that it is made by a gradation of different grain sizes.

For temperatures above $T_m/2$, the strength of HP–80C–20M decreases at a faster rate than the strength of CPS–80C–28M. This leads to a ratio of about 4.5 at 2400°F compared to a ratio of about 7.5 for temperatures below $T_m/2$. This is similar to the faster rate of decrease in strength exhibited by HP–90A–10C compared to CPS–90A–10C.

The asociated peak strain variation with temperature, shown in Fig. 6.20, is

Strength of HP and CPS Chromia—Magnesia
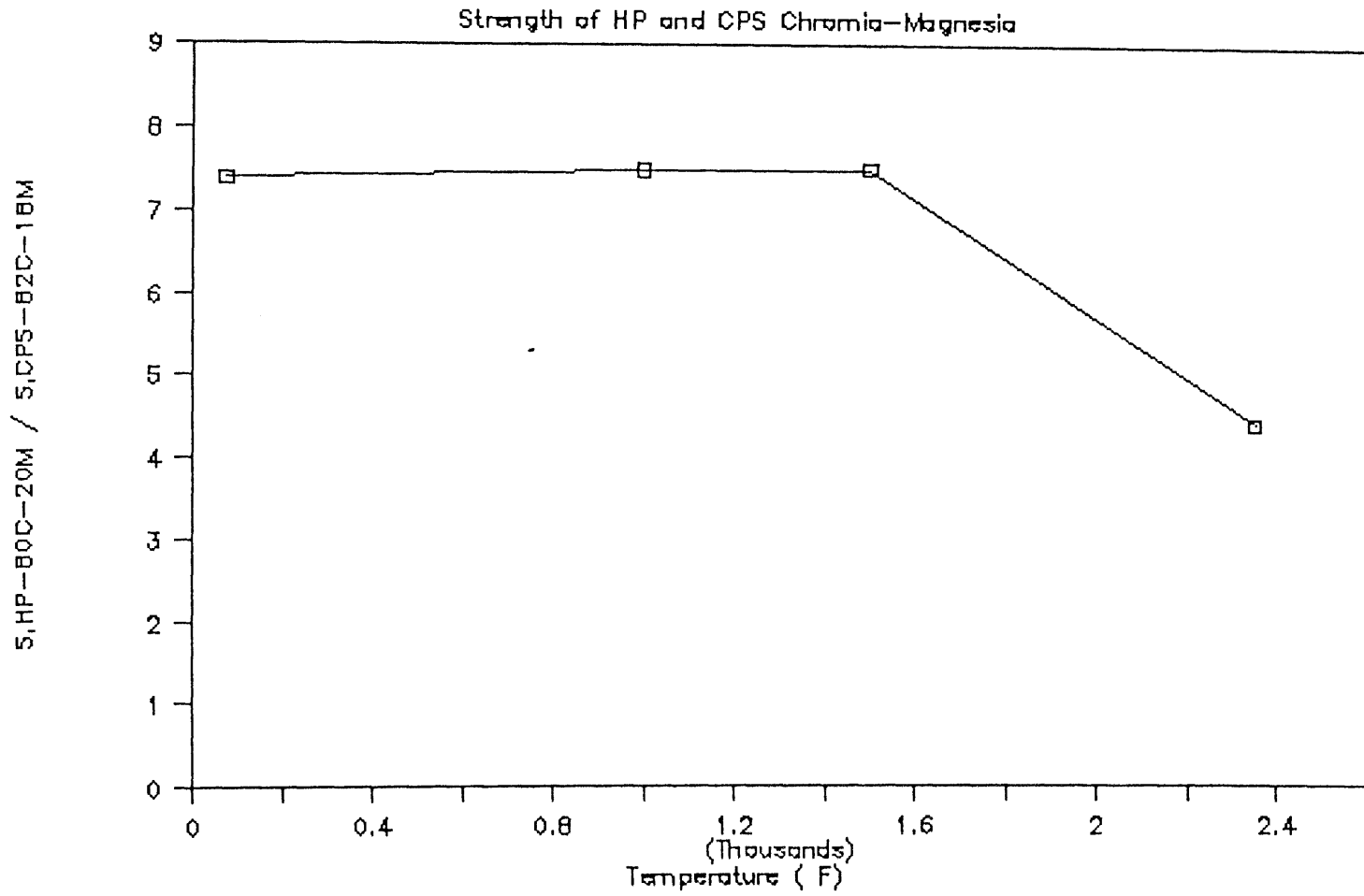
Figure 6.19   Ratio of strength of HP—80C—20M to CPS—82C—18M

As-Manufactured HP-80C-20M
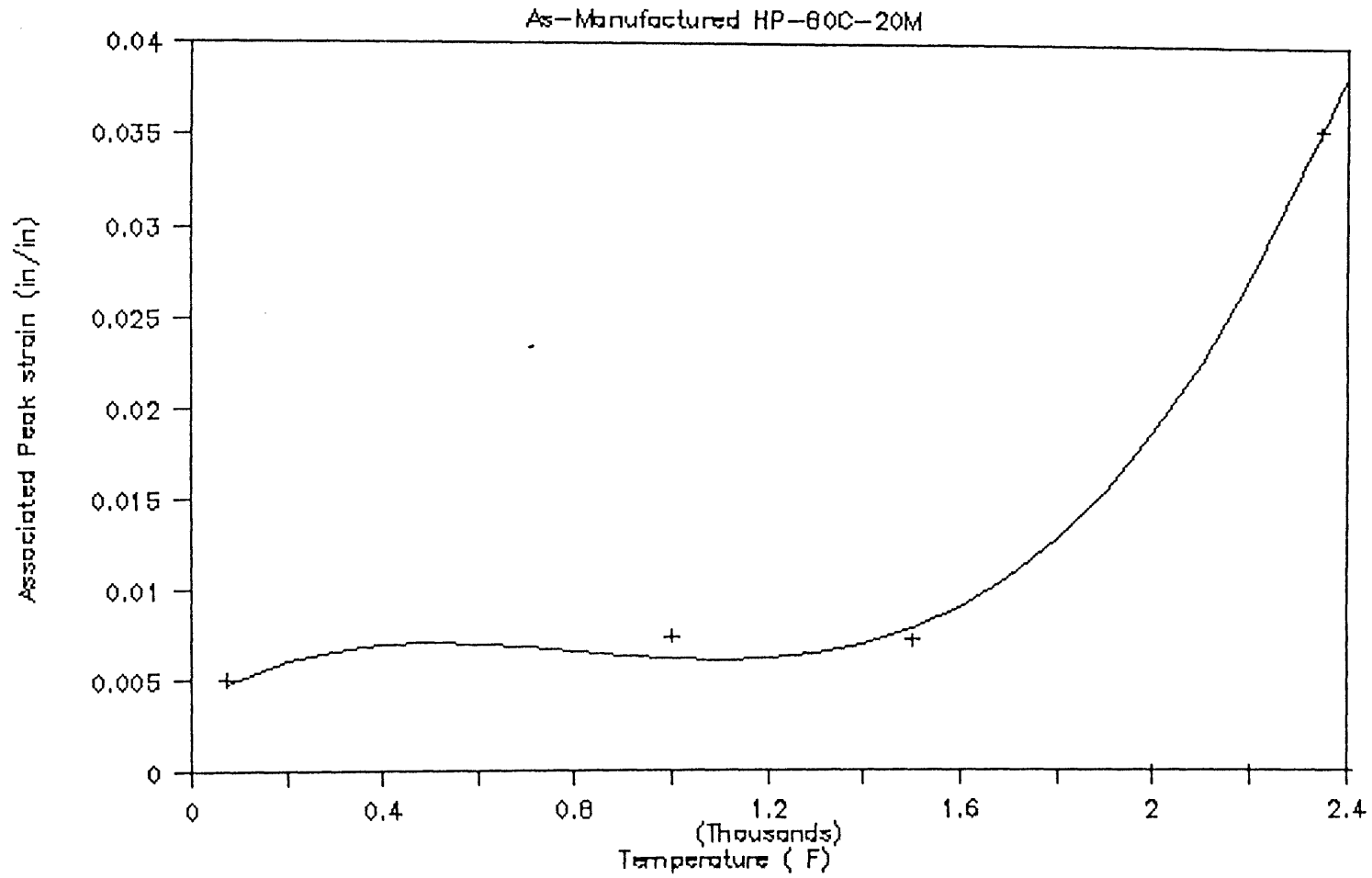
Figure 6.20   Associated peak strain variation with temperature for HP-80C-20M

similar to the other hot–pressed and cold–pressed sintered materials, where the rate of increase in associated peak strain is faster at temperatures above $T_m/2$. The associated peak strain values for HP–80C–20M are larger than the ones for CPS–82C–18M.

The initial stiffness variation with temperature, shown in Fig. 6.21, and the toughness measure variation with temperature, shown in Fig. 6.22, are similar to the previously discussed ones. The ratios of initial stiffness and toughness measure of HP–80C–20M to CPS–82C–18M appears to be about constant.

Material HP–80C–20M exhibits larger strength, associated peak strain, initial stiffness, and toughness measure than CPS–82C–18M. The variations of these properties with temperature are similar for both materials. Based on this, HP–80C–20M appears to be a better candidate material for monotonic compressive loading at high temperatures than CPS–82C–18M.

6.3.2 Behavior Under Constant Compressive Loads at Constant Temperature

The purpose of the constant compressive load tests at constant temperature was to study the nature of the non–linear deformations in monotonic load tests.

Figure 6.23 shows the variation of the creep strain rate for HP–90A–10C at temperature levels of 1500°F (816°C), and 2400°F (1316°C), under 78% and 81% of the uniaxial monotonic strength respectively. The same results are plotted as log ($\dot{\epsilon}_{creep} \times 10^8$) vs. time for different temperature levels, in Fig. 6.24. The measured strain rates are smaller than the ones obtained for cold–pressed sintered materials at the same load level; however at the same % strength level the creep strain rates in the hot–pressed materials are larger..
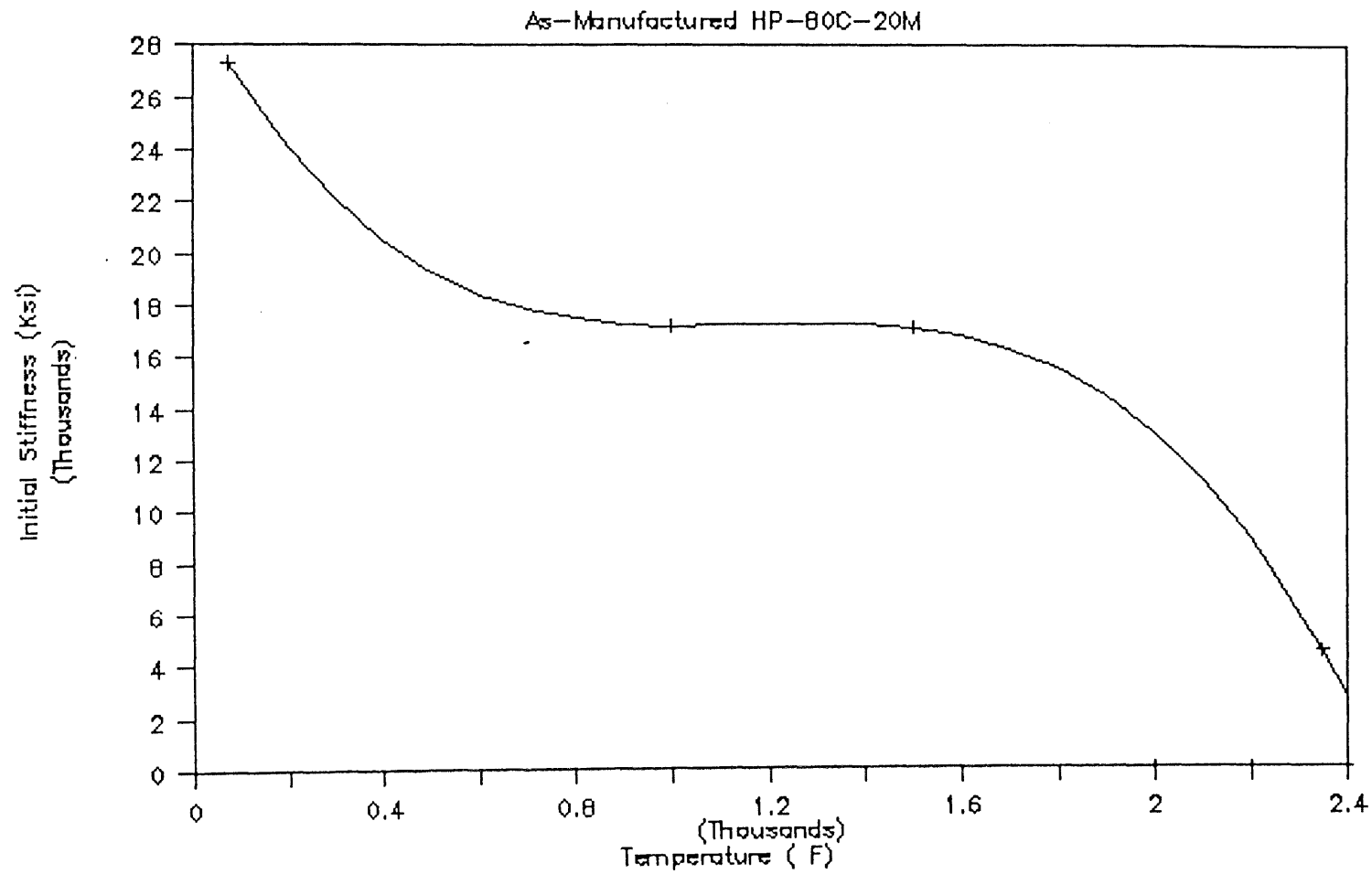
Figure 6.21   Initial stiffness variation with temperature for HP–80C–20M

As-Manufactured HP-80C-20M

Toughness Measure (psi) (Thousands)

Temperature (F) (Thousands)
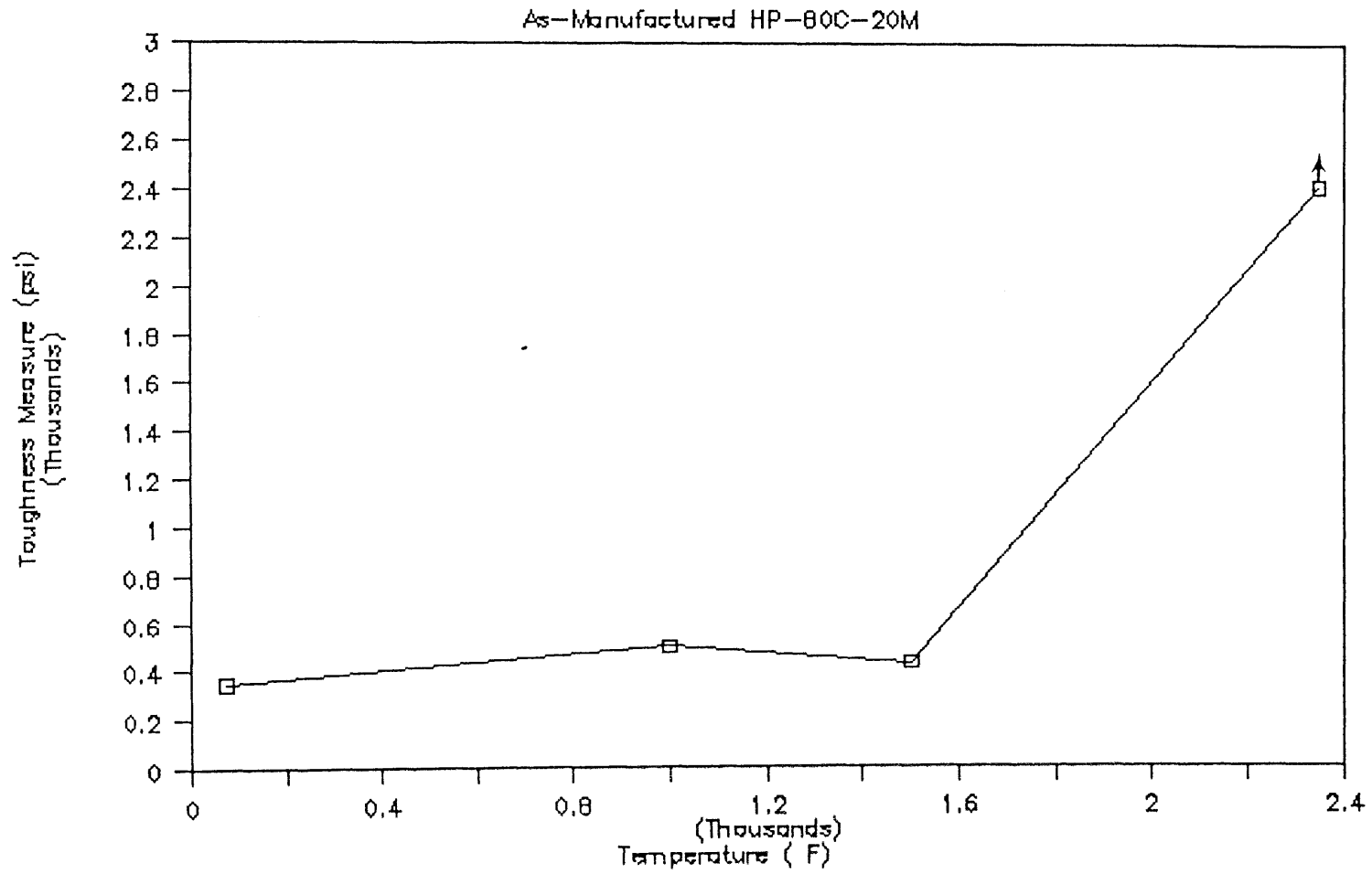
Figure 6.22   Toughness measure variation with temperature for
HP–80C–20M
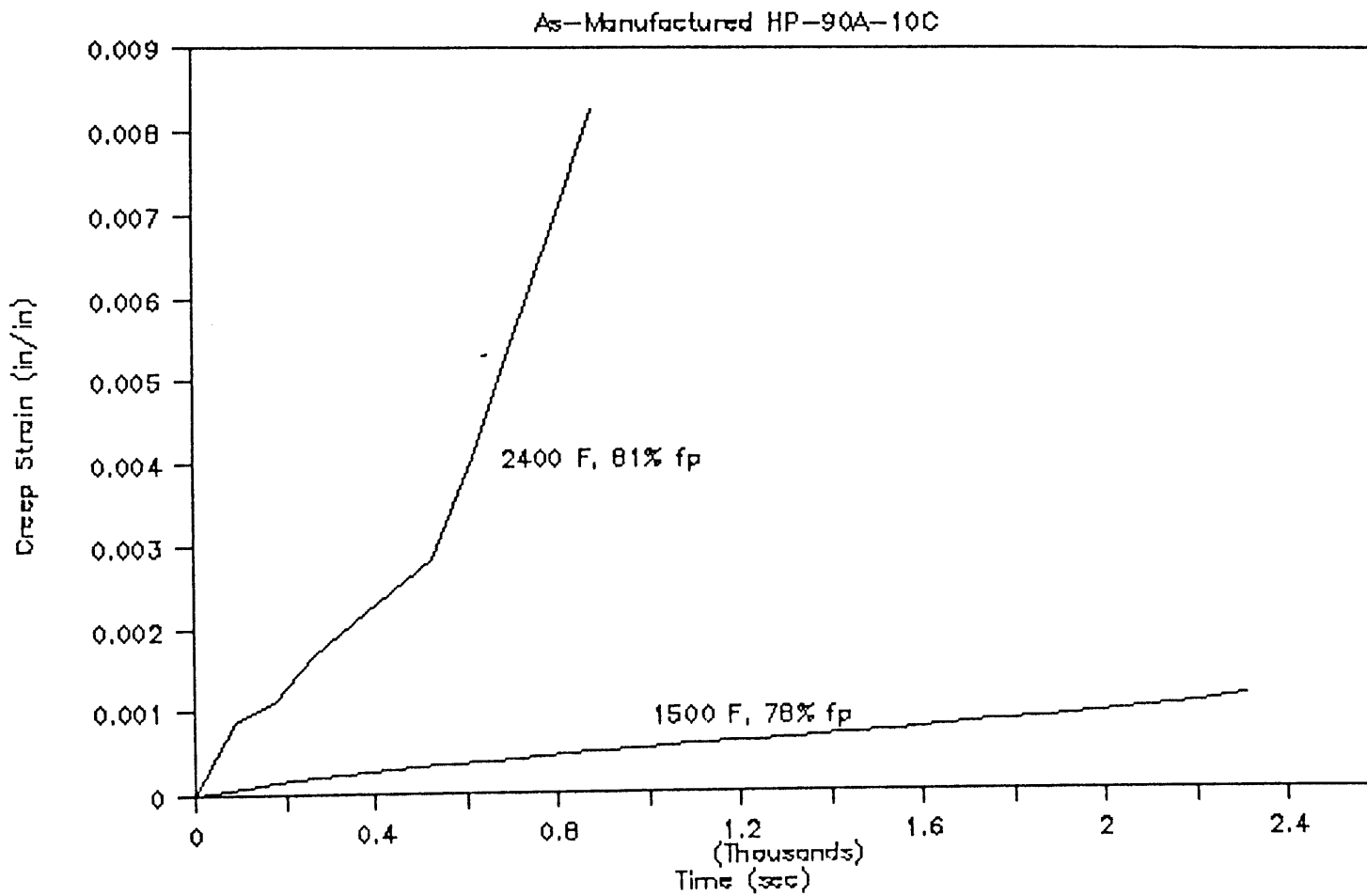
Figure 6.23   Creep strains for HP–90A–10C at different temperature and load levels

As—Manufactured HP—90A—10C
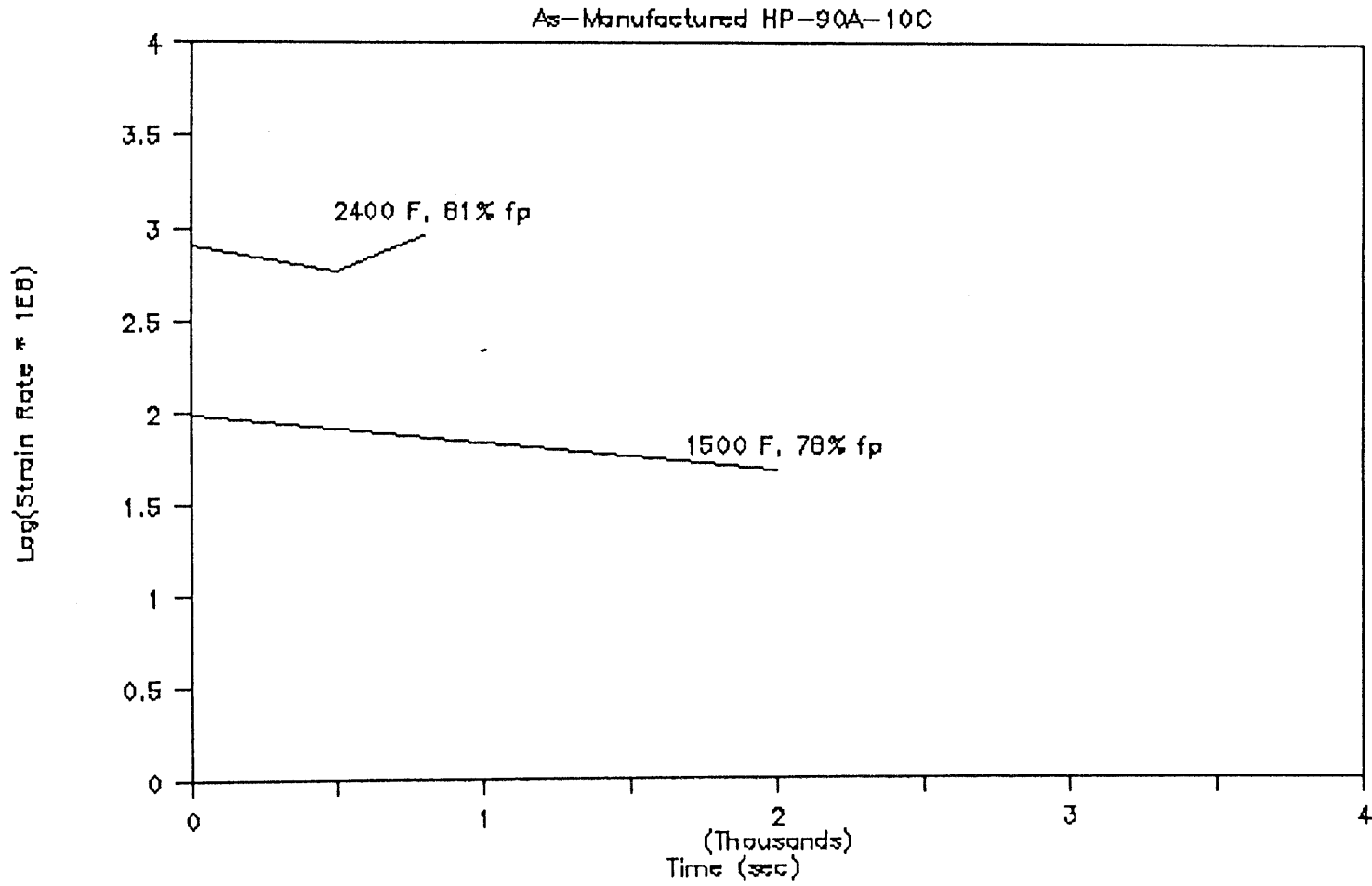
Figure 6.24   Variation of the log of the creep strain rate at different temperature and load levels for HP—90A—10C

6.4 MICROSTRUCTURAL CHARACTERIZATION OF VIRGIN AND TESTED MATERIALS

In this section the microstructural characteristics of as—manufactured HP—90A—10C in the non—tested condition and after testing at $2000^{O}F$ in monotonic compression is examined. The tests performed include observations using the Nomarski and scanning electron microscopes.

Materials CPS—90A—10C and HP—90A—10C have the same chemical composition, however, the microstructure of the as—manufactured HP—90A—10C is much more homogeneous than as—manufactured CPS—90A—10C. Figure 6.25 shows a Nomarski picture of a non—tested material HP—90A—10C at 500X. It can be seen that the grain distribution is much more uniform and that the individual grains are significantly smaller than the grains in CPS—90A—10C. Figure 6.26 shows a picture of a large grain of alumina taken using the Nomarski at 1500X. The grain in Fig. 6.26 was the largest observed in this specimen and is about 0.001" long (compared to largest grains of 0.25" in CPS—90A—10C). The finer and more homogeneous microstructure seems to be the reason for the larger strength observed for material HP—90A—10C. The non—tested HP—90A—10C pore structure was examined under the scanning electron microscope, and is shown in Fig. 6.27. The darker regions are not all pores. In order to determine which ones are pores, the matrix is put out of focus, and the particles inside the pore become in focus. It is estimated that about 9% porosity exists in HP—90A—10C. This is contrasted to about 17% porosity in the cold—pressed sintered CPS—90A—10C with the same chemical composition. The cracking pattern of as—manufactured HP—90A—10C tested at $2000^{O}F$ is also more homogeneous as shown in Fig. 6.28, taken by SEM at 33X. The test was stopped just before final fracture, after the stress started to decrease. The crack that is thought responsible for the stress decrease started at the bottom right of the picture by an en passant formation, and

Figure 6.25   Nomarski microscope picture of virgin HP–90A–10C at 500X showing a more homogeneous microstructure compared to CPS–90A–10C

Figure 6.26   Nomarski microscope picture of virgin HP—90A—10C at 1500X showing a large grain
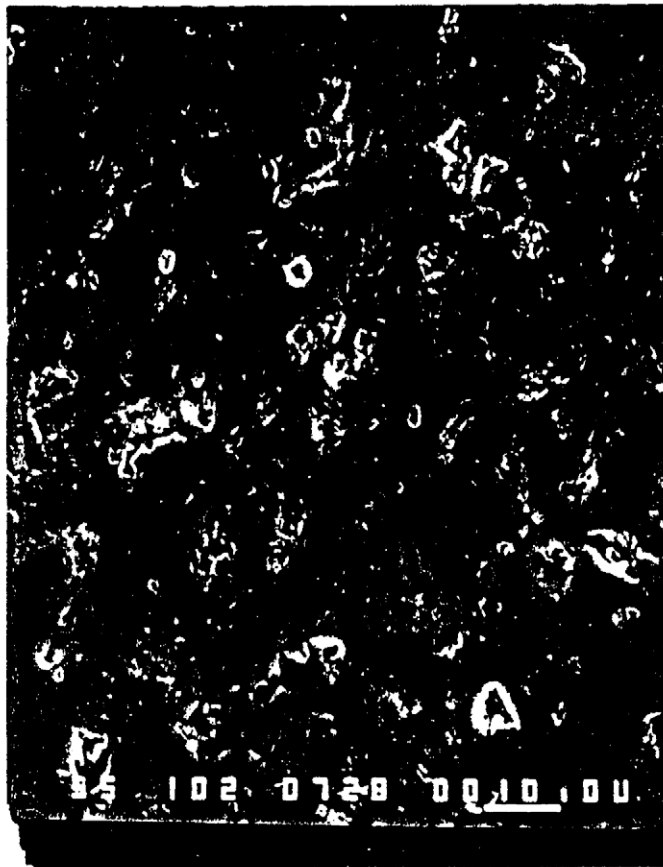
Figure 6.27   SEM picture of HP–90–10C at 1000X showing the fine microstructure of pores and grains in the solid solution matrix
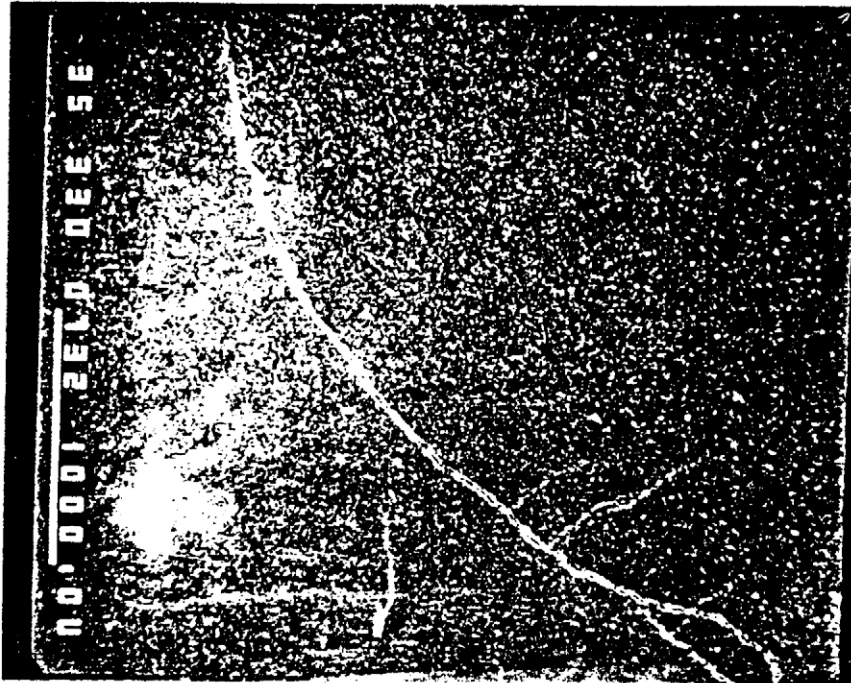
Figure 6.28   SEM picture of HP–90A–10C at 33X tested under monotonic compression to just below the peak stress at 2000°F showing a crack starting by an "en–passant" formation and curving in the direction of the maximum principal stress

propagated at first in a direction inclined to the applied stress direction. It then curved in a direction parallel to the applied load direction. The middle of the specimen did not shown any damage, as shown in Fig. 6.29 by a Nomarski picture at 500X. This seems to support the assumption that in the brittle regime for temperatures below $T_m/2$, fracture starts just prior to the peak stress and final fracture. It is very difficult to stop the test before final fracture.

The results of mercury porosimeter tests indicate that open porosity of hot—pressed materials is insignificant.

6.5 SUMMARY

Similarly to cold—pressed sintered materials, the hot—pressed materials follow two distinct behavioral trends with respect to temperature: (1) for temperatures below $T_m/2$ the deformations are linear and the final fracture is brittle; and (2) for temperatures above $T_m/2$ significant non—linear deformations occur before the final fracture.

No relation was found between the strength of HP—90A—10C and that of CPS—90A—10C with the same chemical composition. On the other hand, the ratio of strength of HP—80C—20M to that of CPS—82C—18M with about the same chemical composition is found to be a constant (about 8) for temperatures below $T_m/2$; this constant seems to be related to the inverse ratio of grain sizes of the two materials.

The variation of strength, associated peak strain, initial stiffness and measure of toughness are compared for the three hot—pressed alumina—chromia refractories HP—90A—10C, HP—50A—50C and HP—25A—75C. The strength of hot—pressed alumina—chromia refractories seem to increase monotonically with chromia content. Material HP—25A—75C (with 75% Cr_2O_3) has the highest strength of the three tested
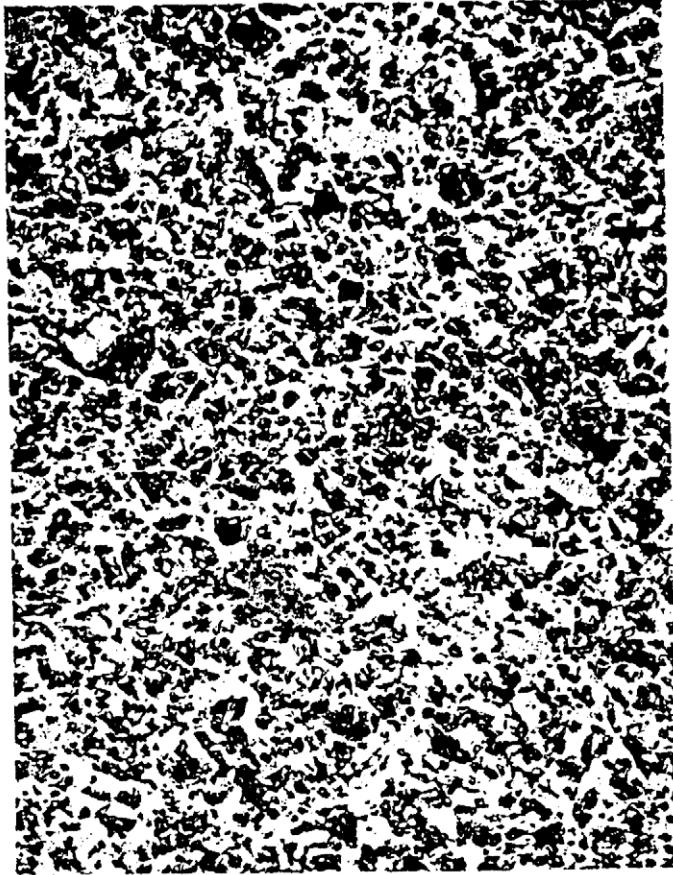
Figure 6.29   Middle portion of specimen shown in Fig. 6.27 showing no
cracks taken by Nomarski at 500X

alumina–chromia. However, it is possible that a chromia content between 50% and 75% might give a higher strength, and it is suggested to test a 62% Cr_2O_3 – 38% Al_2O_3 hot–pressed refractory to check this hypothesis. Material HP–25A–75C has approximately the same associated peak strain values than HP–50A–50C and HP–90A–10C. Both the initial stiffness and measure of toughness increase with increased chromia content. It appears that hot–pressed chromia–alumina refractories with higher chromia contents are better candidate materials under monotonic compression. However, it is to be noted that in the same temperature range, HP–25A–75C has a larger rate of decrease in strength than HP–90A–10C.

The creep strain rates for HP–90A–10C are smaller than the ones for CPS–90A–10C at the same load level. However, at the same % of the strength the creep strain rates for HP–90A–10C are are higher than the ones for CPS–90A–10C.

The microstructure of hot–pressed refractories is more homogeneous than the one of cold–pressed sintered materials. The maximum observed grain size of HP–90A–10C is about 250 times smaller than the maximum grain size of CPS–90A–10C. The porosity of HP–90A–10C is smaller than the one for CPS–90A–10C, but the open porosity of HP–90A–10C is insignificant.

A specimen loaded in monotonic compression at $2000^{\circ}F$ was removed at loads slightly below the peak load determined from previous tests, and no microcraks were observed in the middle portion of the specimen. This seems to indicate that for temperatures below $T_m/2$ fracture initiates at stresses very close to the peak and propagates rapidly to final fracture.

CHAPTER 7
FUSED–CAST HIGH–CHROMIA MATERIALS

7.1 SYNOPSIS

In the case of fused–cast bricks the brick characterization described in Section 7.2 is important in order to be able to interpret the results of thermomechanical tests. The behavior of fused–cast high chromia FC–7A–78C–8M under short–term uniaxial monotonic and constant compressive loads at elevated temperatures in air atmosphere is described in Section 7.3. Similarly to Chapters 5 and 6, this is followed by the microstructural characterization of virgin and tested materials in Section 7.4.

7.2   SPECIMEN PREPARATION AND BRICK CHARACTERIZATION

Fused–cast materials were received as bricks from the manufacturers. The bricks were all rectangular with different sizes. Standard bricks have the same size as the cold–pressed sintered bricks (Fig. 7.1a). But fused–cast long bricks (Fig. 7.1b), or bulky big bricks (Fig. 7.1c) have also been received. Similarly to the cold–pressed sintered material, cylindrical cores were extracted from the fused–cast bricks and prepared following the same guidelines outlined in Section 5.2.

The brick characterization study is interesting in the case of the fused–cast materials, because variations of material behavior may be expected within the same brick, and between different bricks with different sizes due to different cooling rates during the cooling–down process.
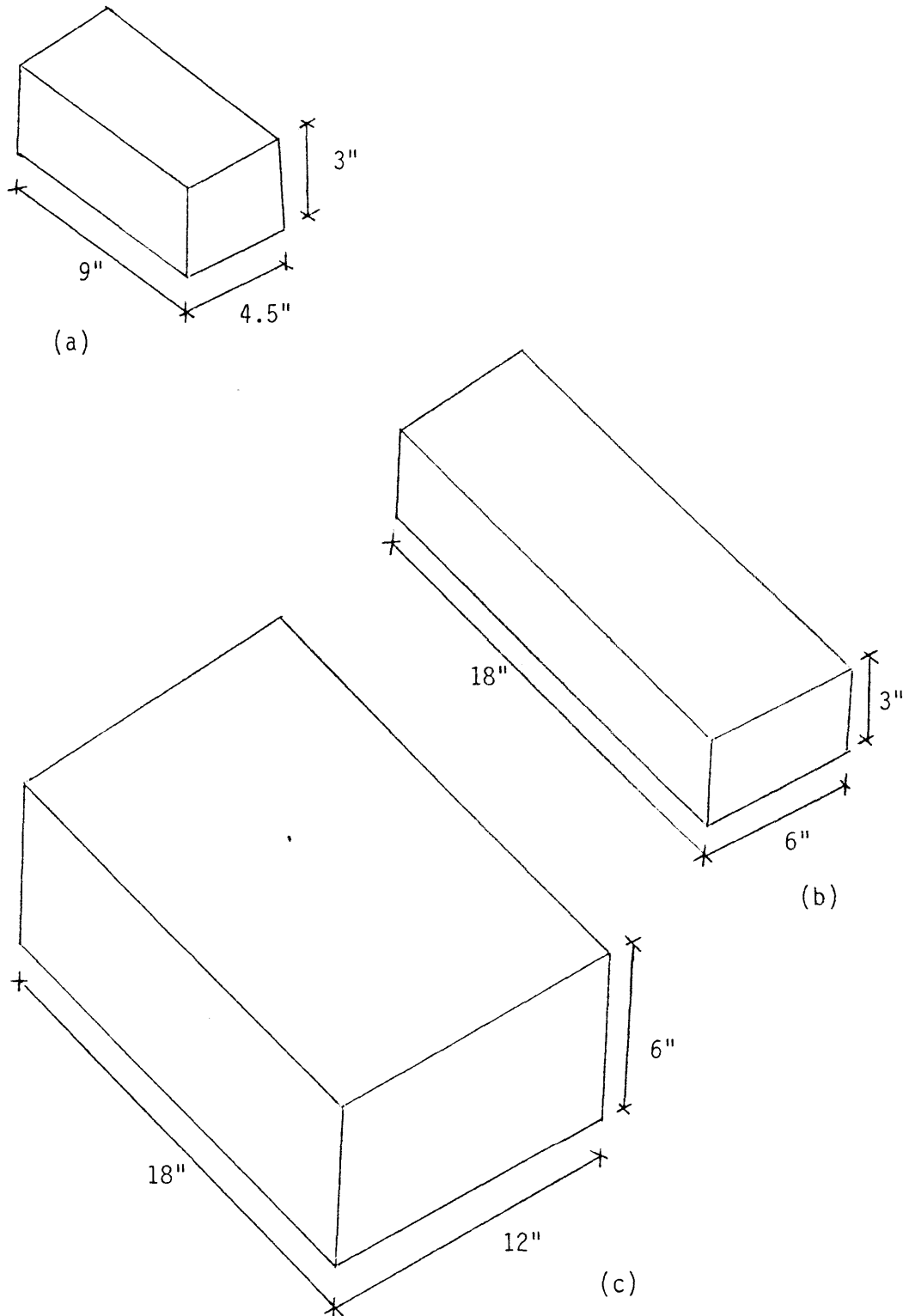
Figure 7.1　　　　Typical shapes and sizes of as—received as—manufactured fused—cast bricks

Fused—cast bricks were also found to be inhomogeneous and anisotropic. Furthermore, the mechanical properties also vary with depth in a fused—cast brick. Figure 7.2 shows average strength values for specimens cored from the top of a FC—59A—27C—6M brick at an interior location, and from the bottom at an interior and corner locations. The bottom exhibits a greater strength, and this may be attributed to the slower cooling rate of the bottom material. Figure 7.3 shows average strengths of specimens cored out from different directions for interior locations from a FC—59A—27C—6M brick. A large variation is observed. Fused—cast bricks, are thus, anisotropic and inhomogeneous. Furthermore, since the rate of cooling is dependent on the size of the brick, the strength values are different for bricks of different sizes. This is shown in Figure 7.4 for a 3" x 6" x 18" FC—59A—27C—6M brick, where an interior specimen cored out from the top exhibits a strength of 32.2 ksi. It is noted that in this case there is no distinction between top and bottom since the specimen height is equal to the brick depth. This can be compared to a strength of 20.1 ksi for a top interior specimen and 26.3 ksi for a bottom interior specimen cored out from a 6" 10" x 13" FC—59A—27C—6M brick shown in Fig. 7.4.

7.3 ELEVATED TEMPERATURE BEHAVIOR OF AS—MANUFACTURED MATERIALS UNDER UNIAXIAL SHORT—TERM MONOTONIC AND CONSTANT COMPRESSIVE LOADS IN AIR ATMOSPHERE

The behavior of fused—cast FC—7A—78C—8M at elevated temperatures under uniaxial short—term compressive loads is examined first. The stress strain curves for FC—7A—78C—8M at different temperature levels and a constant displacement rate of 7.218×10^{-5} in/sec are shown in Fig. 7.5. The two behavioral regions previously identified for cold—pressed sintered and hot—pressed materials are found for
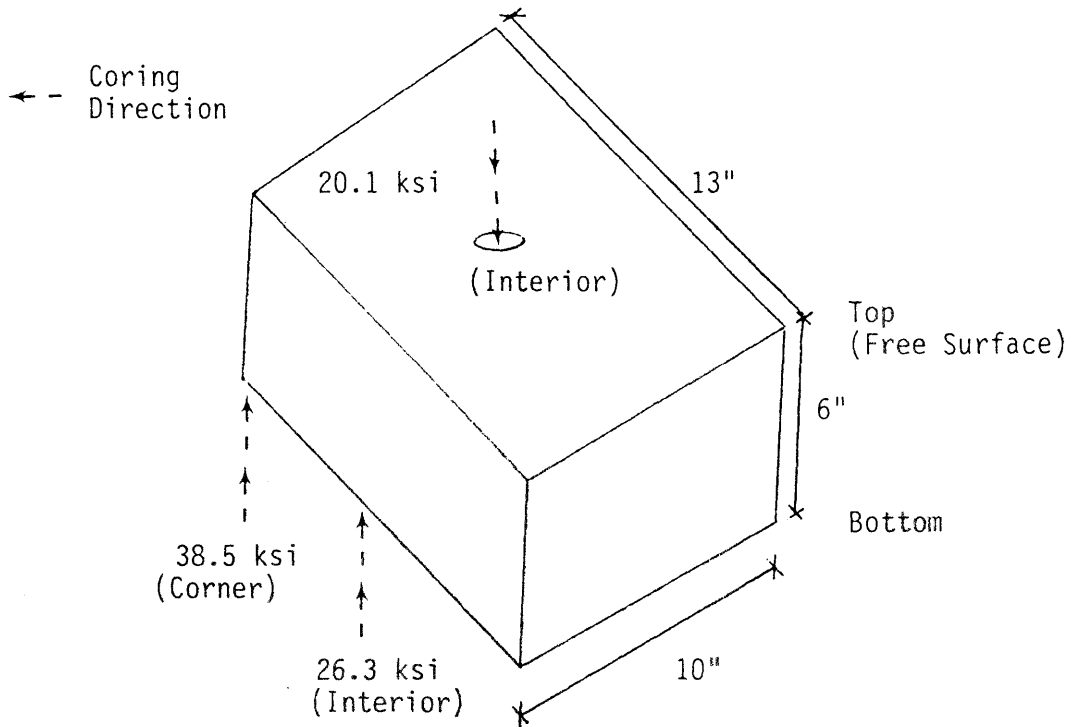
Figure 7.2   Strength variation with location of coring for FC–59A–27C–6M
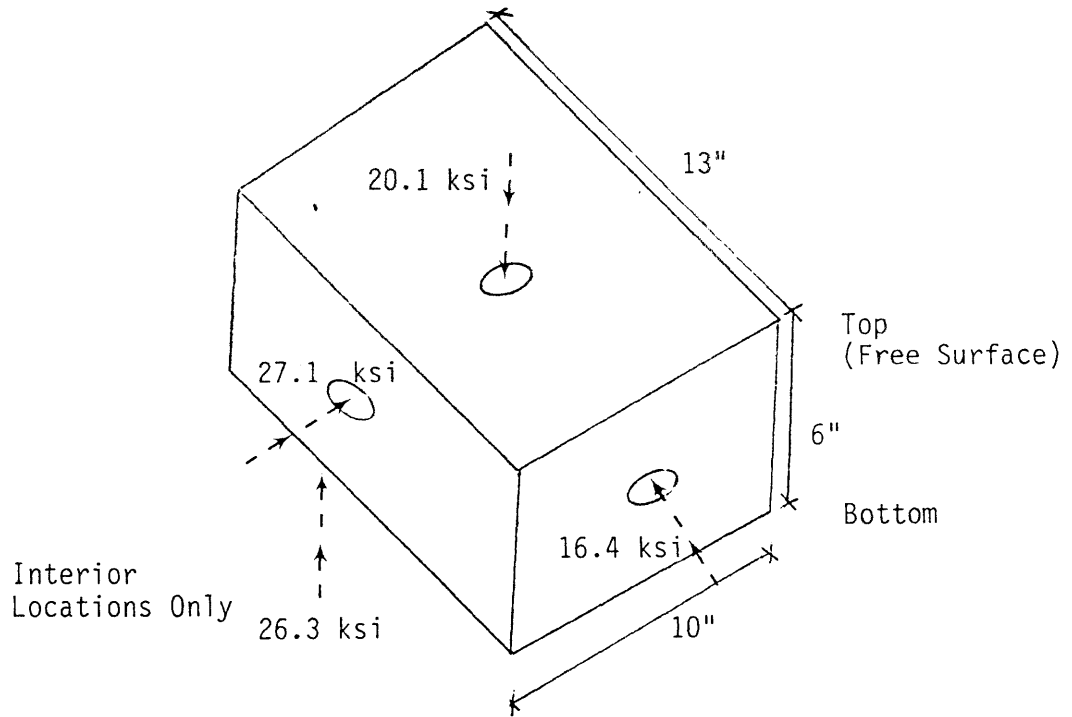
Figure 7.3   Strength variation with direction of coring for FC–59A–27C–6M
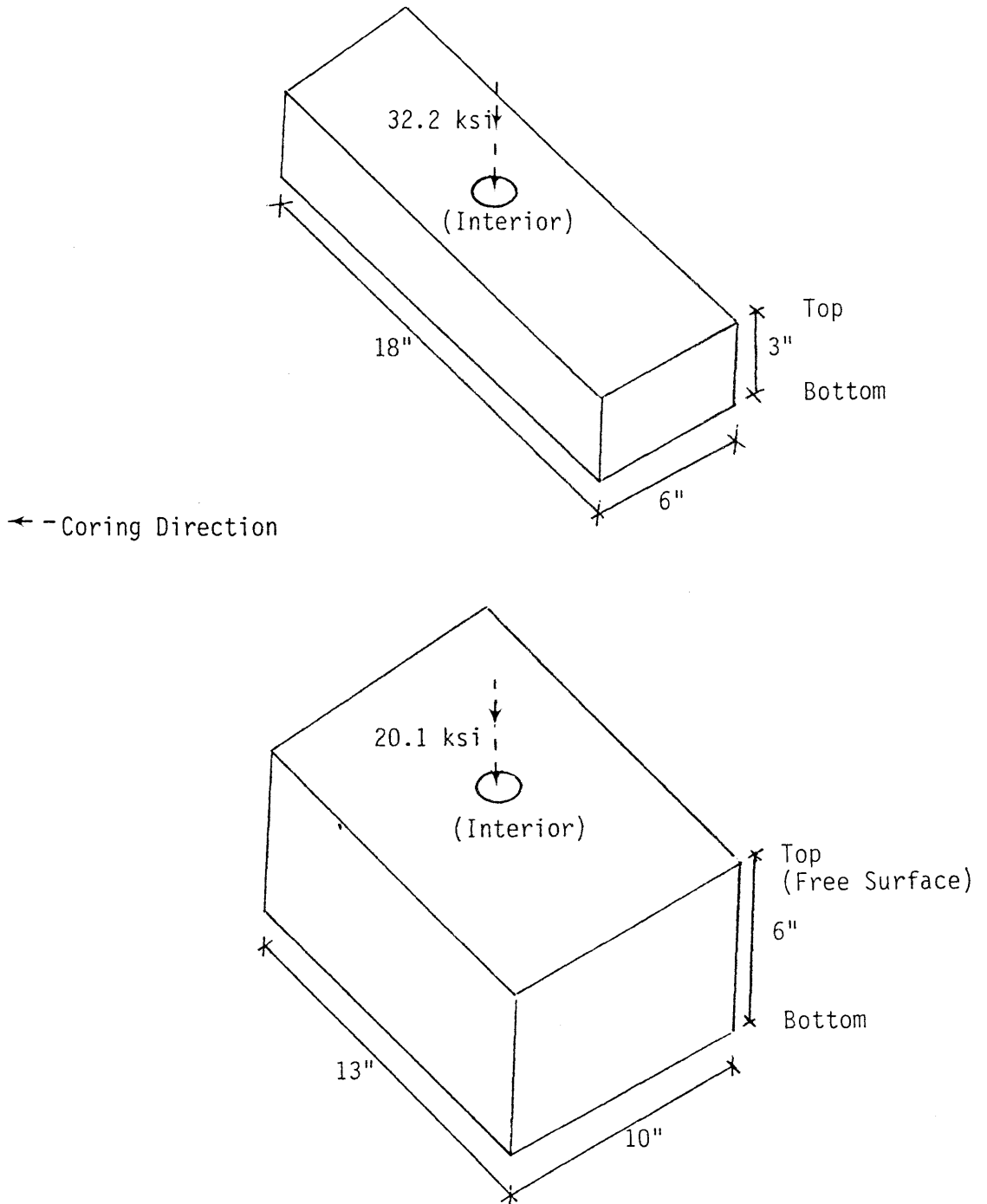
Figure 7.4   Strength variation with brick size for FC–59A–27C–6M
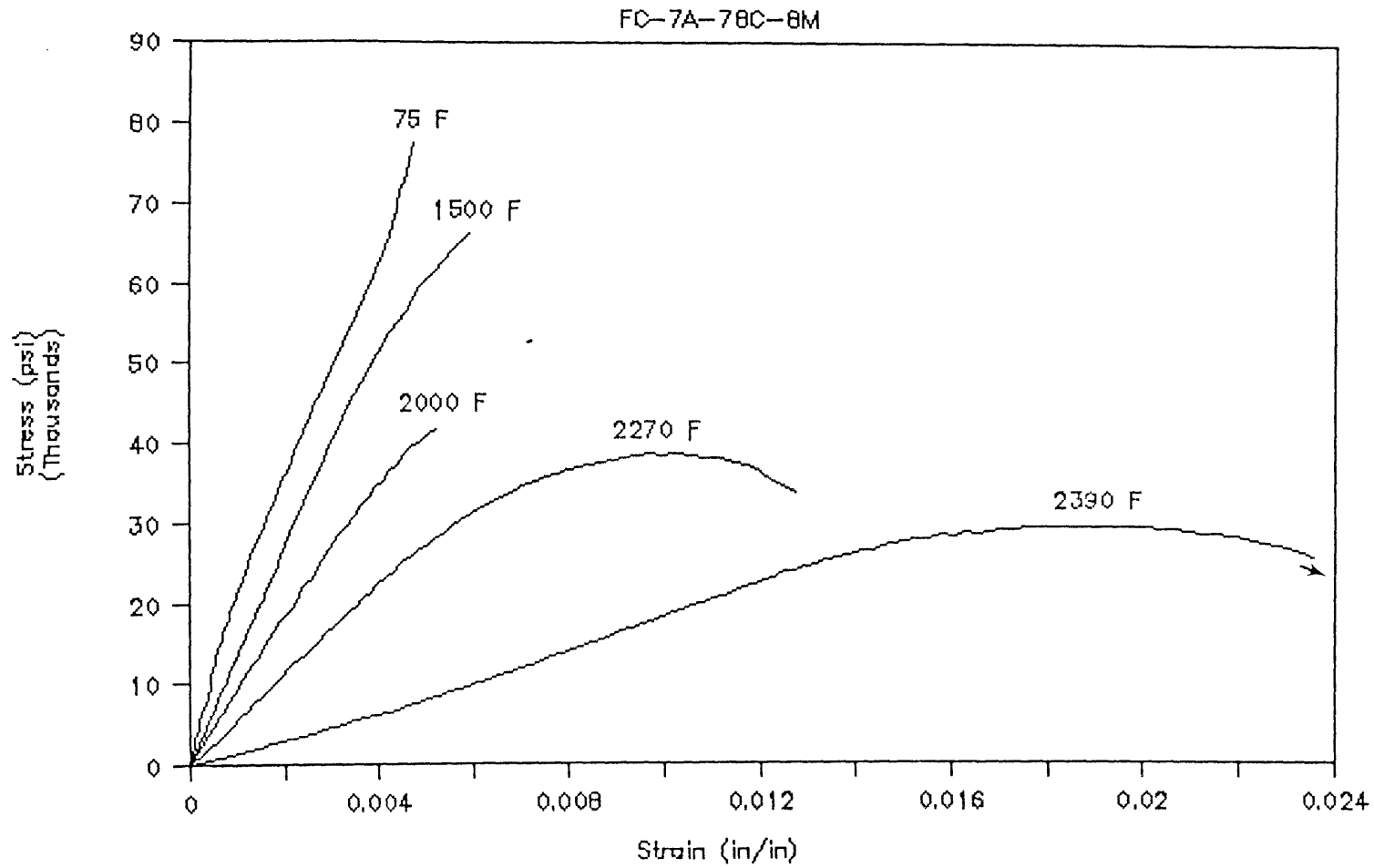
Figure 7.5   Stress strain curves for FC–7A–78C–8M at different
temperature levels and a constant displacement rate of 7.218
$\times 10^{-5}$ in/sec

FC–7A–78C–8M as well. For temperatures below or equal to 2000°F linear deformations with brittle fracture are observed. At 2270°F some non–linear deformations develop specially in the post–peak region, and the final fracture of the specimen occurs in a range of strains that is still comparable to the strains measured in the specimens at temperatures below or equal to 2000°F. At 2390°F significant non–linear deformations occur, and the final fracture does not happen after developed strains about twice as large as the final fracture strain at 2270°F.

The strength variation of FC–7A–78C–8M with temperature is shown in Fig. 7.6. The rate of decrease in strength is slower from room temperature to 1500°F, and is significantly larger for temperatures above 2270°F. The fit of equations (5.1) and (5.2) is shown in Fig. 7.6 as well. It is noticed that in the case of FC–7A–78C–8M the transition temperature is not as well defined. The strength of the fused–cast high–chromia (FC–7A–78C–8M) is higher than the strength of cold–pressed sintered high–chromia (CPS–82C–18M); the ratio of the strength of FC–7A–78C–8M to CPS–82C–18M varies from about 4 at room temperature to about 3 at 2270°F. The strength of FC–7A–78C–8M is lower than the one of the hot–pressed high–chromia (HP–80C–20M); HP–80C–20M is about twice as strong as FC–7A–78C–8M at room temperature, and has about 1.5 times the strength at temperature levels around 2300°F. It is also noticed that cold–pressed high–chromia materials exhibit the smallest rate of decrease in strength, followed by fused–cast high–chromia; hot–pressed high–chromia show the largest rate of decrease in strength.

The associated peak strain variation with temperature for FC–7A–78C–8M is shown in Fig. 7.7. The peak strain increases slowly for temperatures below 2000°F. On the other hand, for temperatures above 2000°F a sharp increase in peak strain is observed. This is similar to the observed behavior for cold–pressed sintered and

As—Manufactured FC—78C—8A—8M
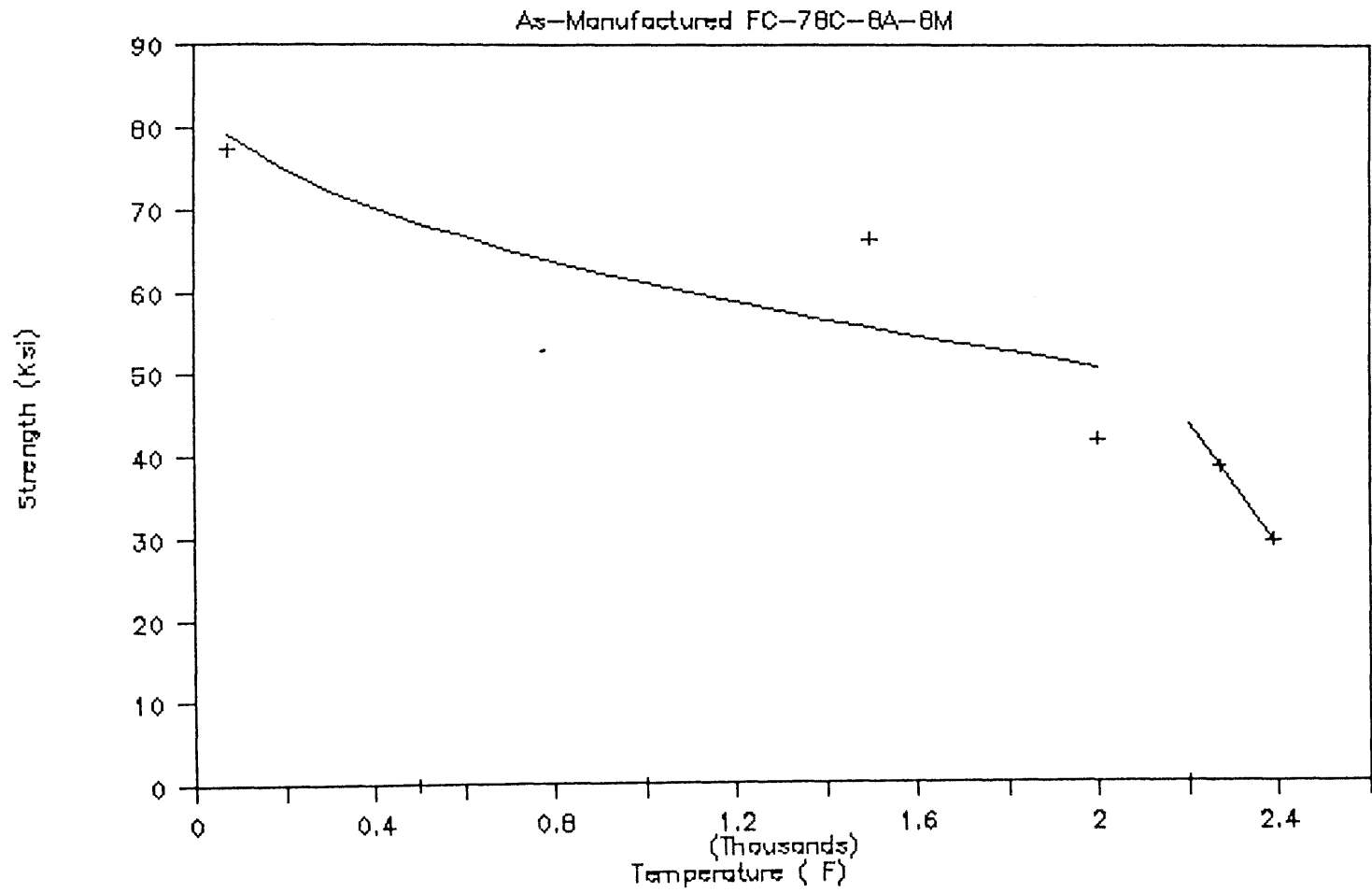
Figure 7.6   Strength variation with temperature for FC–7A–78C–8M
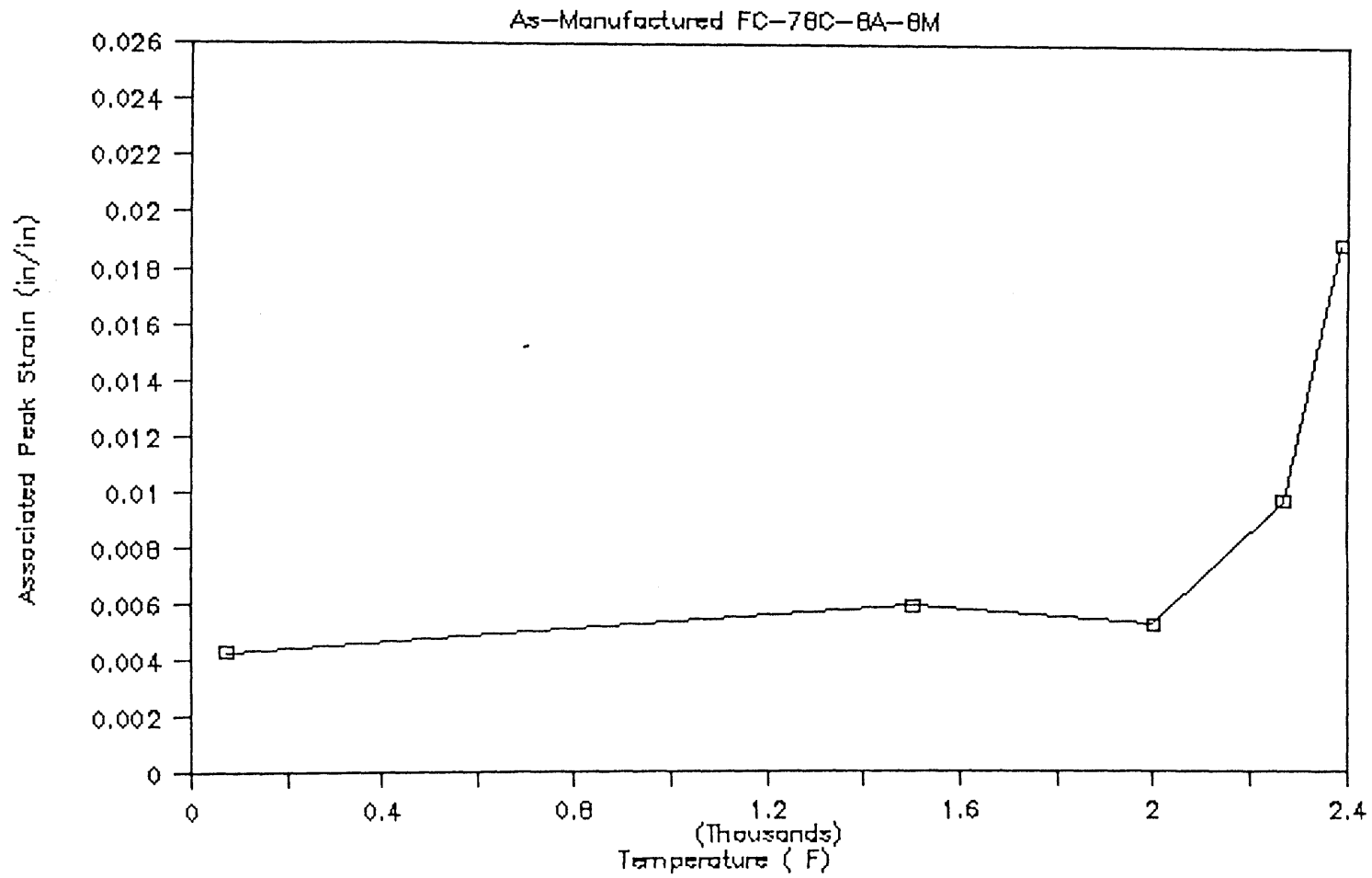
Figure 7.7   Associated peak strain variation with temperature for
FC–7A–78C–8M

hot—pressed materials. The associated peak strains for FC–7A–78C–8M are about twice as large as the peak strains for CPS–82C–18M at room temperature and about three times larger than the peak strains for CPS–82C–18M at temperatures around 2300°F. Compared to the peak strains for HP–80C–20M, the peak strains for FC–7A–78C–8M are about 20% lower at room temperature, and about 50% lower at temperatures around 2300°F. For the three kinds of manufacturing processes, the final fracture strains are significantly larger than the associated peak strains. The rate of increase of the associated peak strains with temperatures above roughly $T_m/2$ is largest for hot—pressed refractories, followed by fused—cast refractories, and the smallest rate of increase is observed for cold—pressed sintered refractories.

The variation of the initial stiffness with temperature for FC–7A–78C–8M is shown in Fig. 7.8. Larger rates of decrease in initial stiffness are observed at elevated temperatures, specially above 2000°F. This is similar to the variation observed for cold—pressed sintered and hot—pressed refractories. The initial stiffness of FC–7A–78C–8M is about three times larger than the one for CPS–82C–18M and about the same as the one for HP–80C–20M at room temperature. At temperatures around 2350°F the initial stiffness of FC–7A–78C–8M is about equal to the one for CPS–82C–18M, and about one—half the initial stiffness of HP–80C–20M. The rate of decrease in initial stiffness is largest for the fused—cast high—chromia, followed by the hot—pressed high—chromia, and is smallest for cold—pressed high—chromia.

The toughness measure variation with temperature for FC–7A–78C–8M is shown in Fig. 7.9. The decrease in the toughness measure at 2000°F is not expected; a similar decrease was observed at 2000°F for HP–50A–50C. The rate of increase in toughness measure for temperatures above 2000°F is higher than the one for temperatures below 1500°F, and this trend is similar to the one observed for the

As—Manufactured FC—78C—8A—8M
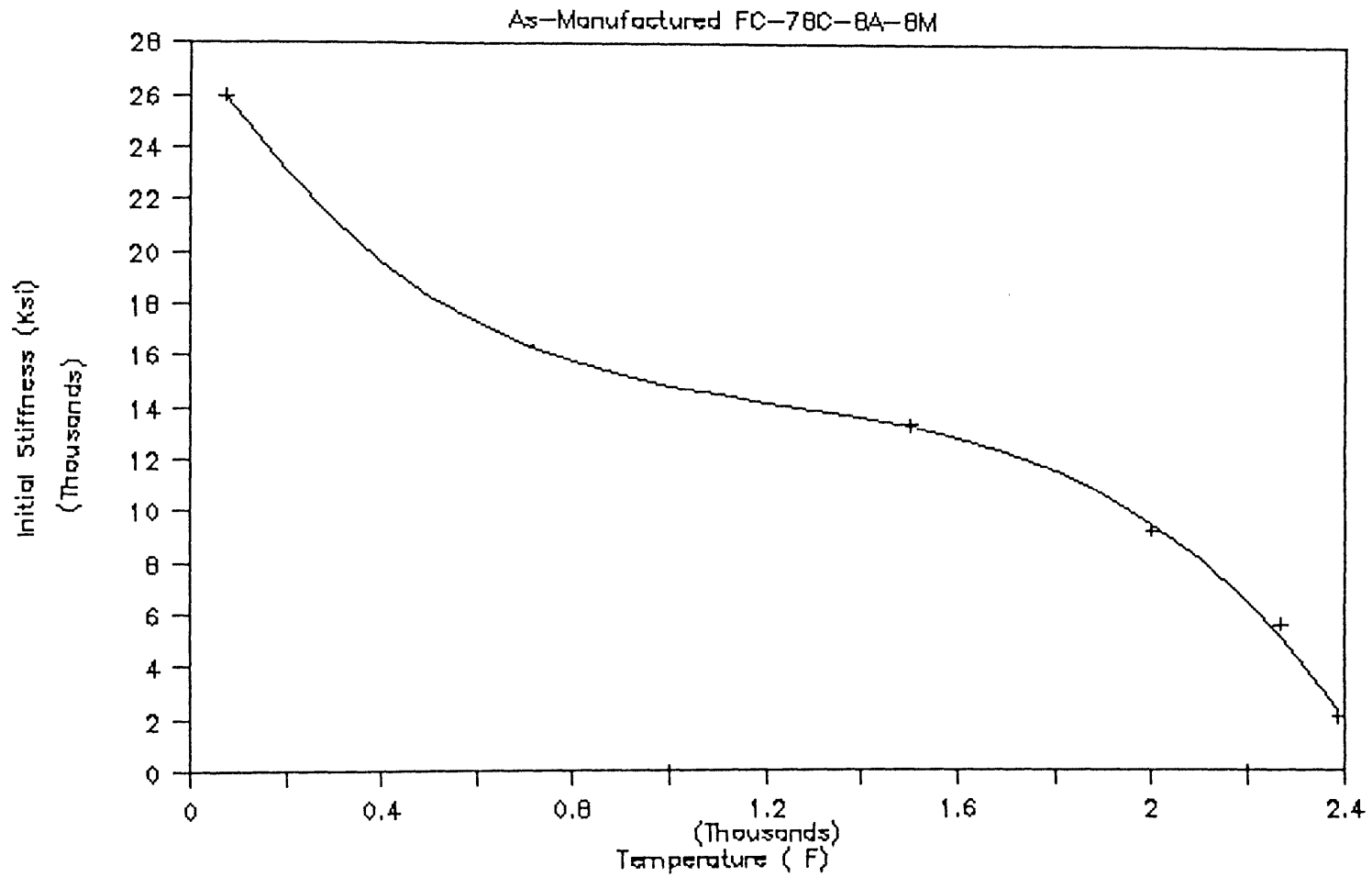
Figure 7.8   Initial stiffness variation with temperature for FC—7A—78C—8M

As-Manufactured FC-78C-8A-8M
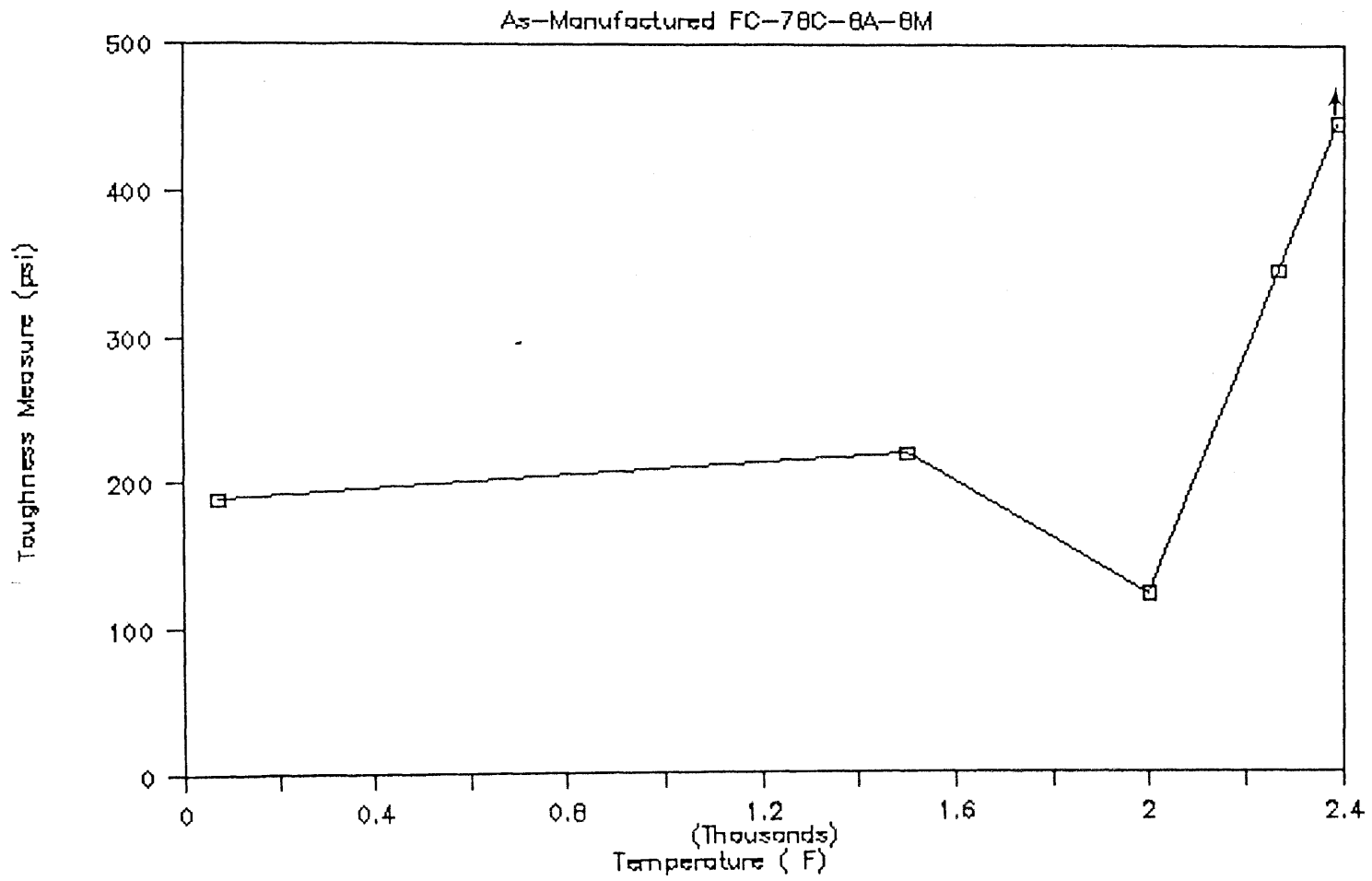
Figure 7.9   Toughness measure variation with temperature for FC–7A–78C–8M

previously tested materials. The toughness measure for FC–7A–78C–8M at room temperature is about 7.5 times larger than the one for CPS–82C–18M, and is only one–half of the one for HP–80C–20M. At temperatures of about 2350°F, the toughness measure of FC–7A–78C–8M is significantly smaller than the one for HP–80C–20M, and about four times larger than the one for CPS–82C–18M. The rate of increase of toughness measure with temperature is largest for HP–80C–20M, and is smallest for FC–7A–78C–8M.

The behavior of FC–7A–78C–8M under short–term uniaxial compressive loads is examined next. Only selected temperature and load levels were used, since the object of the present study on fused–cast materials is to compare their short–term creep behavior to the one of cold–pressed sintered and hot–pressed materials. Figures 7.10 and 7.11 show the variation of the creep strain with time and the variation of the log of the creep strain rate with time respectively for FC–7A–78C–8M at 2000°F and 83% of the monotonic strength. The specimen did not fail in the two hours duration of this short–term creep test. Comparing this behavior to the failure of hot–pressed high–alumina specimens at 1500°F and 78% f_p, it seems that the fused–cast high–chromia are more creep resistant than the hot–pressed high–alumina under the same % strength level. However, more data is needed to compare the strain rates of both materials at the same load levels.

7.4 MICROSTRUCTURAL CHARACTERIZATIONS OF VIRGIN AND TESTED MATERIALS

In tl⸱ ⸱ section the microstructural characteristics of fused–cast FC–7A–78C–8M are studied using a Nomarski and scanning electron microscopes and X–ray microanalysis. Microstructure is very much influenced by the rate of cooling. Different microstructures develop at different locations and depths in the
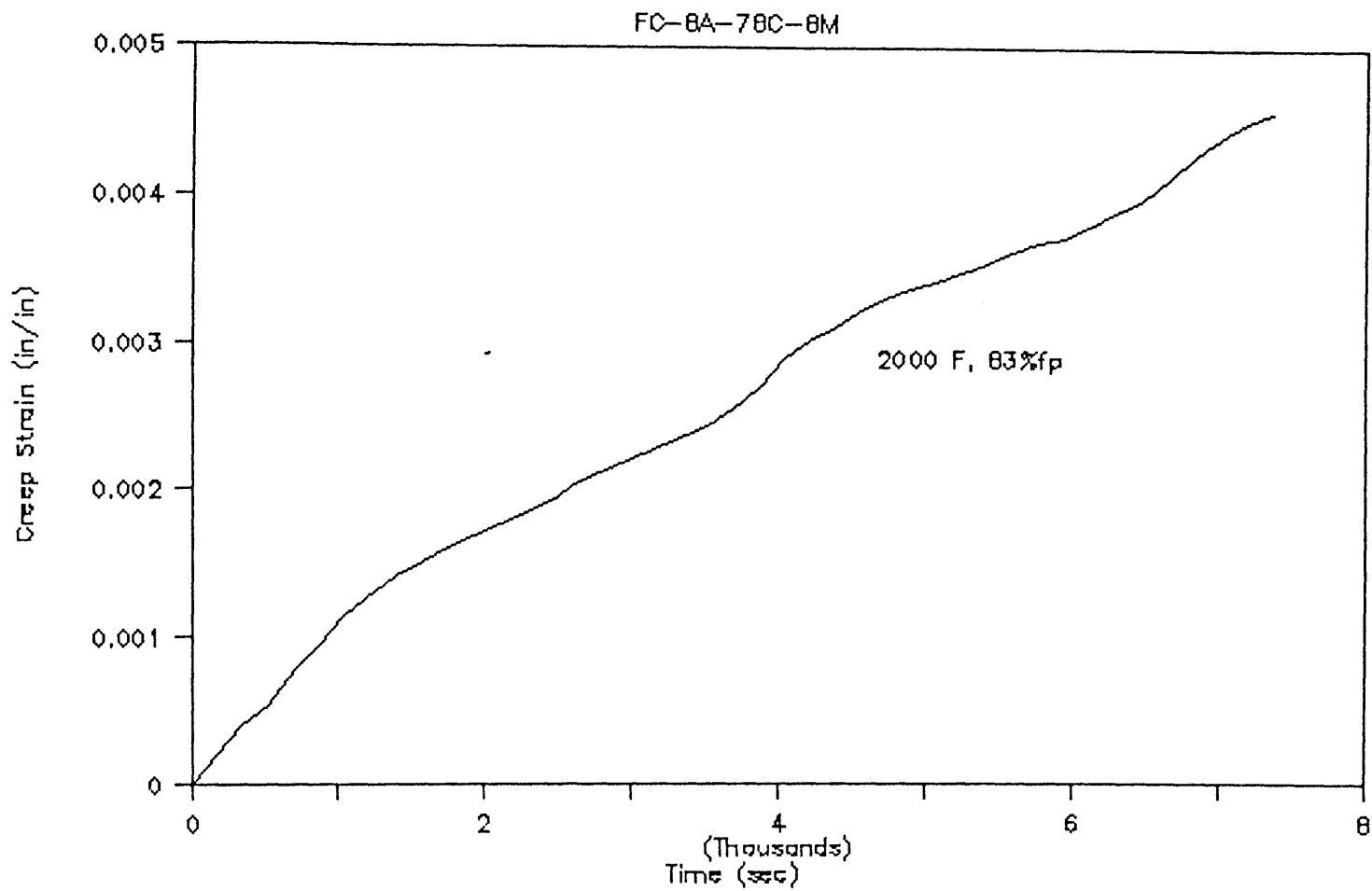
Figure 7.10   Creep strain for FC–7A–78C–8M at $2000^{\circ}F$ under 83% of the monotonic strength
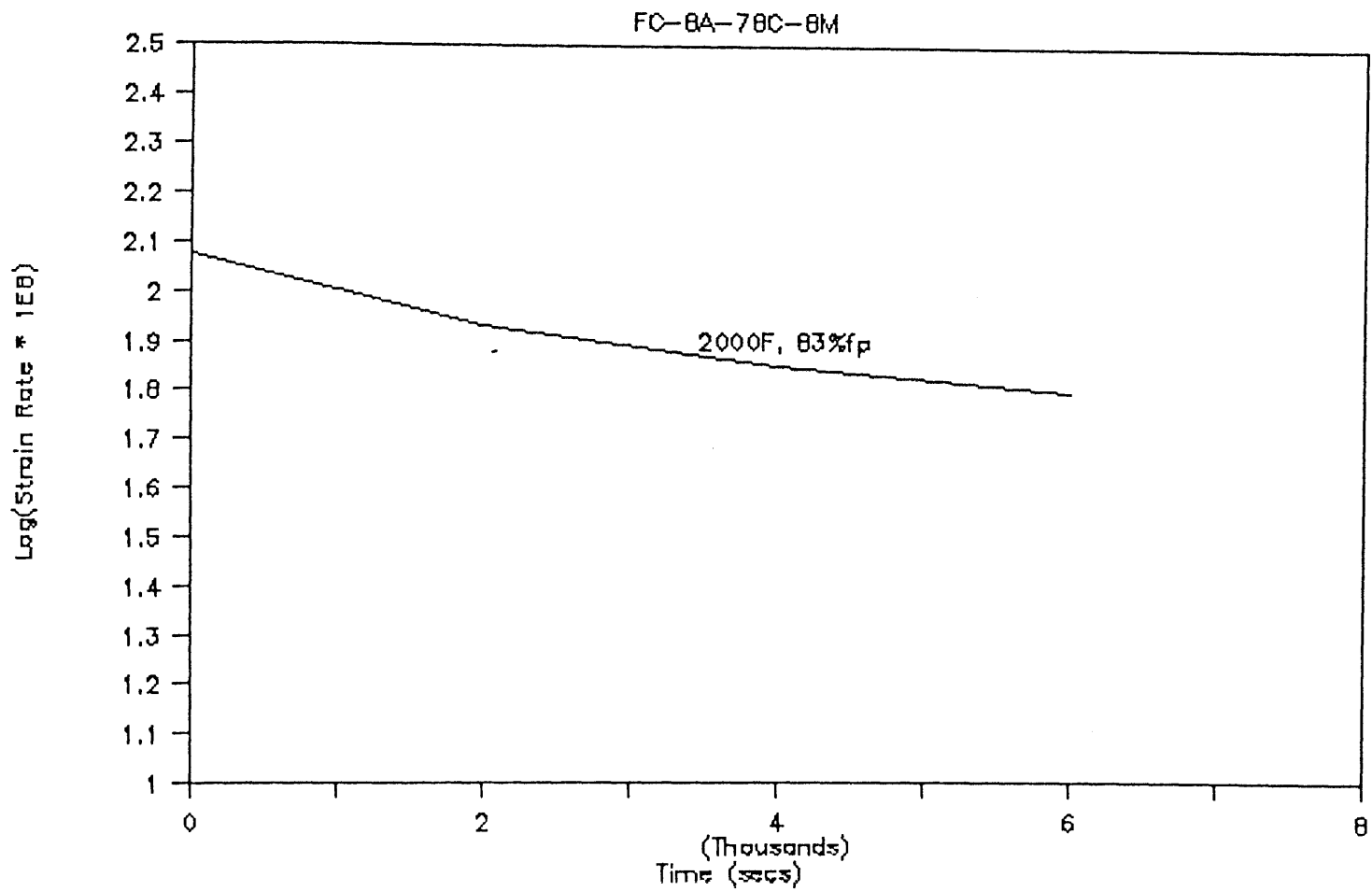
Figure 7.11   Variation of the log of the creep strain rate at different temperature and load levels for FC—7A—78C—8M

brick, due to different cooling rates. Figure 7.12 shows the characteristics of non–tested FC–7A–78C–8M using a Nomarski at 20X. Needle–like grains are observed with no specific orientation. The black dots shown in the picture are pores and the different phases present show as various gradations from gray to white. The long needle–like grains are shown in Fig. 7.13 at 320X for material FC–7A–78C–8M tested at $2300^{\circ}F$ under monotonic compression. Small cavities have developed under loading adjacent to the long grains, at the interface with the spinel matrix. Similarly to the as–manufactured hot–pressed material and slag–impregnated cold–pressed sintered materials, the cracking pattern of material FC–7A–78C–8M is more homogeneous than for the as–manufactured cold–pressed sintered materials. Figure 7.14 shows an array of vertical cracks that joint together in en echelon formation to probably cause the final fracture of the FC–7A–78C–8M specimen at $2300^{\circ}F$. Contrary to the case of as–manufactured cold–pressed sintered materials, cavitation does not seem to be an important factor in the deformation process for cold–pressed sintered materials. The different phases present in material FC–7A–78C–8M do not show very well in black and white pictures although they can be noticed on color prints using the Nomarski. In order to characterize these different phases, SEM pictures have been taken. Figures 7.15a, 7.15b and 7.15c show the same area of FC–7A–78C–8M photographed using secondary electrons imaging, backscattered electrons imaging in the compositional mode, and backscattered electrons imaging in the topographical mode respectively. The secondary electron imaging shows the pore structure, but does not give clear compositional changes (Fig. 7.15a). However, the backscattered electron imaging shows the long grains, inside the spinel matrix, and gives a very good contrast between the two phases (Fig. 7.15b). Since the specimen surface was polished and is completely flat, the backscattered

Figure 7.12   Nomarski microscope picture of virgin FC–7A–78C–8M at
                     20X showing needle–like grains and spinel matrix

Figure 7.13   Nomarski picture of FC–7A–78C–8M at 320X tested to failure under monotonic compression at $2300^{O}F$ showing needle–like grains and intra–granular cavities
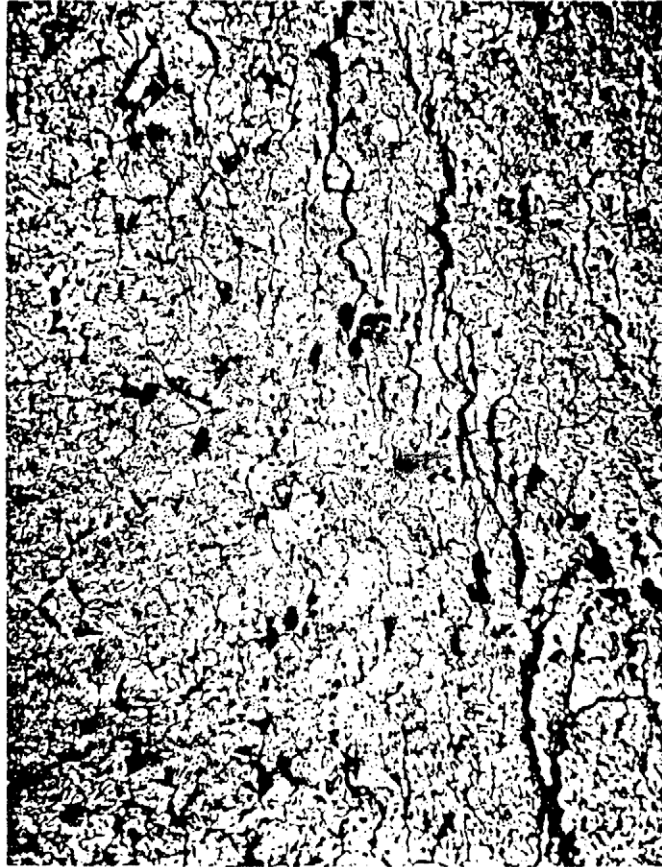
Figure 7.14   Nomarski picture of FC—7A—78C—8M at 12.8X tested to
failure under monotonic compression at $2300^{O}F$ showing
networks of cracks parallel to the principal stress direction

Figure 7.15a

SEM picture of FC–7A–78C–8M at 320X using secondary electron imaging

Figure 7.15b

SEM picture of FC–7A–78C–8M at 320X using the backscattered electron imaging in the compositional mode

Figure 7.15c

SEM picture of FC–7A–78C–8M at 320X using the
backscattered electron imaging in the topographical mode

electron imaging in topographical mode does not show any interesting information (Fig. 7.15c).

An X—ray microanalysis was carried out to differentiate between the grains and the matrix. As expected, the grains showed more Fe and Ca, and not much Mg (Fig. 7.16a). On the other hand, the matrix showed an Mg peak and reduced Fe content (Fig. 7.16b).

7.5 SUMMARY

The behavior of fused—cast bricks was found to be not only anisotropic and inhomogeneous, but to also depend on the size of the brick. This is explained by the fact that different size bricks have different cooling rates. The following variations in strength properties were observed for FC—59A—27C—6M: the top is about 22% weaker than the bottom of the brick, the corner is 31% stronger than the interior, a maximum difference of 26% between cores extracted with their axis parallel to and the ones with their axis perpendicular to the free surface, and about 37% increase for a shallow long block compared to a deep square brick. The variation of material properties within a fused—cast brick is higher than the one within a cold—pressed sintered brick.

The fused—cast materials exhibit similar behavioral trends with respect to temperature than the cold—pressed sintered and hot—pressed materials. The variations with temperature of the strength, associated peak strain, initial stiffness and equivalent measure of toughness of FC—7A—78C—8M are also similar to the variations exhibited by CPS—82C—18M and HP—80C—20M. The creep strain rates of fused—cast materials are comparable to the ones of the hot—pressed materials.

The microstructure of FC—7A—78C—8M consists of needle—like grains in a
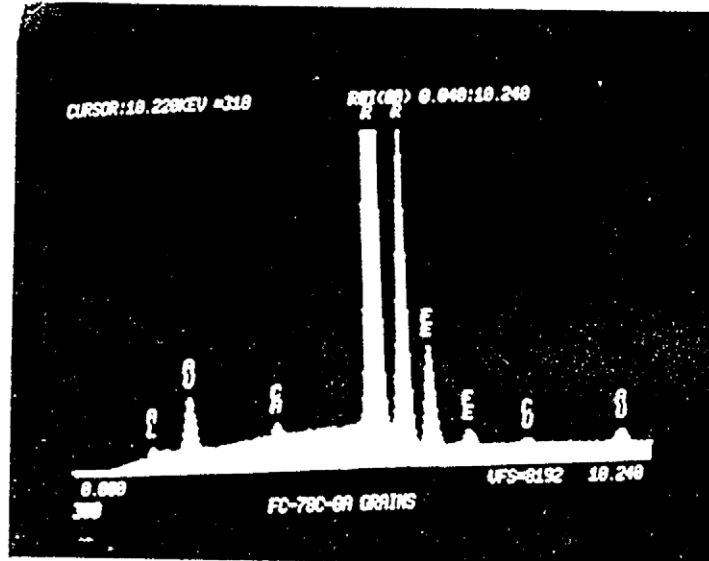
Figure 7.16a   X—ray diffraction for the grains of FC—7A—78C—8M
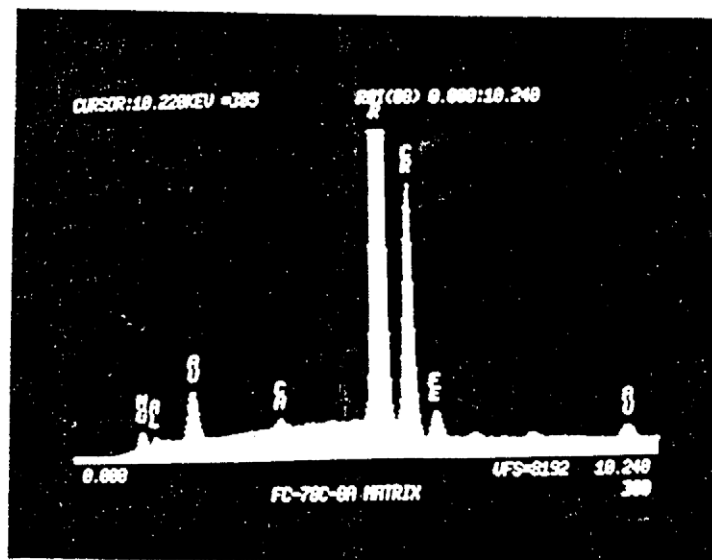
Figure 7.16b   X—ray diffraction for the matrix of FC—7A—78C—8M

high–chromia spinel matrix. The microstructure of FC–7A–78C–8M is finer than the one observed for the CPS materials, but coarser than the one observed for the HP materials.

Comparing the three different manufacturing processes for the materials tested, going from cold–pressed sintered (CPS) materials to fused–cast (FC) materials to hot–pressed (HP) materials, the following is observed:

– the monotonic strength increases; however the rate of decrease in strength with temperature is larger;

– the associated peak strain increases;

– the equivalent measure of toughness increases;

– the creep strain rates seem to decrease for materials with the same chemical composition at the same load level;

– the microstructure is finer and more homogeneous;

– the porosity decreases; and

– the cost of the material is higher.

CHAPTER 8
MATERIAL DATABASE

A material database of thermomechanical and thermophysical properties for refractory materials has been developed. It summarizes the thermomechanical data obtained at MIT under the current project and includes a collection of thermomechanical and thermophysical data assembled from the manufacturers or the literature. The thermomechanical data was unavailable in the past, and was produced by the current MIT Project. The material database may be useful to manufacturers and users of refractory materials. The developed material database can be found in Appendices A and B. This short chapter only describes the materials and properties included in the database.

Table 8.1 shows the different materials included in this database. They represent 14 dense refractory bricks tested at MIT under the current DOE project, 15 dense commercial refractory bricks from different manufacturers, 4 dense refractory bricks from the literature, 4 insulating commercial bricks, 1 dense and 1 insulating refractory castables tested at MIT under a previous DOE project, 1 commercial refractory castable, and 1 Portland Cement Concrete from the literature. It should be noted that there is some overlap between the bricks tested at MIT and the commercial bricks.

Under the current MIT project, nine different materials have been tested at high temperatures and are shown in Table 8.1a. These include two as—manufactured cold—pressed and sintered refractories, two slag—impregnated cold—pressed and

Material Classifi- cation	Chemical Composition	Manufacturing Process	Testing After Slag Impregnation
CPS-90A-10C	$90\%Al_2O_3, 10\%Cr_2O_3$	Cold Pressing and Sintering	Yes
CPS-82C-18M	$82\%Cr_2O_3, 18\%MgO$	Cold Pressing and Sintering	Yes
HP-90A-10C	$90\%Al_2O_3, 10\%Cr_2O_3$		No
HP-50A-50C	$50\%Al_2O_3, 50\%Cr_2O_3$	Hot-Pressing	No
HP-25A-75C	$25\%Al_2O_3, 75\%Cr_2O_3$		No
HP-80C-20M	$80\%Cr_2O_3, 20\%MgO$	Hot-Pressing	No
FC-78C-8A	$78\%Cr_2O_3, 8\%Al_2O_3$	Fusion-Casting	No

Table 8.1a

Materials used at MIT under current project for thermomechanical testing

sintered refractories, four as—manufactured hot—pressed refractories, and one as—manufactured fused—cast refractory. Limited room temperature data has been developed for seven other materials shown in Table 8.1b. These include five as—manufactured cold—pressed and sintered refractories, and two as—manufactured fused—cast refractories.

Thermomechanical data on the elevated temperature behavior of refractory castables have been collected from the literature as well, and included in the database. The data gathered is from monotonic load tests to failure, at elevated temperatures, in air atmosphere (Category A in the MIT program). Four different materials were surveyed, and are shown in Table 8.1c. These include a dense and an insulating refractory concrete tested at MIT under a previous DOE project, one commercial refractory concrete, and a Portland Cement concrete.

Modulus of rupture data has been collected from the literature, and from manufacturers information for fifteen different as—manufactured materials shown in Table 8.1d. The materials include four cold—pressed sintered, three fused—cast, four insulating, and four alumina—silica refractories.

Thermophysical properties have been collected from the literature and manufacturers data for twenty different as—manufactured materials shown in Table 8.1e. These include eight cold—pressed sintered, three hot—pressed, three fused—cast, four insulating, and two castable refractories.

The database includes over thirty different materials and consists of over fifty tables, over one hundred equations, and about ninety graphs. The bulk of the material database can be found in Appendices A and B.

Material Classifi-cation	Chemical Composition	Manufacturing Process
CPS-16A-62C	$62\%Cr_2O_3$, $16\%Al_2O_3$ $12\%ZrO_2$, $7\%SiO_2$	Cold Pressing & Sintering
CPS-9A-81C	$81\%Cr_2O_3$, $9\%Al_2O_3$ $6\%ZrO_2$, $2.5\%SiO_2$	Cold Pressing & Sintering
CPS-23A-75C	$75\%Cr_2O_3$, $23\%Al_2O_3$	Cold Pressing & Sintering
CPS-80C-18.5M	$80\%Cr_2O_3$, $18.5\%MgO$	Cold Pressing & Sintering
CPS-79C-19.5M	$79\%Cr_2O_3$, $19.5\%MgO$	Cold Pressing & Sintering
FC-15A-83C	$83\%Cr_2O_3$, $15\%Al_2O_3$	Fusion-Casting
FC-50A-28C	$28\%Cr_2O_3$, $50\%Al_2O_3$	Fusion-Casting

Table 8.1b

Materials used at MIT under current project
for preliminary room temperature characterization

Material	Characteristics	Source of Information
Dense Refractory Concrete	Castable Refractory, Alumina Cement, 8% Water by Weight, Curing at 225°F, 5" x 5" x 1" Flat Plates.	Tseng, 82
Insulating Refractory Concrete	Castable Refractory, Alumina Cement, 21% Water by Weight, Curing at 225°F, 5" x 5" x 1" Flat Plates.	Tseng, 82
Commercial Refractory Concrete	Castable Refractory, Alumina Cement.	Wygant and Buckley, 54
Portland Cement Concrete	Standard Portland Cement, Sand:Cement ratio = 2.88, Aggregate:Cement ratio = 1.92, Quartzite Aggregate (8 - 12mm), 75mm diam x 150mm heigh cylinder	Anderberg and Thelandersson, 76

Table 8.1c

Castables compiled in the database for
thermomechanical properties in compression

Material	Description	Source of Information
AX581 TX591 AX565	Cold-Pressed Sintered Dense Refractory Bricks	Norton Company
HW25-83		Harbison Walker
SOHIO B SOHIO E SOHIO K3	Fused-Cast Dense Refractory Bricks	Sohio Engineered Materials Company
JM-20 JM-23 JM-30 JM-32	Insulating Refractory Bricks	Eastern Refractories
50% Alumina 60% Dense Alumina 90% Dense Alumina 99% Alumina	Alumina-Silica Refractory Bricks	Miller and Davis, 66

Table 8.1d

Materials compiled for modulus of Rupture data

Material	Description	Source of Information
AX581, TX591, AX565	Cold-Pressed Sintered Refractories	Norton Company
HW25-83		Harbison Walker
Radex BCF86C Radex BCF812		General Refractories
Zirchrom 60 Zirchrom 80		National Refractories
AX627B, AX627D, TX628	Hot-Pressed Refractories	Norton Company
Sohio E, Sohio B, Sohio K3	Fused-Cast Refractories	Sohio Engineering Materials Company
JM20, JM23, JM30, JM32	Insulating Refractories	Eastern Refractories
Dense and Insulating Refractory Concretes	Castable Refractories	Tseng, 82

Table 8.1e
Materials compiled in the database for thermophysical information

CHAPTER 9
SUMMARY, CONCLUSIONS, AND SUGGESTIONS
FOR FUTURE RESEARCH

9.1 SUMMARY OF THE PRESENT WORK

The general application area studied is the analysis and design of linings for high temperature process vessels, with a focus on slagging coal gasifiers. Previous projects at MIT concentrated on modeling the material behavior and using finite element analysis to arrive at recommendations for the design of the linings. There was a need to generate a fundamental understanding and characterization of the behavior of different refractory material systems manufactured by various processes in slagging coal gasifier environments. The objective of this work is to characterize the short–term compressive behavior of refractory ceramic oxides at elevated temperatures, with a focus on candidate materials for slagging coal gasifier linings.

The materials studied for thermomechanical properties were alumina–chromia and chromia–magnesia refractories manufactured by cold–pressing and sintering (CPS), hot–pressing (HP) or fusion–casting (FC). The cold–pressed sintered alumina–chromia is a high–alumina system consisting of 90% Al_2O_3 (A) and 10% Cr_2O_3 (C), thus denoted CPS–90A–10C, with an alumina–chromia solid solution and tabular alumina grains. The cold–pressed chromia–magnesia is a high–chromia system consisting of 82% Cr_2O_3 and 18% MgO (M), thus denoted CPS–82C–18M, with a picrochromite ($MgCr_2O_4$) spinel matrix and fused picrochromite grains. Three hot–pressed alumina–chromia systems were tested with different alumina contents and the balance consisting of chromia, namely, 90% Al_2O_3 (HP–90A–10C),

50% Al_2O_3 (HP–50A–50C) and 25% Al_2O_3 (HP–25A–75C). One hot–pressed chromia–magnesia material, HP–80C–20M, was tested with about the same chemical composition as the cold–pressed sintered chromia–magnesia. Finally a high–chromia fused–cast refractory, FC–7A–78C–8M was also tested. In a separate test category, the cold–pressed sintered refractories were studied after impregnation with western acid slag which is very rich in SiO_2, Al_2O_3, CaO and Fe_2O_3.

The approach followed in conducting the research can be summarized in the following steps:

o   development of a testing system for uniaxial compressive and flexural load applications (up to 50,000 lb) at elevated temperatures (up to $2800^{o}F$) under controlled gas environments (see Table 9.1);

o   development of testing and specimen preparation procedures; characterization of refractory brick properties (such as anisotropy and inhomogeneity within a brick) and property variation between bricks from the same production batch and bricks from different production batches;

o   characterization of the deformation and fracture behavior of refractory ceramics under compressive loading and elevated temperatures ($70^{o}F$ to $2500^{o}F$); the following factors are considered:

     —   monotonic, cyclic (up to 70% to 90% of monotonic strength), and creep (from 55% to 85% of monotonic strength) loads,

     —   constant, and increasing temperatures,

     —   air and reducing atmospheres ($P_{0_2} = 10^{-8}$ atm),

     —   as–manufactured and slag–impregnated materials,

     —   strain rate effects in monotonic tests (from 10^{-4} to 10^{-6} sec^{-1}),

Furnace:	- split type with SiC resistance elements - maximum temperature of 2800 Fahrenheits (F) - temperature setpoint achieved with accuracy of 2 F - controlled up to 252 thermal cycles with 8 ramp or soak periods per cycle
Retort System:	- SiC rods joining to stainless steel water-cooled rods - maximum load of 50,000 lb at 2800 F - bellows assembly allows up to 1" of deformation in controlled environments - water cooling of six chambers is done in parallel - two clamping systems for tests with and without muffle tube
Gas Control System:	- controlled gas environment inside alumina muffle tube - pressure relief valves, check valve, flowmeter, suction pump
Partial Oxygen Pressure:	- measured partial oxygen pressures as low as 1E-13 atm using a 5% ammonia - 95% nitrogen mixture - output gas through acid bubbler
Data Acquisition and Control System:	- microcomputer for load control - microprocessor for temperature control - intelligent front end linked to personal computer for data acquisition

Table 9.1

High Temperature Test Facility

- heating rate effects in increasing temperature tests (from 100°F/hr to 250°F/hr),

- effect of manufacturing process (cold–pressing and sintering, hot–pressing, and fusion–casting),

- different chromia contents in the hot–pressed alumina–chromia system (10%, 50% and 75% Cr_2O_3), and

- study of the variability of macroscopic properties;

o microstructural characterization of virgin and tested, as–manufactured and slag–impregnated materials:

- stereoscopic optical microscope,

- nomarski optical microscope,

- scanning electron microscope,

- x–ray diffraction,

- mercury porosimeter tests, and

- density measurements;

o development of a database, which may be useful to the manufacturers and users of refractory materials, for the obtained thermomechanical properties in compression, and assembed modulus of rupture data and thermophysical properties; and

o study the relation of the deformation and fracture behavior at macroscopic level to microstructural characterization.

Under the current MIT project a total of over 300 short–term compression tests (not including preliminary tests) have been carried out. Over 150 compression tests were performed at room temperature to establish standard specimen preparation procedures, and characterize brick behavior. About 150 other compression tests were

carried out in controlled gas environments to characterize deformation and fracture behavior at high temperatures. All thermomechanical tests were carried under short—term uniaxial compression under five categories of loading:

A — monotonically increasing loads to failure, under pre—determined constant temperatures, in air;

B — monotonically increasing loads to failure, under pre—determined constant temperatures, in reducing atmosphere with a partial oxygen pressure (P_{O_2}) of 10^{-8} atm.

C — cyclically varying loads, under pre—determined constant temperatures, in air;

D — constant loads, under constant pre—determined temperatures, in air; and

E — constant loads, under monotonically increasing temperatures, in air.

9.2 SUMMARY OF THE MAIN FINDINGS

9.2.1 Testing Methodology

A testing methodology has been developed which consists of three main components: calibrating the high temperature test facility and establishing testing procedures, recommending specimen preparation procedures and characterizing the variability in the brick behavior as well as the variability in behavior of the bricks from different batches of the production line. The last two components are discussed further in this section.

Specimen Preparation Procedures (Table 9.2)

The following parameters were studied for recommending specimen preparation procedures:

Cross Section:	– circular was preferred to rectangular for:
	   – load uniformity
	   – temperature uniformity
	   – minimizing end effects

Size:	– diameter > 4 x maximum grain size – height = 3 x diameter
Coring Speed:	– strength at 375 RPM was 38% > strength at 1400 RPM – " " was 3% > " at 525 RPM – 375 RPM was adopted for extracting cylindrical cores from brick
End Surfaces:	– high temperature capping avoided to keep consistent system deformation – grinding caused grain separation – automatic slow speed sawing at feed rate of 0.02"/min was adopted
Skill of Operator:	– strength for experienced in coring was 34% > inexperienced in coring – " " sawing was 5% > " in sawing
Slag Impregnation Position:	– horizontal impregnation results in length uniformity – vertical " " in cross section " – vertical position adopted for slag impregnation

Table 9.2

Specimen Preparation Procedures

Note: Strength values are reported for CPS-82C-18M.

1. specimen shape: circular cross—sections are preferred to rectangular ones for temperature uniformity, load uniformity and minimizing end effects;

2. specimen size: the diameter was chosen to be larger than three to four times the diameter of the maximum grain (1" for cold—pressed sintered materials); a height to diameter ratio of 3 was used to minimize end effects;

3. coring speed: higher coring speeds were found to cause damage in the specimen and decrease its strength (strength decrease of about 40% was observed at 1400 RPM compared to 375 RPM); damage due to coring at 375 RPM was found to be small enough, and 375 RPM is adopted;

4. end surfaces preparation: high temperature capping was not used to maintain consistent system deformation; grinding was found to cause grain separation at end surface; automatic slow—speed sawing of end surfaces at a feed rate of 0.02"/min is adopted;

5. skill of operator: unskilled operators were found to produce weaker specimens; this parameter could be related to the feed rate whereas unskilled operators do not maintain the proper feed rate during coring or sawing; and

6. slag impregnation method: impregnation uniformity along the length or across the cross—section of the specimen were observed for horizontal and vertical positions of slag impregnation; the vertical position is adopted for further testing.

Brick Characterization (Table 9.3)

Cold—pressed sintered bricks are inhomogeneous and anisotropic (Fig. 5.9). In

	Cold-Pressed Sintered 82C-18M	Fused-Cast FC-59A-27C-6M
Inhomogeneity:	– interior strength 8% > corner	– top strength 22% < bottom – interior strength 31% < corner

Anisotropy:	– orthotropic
	– core parallel to pressing direction
	  is 15% stronger core perpendicular
		– anisotropic
		– no correlation between parallel and
		  perpendicular to free surface
		– <26% difference transverse strength

Size of Brick:	———	– strength of long shallow brick 37% > strength of above deep square one
Production Batch:	Variability between bricks from different production batches is twice as large as between bricks from same production batch	———

Table 9.3

Brick Characterization

CPS–82C–18M an 8% increase in strength was observed for interior specimens compared to corner specimens. This may be related to the increased friction between the material and the mold at the corners during cold–pressing that might be resulting in a more porous material next to the corners. Specimens extracted in the direction parallel to the pressing direction were found to be 15% stronger than those in the perpendicular direction.

The behavior of fused–cast bricks is not only anisotropic and inhomogeneous (Figs. 7.2 and 7.3), but also depends on the size of the brick (Fig. 7.4). This is explained by the fact that different size bricks have different cooling rates during processing. The following variations in strength properties were observed for FC–59A–27C–6M: the top is about 22% weaker than the bottom of the brick, the corner is 31% stronger than the interior, a maximum difference of 26% between cores extracted with their axis parallel to and the ones with their axis perpendicular to the free surface, and about 37% increase for a shallow long brick compared to a deep square brick.

The variation in properties between bricks belonging to different production batches was found twice as large as the one for bricks from the same production batch.

All standard specimens used in the current thermomechanical testing were extracted from an interior position on the brick in a direction parallel to the pressing direction in cold–pressed sintered materials and perpendicular to the free surface in fused–cast materials. All specimens were taken from the same production batch.

9.2.2 Behavior Under Monotonic or Constant Compressive Loads

Macroscopic Deformation and Fracture Behavior

Behavior Under Monotonic Loads (Table 9.4)

For all the materials studied, two distinct behavioral trends were observed with respect to temperature: (1) at temperatures below a transition temperature, roughly equal to $T_m/2$ (where T_m is the melting temperature of the material), the deformation behavior is linear elastic with a brittle final fracture; and (2) at temperatures greater than this transition temperature, significant non–linear deformations were observed (Figs. 5.11, 6.3, and 7.5).

The material behavior does not seem to be affected by various strain rates for temperatures below $T_m/2$ (Fig. 5.13). For temperatures above $T_m/2$ three distinct behavioral trends were observed with respect to strain rate (fig. 5.15): (1) for strain rates higher than $\dot{\epsilon}_{trans}$ (where $\dot{\epsilon}_{trans}$ is a transition strain rate dependent on the material and temperature) linear inelastic deformations were observed with a brittle final fracture; (2) for strain rates around $\dot{\epsilon}_{trans}$ fracture initiates prior to the peak load, and crack growth is unstable until final fracture at loads slightly lower than the peak load; and (3) for strain rates lower than $\dot{\epsilon}_{trans}$, fracture initiates prior to the peak load, and crack growth is stable until final fracture at loads reduced almost to zero.

Variation of the Material Properties with Temperature (Table 9.4)

The material properties also appear to follow two different trends above and below a transition temperature roughly equal to $T_m/2$. Two different strength variations with temperature were observed depending on the materials. For all materials (Figs. 5.17, 6.6 and 7.6), except the cold–pressed sintered high–alumina, a

	Room T $<$ Temperature $<$ 0.5 T_m	0.5 T_m $<$ Temperature $<$ 0.7 T_m
Stress-strain Curves:	- linear elastic deformations - brittle final fracture	- significant non-linear deformations especially in post-peak region
Strain Rate Effects:	- no effect for $1E-4/\text{sec} < \dot{\epsilon} < 1E-6/\text{sec}$ - CPS-82C-18M: $(\Delta S/S)/\ln\Delta\dot{\epsilon} = -0.009$ $(\Delta\epsilon_f/\epsilon_f)/\ln\Delta\dot{\epsilon} = +0.035$	- transition $\dot{\epsilon}$ observed: non-linear deformations & unstable fracture - $\dot{\epsilon} >$ trans: linear def, brittle fract - " $<$ " : non-linear def, stable frac $(\Delta S/S)/\ln\Delta\dot{\epsilon} = -0.05$ $(\Delta\epsilon_f/\epsilon_f)/\ln\Delta\dot{\epsilon} > +0.13$
Strength:	- slower rate of change with T (K) $(\Delta S/S)/(\Delta T/T_m) =$ + 0.3 for CPS-90A-10C - 0.6 for CPS-82C-18M - 1.3 for HP-90A-10C	- higher rate of change with T (K) $(\Delta S/S)/(\Delta T/T_m) =$ - 1.5 for CPS-90A-10C -10.2 for CPS-82C-18M - 7.4 for HP-90A-10C
Associated Peak ϵ:	- slower rates of increase with T 0.2% to 0.45% for CPS-90A-10C	- higher rates of increase with T 0.45% to 1.35% for CPS-90A-10C
Area: $\int\sigma d\epsilon$	- almost constant 30 psi to 60 psi for CPS-90A-10C 800 psi to 1200 psi for HP-75A-25C	- increases with T 60 psi to 300 psi for CPS-90A-10C 1200 psi to 2000 psi for HP-75A-25C
Macrocrack θ from Compressive Axis:	- 0 degrees or - 15 to 60 degrees	- 15 to 60 degrees
Variability: Standard Deviation	- Strength of CPS-90A-10C: S.D. of 10% @ 75F vs. S.D. of 1.2% @ 2000F - Peak strain of CPS-90A-10C: S.D. of 19% @ 75F vs. 6% @ 2000F	

Table 9.4
Findings from Monotonic Tests

slow rate of decrease in strength was observed for temperatures below transition (strength decrease was proportional to $T^{1/2}$, Eq. 5.1), and a faster rate of decrease in strength was observed for temperatures above transition (strength decrease was proportional to T, Eq. 5.2). For the cold–pressed sintered high–alumina, the maximum strength was observed at about $T_m/2$, and the strength decreased for temperatures higher than $T_m/2$ (Fig. 5.18).

For all materials, the variations with temperature of the associated peak strain, fracture stress and fracture strain, and equivalent measure of toughness were found to be similar. Peak strains (associated with the peak stress on the stress–strain curve) as well as fracture strains (strains at final fracture) showed higher rates of increase with temperatures above transition (Fig. 5.22). For the same temperature above transition, the peak and fracture strains increased significantly with decreasing strain rates for cold–pressed sintered materials. For temperatures below transition, the strains were linear elastic with insignificant inelastic part. However, for temperatures above transition significant inelastic non–linear strains developed. Initial stiffnesses on the stress–strain curve showed higher rates of decrease with temperatures above transition. For the same temperature above transition, the initial stiffness decreased with decreasing strain rates for cold–pressed sintered materials. The equivalent toughness (defined as the area under the stress strain curve) showed higher rates of increase with temperatures above transition (Figs. 5.25, 6.15 and 7.9).

The variability in material properties (such as Table A.9) was smaller at elevated temperatures (such as a standard deviation, expressed as % of the mean, in strength values of 10% at 75°F compared to 1.2% at 2000°F for CPS–90A–10C). The variability in associated peak strains was larger than the one for strength

(standard deviation of 6% in associated peak strains at 2000°F for CPS–90A–10C).

At room temperature both vertical and inclined macrocracks seemed to cause final fracture, while at elevated temperatures inclined macrocracks seemed to be predominant (Fig. 5.26).

Behavior under Constant Loads (Table 9.5)

Short–term creep tests were conducted at constant temperatures to examine the nature of non–linear deformations. At temperatures lower than $T_m/2$ creep strains under constant loads were small compared to the elastic strains that developed in the material in monotonic tests. At temperatures above $T_m/2$ the creep strains under constant loads were of the order of the strains that developed in the material in monotonic tests (Fig. 5.28). A significant part of the non–linear deformations in monotonic tests at temperatures above transition appeared to be due to short–term creep. The results of the short–term creep tests were combined with long–term creep results on similar materials by McGee and Konrady (1983–1987) to produce deformation maps (Figs. 5.34 to 5.36). The comparison of a deformation map for CPS–90A–10C with a Gandhi and Ashby's (1983) map for alumina predicts two major mechanisms: brittle intergranular fracture and intergranular creep fracture. An activation energy of 185 kJ/mole was found for CPS–90A–10C between 1500°F and 2400°F at 13 ksi. This is in the same range as activation energies reported by other researchers (McGee and Wiedemeier, 1985a). An obtained stress exponent of 1.83 indicates the importance of diffusional mechanisms.

Constant Load, Constant T Tests:	- creep rates for $T < 0.5\ T_m$ are small (2E-8/sec @ 60%S, 1500F, CPS-90A-10C) - " " $T > 0.5\ T_m$ significant (2E-6/sec " , 2400F, ") - CPS-82C-18M exhibit higher creep rates than CPS-90A-10C (4E-6/sec @ 60%S, 2400F, CPS-82C-18M) - activation energy of 185 kJ/mole compares well with other researchers - stress exponent of 1.83 showing importance of diffusion mechanisms
Mechanism Maps:	- comparison of obtained maps for CPS-90A-10C with alumina map from Ghandi & Ashby shows two mechanisms: brittle intergranular fracture (high σ) and intergranular creep fracture (low σ); good correlation
Constant Load, Increasing T Tests	- slower heating rates (100°F/hr vs. 250°F/hr) produce higher final strains and smaller deformation rates

Table 9.5

Constant Load Tests

Constant loads, increasing temperature tests were carried to provide a measure of the transient strain (Fig. 5.38). Slower heating rates (100°F/hr) were observed to produce higher final strains, and slower creep strain rates than faster heating rates (250°F/hr). For CPS–90A–10C, at a temperature of about 1300°F the creep strain rate increased abruptly for both heating rates. This temperature seems to be a material property.

The three previously mentionned tests, i.e. monotonic loads at constant temperature, constant loads at constant temperature and constant loads under increasing temperatures are needed to validate constitutive models of the material behavior under the complex load and temperature histories encountered in the process vessels.

Microscopic Mechanisms (Table 9.6)

The microstructure of materials tested under monotonic loads is examined first. As test temperature increases the total % cavity volume of microcavities (Figs. 5.63 and 5.64b) increases significantly (14%, 20% and 34% for CPS–90A–10C non–tested, tested at 1500°F and tested at 2400°F respectively). Two different deformation mechanisms seem to control at temperatures above and below the previously observed transition temperature of roughly $T_m/2$. For temperatures lower than transition, narrow cavities with a width to length ratio (W/L) smaller than 1/8, and orientations from 15° to 60° to the applied compression direction seem to dominate; in cold–pressed sintered materials most of these narrow cavities occur at the interface between the grains and the matrix (Figs. 5.59 and 5.65). For temperatures above transition, large pores with no specific orientation seem to be the major factor in the deformation mechanism (Figs. 5.60 and 5.65).

	Room T < Temperature < 0.5 T_m	0.5 T_m < Temperature < 0.7 T_m
Cavity W/L: Monotonic CPS-A-C	– number of cavities, W/L < 1/4: 40% – cavity volume, W/L < 1/4: 50%	– number of cavities, W/L < 1/8: 55% – cavity volume, W/L > 3/4: 80%

Cavity orientation
θ to applied load:
Monotonic CPS-A-C
	– cavity volume =
	    26% for 15 < θ < 30 degrees
	    36% 45 < θ < 60 degrees
		– number of cavities with 0<θ<15 deg
		  = 31%
		– volume of cavities with no specific
		  orientation = 80%

Controlling Factor
Monotonic Tests:
	– narrow interface cavities with
	  15-60 deg. orientation
		– large pores with no specific
		  orientation

Other Factors, Monotonic Tests:		– large number transgranular cavities – grain growth
Cavity: Creep Tests	– insignificant cavity volume increase wrt virgin material	– significant large pores – creep cavitation is major mechanism

Table 9.6
Microstructural Characterization for Monotonic and Creep Tests

The observations made on specimens tested under creep loads correlate well with the previous discussion. For temperatures below $T_m/2$ insignificant cavity volume was observed, indicating insignificant contributions of creep to the total deformation (Fig. 5.66). For temperatures above $T_m/2$ large pores, similar to the ones in monotonically tested specimens, were observed (Fig. 5.67). Creep cavitation seems to be the major deformation mechanism at temperatures above transition in the studied material. The cavity volume in CPS–82C–18M is larger than the one in CPS–90A–10C (Figs. 5.69 and 5.70), that also correlates with the higher creep strain rates (by about an order of magnitude) observed in CPS–82C–18M compared to CPS–90A–10C.

For temperatures above transition, the number of intra–granular cavities with both dimensions smaller than 6 μm increases significantly and grain growth is observed.

The microscopic cracking patterns seem to be affected by the homogeneity of the microstructure. Going from the cold–pressed sintered to the fused–cast to the hot–pressed materials, a more homogeneous microstructure was observed (Figs. 5.58, 6.25 and 7.12) that correlates with more defined cracking patterns.

The two main observed interactions of microcracks are "en echelon" and "en passant". In an "en echelon" interaction the microcracks extend first by kinking (Fig. 5.74), and then join to form longer networks. In an "en passant" interaction parallel microcracks join along directions perpendicular to their propagation direction (Fig. 5.73). Interactions of various "en passant" formations were also observed.

The bulk density measurements confirm the microscopic observations. The bulk density decreases at higher test temperatures indicating higher amounts of

microcracking at higher temperatures. The density after testing shows higher rates of decrease for temperatures above $T_m/2$, indicating higher cavity volume for temperatures above $T_m/2$. The fracture strains increase with the decrease in density (Fig. 5.76). The fracture strains are proportional to 3/2 power of the density decrease for temperatures below $T_m/2$. The open porosity is also found to decrease with higher test temperature.

9.2.3 Behavior Under Cyclic Compressive Loads (Table 9.7)

The deformations under cyclic loads appeared to follow two distinct trends below and above a similar transition temperature of roughly $T_m/2$ observed in previous results. At temperatures below transition initial cycles produced significant amounts of inelastic strains, and later cycles accumulated relatively less inelastic strains. Large amounts of inelastic strains were observed immediately before final fracture (Fig. 5.41). At temperatures above $T_m/2$ all cycles accumulated about the same amount of inelastic strains (Fig. 5.42).

Cyclic test results àt elevated temperatures were used to produce three—dimensional failure surfaces showing the interaction of temperature, stress as % of monotonic strength and number of cycles at failure (Fig. 5.44). At high temperatures the final fracture of the specimen occurs after a few cycles (such as 4 cycles at 2400^OF and 90% of the monotonic strength, f_p, and 15 cycles at 2400^OF and 80% f_p). At lower temperatures the material can sustain a greater number of cycles before final fracture (75 cycles at 75% f_p and room temperature).

9.2.4 Effect of Environmental Factors on the Material Behavior (Table 9.8)

	Room T $<$ Temperature $<$ 0.5 T_m	0.5 T_m $<$ Temperature $<$ 0.7 T_m
Deformations Under Cyclic Loads	− initial cycles −> large inelastic ϵ − intermadiate " −> less " " − final cycle before final fracture −> large deformation	− all cycles exhibit similar deformations

Number of Cycles to Failure	CPS-90A-10C:
	   75F & 80%S −> N = 68
	   75F & 90%S −> N = 20
	
	 1500F & 80%S −> N = 36
	 1500F & 90%S −> N = 17
	
	Three dimensional failure surfaces: T − %S − N; may be useful to designers
		CPS-90A-10C:
		
		  2400F & 80%S −> N = 15
		  2400F & 90%S −> N = 4

Table 9.7

Findings from Cyclic Tests

342

	Room T < Temperature < $0.5\ T_m$	$0.5\ T_m$ < Temperature < $0.7\ T_m$
Slag Impregnation:	– slag-impregnated materials exhibit higher strength (3 times stronger for CPS-90A-10C) and stiffness than as-manufactured materials	– for T above 2400F ($0.6\ T_m$) slag-impregnated CPS-90-10C is weaker than as-manufactured CPS-90A-10C
Reducing atmosphere (partial oxygen pressure= 1E-8 atm)	– no adverse effect on as-manufactur. and slag-impregnated materials	– no adverse effect on as-manufactur. materials and slag-impregnated CPS-90A-10C – reduces strength of slag-impregnat. CPS-82C-18M by about one-half
X-Ray Diffraction:	– x-ray diffraction indicates that open porosity is a major factor for penetration into refractory – %Si: as-manufac. CPS-90A-10C: No Si, slag: 46.4% Si; vs. in slag-impregn. CPS-90A-10C: matrix: 4.5% Si, next to pore: 10.3% Si, inside pore:22.8% Si	
Porosimeter Tests:	– confirm results of x-ray diffraction as-manufactured CPS-90A-10C: 16.5% open pores slag-impregnated CPS-90A-10C: 2.7 open pores	
Mechanism of Slag Penetration:	– slag penetrates material through open porosity, solidifies and acts as glassy bond to strengthen matl.	– as T > $0.6\ T_m$ slag in pores weakens material, thus, facilitates corrosion process

Table 9.8
Environmental Effects on Material Behavior

Effect of Slag–Impregnation at the Macroscopic Level

The room temperature strength of slag–impregnated materials was found higher than the one for as–manufactured materials (77 ksi and 23 ksi at $75^{\circ}F$ for slag–impregnated and as–manufactured CPS–90A–10C respectively, Fig. 5.49). However, at elevated temperatures the strength of slag–impregnated materials was lower than the one of as–manufactured materials (20 ksi and 22 ksi at $2400^{\circ}F$ for as–manufactured and slag–impregnated CPS–90A–10C respectively, Fig. 5.49). The initial stiffness of the slag–impregnated materials showed a higher rate of decrease with temperatures above $T_m/2$ compared to as–manufactured materials. The results obtained for thermomechanical properties of slag–impregnated materials correlate well with the ones obtained from corrosion tests (Bakker et. al., 198x) that show insignificant corrosion at low temperatures.

Microscopic Observations in Slag–Impregnated Materials

Due to slag–impregnation grain growth was observed in both the alumina–chromia and chromia–magnesia systems (Fig. 5.72). Various new phases were observed as well.

X–ray microanalysis showed that open porosity is a major factor in slag–impregnation (Table 5.3). This was concluded by observing the changes in chemical compositions in regions with no–pores, next to a pore, and inside a pore (such as the change in Si content). The as–manufactured CPS–90A–10C contained negligible amounts of Si compared to about 46% Si in the Western acid slag. The slag penetration in CPS–90A–10C in a no–pores region was not significant (4% Si); however, the slag penetration was significant in regions next to a pore (10% Si), and extensive inside the pores (23% Si).

The results from the mercury porosimeter tests confirm that open—porosity was a major factor in slag—penetration (16% and 2.5% open porosity for as—manufactured and slag—impregnated CPS—90A—10C respectively, Table 5.4).

Effect of Reducing Atmospheres

A reducing atmosphere (partial oxygen pressure (P_{0_2}) of 10^{-8} atm) did not seem to affect the behavior of as—manufactured CPS—90A—10C; it does affect, however, the behavior of as—manufactured CPS—82C—18M, where an increase of about one third in initial stiffness was observed at $2200^\circ F$ (Fig. 5.47).

Reducing atmospheres did not seem to affect the behavior of slag—impregnated CPS—90A—10C but significantly reduced the strength of slag—impregnated CPS—82C—18M at temperatures above $T_m/2$ (Fig. 5.55).

9.2.5 Material Selection (Table 9.9)

Manufacturing Process

Comparing the three different manufacturing processes for the materials tested, going from cold—pressed sintered (CPS) materials, to fused cast (FC) materials, to hot—pressed (HP) materials, the following is observed:

— the monotonic strength increases (19 ksi for CPS—82C—18M, 78 ksi for FC—7A—78C—8M and 144 ksi for HP—80C—20M at $70^\circ F$); however, the rate of decrease in strength with temperature is greater;

— the associated peak strain and the final fracture strain increase;

— the equivalent measure of toughness increases;

— the creep strain rates seem to decrease for materials with the same chemical composition at the same load level (and to increase at the same % of

Manufacturing Process: Going CPS -> FC -> HP	- maximum grain size decreases; 0.25" for CPS-90A-10C, 0.001" for HP-90A-10C - homogeneity of microstructure increases - porosity decreases - strength increases; 19ksi:CPS-82C-18M, 78ksi:FC-78C-8M, 144ksi:HP-80C-20M - rate of strength decrease with T is greater - associated peak and final fracture strains increase - creep strains decrease at same load level (increase at same % strength) - cost of the material increases
Alumina-Chromia vs Chromia-Magnesia:	- alumina-chromia is preferred for thermomechanical properties - chromia-magnesia is preferred for penetration by slags
$%Cr_2O_3$ Content in Alumina-Chromia:	- higher chromia contents in the hot-pressed alumina-chromia seem to result in improved thermomechanical properties
Tabular vs. Fused-Cast Grains:	- as-received fused picrochromite grains (before manufacturing) were cracked - tabular alumina grains were not cracked after their use in manufacturing
Material Database:	- material database is assembled for obtained thermomechanical data and compiled modulus of rupture and thermophysical data

Table 9.9
Material Selection

346

monotonic strength level);

— the microstructure is finer and more homogeneous (maximum grain size of 0.25" for CPS–90A–10C compared to 0.001" for HP–90A–10C);

— the total porosity and the open porosity decrease; for HP materials a decrease of slag penetration is expected compared to CPS; and

— the cost of the material increases based on information from various manufacturers.

Comparison of the Alumina–Chromia and Chromia–Magnesia Systems

Comparing the alumina–chromia and the chromia–magnesia materials, it is noted that alumina–chromia materials manifested better thermomechanical properties in monotonic compression (such as higher strength, smaller rates of decrease in strength with temperature, higher associated peak strains, and higher equivalent measures of toughness). The alumina–chromia materials also showed smaller creep strain rates. On the other hand, the chromia–magnesia materials exhibited smaller degrees of impregnation by slags.

Effect of Chromia Content in the Hot–Pressed Alumina–Chromia System

The tests on three hot–pressed alumina–chromia (with 90%, 50% and 25% Al_2O_3 and the balance of Cr_2O_3) give some indications of the variation in thermomechanical properties with chemical composition. The strength of hot–pressed alumina–chromia refractories seemed to increase monotonically with chromia content. Material HP–25A–75C (with 75% Cr_2O_3) had the highest strength of the three tested alumina–chromia. However, it is possible that a chromia content between 50% and 75% might give the highest strength, and it suggested to test a

62% Cr_2O_3–38% Al_2O_3 hot–pressed refractory to check this assumption. Material HP–75A–25C had approximately the same associated peak strain values than that of HP–50A–50C and HP–90A–10C. Both the initial stiffness and measure of toughness increased with increased chromia content. It appears that hot–pressed chromia–alumina refractories with higher chromia contents are probably better candidate materials under monotonic compression. However, it is noted that in the same temperature range, HP–25A–75C has a greater rate of decrease in strength than HP–90A–10C.

Open Porosity

Open porosity was found to be a major factor for slag penetration into the material. Materials with less open porosity are preferred to reduce the extent of slag–impregnation.

Material Database

A preliminary material database of thermomechanical and thermophysical properties summarizes the data obtained from the completed test program, and data compiled from manufacturers and the literature.

9.3 CONCLUSIONS

Within the limitations of the present test program with respect to the loading conditions and materials studied, the following conclusions from this study are highlighted:

1. A transition temperature roughly equal to one–half the melting temperature of the material is observed to separate two behavioral regions. Below this transition temperature linear elastic

deformations are observed with a brittle final fracture. Above this transition temperature the material behavior is strain rate dependent, and the material behavior follows three different trends related to a temperature dependent transition strain rate: (a) for strain rates above transition, linear inelastic deformations with brittle final fracture are observed, (b) for strain rates around transition, significant non—linear inelastic deformations in the pre— and post—peak regions with unstable fracture propagation and final fracture at loads slightly less than peak are observed, and (c) for strain rates below transition, non—linear inelastic deformations in the pre— and post—peak regions with stable fracture propagation and final fracture at loads almost reduced to zero are observed.

2. Short—term creep seems to be the major factor in non linear deformations above the transition temperature. Obtained activation energies are in the same range as those obtained by other researchers. Stress exponents lower than 2 indicate the presence of diffusional mechanisms. Comparison of established deformation maps with mechanism maps from Ghandi and Ashby (1983) indicates brittle intergranular and creep intergranular fracture as major mechanisms.

3. For temperatures below transition, microscopic cavities with small width to length ratios oriented at 15° to 60° to the direction of the applied compression seem to be the major factor in the deformation and fracture mechanism. At temperatures above transition, large pores with no specific orientation are predominant. The coalescence and growth of these large pores seems to be occurring under creep, and creep cavitation seems to be a major deformation and fracture mechanism for temperatures above transition. Significant transgranular cavitation and grain growth are also observed at temperatures above transition.

4. The study of the material behavior should be carried out keeping in mind the inhomogeneity and anisotropy in the material behavior and the variability of the material properties.

5. In cyclic load tests at temperatures below transition the first loading cycles and the last cycle before final fracture exhibit larger deformations than intermediate ones, while at temperatures above transition the deformation of all cycles is similar. The number of cycles to final fracture decrease with temperature and load level. The rate of decrease in number of cycles to final fracture with temperature is greater than the rate of decrease load level.

6. Open porosity is found to be the major factor for slag impregnation. Slag is observed to fill the material pores and act as a glassy bond at temperatures below transition to increase the material strength and stiffness. At temperatures above transition slag—impregnated materials exhibit higher rate of strength dec ase with temperature than as—manufactured ones, and at $2400^{\circ}F$ the strength of slag—impregnated alumina—chromia is smaller than the as—manufactured one.

7. Reducing atmospheres do not seem to adversely affect the properties of as—manufactured alumina—chromia and chromia—magnesia. Reducing atmospheres decrease the strength of slag—impregnated chromia—magnesia at temperatures above transition.

8. For the same material system, going from cold—pressed sintered to fused—cast to hot—pressed materials, the grain size decreases, the homogeneity of the microstructure increases, the strength increases (but the rate of decrease in strength also increases), the creep strain rates decrease at same load level, and the cost of the material is higher.

9. The alumina–chromia system may be preferred to the chromia–magnesia for its thermomechanical properties, and the chromia–magnesia system may be preferred for its smaller degree of slag–impregnation. An increase in the chromia content in hot–pressed alumina–chromia seems to produce better thermomechanical properties. Tabular grains seem to result in better thermomechanical properties than fused grains.

9.4 SUGGESTIONS FOR FUTURE RESEARCH

Additional Characterization of the Material Behavior

The completed test program led to the development and evaluation of new material data which provides insight into the understanding of the thermomechanical behavior of refractories. The quantitative information developed constitutes a part of the data base necessary for use in the development of predictive design methods. There is a need for a more in depth study of specific parameters, and there is a need for evaluating different materials under different loading conditions.

Based on the conclusions from the current study, more in–depth characterization of specific parameters is needed, such as the effect of open porosity and chromia content on the material behavior and a more precisely determined transition behavior with respect to temperature and strain rate. Open porosity was found to be a major factor in slag–impregnation. It can be useful to study the effect of slag–impregnation on hot–pressed materials (with closed pores) at both macroscopic and microscopic levels to verify current findings. Chromia content in the alumina–chromia system was found to improve the thermomechanical properties of the hot–pressed refractory. It can be interesting to study one more composition for the hot–pressed alumina–chromia, namely, 62% Cr_2O_3 and 38% Al_2O_3 to confirm the obtained results with respect to strength and toughness measure increase; and to

study the effect of chromia increase in the cold—pressed sintered alumina—chromia refractories and try to deduce if this effect is independent of the manufacturing process. The transition temperature and the effect of strain rate on this transition temperature need to be determined more precisely.

There is a need to characterize different types of refractory materials and to examine different loading conditions. Data is needed on the behavior of refractoriy materials used in the steel industry or petrochemical plants, as well as other types of refractory materials such as insulating refractories or elastomeric materials. Characterizing the material behavior under tensile loading, multiaxial loading or higher temperatures is needed as well. The test setup for multiaxial loading can be quite complex. It can be done by using a muffle tube capable of sustaining internal pressures along with the present test system (high temperature, low pressure), or heat—up the liquid around the specimen in a triaxial loading cell (low temperature, high pressure). The present test system limits the maximum test temperature to 2800°F. It can be interesting to characterize the thermomechanical material behavior up to the melting point.

Modeling of the Material Behavior

The conducted research effort led to the identification of some macroscopic behavior and microscopic mechanisms. There is a need for a better link between the two. This includes establishing the relations of the different kinds of mechanisms observed at temperatures below transition (narrow cavities mostly at interfaces and oriented at 15° to 60° to applied compression) and above transition (large pores with no specific orientation that seem to arise from creep cavitation) to the observed macroscopic behavioral trends below transition (linear deformations and brittle

fracture) and above transition (non linear deformations). The effect of using different kinds of grains (tabular or fused) on the material behavior needs to be quantified as well. The macroscopic behavior can be related to the different mineralogical phases present in the materials. These mineralogical phases can in turn be related to the various manufacturing processes. There is also a need to model the effect of slag–impregnation with respect to open porosity.

Previous projects at MIT in this area led to the development of constitutive material models that are linked to a finite element analysis capability. There is a need for re–evaluating these models based on the current findings. The re–evaluation will lead to the generation of new constitutive models if needed, or the calibration of the existing models.

Development of a Knowledge–Based System for Design of the Linings

Research has been conducted at the Massachusetts Institute of Technology and elsewhere on the analysis and design of linings for high temperature process vessels and on the characterization of candidate materials to be used in these linings. Knowledge is available from different sources and there is a need to organize this knowledge and to transfer it to the industry by building a knowledge–based system. This can be achieved by developing a computer system that would enable users to:

o   have access to design guidelines and to perform preliminary design;

o   perform detailed finite element analysis for final design; and

o   allow experienced engineers to modify existing or to add new capabilities through a modular program structure.

This software capability can consist of two components: a knowledge–based preliminary design advisor, and a user–friendly finite element analysis system.

REFERENCES

ACI publication SP 74 (1982), Monolithic Refractories, Lankard, D.R., editor, American Concrete Institute, Detroit, Michigan.

Air Force Materials Lab (1963), Refractory Ceramics of Interest in Aerospace Structural Applications – A Materials Selection Handbook, Report No. ASD–TRD–63–4102, Wright–Patterson Air Force Base, Ohio.

Alper, A. M., McNally R. N., Doman R. C. and Keihn, F. G. (1964), Journal of the American Cermaic Society, Vol. 47, No. 1.

Ameur–Moussa, R. (1987), "Constitutive Modeling of Concrete in Finite Element Analysis," M.S. Thesis, MIT, Cambridge, MA, June.

Anderberg, Y. and Thelanderson, S. (1976), "Stress and Deformation Characteristics of Concrete at High Temperatures," Lund Inst. of Technology, Lund, Sweden, Division of Structural Mechanics and Concrete Construction, Bulletin 54, August..

Argon, A. S., Im, J. and Safoglu, R. (1975), "Cavity Formation from Inclusions in Ductile Fracture," Metallurigan Transactions, Vol. 6A, April, pp. 825–837.

Argon, A. S. (1983), "Inhomogeneities in Creep," ASM Material Science Seminar, Philadelphia, PA., October 1–2.

ASCE Report (1982), "Finite Element Analysis of Reinforced Concrete," American Society of Civil Engineers, pp. 34–110.

ASTM (1986), Annual Book of ASTM Standards, American Society for Testing and Materials, Easton, MD.

Award, M.E. and Hilsdorf, H.K. (1972), "Strength and Deformation Characteristics of Plain Concrete Subjected to High Repeated and Sustained Loads," Civil Engineering Studies, SRS No. 372, University of Illinois, Urbana, February, 7 pp.

Baecher, G. B., and Einstein, H. H. (1981), "Size Effect in Rock Testing," Geophysical Research Letters, Vol. 8, No. 7, pp. 671–674, July.

Bakker, W. T. and Stringer, J. (1981), "Materials for Coal Gasification Combined Cycle Power Plants," Sixth Annual Conference on Material for Coal Conversion and Utilization, October.

Bakker, W. T., Greensberg, S., Trondt, M., and Gerhardus, U. (1984), "Refractory Practice in Slagging Gasifiers," American Ceramic Society Bulletin, Vol. 63, No. 7.

Bandyopadhyay, G., Chen, J., Kennedy, C. R., Diereks, D. R. (1983), "Thermal–Shock Damage of Refractories for Application in Slagging Coal Gasifiers," Journal of Materials for Energy Systems, Vol. 4, No. 4, March.

Batchelor, G. K. (1967), "An Introduction to Fluid Dynamics," Cambridge University Press, Cambridge.

Batdorf, S. B. and Heinisch, H. L. Jr. (1978), "Weakest Link Theory Reformulated for Arbitrary Fracture Criterion," Journal of the American Ceramic Society, Vol. 61, No. 7–8, July–August.

Batdorf, S. B., and Crose, J. G. (1974), "A Statistical Theory for the Fracture of Brittle Structures Subjected to Nonuniform Polyaxial Stresses," Journal of Applied Mechanics, June, pp. 459–464.

Bazant, Z.P. and Oh, B.H., (1982), "Strain–Rate Effect in Rapid Triaxial Loading of Concrete,"Journal of the Engineering Mechanics Division, ASCE, Vol. 108, No. EM5, October, pp. 764–782.

Bazant, Z.P. and Bhat, P.D., (1976), "Endochronic Theory of Inelasticity and Failure of Concrete," Journal of the Engineering Mechanics Division, ASCE, Vol. 102, No. EM4, Proc. Paper 12360, August, pp. 701–721.

Bazant, Z.P. and Shieh, C.L., (1980), "Hysteretic Fracturing Endochronic Theory for Concrete," Journal of the Engineering Mechanics Division, ASCE, Vol. 106, No. EM5, Proc. Paper 15781, October, pp. 929–950.

Bazant, Z.P. and Kim, S.S. (1979), "Plastic–Fracturing Theory of Concrete," Journal of the Engineering Mechanics Division, ASCE, Vol. 105, No. EM3, Proc. Paper 14653, June, pp. 407–428.

Bazant, Z. P., and Tsubaki, T. (1980), "Total Strain Theory and Path–Dependence f Concrete," Journal of the Engineering Mechanics Division, Journal of Engineering Mechanics, Vol. 106, December..

Berg, C. A. (1961), "The Influence of Viscous Deformation on Brittle Fracture," Ph.D. Thesis, Department of Mechanical Engineering, M.I.T., June.

Berry, T. F., Allen, W. C., Snow, R. B (1950), "Chemical Changes in Basic Brick During Service," Journal of the American Ceramic Society, Vol. 33. No. 4.

Bertrand, P. T., et al (1988), "Strengths of Fused and Tabular Alumina Refractory Grains," Ceramic Bulletin, Vol. 67, No. 7.

Bieniawaski, Z. T. and van Heerden, W. L. (1975), "The Significance of In Situ Tests on Large Rock Specimens," International Journal of Rock Mechanics and Mining Sciences, Vol. 12, pp. 101–113.

Boland, J.N. and Hobbs, B.E. (1973) "Microfracturing Processes in Experimentally Deformed Periolotite," International Journal of Rock Mechanics and Mining Sciences, Vol. 10, pp. 623–626.

Bonar, J. A., Kennedy, C. R., and Swaroop, R. G. (1980), "Coal–Ash Slag Attack and Corrosion of Refractories," American Ceramic Society Bulletin, Vol. 59, No. 4.

Bortz, S.A., and Burton, K.T. (1969), "Analysis and Review of Mechanical Testing Procedures for Brittle Materials," Structural Ceramics and Design, Gordon and Breach Publishers, New York, NY.

Bowen, D. H. (1968), "Fiber–Reinforced Ceramics," Fibre Science and Technology, Vol. 1, No. 1, July.

Brace, W.F. and Bombolakis, E.G. (1963), "A Note on Brittle Crack Growth Compression," Journal of Geophysical Research, Vol. 68, pp. 3709–3713.

Brace, W.F. and Martin, R.J. (1968), "A Test of the Law of Effective Stress for Crystalline Rocks of Low Porosity," International Journal of Rock Mechanics and Mining Sciences, Vol. 5, p. 415.

Bray, D. J., Smyth, J. R. and McGee, T. D. (1980), "Creep of 90% Al_2O_4 Refractory Concrete," American Ceramic Society Bulletin, Vol. 64, No. 7.

Bremser, A.H. and Buyukozturk, O., (1982), "Biaxial Compressive Testing of Refractory Concretes," Proceedings of the Conference on Advances in Material Characterization, Alfred University, Alfred, N.Y., August.

Bremser, A. H. et al. (1981), "Refractory Material Property Testing," The Babcock and Wilcox Company, Alliance, Ohio.

Bresler, B. and Pister, K.S., (1958), "Strength of Concrete Under Combined Stresses," American Concrete Institute Journal, Vol. 55, September, pp. 321–345.

Bresler, B. (1976), "Reinforced Concrete Engineering," Volume 1, Materials, Structural Elements, Safety, Wiley, New York.

Brezny, R. and Semler, C. E. (1984), "Oxidation and Diffusion in Selected Pitch–Bonded Magnesia Refractories," Journal of the American Ceramic Society, Vol. 67.

Brockenbrough, J. R., Forsythe, L. Ed. and Rolf, R. L., (1986), "Reliability of Brittle Materials in Thermal Shock,," Journal of the American Ceramic Society, 69, [8], pp. 634–637, August.

Brockenborough, J. R. and Suresh, S. (1987), "Constitutive Behavior of a Microcracking Brittle Solid in Cyclc Compression," J. Mech. Phys. Solids, February.

Brown, J. J. (1983), "Co–Disintegration of High Alumina Castables for Coal Gasifiers," Department of Materials Engineering, Virginia Polytechnic Institute and State University, Blacksburg, VA.

Brown, N. R. (1983), "Gaseous Corrosion Resistance of Refractories for Coal Gasifiers," U. S. Bureau of Mines.

Budiansky, B. (1983), "Micromechanics," Computers & Structures, Vol. 16, No. 1–4, pp. 3–12.

Budnikov, P. P. (1964), "The Technology of Ceramics and Refractories," The MIT Press, Cambridge, MA.

Bunting, E. N. (1931), Bureau of Standards Journal of Research, Vol. 6, No. 6, p. 948.

Buyukozturk, O. and Tseng, T.M. (1982), "Thermomechanical Behavior of Refractory Concrete Linings," Journal of the American Ceramic Society, Vol. 65, No. 6, June.

Buyukozturk, O. and Tseng, T.M. (1983), "Heat Conduction through Layered Refractory Linings," Journal of Engineering Mechanics Division, ASCE, Vol. 109, No. EM3, June.

Buyukozturk, O. and Shareef, S.S. (1983), "Constitutive Modeling of Concrete in Finite Element Analysis," Research Report R83–16, MIT, Department of Civil Engineering, December.

Buyukozturk, O. and Shareef, S. S. (1984), "Constitutive Modeling of Concrete in Finite Element Analysis," Computers and Structures, Vol. 21, No. 3, Pergamon Press, pp. 581–610.

Buyukozturk, O., (1977), "Nonlinear Analysis of Reinforced Concrete Structures," Journal of Computers and Structures, Vol. 7, February, pp. 149–156.

Buyukozturk, O., Nilson, A.H. and Slate, F.O. (1972), "Deformation and Fracture of Particulate Composite," Journal of the Engineering Mechanics Division, ASCE, June, pp. 581–593.

Buyukozturk, O. and Connor, J., (1979), "A Numerical Thermomechanics Model for Refractory Liner–Anchor Interactions," (Summary), Proceedings of the Fourth Annual Conference on Materials for Coal Conversion and Utilization, Gaithersbury, Maryland, October.

Buyukozturk, O., (1981), "Analysis of Coal Gasification Vessels," (Summary), Proceedings of the Sixth Annual Conference on Materials for Coal Conversion and Utilization, Gaithersburg, Maryland, October.

Buyukozturk, O., (1982), "Behavior of Coal Gasification Vessels," (Summary), Proceedings of the Seventh Annual Conference on Materials for Coal Conversion and Utilization, Gaithersburg, Maryland, November.

Campbell, R. H. and Tobin, R. E. (1967), "Core and Cylinder Strengths of Natural and Lightweight Concrete," ACI Journal, October.

Casey, J. and Naghdi, P. M. (1984), Computational Aspects of Strain–Space Plasticity,," Discussion, Journal of the Engineering Mechanics Division, ASCE, Vol. 110, No. 3, March, pp. 485–488.

Chehayeb, F. S. (1985), "Interactive Computer Analysis of Reinforced Concrete Using Finite Elements," Degree in Master of Science, Department of Civil Engineering, Massachusetts Institute of Technology, May.

Chen, E. S. (1984), "Behavior of Refractory Linings for Slagging Gasifiers," Ph.D. Thesis, Massachusetts Institute of Technology.

Chen, E.S. and Buyukozturk, O., (1984), "Behavior of Refractory Linings for Slagging Gasifiers," MIT, Research Report, June.

Chen, E. S. and Buyukozturk, O. (1985a), "Methodology for Thermomechanical Analysis of Brittle Systems," American Ceramic Society Bulletin, Refractories Issue, July.

Chen, E.S. and Buyukozturk, O. (1985b), "Thermomechanical Behavior of Refractory Linings in Slagging Gasifiers, " American Ceramic Society Bulletin, Refractories Issue, July.

Chen, E. S. and Buyukozturk, O. (1985c), "Modeling of Long Term Corrosion Behavior of Refractory Linings in Slagging Gasifiers," American Ceramic Society Bulletin, Refractories Issue, July.

Chen, W.F., (1982), "Plasticity in Reinforced Concrete, McGraw—Hill Book Co., Inc., New York, N.Y.

Chen, A.C.T. and Chen W.F., (1975), "Constitutive Relations for Concrete,"Journal of the Engineering Mechanics Division, ASCE, Vol. 101, No. EM4, Proc. Paper 11529, August, pp. 465–481.

Chen, Y. T., Lee, T. F., Pan, H. C. and Ko, Y. C. (1984), "Effect of Cr_2O_3 on Creep Resistance of High Alumina Bauxite Refractories," American Ceramic Society Bulletin, Vol. 63, No. 7.

Chesters, J. H. (1973), Refractories Production and Properties, Iron & Steel Institute, London.

Clarke, D. R. (1983), "High Temperature Environmental Strength Degradation of a Hot—Pressed Silicon Nitride: An Experimental Test," Journal of the American Ceramic Society, Vol. 66, No. 2.

Claytor, T. N. and Ellingson, W. A. (1984), "State—of—the—Art Review of Acoustic Techniques for Application to the Nondestructive Evaluation of Refractory Concrete for Coal Gasification," Argonne National Laboratory, Argonne, Illinois, prepared for the US DOE under contract W—31—109—Eng—38
Report ANL/FE—83—23.

Coble, R. L. (1963), "A Model for Boundary Diffusion Controlled Creep in Polycrystalline Materials," Journal of Applied Physics, Vol. 34, No. 6, June.

Cooper, A. R. (1981), "Kinetics of Refractory Corrosion," Ceramic Engineering and Science Proceedings, Published by American Ceramic Society, Vol. 2, No. 11–12.

Cooper, B. R. and Ellington, W. A., Ed (1984), The Science and Technology of Coal and Coal Ultilization, Plenum Press.

Crowley, M. S. (1970), "Inspection and Repair of Refractory Concrete Linings," Chemical Engineernig Progress, Vol. 66, No. 8.

Crowley, M. S. and Johnson, R. C. (1972), "Guidelines for Installing Refractory Concrete Linings in Cold Weather," Ceramics Bulletin, Vol. 51, No. 2.

Crowley, M. S. (1975), "Refractory Problems in Coal Gasification Reactors," Ceramic Society Bulletin, Vol. 51, No. 12.

Crowley, M. S. and Wygant, J. F. (1973), "Critical Ceramic Applications in Fossil Fuel Processing," American Ceramic Society Bulletin, Vol. 52, No. 11.

Crowley, M. S. (1984), "Refractory Usage in the Process Industries," Standard Oil Company, Indiana.

Cruz, C. R., "Elastic Properties of Concrete at High Temperatures," Journal of the PCA Research and Development Lab, January 1966.

Dafalias, Y.F., (1986), "Bounding Surface Plasticity. I: Mathematical Foundation and Hypoplasticity," Journal of Engineering Mechanics, Vol. 112, No. 9, September, pp. 966–987.

Duffy, J. I. (1980), Refractory Materials, Noyes Data Corporation, Park Ridge, N.J.

Easler, T. E., Tan, C. and Putz, L. M. (1985), "Influence of Oxidizing and Reducing Environments on Coal–Slag–Induced Corrosion of Silicon Carbide Ceramics," Argonne National Laboratory, Argonne, Illinois.

Easler, T. E. (1985), "Effects of Coal Gasification Environments on Corrosion Behavior and Mechanical Properties of Siliconized Silicon Carbide," Argonne National Laboratory, Argonne, Illinois, for the US DOE, under contract W–31–109–Eng–38, ANL/FE–866.

Einstein, H. H., Baecher, G. B., and Hirschfeld, R. C. (1970), "The Effect of Size on Strength of a Brittle Rock," Proceedings of the 2nd International Congress on Rock Mechanics, Belgrade.

Elwi, A.A. and Murray, D.W., (1979), "A 3–D Hypoelastic Concrete Constitutive Relationship," Journal of the Engineering Mechanics Division, ASCE, Vol. 105, No. EM4, August, pp. 623–641.

Endell, K., Fehling, R., Kley, R. (1939), "Influence of Fluidity, Hydrodynamic Characteristics, and Solvent Action of Slag on the Destruction of Refractories at High Temperatures," Journal of the American Ceramic Society, Vol. 22.

Eusner, G. R. and Kappmeyer, K. K. (1962), "Rating of Fireclay Brick," American Ceramic Society Bulletin, Vol. 41, No. 1.

Evans, A. G., Russel, L. R. and Richerson, D. W. (1975), "Slow Crack Growth in Ceramic Materials at Elevated Temperatures," Metallurigical Transactions A, Vol. 6A, April, pp. 707–716.

Evans, A. G., (1978), "A General Approach for the Statistical Analysis of Multiaxial Fracture," Journal of the American Ceramic Society, Vol. 61, No. 7–8, pp. 302–308, July–August.

Evans, A. G., and Langdon, T. G. (1976), Structural Ceramics, Progress in Materials Science, Vol. 21, pp. 171–441.

Ewart L. and Suresh S. (1987), "Crack Propagation in Ceramics Under Cyclic Loads," Journal of Materials Science, Vol. 22.

Fardis, M. N., Alibe, B. and Tassoulas, J. L. (1983), "Monotonic and Cyclic Constitutive Law for Concrete," Journal of Engineering Mechanics, ASCE, Vol. 109, No. EM2, Proc. Paper 17871, April, pp. 516–536.

Folk, H. F., Bohling, W. C (1968), "High Temperature Strength of High Alumina Refractories," American Ceramic Society Bulletin, Vol. 47, June.

Fonseka, G. M., Murrell, S. A. F. and Barnes, P. (1985), "Scanning Electron Microscope and Acoustic Emission Studies of Crack Development in Rocks," Int. J. Rock Mech. Min. Sci. & Geomech. Abstr., Vol. 22, No. 5, pp. 273–289.

Frost, H. J., and Ashby, M. F. (1982), Deformation Mechanism Maps, Pergamon Press, Elmsford, N.Y.

Furamura, F. (1966), "The Stress–Strain Curve of Concrete at High Temperature," Tokyo Institute of Technology, Report of Meeting at Architectural Institute of Japan.

Gac, F. D. et al., (1983), "Ceramic Application Technology," Surface Gasification Materials Program Review.

Garmong, G., Paton, N. E. and Argon, A. S. (1975), "Attainment of Full Interfacial Contact During Diffusion Bonding," Metallurgical Transactions A, Vol. 6A, June, pp. 1269–1279.

Gentile, M., Sun, T. and Brown J.J. (1987), "Alkali Attack of Coal Gasifier Refractory Linings," Department of Materials Engineering, Virginia Polytechnic Institute and State University, Report ORNL/85–43397, prepared for Oak Ridge National Laboratory.

Gerstle, K. H., Aschl, H., Bellotti, R., Bertacchi, P., Kotsovos, M. D., Ko, H. Y., Linse, D., Newman, J. B., Rossi, P., Schickert, G., Taylor, M. A., Traina, L. A., Winkler, H., and Zimmerman, R. M., (1980), "Behavior of Concrete Under Multiaxial Stress States," Journal of Engineering Mechanics, Vol. 6, December.

Gilchrist, J. D. (1977), Fuels, Furnaces and Refractories, Pergamon Press, Oxford, England.

Greenberg, S. and Peoppel, R. B. (1985), "The Corrosion of Ceramic Refractories Exposed to a Synthetic Coal Slag by Means of the Rotating–Drum Technique," Argonne National Latoratory, Argonne, Illinois, prepared for the US DOE, under contract W–31–109–Eng–38, ANL/FE–85–9.

Griffith, A.A. (1924), "Theory of Rupture," Proceedings of the First International Congress for Applied Mechanics, pp. 55–63.

Griggs, D.T., Turnes, F.J., and Heard, H.C. (1960), "Deformation of Rocks at 500°C to 800°C," Griggs, D. and Hardin, J., editors, Rock Deformation, GSA Memoir.

Han, D.J. and Chen, W.F. (1985), "A Non–uniform Hardening Plasticity Model for Concrete Materials," Journal of Mechanics of Materials, Vol. 4, No. 4, December, pp. 283–302.

Hamdin, J. and Hager, R.V. (1958), "Experimental Deformation of Sedimentary Rock Under Confining Pressure: Tests at High Temperature," Bulletin American Association Petroleum Geology, Vol. 42, p. 2892.

Hansen, W. C. and Livovich, A. F. (1953), "Thermal Conductivity of Refractory Insulating Concrete," Journal of the American Ceramic Society, Vol. 36, No. 11.

Hasselman, D.P.H. (1963), "Thermal Shock by Radiation Heating," Journal of the American Ceramic Society, Vol. 46, No. 5.

Hausner, H. H. and Bowman, M. G. (1968), Fundamentals of Refractory Compounds, Plenum Press, New York, NY.

Hein and Best (1980), College Chemistry, Brooks/Cole Publishing, Monterey, California.

Heindl, R. A. and Post, Z. A. (1954), "Refractory Castables: Some Properties, and Effects of Heat Treatments," Journal of the American Ceramic Society, Vol. 37, No. 5.

Hens, H. J. (1986), "An Interactive Analysis Capability for Complex Structures and High Temperature Applications," Master of Science Degree, Department of Civil Engineering, Massachusetts Institute of Technology, February.

Hens, H.J., Chehayeb, F.S., and Tamer, F.G. (1986a), 'Arc–C: A Computer Program for the Three Dimensional Finite Element Analysis of Reinforced and Prestressed Concrete Structures," User Manual, Department of Civil Engineering, Massachusetts Institute of Technology, March.

Hens, H.J., Chehayeb, F.S., and Tamer, F.G. (1986b), "Arc–R: A Computer Program for the Three Dimensional Finite Element Analysis of Refractory Concrete Structures," User Manual, Department of Civil Engineering, Massachusetts Institute of Technology, March.

Herring, (1950), "Diffusional Viscosity of a Polycrystalline Solid," Journal of Applied Physics, Vol. 21, May. pp. 437–445.

Heuze, F. E. (1983), "High–temperature Mechanical, Physical and Thermal Properties of Granitic Rocks – A Review," Int. J. Rock Mech. Min. Sci. & Geomech. Abstr., Vol. 20, No. 1, pp. 3–10.

Hill, V. L. (1976), "Corrosion and Erosion–Corrosion of Materials in Coal Gasification Environments," Proceedings of th Eighth Synthetic Pipeline Gas Symposium, Chicago, Illinois, October.

Hoek, E. and Bieniawski, F.T. (1965), "Brittle Fracture Propagation in Rock Under Compression," International Journal of Fracture Mechanics, Vol. 1, pp. 137–155.

Holmen, J.O. (1982), "Fatigue of Concrete by Constant and Variable Amplitude Loading," American Concrete Institute, Special Publication SP–75, pp. 71–109.

Hsu, T.T. (1981), "Fatigue of Plain Concrete," Journal of the American Concrete Institute, July/August, pp. 292–305.

Huggett, L. G. (1966), "Lining of Secondary Reformers," Proc. Mat. Tech. Symposium, Pergamon Press.

Hunt, E.B., and Bradley, R.S. (1941), "Description of Hot Modulus of Rupture and Hot Crushing Strength Test and Discussion of Results," American Ceramic Society Bulletin, Vol. 20, No. 8.

ISI Publication 116, (1968), Blast–furnace refractories, Iron and Steel Institute, London, England.

Jakus, K., Wiederhorn, S. M., and Hockey, B. J. (1986), "Nucleation and Growth of Cracks in Vitreous–Bonded Aluminum Oxide at Elevated Temperatures," Journal of the American Ceramics Society, Vol. 69 [10], pp. 725–731.

Johnson–Walls, D., and Evans, A.G. (1986), "Residual Stresses in Machined Ceramic Surfaces," Journal of the American Ceramic Society, Vol. 69, No. 1, January.

Judkins, R.R., and Carlson, P.T. (1987), Introduction of the Semi–Annual Progress Reports of the US DOE, AR&TD Fossil Energy Materials Program, Oak Ridge National Laboratory, Oak Ridge, Tennesse.

Kachanov, M. L. (1982a), "A Microcrack Model of Rock Inelasticity Part I: Frictional Sliding on Microcracks," Mechanics of Materials, 1, pp. 19–27.

Kachanov, M. L. (1982b), "A Microcrack Model of Rock Inelasticity Part II: Propagation of Microcracks," Mechanics of Materials, 1, pp. 29–41.

Karfakis, M. G. (1985), "Drilling Mechanisms at Elevated Rock Temperatures," Int. J. Rock Mech. Min. Sci. Geomech. Abstr., Vol. 22, No. 6, pp. 407–417.

Kennedy, C. R. (1979), "Refractories for Application in Slagging Gasifiers," Fourth Annual Conference on Materials for Coal Conversion and Utilization, October.

Kennedy, C. R. (1980), "Compatability of Water–Cooled Refractories with a Basic Coal–Ash Slag at $1500^{\circ}C$," Journal of Materials for Energy Systems, Vol. 2, September.

Kennedy, C. R. (1981a), "Compatability of Water–Cooled Chromia Containing Refractories with a High Iron Oxide Acidic Coal Ash Slag at $1575^{\circ}C$, Journal of Materials for Energy Systems, Vol. 3, No. 3.

Kennedy, C. R. (1981b), "Coal Slag–Refractory Compatibility Studies: Progress to Date," American Ceramic Society Proceedings, Vol. 2.

Khoury, G. A., Grainger, B. N. and Sullivan, P J. E. (1985), "Transient Thermal Strain of Concrete: Literature Review, Conditions Within Specimen and Behavior of Individual Constituents," Magazine of Concrete Research, Vol. 37, No. 132.

Kingery, W. D., Bowen, H. U., and Uhlmann, D. R. (1976), Introduction to Ceramics, John Wiley & Sons, New York, N.Y.

Kotsovos, M.D. (1983), "Effect of Testing Techniques on the Post–Ultimate Behavior of Concrete in Compression," Materiaux et Constructions, Vol. 16, No. 91.

Krajcinovic, D. and Fonseka, G. U. (1981), "The Continuous Damage Theory of Brittle Materials, Part 1: General Theory," Journal of Applied Mechanics, Vol. 48, pp. 808–815.

Kranz, R. L. (1979), "Crack Growth and Development During Creep of Barre Granite," Int. J. Rock Mech. Min. Sci. & Geomech. Abstr., Vol. 16, pp. 23–35.

Kranz, R. L. (1979), "Crack–Crack and Crack–Pore Interactions in Stressed Granite," Int. J. Rock Mech. Min. Sci. & Geomech. Abstr., Vol. 16, pp. 37–47.

Krishnaswamy, K.T. (1971), "Mechanism of Failure and Microcracking of Plain Concrete Under Uniaxial Tensile Loading," Indian Concrete Journal, Vol. 45, May, pp. 204–208.

Kromp, K. and Pabst, R. F. (1983), "Application of the J Concept to Alumina at High Temperatures," Journal of the American Ceramic Society, Vol. 66, No. 2.

Kschinka, B. A., Perrella, S., Nguyen, H. and Bradt, R. C. (1986), "Strengths of Glass Spheres in Compression," Journal of the American Ceramic Society, 69, [6], pp. 467–472, August.

Kuczynski, G. (1977), "Science of Sintering," Science of Sintering, Vol. 9, No. 3, pp. 243–264.

Kupfer, H. B., and Gerstle, K. H. (1973), "Behavior of Concrete Under Biaxial Stresses," Journal of the Engineering Division, Vol. 4, August.

Lade, P.V. (1982), "Three—Parameter Failure Criterion for Concrete," Journal of the Engineering Mechanics Division, ASCE, Vol. 108, No. EM5, October.

Lam, Y.Y. (1980), "Behavior of Plain Concrete Under Cyclic Compressive Loading," S.M. Thesis, Department of Civil Engineering, M.I.T., September, 86 pp.

Lange, F.F. (1968), "Interaction Between Overlapping Parallel Cracks: a Photoelastic Study," International Journal of Fracture Mechanics, Vol. 4, pp. 287–294.

Langford, J. (1977), "Compressive Strength and Microplasticity in Polycrystalline Alumina," Journal of Material Science, Vol. 12.

Lankard, D. R. (1984), "Factors Affecting Selection and Performance of Steel—Fiber—Reinforced Monolithic Refractories," Ceramic Bulletin, Vol. 63, No. 7.

Lim, K. H. (1983), "Investigations and Design Considerations for the Refractory Lining of Coal Gasifiers," Interceramics, Vol. 33, No. 4.

Lyle, F. F., Jr. (1976), "Engineering Properties of Materials in Coal Gasifications Environments," Proceedings of the Eighth Synthetic Pipeline Gas Symposium, Chicago, Illinois, October.

MacGregor, C. W. and Fisher, J. C. (1946), "A Velocity Modified Temperature for the Plastic Flow of Metals," Journal of Applied Mechanics, March.

MacNab, A. J. (1975), "Design and Materials Need for Coal Gasification," Chemical Engineering Process, Vol. 71, No. 11.

McGee, T.D. (1984), "High Temperature Creep of Refractories for Coal Processing Vessels," U.S. Department of Energy, Fossil Energy Advanced Research and Technology Development Reports, ONRL/FMP—83/3—5; ONRL/FMP—84/1.

McGee, T.D., and Konrady, R. (1983–87), "High Temperature Creep Behavior of Refractory Bricks," Quarterly Reports published by the US DOE Fossil Energy Program.

McClintock, F. A. (1955a), "The Statistical Theory of Size and Shape Effects in Fatigue," Journal of Applied Mechanics, Vol. 22, No. 3, p. 421.

McClintock, F. A., (1955b), "A Criterion for Minimum Scatter in Fatigue Testing," Journal of Applied Mechanics, Vol. 22, No. 3, p. 427.

McClintock, F. A. (1956), "Variability in Fatigue Testing: Sources and Effect on Notch Sensitivity," Proc. Intl. Colloq. on Fatigue, pp. 171–177.

McClintock, F. A. and Mayson, H. J. (1976), "Principal Stress Effects on Brittle Crack Statistics," The effects of voids on material deformation, ASME, New York, NY.

McClintock, F. A. and Zaverl, F. Jr. (1979), "An Analysis of the Mechanics and Statistics of Brittle Crack Initiation," International Journal of Fracture, Vol. 15, No. 2, April.

McClintock, F. A. and Walsh, J. B. (1962), "Friction on Griffith Cracks in Rocks Under Pressure," Proceedings of the 4th U.S. National Congress of Applied Mechanics 2:1015.

McCullough, J. M. and Rigby, G. R. (1971), "Mechanical Properties of Refractory Castables," Journal of British Ceramic Society, Vol. 71, No. 7.

McGannon, E. (1964), "The Making, Shaping and Treating of Steel," United States Steel Corporation, eighth edition.

McGee, T.D. (1984), "High Temperature Creep of Refractories for Coal Processing Vessels," U. S. Department of Energy, Fossil Energy Advanced Research and Techology Development Reports, ONRL/FMP–83/3–5; ONRL/FMP–84/1.

McGee, T. D. and Konrady, R. (1983–1987), "High Temperature Creep Behavior of Refractory Bricks," Quarterly Reports published by the US DOE Fossil Energy Program.

Megusar. J., Argon, A. S., and Grant, N. J. (1979), "Plastic Flow and Fracture in $Pd_{80}Si_{20}$ near T_g," Materials Science and Engineering, 38, pp 63–72.

Miller, E. D. and Davis, B. (1966), "Modulus of Rupture of Alumina–Silica Refractories at Elevated Temperatures," American Ceramic Society Bulletin, Vol. 45, No. 8.

Muan, A. (1983), "Refractories in Slagging Gasifiers," Presentation at the Fossil Energy Materials Program Review Meeting, Oak Ridge, TN, May.

Muan, A. (1987), "Thermodynamic Properties and Phase Relations for Refractory Slag Reactions in Slagging Coal Gasifiers," Pennsylvania State University Report Prepared under ORNL Subcontract No. 19X–09006C, December.

NMAB (1983), National Materials Advisory Board, Chairman: Argon, A. S., "Fracture in Compression of Brittle Solids," Report of the Committee on Fracture in Compressive Stress Fields, NMAB–404.

Nemat–Nasser, S. and Horii, H. (1982), "Compression–Induced Nonplanar Crack Extension with Application to Splitting, Exfoliation, and Rockburst," Journal of Geophysics Research, Vol. 87, pp. 6805–6821.

Neville, A.M. (1959), "Some Aspects of the Strength of Concrete," Civil Engineering and Public Works Review, London.

Newbury, D. E. Joy, D.C., et al (1986), "Advanced Scanning Electron Microscopy, and X–ray Microanalysis, Plenum Press.

Nielsen, L. F. (1984), "Elasticity and Damping of Porous Materials and Impregnated Materials," Journal of the American Ceramic Society, Vol. 67, No. 2.

Norton, F. H. (1968), Refractories, McGraw–Hill, N.Y.

Okubo, S. and Nishimatsu, Y. (1985), "Uniaxial Compression Testing Using a Linear Combination of Stress and Strain as the Control Variable," Int. J. Rock Mech. Min. Sci & Geomech. Abstr. Vol. 22, No. 5, pp. 323–330.

Orowan, E. (1949), "Fracture and Strength of Solids," Reports on Progress in Physics, The Physical Society, Vol. 12, pp. 185–232.

Ottosen, N.S. (1977), "A Failure Criterion for Concrete," Journal of the Engineering Mechanics Division, ASCE, Vol. 103, August, pp. 527–535.

Pampuch, R. (1976), Ceramic Materials, Elsevier Scientific Publishing Co., Warzawa, Poland.

Paterson, M.S. (1978), Experimental Rock Deformation–The Brittle Field, Springer, Verlag, New York, N.Y.

Paul, W. B., Jr. (1954), "Monolithic Refractories in Fluid Catalytic Cracking Refinery Units," American Ceramic Society Bulletin, Vol. 33, No. 4.

Peck, L., Barton, C. C. and Gordon, R. B. (1985), "Microstructure and the Resistance of Rock to Tensile Fracture," Journal of Geophysical Research, Vol. 90, No. B13, pp. 11,533–11,546.

Pike, P.J., Buyukozturk, O. and Connor, J. (1980), "Thermomechanical Analysis of Refractory Concrete–Lined Coal Gasification Vessels," Research Report R80–2, M.I.T., Department of Civil Engineering, January 1980.

Potter, R. A. (1981), "Improvement of the Mechanical Reliability of Monolithic Refractory Linings for Coal Gasification Process Vessels," Prepared for the United States Departemnt of Energy.

Raithby, K.D. (1979), "Behavior of Concrete Under Fatigue Loading," Developments in Concrete Technology, edited by F.D. Lydon, Applied Science Publishers, Ltd., London.

Raju, N.K. (1970), "Small Concrete Specimens Under Repeated Compression Loads by Pulse Velocity Technique," Journal of Materials, JMLSA, Vol. 5, June, pp. 262–272.

Raleigh, C.B. and Paterson, M.S. (1965), "Experimental Deformation of Serpentinite and its Tectonic Implications," Journal of Geophysical Research, Vol. 70, p. 3965.

Reimann, K. J. (1984), "Electromagnetic Acoustic Transducers (EMATs) for Erosion Monitoring," Argonne National Laboratory, Argonne, Illinois.

Rigby, G. R. and Hutton, R. (1962), "Action of Alkali and Alkali–Vanadium Oxide Slags on Alumina–Silica Refractories," Journal of the American Ceramic Society, Vol. 45, No. 2.

Ritter, J. E. Jr. and Davidge, R.W. (1984), "Strength and its Variability in Ceramics with Particular Reference to Alumina," Journal of the American Ceramic Society, Vol. 67, No. 6.

Robbins, C. R. and Mauer, F. A. (1981), "Chemical Degradation of Castable Refractories in Coal Gasification Process Environments," Journal of Materials for Energy Systems, Vol. 3.

Robinson, G.S. (1965), "The influence of Microcracking and State of Stress on the Elastic Behavior and Discontinuity of Concrete," Theory of Arch Dams: Proceedings of an International Symposium, Southampton, 1964, Edited by J.R. Rydzewski, pp. 713–721.

Ruh, E. and Renkey, A. L. (1963), "Thermal Conductivity of Refractory Castables," Journal of the American Ceramic Society, Vol. 46, No. 2.

Ruprecht, B. C. et al. (1934), "A Study of the Effect of Natural Gas and of Hydrogen Upon Various Refractories," Research Department, Harbison Walker Refractories Company, Pittsburgh, PA, July.

Sadler, L. Y., Raymon, N. S., Ivey, K. H., and Heystek, H. (1979), "Evaluation of Refractory Liner Materials for Use in Nonslagging, High Btu Coal–Gasifier Reactors," American Ceramic Society Bulletin, Vol. 58, No. 7.

Samsonov, G. V. (1964), High Temperature Materials, Properties Indux, Plenum Press, N.Y.

Schafter, P. B. (1964), High Temperature Materials, Materials Index, Plenum Press, N.Y.

Schurelht, H. G. (1938), "Reactions of Slag with Refractories: Surface Reactions," Presented at the 40th Annual Meeting, American Ceramic Society, New Orleans, LA.

Schick, H. L. (1966), Thermodynamics of Certain Refractory Compounds, Academic Press, N.Y.

Sedlacek, R. (1968), "Investigation of Elasticity and Strength of Ceramics Subjected to Tensile and Compressive Loads," Air Force Materials Laboratory Technical Report No. AFML–TR–68–231.

Shah, S.P. and Chandra, S. (1970), "Mechanical Behavior of Concrete Examined by Ultrasonic Measurements," Journal of Materials, JMLSA, Vol. 5, September, pp. 550–563.

Shah, S.P. and Slate, F.O. (1965), "Internal Microcracking, Mortar—Aggregate Bond and the Stress—Strain Curve of Concrete," International Conference on the Structure of Concrete, pp. 1–11.

Shaw, K. (1972), Refractories and Their Uses, John Wiley & Sons, New York, N.Y.

Shrive, N.G. and El—Rahman, M. (1985), "Understand the Cause of Cracking in Concrete: A Diagonistic Aid," Concrete International, Vol. 7, May, pp. 39–44.

Shultz, A. H. and Stubican, V. S. (1970), "Separation of Phases by Spinoidal Decomposition in the System Al_2O_3–Cr_2O_3–Fe_2O_3," Journal of the American Ceramic Society, Vol. 53, No. 22, November.

Sines, G., and Adams, M. (1978), "Compression Testing of Ceramics," Fracture Mechanics of Ceramics, Vol. 3, Plenum Press, New York.

Sines, G., Okada, T., and Mark, S. (1983), "Fixture for Accurate Load Path in Axial Compression," ASTM STP 808, pp. 97–108.

Snyder, J. E. and Petit, M. R. (1982), "Refractory Fiber Lining Design for High Temperature Metal—Heating Furnaces," Presented at the American Ceramic Society Refractories Meeting, Bedford Springs, PA, Vol. 61, No. 7.

Soon, K.A. (1987), "Behavior of Pressure Confined Concrete in Monotonic and Cyclic Loadings," Ph.D. Thesis, Department of Civil Engineering, Massachusetts Institute of Technology, May, 813 pp.

Sparks, P. R. (1982), "The Influence of Rate of Loading and Material Variability on the Fatigue Characteristics of Concrete," ACI, SP 75–16, pp. 331–341.

Spunt, E. and Brace, W.F. (1974), "Direct Observations of Microcavities in Crystalline Rocks," International Journal of Rock Mechanics, Mining Sciences and Geomechanical Abstracts, Vol. 11, pp. 139–150.

Stahl, N. (1976), "Laser Measurements of the Lining Wear of Steel Furnaces," Scandanavia Journal of Metallurgy, 1976, No. 6.

Stout, M. G. and Petrovic, J. J. (1984), "Multiaxial Loading Fracture of Al_2O_3 Tubes: I, Experiments," Journal of the American Ceramic Society, Vol. 67, No. 1, January.

Stringer, J. (1981), "High Temperature Corrosion Problems in the Electric Power Industry and Their Solution," High Temperature Corrosion Conference, San Diego, California, March.

Stroeven, P. (1979), "Mechanics of Microcracking in Concrete Subjected to Fatigue Loading," International Conference on the Mechanical Behavior of Materials, Vol. 3, August, pp. 141–150.

Suaris, W. and Shah, S. P. (1984), "Rate–Sensitive Damage Theory for Brittle Solids," Journal of Engineering Mechanics, Vol. 110, No. 6, June.

Suresh, S. and Brockenborough, J. R. (1987), "Theory and experiments of fracture in Cyclic Compression: Single Phase Ceramics, Transforming Ceramics and ceramic Composites," Acta Met., April 1987.

Swain, M.V. and Hagan, J.T. (1978), "Some Observations of Overlapping Interacting Cracks," Engineering Fracture Mechanics, Vol. 10, pp. 299–304.

Sweeney, J. and Cross, M. (1982), "Analysis of the Stress Response of Commercial Refractory Structures in Service at High Temperature: II, A Thermal Stress Model for Refractory Structures," British Ceramic Society Transactions and Journal, Vol. 81, No. 1.

Takeuchi, S. and Argon, A. S. (1976), "Review, Steady–State Creep of Single–Phase Crystalline Matter at High Temperature," Journal of Materials Science, 11, pp. 1542–1566.

Tapponnier, P. and Brace, W. F. (1976), "Development of Stress–Induced Microcracks in Westerly Granite," Int. J. Rock. Mech. Min. Sci. & Geomech. Abstr., Vol. 13, pp. 103–112.

Tepfers, R. (1982), "Fatigue of Plain Concrete Subjected to Stress Reversals," American Concrete Institute, SP–75, pp. 195–215.

Thelandersson, S. (1974), "Mechanical Behavior of Concrete Under Torsional Loading at Transient, High Temperature Conditions," Lund Institute of Technology, Bulletin 46, Lund, Sweden, November.

Tracy, C.A. (1987), "A Compression Test for High Strength Ceramics," ASTM, Journal of Testing and Evaluation, ASTM, January.

Tseng, T. M. (1982), "Thermomechanical Behavior of Refractory Concrete Lined Vessels," Research Report No. R82–11, Massachusetts Institute of Technology.

Tseng, T.M. and Buyukozturk, O., "Thermomechanical Behavior of Refractory Concrete–Lined Vessels," Research Report R82–44, M.I.T., Department of Civil Engineering, August, 1982.

Tseng, T.M. and Buyukozturk, O., "Refractory Concretes: Constitutive Model and Application," Proceedings of the International Conference on Constitutive Laws of Engineering Materials: Theory and Application, University of Arizona, Tucson, Arizona, January 1983.

Tvergaard, V. and Hutchinson, J. W. (1987), "Micro–Cracking in Ceramics Induced by Thermal Expansion or Elastic Anisotropy," May.

Venable, C. R. Jr. (1977), "Right Refractory is Key to Good Linings," The Oil and Gas Journal, October, pp. 143–147.

Venkatachari, K. R., and Raj, R. (1986), "Superplastic Flow in Fine—Grained Alumina," Journal American Ceramic Society, 69 [2], pp. 135–138.

Vorres, K. S., Greenberg, S. and Poeppel, R. B., (1985), "Viscosity of Synthetic Coal Ash Slags," Argonne National Laboratory, Argonne, IL.

Washburn, M. E. (1982), "Rotating Sample Slag Test for Refractories," Seventh Annual Conference on Materials for Coal Conversion and Utilization, November.

Washburn, M. E. (1983), "Comparative Rotating Sample Slag Test," Presented on April 25, 1983 at the Ceramic Society 85th Annual Meeting, Chicago, IL.

Washburn, M. E. (1985), Private Communication, MIT, Cambridge, MA.

Watt, I. M., (1985), "The Principles and Practice of Electron Microscopy," Cambridge University Press, Cambridge.

Weibull, W. (1939), "Statistical Theory of the Strength of Materials," Ingenioers Vetenskaps Akad. Handl., No. 151.

Wiederhorn, S. M. and Krause, R. F. (1986), "Effect of Slag Penetration on the Mechanical Properties of Refractories," NBS Final Report prepared for the DOE under ONRL contract number DE—AI05—830R21349.

Wiederhorn, S. M. and Krause, R. F. (1988), "Effect of Coal Slag on the Microstructure and Creep Behavior of a Magnesium—Chromite Refractory," Ceramic Bulletin, Vol. 67, No. 7.

William, K.J., and Warnke, E.P. (1974), "Constitutive Model for the Triaxial Behavior of Concrete," International Association of Bridge and Structural Engineers Seminar on Concrete Structures Subjected to Triaxial Stresses; Paper III–1, Italy, May 17–19.

Wong, T. F. (1982a), "Micromechanics of Faulting in Westerly Granite," Int. J. Rock Mech. Min. Sci. & Geomech. Abstr., Vol. 19, pp. 49–64.

Wong, T. F. (1982b), "Effects of Temperature and Pressure on Failure and Post—Failure Behavior of Westerly Granite," Mechanics of Materials, Vol. 1, pp. 3–1.

Wong, T.F. and Brace, W.F. (1979), "Thermal Expansion of Rocks: Some Measurements at High Pressures," Tectonophysics, Vol. 57, pp. 95–117.

Wygant, J. F. and Bulkley, W. L., (1954), "Refractory Concrete for Refinery Vessel Linings," American Ceramic Society Bulletin, 33 (1), pp. 233–239.

Wygant, J. R. and Crowley, M. S. (1958), "Effects of High—Conductivity Gases on he Thermal Conductivity of Insulating Refractory Concrete," Journal of American Ceramic Society, Vol. 41, [5].

Wygant, J. F. and Crowley, M. S. (1964), "Designing Monolithic Refractory Vessel Linings," American Ceramic Society Bulletin, Vol. 43, No. 3.

Yang, B.L., Dafalias, Y.F., and Herrmann, L.R. (1985), "A Bounding Surface Plasticity Model for Concrete," Journal of Engineering Mechanics, ASCE, Vol. 111, No. 3, March.

Zielinski, A. J. (1983), "Model for Tensile Fracture of Concrete at High Rates of Loading," Cement and Concrete Research, Vol. 14, pp. 215–224.

LIST OF FIGURES

LIST OF TABLES

APPENDIX A
MATERIAL DATABASE

The assembled material database is extensive, and is expected to be useful to manufacturers of refractory materials, and designers of refractory linings. The thermomechanical data in compression was unavailable in the past, and was produced by the current MIT Project. The modulus of rupture data and the thermophysical information have been compiled from manufacturers' data or from the literature. Table A.1 shows the different materials and properties that are presented in this appendix. References are made to Chapter 8 for more details about the materials and sources of information. The thermomechanical properties are presented in Section A.1, while the thermophysical properties are presented in Section A.2. At the beggining of both Sections A.1 and A.2 Tables summarizing the organization of the data in the database are given.

A.1   THERMOMECHANICAL PROPERTIES

The thermomechanical data is presented in this Section. The completed MIT project, on the high temperature characterization of refractory oxides under short—term compressive loads in controlled gas environments, is summarized in Table A.2 along with the appropriate tables of results. Tables A.3 to A.8 summarize the organization of the thermomechanical test results from MIT and elsewhere. The thermomechanical data is presented in Tables A.9 to A.37, and Equations A.1 to A.46. The thermomechanical data presented on dense refractory bricks, with the exception of

Material Classes and Properties Included in the Database	Reference for More Detailed Information
Refractory Bricks Used for Thermomechanical Testing in Compression	Table 8.1a
Refractory Bricks Used for Room Temperature Characterization in Compression	Table 8.1b
Castable Refractories Assembled for Thermomechanical Properties in Compression	Table 8.1c
Refractory Bricks and Castables Assembled for Modulus of Rupture Data	Table 8.1d
Refractory Bricks and Castables Assembled for Thermophysical Properties	Table 8.1e

Table A.1

Summary of Materials and Properties
Included in the Database

Short-Term Uniaxial Compression Tests				
Displacement Control. Linear variation with time		Load Control. Haversine variation with time	Load Control. Fixed constant level with time	
Average $\dot{\epsilon}$ is in the range $10^{-4} \sec^{-1}$ to $10^{-6} \sec^{-1}$		f in the range 10^{-3} - 10^{-4} Hz	$\dot{\epsilon}$ is a test result	Heating rates: 100 to 250°F/hr
Constant T in the range 70°F to 2500°F				Increasing T from 70° to 2400°F
Monotonic P to failure		Cyclic P 75% - 90% f_p	Constant P between 55% f_p and 85% f_p	
Air	$P_{O_2} = 10^{-8}$ atm.	Air	Air	
CATEGORY	A	B	C	D	E
Mat. CPS-90A-10C As-Manufactured	A.9	A.20	A.22 & A.23	A.25	A.29
Mat. CPS-90A-10C Slag-Impregnated	A.10 & A.11	A.11			
Mat. CPS-82C-18M As-Manufactured	A.12	A.21	A.24	A.26	
Mat. CPS-82C-18M Slag-Impregnated	A.13 & A.14	A.13 & A.14			
Materials HP-90A-10C HP-50A-50C HP-25A-75C As-Manufactured	A.15 A.16 A.17			A.27	
Material HP-80C-20M As-Manufactured	A.18				
Material FC-78C-8A As-Manufactured	A.19			A.28	

$\dot{\epsilon}$ - strain rate   f - cyclic test frequency
P - mechanical load   T - temperature
P_{O_2} - partial oxygen pressure f_p - monotonic material strength

Table A.2 Thermomechanical Test Program Under Current Project

Note: Table A.30 presents results of limited thermal cyclic tests.

MOR data, have been obtained at MIT under the current project. Fit of Equations A.1 to A.46 with the test data is shown in Appendix B.

A.1.1   Tabular Representation of Thermomechanical Properties

The following Tables (Tables A.3 to A.37) present some of the thermomechanical data. The following definitions have been used for the tables:

- o   Strength is defined as the peak stress on the stress–strain curve;

- o   Associated peak strain is defined as the strain associated with the peak stress on the stress–strain curve;

- o   Final fracture stress is defined as the stress at which the specimen cannot carry any more load;

- o   Final fracture strain is defined as the strain associated with the final fracture stress on the stress–strain curve;

- o   Toughness measure is defined as the area under the stress–strain curve between zero and the final fracture load;

- o   Initial stiffness is defined as the initial slope of the stress–strain curve;

- o μ is defined as the mean of the results for a series of specimens;

- o   S.D. is defined as the unbiased standard deviation of the results of a series of specimens and is expressed as % of μ;

- o   n is the number of tests reported by category; and

- o P_{O_2} refers to the partial oxygen pressure defined as the molar content of oxygen in the atmosphere.

Table A.3

Thermomechanical Properties - Category A - Source: MIT

Monotonically Increasing Compressive Load Tests at Constant Temperatures in Air Atmosphere

Material	Complete Stress Strain Curves	Strength vs. T	Associated Peak Strain vs. T	Initial Modulus E vs. T	Final Fracture Stress vs. T	Final Fracture Strain vs. T	Toughness Measure vs. T	Assessment of Strain rate effects
CPS-90A-10C As-Manufactured (Current Project)	Yes	Eq. A.1	Eq. A.2	Eq. A.3	Table A.9			Yes
CPS-90A-10C Slag-Impregnated (Current Project)	Yes	Eq. A.4	Eq. A.5	Eq. A.6	Tables A.10 and A.11			No
CPS-82C-18M As-Manufactured (Current Project)	Yes	Eq. A.7	Eq. A.8	Eq. A.9	Table A.12			Yes
CPS-82C-18M Slag-Impregnated (Current Project)	Yes			Eq. A.10	Tables A.13 and A.14			No

HP-90A-10C (Current Project)	Yes	Eq. A.11	Eq. A.12	Eq. A.13 Table A.15		No
HP-50A-50C (Current Project)	Yes	Eq. A.14	Eq. A.15	Eq. A.16 Table A.16		No
HP-25A-75C (Current Project)	Yes	Eq. A.17	Eq. A.18	Eq. A.19 Table A.17		No
HP-80C-20M (Current Project)	Yes	Eq. A.20	Eq. A.21	Eq. A.22 Table A.18		No
FC-78C-8A (Current Project)	Yes	Eq. A.23	Eq. A.24	Eq. A.25 Table A.19		No
6 dense and 4 insulating refractory bricks (Manufacturers Data)	No	Strength Data in Table A.31	No			No
Dense Refractory Concrete (Tseng,82)	(See Tseng,82)	Eq. A.26 Strength, Peak strain and Initial Modulus Data Only Table A.32	Eq. A.27	Eq. A.28	No	No
Insulating Refractory Concrete (Tseng,82)	(See Tseng,82)	Eq. A.29 Strength, Peak strain and Initial Modulus Data Only Table A.33	Eq. A.30	Eq. A.31	No	No

Commercial Refractory Concrete (Wygant and Buckley,54)	No	Eq. A.32 Strength Data Only Table A.34			No	No
Portland Cement Concrete (Thelandersson,76)	(See Thelandersson,76)	Eq. A.33	Eq. A.34	Eq. A.35	No	No
		Strength, Peak strain and Initial Modulus Data Only Table A.35				

Table A.4

Thermomechanical Properties - Category B - Source: MIT

Monotonically Increasing Compressive Load Tests at Constant Temperatures
in Reducing Atmosphere

Material	E vs. T	$E(P_{O_2})/E_{AIR}$ vs. T
CPS-90A-10C	Eq. A.36	Table A.20
Slag-Impregnated CPS-90A-10C	Eq. A.37	Table A.11
CPS-82C-18M	Eq. A.38	Table A.21
Slag-Impregnated CPS-82C-18M	Eq. A.39	Tables A.13 and A.14

Table A.5

Thermomechanical Properties - Category C - Source: MIT

Cyclically Varying Compressive Load Tests at
Constant Temperature Levels in Air Atmosphere

Material	Number of Cycles to Failure vs. Load Level	Number of Cycles to Failure vs. T	Cyclic Load-Deformation Curves
CPS-90A-10C	Tables A.22 and A.23		Yes
CPS-82C-18M	Table A.24		Yes

Table A.6

Thermomechanical Properties - Category D - Source: MIT

Constant Compressive Load Tests at Constant
Temperature Levels in Air Atmosphere

Material	Time-Dependent Strain Variation vs. Load Level	Time-Dependent Strain Variation vs. T	Deformation Maps by combining our data with other's data
CPS-90A-10C	Table A.25		Yes
CPS-82C-18M	Table A.26		Yes
HP-90A-10C	Table A.27		No
FC-8A-78C	Table A.28		No

400

Table A.7

Thermomechanical Properties – Category E – Source: MIT

Constant Compressive Loads, Increasing Temperature Tests in
Air Atmosphere

Material	Effect of Different Heating Rates	Time Dependent Strain Variation
CPS-90A-10C	Table A.29	

Table A.8

Thermomechanical Properties - Category F - Source: Manufacturer's Data

Modulus of Rupture (MOR) Data

Material	MOR at Room T	MOR at Elevated Temperatures
	Table A.36 and	
AX581 (Norton)		Eq. A.40
TX591 (Norton)		Eq. A.41
AX565 (Norton)		Eq. A.41
HW25-83 (Harbison-Walker)		
SOHIO B (Sohio)		
Sohio E (Sohio)	Table A.36	No
Sohio K3 (Sohio)		
JM-20 (Eastern Ref.)		
JM-23 (Eastern Ref.)		
JM-30 (Eastern Ref.)		
JM-32 (Eastern Ref.)		
	Table A.37 and	
Alumina-Silica Bricks (Miller and Davies,66) 50% Alumina		Eq. A.43
Dense 60% Alumina		Eq. A.44
Dense 90% Alumina		Eq. A.45
99% Alumina		Eq. A.46

Constant Temperature, Monotonically Increasing Crosshead
Displacement Tests, Under Air Atmosphere, on As-Manufactured Materials

Table A.9   Material CPS-90A-10C, As Manufactured

	AIR ATMOSPHERE					
Temperature	Strength (ksi)	Associated Peak Strain (in/in) $* 10^3$	Final Fracture Stress (ksi)	Final Fracture Strain (in/in) $* 10^3$	Average Strain Rate (in/in/ sec)$*10^6$	Dis- placement Rate (in/ sec) $* 10^5$
n = 3 73°F (23°C)	μ = 22.76 S.D.=2.96	μ = 2.38 S.D.=0.47	SAME AS STRENGTH	SAME AS PEAK STRAIN	μ = 9.82 S.D.=1.14	7.218
500°F (260°C)	23.67	x			-	7.218
n = 2 1000°F (538°C)	μ = 21.52 S.D.=2.30	μ = 3.00 S.D.=0.07			μ = 6.2 S.D.=0.7	7.218
n = 4 1500°F (816°C)	μ = 19.29 S.D.=0.05	μ = 3.37 S.D.=0.44			μ = 6.6 S.D.=0.6	7.218
n = 4 2000°F (1093°C)	μ = 25.39 S.D.=0.3	μ = 4.86 S.D.=0.33			μ = 8.39 S.D.=1.2	7.218
2200°F (1204°C)	24.46	8.34	23.58	9.28	15.08	7.218
2440°F (1338°C)	22.74	13.62	< 21.5	> 16.45	20.31	7.218
2440°F (1338°C)	22.85	6.56	22.85	6.56	35.65	21.65
1500°F (816°C)	18.29	3.09	17.63	3.34	1.91	1.444

Constant Temperature, Monotonically Increasing Crosshead
Displacement Tests, Under Air Atmosphere, on As-Manufactured Materials

Table A.9 (continued)   Material CPS-90A-10C, As Manufactured

Temperature	AIR ATMOSPHERE			
	Toughness Measure (psi)	Average Initial Stiffness (ksi) $* 10^{-3}$	Average Strain Rate (in/in/ sec)$*10^6$	Displacement Rate (in/ sec) $* 10^5$
n = 3 73°F (23°C)	$\mu = 30.18$ S.D. =9.95	$\mu = 10.98$ S.D. =0.35	$\mu = 9.82$ S.D. =1.14	7.218
500°F (260°C)	-	-	-	7.218
n = 2 1000°F (538°C)	$\mu = 41.86$ S.D.=8.73	$\mu = 7.74$ S.D.=0.59	$\mu = 6.2$ S.D. =0.7	7.218
n = 4 1500°F (816°C)	$\mu = 37.12$ S.D.=0.06	$\mu = 6.25$ S.D.=1.16	$\mu = 6.6$ S.D.=0.6	7.218
n = 4 2000°F (1093°C)	$\mu = 63.04$ S.D.=0.95	$\mu = 5.27$ S.D.=0.53	$\mu = 8.39$ S.D.=1.2	7.218
2200°F (1204°C)	163.27	5.03	15.08	7.218
2440°F (1338°C)	> 287.19	3.91	20.31	7.218
2440°F (1338°C)	67.54	4.67	35.65	21.65
1500°F (816°C)	41.41	8.00	1.91	1.444

Constant Temperature, Monotonically Increasing Crosshead
Displacement Tests, Under Air and Controlled Gas Atmosphere,
Slag-Impregnated Materials

Material CPS-90A-10C Slag-Impregnated   Table A.10

Temperature	Atmosphere	Strength (ksi)	Associated Peak Strain (in/in) $* 10^3$	Final Fracture Stress (ksi)	Final Fracture Strain (in/in) $* 10^3$	Dis-placement Rate (in/sec) $* 10^5$
n = 3 73°F (23°C)	Air	μ = 77.29 S.D.= 14.28	μ = 3.73 S.D.= 0.69	SAME AS STRENGTH	SAME AS PEAK	6.67
2400°F (1316°C)	Air	20.19	8.79	< 20.18	> 9.29	7.218

Temperature	Atmosphere	Toughness Measure (psi)	Average Initial Stiffness (ksi) $* 10^{-3}$	Dis-placement Rate (in/sec) $* 10^5$
n = 3 73°F (23°C)	Air	μ = 198.31 S.D.= 43.57	μ = 22.07 S.D.= 3.39	6.67
2400°F (1316°C)	Air	> 134.73	4.74	7.218

Constant Temperature, Monotonically Increasing Crosshead
Displacement Tests, Under Air and Controlled Gas Atmosphere,
Slag-Impregnated Materials

Material CPS-90A-10C, Slag-Impregnated   Table A.11

Temperature	Air		$P_{O_2} = 10^{-8}$ atm.	
	Average Initial Stiffness (ksi) $* 10^{-3}$	Displacement Rate (in/sec) $* 10^5$	Average Initial Stiffness (ksi) $* 10^{-3}$	Displacement Rate (in/sec) $* 10^5$
$n = 3$ $73^\circ F$ $(23^\circ C)$	$\mu = 22.07$ S.D. $= 3.39$	6.67	-	-
$n = 2$ $1000^\circ F$ $(538^\circ C)$	$\mu = 21.97$ S.D. $= 1.35$	7.218	16.35	7.218
$n = 2$ $1500^\circ F$ $(816^\circ C)$	$\mu = 18.41$ S.D. $= 2.56$	7.218	15.05	7.218
$2000^\circ F$ $(1093^\circ C)$	12.67	7.218	-	-
$2200^\circ F$ $(1204^\circ C)$	8.36	7.218	7.89	7.218
$2400^\circ F$ $(1316^\circ C)$	4.74	7.218	-	-

Constant Temperature, Monotonically Increasing Crosshead
Displacement Tests, Under Air Atmosphere, on As-Manufactured Materials

Table A.12   Material CPS-82C-18M, As Manufactured

	AIR ATMOSPHERE					
Temperature	Strength (ksi)	Associated Peak Strain (in/in) $* 10^3$	Final Fracture Stress (ksi)	Final Fracture Strain (in/in) $* 10^3$	Average Strain Rate (in/in/ sec)$*10^6$	Dis- placement Rate (in/ sec) $* 10^5$
n = 3 73°F (23°C)	$\mu = 19.36$ S.D.=1.31	$\mu = 2.53$ S.D.=0.07	SAME AS STRENGTH	SAME AS PEAK STRAIN		7.218
500°F (260°C)	22.28	X			-	7.218
1000°F (538°C)	16.46	3.15			11.26	7.218
n = 3 1500°F (816°C)	$\mu = 15.35$ S.D. =0.7	$\mu = 3.39$ S.D. =0.4			$\mu = 10.64$ S.D.=0.05	7.218
n = 2 2000°F (1093°C)	$\mu = 14.73$ S.D.=1.30	$\mu = 4.11$ S.D.=0.3			$\mu = 12.86$ S.D.=0.56	7.218
2275°F (1246°C)	12.52	6.82	< 9.2	> 10.26	18.78	7.218
2400°F (1316°C)	7.40	6.16	< 5.9	> 10.29	21.21	7.218
2000°F (1093°C)	16.36	7.06	15.82	7.82	3.11	1.444
2275°F (1246°C)	8.72	9.49	< 0.7	> 24.28	4.14	1.444
2275°F (1246°C)	13.15	4.77	13.15	4.77	39.16	21.65

<u>Constant Temperature, Monotonically Increasing Crosshead</u>
<u>Displacement Tests, Under Air Atmosphere, on As-Manufactured Materials</u>

<u>Table A.12 (continued)</u>   <u>Material CPS-82C-18M, As Manufactured</u>

Temperature	AIR ATMOSPHERE			
	Toughness Measure (psi)	Average Initial Stiffness (ksi) $* 10^{-3}$	Average Strain Rate (in/in/ sec)$*10^{6}$	Displacement Rate (in/ sec) $* 10^{5}$
n = 3 $73^{o}F$ ($23^{o}C$)	$\mu = 25.11$ S.D.= 3.31	$\mu = 7.64$ S.D. = 0.31		7.218
$500^{o}F$ ($260^{o}C$)	-	-	-	7.218
$1000^{o}F$ ($538^{o}C$)	25.89	5.12	11.26	7.218
n = 3 $1500^{o}F$ ($816^{o}C$)	$\mu = 28.64$ S.D.= 1.16	$\mu = 4.48$ S.D.= 0.42	$\mu = 10.64$ S.D.= 0.05	7.218
n = 2 $2000^{o}F$ ($1093^{o}C$)	$\mu = 33.01$ S.D.= 3.05	$\mu = 3.73$ S.D.= 0.16	$\mu = 12.86$ S.D.= 0.56	7.218
$2275^{o}F$ ($1246^{o}C$)	>94.69	2.72	18.78	7.218
$2400^{o}F$ ($1316^{o}C$)	>59.24	2.02	21.21	7.218
$2000^{o}F$ ($1093^{o}C$)	83.74	3.45	3.11	1.444
$2275^{o}F$ ($1246^{o}C$)	>138.51	1.59	4.14	1.444
$2275^{o}F$ ($1246^{o}C$)	33.38	2.89	39.16	21.65

Constant Temperature, Monotonically Increasing Crosshead
Displacement Tests, Under Air and Controlled Gas Atmosphere,
Slag-Impregnated Materials

Material CPS-82C-18M, Slag-Impregnated   Table A.13

Temperature	Atmosphere	Strength (ksi)	Associated Peak Strain (in/in) $* 10^3$	Final Fracture Stress (ksi)	Final Fracture Strain (in/in) $* 10^3$	Dis-placement Rate (in/sec) $* 10^5$
n = 3 $73^{\circ}F$ $(23^{\circ}C)$	Air	$\mu = 21.86$ S.D.= 4.26	$\mu = 1.97$ S.D.= 0.44	SAME AS	SAME AS	6.67
$2200^{\circ}F$ $(1204^{\circ}C)$	$P_{O_2} = 10^{-8}$ atm.	3.14	4.8	STRENGTH	PEAK	7.218

Temperature	Atmosphere	Toughness Measure (psi)	Average Initial Stiffness (ksi) $* 10^{-3}$	Dis-placement Rate (in/sec) $* 10^5$
n = 3 $73^{\circ}F$ $(23^{\circ}C)$	Air	$\mu = 22.14$ S.D.= 5.11	$\mu = 11.26$ S.D.= 2.06	6.67
$2200^{\circ}F$ $(1204^{\circ}C)$	$P_{O_2} = 10^{-8}$ atm.	7.86	0.94	7.218

Constant Temperature, Monotonically Increasing Crosshead
Displacement Tests, Under Air and Controlled Gas Atmosphere,
Slag-Impregnated Materials

Material CPS-82C-18M, Slag-Impregnated   Table A.14

Temperature	Air		$P_{O_2} = 10^{-8}$ atm.	
	Average Initial Stiffness (ksi) $* 10^{-3}$	Dis-placement Rate (in/sec) $* 10^{5}$	Average Initial Stiffness (ksi) $* 10^{-3}$	Dis-placement Rate (in/sec) $* 10^{5}$
n = 3 73°F (23°C)	μ = 15.38 S.D. = 2.06	6.67	-	-
1200°F (649°C)	10.72	7.218	10.17	7.218
1500°F (816°C)	4.83	7.218	4.57	7.218
2200°F (1204°C)	5.24	7.218	0.94	7.218

Constant Temperature, Monotonically Increasing Crosshead
Displacement Tests, Under Air Atmosphere, on As-Manufactured Materials

Table A.15   Material HP-90A-10C, As Manufactured

	AIR ATMOSPHERE				
Temperature	Strength (ksi)	Associated Peak Strain (in/in) $* 10^3$	Final Fracture Stress (ksi)	Final Fracture Strain (in/in) $* 10^3$	Displacement Rate (in/sec) $* 10^5$
73°F (23°C)	155.18	9.74	SAME	SAME	7.218
n = 3 1500°F (816°C)	μ=103.84 S.D.= 3.67	μ = 10.73 S.D. = 0.07	AS STRENGTH	AS PEAK	7.218
2000°F (1093°C)	96.35	10.4		STRAIN	7.218
2340°F (1282°C)	68.69	20.24	55.95	24.23	7.218

Constant Temperature, Monotonically Increasing Crosshead
Displacement Tests, Under Air Atmosphere, on As-Manufactured Materials

Table A.15 (continued)   Material HP-90A-10C, As Manufactured

Temperature	AIR ATMOSPHERE		
	Toughness Measure (psi)	Average Initial Stiffness (ksi) $* 10^{-3}$	Displacement Rate (in/sec) $* 10^{5}$
$73^{\circ}F$ ($23^{\circ}C$)	809.41	17.71	7.218
n = 3 $1500^{\circ}F$ ($816^{\circ}C$)	$\mu = 565.95$ S.D.=24.82	$\mu = 9.51$ S.D. = 0.07	7.218
$2000^{\circ}F$ ($1093^{\circ}C$)	562.55	10.76	7.218
$2340^{\circ}F$ ($1282^{\circ}C$)	999.65	3.59	7.218

Constant Temperature, Monotonically Increasing Crosshead
Displacement Tests, Under Air Atmosphere, on As-Manufactured Materials

Table A.16   Material HP-50A-50C, As Manufactured

	AIR ATMOSPHERE				
Temperature	Strength (ksi)	Associated Peak Strain (in/in) $* 10^3$	Final Fracture Stress (ksi)	Final Fracture Strain (in/in) $* 10^3$	Displacement Rate (in/sec) $* 10^5$
73°F (23°C)	187.96	8.15	SAME	SAME	7.218
1500°F (816°C)	166.97	10.81	AS STRENGTH	AS PEAK	7.218
2000°F (1093°C)	115.73	12.28		STRAIN	7.218

Constant Temperature, Monotonically Increasing Crosshead
Displacement Tests, Under Air Atmosphere, on As-Manufactured Materials

Table A.16 (continued)   Material HP-50A-50C, As Manufactured

Temperature	AIR ATMOSPHERE		
	Toughness Measure (psi)	Average Initial Stiffness (ksi) $* 10^{-3}$	Dis-placement Rate (in/sec) $* 10^{5}$
$73^{\circ}F$ ($23^{\circ}C$)	735.15	20.85	7.218
$1500^{\circ}F$ ($816^{\circ}C$)	943.19	16.97	7.218
$2000^{\circ}F$ ($1093^{\circ}C$)	802.12	10.85	7.218

Constant Temperature, Monotonically Increasing Crosshead
Displacement Tests, Under Air Atmosphere, on As-Manufactured Materials

Table A.17   Material HP-25A-75C, As Manufactured

	AIR ATMOSPHERE				
Temperature	Strength (ksi)	Associated Peak Strain (in/in) $* 10^3$	Final Fracture Stress (ksi)	Final Fracture Strain (in/in) $* 10^3$	Dis-placement Rate (in/sec) $* 10^5$
73°F (23°C)	213.98	7.47	SAME	SAME	7.218
1500°F (816°C)	166.63	10.27	AS	AS	7.218
2000°F (1093°C)	130.89	16.29	STRENGTH	PEAK STRAIN	7.218
2400°F (1316°C)	80.89	18.41	< 42.25	> 38.66	7.218

Constant Temperature, Monotonically Increasing Crosshead
Displacement Tests, Under Air Atmosphere, on As-Manufactured Materials

Table A.17 (continued)   Material HP-25A-75C, As Manufactured

Temperature	AIR ATMOSPHERE		
	Toughness Measure (psi)	Average Initial Stiffness (ksi) $* 10^{-3}$	Dis-placement Rate (in/sec) $* 10^{5}$
$73^{o}F$ ($23^{o}C$)	790.30	25.08	7.218
$1500^{o}F$ ($816^{o}C$)	939.26	19.90	7.218
$2000^{o}F$ ($1093^{o}C$)	1231.14	9.67	7.218
$2400^{o}F$ ($1316^{o}C$)	>2014.17	5.12	7.218

Constant Temperature, Monotonically Increasing Crosshead
Displacement Tests, Under Air Atmosphere, on As-Manufactured Materials

Table A.18   Material HP-80C-20M, As Manufactured

Temperature	AIR ATMOSPHERE				
	Strength (ksi)	Associated Peak Strain (in/in) $* 10^3$	Final Fracture Stress (ksi)	Final Fracture Strain (in/in) $* 10^3$	Displacement Rate (in/sec) $* 10^5$
73°F (23°C)	143.10	5.03	SAME	SAME	7.218
1000°F (538°C)	123.14	7.34	AS STRENGTH	AS PEAK STRAIN	7.218
1500°F (816°C)	115.04	7.17			7.218
2350°F (1288°C)	43.53	35.42	<37.67	>67.14	7.218

Constant Temperature, Monotonically Increasing Crosshead
Displacement Tests, Under Air Atmosphere, on As-Manufactured Materials

Table A.18 (continued)   Material HP-80C-20M, As Manufactured

Temperature	AIR ATMOSPHERE		
	Toughness Measure (psi)	Average Initial Stiffness (ksi) $* 10^{-3}$	Dis-placement Rate (in/sec) $* 10^{5}$
$73^{\circ}F$ $(23^{\circ}C)$	347.89	27.31	7.218
$1000^{\circ}F$ $(538^{\circ}C)$	496.79	17.15	7.218
$1500^{\circ}F$ $(816^{\circ}C)$	426.16	17.06	7.218
$2350^{\circ}F$ $(1288^{\circ}C)$	>2407.94	4.48	7.218

Constant Temperature, Monotonically Increasing Crosshead
Displacement Tests, Under Air Atmosphere, on As-Manufactured Materials

Table A.19   Material FC-78C-8A, As Manufactured

Temperature	AIR ATMOSPHERE				
	Strength (ksi)	Associated Peak Strain (in/in) $* 10^3$	Final Fracture Stress (ksi)	Final Fracture Strain (in/in) $* 10^3$	Displacement Rate (in/sec) $* 10^5$
73°F (23°C)	77.39	4.3	SAME AS STRENGTH	SAME AS PEAK STRAIN	7.218
1500°F (816°C)	66.29	5.9			7.218
2000°F (1093°C)	41.86	5.23			7.218
2270°F (1243°C)	38.52	9.7	33.84	12.76	7.218
2390°F (1310°C)	29.53	18.90	< 25.52	> 23.59	7.218

Constant Temperature, Monolitically Increasing Crosshead
Displacement Tests, Under Air Atmosphere, on As-Manufactured Materials

Table A.19 (continued)   Material FC-78C-8A, As Manufactured

Temperature	AIR ATMOSPHERE		
	Toughness Measure (psi)	Average Initial Stiffness (ksi) $* 10^{-3}$	Dis- placement Rate (in/ sec) $* 10^5$
$73^{\circ}F$ ($23^{\circ}C$)	188.67	26.0	7.218
$1500^{\circ}F$ ($816^{\circ}C$)	219.14	13.34	7.218
$2000^{\circ}F$ ($1093^{\circ}C$)	121.9	9.26	7.218
$2270^{\circ}F$ ($1243^{\circ}C$)	345.15	5.62	7.218
$2390^{\circ}F$ ($1310^{\circ}C$)	446.13	2.09	7.218

Constant Temperature, Monotonically Increasing Crosshead
Displacement Tests, Under Controlled Atmosphere

As-Manufactured Materials

Material CPS-90A-10C, As-Manufactured

Table A.20

Temperature	$P_{O_2} = 10^{-8}$ atm.		
	Avg. Initial E E_{air}	Average Strain Rate (in/in/sec) $* 10^6$	Displacement Rate (in/sec) $* 10^5$
n = 2 $73^{\circ}F$ $(23^{\circ}C)$	$\mu = 0.92$ S.D. = 0.144	$\mu = 6.99$ S.D. = 0.20	7.218
n = 2 $1000^{\circ}F$ $(538^{\circ}C)$	$\mu = 1.21$ S.D. = 0.18	$\mu = 6.86$ S.D. = 0.55	7.218
n = 2 $1500^{\circ}F$ $(816^{\circ}C)$	$\mu = 1.32$ S.D. = 0.096	$\mu = 6.21$ S.D. = 0.19	7.218
n = 2 $2000^{\circ}F$ $(1093^{\circ}C)$	$\mu = 1.19$ S.D. = 0.24	$\mu = 6.72$ S.D. = 0.42	7.218

Definitions

- P_{O_2} refers to the partial oxygen pressure defined as the molar content of oxygen in the atmosphere.

- Avg. Initial E refers to the ratio of the average initial stiffness in an E_{air} environment with $P_{O_2} = 10^{-8}$ atm., to the average initial stiffness in air atmosphere.

Note: For this table different specimens are compared for tests in air and reduced atmospheres.

Constant Temperature, Monotonically Increasing Crosshead
Displacement Tests, Under Controlled Atmosphere

As-Manufactured Materials

Material CPS-82C-18M, As-Manufactured

Table A.21

	$P_{O_2} = 10^{-8}$ atm.		
Temperature	Avg. Initial E $\frac{}{E_{air}}$	Average Strain Rate (in/in/sec) $* 10^6$	Displacement Rate (in/sec) $* 10^5$
n = 2 73°F (23°C)	μ = 1.114 S.D. = 0.175	μ = 5.11 S.D. = 0.22	7.218
n = 2 1000°F (538°C)	μ = 0.892 S.D. = 0.105	μ = 4.65 S.D. = 0.03	7.218
n = 2 1500°F (816°C)	μ = 0.875 S.D. = 0.061	μ = 4.23 S.D. = 0.16	7.218
n = 2 2000°F (1093°C)	μ = 1.359 S.D. = 0.27	μ = 5.76 S.D. = 0.44	7.218

Note: For the series of test reported in this table, the same specimen is used for
test in air and in reducing atmosphere. A different specimen is used for
each temperature level.

Cyclic Mechanical Load Tests, Between Zero Load and a Fixed Load Level

Material CPS-90A-10C, As-Manufactured

Room Temperature Tests   Table A.22
Air Atmosphere

Fixed load level as % of monotonic strength	Number of cycles to failure
75%	74
80%	μ = 68 S.D. = 6 n = 3
90%	μ = 20 S.D. = 4 n = 2

Cyclic Mechanical Load Tests, Between Zero Load and a Fixed Load Level

Material CPS-90A-10C, As-Manufactured

Elevated Temperature Tests   Table A.23

Temperature	Fixed load level as % of monotonic strength	Number of cycles to failure
1500°F (816°C)	75%	45
1500°F (816°C)	80%	36
1500°F (816°C)	90%	17
2400°F (1316°C)	80%	15
2400°F (1316°C)	90%	4

Cyclic Mechanical Load Tests, Between Zero Load and a Fixed Load Level

Material CPS-82C-18M, As-Manufactured

Room Temperature Tests   Table A.24
Air Atmosphere

Fixed load level as % of monotonic strength	Number of cycles to failure
73%	59
77%	μ = 35 S.D. = 9 n = 3
88%	μ = 20 S.D. = 6 n = 3
92%	μ = 17 S.D. = 6 n = 2
95%	μ = 14 S.D. = 5 n = 2

Short Term Creep Tests, Material CPS-90A-10C, As-Manufactured

Air Atmosphere   Table A.25

Temperature	Constant load as % of monotonic strength at corresponding temperature level	Strain rates corresponding to time$_c$ (in/in/sec) $* 10^8$	Time$_c$ = Time after reaching constant load level (sec)
75°F (23°C)	62		0 2000 4000
1500°F (816°C)	66	4.05 1.99 1.95	0 2000 4000
2000°F (1093°C)	55	23.32 21.56 19.06	0 2000 4000
2400°F (1316°C)	57 57 57 74	389.59 171.94 146.79	0 2000 4000 >4000
2400°F (1316°C)	74	611.64 363.89 FAILURE	0 2000 2310

Short Term Creep Tests, Material CPS-82C-18M, As-Manufactured

Air Atmoshpere   Table A.26

Temperature	Constant load as % of monotonic strength	Strain rates corresponding to time$_c$ (in/in/sec) $* 10^8$	Time$_c$ = Time after reaching constant load level (sec)
75°F (23°C)	67%		0 2000 4000
1500°F (816°C)	84%	23.4 21.3 18.8	0 2000 4000
2300°F (1260°C)	55% 55% 68% 68%	368.25 153.08 522.82 FAILURE	0 1000 2000 2142

Short Term Creep Tests, Material HP-90A-10C, As-Manufactured

Air Atmoshpere   Table A.27

Temperature	Constant load as % of monotonic strength	Strain rates corresponding to time$_c$ (in/in/sec) $* 10^8$	Time$_c$ = Time after reaching constant load level (sec)
1500°F (816°C)	78	95.59	0
		46.93	2000
		FAILURE	2310
2400°F (1316°C)	81	802.95	0
		587.60	500
		902.33	800
		FAILURE	880

Short Term Creep Tests, Material FC-78C-8A, As-Manufactured

Air Atmoshpere   Table A.28

Temperature	Constant load as % of monotonic strength	Strain rates corresponding to time$_c$ (in/in/sec) $* 10^8$	Time$_c$ = Time after reaching constant load level (sec)
2000°F (1093°C)	83	119.09 85.16 70.72 62.40	0 2000 4000 6000

Constant Load Tests, Varying Temperatures, Material CPS-90A-10C,
As-Manufactured

Air Atmosphere   Table A.29

Constant load % of monotonic strength	Temperature variation (^{o}F)	Creep Strain variations (in/in)
Stress = 14021 psi 62% at 73°F	Increasing from 73°F to 2400°F at 250°F/hr	0 to 0.016 in 18100 sec Attains 0.034 at 2350°F
Stress = 14021 psi 62% at 73°F	Increasing from 73°F to 2400°F at 100°F/hr	0 to 0.015 in 44200 sec Attains 0.036 at 2300°F

Thermal Cycling at Zero Load, followed by
Monotonically Increasing Crosshead Displacement Tests

Material CPS-82C-18M, As-Manufactured

Table A.30

Condition	Average Initial Stiffness Variation	Displacement Rate (in/sec)
One thermal cycle at no load between 73°F (23°C) and 2200°F (1204°C), in air atmosphere	Reduced by μ = 6.19 % S.D. = 2.17 %	7.218 x 10^{-5}
One thermal cycle at no load between 73°F (23°C), and 2200°F (1204°C) in reducing atmosphere (P_{O_2} = 10^{-8} atm.)	Reduced by 3.5%	7.218 x 10^{-5}

Table A.32

Dense Refractory Concrete (Tseng,82)

T ($^{\circ}$F)	Strength (Ksi)	Peak Strain $*10^3$ (in/in)	Initial Modulus $*10^{-3}$ (Ksi)
70	9.48	0.8	5.36
500	-	-	3.44
1000	9.36	2.7	2.08
1500	10.52	7.5	1.29
2000	10.64	33	0.83
2500	-	-	0.57

Table A.33

Insulating Refractory Concrete (Tseng,82)

T ($^{\circ}$F)	Strength (Ksi)	Peak Strain $*10^3$ (in/in)	Initial Modulus $*10^{-3}$ (Ksi)
70	0.78	3.0	1.97
500	2.56	3.6	0.85
1000	2.56	3.3	0.50
1500	3.48	19.4	0.42
2000	-	-	0.40
2500	-	-	0.39

Strength of Commercial Refractory Concrete
(Wygant & Buckley, 54)

T (°F)	S (Ksi)
100	2.00
420	1.51
770	1.00
1370	0.53
1530	0.47
1670	0.53
1950	0.99
2000	1.23
2170	1.00

Portland Cement Concrete

T (°F)	E (Ksi)	S (Ksi)	ϵ_p (in/in) $*10^3$
77	14.47	14.47	3.0
272	13.03	14.84	2.8
362	10.61	14.23	2.8
505	8.44	13.75	3.8
752	7.00	13.87	5.5
827	6.27	11.10	6.7
932	5.79	8.44	6.2
1202	2.65	5.07	8.2
1412	1.69	3.38	8.2

Modulus of Rupture Data
Air Atmosphere

Table A.36

Material	Source of Information	Room T	2280°F 1250°C	2640°F 1450°C	2700°F 1480°C
AX565	Norton Co.	5700 psi 39 MPa	6000 psi 41 MPa	3800 psi 26 MPa	
AX581	Norton Co.	4700 psi 32 MPa	4700 psi 32 MPa	4200 psi 29 MPa	
TX591	Norton Co.	3400 psi 23 MPa	2200 psi 18.5 MPa	1950 psi 13.4 MPa	
HW25-83	Harbison Walker	4410 psi			1340 psi
Sohio E	Sohio Eng. Matls. Co.	5600 psi			
Sohio K3	Sohio Eng. Matls. Co.	8000 psi			
Sohio B	Sohio Eng. Matls. Co.	5600 psi			

434

Modulus of Rupture (psi) of Alumina-Silica Bricks

Source: Miller and Davies (1966)

Table A.37

Temperature	50% Alumina	Dense 60% Alumina	Dense 90% Alumina	99% Alumina
Room	1060	1750	3300	1900
500°F	1070	1980	2730	1720
1000°F	1080	2100	2390	1490
1500°F	1090	2100	2560	1500
1750°F	1170	1980	2520	
1850°F	-	1960		1310
2000°F	2210	2280	3480	1280
2300°F	1020	1870	2800	890
2500°F	180	900	2380	630
2700°F			1480	
2900°F		390	1430	

A.1.2 Functional Representation of Thermomechanical Properties in

Monotonic Compression in Air

The following properties are expressed in the English system of units. The following are the symbols that have been used:

o S (ksi) is the strength of the material, defined as the peak strength on the stress strain curve, expressed in 'ksi';

o ϵ_p (in/in) is the strain associated with the peak stress on the stress strain curve, expressed as 'in/in';

o E_i (x1000 ksi) is the initial stiffness of the stress strain curve, expressed in thousands of 'ksi'; and

o T is the temperature, expressed in ^OF.

To convert to the International System of units (SI) the following can be used:

o $T\ (^OC) = [T\ (^OF) - 32]\ /\ 1.8$;

o 1 MPa = 144.74 psi (for S or E); and

o ϵ (in/in) = ϵ (m/m) = 0.01 ϵ (%).

In what follows the selected thermomechanical properties obtained from short term compression tests at constant temperatures in air at a constant displacement rate of 7.218 x 10^{-5} in/sec. are presented. They are classified by materials. The variations with temperature of the strength, associated peak strain, and initial stiffness of the stress strain curve are given.

1. As-Manufactured CPS-90A-10C (Completed MIT Project)

a) Strength

- Brittle Region: (T < 2100°F)

$$S = 22.2400 \left(1 - \sqrt{T/9.2849 \times 10^{14}}\right) \tag{A.1a}$$

- Ductile Region: (T > 2100°F)

$$S = -7.1667 \times 10^{-3} T + 40.2267 \tag{A.1b}$$

- Complete Temperature Range: (70°F - 2500°F)

$$S = -2.3960 \times 10^{-9} T^3 + 1.0667 \times 10^{-5} T^2 - 0.011806 T + 23.7152 \tag{A.1c}$$

b) Associated Peak Strain

- Brittle Region: (T < 2100°F)

$$\epsilon_p = 2.2127 \times 10^{-3} \times 10^{(1.5051 \times 10^{-4}T)} \tag{A.2a}$$

- Complete Temperature Range: (70°F - 2500°F)

$$\epsilon_p = 3.6896 \times 10^{-12} T^3 - 1.0178 \times 10^{-8} T^2 + 7.6469 \times 10^{-6} T$$
$$+ 1.6007 \times 10^{-3} \tag{A.2b}$$

c) Initial Stiffness

- Complete Temperature Range: (70°F - 2500°F)

$$E_i = -4.4460 \times 10^{-10} T^3 + 0.000002 T^2 - 0.005360 T + 11.3750 \tag{A.3}$$

2. Slag-Impregnated CPS-90A-10C (Completed MIT Project)

- Complete Temperature Range: (70°F - 2500°F)

a) Strength

$$S = -0.024538 T + 79.0813 \tag{A.4}$$

b) Associated Peak Strain

$$\epsilon_p = 2.1745 \times 10^{-6} T + 3.5713 \times 10^{-3} \tag{A.5}$$

c) Initial Stiffness

$$E_i = -7.7902 \times 10^{-10} \, T^3 - 2.5183 \times 10^{-6} \, T^2 + 3.3608 \times 10^{-3} \, T$$
$$+ \; 21.8435 \qquad\qquad\qquad\qquad\qquad\qquad (A.6)$$

3. As-Manufactured CPS-82C-18M (Completed MIT Project)

a) Strength

- Brittle Region: (T < 2100°F)

$$S = 20.4758 \, (1 - \sqrt{T/25017.15}) \qquad\qquad (A.7a)$$

- Ductile Region: (T > 2100°F)

$$S = -0.04096 \, T + 105.704 \qquad\qquad (A.7b)$$

- Complete Temperature Range: (70°F - 2500°F)

$$S = -4.6737 \times 10^{-9} \, T^3 + 0.000016 \, T^2 - 0.015724 \, T + 20.5033 \qquad (A.7c)$$

b) Associated Peak Strain

- Brittle Region: (T < 2100°F)

$$\epsilon_p = 2.4642 \times 10^{-3} \times 10^{(1.0469 \times 10^{-4} \, T)} \qquad\qquad (A.8a)$$

- Complete Temperature Range: (70°F - 2500°F)

$$\epsilon_p = 1.0180 \times 10^{-12} \, T^3 - 2.6975 \times 10^{-9} \, T^2 + 2.4131 \times 10^{-6} \, T$$
$$+ \; 2.3761 \times 10^{-3} \qquad\qquad\qquad\qquad (A.8b)$$

c) Initial Stiffness

- Complete Temperature Range: (70°F - 2500°F)

$$E_i = -1.0994 \times 10^{-9} \, T^3 + 4.0931 \times 10^{-6} \, T^2 - 0.005987 \, T + 8.0615 \qquad (A.9)$$

4. Slag-Impregnated CPS-82C-18M (Completed MIT Project)

- Complete Temperature Range: (70°F - 2500°F)

$$E_i = 3.9323 \times 10^{-9} \, T^3 - 1.2789 \times 10^{-5} \, T^2 + 4.6574 \times 10^{-3} \, T + 14.919 \qquad (A.10)$$

5. As-Manufactured HP-90A-10C (Completed MIT Project)

a) Strength

- Brittle Region: (T < 2100°F)

$$S = 169.0638 \ (1 - \sqrt{T/10494.578})$$
(A.11a)

- Ductile Region: (T > 2100°F)

$$S = -0.10313 \ T + 310.0025$$
(A.11b)

- Complete Temperature Range: (70°F - 2500°F)

$$S = -3.9661 \times 10^{-8} \ T^3 + 1.5260 \times 10^{-4} \ T^2 - 0.18224T + 167.6853$$
(A.11c)

b) Associated Peak Strain

- Brittle Region: (T < 2100°F)

$$\epsilon_p = 8.1104 \times 10^{-3} \times 10^{(1.2773 \times 10^{-4} \ T)}$$
(A.12a)

- Complete Temperature Range: (70°F - 2500°F)

$$\epsilon_p = 4.8509 \times 10^{-12} \ T^3 - 1.3904 \times 10^{-8} \ T^2 - 1.0428 \times 10^{-5} \ T$$
$$+ 8.8355 \times 10^{-3}$$
(A.12b)

c) Initial Stiffness

- Temperature Range: (70°F - 2500°F)

$$E_i = -1.1941 \times 10^{-3} \ T^2 - 2.6074 \ T + 1.7749 \times 10^4$$
(A.13)

6. As-Manufactured HP-50A-50C (Completed MIT Project)

- Temperature Range: (70°F - 2000°F)

a) Strength

$$S = -2.3514 \times 10^{-5} \ T^2 + 1.4790 \times 10^{-2} \ T + 185.48$$
(A.14)

b) Associated Peak Strain

$$\epsilon_p = 5.5836 \times 10^{-10} T^2 + 9.8576 \times 10^{-7} T + 8.0751 \times 10^{-3} \qquad (A.15)$$

c) Initial Stiffness

$$E_i = -3.0546 \times 10^{-3} T^2 + 1.5221 T + 2.0487 \times 10^{-4} \qquad (A.16)$$

7. As-Manufactured HP-25A-75C (Completed MIT Project)

a) Strength

- Brittle Region: $(T < 2100^{\circ}F)$

$$S = 233.7012 \left(1 - \sqrt{T/12857.57}\right) \qquad (A.17a)$$

- Ductile Region: $(T > 2100^{\circ}F)$

$$S = -0.19453 T + 547.77 \qquad (A.17b)$$

- Complete Temperature Range: $(70^{\circ}F - 2500^{\circ}F)$

$$S = -1.7014 \times 10^{-8} T^3 + 4.0917 \times 10^{-5} T^2 - 0.05731 T + 217.9521 \qquad (A.17c)$$

b) Associated Peak Strain

- Brittle Region: $(T < 2100^{\circ}F)$

$$\epsilon_p = 6.8541 \times 10^{-3} \times 10^{(1.7045 \times 10^{-4} T)} \qquad (A.18a)$$

- Complete Temperature Range: $(70^{\circ}F - 2500^{\circ}F)$

$$\epsilon_p = -5.3950 \times 10^{-14} T^3 + 2.5434 \times 10^{-9} T^2 - 1.1436 \times 10^{-6} T$$
$$+ 7.6571 \times 10^{-3} \qquad (A.18b)$$

c) Initial Stiffness

- Complete Temperature Range: $(70^{\circ}F - 2500^{\circ}F)$

$$E_i = -3.7138 \times 10^{-7} T^3 - 2.9046 \times 10^{-3} T^2 + 0.16713 T$$
$$+ 2.4867 \times 10^4 \qquad (A.19)$$

8. As-Manufactured HP-80C-20M (Completed MIT Project)

a) Strength

- Brittle Region: (T < 2100°F)

$$S = 151.1203 (1 - \sqrt{T/27360.33}) \tag{A.20a}$$

- Ductile Region: (T > 2100°F)

$$S = -0.2628\ T + 661.298 \tag{A.20b}$$

- Complete Temperature Range: (70°F - 2500°F)

$$S = -2.3739 \times 10^{-8}\ T^3 + 6.4818 \times 10^{-5}\ T^2 - 0.065482\ T + 147.544 \tag{A.20c}$$

b) Associated Peak Strain

- Brittle Region: (T < 2100°F)

$$\epsilon_p = 5.1004 \times 10^{-3} \times 10^{(1.1659 \times 10^{-4}T)} \tag{A.21a}$$

- Complete Temperature Range: (70°F - 2500°F)

$$\epsilon_p = 8.9507 \times 10^{-12}\ T^3 - 2.1810 \times 10^{-8}\ T^2 + 1.5272 \times 10^{-5}\ T$$
$$+\ 3.73887 \times 10^{-3} \tag{A.21b}$$

c) Initial Stiffness

- Complete Temperature Range: (70°F - 2500°F)

$$E = -8.0738 \times 10^{-9}\ T^3 + 2.8328 \times 10^{-5}\ T^2 - 3.2650 \times 10^{-2} + 29.546 \tag{A.22}$$

9. As-Manufactured FC-7A-78C-8M (Completed MIT Project)

a) Strength

- Brittle Region: (T < 2100°F)

$$S = 85.8637 (1 - \sqrt{T/12018.92}) \tag{A.23a}$$

- Ductile Region: ($T > 2100^\circ F$)

$$S = -0.074917\ T + 208.581 \tag{A.23b}$$

- Complete Temperature Range: ($70^\circ F - 2500^\circ F$)

$$S = -2.2092 \times 10^{-9}\ T^3 - 2.4846 \times 10^{-6}\ T^2 - 1.2373 \times 10^{-3} T + 77.148 \tag{A.23c}$$

b) Associated Peak Strain

- Brittle Region: ($T < 2100^\circ F$)

$$\epsilon_p = 4.3788 \times 10^{-3} \times 10^{(5.5625\ \times\ 10^{-5} T)} \tag{A.24a}$$

- Complete Temperature Range: ($70^\circ F - 2500^\circ F$)

$$\epsilon_p = 7.4951 \times 10^{-12}\ T^3 - 2.3202 \times 10^{-8}\ T^2 + 1.8305 \times 10^{-5}\ T$$
$$+ 2.7989 \times 10^{-3} \tag{A.24b}$$

c) Initial Stiffness

- Complete Temperature Range: ($70^\circ F - 2500^\circ F$)

$$E_i = -5.5779 \times 10^{-9}\ T^3 + 2.0663 \times 10^{-5}\ T^2 - 2.8226 \times 10^{-2}\ T + 27.955 \tag{A.25}$$

10. Dense Alumina Refractory Castable (Tseng, 82)

a) Strength

- Temperature Range: ($70^\circ F - 2000^\circ F$)

$$S = -8.3485 \times 10^{-10}\ T^3 + 3.0396 \times 10^{-6}\ T^2 - 2.2347 \times 10^{-3}\ T + 9.6731 \tag{A.26}$$

b) Associated Peak Strain

- Temperature Range: ($70^\circ F - 2000^\circ F$)

$$\epsilon_\rho = 1.4523 \times 10^{-11}\ T^3 - 2.9040 \times 10^{-8}\ T^2 + 1.6628 \times 10^{-5}\ T$$
$$- 4.4438 \times 10^{-4} \tag{A.27}$$

c) Initial Stiffness

- Temperature Range: ($70^\circ F - 2500^\circ F$)

$$E_i = 5.570\ \exp\ (-0.00108\ T) + 0.192 \tag{A.28a}$$

$$E_i = -3.24073 \times 10^{-10} \, T^3 + 2.1992 \times 10^{-6} \, T^2 - 5.5384 \times 10^{-3} \, T$$
$$+ 5.7268 \tag{A.28b}$$

11. Insulating Alumina Refractory Castable (Tseng, 82)

a) Strength

- Temperature Range: $(70°F - 1500°F)$

$$S = 4.3994 \times 10^{-9} \, T^3 - 1.1358 \times 10^{-5} \, T^2 + 9.3383 \times 10^{-3} \, T + 0.18047 \tag{A.29}$$

b) Associated Peak Strain

- Temperature Range: $(70°F - 1500°F)$

$$\epsilon_\rho = 2.2417 \times 10^{-11} \, T^3 - 3.5767 \times 10^{-8} \, T^2 + 1.4848 \times 10^{-5} \, T$$
$$+ 1.9233 \times 10^{-3} \tag{A.30}$$

c) Initial Stiffness

- Temperature Range: $(70°F - 2500°F)$

$$E_i = 1.940 \exp(-0.00290 \, T) + 0.390 \tag{A.31a}$$

$$E_i = -4.0622 \times 10^{-10} \, T^3 + 2.0936 \times 10^{-6} \, T^2 - 3.41496 \times 10^{-3} \, T$$
$$+ 2.1683 \tag{A.31b}$$

12. Commercial Refractory Castable (Wygant and Buckley, 54)

Strength

- Temperature Range: $(70°F - 2170°F)$

$$S = 1.6339 \times 10^{-10} \, T^3 + 3.6879 \times 10^{-7} \, T^2 - 2.0349 \times 10^{-3} \, T$$
$$+ 2.2344 \tag{A.32}$$

13. Portland Cement Concrete (Anderberg and Thelandersson, 76)

- Temperature Range: $(70^{\circ}F - 1400^{\circ}F)$

a) Strength

$$S = 7.7947 \times 10^{-9} T^3 - 2.4956 \times 10^{-5} T^2 + 0.0124\, T + 13.308 \qquad (A.33)$$

b) Associated Peak Strain

$$\epsilon_{\rho} = -8.2864 \times 10^{-12} T^3 + 1.8810 \times 10^{-8} T^2 - 6.6223 \times 10^{-6} T$$
$$+ 3.3479 \times 10^{-3} \qquad (A.34)$$

c) Initial Stiffness

$$\frac{E_i}{1000} = -1.5432 \times 10^{-9} T^3 + 6.1706 \times 10^{-6} T^2 - 0.015809T + 15.9044 \qquad (A.35)$$

A.1.3 Functional Representation of Thermomechanical Properties in Compression and Low P_{O_2}

In this section the stiffness variation of as–manufactured and slag–impregnated refractories in reducing atmospheres ($P_{O_2} = 10^{-8}$ atm) is given functionally. The units and symbols are the same as for Section A.2.1.

1. <u>As-Manufactured CPS-90A-10C</u> (Completed MIT Project)

$$\frac{E_i \; (P_{O_2} = 10^{-8} \; atm)}{E_i \; (air)} = -2.1533 \times 10^{-10} \; T^3 + 4.8899 \times 10^{-7} \; T^2$$

$$+2.0350 \times 10^{-5} \; T + 0.91599 \qquad (A.36)$$

2. <u>Slag-Impregnated CPS-90A-10C</u> (Completed MIT Project)

$$E_i \; (P_{O_2} = 10^{-8} \; atm) = 2.0567 \times 10^{-11} \; T^3 - 6.7141 \times 10^{-8} \; T^2$$

$$+ 2.1616 \times 10^{-4} \; T + 0.57441 \qquad (A.37)$$

3. <u>As-Manufactured CPS-82C-18M</u> (Completed MIT Project)

$$\frac{E_i \; (P_{O_2} = 10^{-8} \; atm)}{E_i \; (air)} = 4.4525 \times 10^{-10} \; T^3 - 1.0016 \times 10^{-6} \; T^2$$

$$+ 3.5515 \times 10^{-4} \; T + 1.0932 \qquad (A.38)$$

4. <u>Slag-Impregnated CPS-82C-18M</u> (Completed MIT Project)

- Temperature range : $(1200^\circ F - 2200^\circ F)$

$$E_i \; (P_{O_2} = 10^{-8} \; atm) = 1.3481 \times 10^{-5} \; T^2 - 0.055065 \; T + 56.8357 \qquad (A.39)$$

A.1.4 Functional Representation of Modulus of Rupture Data at Elevated

Temperatures in Air

In this Section the variation with temperature of the modulus of rupture is given. The data has been obtained from manufacturer's information or from the literature. The following symbols are used:

o   MOR (ksi) refers to the modulus of rupture expressed in 'ksi'; and

o   T is the temperature expressed in ^{O}F.

English units are used, and the conversion factors are the same as the one in Section A.2.1.

1. __AX581__ (Norton Company)

$$MOR = -1.6728 \times 10^{-7} T^2 + 3.2050 \times 10^{-4} T + 4.6465 \tag{A.40}$$

2. __TX591__ (Norton Company)

$$MOR = -5.8714 \times 10^{-8} T^2 - 4.0557 \times 10^{-4} T + 3.4299 \tag{A.41}$$

3. __AX565__ (Norton Company)

$$MOR = -7.6426 \times 10^{-7} T^2 + 1.6215 \times 10^{-3} T + 5.4200 \tag{A.42}$$

4. __Alumina-Silica Brick, 50% Alumina__ (Miller and Davies, 66)

- $T < 2000^{\circ}F$

$$MOR = 5.1430 \times 10^{-5} T + 1.0444 \tag{A.43a}$$

- $T \geq 2000^{\circ}F$

$$MOR = -4.0526 \times 10^{-3} T + 10.323 \tag{A.43b}$$

- Complete Temperature Range: $(70^{\circ}F - 2500^{\circ}F)$

$$MOR = -8.1978 \times 10^{-10} T^3 + 2.8125 \times 10^{-6} T^2 - 2.2892 \times 10^{-3} T$$
$$+ 1.3417 \tag{A.43c}$$

5. __Dense Alumina-Silica Brick, 60% Alumina__ (Miller and Davies, 66)

- $T < 2000^{\circ}F$

$$MOR = 1.0017 \times 10^{-4} T + 1.8669 \tag{A.44a}$$

- $T \geq 2000^{\circ}F$

$$MOR = -2.2222 \times 10^{-3} T + 6.7489 \tag{A.44b}$$

- Complete Temperature Range: $(70^{\circ}F - 2900^{\circ}F)$

$$MOR = -2.1531 \times 10^{-10} \, T^3 + 3.9398 \times 10^{-7} \, T^2 + 1.6957 \times 10^{-4} \, T$$

$$+ 1.7605 \tag{A.44c}$$

6. Dense Alumina-Silica Brick, 90% Alumina (Miller and Davies, 66)

- $T < 2000^{\circ}F$

$$MOR = -4.0521 \times 10^{-4} \, T + 3.0909 \tag{A.45a}$$

- $T \geq 2000^{\circ}F$

$$MOR = -2.4602 \times 10^{-3} \, T + 8.4154 \tag{A.45b}$$

- Complete Temperature Range: $(70^{\circ}F - 2900^{\circ}F)$

$$MOR = -7.0289 \times 10^{-10} \, T^3 + 2.9185 \times 10^{-6} \, T^2 - 3.3808 \times 10^{-3} \, T$$

$$+ 3.6021 \tag{A.45c}$$

7. Alumina-Silica Brick, 99% Alumina (Miller and Davies, 66)

- $T < 2000^{\circ}F$

$$MOR = -2.9658 \times 10^{-4} \, T + 1.8803 \tag{A.46a}$$

- $T \geq 2000^{\circ}F$

$$MOR = -1.3000 \times 10^{-3} \, T + 3.8800 \tag{A.46b}$$

- Complete Temperature Range: $(70^{\circ}F - 2500^{\circ}F)$

$$MOR = -2.5746 \times 10^{-10} \, T^3 + 8.2495 \times 10^{-7} \, T^2 - 9.9879 \times 10^{-4} \, T$$

$$+ 1.9872 \tag{A.46c}$$

A.2 THERMOPHYSICAL PROPERTIES

The thermophysical data is presented in this Section. The organization of the thermophysical data is given in Table A.38. The thermophysical data is presented in Tables A.39 to A.51, and Equations A.47 to A.74. Fit of Equations A.47 to A.74 to the data is presented in Appendix B.

A.2.1 Tabular Representation of Thermophysical Properties

The following tables (Tables A.39 to A.51) present some of the thermophysical data.

Table A.38

Thermophysical Properties

Material	Source of Information	Thermal Conductivity K	Coefficient of Linear Expansion α	Thermal Diffusivity	Density ρ	Specific Heat C_p
		vs. T	vs. T	$= \dfrac{K}{\rho C_p}$ vs. T	vs. T	vs. T
AX581 Norton Sintered 90% Al_2O_3 10% Cr_2O_3	Norton Co.	Eq. A.47	Eq. A.48	–		Eq. A.49 Table A.39
TX591 Norton Sintered 82% Cr_2O_3 18% MgO	Norton Co.	Eq. A.50	Eq. A.51	–		Eq. A.52 Table A.39
AX565 Norton Sintered 50% Al_2O_3 50% Cr_2O_3	Norton Co.	–	Table A.39	–	Table A.39	–

Norton AX627-D Hot Pressed 75% Cr_2O_3 25% Al_2O_3	Norton Co.	Eq. A.53 Table A.40	–	Eq. A.54 Table A.40	Eq. A.55 Table A.39
Norton AX627-B Hot Pressed 50% Al_2O_3 50% Cr_2O_3	Norton Co.	Eq. A.56 Table A.41	–	Eq. A.57 Table A.41	Eq. A.58 Table A.39
TX628 Norton Hot Pressed 80% Cr_2O_3 20% MgO	Norton Co.	Eq. A.59 Table A.42	–	Eq. A.60 Table A.42	Eq. A.61 Table A.39
Harbison Walker HW25-83 75% Cr_2O_3 23.4% Al_2O_3 Sintered	Harbison Walker	Eq. A.62 Table A.43	Eq. A.63 Table A.44	–	Table A.39	–
Sohio E 78% Cr_2O_3 8% Al_2O_3 Fused-Cast	Sohio Engineered Materials Co.	Eq. A.64 Table A.45	Eq. A.65 Table A.46	–	Table A.39	–

Sohio K3 59% Al_2O_3 27% Cr_2O_3 Fused Cast	Sohio Engineered Materials Co.	Eq. A.66 Table A.47	Eq. A.67 Table A.48	–	Table A.39	–
Sohio B 82% Cr_2O_3 14% Al_2O_3 Fused Cast	Sohio Engineered Materials Co.	–	Eq. A.65	–	Table A.39	–
Radex BCF-812 79% Cr_2O_3 19.5% MgO Sintered	General Refractories	Table A.39	Table A.39 Temperature Independent	–	Table A.39 Temperature Independent	Temperature Independent
Radex BCF-86C 80% Cr_2O_3 18.5% MgO Sintered	General Refractories	Table A.39	Table A.39 Temperature Independent	–	Table A.39 Temperature Independent	Temperature Independent
ZIRCHROM 60 62% Cr_2O_3 16% Al_2O_3 Sintered	Savoie Refractories	Table A.39	Table A.39 Average Value	–	Table A.39 Temperature Independent	–
ZIRCHROM 80 81% Cr_2O_3 9% Al_2O_3 Sintered	Savoie Refractories	–	Table A.39 Average Value	–	Table A.39 Temperature Independent	–

JM-20 $31.4\%Al_2O_3$ $53.9\%SiO_2$ Insulating	Eastern Refractories	Eq. A.68 Table A.49	Table A.39	–	Table A.39	–
JM-23 $31.4\%Al_2O_3$ $53.9\%SiO_2$ Insulating	Eastern Refractories	Eq. A.69 Table A.49	Table A.39	–	Table A.39	–
JM-30 $77.9\%Al_2O_3$ $20.7\%SiO_2$ Insulating	Eastern Refractories	Eq. A.70 Table A.49	Table A.39	–	Table A.39	–
JM-32 $34.1\%Al_2O_3$ $59.4\%SiO_2$ Insulating	Eastern Refractories	Eq. A.71 Table A.49	Table A.39	–	Table A.39	–
Dense Refractory Alumina Concrete	(Tulga,79; Pike et. al.,80)	–	Eq. A.72 Table A.50	–	–	–
Insulating Refractory Alumina Concrete	(Tulga,79; Pike et. al.,80)	Eq. A.73 Table A.51	Eq. A.74 Table A.50	–	–	–

Table A.39

Thermophysical Properties

Material	Source of Information	Thermal Conductivity K vs. T	Coefficient of Linear Expansion α vs. T	Density ρ vs. T	Specific Heat C_p vs. T
AX581 Norton Sintered 90% Al_2O_3 10% Cr_2O_3	Norton Co.			3.3 g/cc	
TX591 Norton Sintered 82% Cr_2O_3 18% MgO	Norton Co.			3.8 g/cc	
AX565 Norton Sintered 90% Al_2O_3 10% Cr_2O_3	Norton Co.		0.08% @ 1750°C	3.3 g/cc	

Norton AX627-D Hot Pressed 75% Cr_2O_3 25% Al_2O_3	Norton Co.		4.73 g/cc	0.25 Cal/g^{o}C
Norton AX627-B Hot Pressed 50% Al_2O_3 50% Cr_2O_3	Norton Co.		4.4 g/cc	0.25 Cal/g^{o}C
TX628 Norton Hot Pressed 80% Cr_2O_3 20% MgO	Norton Co.		4.16 g/cc	0.21 Cal/g^{o}C
Harbison Walker HW25-83 75% Cr_2O_3 23.4% Al_2O_3 Sintered	Harbison Walker	250 pcf		
Sohio E 78% Cr_2O_3 8% Al_2O_3 Fused Cast	Sohio Engineered Materials Co.	4.25 g/cc		

Sohio K3 59% Al_2O_3 27% Cr_2O_3 Fused Cast	Sohio Engineered Materials Co.			3.83 g/cc	
Sohio B 82% Cr_2O_3 14% Al_2O_3 Fused Cast	Sohio Engineered Materials Co.			4.57 g/cc	
Radex BCF 812 79% Cr_2O_3 19.5% MgO Sintered	General Refractories	2.5-3 W/M^{o}K @ 600°C 2-2.5 W/M^{o}K @ 1200°C	8.5×10^{-6}/^{o}K	3.7-3.9 g/cc	0.75 (KJ/Kg ^{o}K)
Radex BCF 86C 80% Cr_2O_3 18.5% MgO Sintered	General Refractories	2.5-3 W/M^{o}K @ 600°C 2-2.5 W/M^{o}K @ 1200°C	8.5×10^{-6}/^{o}K	3.85 g/cc	0.75 (KJ/Kg ^{o}K)
ZIRCHROM 60 62% Cr_2O_3 16% Al_2O_3 Sintered	Savoie Refractories	2 W/M^{o}K @ 1000°C	8.2×10^{-6}/^{o}K	3.70 g/cc	

AX627-D

Table A.40

TEMPERATURE (^{o}C)	THERMAL DIFFUSIVITY (cm^2 s^{-1})	THERMAL CONDUCTIVITY (W/(m.K))	THERMAL CONDUCTIVITY Btu-in/(hr ft^2 ^{o}F)
25	0.0209	10.34	71.7
302	0.015	7.42	51.5
404	0.0135	6.68	46.3
500	0.0128	6.33	43.9
604	0.0118	5.84	40.5
702	0.0114	5.64	39.1
802	0.0109	5.39	37.4
902	0.0106	5.24	36.4
1003	0.0105	5.19	36.0
1100	0.0102	5.05	35.0
1200	0.00997	4.93	34.2
1300	0.00965	4.77	33.1
1400	0.00949	4.70	32.6
1500	0.00945	4.68	32.4
1600	0.00957	4.73	32.9

Source of Information: Norton Company, Worcester, MA.

AX627-B

Table A.41

TEMPERATURE (^{o}C)	THERMAL DIFFUSIVITY ($cm^2 s^{-1}$)	THERMAL CONDUCTIVITY W/(m.K)	THERMAL CONDUCTIVITY Btu-in/(hr ft^2 ^{o}F)
25	0.0253	11.64	80.8
311	0.0142	6.54	45.3
412	0.0129	5.94	41.2
512	0.0112	5.15	35.8
608	0.00986	4.54	31.5
706	0.0093	4.28	29.7
803	0.00909	4.18	29.0
905	0.00879	4.05	28.1
1006	0.00861	3.96	27.5
1100	0.00867	3.99	27.7
1200	0.00871	4.01	27.8
1300	0.00876	4.03	28.0
1400	0.0087	4.00	27.8
1500	0.00864	3.98	27.6
1600	0.00864	3.98	27.6

Source of Information: Norton Company, Worcester, MA.

TX628

Table A.42

TEMPERATURE (°C)	THERMAL DIFFUSIVITY ($cm^2 s^{-1}$)	THERMAL CONDUCTIVITY W/(m.K)	THERMAL CONDUCTIVITY Btu-in/(hr ft^2 °F)
25	0.0148	5.41	37.5
317	0.0133	4.86	33.7
401	0.0119	4.35	30.2
503	0.0114	4.17	28.9
602	0.0113	4.13	28.7
706	0.0111	4.06	28.1
800	0.0109	3.98	27.6
902	0.0107	3.91	27.1
1000	0.0105	3.84	26.6
1100	0.0102	3.73	25.9
1200	0.00987	3.61	25.0
1300	0.0099	3.62	25.1
1400	0.00998	3.65	25.3
1500	0.0101	3.69	25.6
1600	0.0101	3.69	25.6

Source of Information: Norton Company, Worcester, MA.

Table A.43

Thermal Conductivity for HW25-83

T ($^\circ$F)	K_s (Btu-in/ft^2 hr $^\circ$F)
230	23.5
650	25.0
1100	21.0
1550	18.5
1950	17.5

Source: Harbison Walker Refractories

Table A.44

Coefficient of Thermal Expansion for HW25-83

T ($^\circ$F)	α (%)
200	0.02
400	0.11
800	0.30
1200	0.48
1600	0.66
2000	0.87
2400	1.08

Source: Harbison Walker Refractories

Table A.45

Thermal Conductivity for Sohio E

T (^{o}F)	K_s (Btu-in/ft^2 hr ^{o}F)
510	37.14
752	32.14
1112	28.57
1472	30.00
1832	35.00
2098	40.00

Source: Sohio Engineered Materials Company

Table A.46

Coefficient of Thermal Expansion for Sohio E

T (^{o}F)	α
392	0.2
752	0.336
1112	0.464
1472	0.6
1832	0.736
2192	0.871
2552	1.0

Source: Sohio Engineered Materials Company

Table A.47

Thermal Conductivity for Sohio K3

T ($^{\circ}$F)	K_s (Btu-in/ft^2 hr $^{\circ}$F)
392	30
752	25.43
1112	23.57
1472	22.71
1832	22.57
2044	22.43

Source: Sohio Engineered Materials Company

Table A.48

Coefficient of Thermal Expansion for Sohio K3

T ($^{\circ}$F)	α
392	0.110
752	0.271
1112	0.444
1472	0.623
1832	0.81
2192	1.021
2298	1.09

Source: Sohio Engineered Materials Company

Insulating Refractory Bricks
Thermal Conductivity Values
$Btu-in/(ft^2 \, ^oF \, hr)$

Table A.49

Temperature	JM-20	JM-23	JM-30	JM-32
$500\,^oF$	0.92	0.92	2.80	3.90
$1000\,^oF$	1.13	1.13	2.87	4.10
$1500\,^oF$	1.36	1.36	3.05	4.20
$2000\,^oF$	-	1.58	3.31	4.30
Maximum Use Temperature	$2000\,^oF$	$2300\,^oF$	$3000\,^oF$	$3200\,^oF$

Source of Information: Eastern Refractories Company
Auburn, MA

Refractory Concrete Thermal Expansion
(Tseng, 82)

T (^{o}F)	α Dense Refractory	α Insulating Refractory
80	0	0
280	0.070	0.053
400	0.096	0.026
500	0.079	0.004
530	0.053	0.013
1000	0.228	0.123
1250	0.447	0.272
1500	0.579	0.325
1800	0.649	0.412

Refractory Concrete Thermal Conductivity
(Tseng, 82)

T (^{o}F)	ascending T K_s $\frac{Btu-in}{hr\ ft^2\ {}^oF}$	descending T K_s $\frac{Btu-in}{hr\ ft^2\ {}^oF}$
320	1.608	1.275
750	1.431	1.235
1110	1.333	1.235
1470	1.333	1.275
1830	1.373	1.333
2190	1.451	1.441
2275	1.471	1.471

A.2.2 Functional Representation of Thermophysical Properties in Air

Thermophysical properties have been assembled from manufacturers data, and from the literature and are presented in this Section. The properties that have been collected are the thermal conductivity, coefficient of linear expansion, and product of density and specific heat. In some cases the manufacturers data was only given for thermal diffusivity and thermal conductivity; the product of density and specific heat was obtained by dividing the conductivity by the diffusivity. The following symbols and units were used:

o K_s for thermal conductivity, expressed in 'Btu–in/(hr ft^2 $^{\circ}$F)';

o α for coefficient of thermal expansion, expressed per $^{\circ}$F (i.e. '$^{\circ}$F^{-1} ');

o ρ for density, and C_p for specific heat; the product ρC_p is expressed in 'Btu /(in^3 $^{\circ}$F)';

o $\lambda = K_s/\rho C_p$ for thermal diffusivity expressed as 'in^2 /sec'; (the symbol usually used is α, but this would have conflicted with thermal expansion coefficient; and

o T for temperature expressed in '$^{\circ}$F'.

The following are conversion factors to the International System (SI) of units:

o 1 m = 39.370 in;

o 1 kg/m3 = 6.2428x10^{-2} lb/ft^3;

o 1 J/(Kg $^{\circ}$K) = 2.3901x10^{-4} Btu/(lb $^{\circ}$F) = 2.3901x10^{-4} cal/(g $^{\circ}$C);

o 1 W/(m $^{\circ}$K) = 6.9380 Btu in/(hr ft^2 $^{\circ}$F); and

o T ($^{\circ}$C) = [T ($^{\circ}$F) − 32] / 1.8 .

1. AX581 (Norton Company)

a) Thermal Conductivity

$$K_s = 2.8736 \times 10^{-11} T^3 - 1.0536 \times 10^{-7} T^2 + 3.2292 \times 10^{-15} T + 0.3245 \quad \text{(A.47)}$$

b) Coefficient of Thermal Expansion

$$\alpha \ (^{\circ}F^{-1}) = 5.0070 \times 10^{-6} \quad \text{(A.48)}$$

c) Product of Density and Specific Heat

$$\rho C_p = 9.5094 \times 10^{-13} T^3 - 5.4506 \times 10^{-9} T^2 + 1.2340 \times 10^{-5} T$$
$$+ 2.5515 \times 10^{-2} \quad \text{(A.49)}$$

2. TX591 (Norton Company)

a) Thermal Conductivity

$$K_s = -1.4471 \times 10^{-13} T^3 + 5.6285 \times 10^{-9} T^2 - 3.2404 \times 10^{-5} T + 0.2732 \quad \text{(A.50)}$$

b) Coefficient of Thermal Expansion

$$\alpha \ (^{\circ}F^{-1}) = 2.310 \times 10^{-9} T - 6.435 \times 10^{-6} \quad \text{(A.51)}$$

c) Product of Density and Specific Heat

$$\rho C_p = 4.1255 \times 10^{-13} T^3 - 2.3557 \times 10^{-9} T^2 + 6.6212 \times 10^{-6} T$$
$$+ 7.8174 \times 10^{-2} \quad \text{(A.52)}$$

3. AX627D (Norton Company)

a) Thermal Conductivity

$$K_s = -3.4507 \times 10^{-9} T^3 + 2.2732 \times 10^{-5} T^2 - 0.051792 T + 75.03 \quad \text{(A.53)}$$

b) Thermal Diffusivity

$$\lambda = -1.5642 \times 10^{-13} T^3 + 1.0286 \times 10^{-9} T^2 - 2.3414 \times 10^{-6} T$$
$$+ 3.3901 \times 10^{-3} \quad \text{(A.54)}$$

c) Product of Density and Specific Heat

$$\rho C_p = 1.6494 \times 10^{-14} \, T^3 - 6.0994 \times 10^{-11} \, T^2 + 5.9273 \times 10^{-8} \, T$$
$$+ \, 0.042686 \tag{A.55}$$

4. AX627B (Norton Company)

a) Thermal Conductivity

$$K_s = -6.8800 \times 10^{-9} \, T^3 + 4.3474 \times 10^{-5} \, T^2 - 0.088861 \, T$$
$$+ \, 86.5709 \tag{A.56}$$

b) Thermal Diffusivity

$$\lambda = -3.3413 \times 10^{-13} \, T^3 + 2.1 \times 10^{-9} \, T^2 - 4.3146 \times 10^{-6} \, T$$
$$+ \, 4.2045 \times 10^{-3} \tag{A.57}$$

c) Product of Density and Specific Heat

$$\rho C_p = -2.5565 \times 10^{-15} \, T^3 + 1.3318 \times 10^{-11} \, T^2 - 1.0363 \times 10^{-8} \, T$$
$$+ \, 0.039743 \tag{A.58}$$

5. TX628 (Norton Company)

a) Thermal Conductivity

$$K_s = -3.3503 \times 10^{-10} \, T^3 + 3.6880 \times 10^{-6} \, T^2 - 1.2374 \times 10^{-2} \, T$$
$$+ \, 38.521 \tag{A.59}$$

b) Thermal Diffusivity

$$\lambda = -1.9681 \times 10^{-14} \, T^3 + 2.2190 \times 10^{-10} \, T^2 - 7.5002 \times 10^{-7} \, T$$
$$+ \, 0.002351 \tag{A.60}$$

c) Product of Density and Specific Heat

$$\rho C_p = 8.6963 \times 10^{-15} \, T^3 - 4.1639 \times 10^{-11} \, T^2 + 5.3696 \times 10^{-8} \, T$$
$$+ \, 0.031530 \tag{A.61}$$

6. __HW25-83__ (Harbison Walker Refractories)

a) __Thermal Conductivity__

$$K_s = 6.9409 \times 10^{-9} \, T^3 - 2.4139 \times 10^{-5} \, T^2 + 0.019267 \, T + 20.3679 \qquad \text{(A.62)}$$

b) __Coefficient of Thermal Expansion__

$$\alpha = 4.7776 \times 10^{-4} \, T - 0.084108 \qquad \text{(A.63)}$$

7. __SOHIO E__ (Sohio Engineered Materials Company)

a) __Thermal Conductivity__

$$K_s = -3.8332 \times 10^{-9} \, T^3 + 3.0414 \times 10^{-5} \, T^2 - 5.5564 \times 10^{-2} \, T + 58.159 \qquad \text{(A.64)}$$

b) __Coefficient of Thermal Expansion__

$$\alpha = 3.7123 \times 10^{-4} \, T + 0.054549 \qquad \text{(A.65)}$$

8. __SOHIO K3__ (Sohio Engineered Materials Company)

a) __Thermal Conductivity__

$$K_s = -3.2092 \times 10^{-9} \, T^3 + 1.6211 \times 10^{-5} \, T^2 - 0.027597 \, T + 38.490 \qquad \text{(A.66)}$$

b) __Coefficient of Thermal Expansion__

$$\alpha = 5.1407 \times 10^{-4} \, T - 0.1139 \qquad \text{(A.67)}$$

9. __JM-20__ (Eastern Refractories)

__Thermal Conductivity__

$$K_s = 4 \times 10^{-8} \, T^2 + 3.6 \times 10^{-4} \, T + 0.73 \qquad \text{(A.68)}$$

10. JM-23 (Eastern Refractories)

Thermal Conductivity

$$K_s = -4 \times 10^{-11} T^3 + 1.6 \times 10^{-7} T^2 + 2.5 \times 10^{-4} T + 0.76 \qquad (A.69)$$

11. JM-30 (Eastern Refractories)

Thermal Conductivity

$$K_s = -4 \times 10^{-11} T^3 + 3.4 \times 10^{-7} T^2 - 3 \times 10^{-4} T + 2.87 \qquad (A.70)$$

12. JM-32 (Eastern Refractories)

Thermal Conductivity

$$K_s = 1.3333 \times 10^{-10} T^3 - 6 \times 10^{-7} T^2 + 1.0667 \times 10^{-3} T + 3.5 \qquad (A.71)$$

13. Dense Alumina Refractory Castable (Tseng, 82)

a) Coefficient of Thermal Expansion

$$\alpha = -1.7609 \times 10^{-10} T^3 + 6.2009 \times 10^{-7} T^2 - 1.9973 \times 10^{-4} T$$
$$+ 0.044278 \qquad (A.72)$$

b) Thermal Conductivity in Ascending Temperatures

$$K_s = -3.8935 \times 10^{-11} T^3 + 3.7341 \times 10^{-7} T^2 - 8.0599 \times 10^{-4} T$$
$$+ 1.8326 \qquad (A.73a)$$

c) Thermal Conductivity in Descending Temperatures

$$K_s = 7.2134 \times 10^{-12} T^3 + 1.0059 \times 10^{-7} T^2 - 2.0444 \times 10^{-4} T$$
$$+ 1.3297 \qquad (A.73b)$$

14. Insulating Alumina Refractory Castable (Tseng, 82)

Coefficient of Thermal Expansion

$$\alpha = -1.4954 \times 10^{-10} T^3 + 5.4857 \times 10^{-7} T^2 - 2.9782 \times 10^{-4} T$$
$$+ 0.046423 \qquad\qquad (A.74)$$

APPENDIX B
REGRESSION ANALYSIS OF THERMOMECHANICAL
AND THERMOPHYSICAL DATA

This Appendix contains the regression for a part of the data found in the material database. Figures B.1 to B.37 represent the regression of the thermomechanical properties in monotonic compression in air from the present project for as–manufactured and slag–impregnated dense refractory bricks. Figures B.38 to B.49 represent the regression of the thermomechanical properties in monotonic compression in air from the literature for as–manufactured dense and insulating refractory concrete, and Portland cement concrete. Figures B.50 to B.53 represent the regression of the thermomechanical properties in monotonic compression in reducing atmospheres from the present work for as–manufactured and slag–impregnated dense refractory bricks. Figures B.54 to B.64 represent the regression of modulus of rupture data at high temperatures obtained from the literature and manufacturers' data for selected refractory bricks. Finally, Figs. B.65 to B.87 represent the regression of the thermophysical properties from the literature and manufacturers' data for dense and insulating refractory bricks, and dense and insulating refractory concretes.

Figure B.1   Regression of data for Eqs. 8.1a and 8.1b
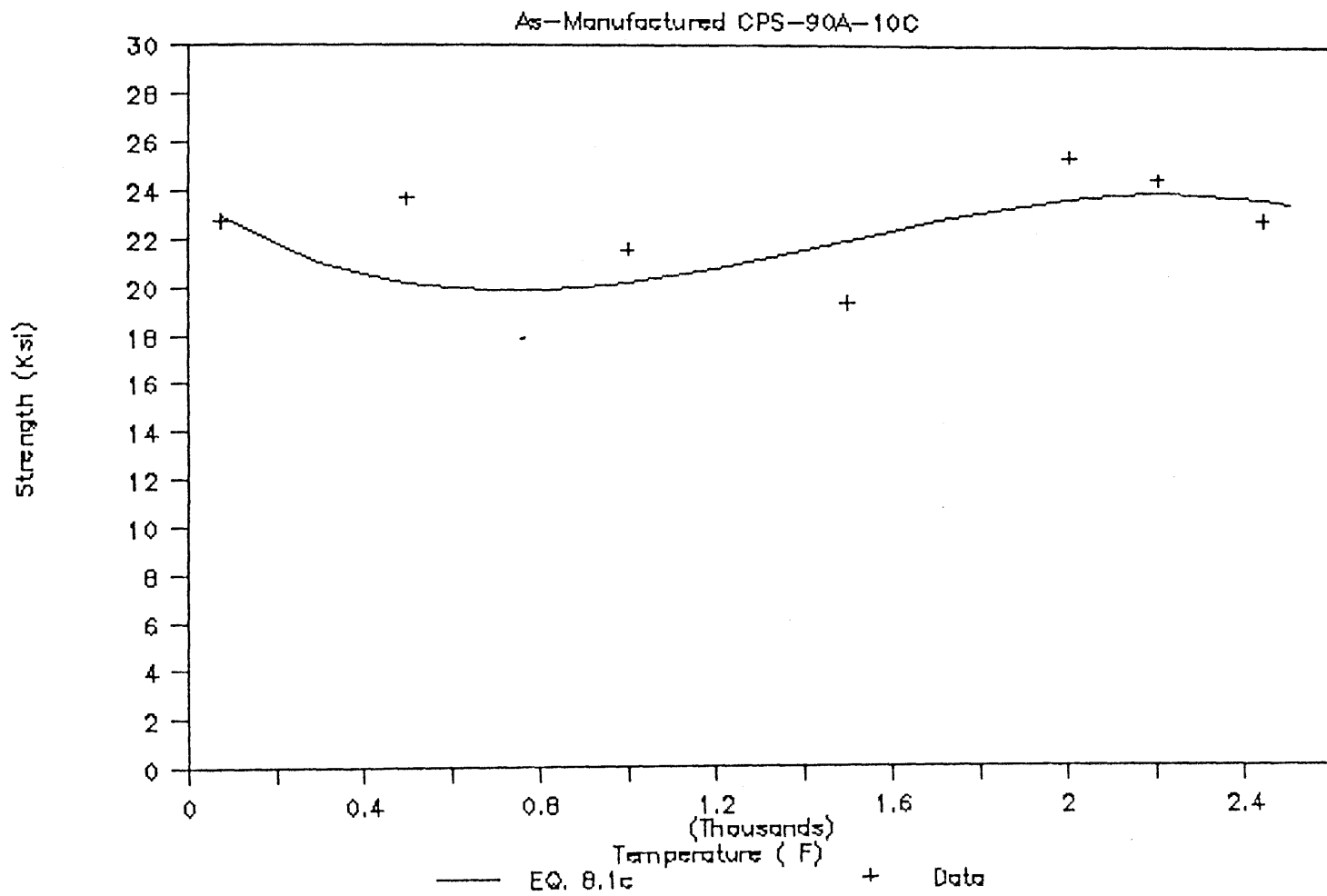
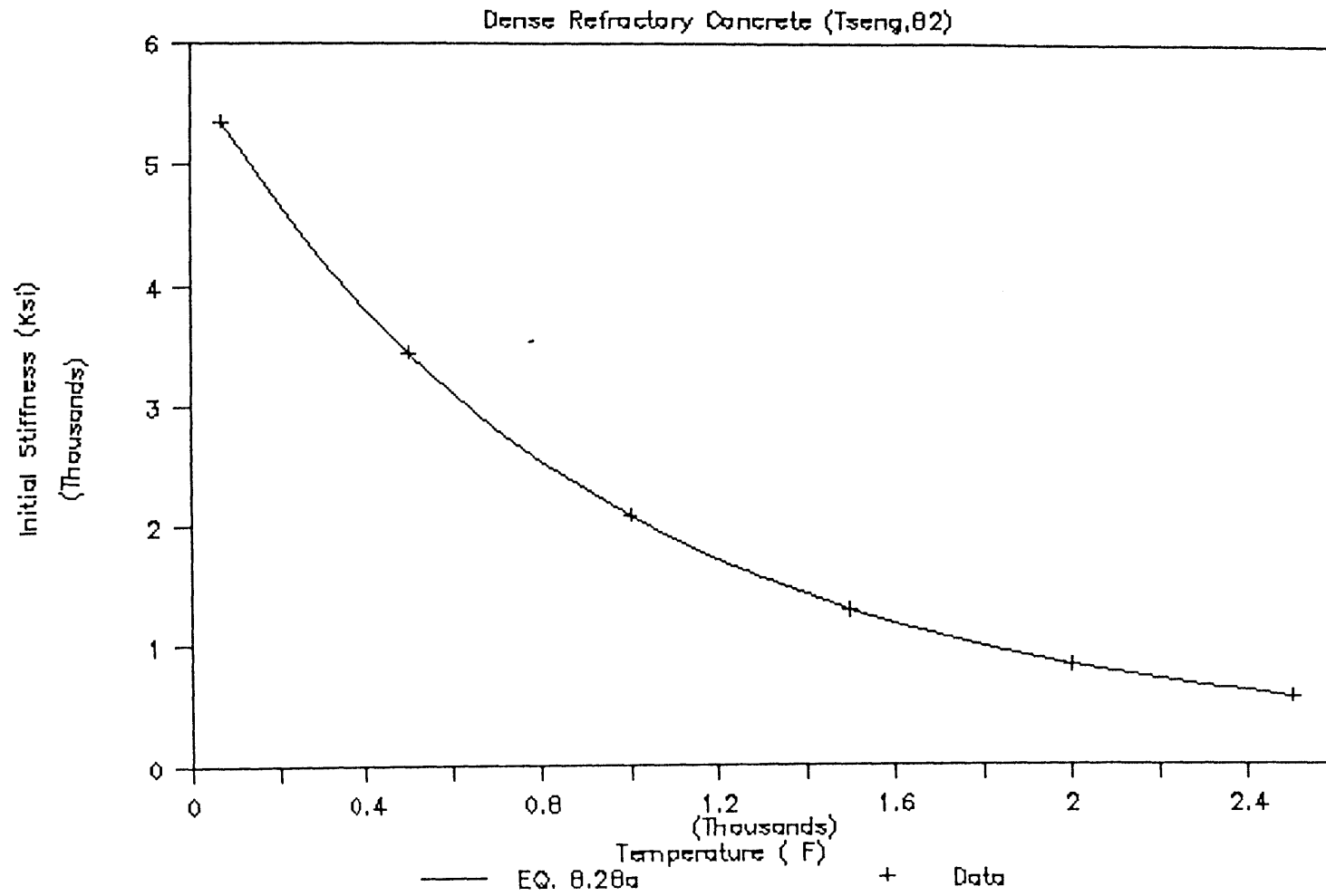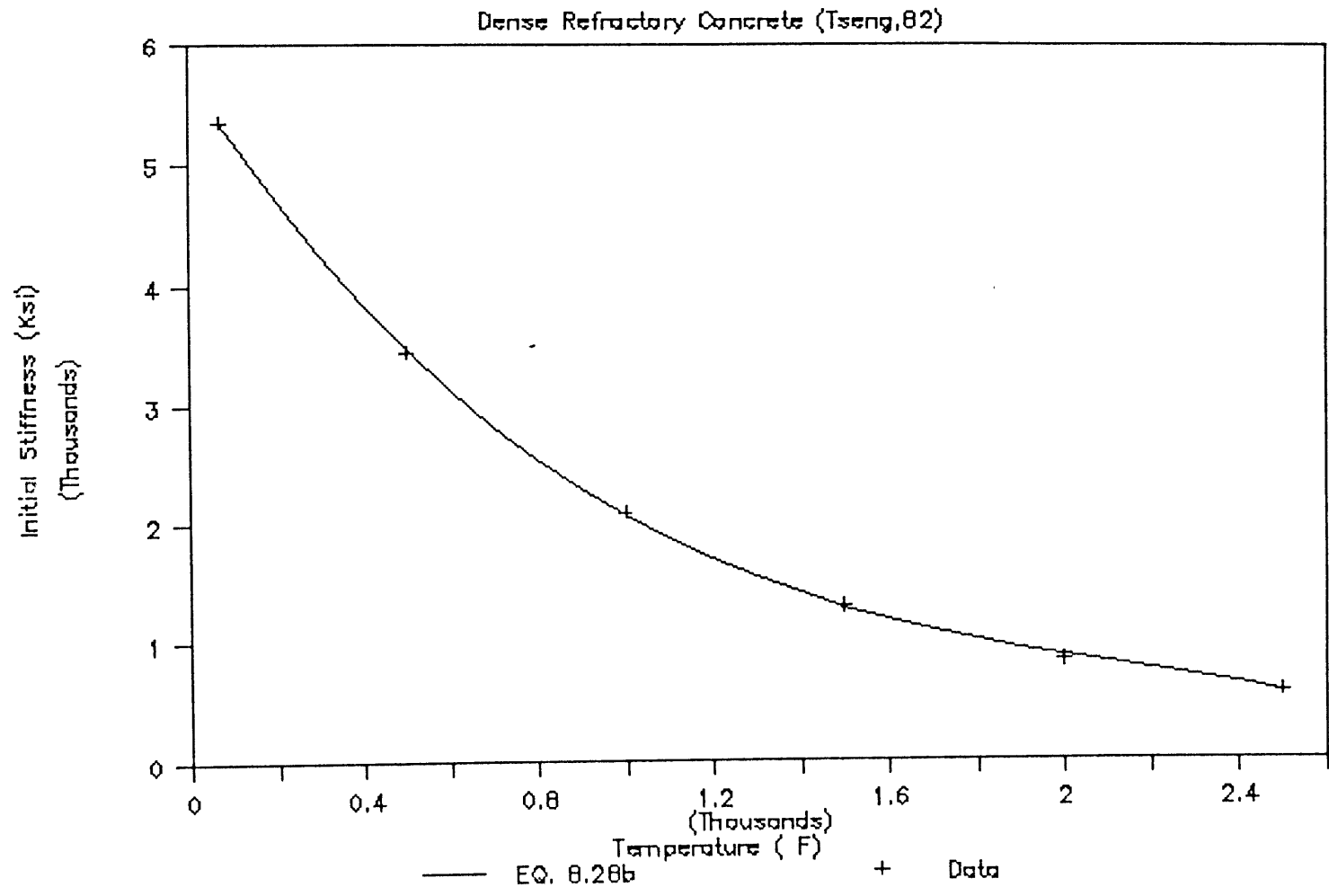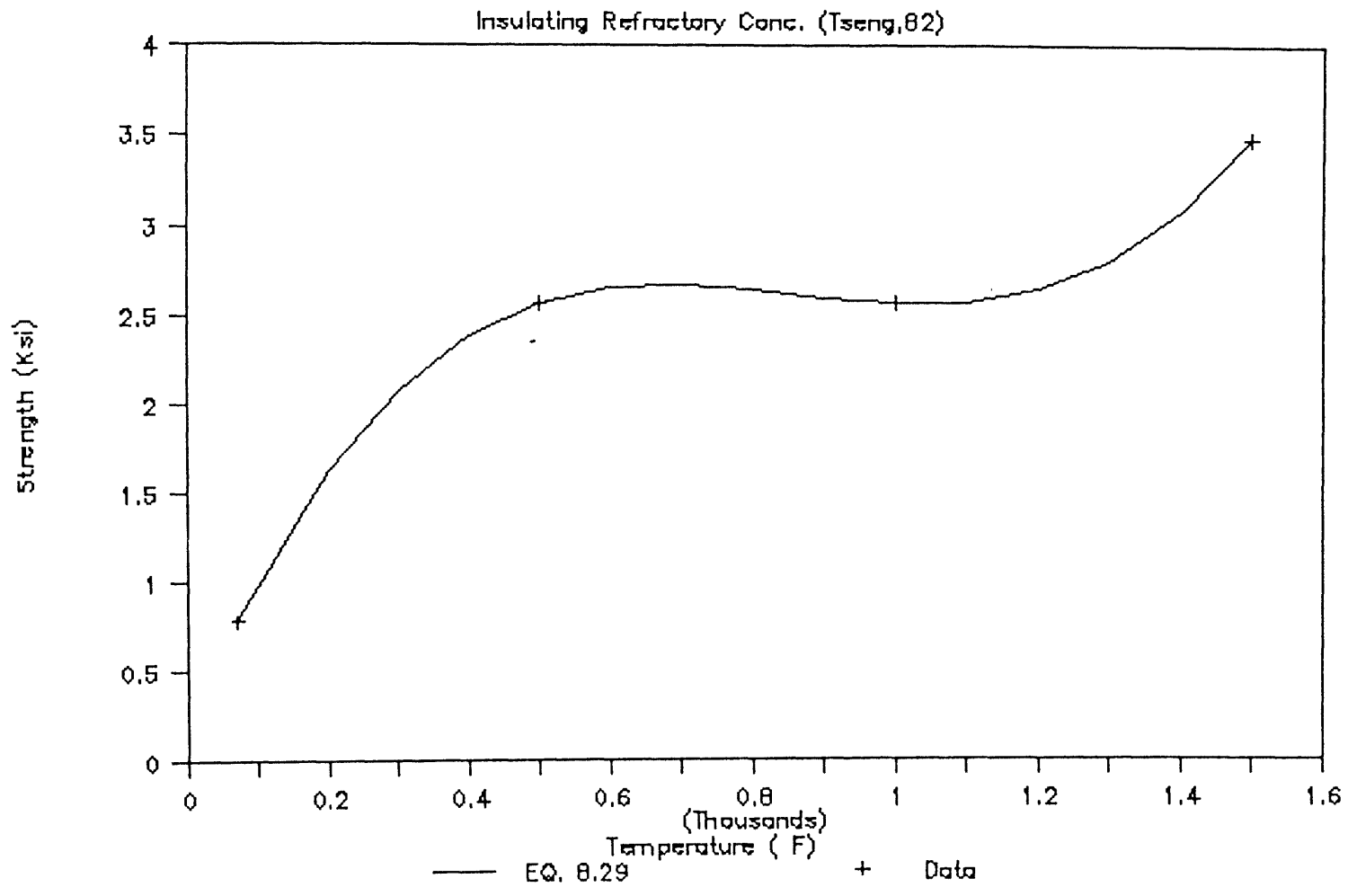Figure B.2   Regression of data for Eq. 8.1c
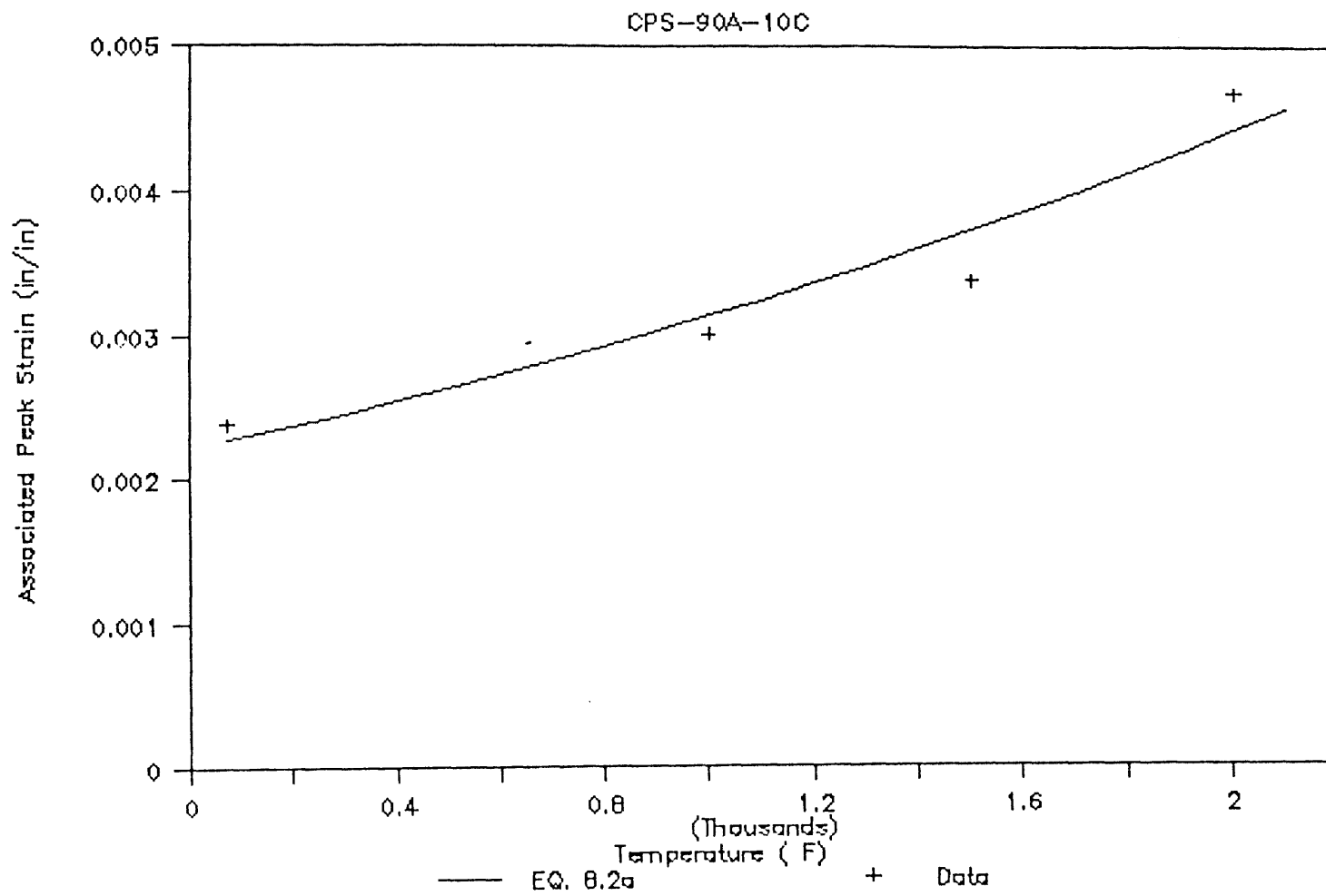
Figure B.3   Regression of data for Eq. 8.2a
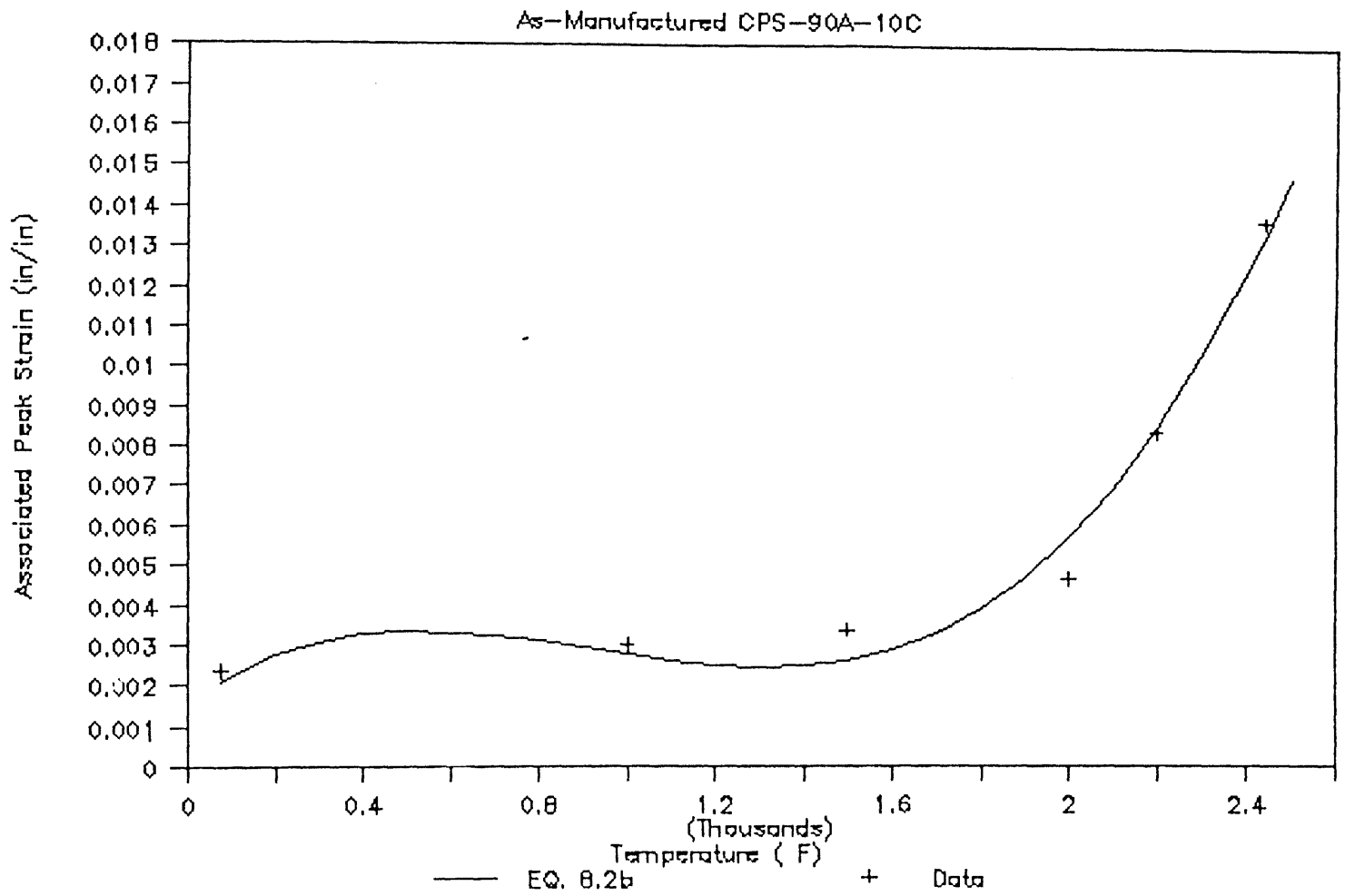
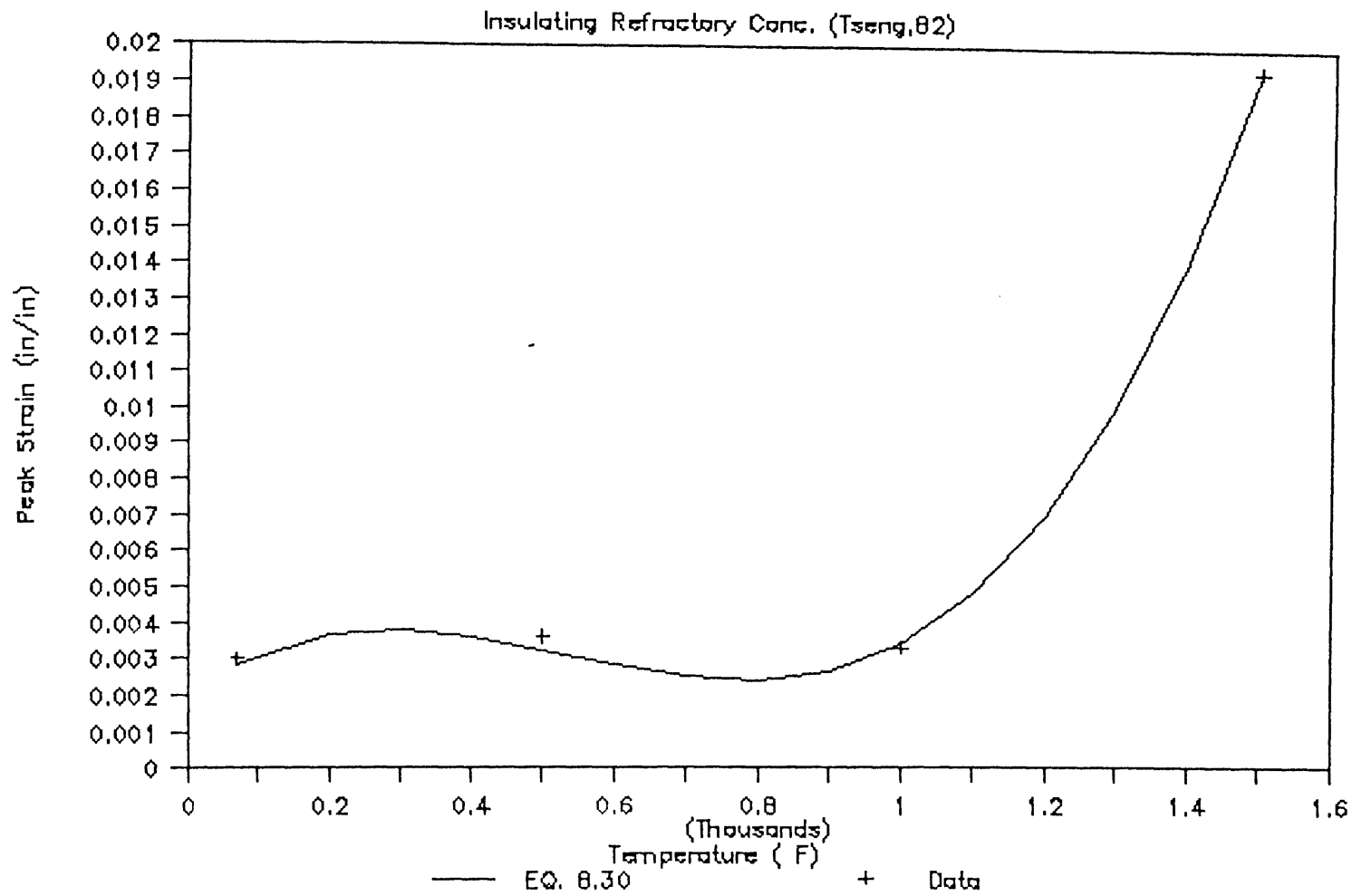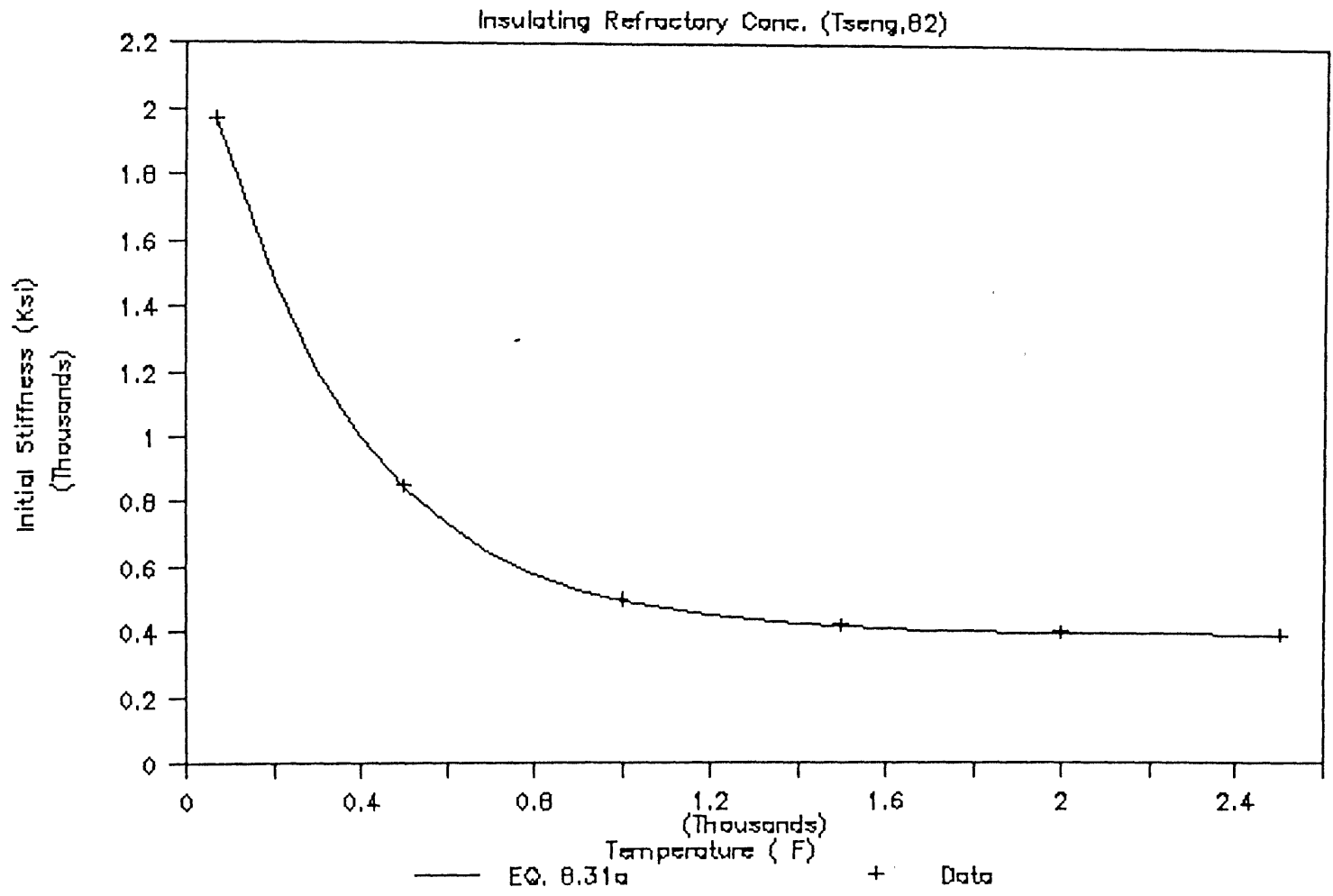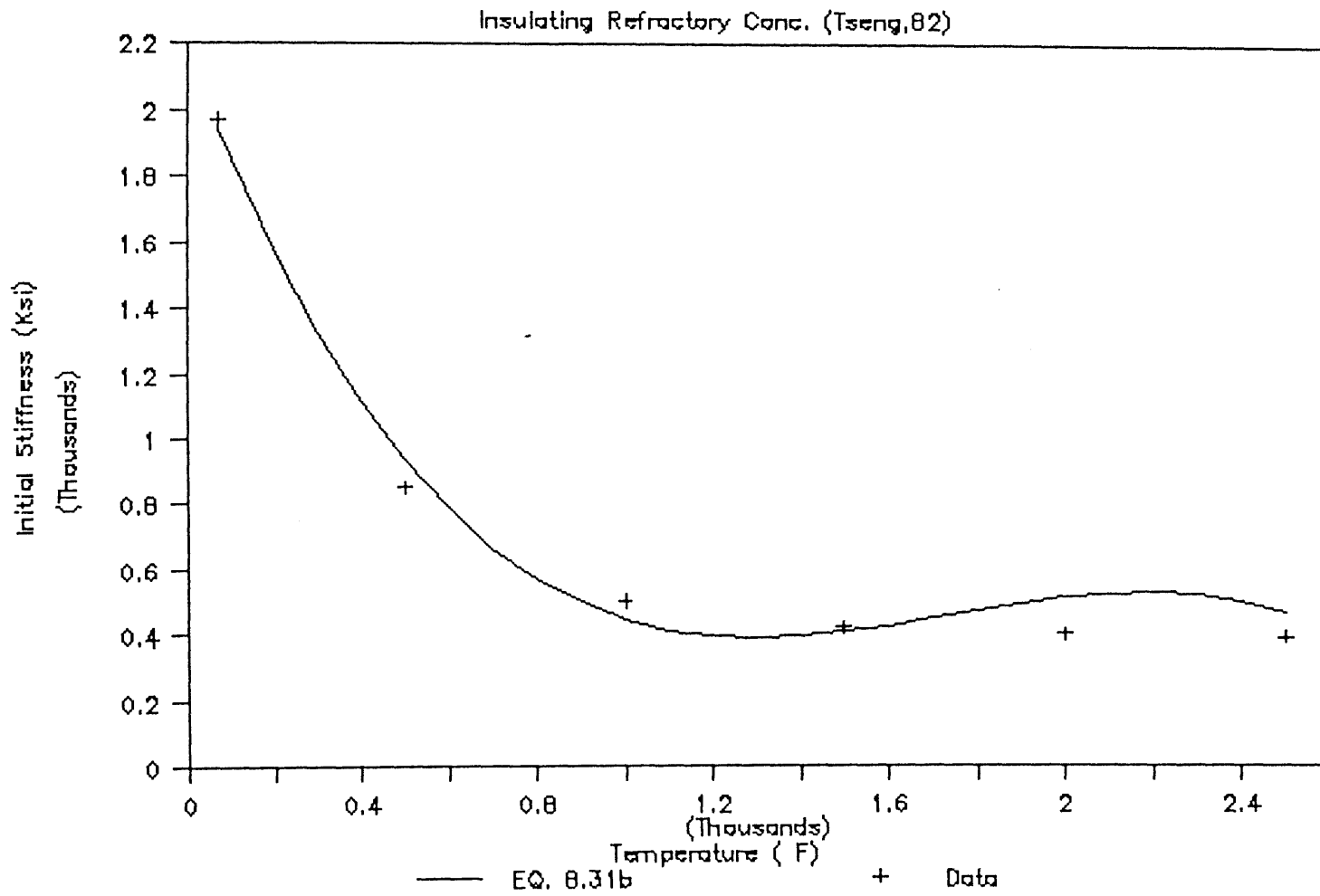Figure B.4   Regression of data for Eq. 8.2b

As-Manufactured CPS-90A-10C
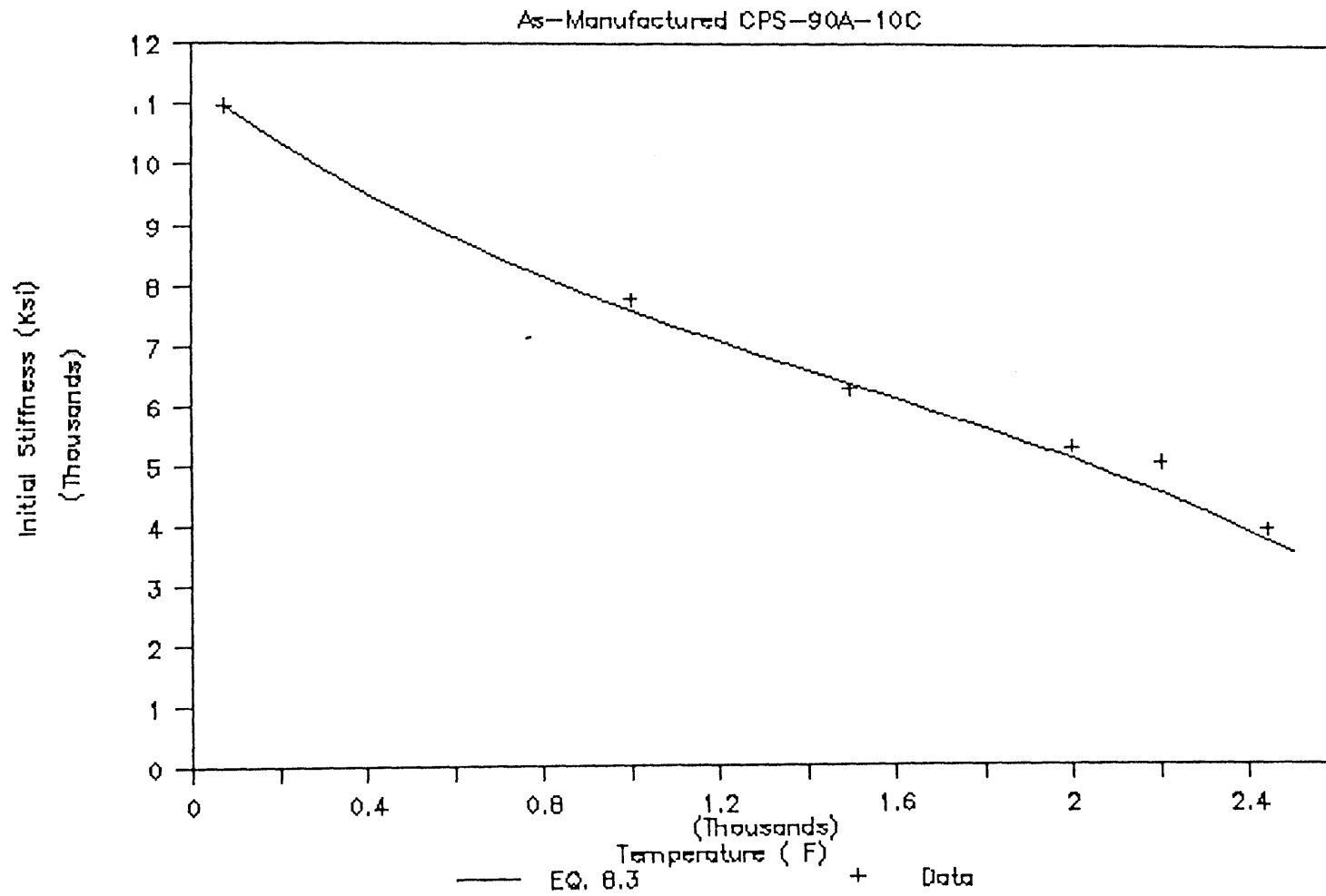
Figure B.5   Regression of data for Eq. 8.3

Slag—Impregnated CPS—90A—10C

Strength (Ksi)

Temperature (F)
(Thousands)

——— EQ. 8.4   +   Data
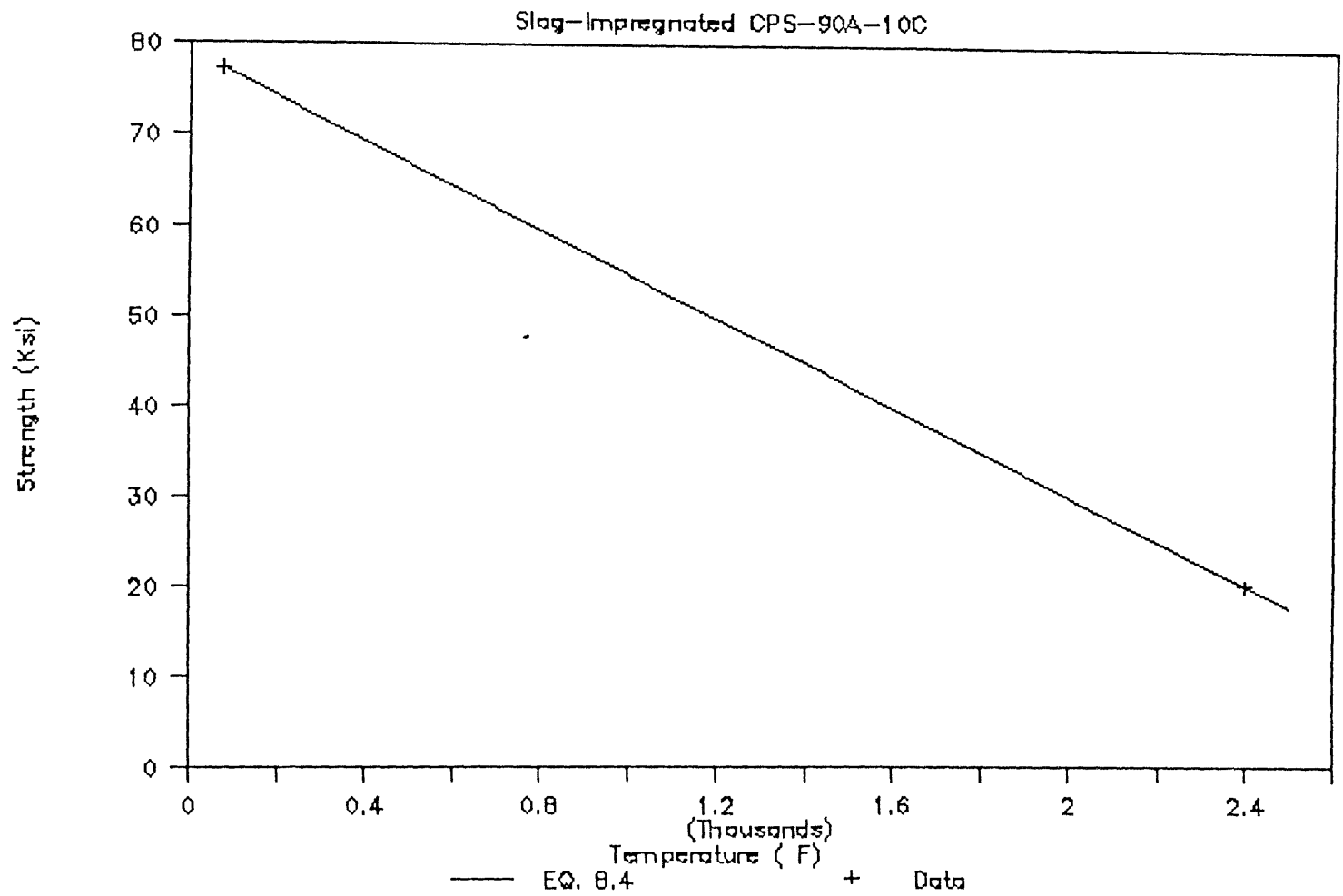
Figure B.6   Regression of data for Eq. 8.4
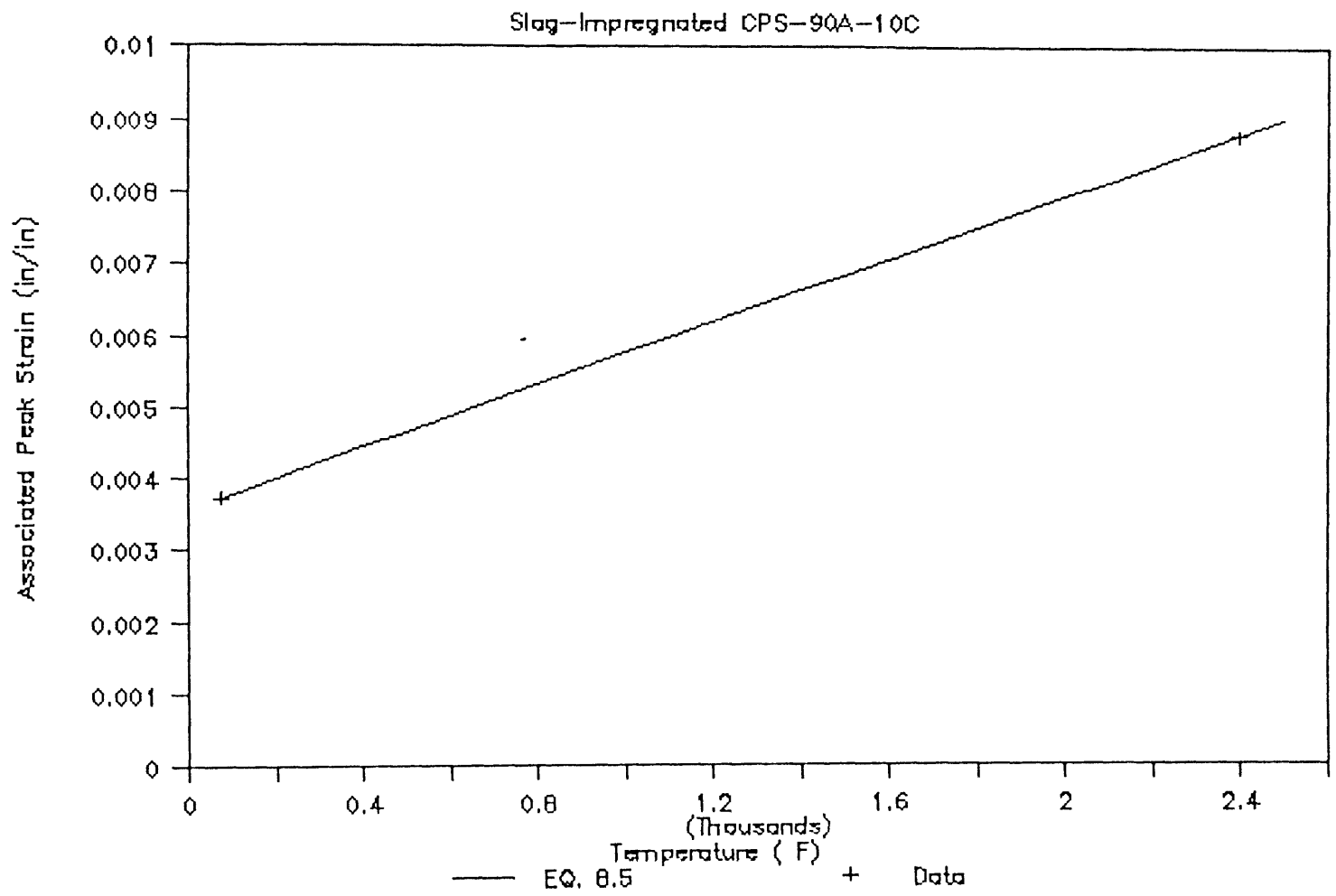
Figure B.7   Regression of data for Eq. 8.5

Slag-Impregnated CPS-90A-10C
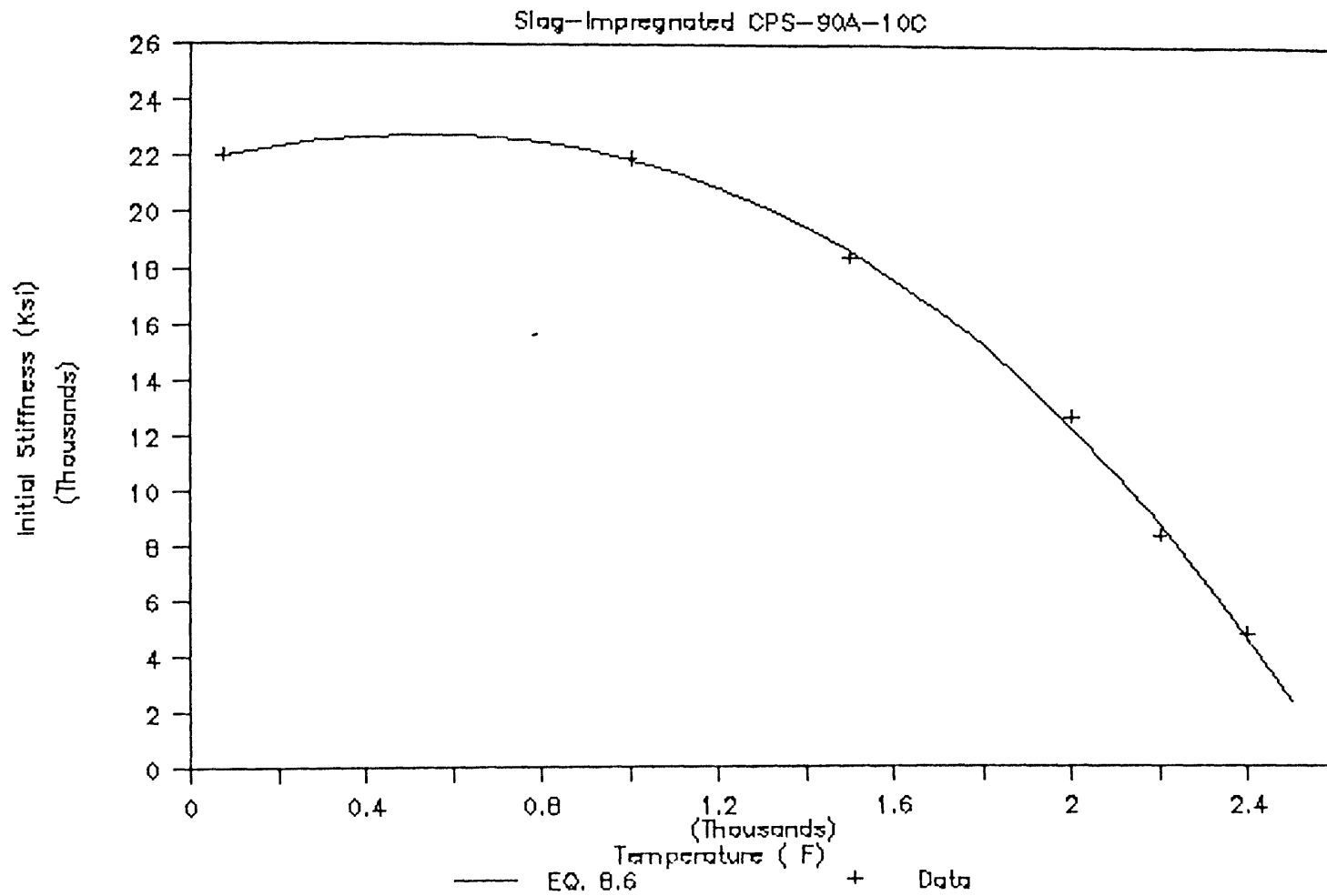
Figure B.8   Regression of data for Eq. 8.6

As—Manufactured CPS—82C—18M
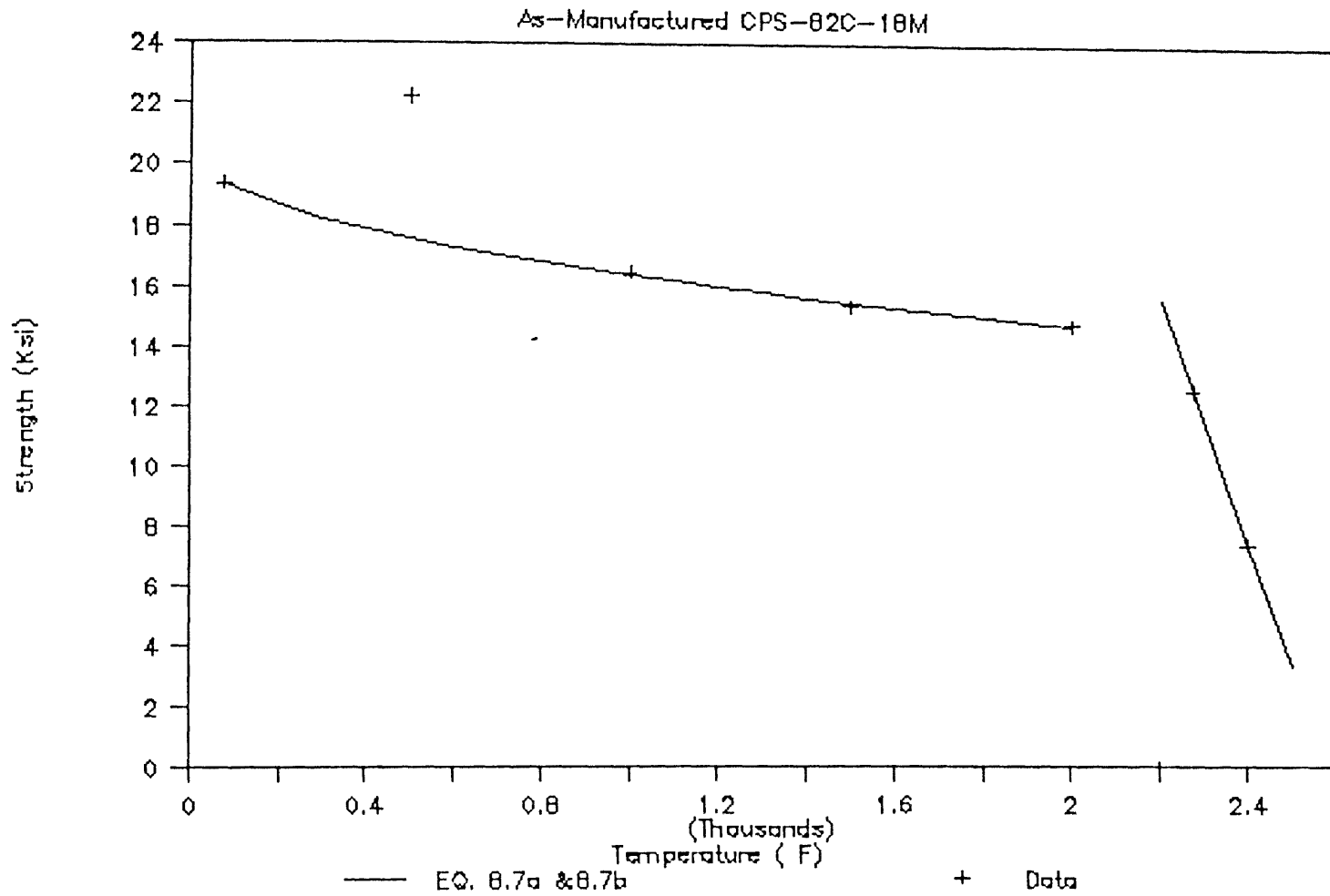
Figure B.9   Regression of data for Eqs. 8.7a and 8.7b

As-Manufactured CPS-82C-18M
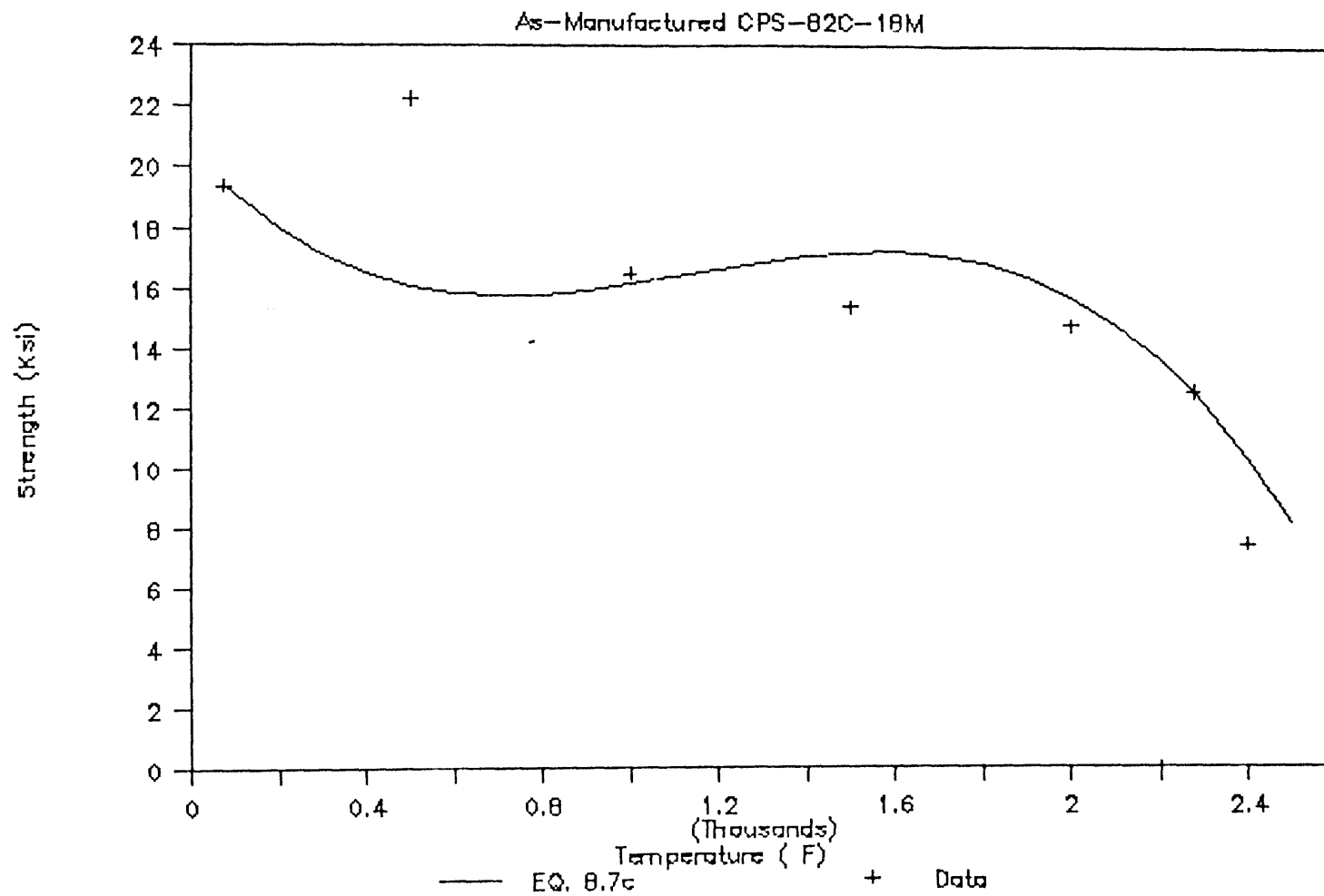
Figure B.10   Regression of data for Eq. 8.7c

As-Manufactured CPS-82C-18M
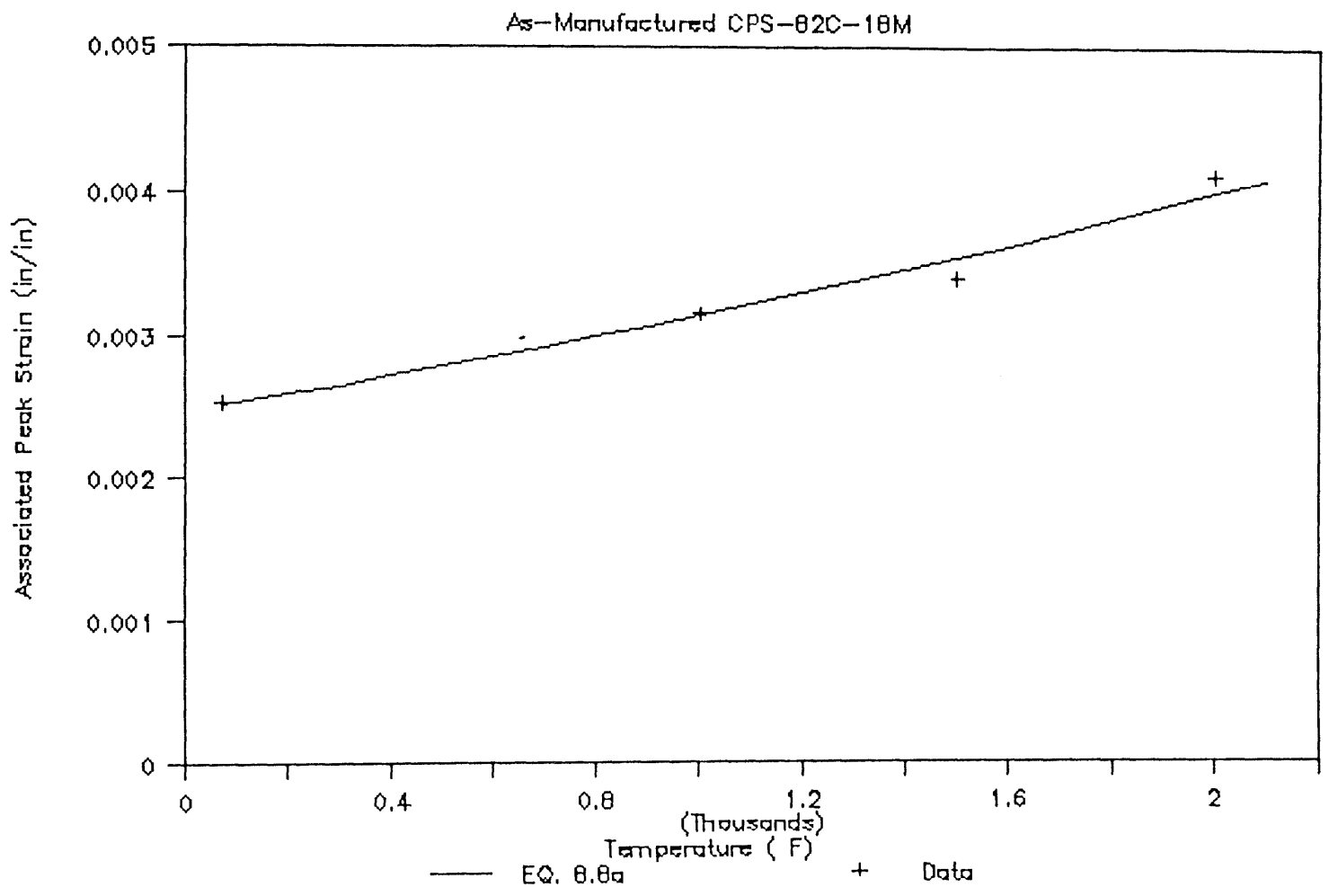
Figure B.11   Regression of data for Eq. 8.8a

As-Manufactured CPS-82C-18M

Associated Peak Strain (in/in)

EQ. 8.8b   +   Data
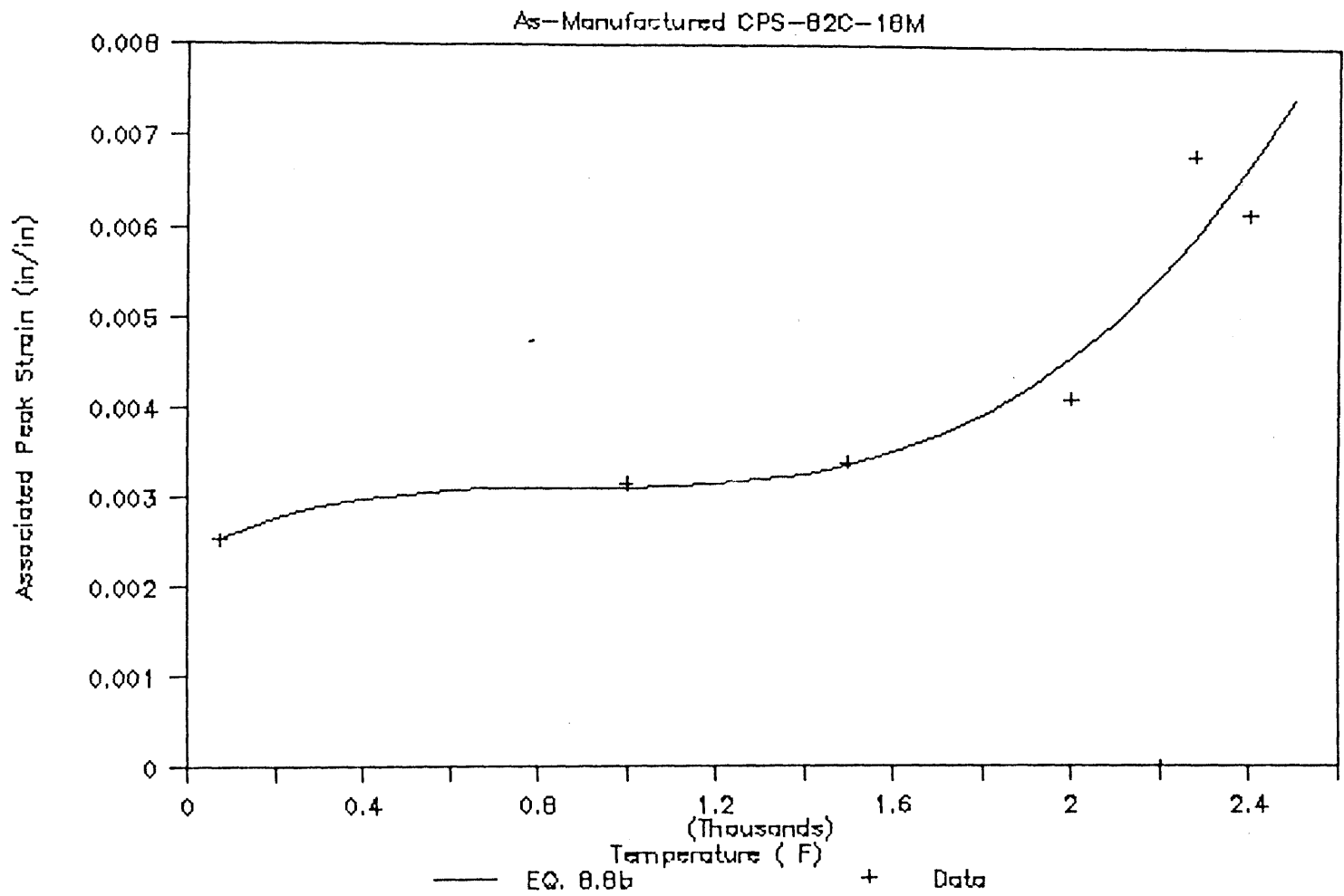
Figure B.12   Regression of data for Eq. 8.8b

484
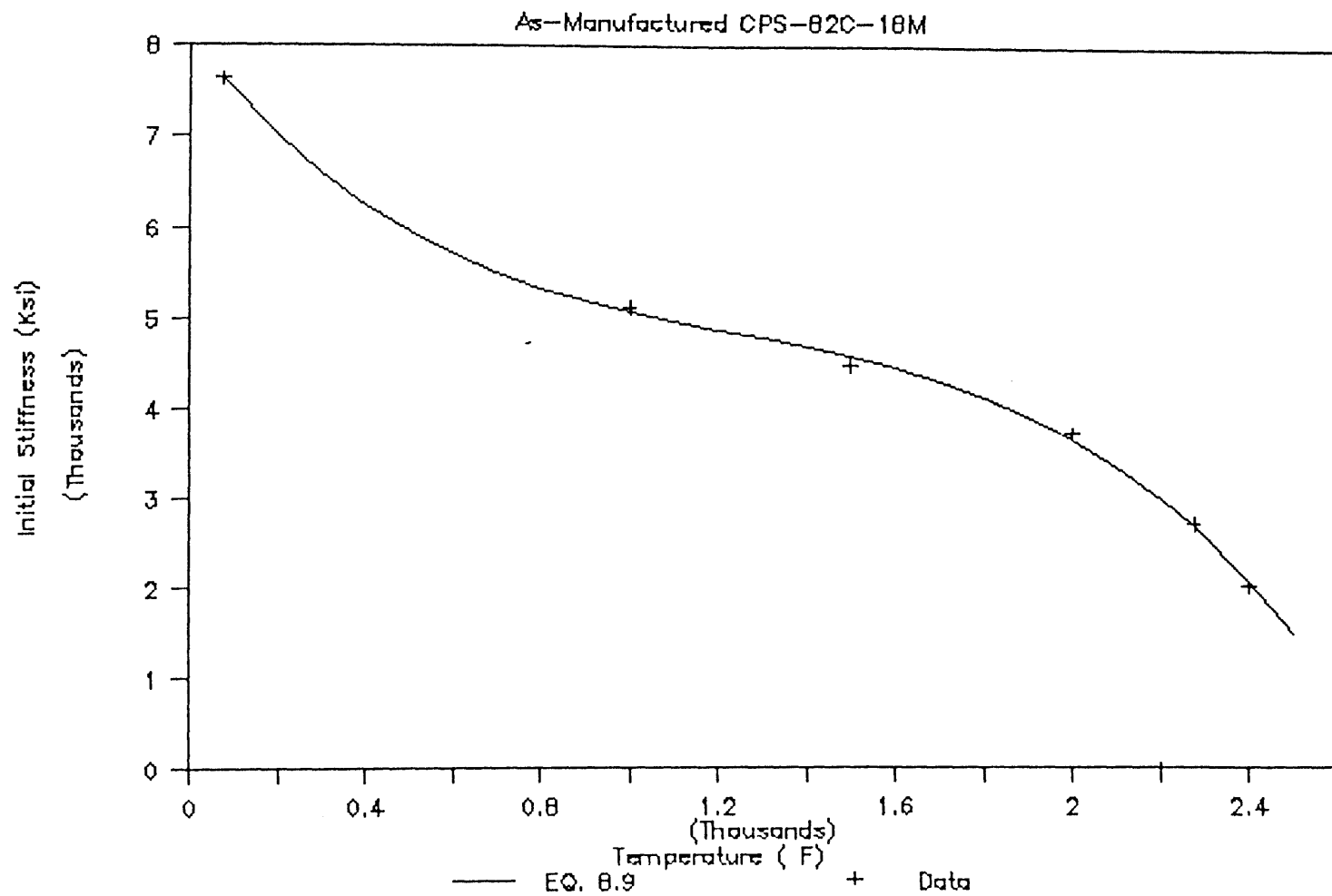
Figure B.13   Regression of data for Eq. 8.9
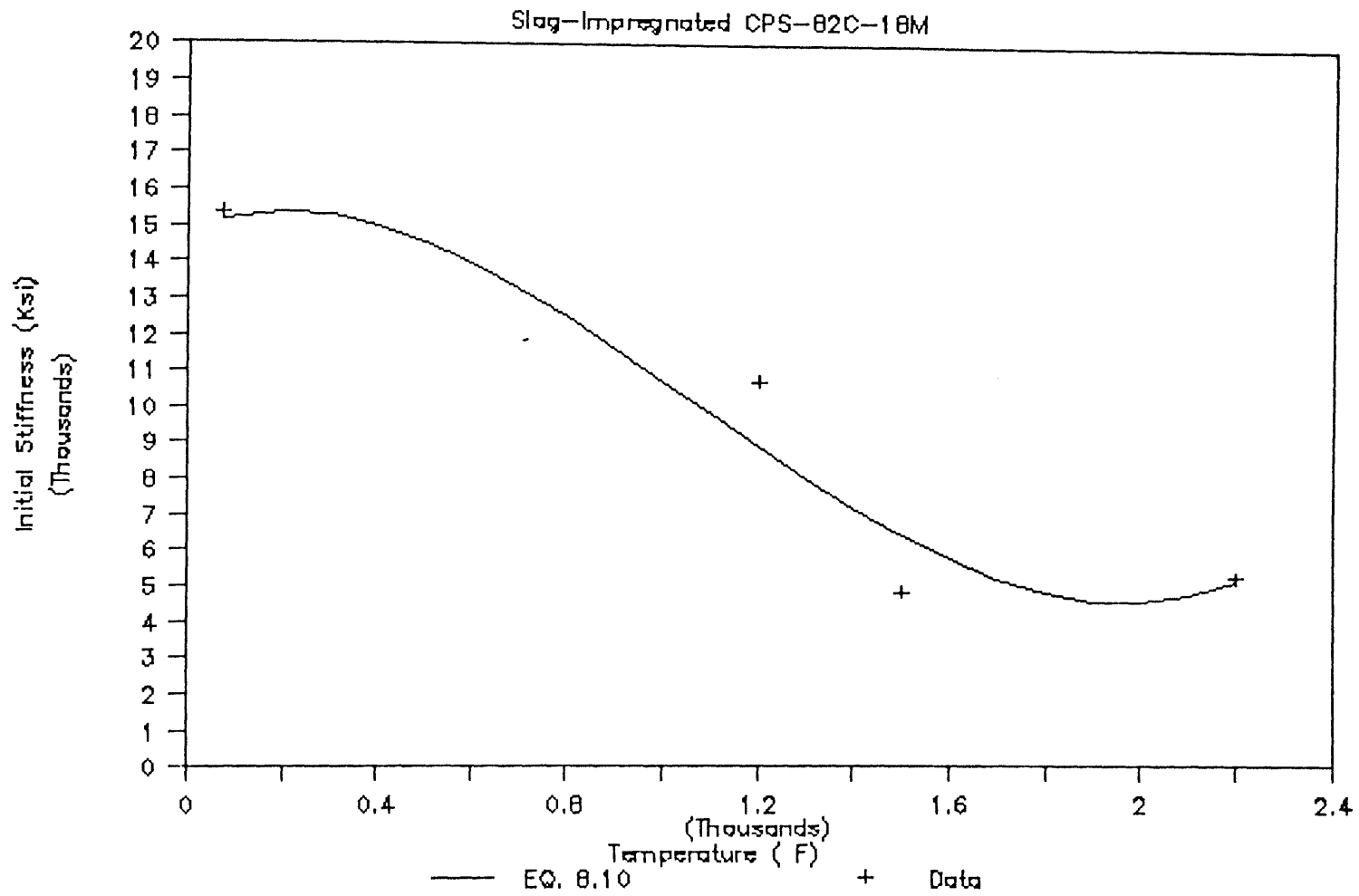
Figure B.14   Regression of data for Eq. 8.10
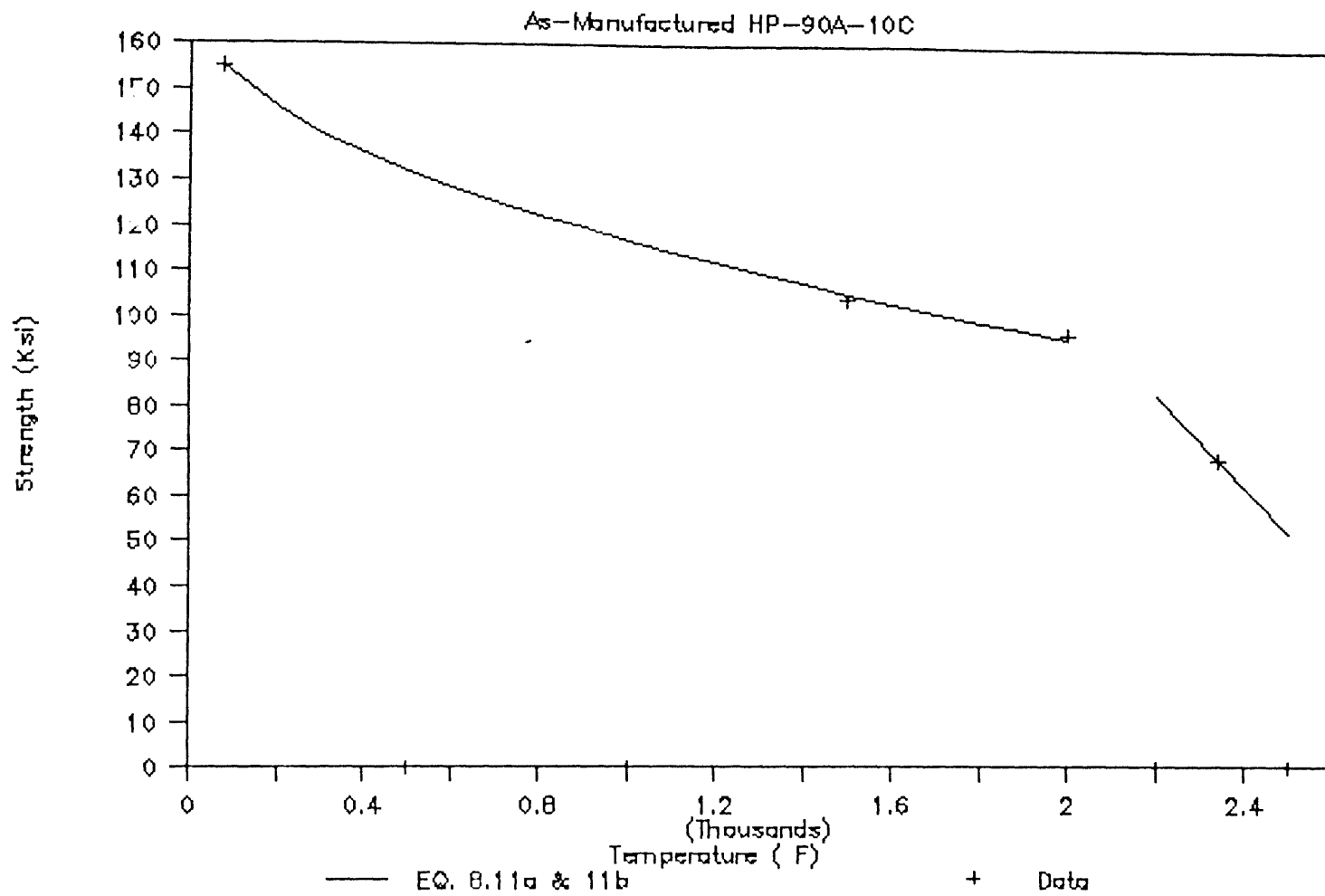
Figure B.15   Regression of data for Eqs. 8.11a and 8.11b

As-Manufactured HP-90A-10C

Strength (Ksi)

(Thousands)
Temperature (F)

———— EQ. 8.11c   +   Data
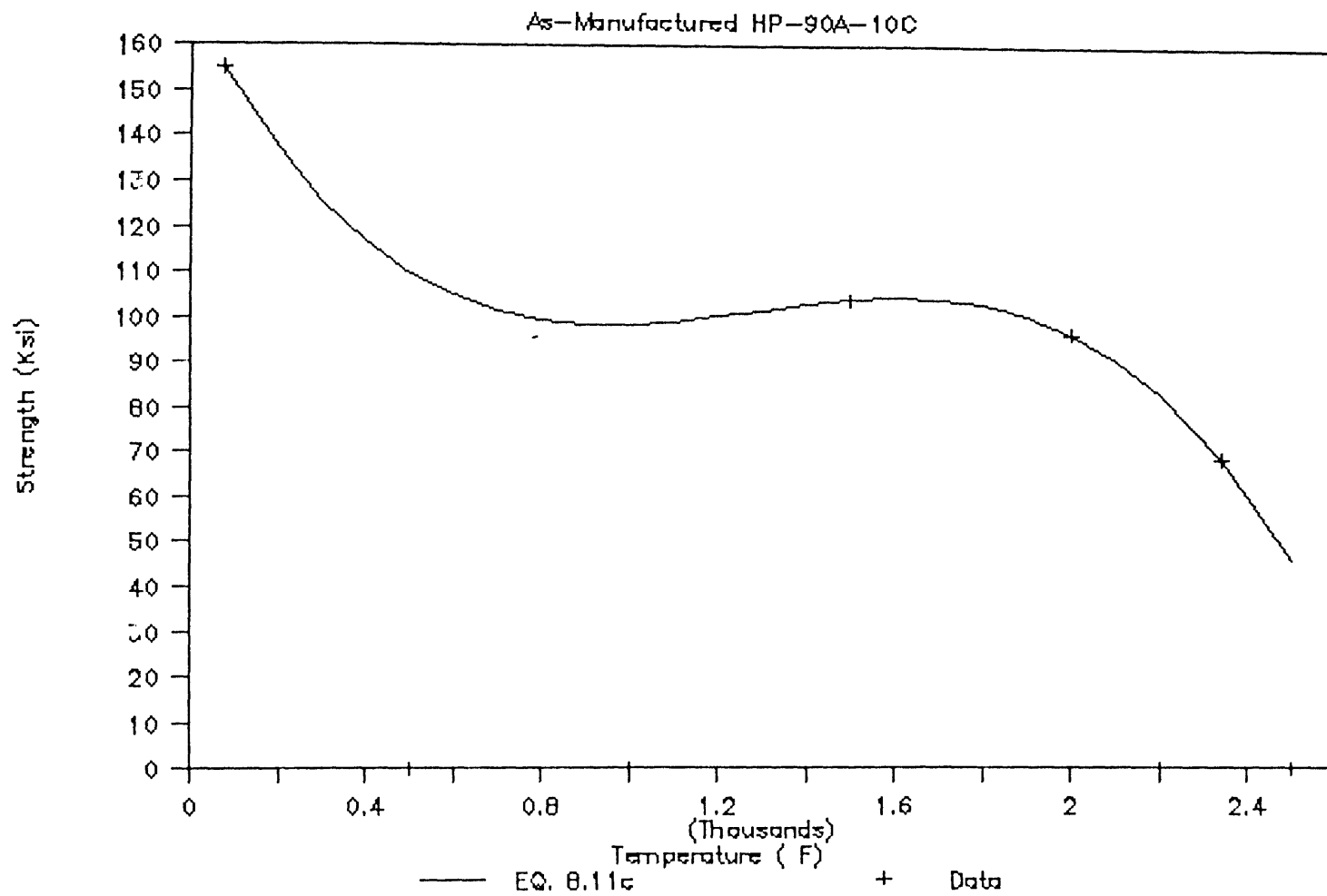
Figure B.16   Regression of data for Eq. 8.11c

As-Manufactured HP-90A-10C
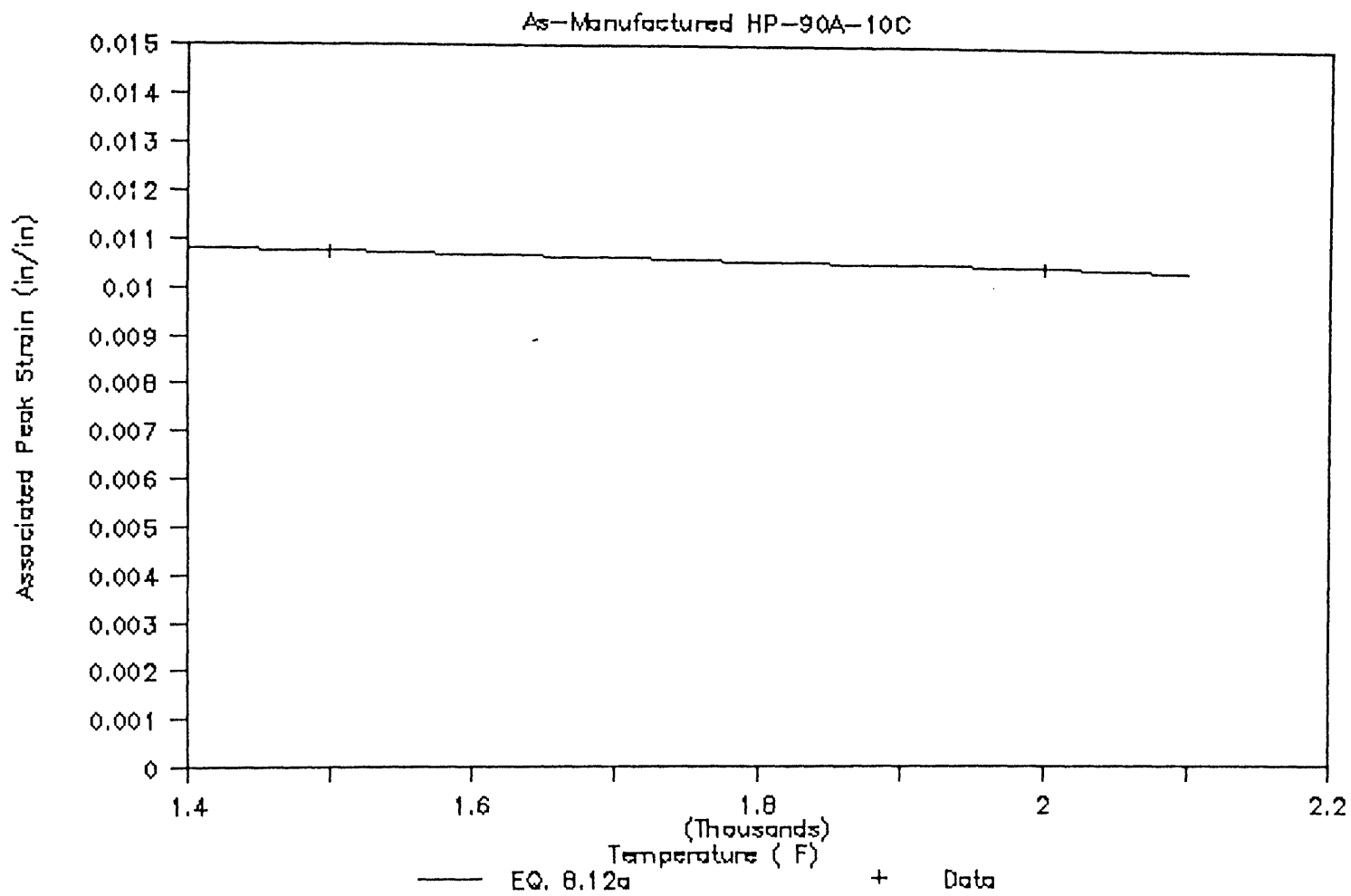
Figure B.17   Regression of data for Eq. 8.12a
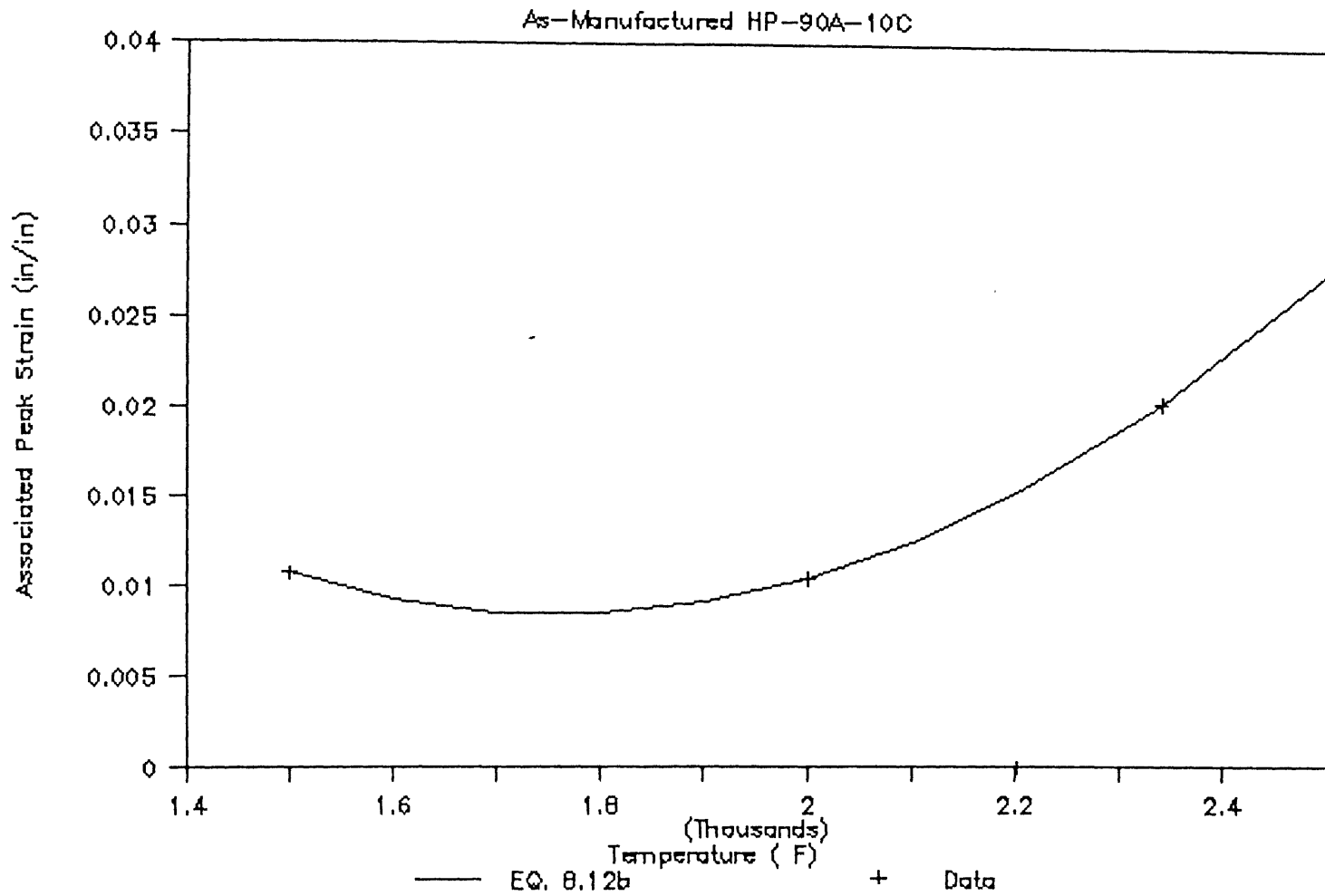
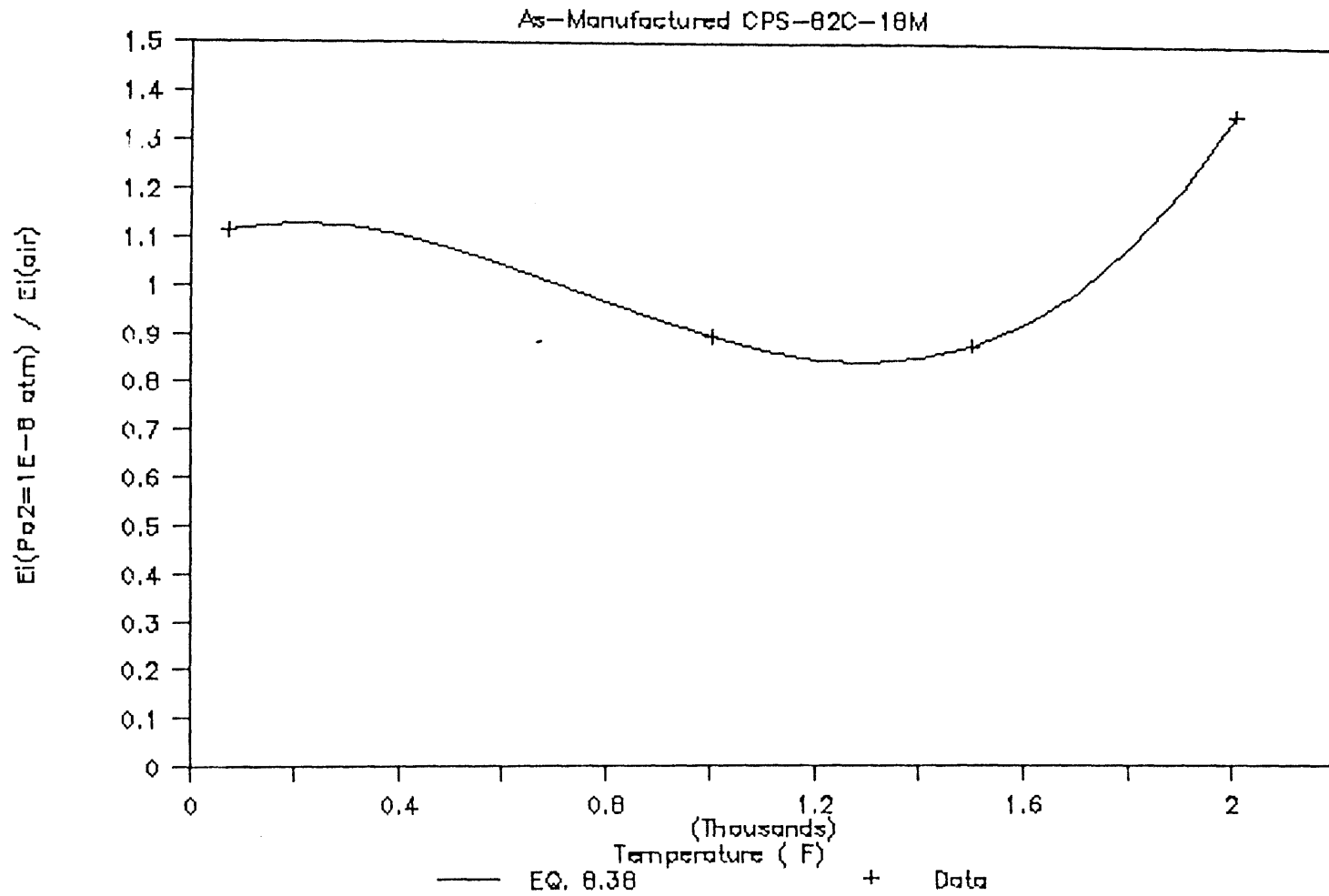Figure B.18   Regression of data for Eq. 8.12b
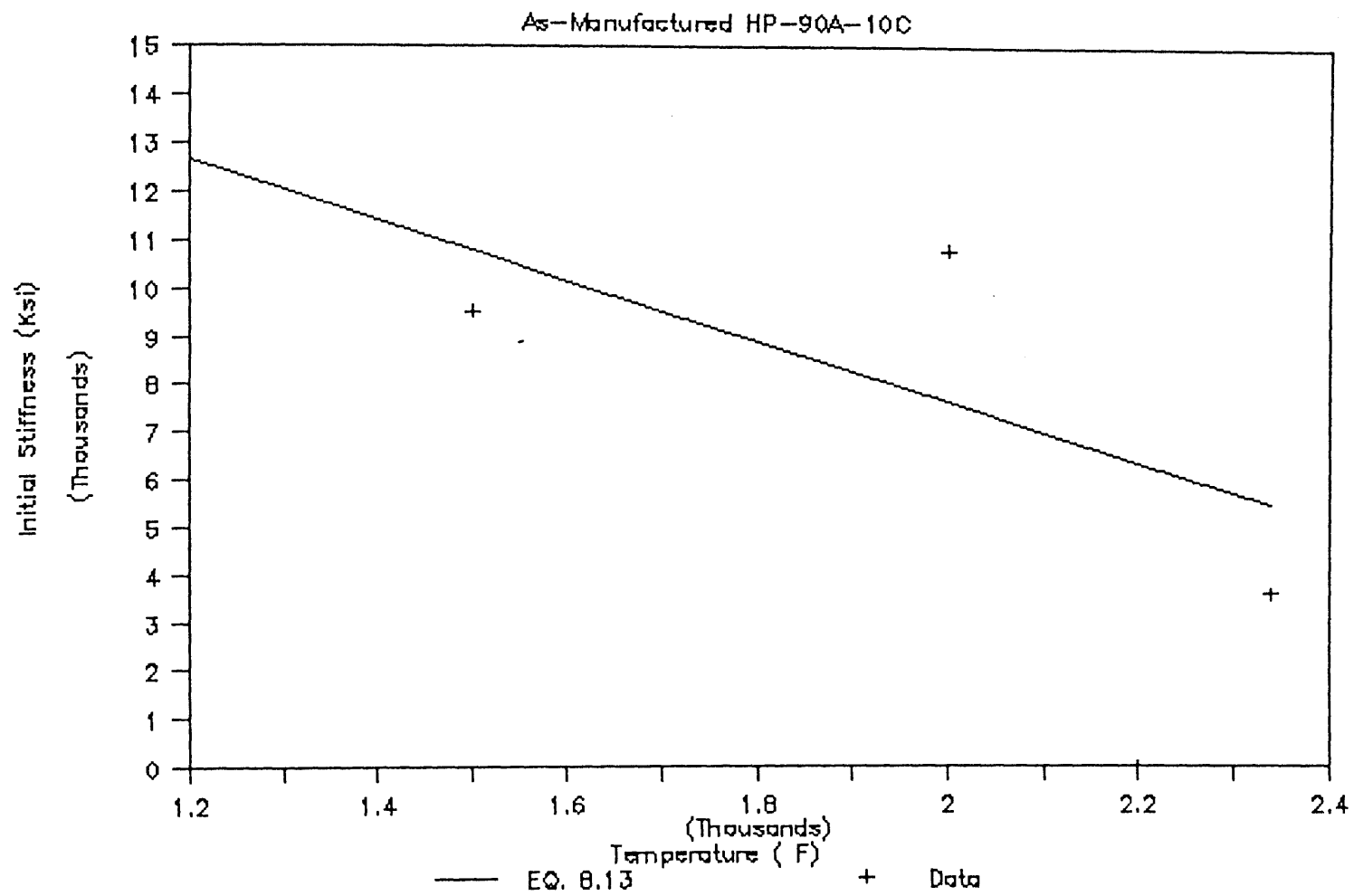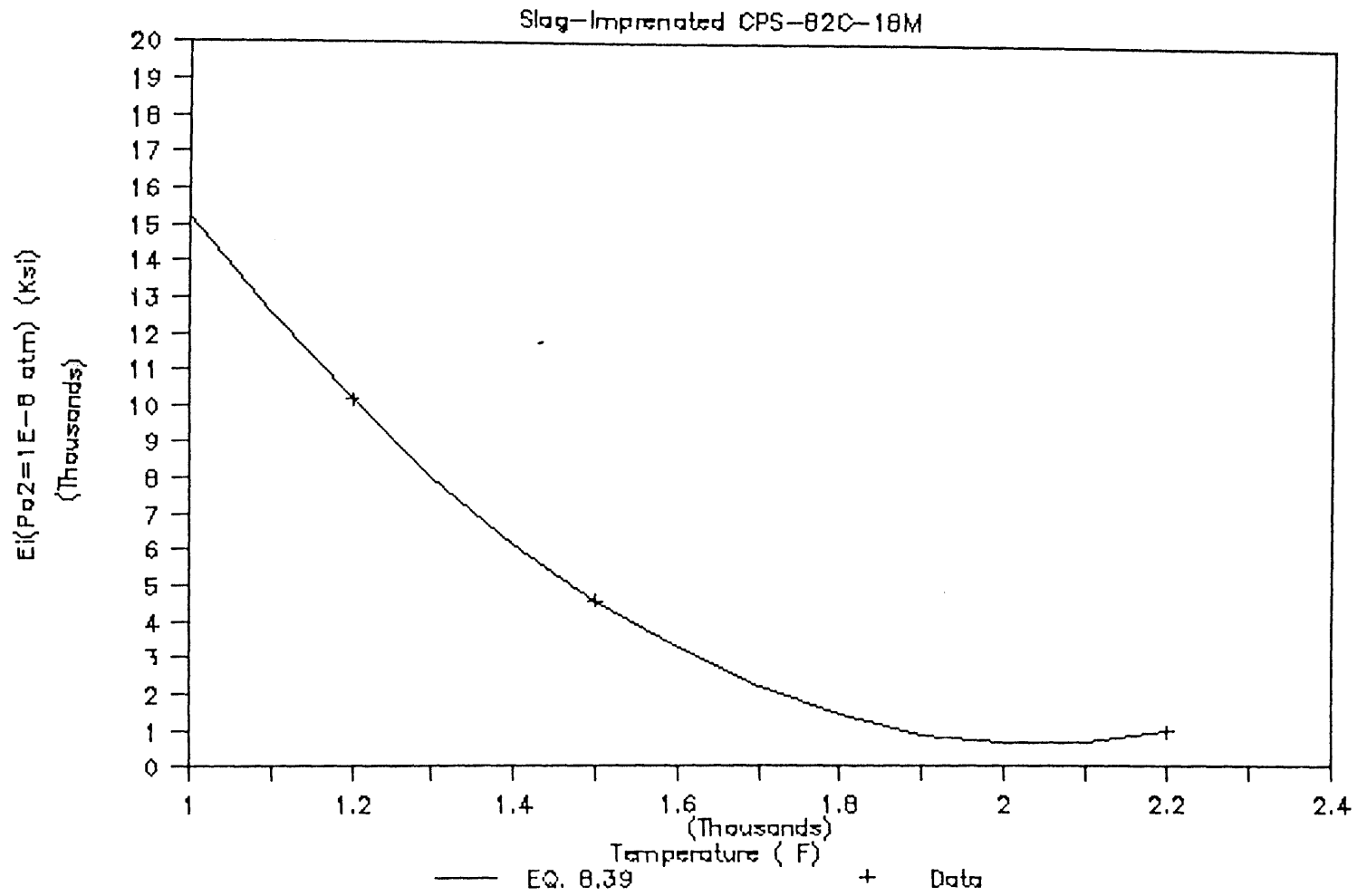
Figure B.19   Regression of data for Eq. 8.13

As-Manufactured HP-50A-50C

Strength (Ksi)

(Thousands)
Temperature (F)

—— EQ. 8.14   +   Data
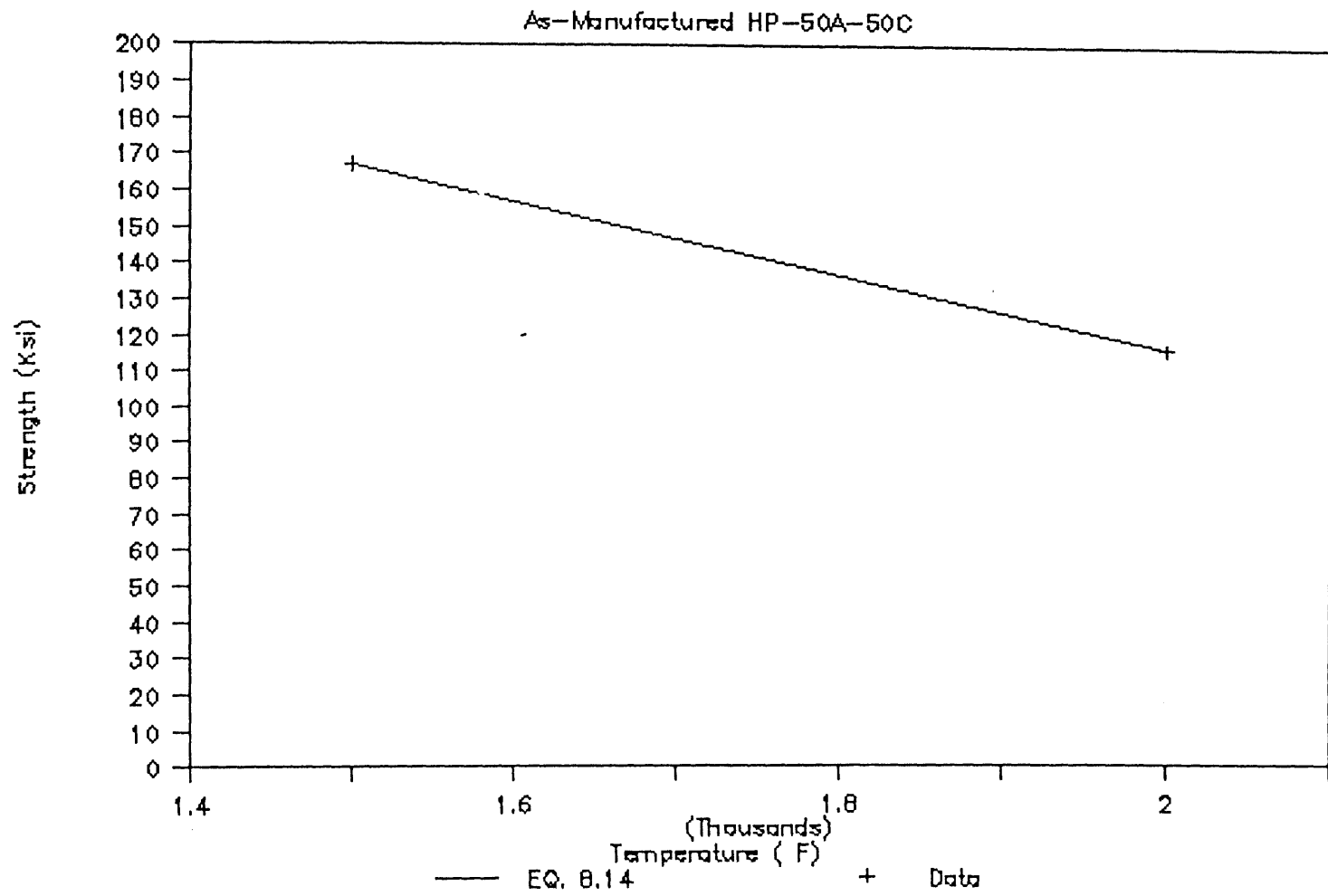
Figure B.20   Regression of data for Eq. 8.14
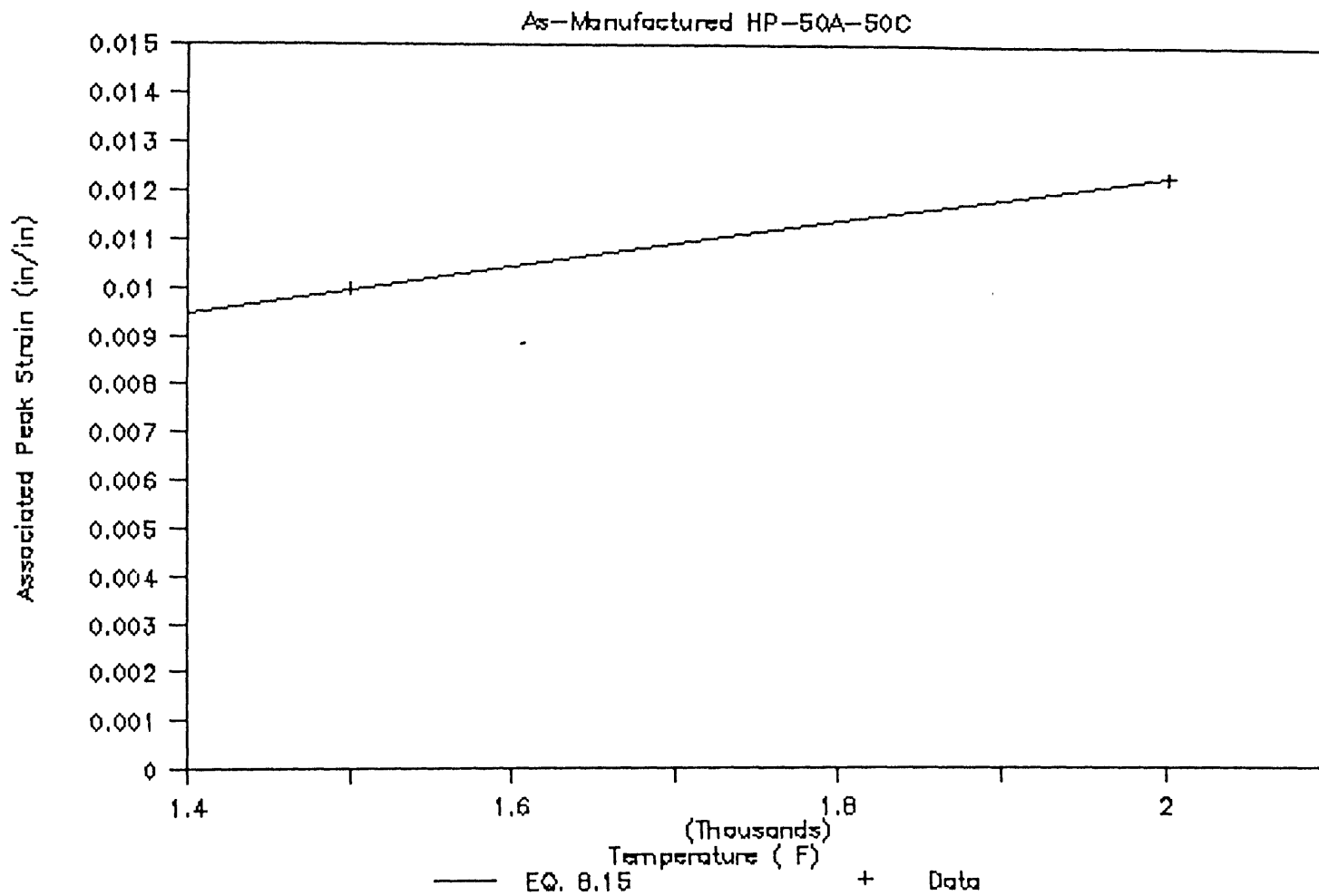
Figure B.21   Regression of data for Eq. 8.15

As-Manufactured HP-50A-50C
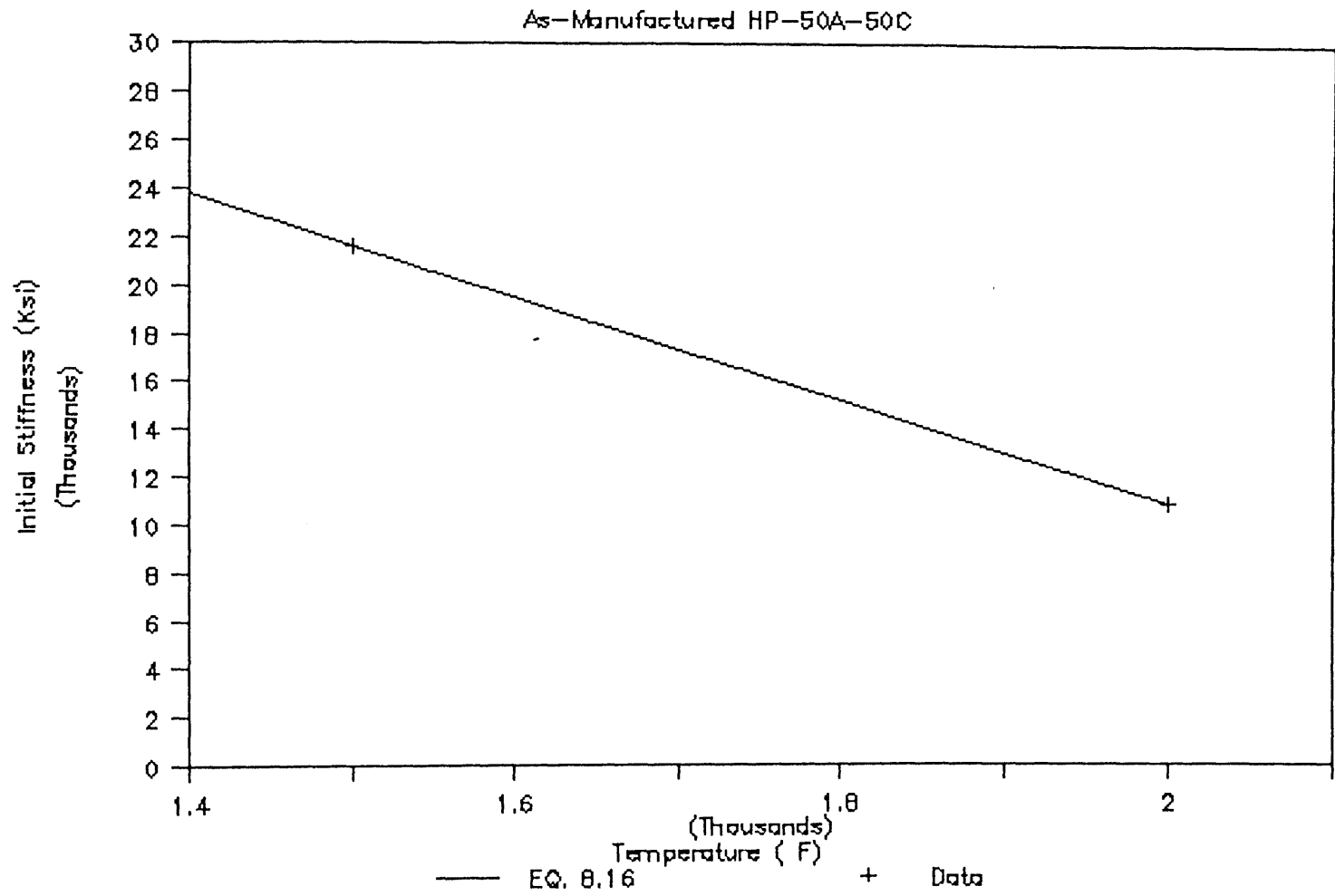
Figure B.22   Regression of data for Eq. 8.16

As—Manufactured HP—25A—75C
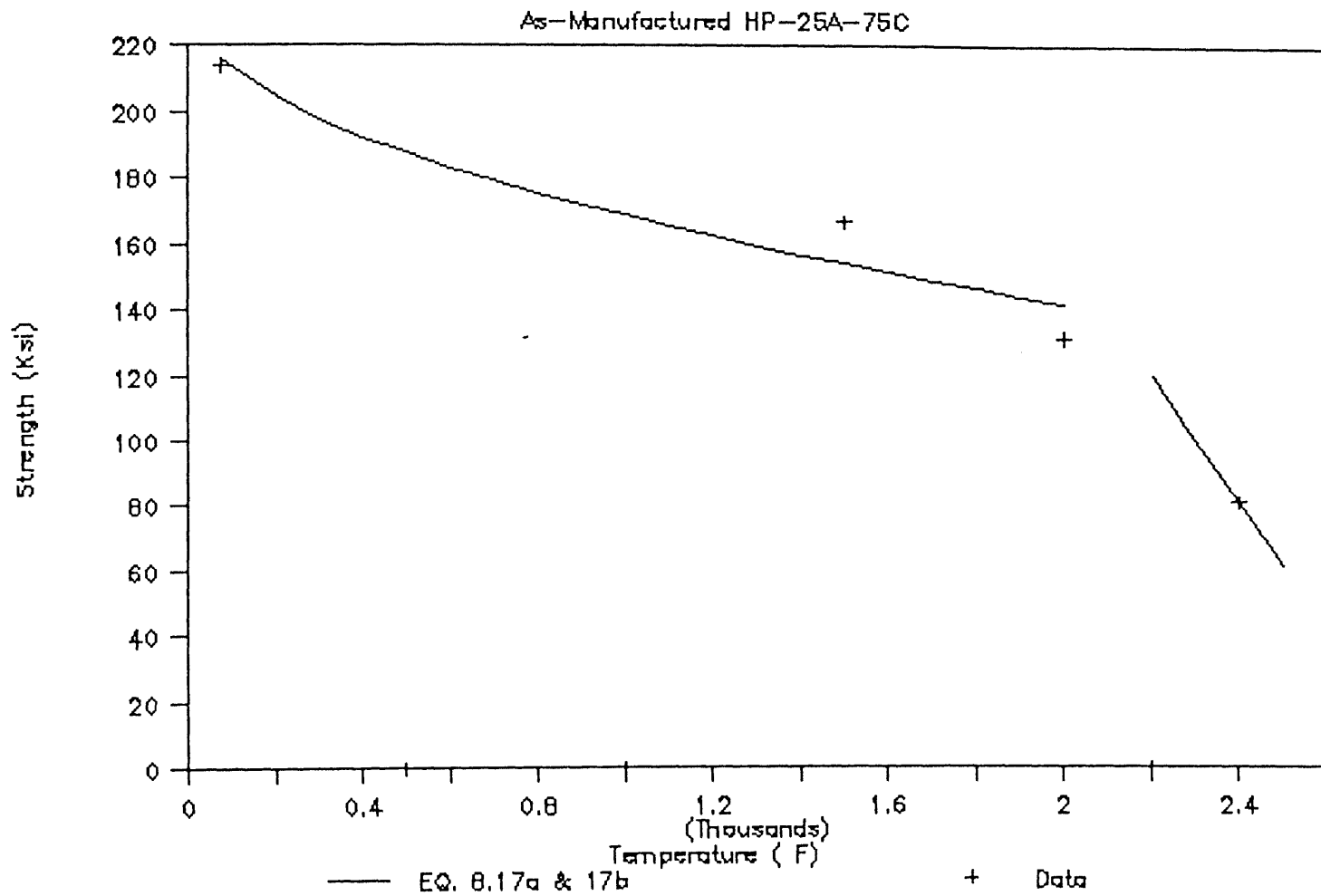
Figure B.23   Regression of data for Eqs. 8.17a and 8.17b

As-Manufactured HP-25A-75C
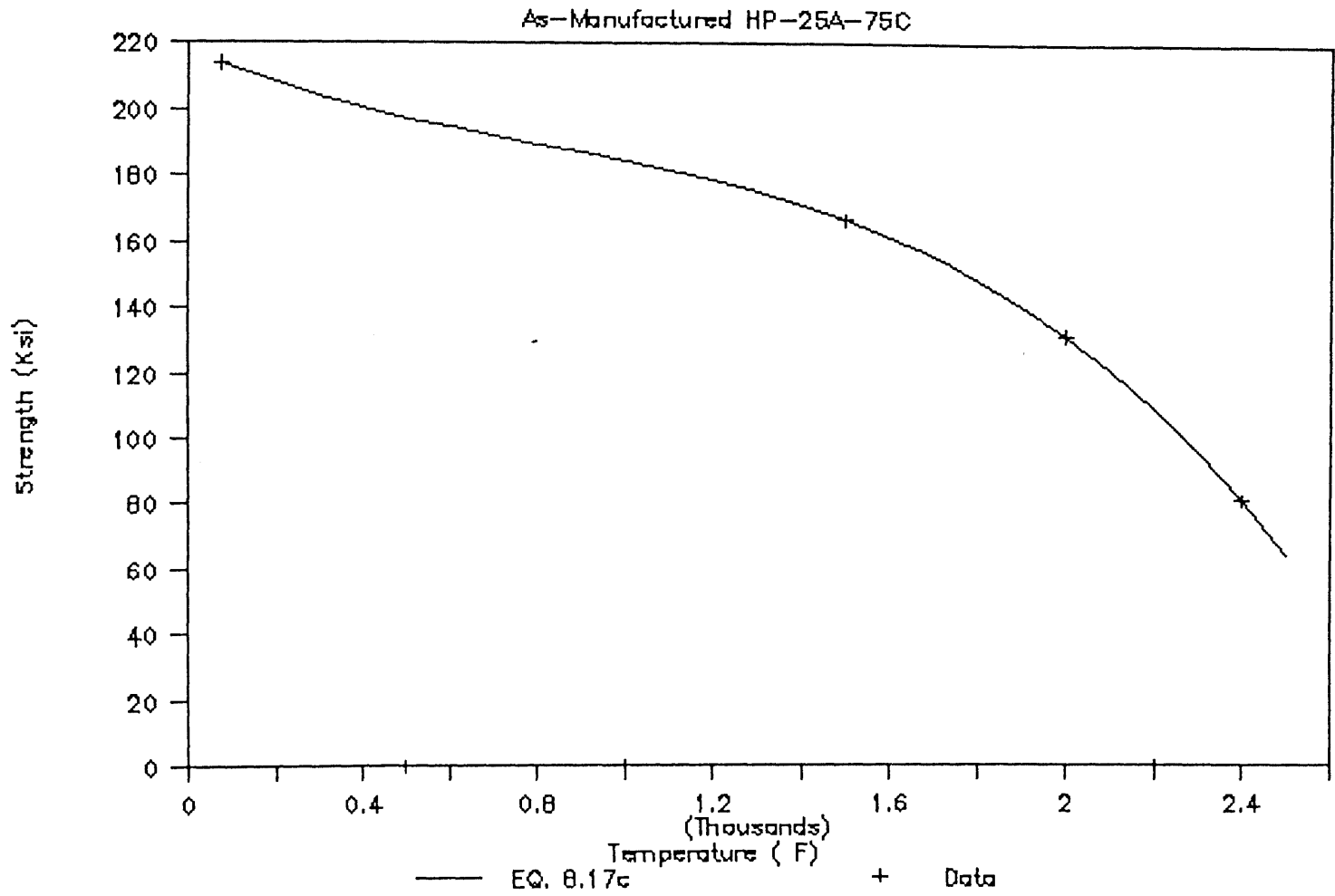
Figure B.24   Regression of data for Eq. 8.17c
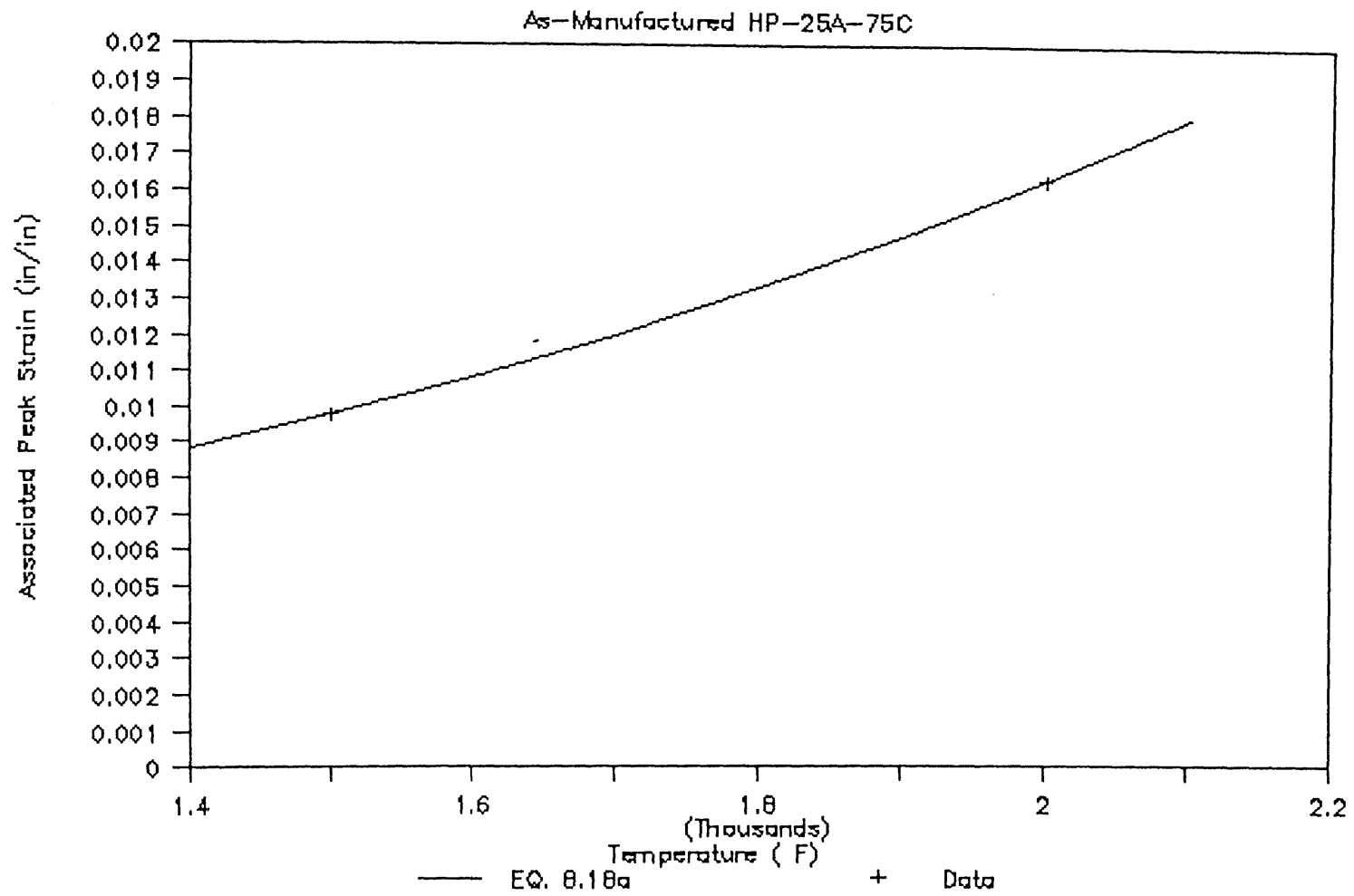
Figure B.25   Regression of data for Eq. 8.18a
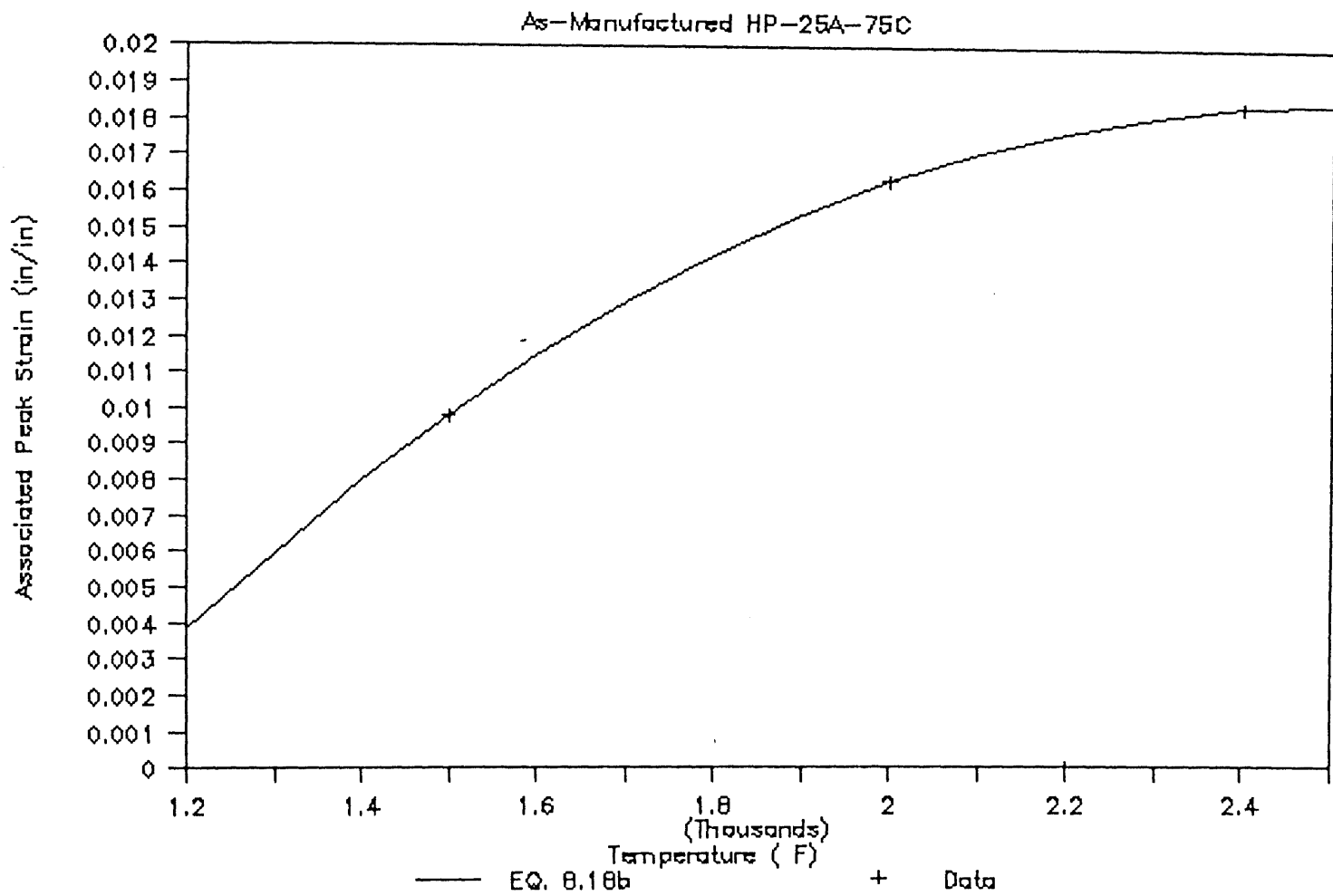
Figure B.26   Regression of data for Eq. 8.18b
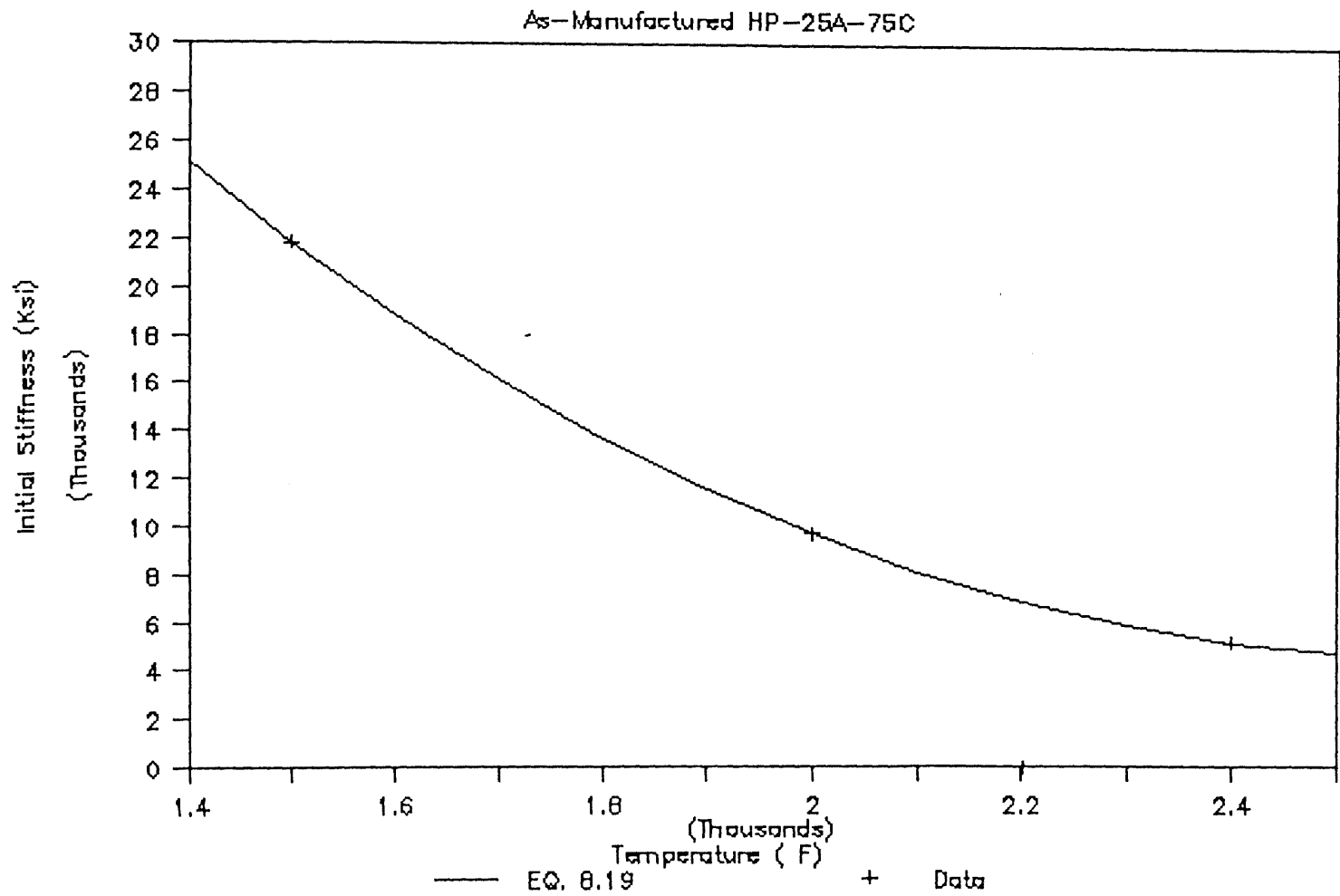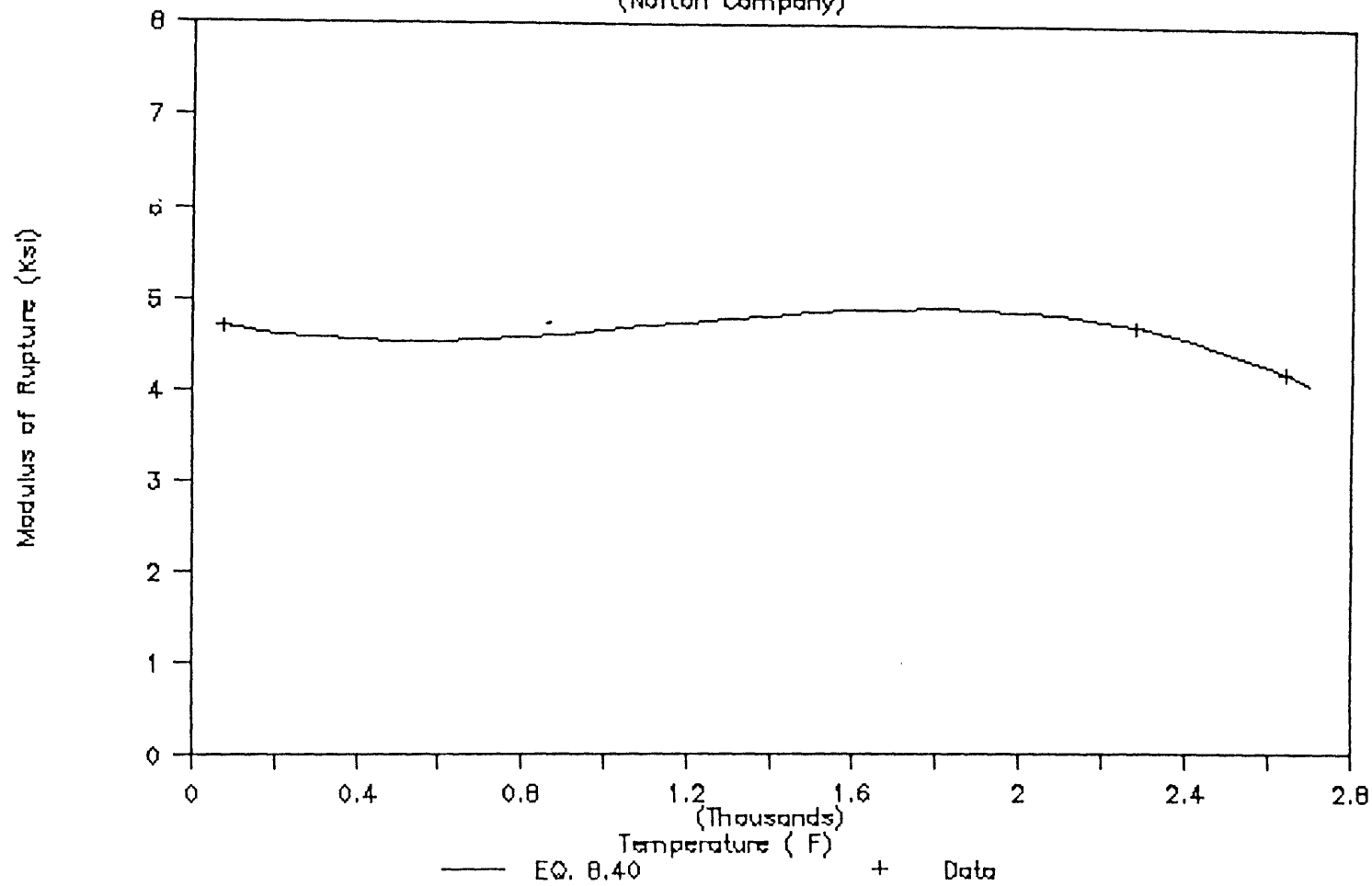
Figure B.27   Regression of data for Eq. 8.19

Figure B.28   Regression of data for Eqs. 8.20a and 8.20b

As—Manufactured HP—80C—20M
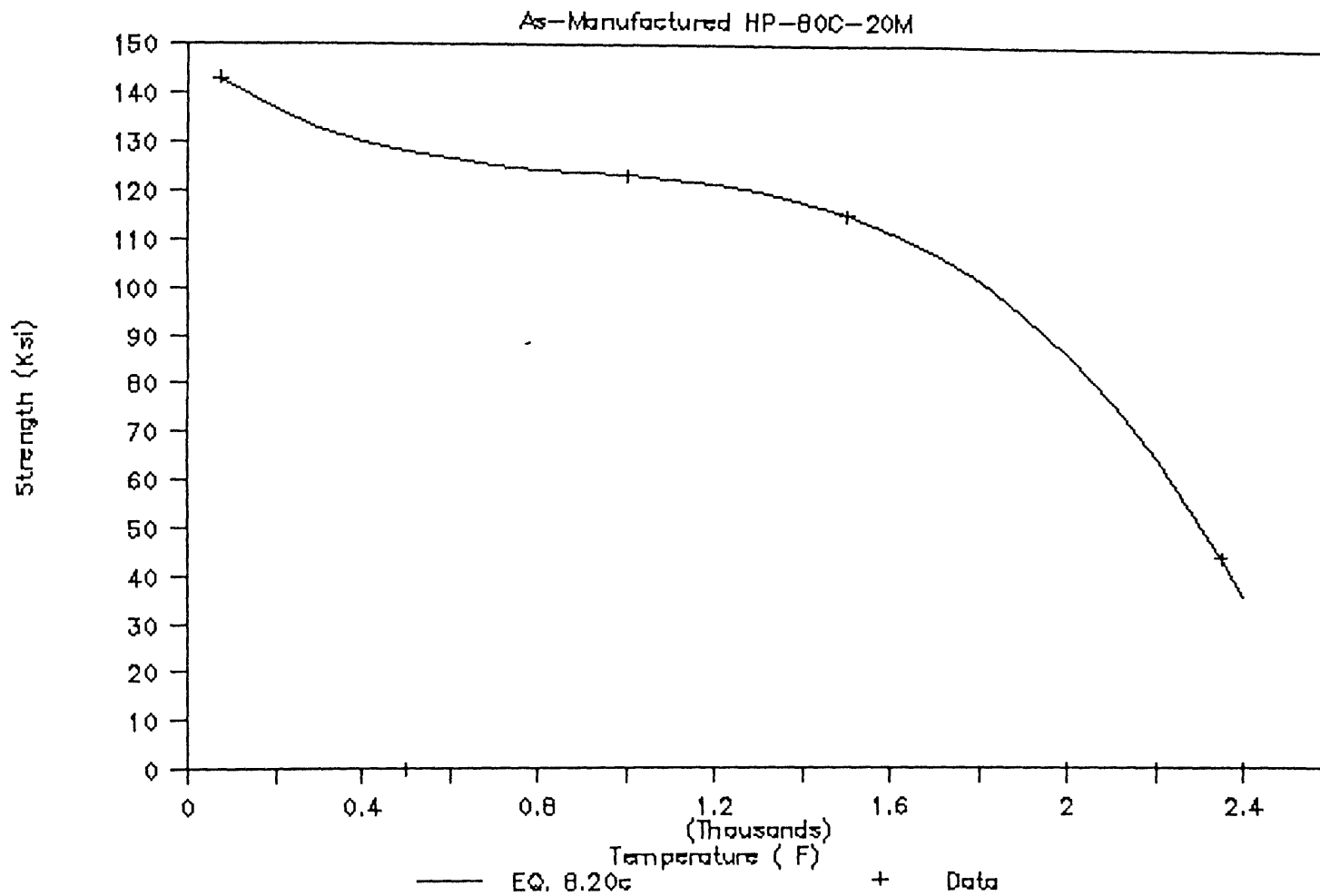
Figure B.29   Regression of data for Eq. 8.20c

As-Manufactured HP-80C-20M
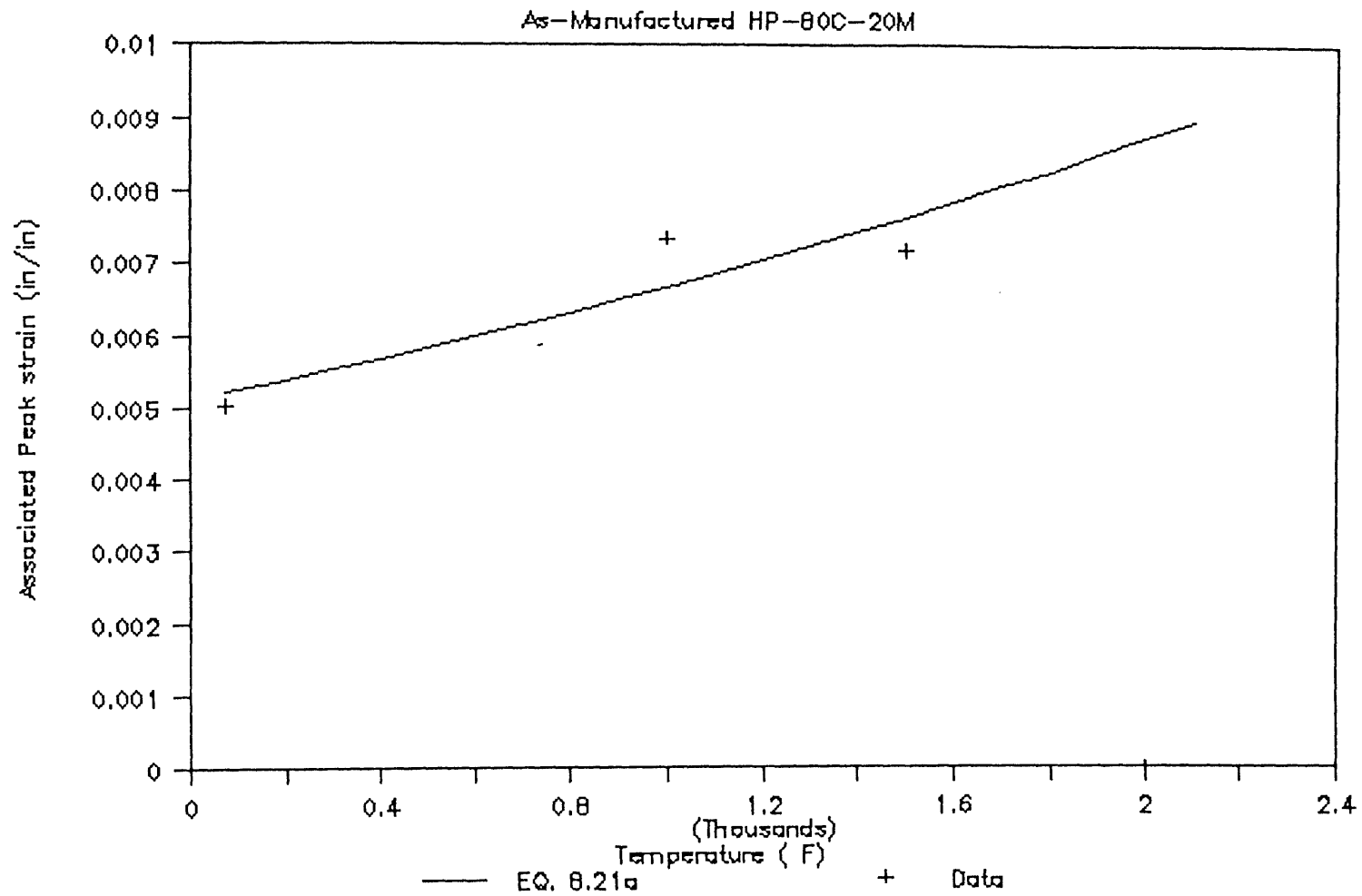
Figure B.30   Regression of data for Eq. 8.21a

As-Manufactured HP-80C-20M
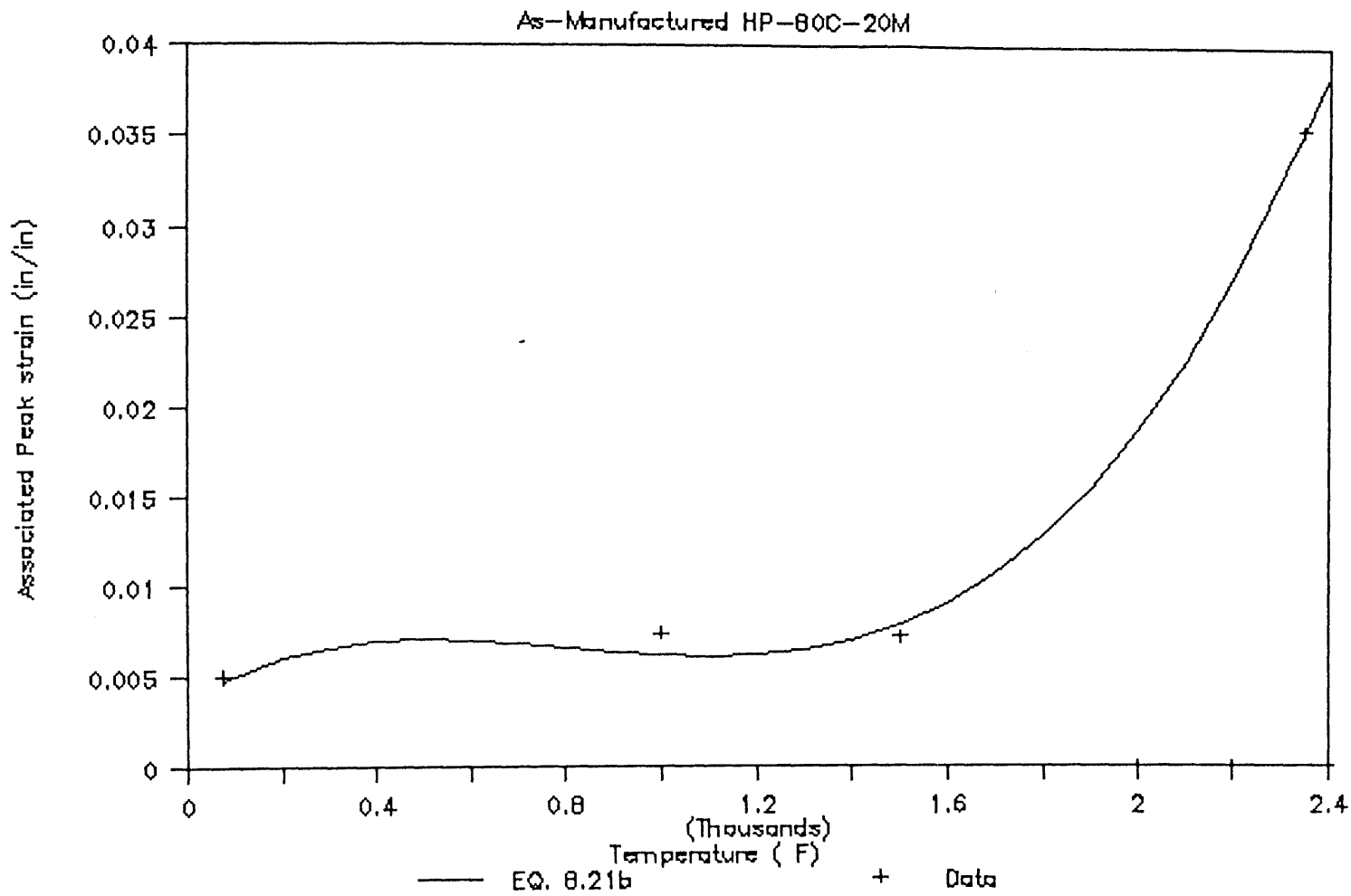
Figure B.31   Regression of data for Eq. 8.21b

As-Manufactured HP-80C-20M
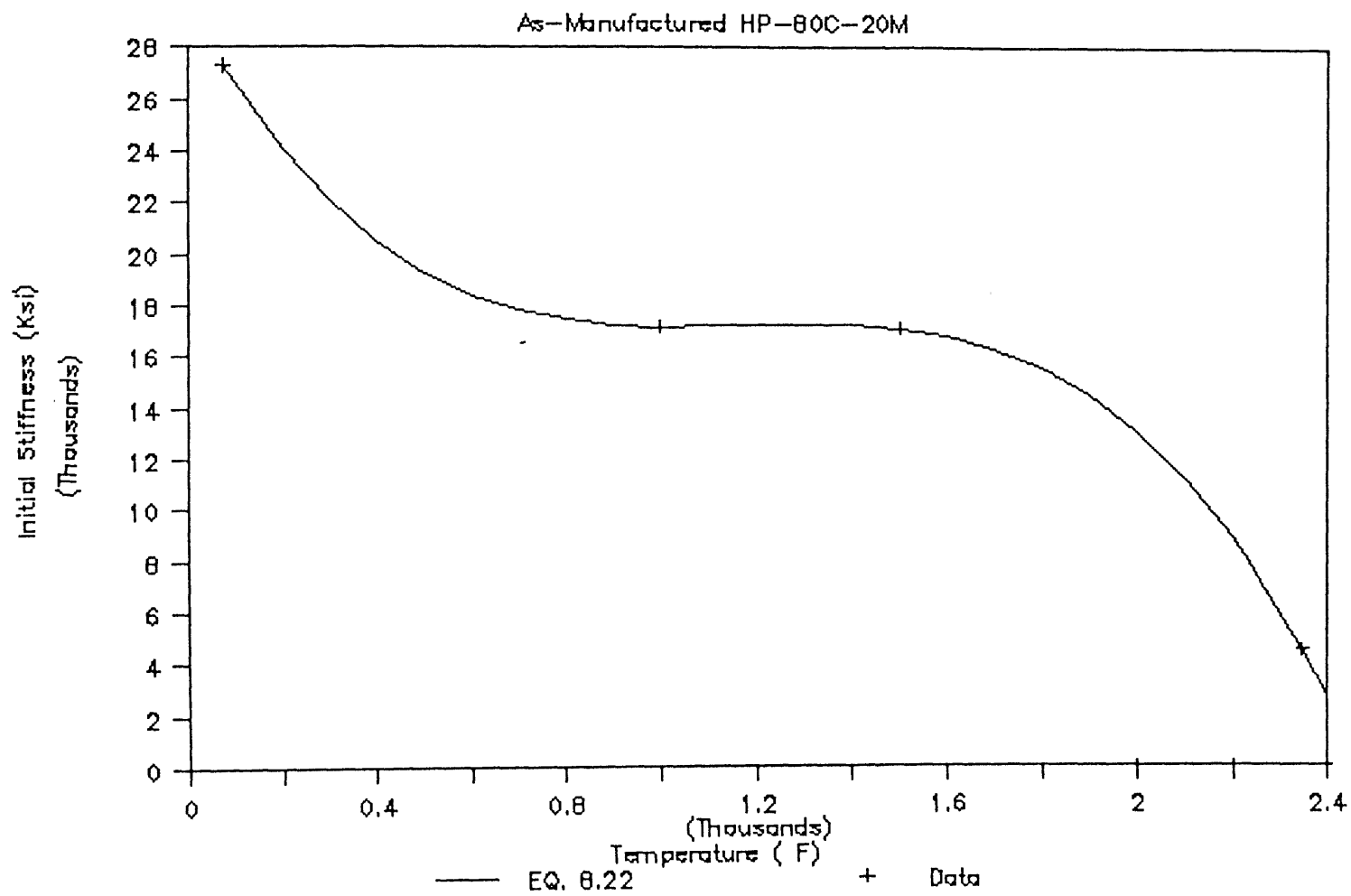
Figure B.32   Regression of data for Eq. 8.22

Figure B.33   Regression of data for Eqs. 8.23a and 8.23b

As—Manufactured FC—78C—8A—8M
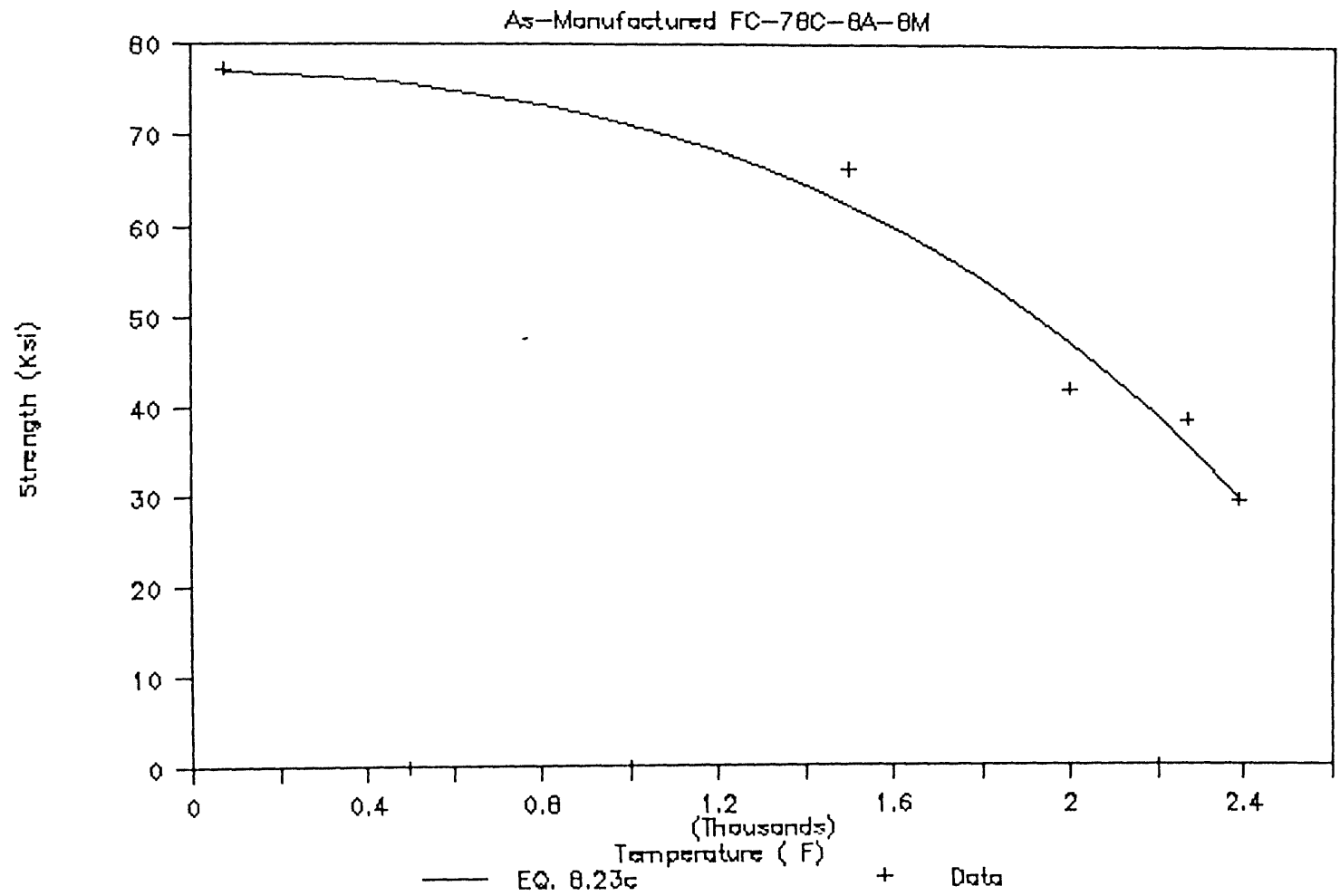
Figure B.34   Regression of data for Eq. 8.23c
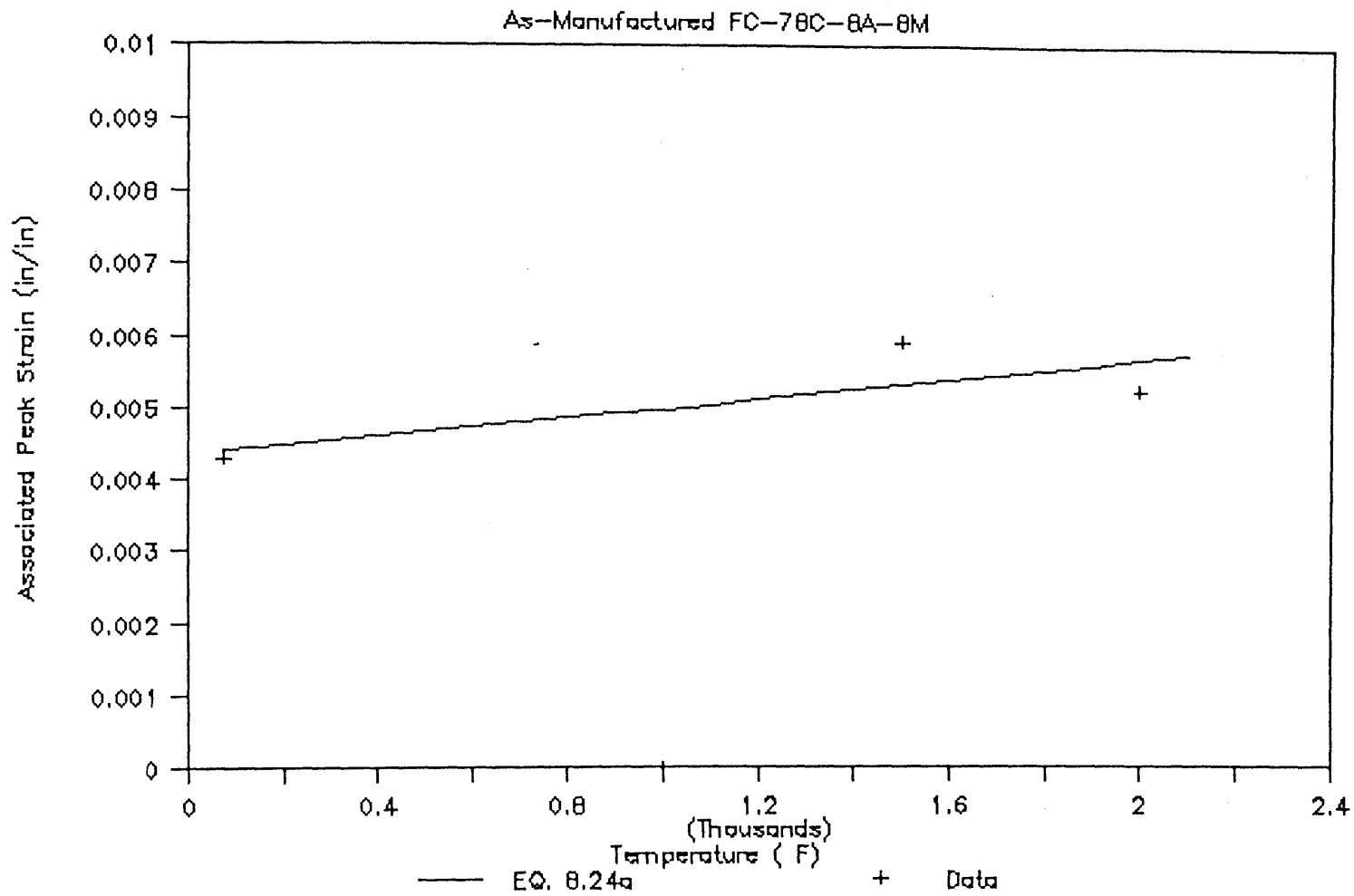
Figure B.35   Regression of data for Eq. 8.24a

As-Manufactured FC-78C-8A-8M
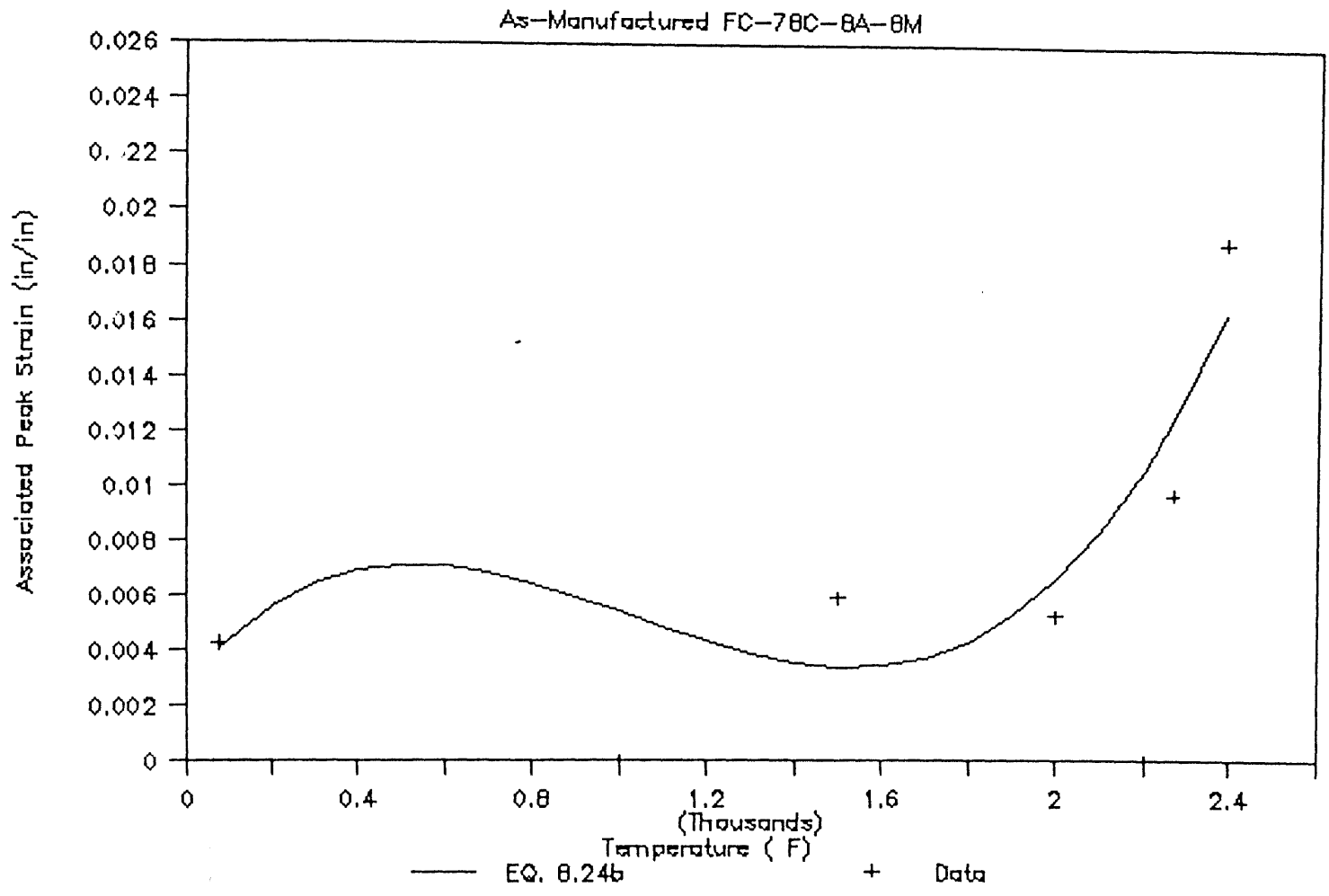
Figure B.36   Regression of data for Eq. 8.24b

As—Manufactured FC—78C—8A—8M

Initial Stiffness (Ksi) (Thousands) vs Temperature (F) (Thousands)

—— EQ. 8.25   + Data
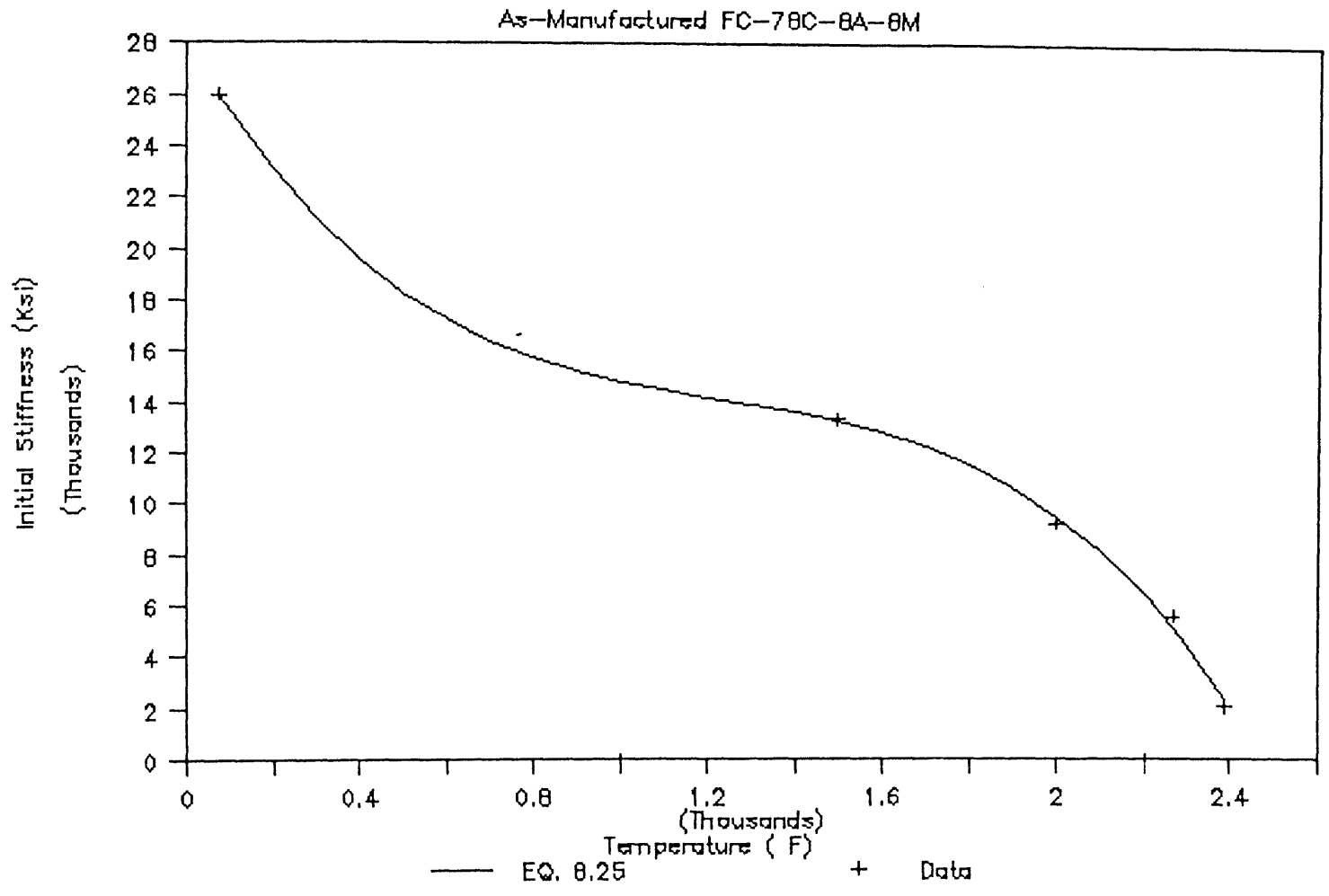
Figure B.37   Regression of data for Eq. 8.25

Dense Refractory Concrete (Tseng,82)
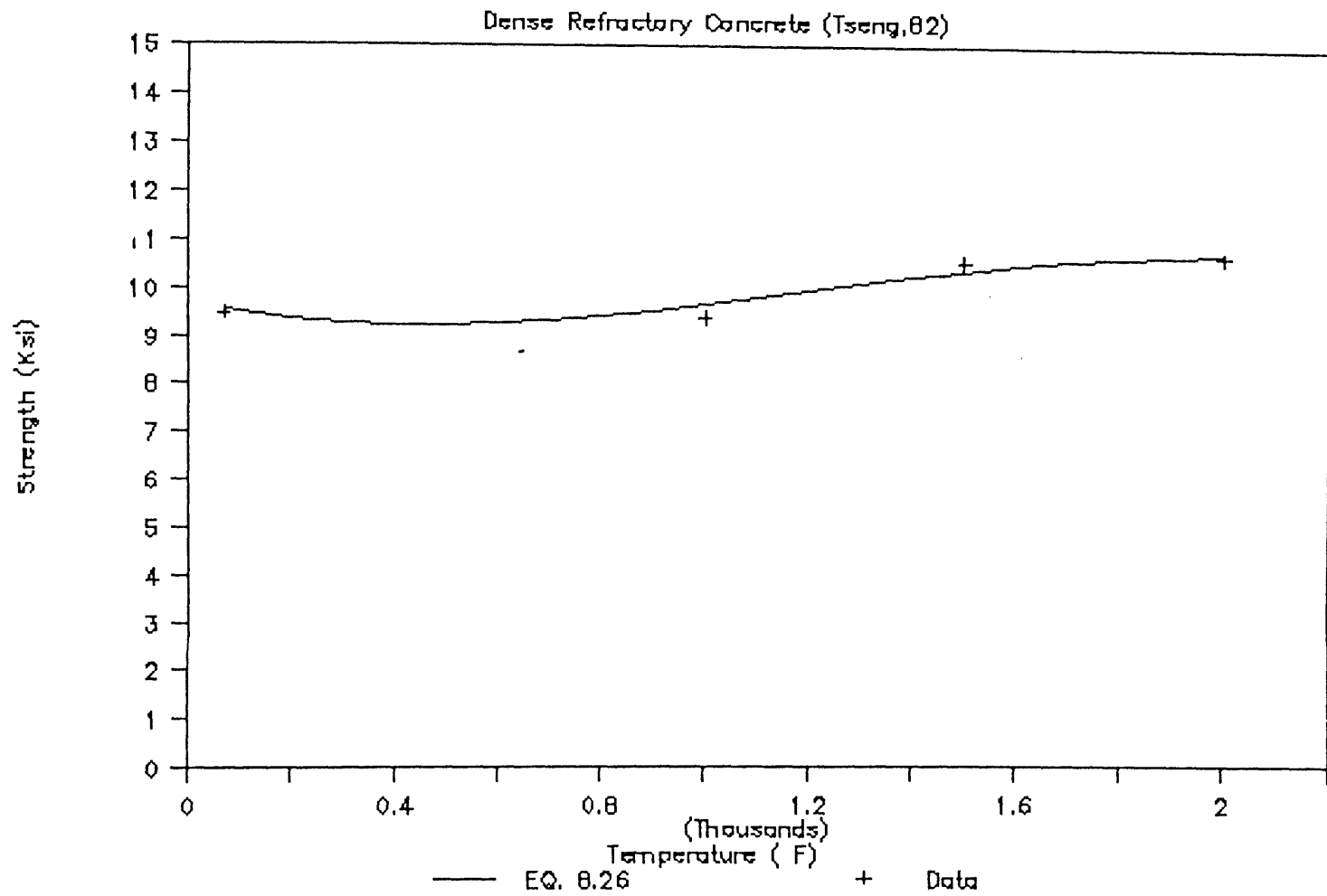
Figure B.38   Regression of data for Eq. 8.26
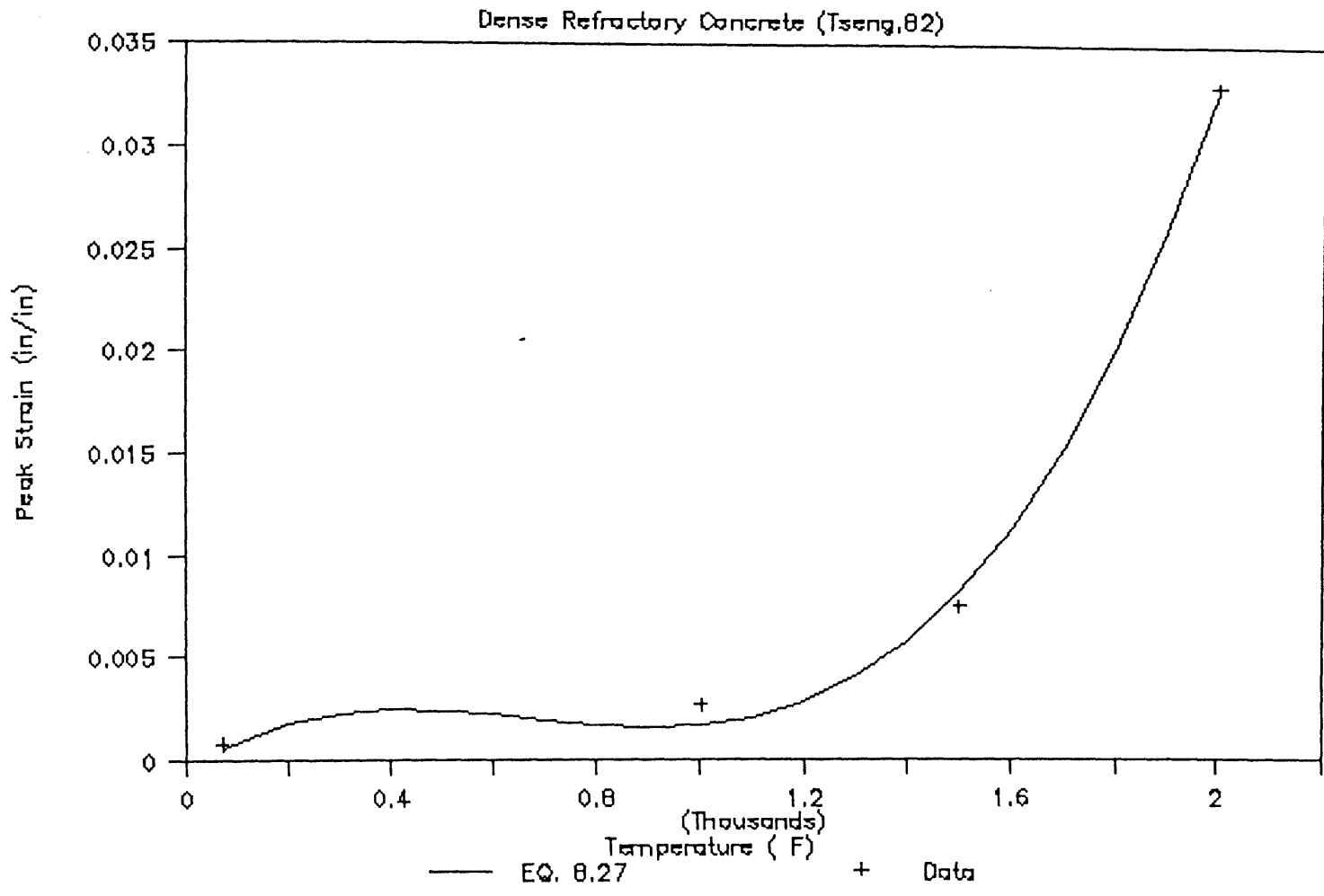
Figure B.39   Regression of data for Eq. 8.27

Dense Refractory Concrete (Tseng,82)

Figure B.40   Regression of data for Eq. 8.28a

Dense Refractory Concrete (Tseng,82)

Initial Stiffness (Ksi)
(Thousands)

Temperature (F)
(Thousands)

———— EQ. 8.28b   +   Data

Figure B.41   Regression of data for Eq. 8.28b

Figure B.42   Regression of data for Eq. 8.29

Figure B.43   Regression of data for Eq. 8.30

Figure B.44   Regression of data for Eq. 8.31a

Figure B.45   Regression of data for Eq. 8.31b

Commercial Refractory Castable
(Wygant and Buckley, 54)
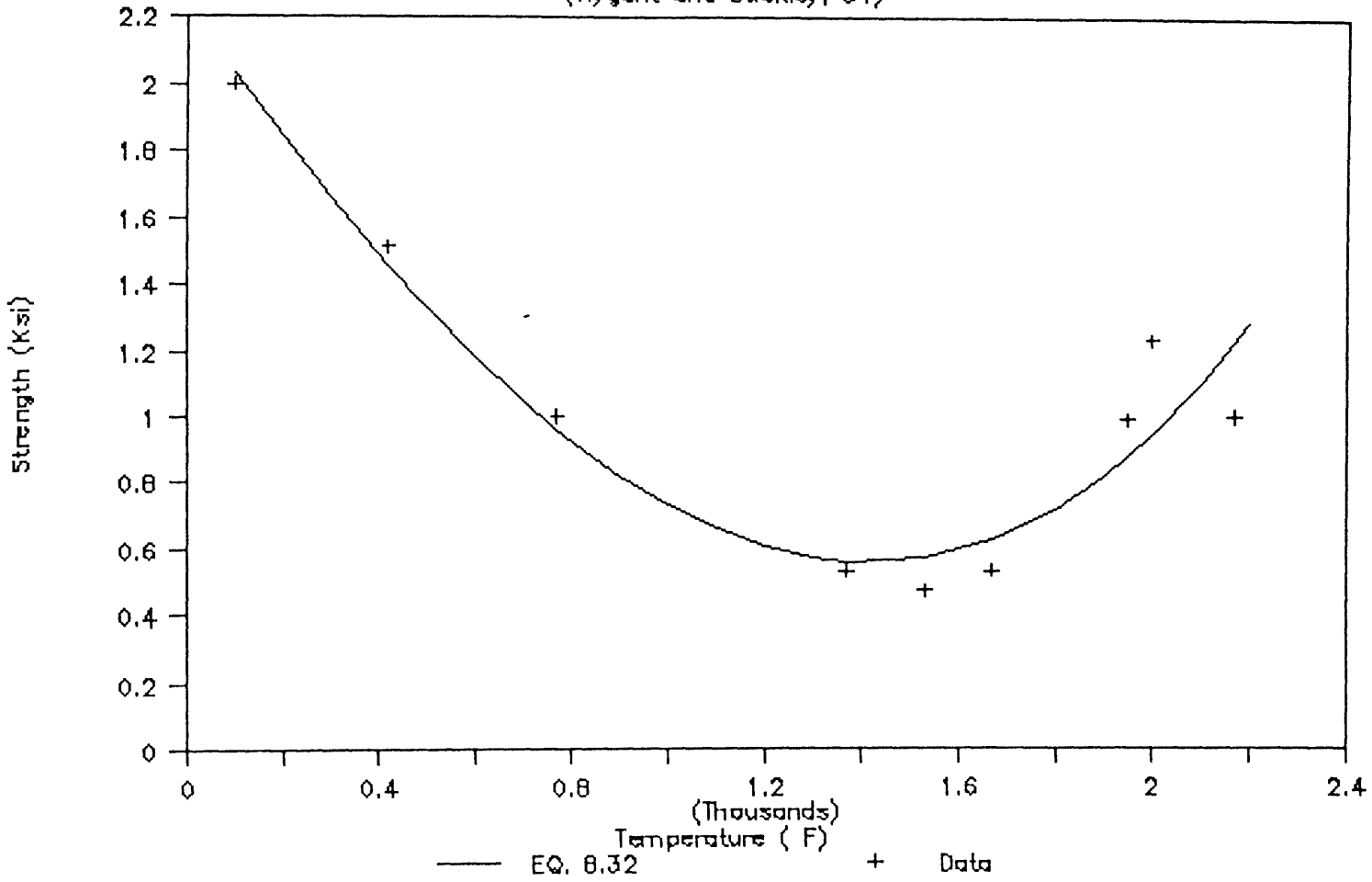
Figure B.46   Regression of data for Eq. 8.32

Portland Cement Concrete
(Anderberg and Thelandersson, 76)

—— EQ. 8.33   +   Data
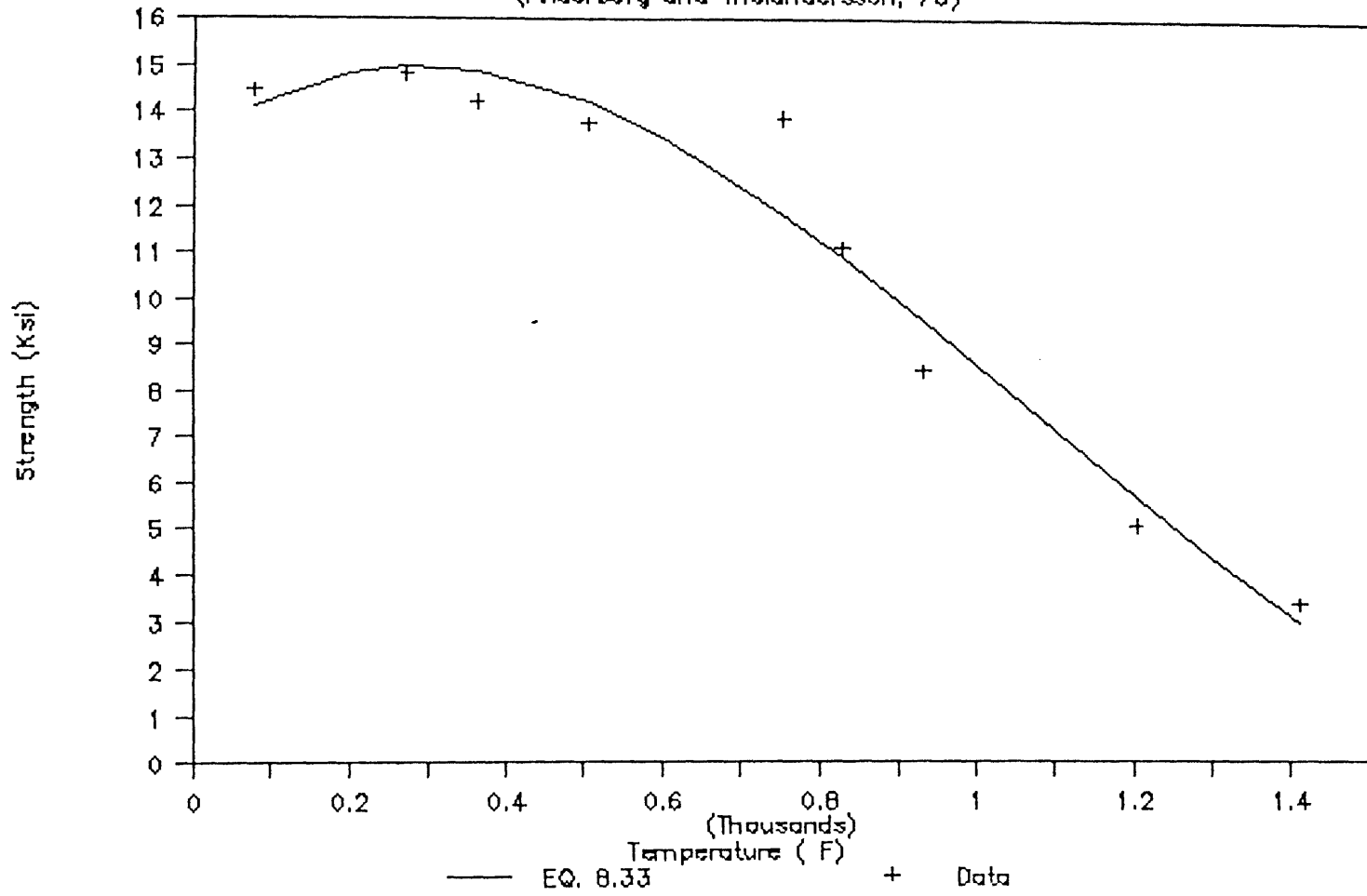
Figure B.47   Regression of data for Eq. 8.33

Portland Cement Concrete
(Anderberg and Thelandersson, 76)
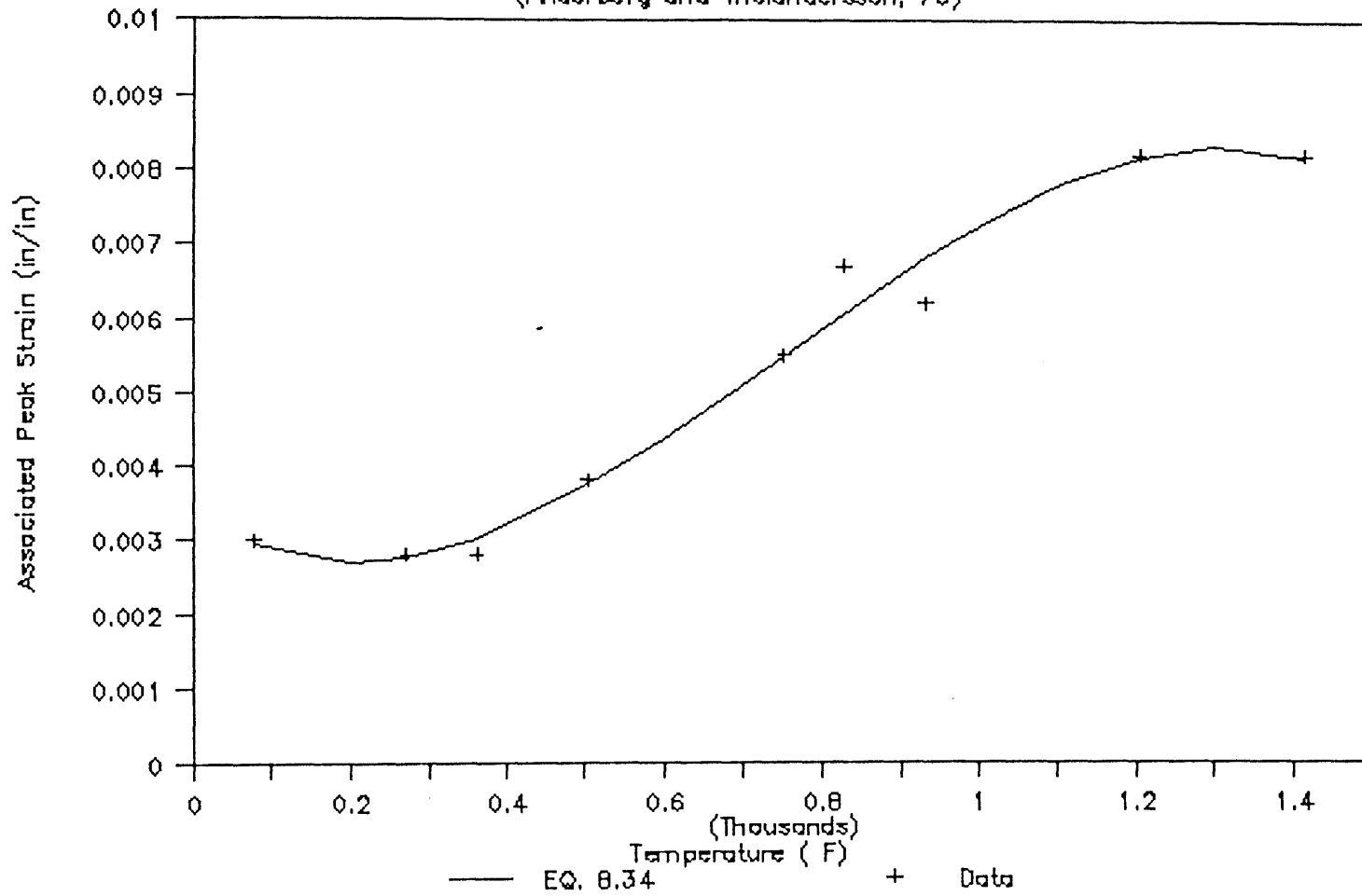
Figure B.48   Regression of data for Eq. 8.34

Portland Cement Concrete

(Anderberg and Thelandersson, 76)
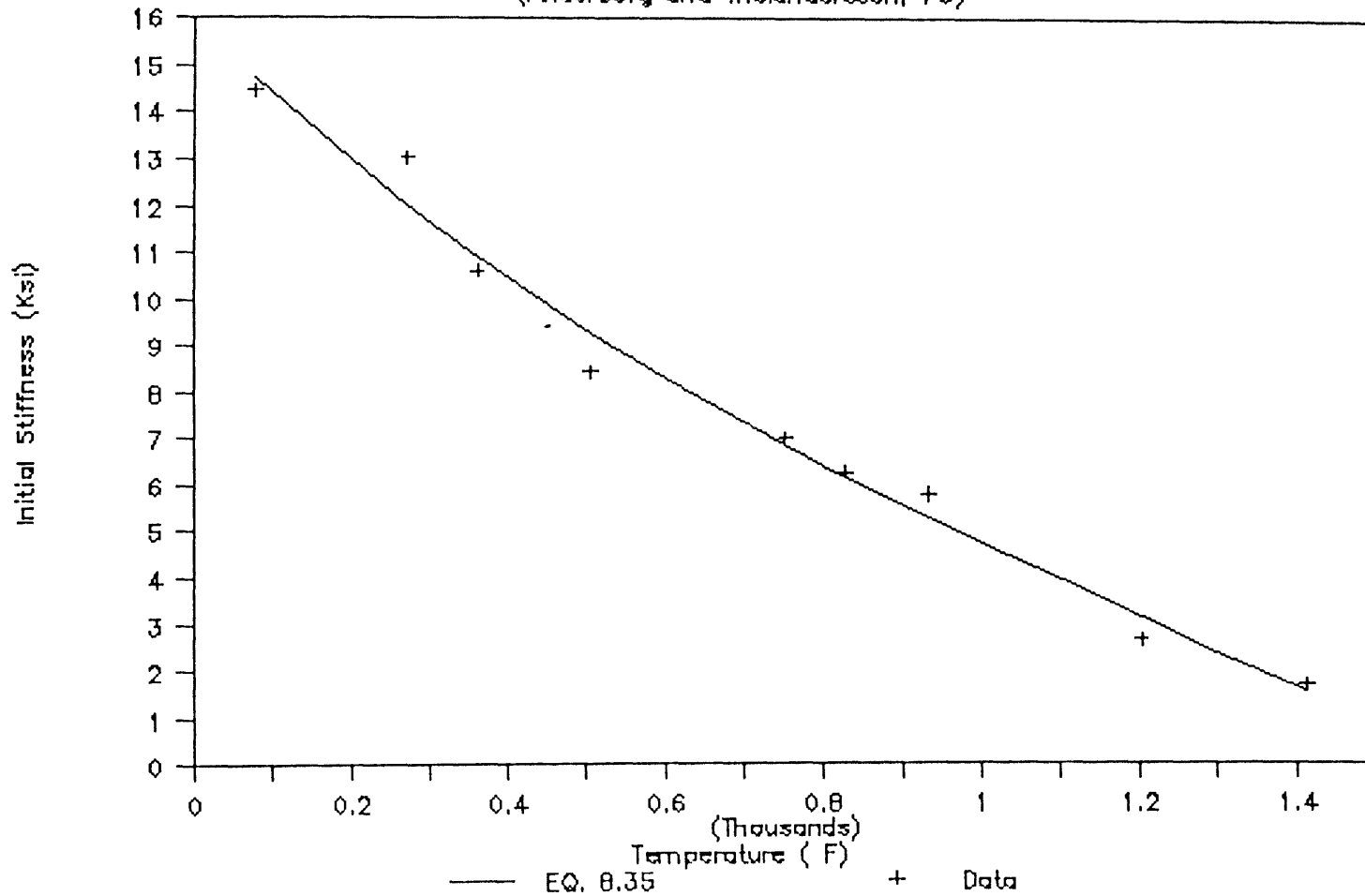
Figure B.49   Regression of data for Eq. 8.35

As-Manufactured CPS—90A—10C
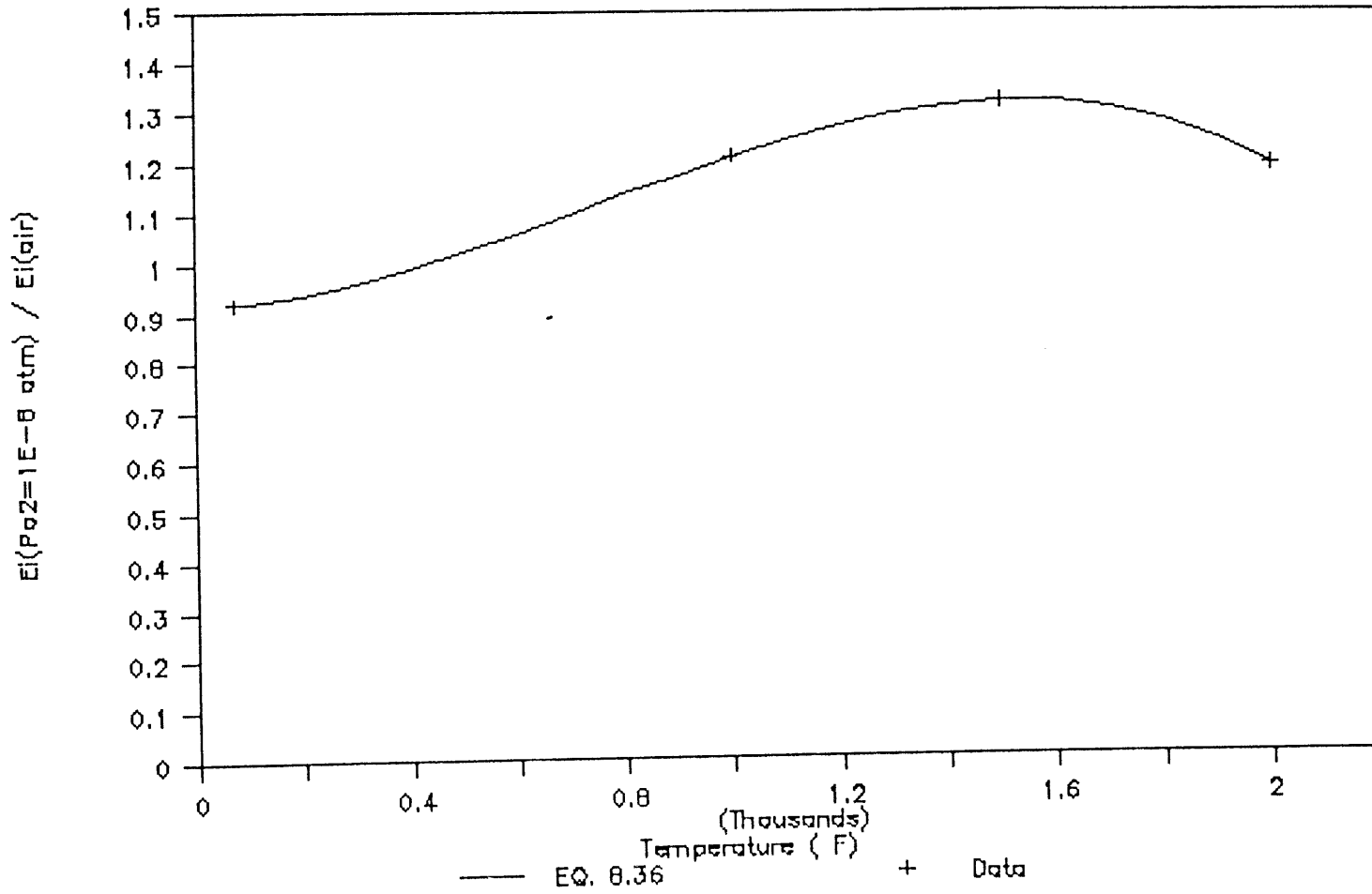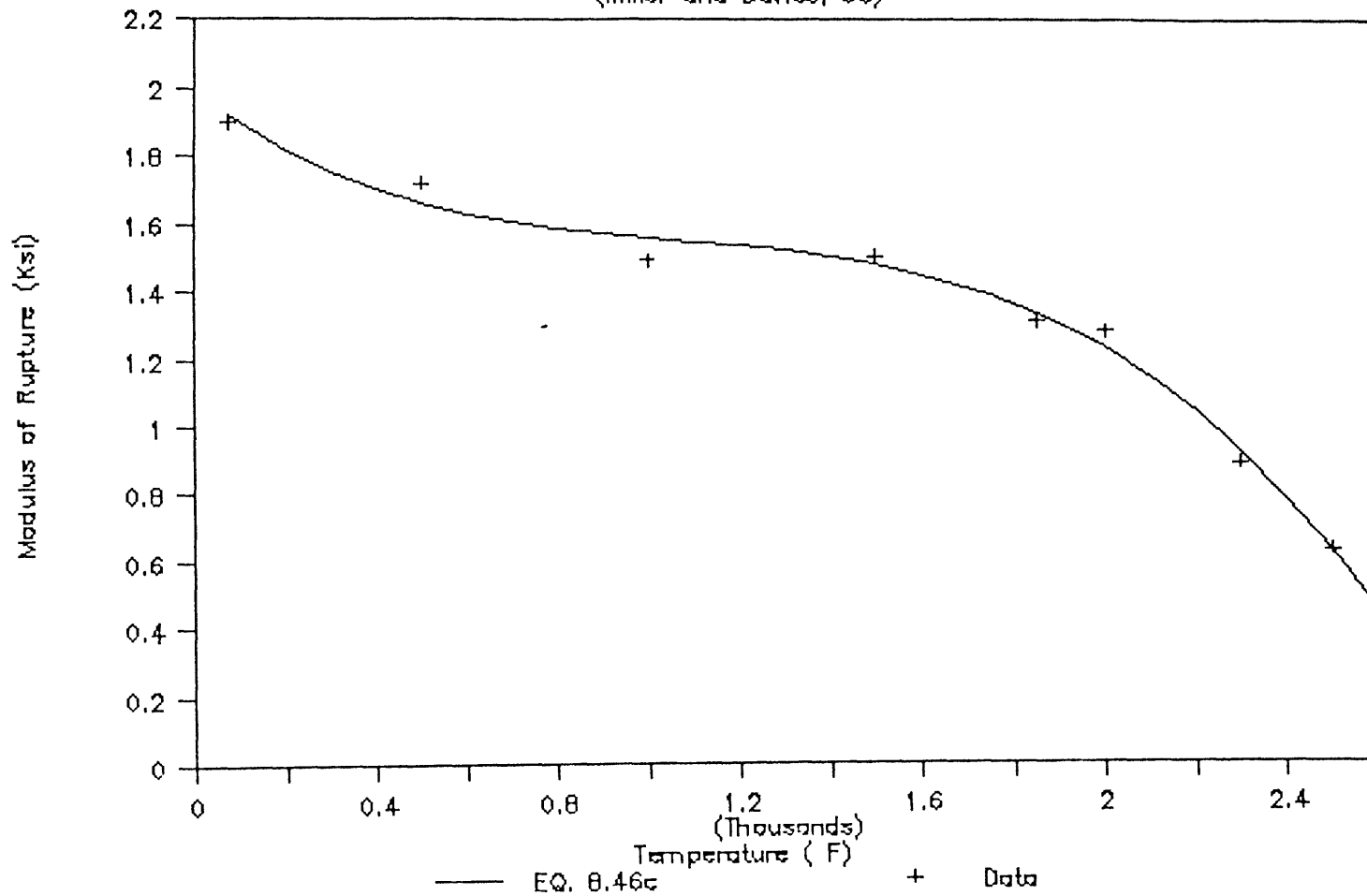
Figure B.50　　　　　Regression of data for Eq. 8.36
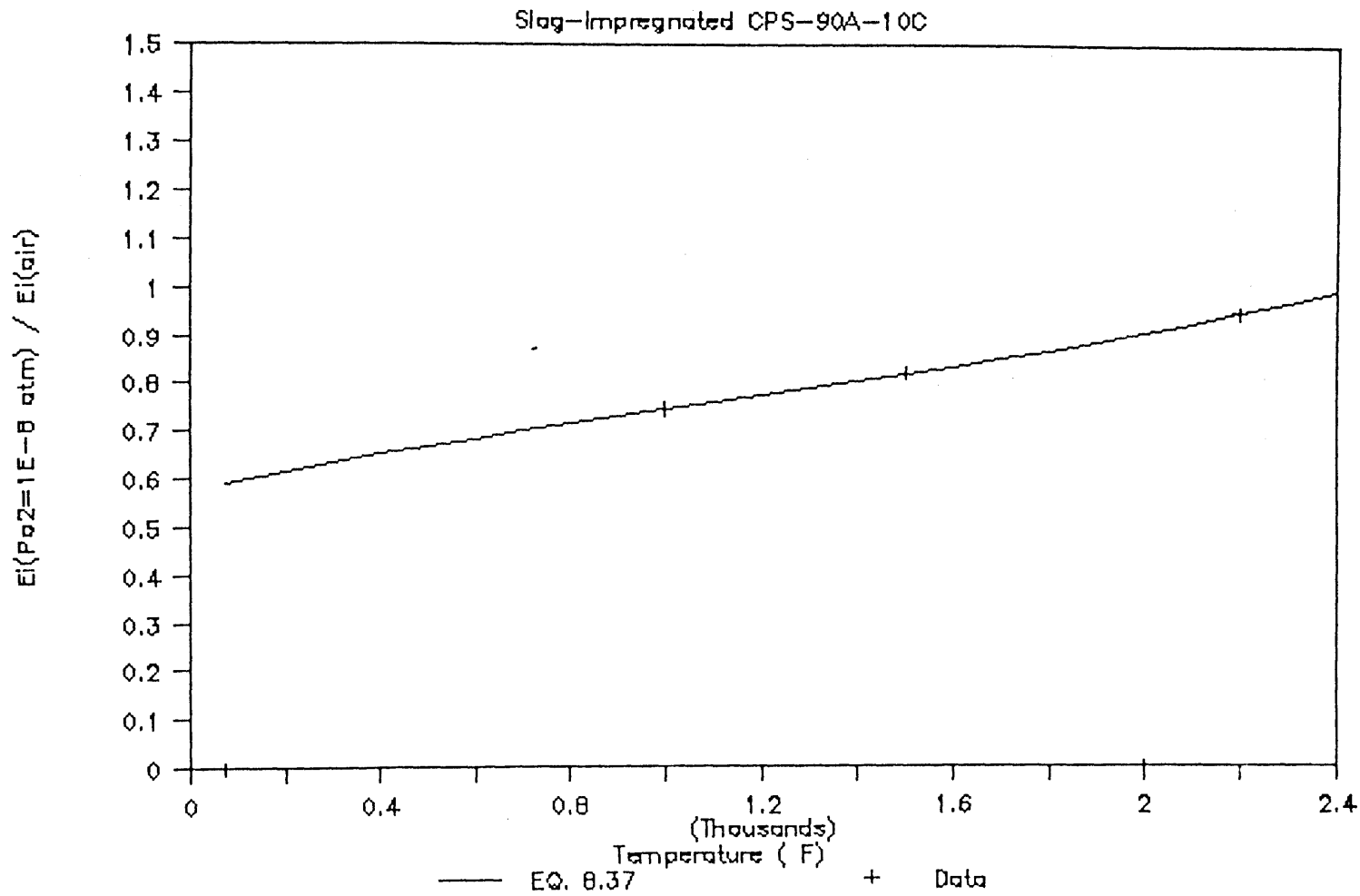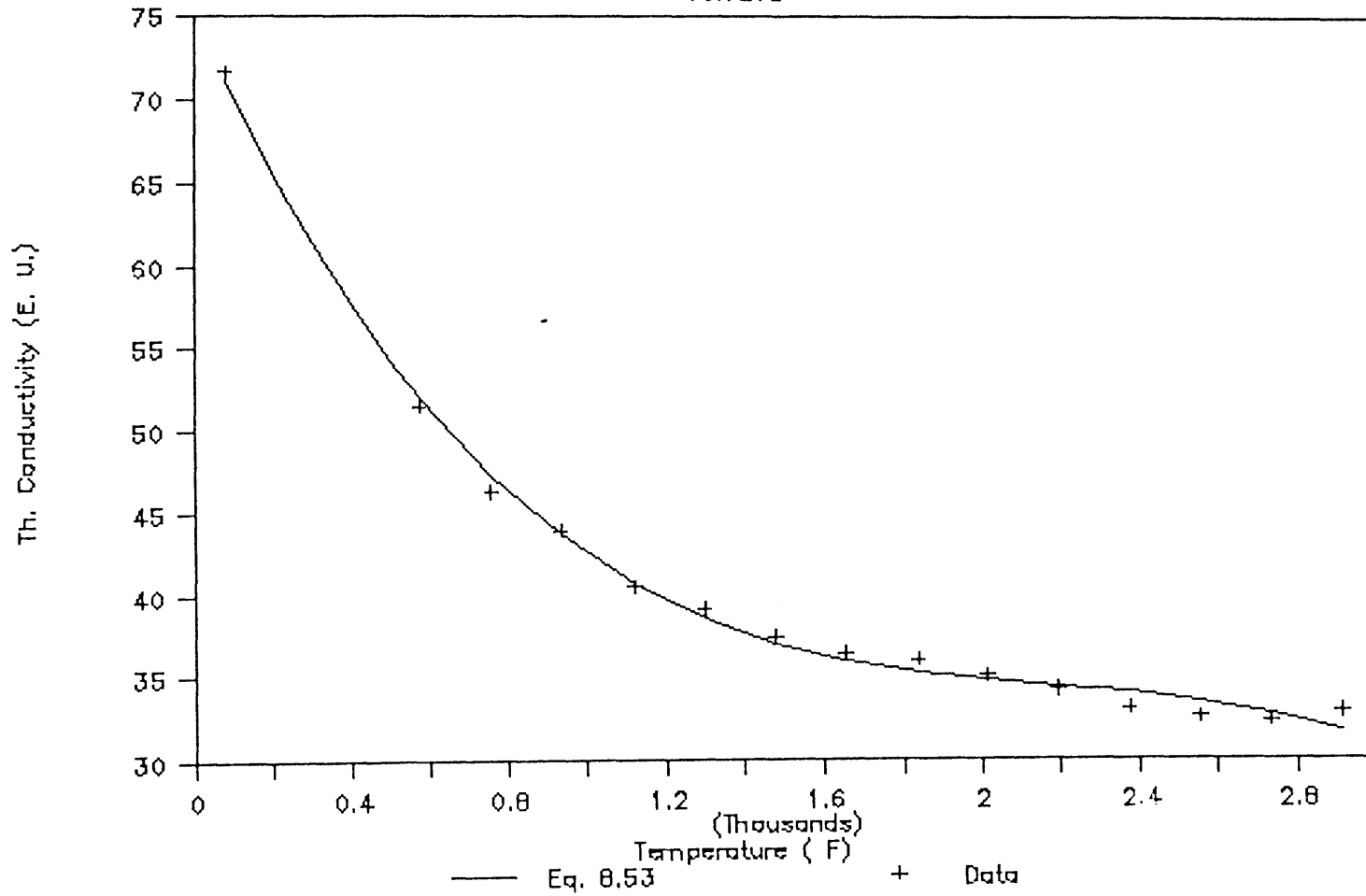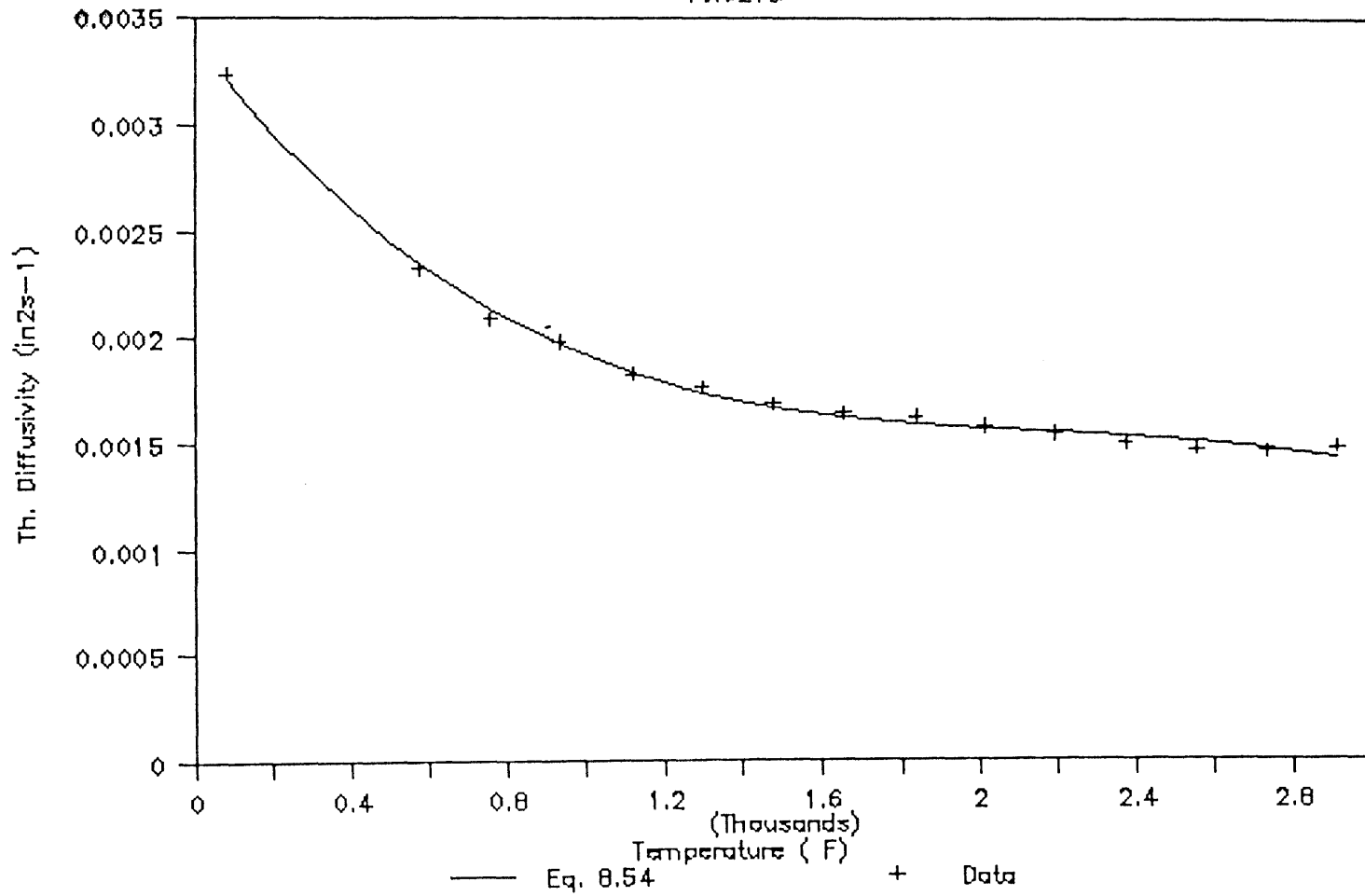
Figure B.51   Regression of data for Eq. 8.37

Figure B.52   Regression of data for Eq. 8.38

Figure B.53   Regression of data for Eq. 8.39

AX581

(Norton Company)

Figure B.54   Regression of data for Eq. 8.40

TX591

(Norton Company)
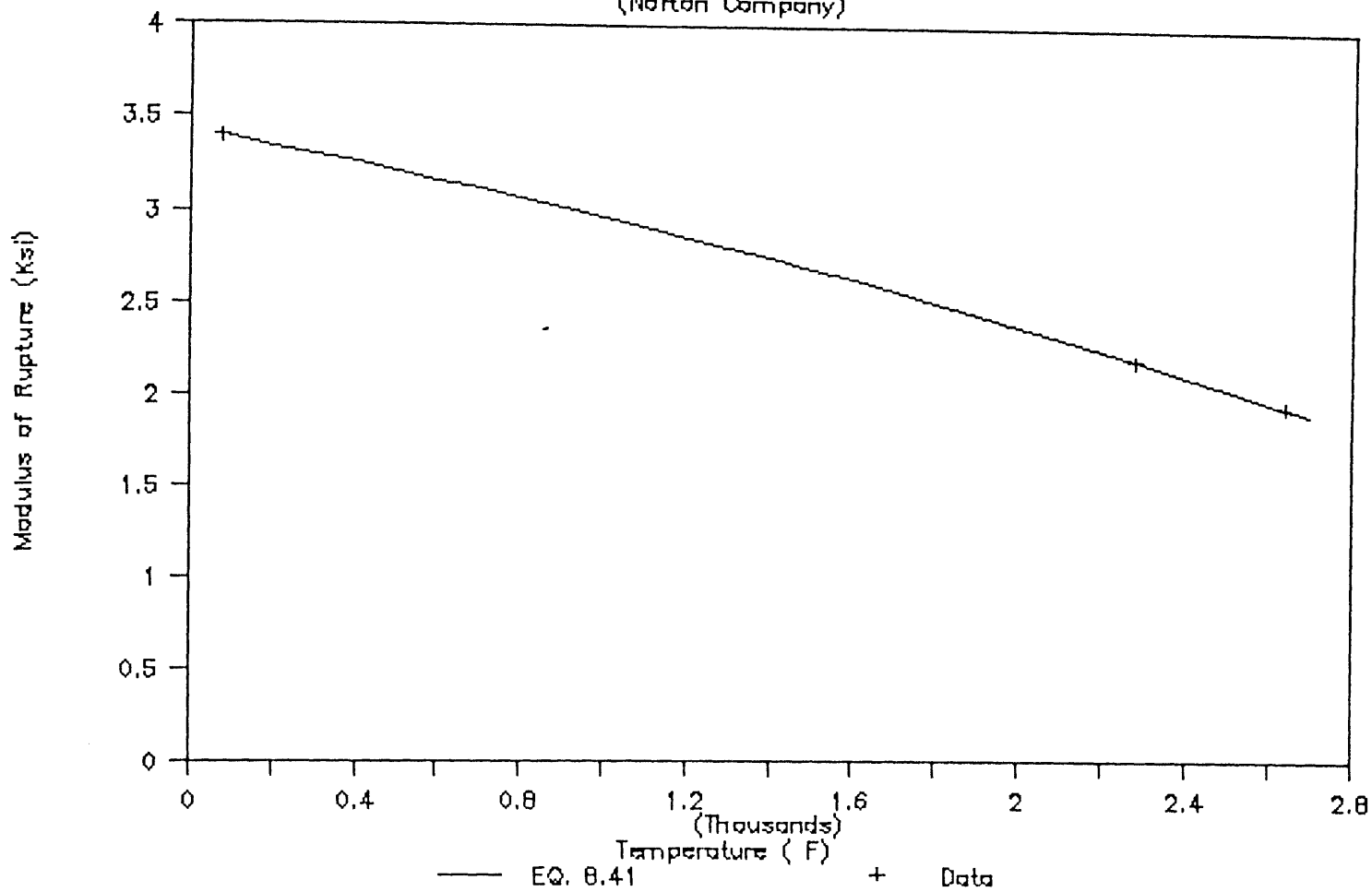
Figure B.55   Regression of data for Eq. 8.41

AX565
(Norton Company)

Modulus of Rupture (Ksi) vs Temperature (°F)

EQ. 8.42   + Data
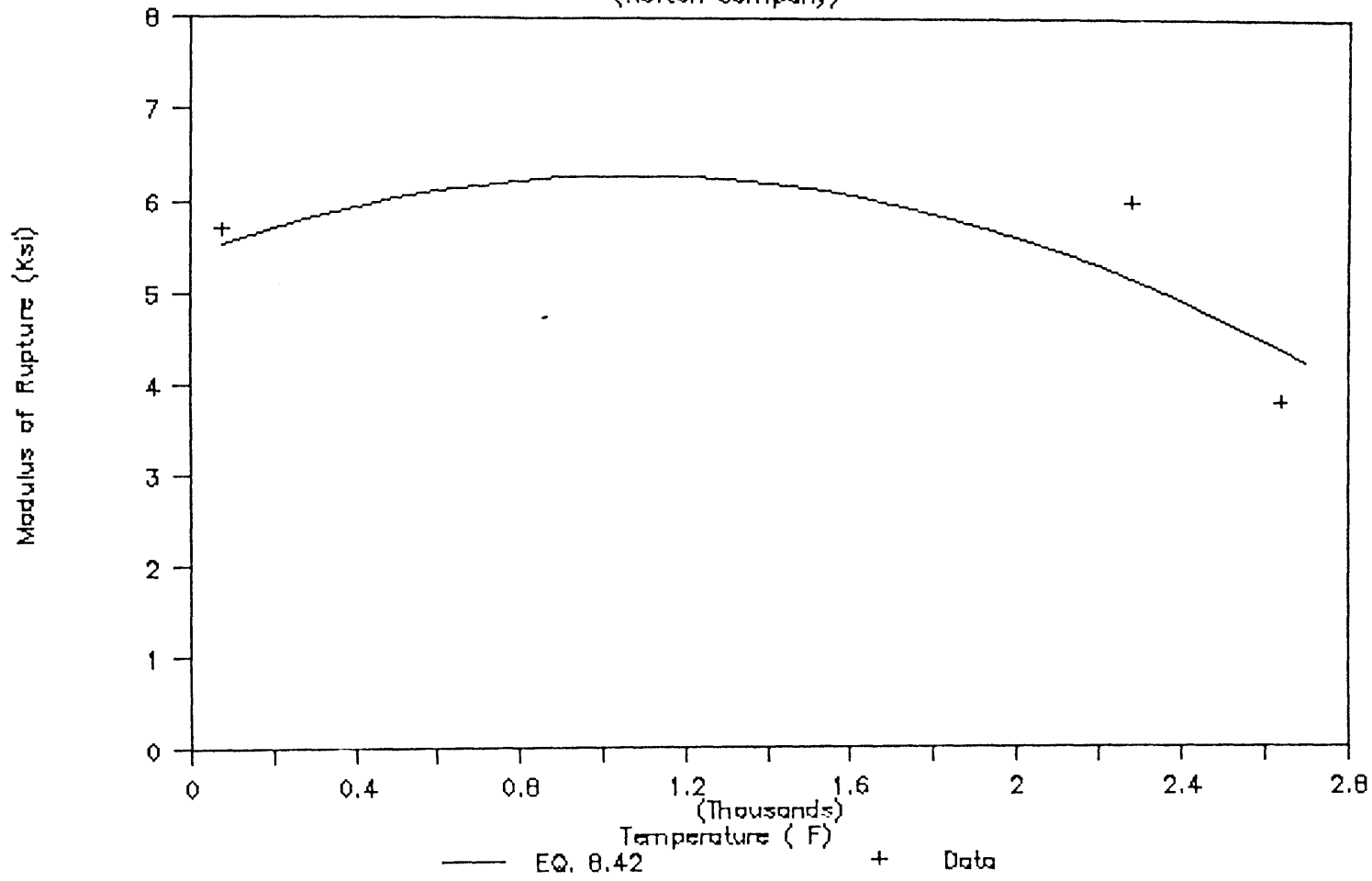
Figure B.56   Regression of data for Eq. 8.42

Alumina–Silica Brick, 50% Alumina
(Miller and Davies, 66)
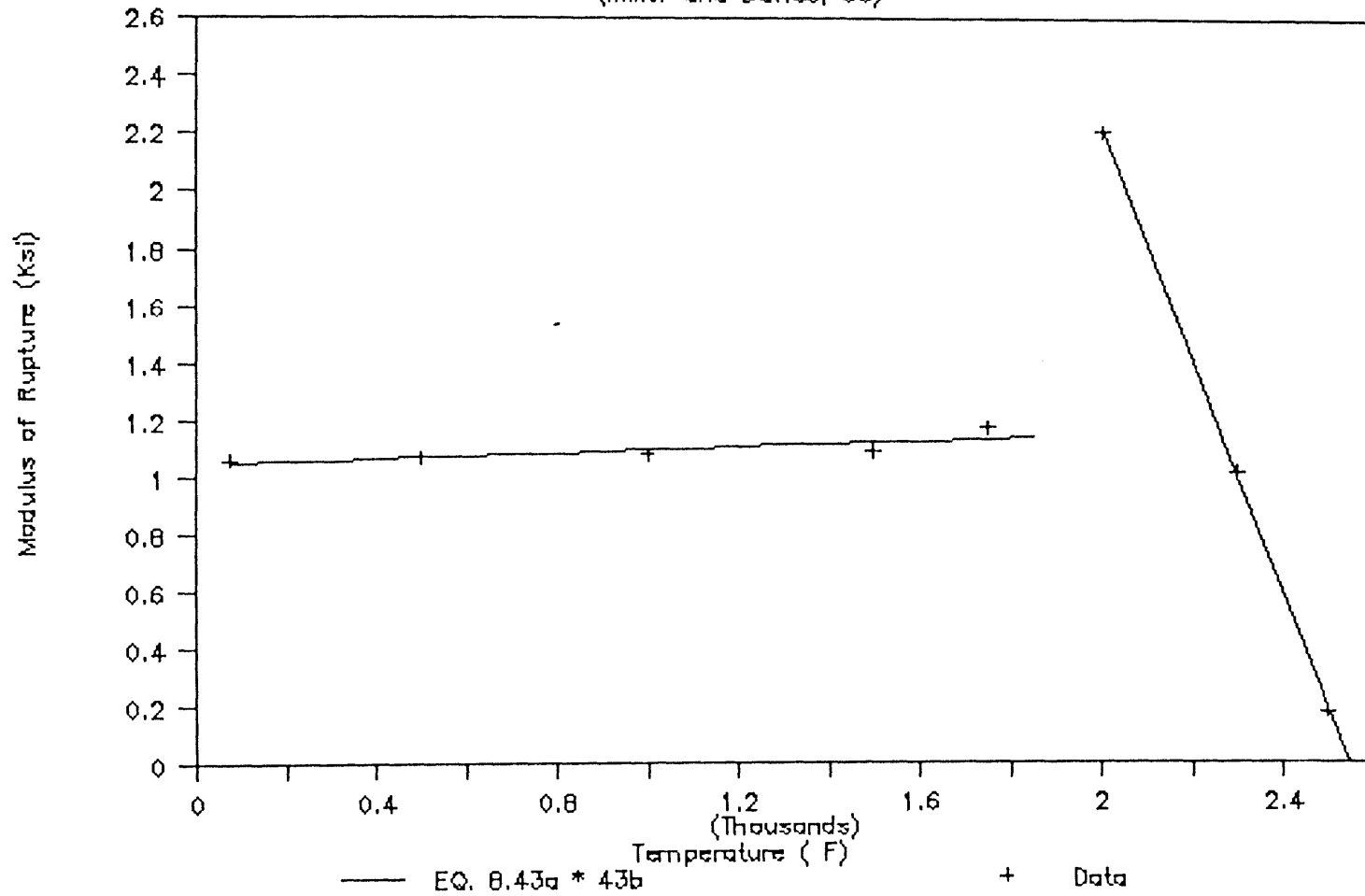
Figure B.57   Regression of data for Eqs. 8.43a and 8.43b

Alumina—Silica Brick, 50% Alumina
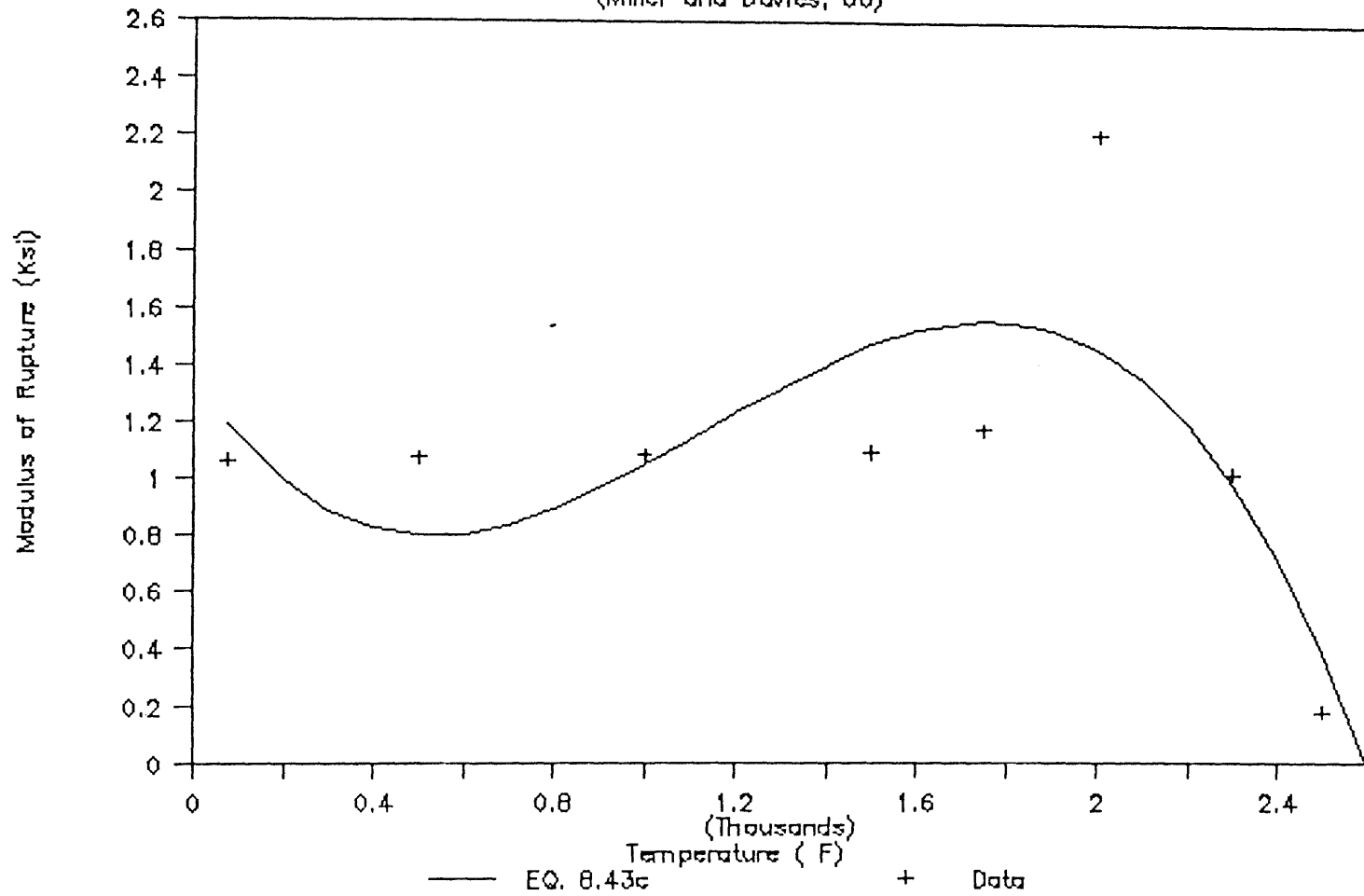
Figure B.58   Regression of data for Eq. 8.43c

Dense Alumina—Silica Brick, 60%Alumina
(Miller and Davies, 66)
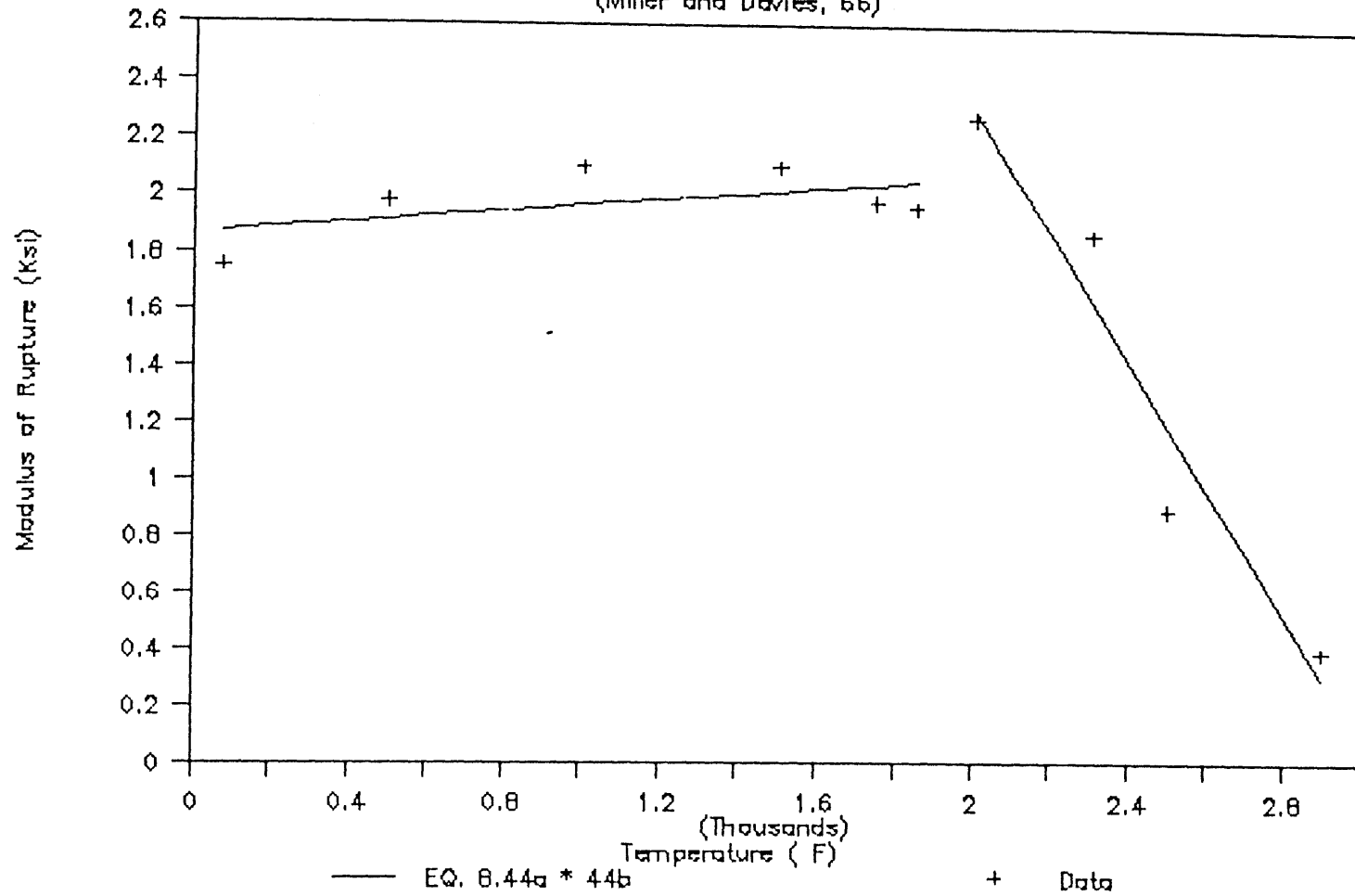
Figure B.59   Regression of data for Eqs. 8.44a and 8.44b

Dense Alumina-Silica Brick, 60%Alumina

(Miller and Davies, 66)
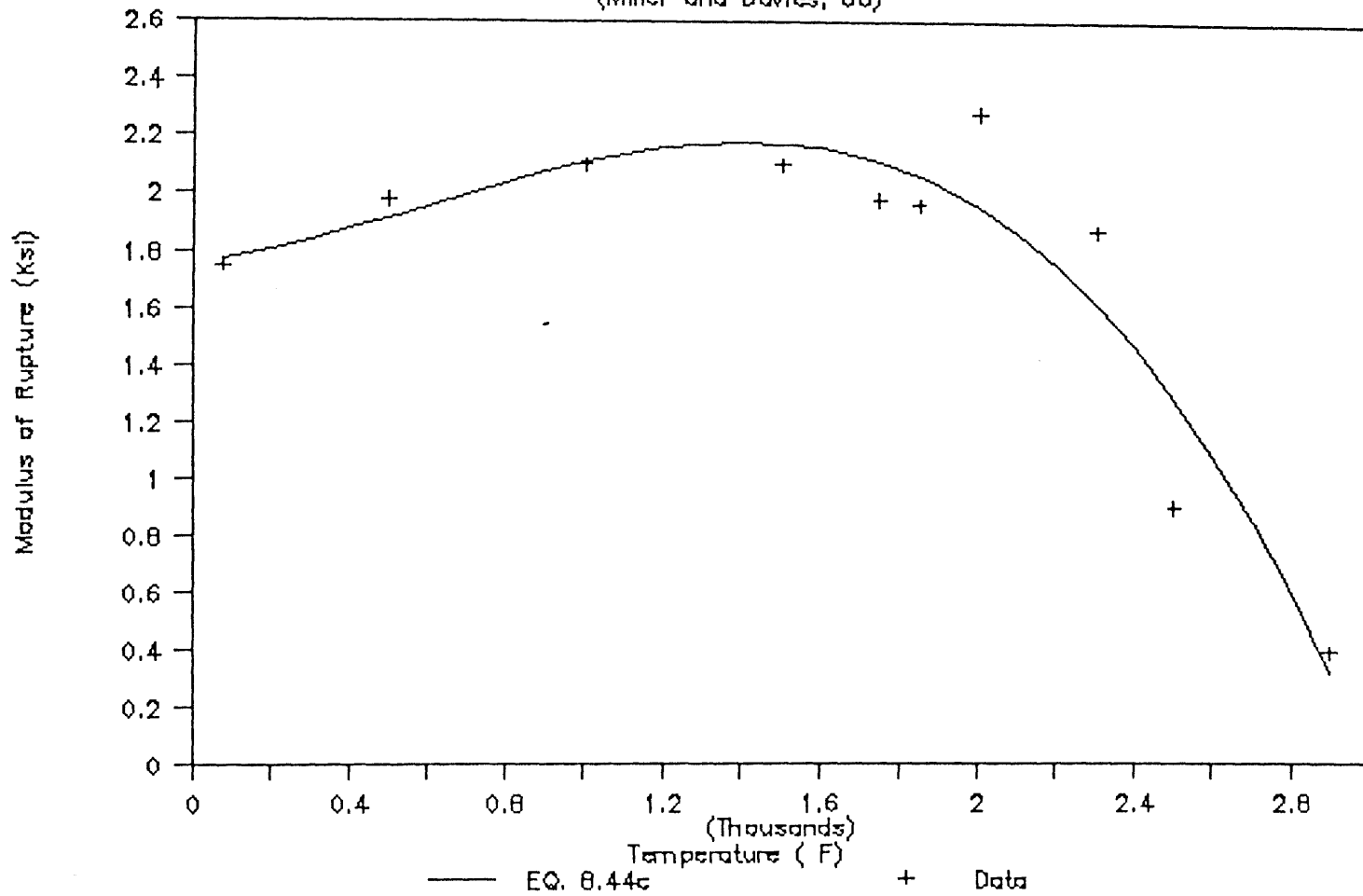
Figure B.60   Regression of data for Eq. 8.44c

Dense Alumina—Silica Brick, 90%Alumina
(Miller and Davies, 66)
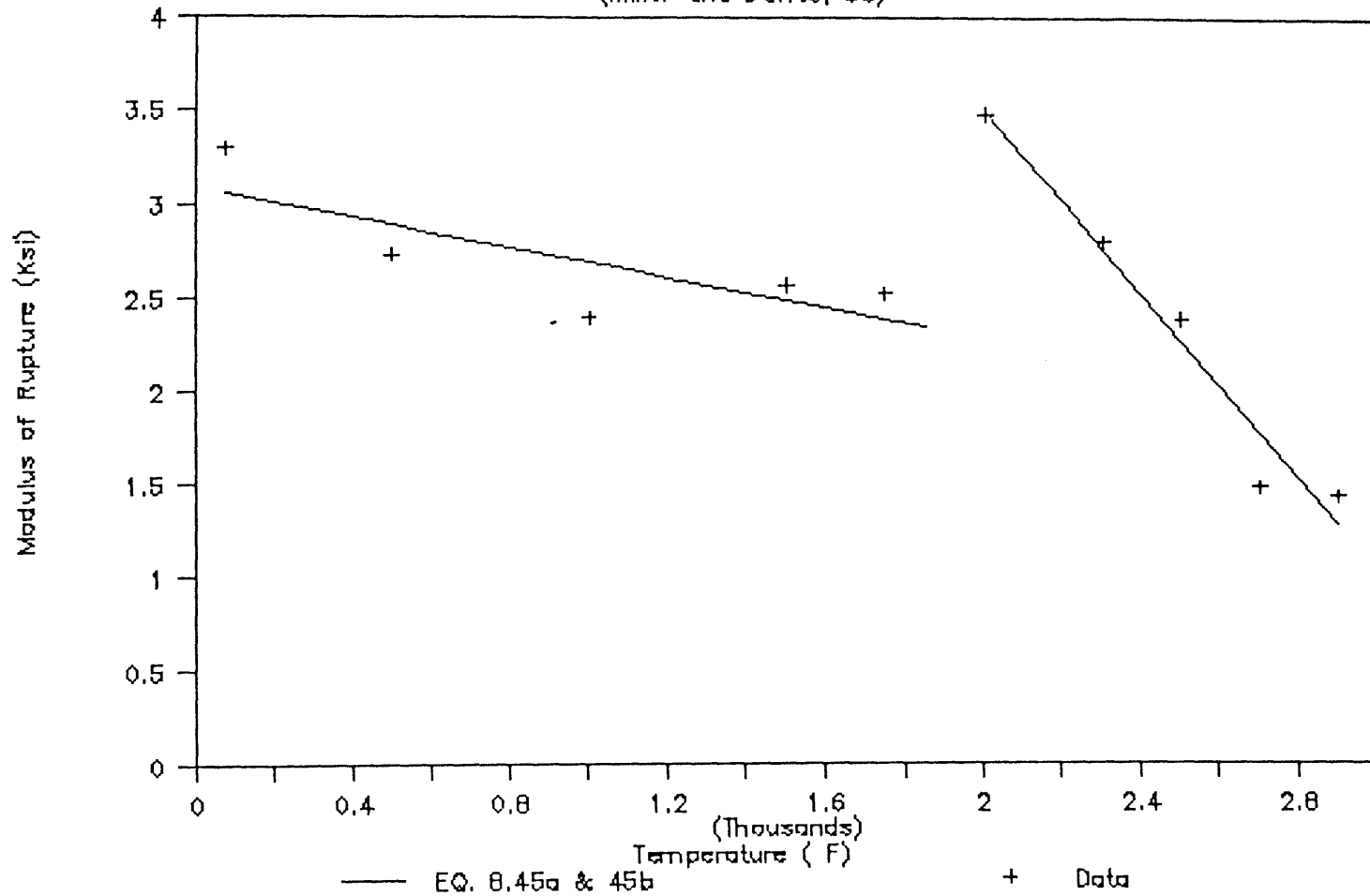
Figure B.61   Regression of data for Eqs. 8.45a and 8.45b

Dense Alumina—Silica Brick, 90%Alumina

(Miller and Davies, 66)
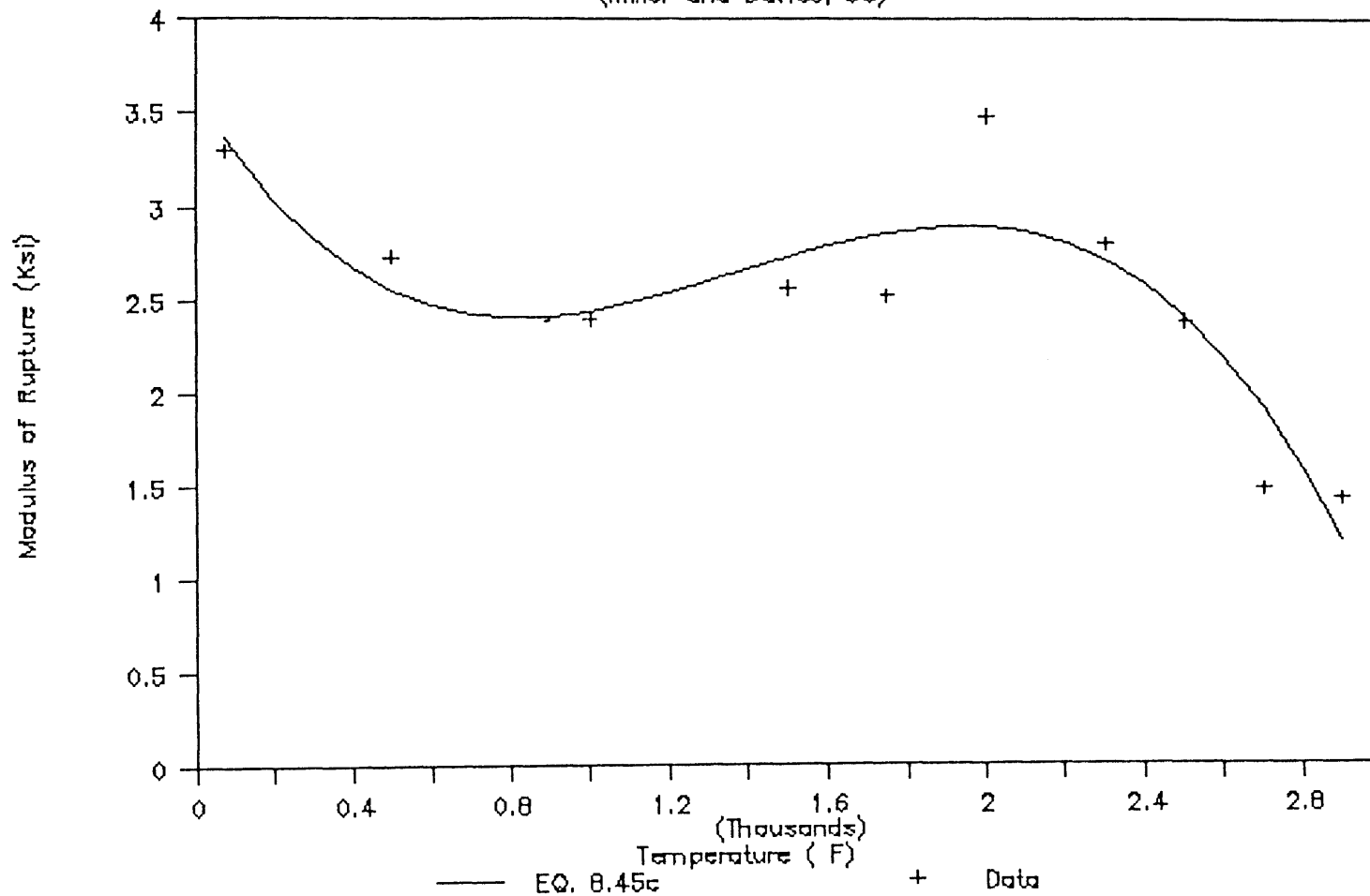
Figure B.62   Regression of data for Eq. 8.45c

Alumina—Silica Brick, 99% Alumina
(Miller and Davies, 66)
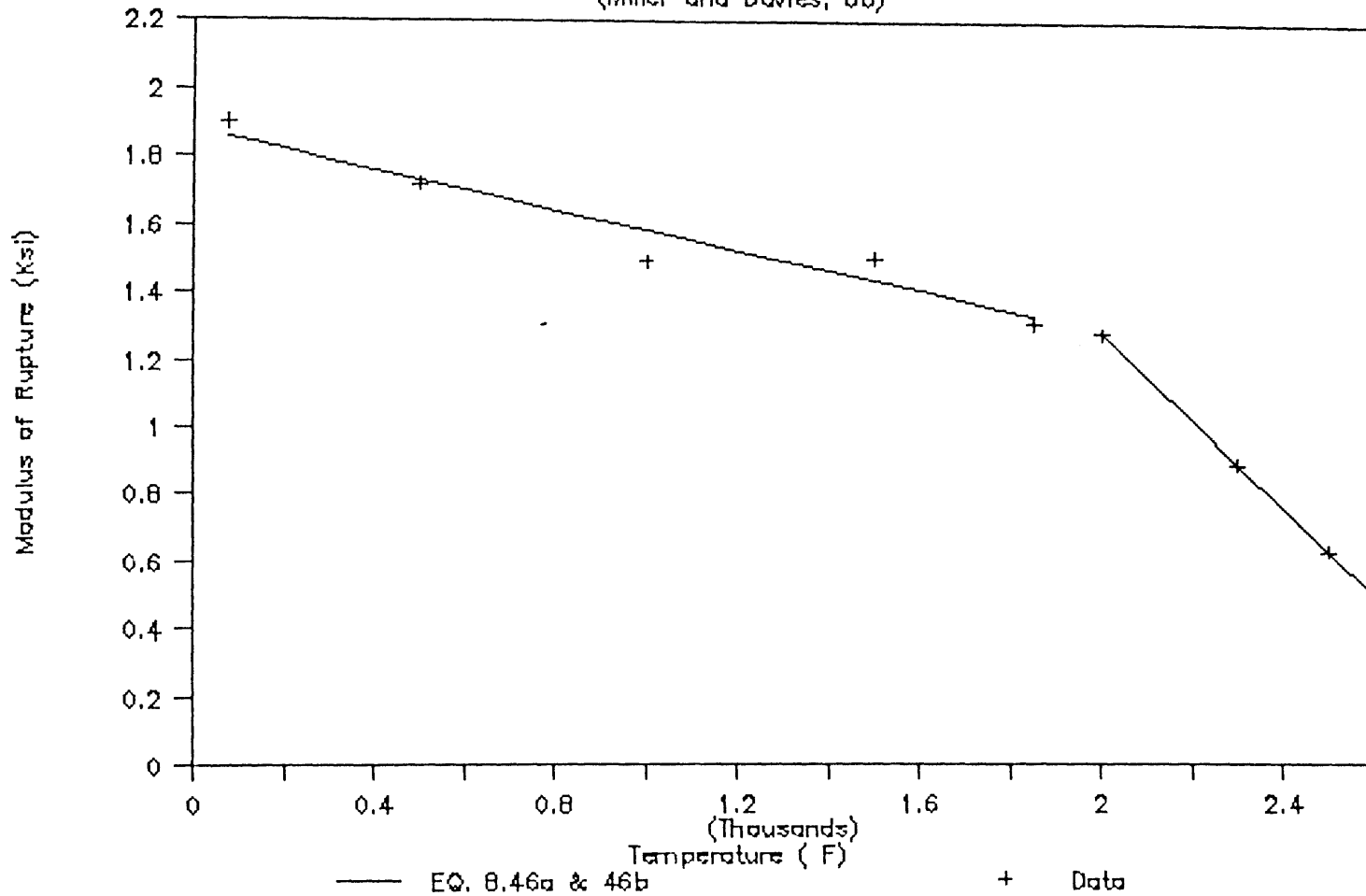
Figure B.63   Regression of data for Eqs. 8.46a and 8.46b

Alumina—Silica Brick, 99% Alumina

Figure B.64   Regression of data for Eq. 8.46c

Figure B.65   Regression of data for Eq. 8.53
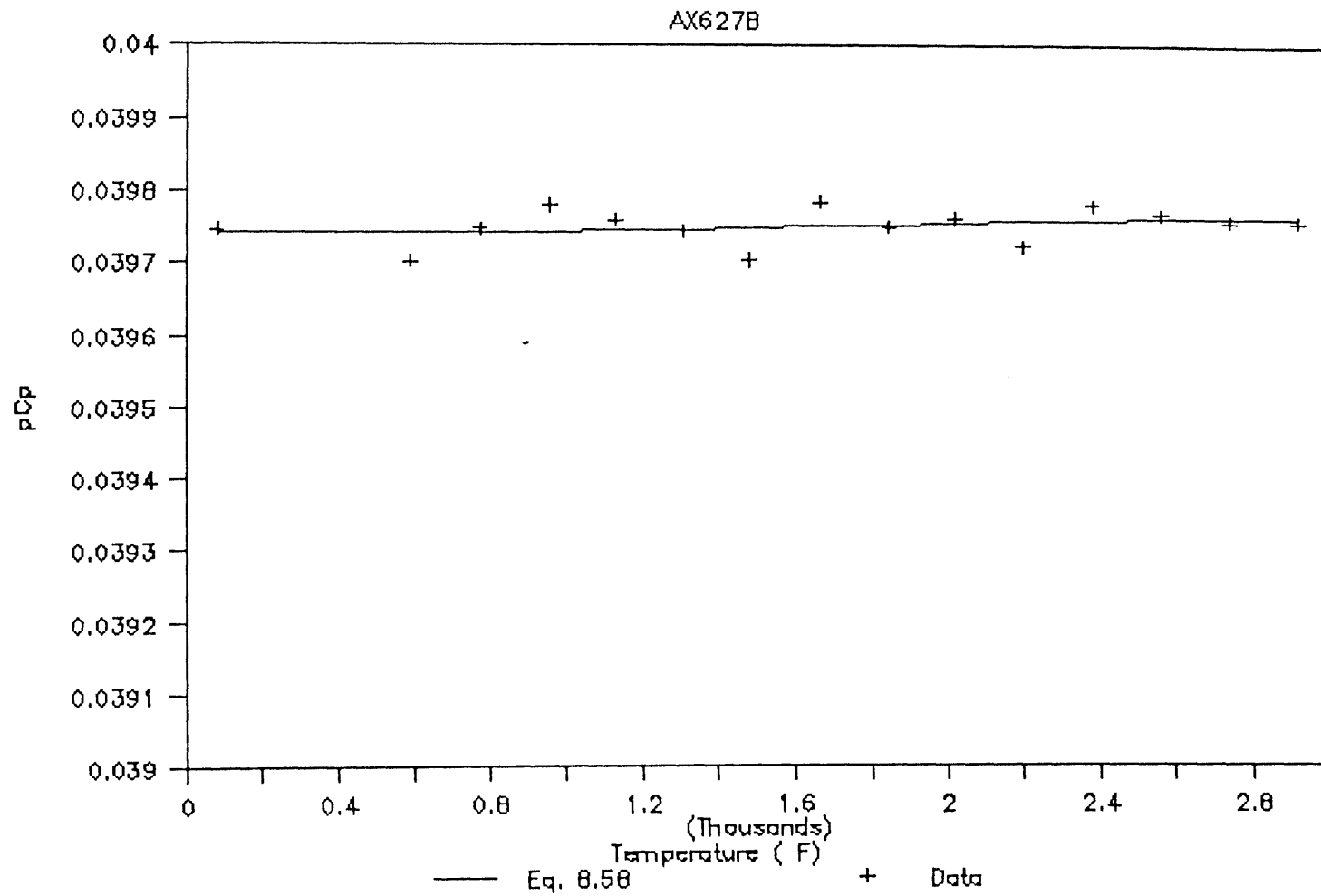
Figure B.66   Regression of data for Eq. 8.54
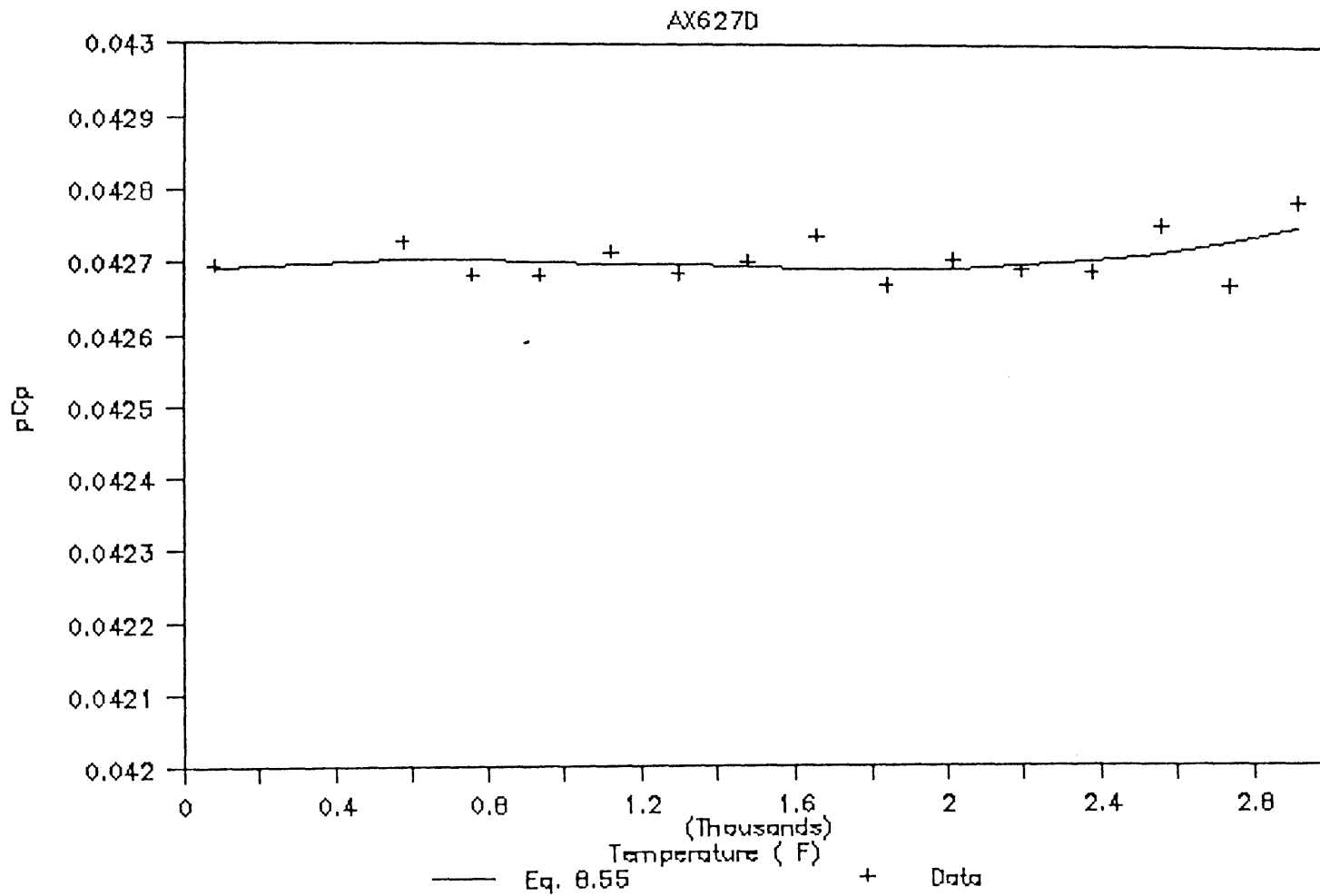
Figure B.67   Regression of data for Eq. 8.55
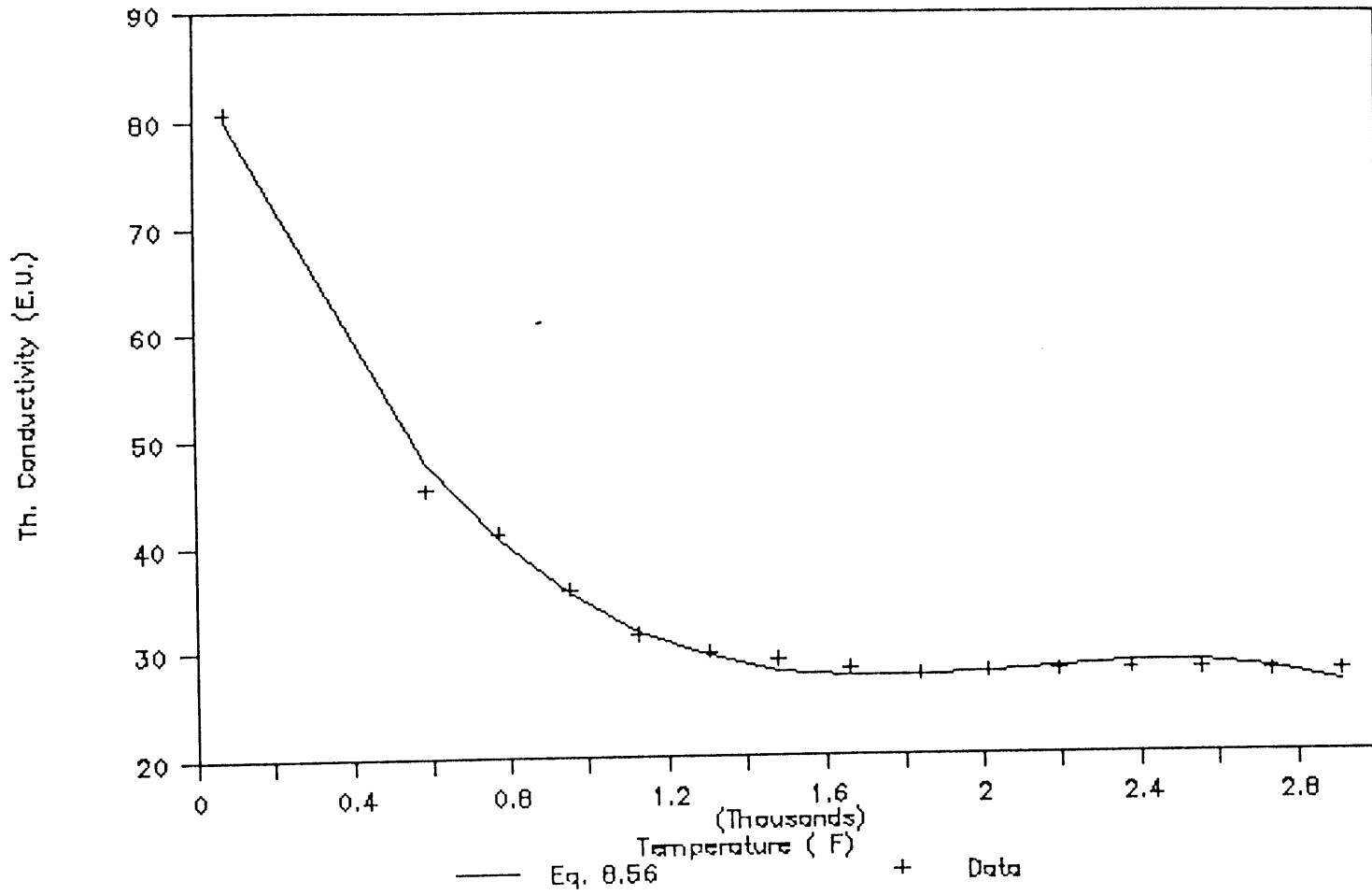
Figure B.68   Regression of data for Eq. 8.56

AX627B
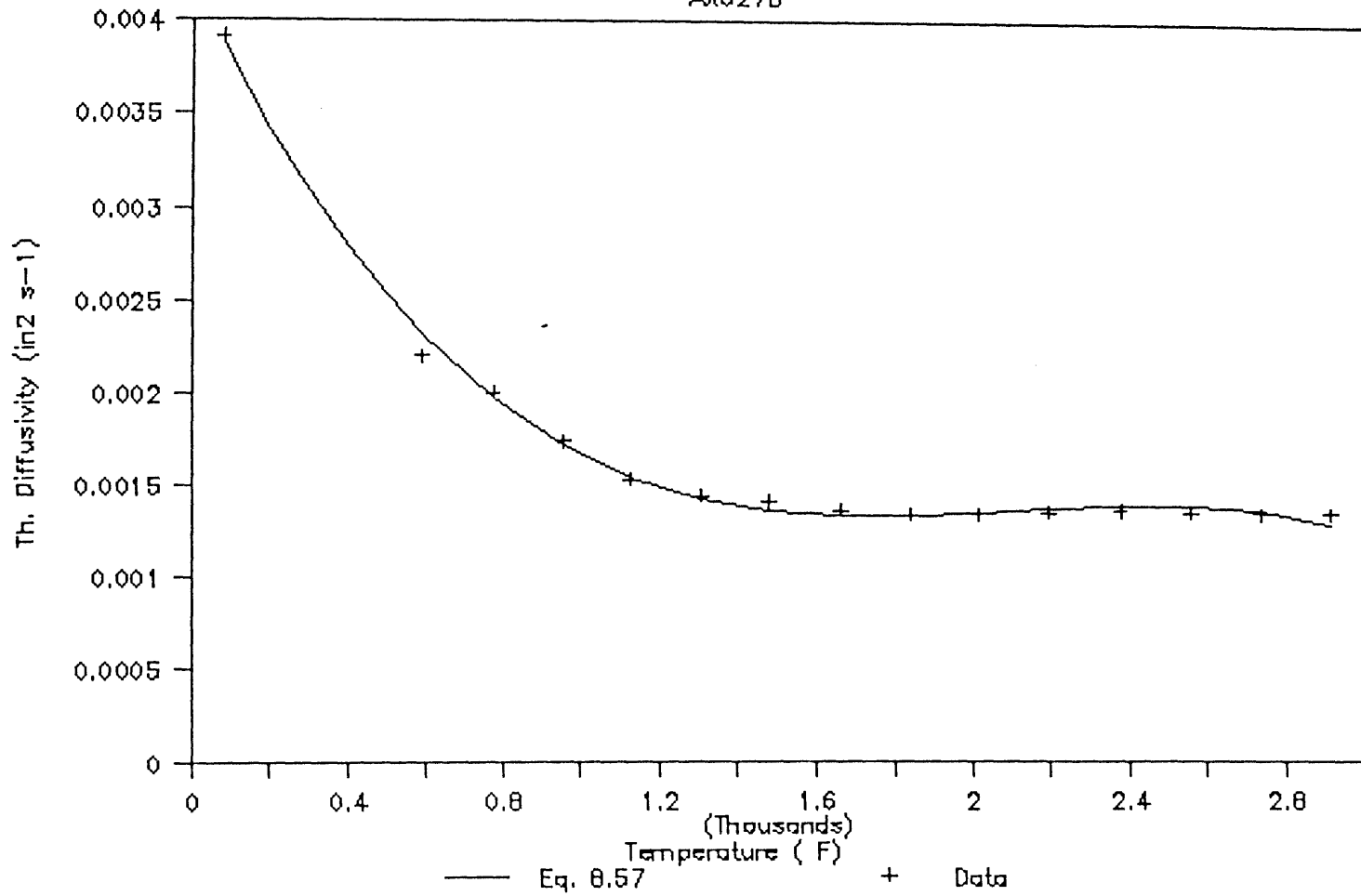
Figure B.69   Regression of data for Eq. 8.57
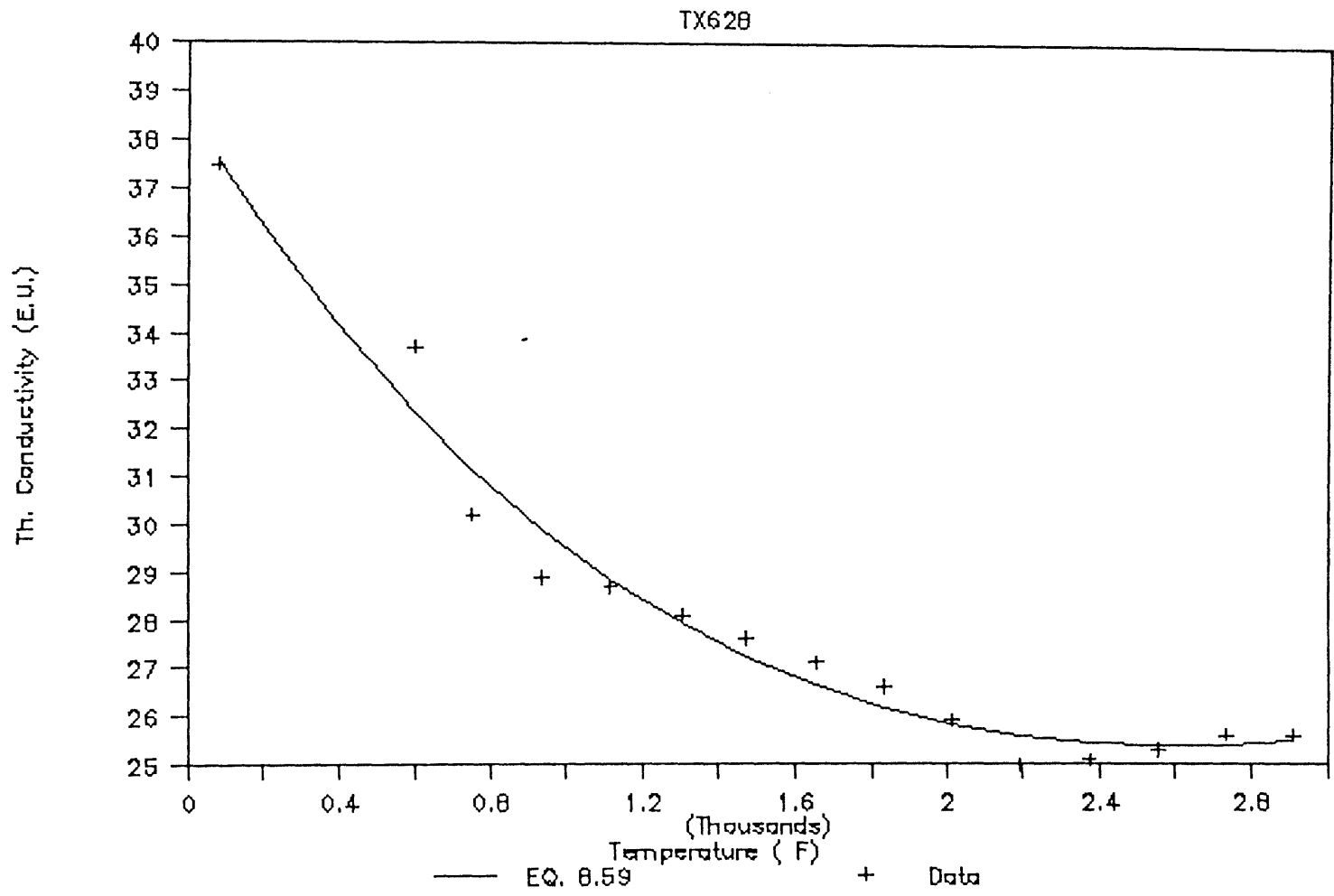
Figure B.70   Regression of data for Eq. 8.58

TX628

Figure B.71   Regression of data for Eq. 8.59
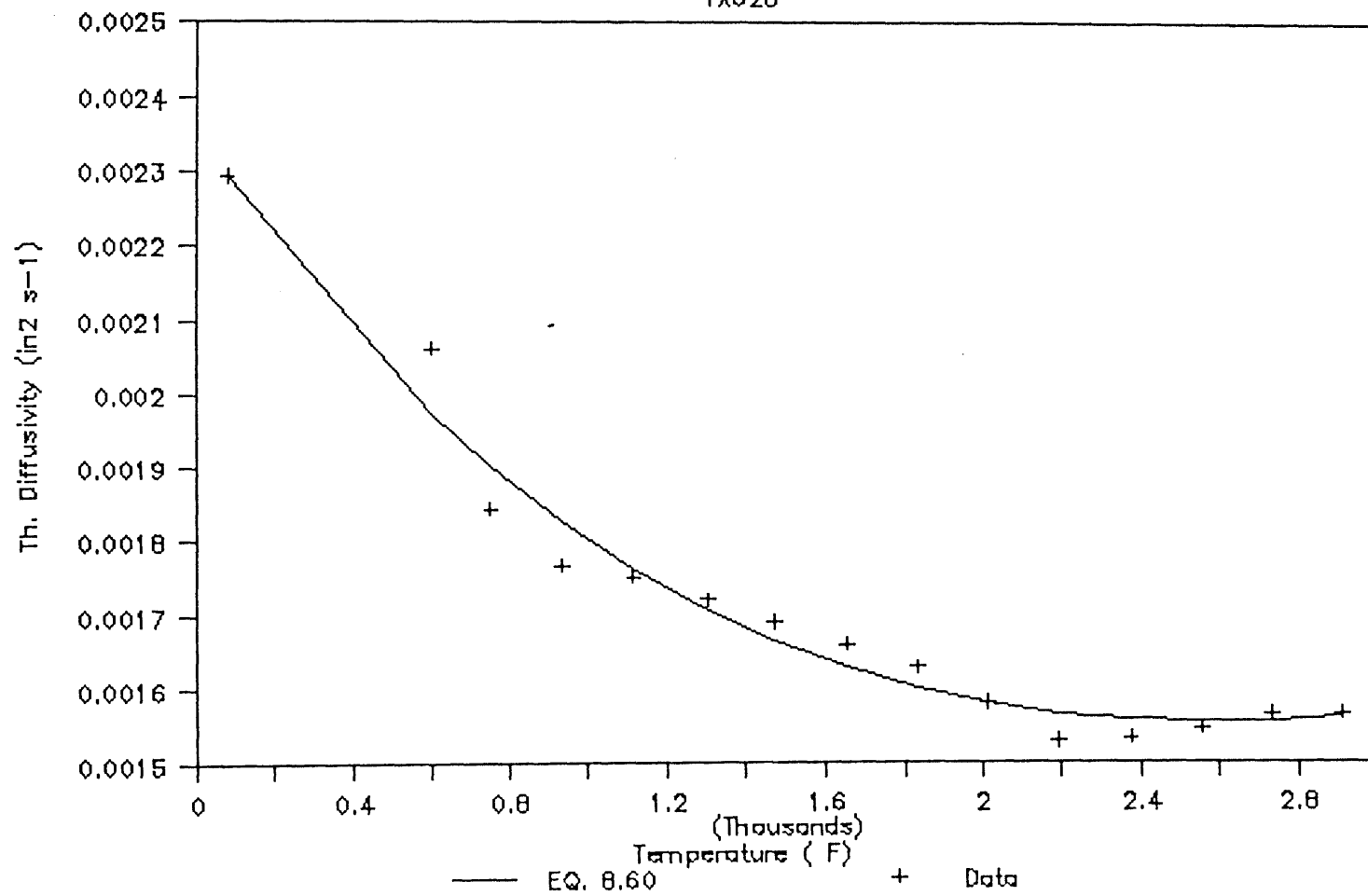
543

Figure B.72   Regression of data for Eq. 8.60

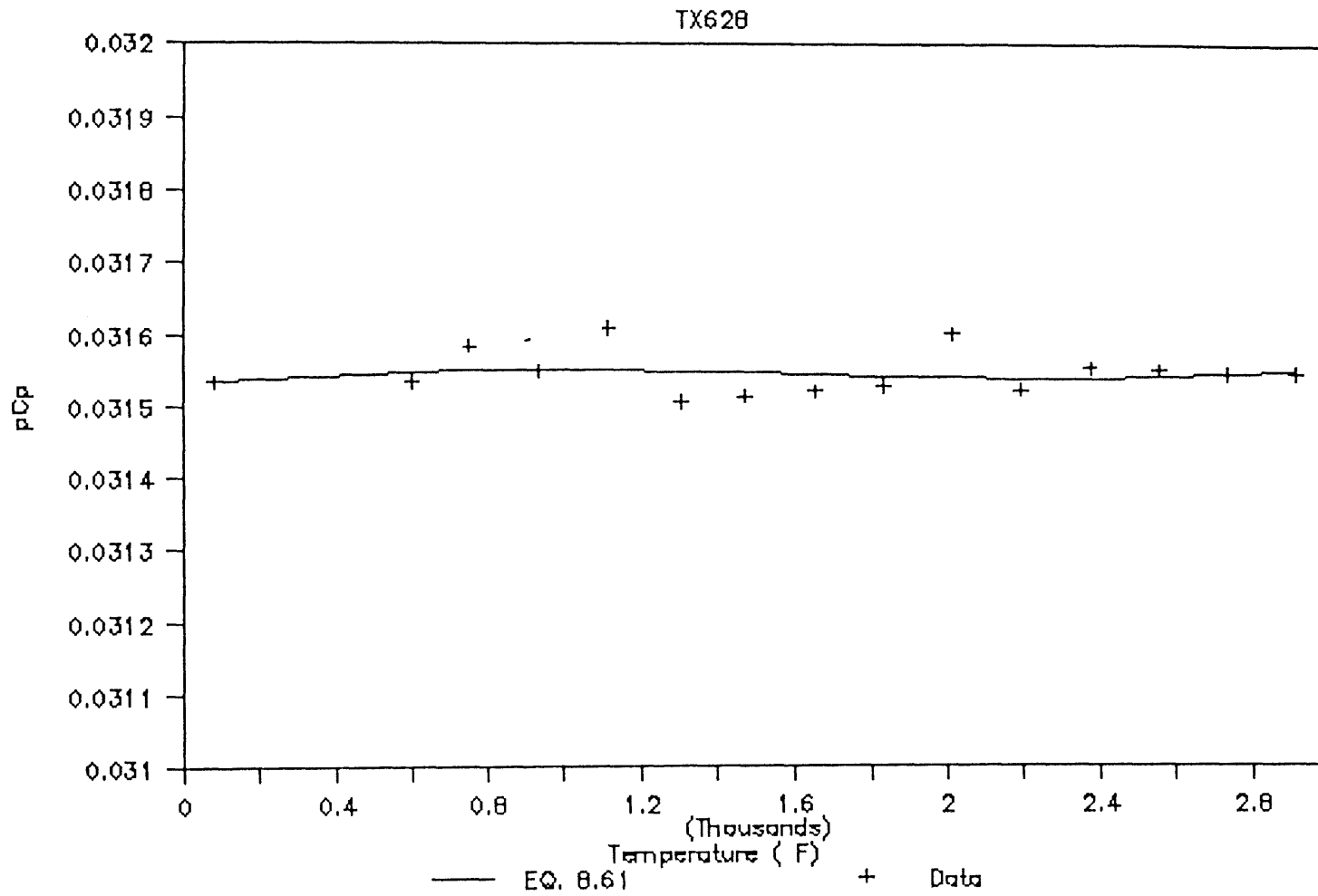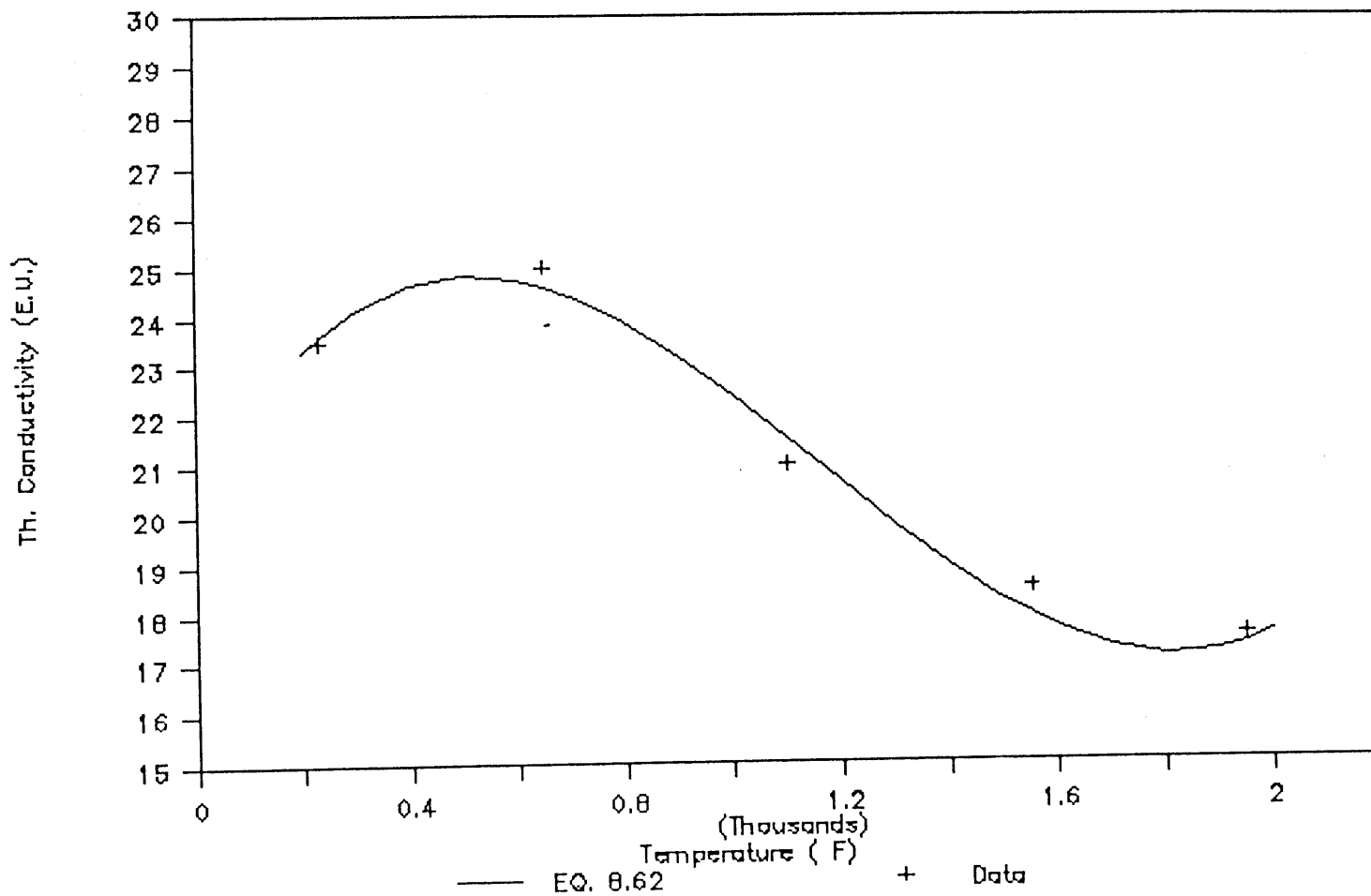Figure B.73   Regression of data for Eq. 8.61
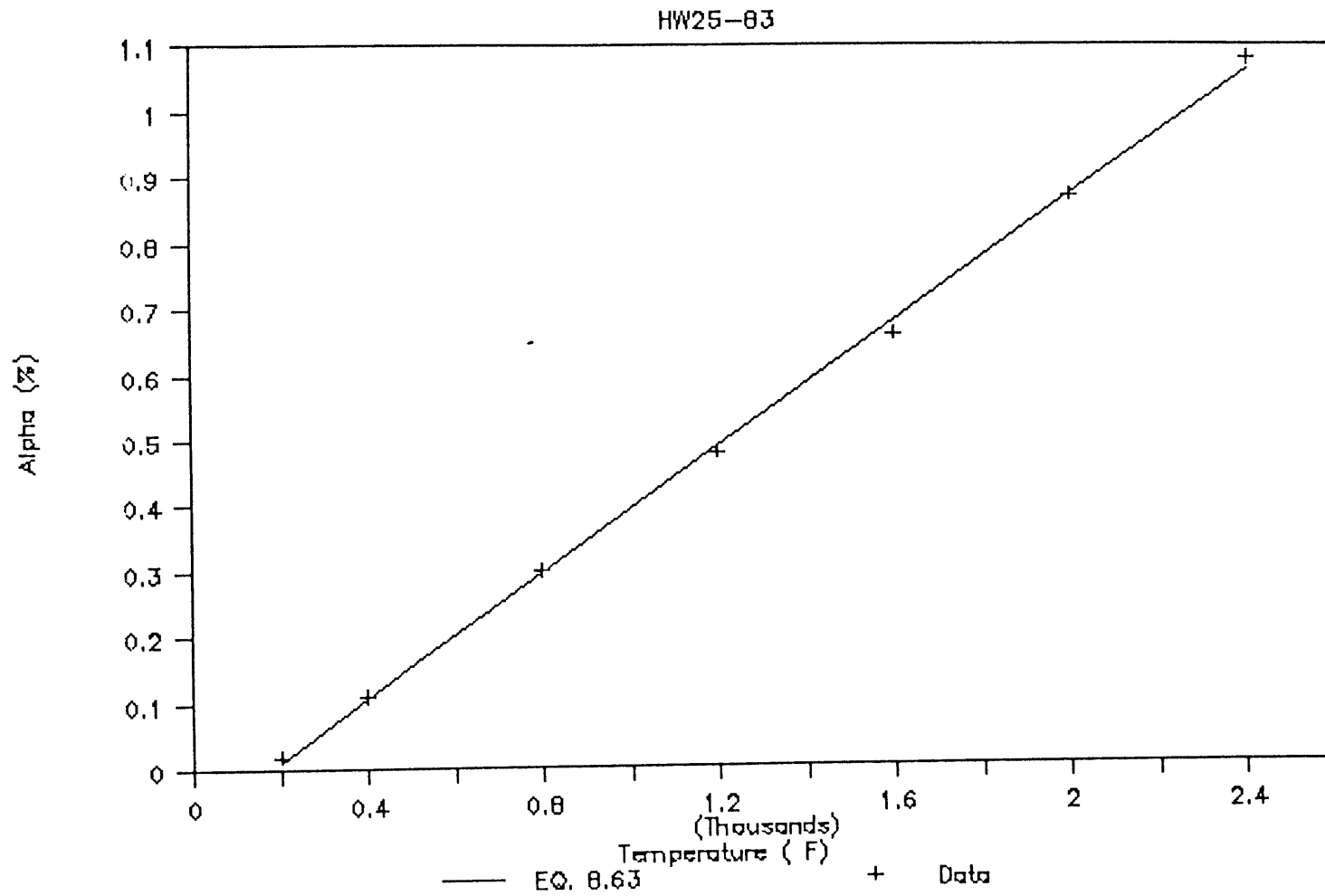
Figure B.74   Regression of data for Eq. 8.62

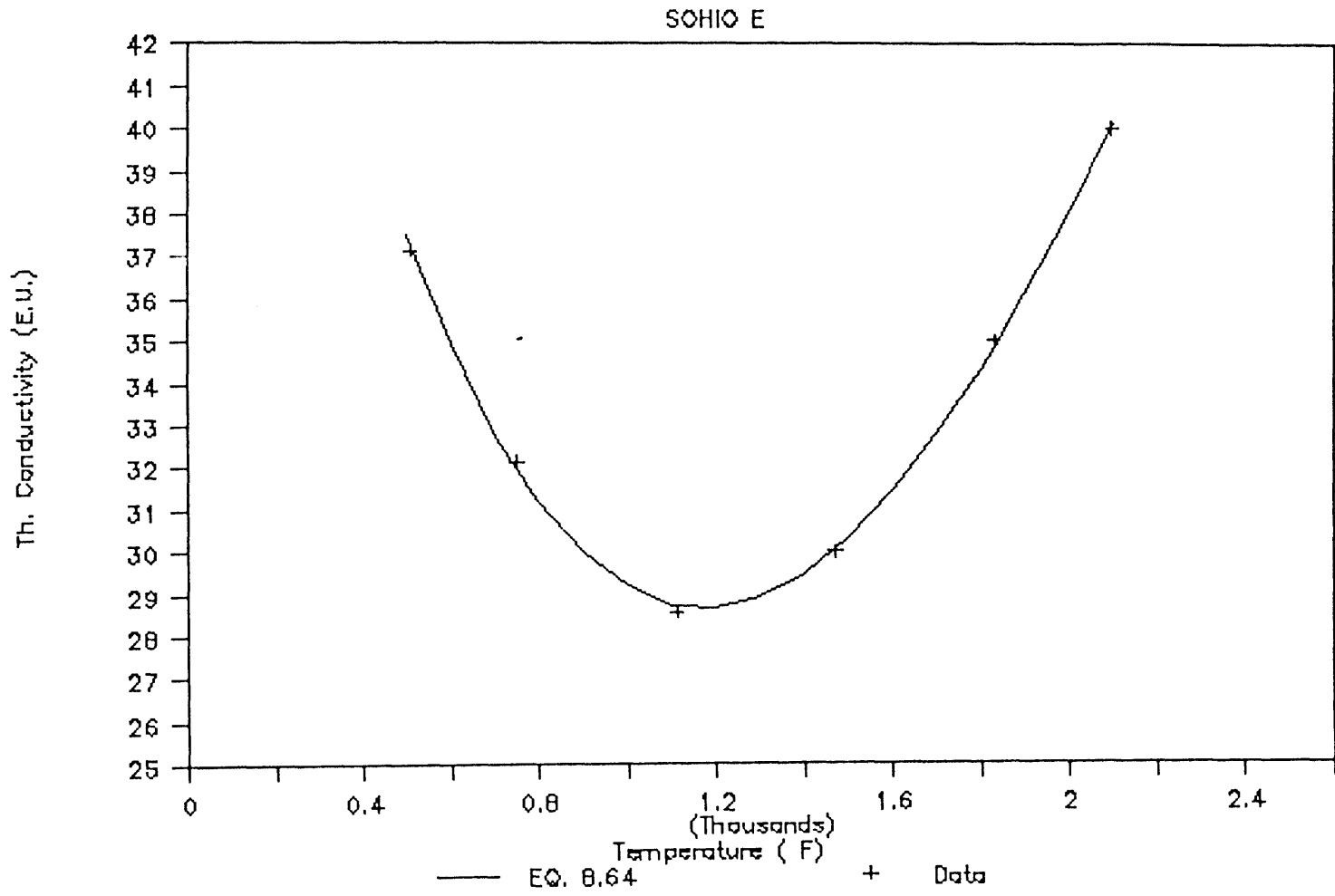Figure B.75   Regression of data for Eq. 8.63

SOHIO E

Figure B.76   Regression of data for Eq. 8.64
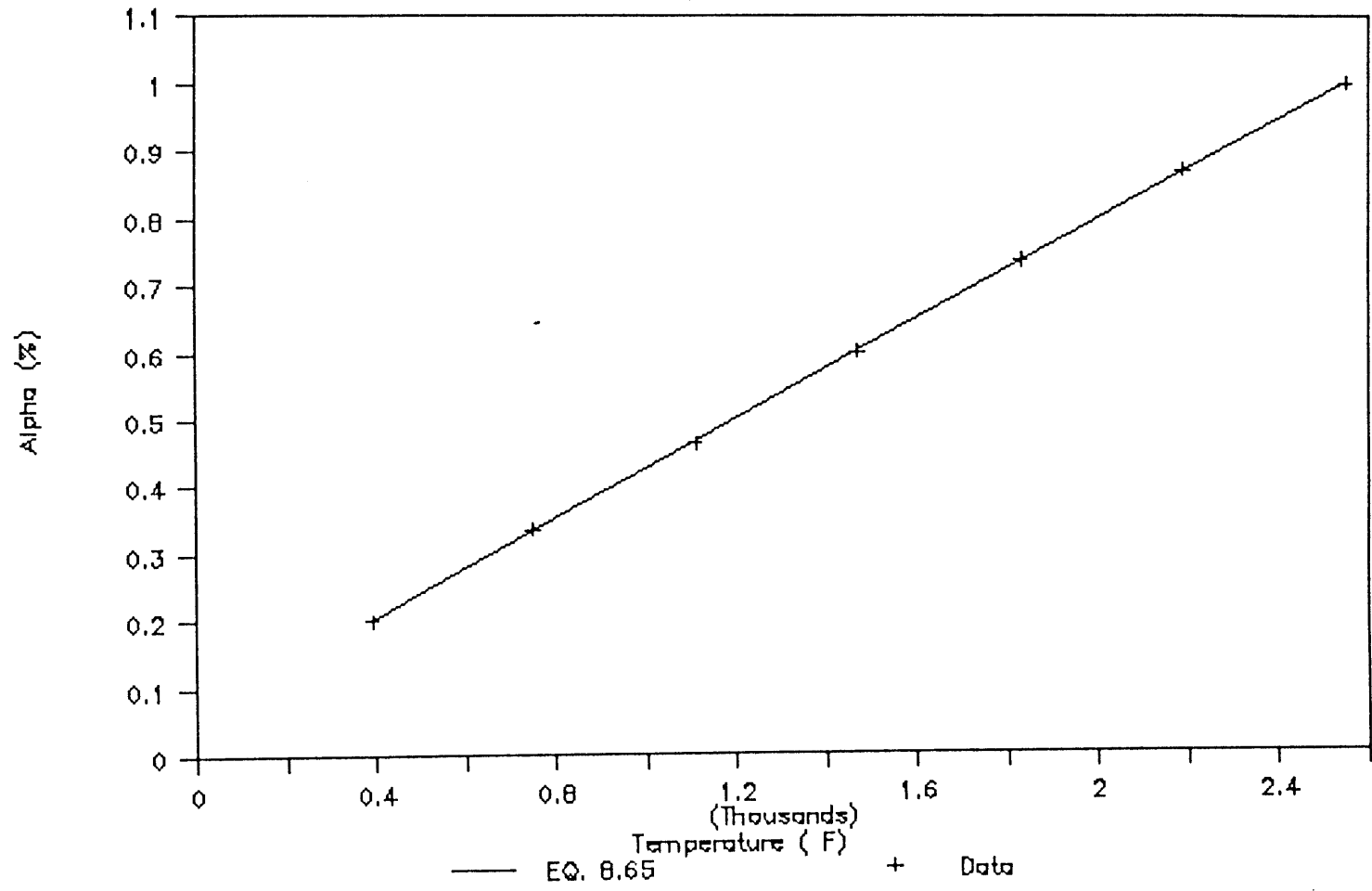
SOHIO E

Figure B.77   Regression of data for Eq. 8.65

Figure B.78   Regression of data for Eq. 8.66

SOHIO K3

Figure B.79   Regression of data for Eq. 8.67

JM-20

Figure B.80   Regression of data for Eq. 8.68

JM—23

Th. Conductivity (E.U.)

Temperature (F)
(Thousands)

——— EQ. 8.69   +   Data

Figure B.81   Regression of data for Eq. 8.69

JM—30

Figure B.82   Regression of data for Eq. 8.70

JM—32
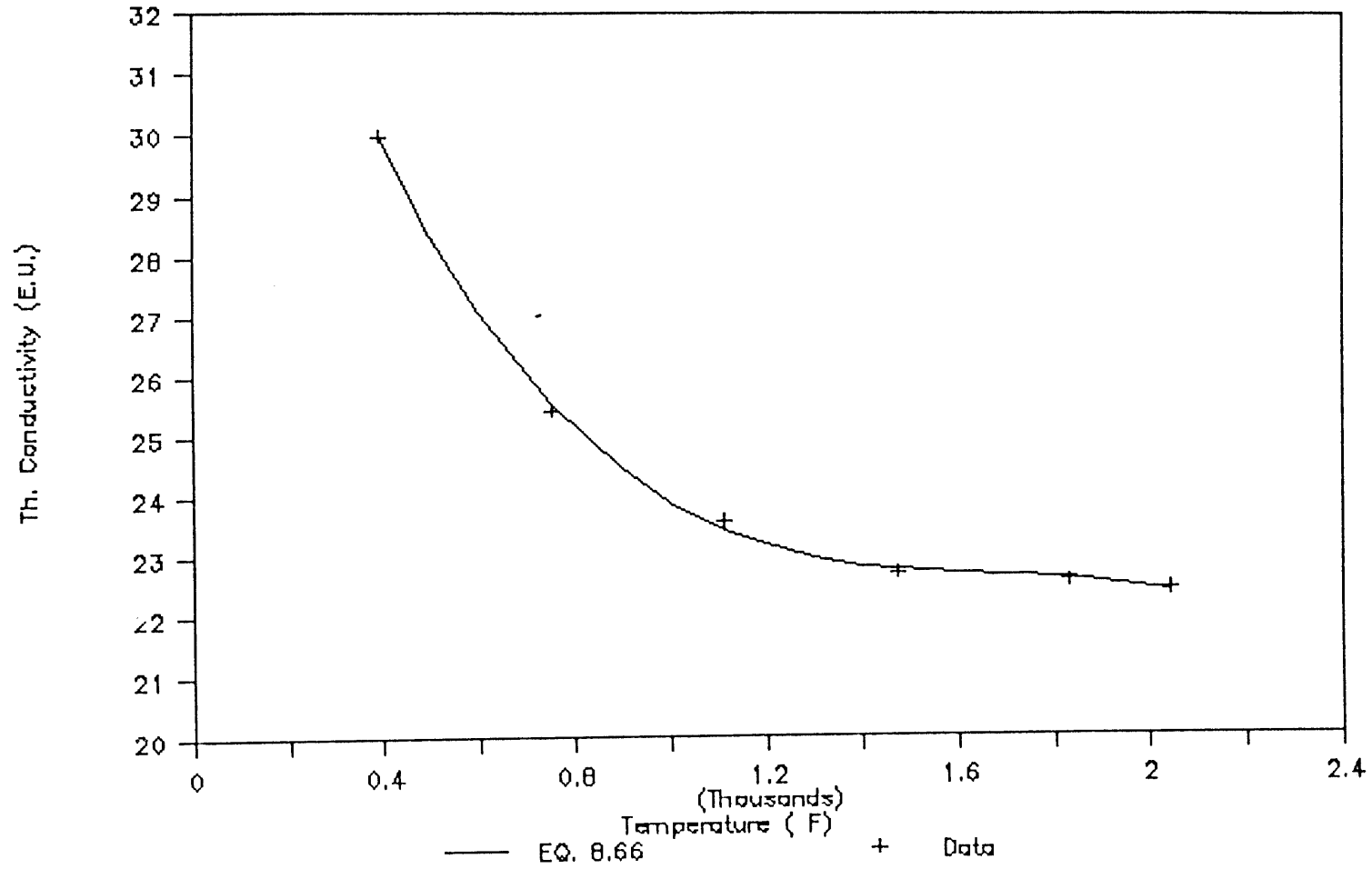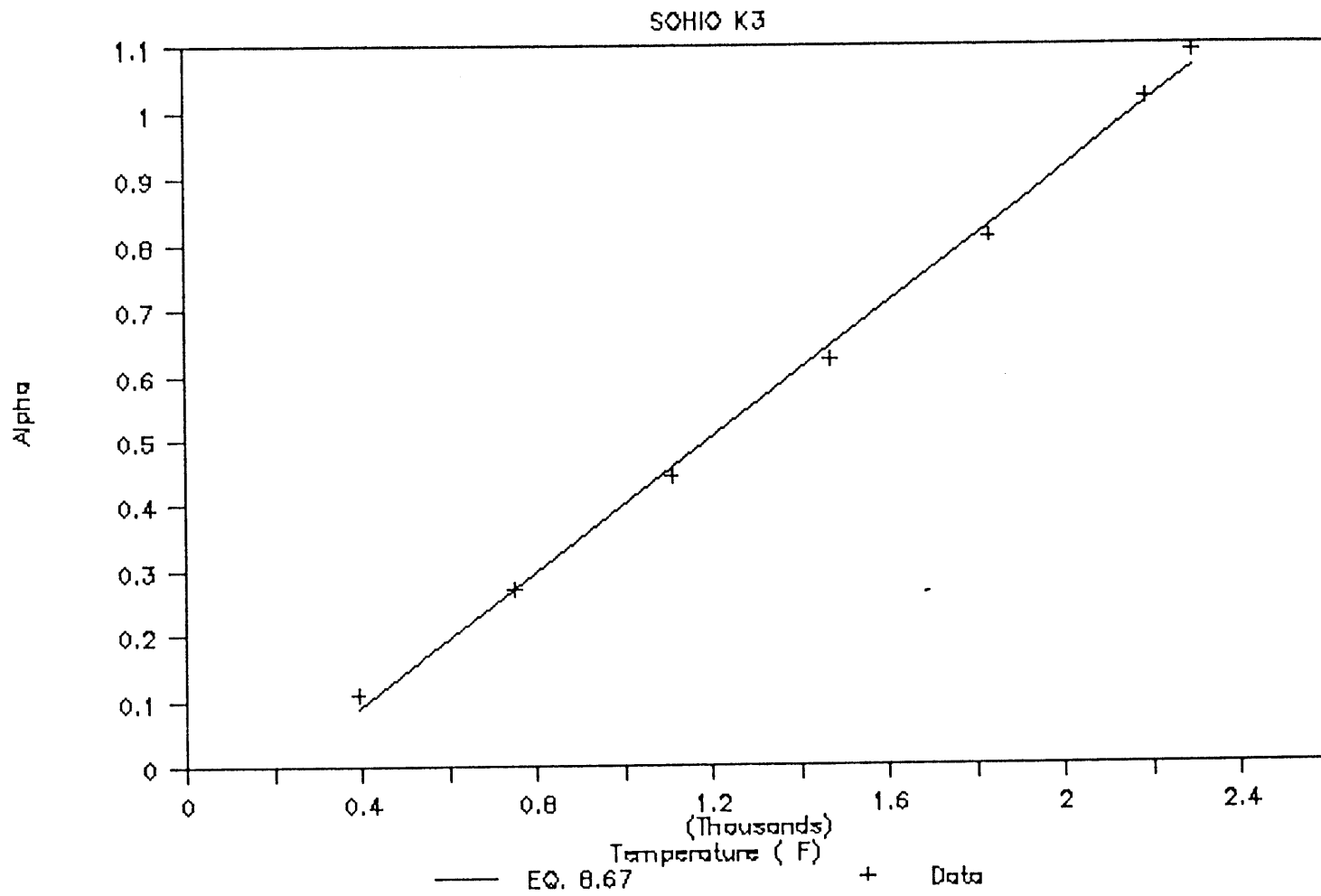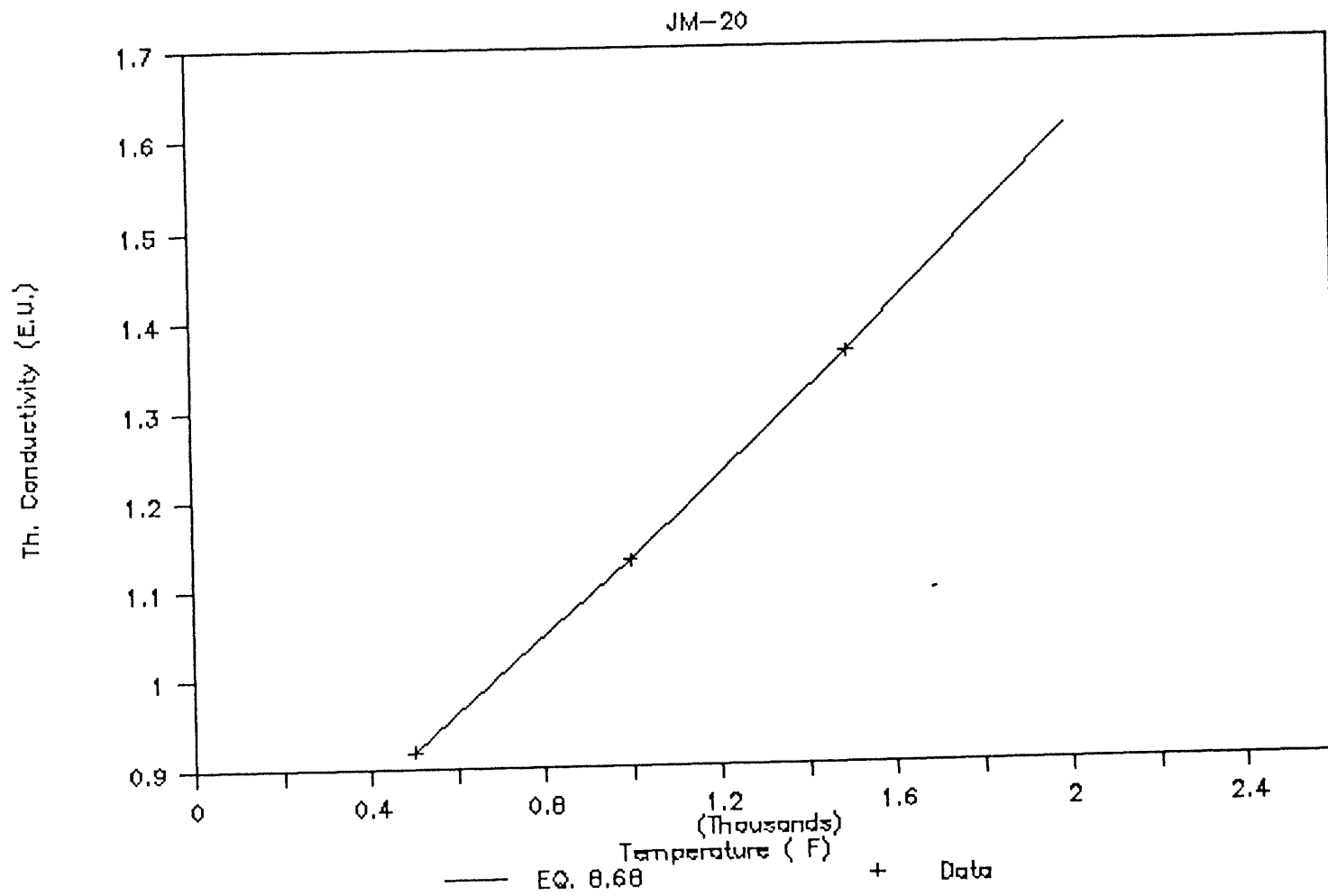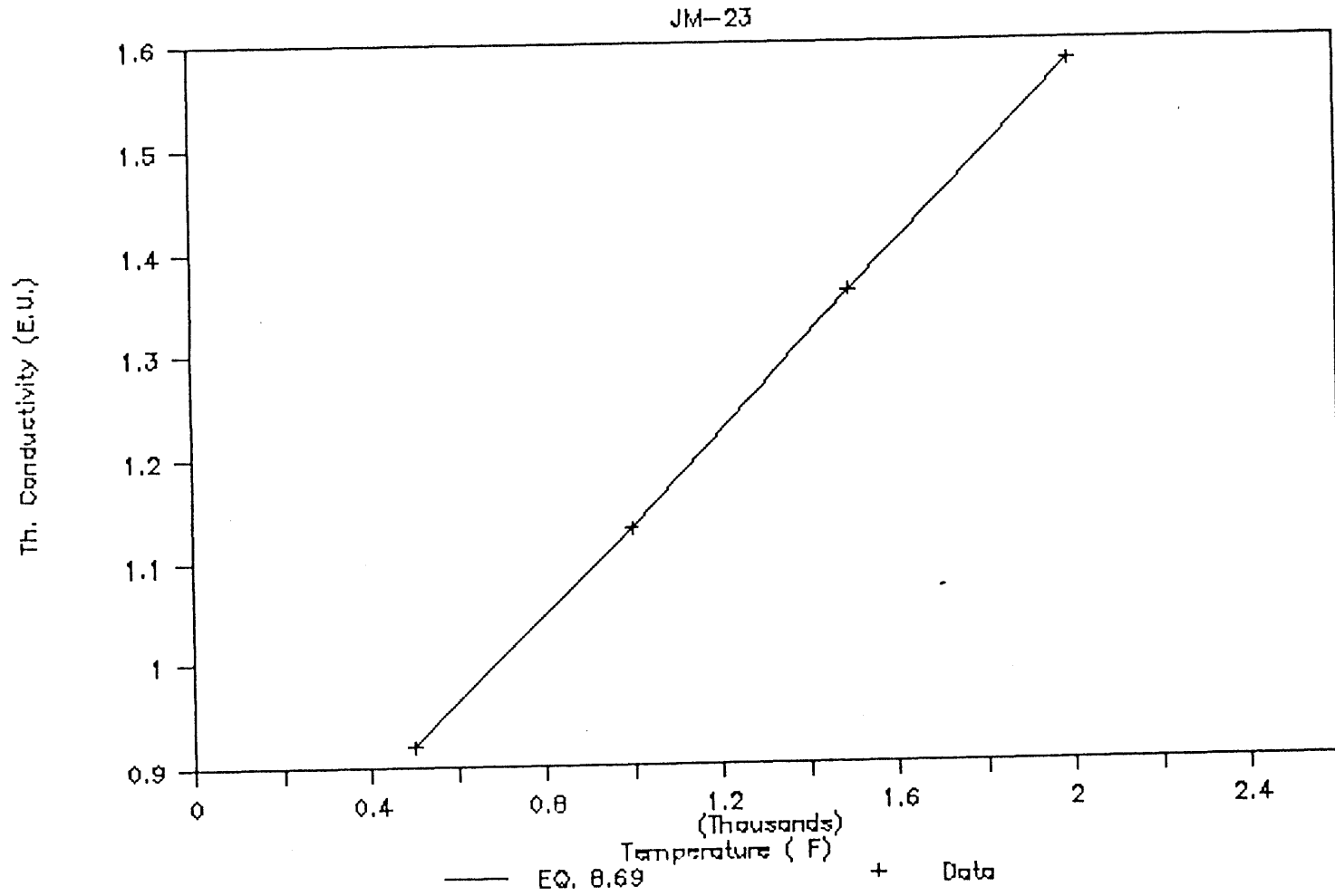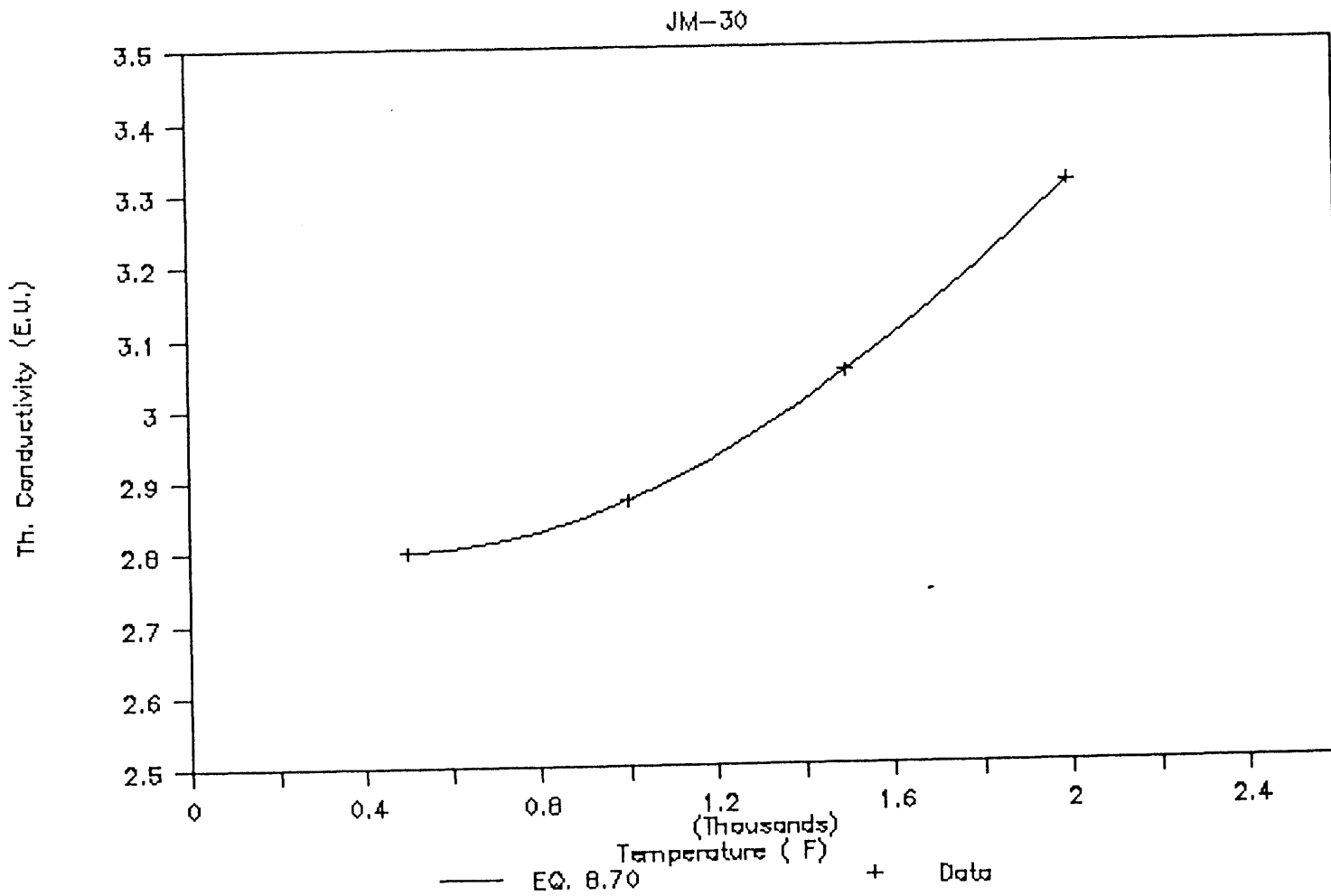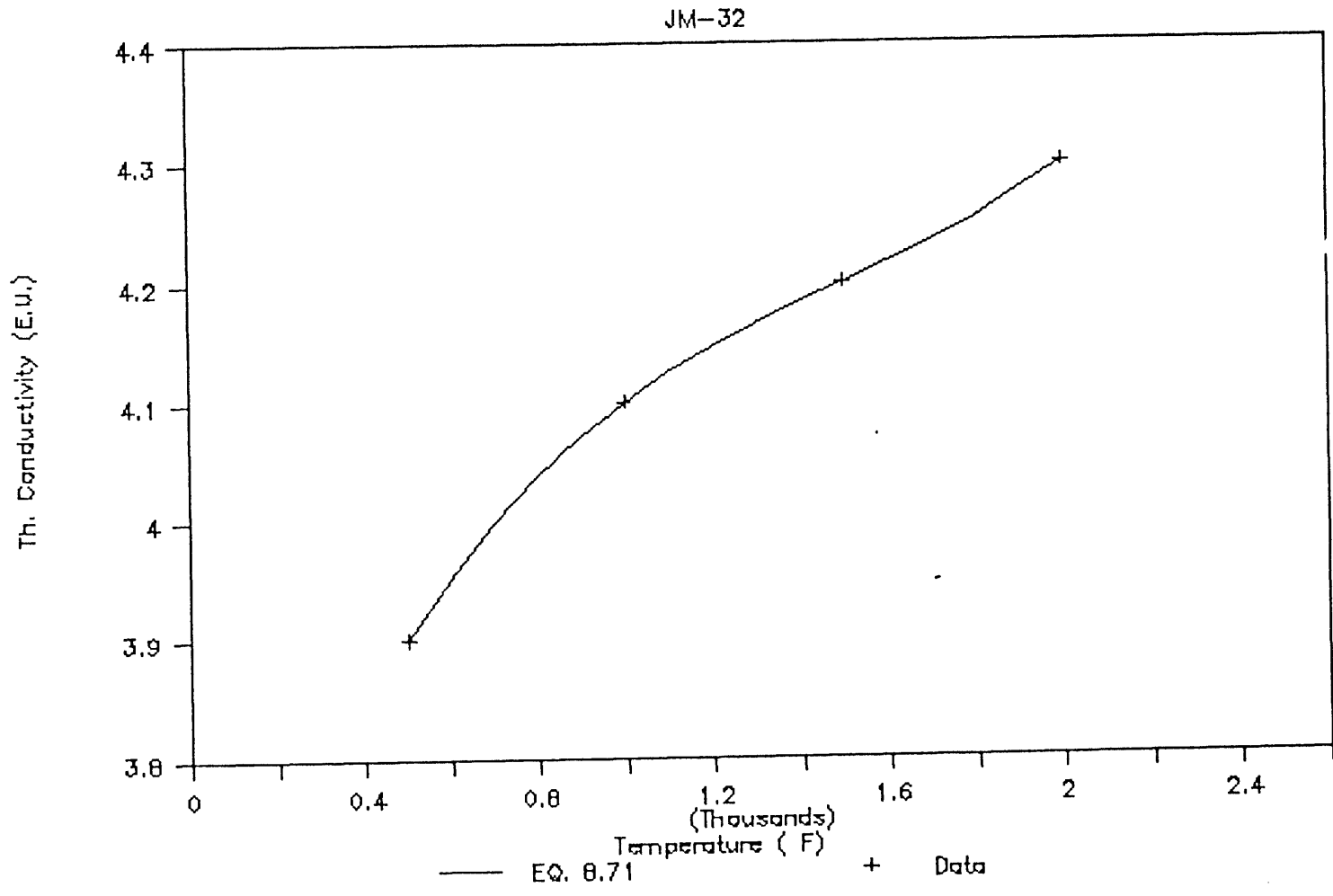

Figure B.83   Regression of data for Eq. 8.71
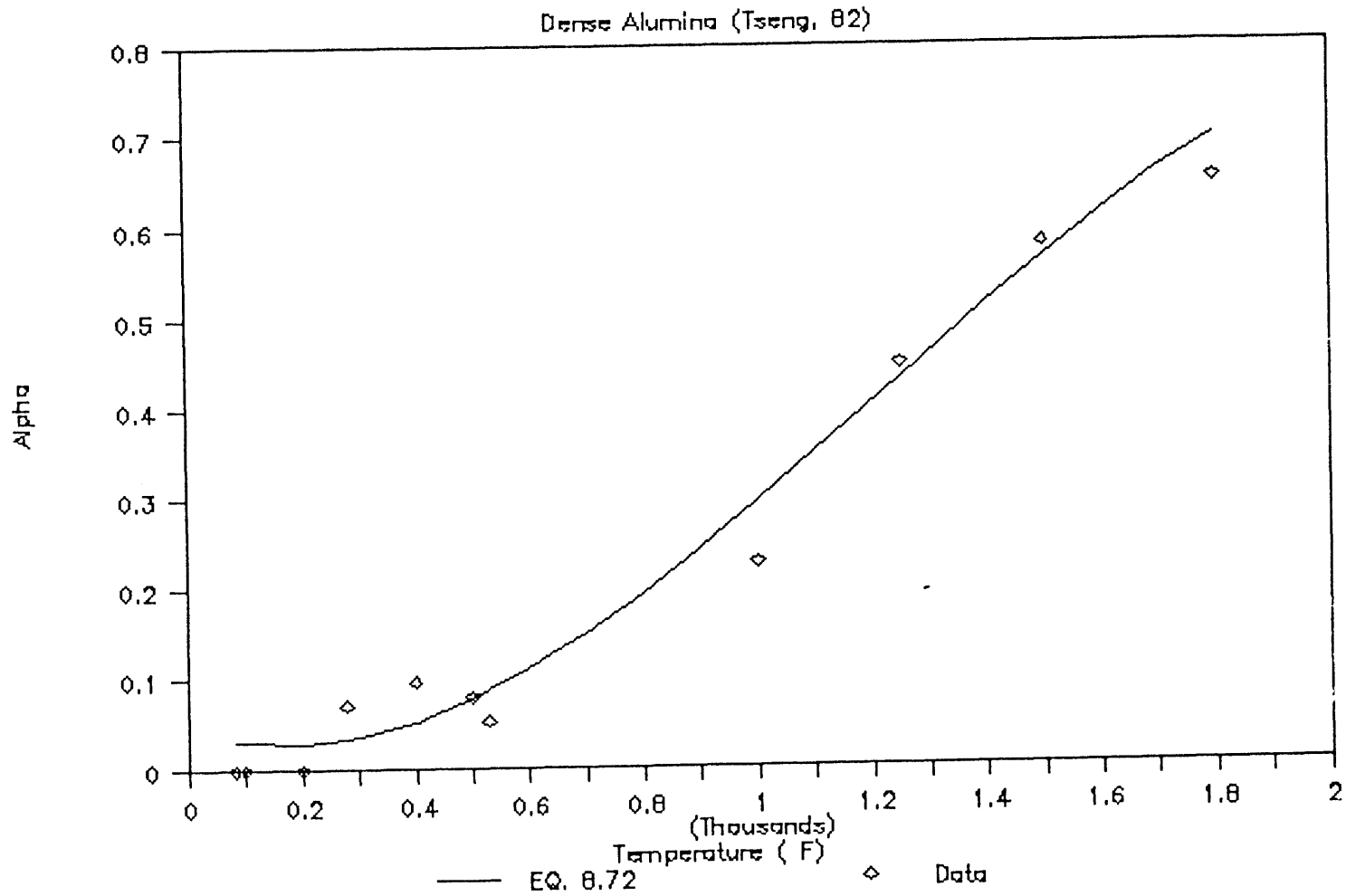
Figure B.84   Regression of data for Eq. 8.72
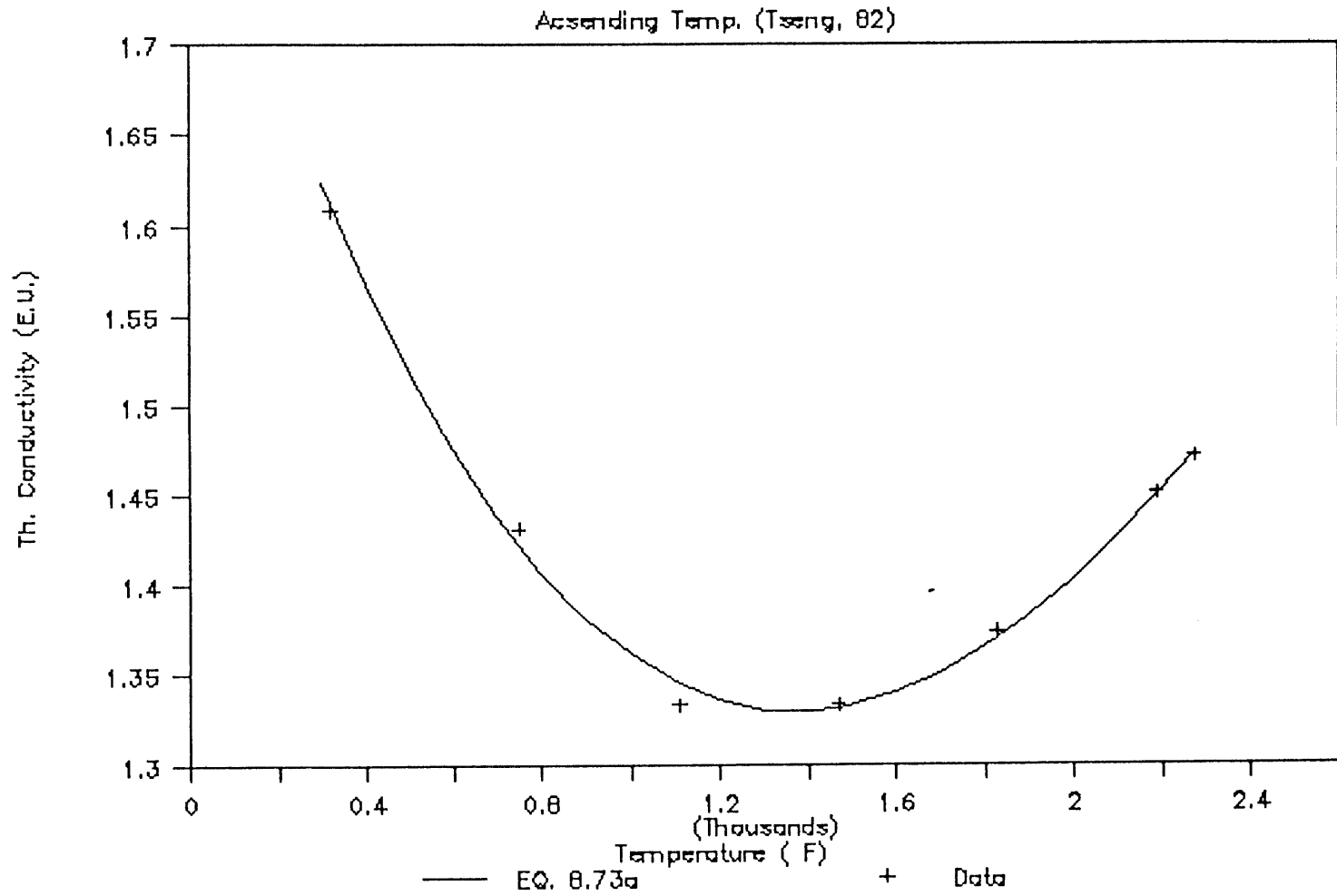
Figure B.85   Regression of data for Eq. 8.73a
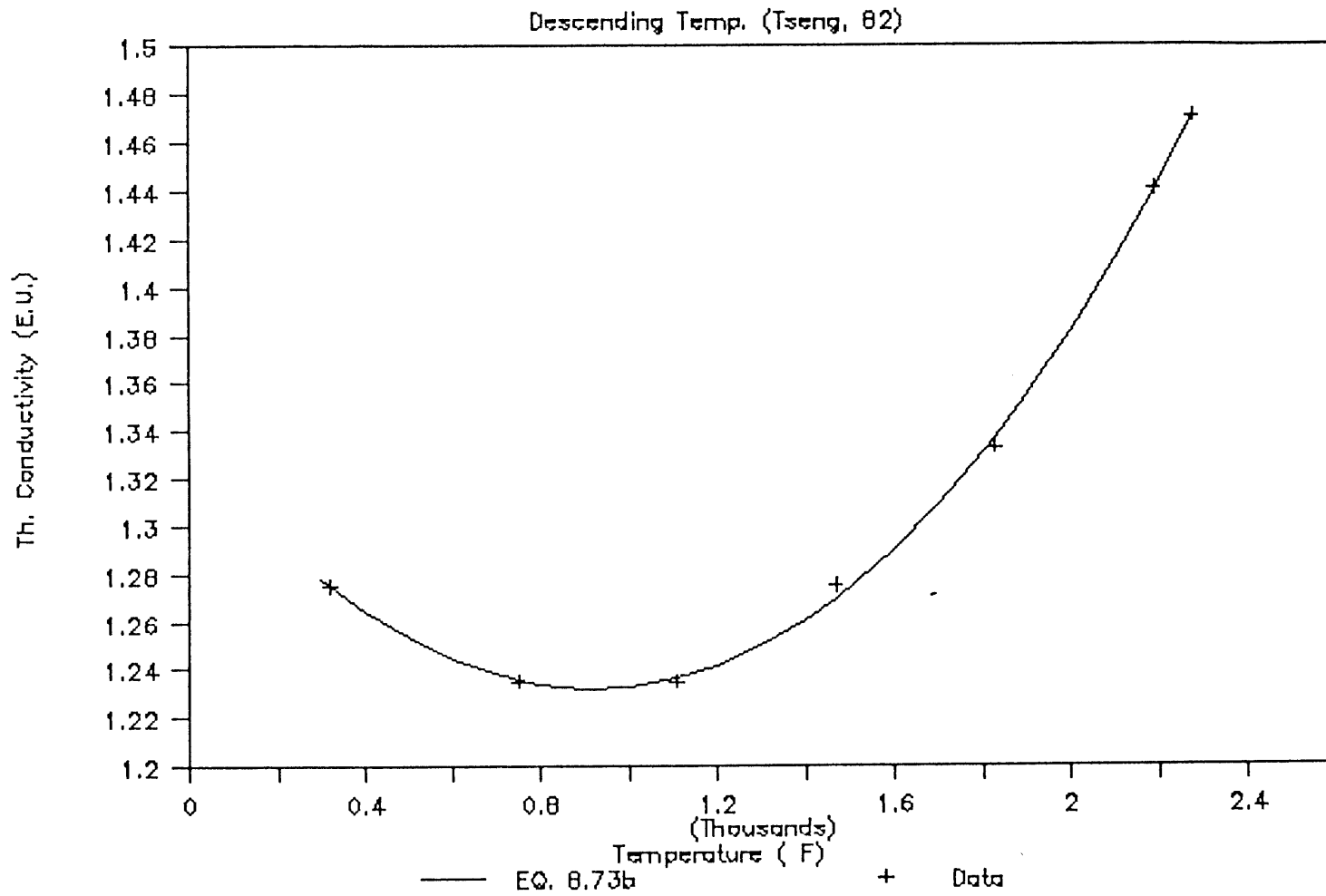
Figure B.86   Regression of data for Eq. 8.73b
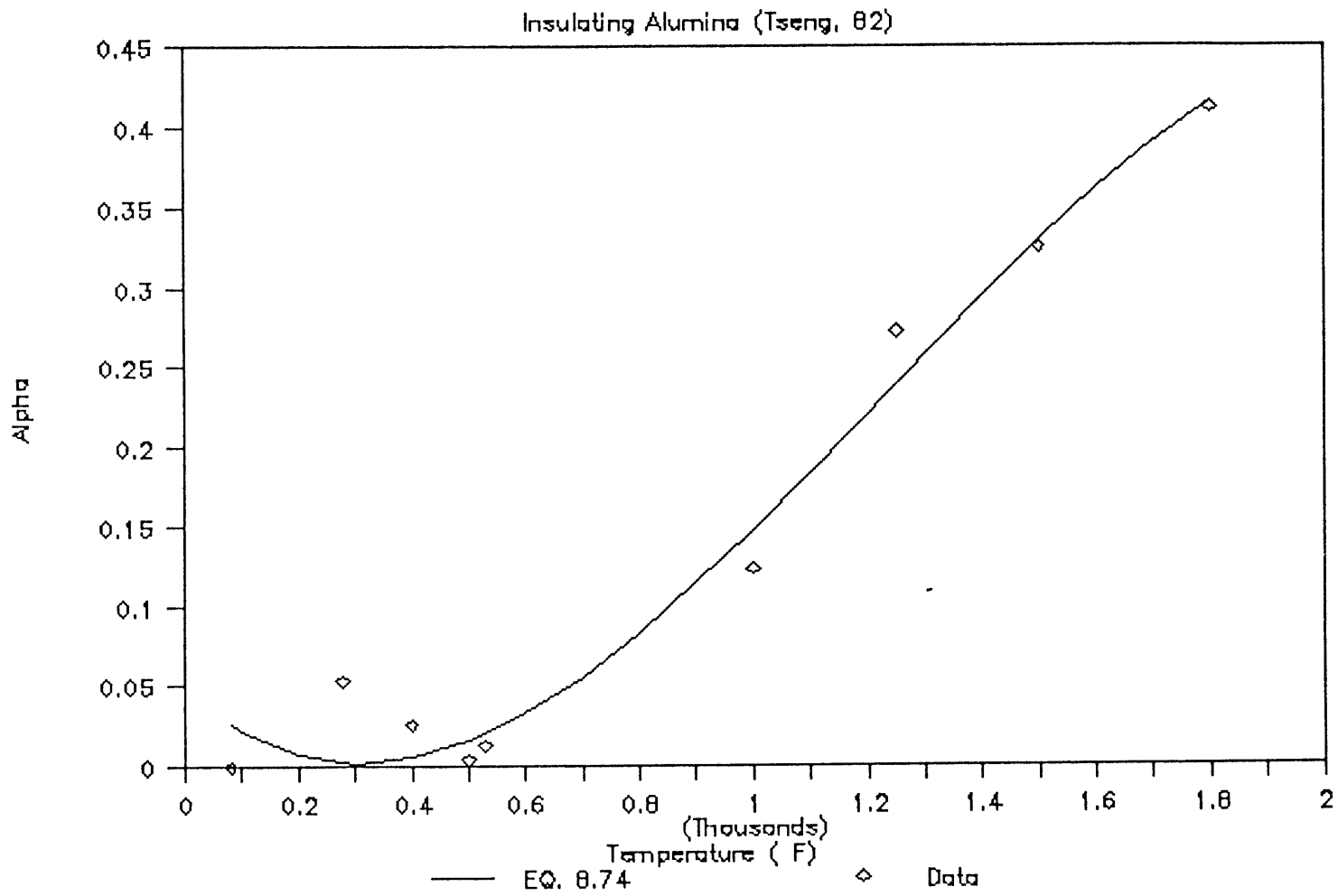
Figure B.87   Regression of data for Eq. 8.74

APPENDIX C
CAVITY CHARACTERIZATION OF CPS MATERIALS
UNDER VARIOUS TESTING CONDITIONS

A quantitative summary of the cavity characterization of cold–pressed sintered (CPS) refractories under different testing conditions is given in this Appendix. The cavity characteristics, determined using a Nomarski optical microscope, of as–manufactured CPS–90A–10C in the non–tested condition and tested at 1500°F and 2400°F are given in Tables C.1 to C.5. The distributions of the number of cavities per mm^2 and the cavity % area are studied with respect to width to length ratios, orientation and type of these cavities. The open porosities of as–manufactured and slag–impregnated CPS–90A–10C and CPS–82C–18M, studied using a mercury porosimeter, are summarized in Tables C.6 and C.7.

Cavity Cumulative Distribution wrt W/L

Cumulative Distribution of Number of Cavities /mm2

W/L smaller than	Not Tested Nb./mm2	Test 1500F Nb./mm2	Test 2400F Nb./mm2
1	5.62	8.86	13.92
0.75	4.92	7.22	12.59
0.625	4.22	6.56	11.51
0.5	3.17	5.91	10.71
0.25	1.76	3.28	9.1
0.125	1.05	1.64	7.23
0.1	0.70	0.66	6.1ᶠ
0	0	0	0
GC (=1)		47.58	189.06
1 with GC		56.44	202.98
1 without GC		8.86	13.92

Cumulative Distribution of Cavity Area (%)

W/L smaller than	Not Tested A%	Test 1500F A%	Test 2400F A%
1	13.20	19.82	33.75
0.75	13.14	16.67	6.92
0.625	9.46	16.47	6.18
0.5	6.34	11.81	4.64
0.25	4.83	9.55	3.78
0.125	0.71	3.23	0.95
0.1	0.44	1.33	0.83
0	0	0	0
GC (=1)		0.08	0.18
1 with GC		19.9	33.93
1 without GC		19.82	33.75

Legend: GC == Intra-Granular Cavities with Both Dimensions Smaller Than 6 microns

Table C.1   Cumulative distributions of number of cavities per mm^2 and of cavity % area with respect to cavity width to length ratio for CPS–90A–10C under different loading conditions

Cavity Distribution wrt Orientation

Distribution of Number of Cavities /mm2

Orientation Theta (deg)	Not Tested Nb./mm2	Test 1500F Nb./mm2	Test 2400F Nb./mm2
0-15	0.62	1.64	4.28
15-30	1.13	0.98	2.41
30-45	1.02	1.31	2.14
45-60	1.08	1.97	1.87
60-75	0.35	0.68	1.61
75-90	0.70	0.64	0.27
Unclass	0.72	1.64	1.34
Total	5.62	8.86	13.92

Distribution of Cavity Area (%)

Orientation Theta (deg)	Not Tested A%	Test 1500F A%	Test 2400F A%
0-15	0.29	1.69	3.71
15-30	2.00	5.11	1.62
30-45	8.01	1.71	0.22
45-60	1.79	7.22	0.85
60-75	0.87	0.43	0.34
75-90	0.18	0.45	0.17
Unclass	0.07	3.21	26.83
Total	13.21	19.82	33.74

Table C.2   Distributions of number of cavities per mm^2 and of cavity % area ith respect to cavity orientation (relative to applied compression force) for CPS–90A–10C under different loading conditions

Cavity Cumulative Distribution wrt Orientation

Cumulative Distribution of Number of Cavities /mm2

Orientation (deg) Smaller than	Not Tested Nb./mm2	Test 1500F Nb./mm2	Test 2400F Nb./mm2
0	0.72	1.64	1.34
15	1.34	3.28	5.62
30	2.47	4.26	8.03
45	3.49	5.57	10.17
60	4.57	7.54	12.04
75	4.92	8.22	13.65
90	5.62	8.86	13.92

Cumulative Distribution of Cavity Area (%)

Orientation (deg) Smaller than	Not Tested A%	Test 1500F A%	Test 2400F A%
0	0.07	3.21	26.83
15	0.36	4.90	30.54
30	2.36	10.01	32.16
45	10.37	11.72	32.38
60	12.16	18.94	33.23
75	13.03	19.37	33.57
90	13.21	19.82	33.74

Table C.3   Cumulative distributions of number of cavities per mm^2 and of cavity % area with respect to cavity orientation (relative to applied compression force) for CPS—90A—10C under different loading conditions

Cavity Distribution wrt Type

Distribution of Number of Cavities /mm2

Type	Not Tested Nb./mm2	Test 1500F Nb./mm2	Test 2400F Nb./mm2
A	0.53	1.97	8.03
B	1.68	3.29	2.94
M	0.79	2.96	1.61
P,U	2.63	0.66	1.34
GC		47.58	189.06
Total, No GC	5.63	8.88	13.92

Distribution of Cavity Area (%)

Type	Not Tested A%	Test 1500F A%	Test 2400F A%
A	0.05	1.9	1.86
B	5.46	11.31	4.88
M	3.77	6.29	0.32
P,U	3.93	0.32	26.7
GC		0.08	0.18
Total, No GC	13.21	19.82	33.76

Table C.4 Distributions of number of cavities per mm^2 and of cavity % area with respect to cavity type for CPS–90A–10C under different loading conditions

Test Condition	Average Width (microns)	Average Length (microns)	Total Cavity Area (%)
Not Tested	66.90	202.91	13.20
Test 1500F	40.64	165.40	19.82
Test 2400F	68.39	255.19	33.75

Table C.5   Average length, width and total cavity % area of the microscopic cavities in CPS–90A–10C under different loading conditions (excluding the intragranular cavities with both dimensions smaller than 6μm)

CPS-90A-10C Open Porosity (%)

Pore Radius Microns	No Test	Test 1500 F	Test 2400 F	Slag Impregn.
60	0	0	0	
6	1.37	0.46	0.91	
4	3.08	1.39	2.74	
3	4.49	2.31	4.26	
2	5.60	3.23	5.79	
1	7.28	5.08	7.15	
0.8	8.40	6.01	7.76	
0.6	12.61	9.70	10.36	
0.5	14.85	13.86	13.24	
0.4	15.97	15.25	14.77	
0.3	16.53	16.17	15.37	
80				0
40				0.72
20				1.44
14				2.02
10				2.16
6				2.31
4				2.45
1				2.74

Table C.6   Cumulative distribution of % open porosity with respect to decreasing pore radius (in μm) for CPS—90A—10C under different conditions

CPS-82C-18M Open Porosity (%)

Pore Radius Microns	No Test	Test 1500 F	Test 2400 F	Slag Impregn.
60	0.3	0	0	
6	1.51	1.13	0.80	
4	3.02	3.02	2.53	
3	5.14	4.41	4.41	
2	7.55	5.98	6.56	
1	10.88	8.56	10.24	
0.8	12.08	9.56	11.16	
0.6	13.60	11.02	12.08	
0.4	15.11	13.09	12.89	
0.3	15.20	14.09	13.23	
80				0
40				1.16
20				1.45
14				1.6
10				2.03
6				3.49
4				4.22
1				4.36

Table C.7   Cumulative distribution of % open porosity with respect to decreasing pore radius (in μm) for CPS–82C–18M under different conditions

Condition	Material Density for CPS-90A-10C (g/cc)
Not Tested	3.25204
Tested at 1000°F n = 2	μ = 3.23522 S.D. = 0.045
Tested at 1500°F n = 2	μ = 3.22490 S.D. = 0.011
Tested at 2000°F n = 2	μ = 3.21253 S.D. = 0.043
Tested at 2400°F	3.18383

Table C.8

APPENDIX D
ADDITIONAL INFORMATION ON THE RETORT SYSTEM

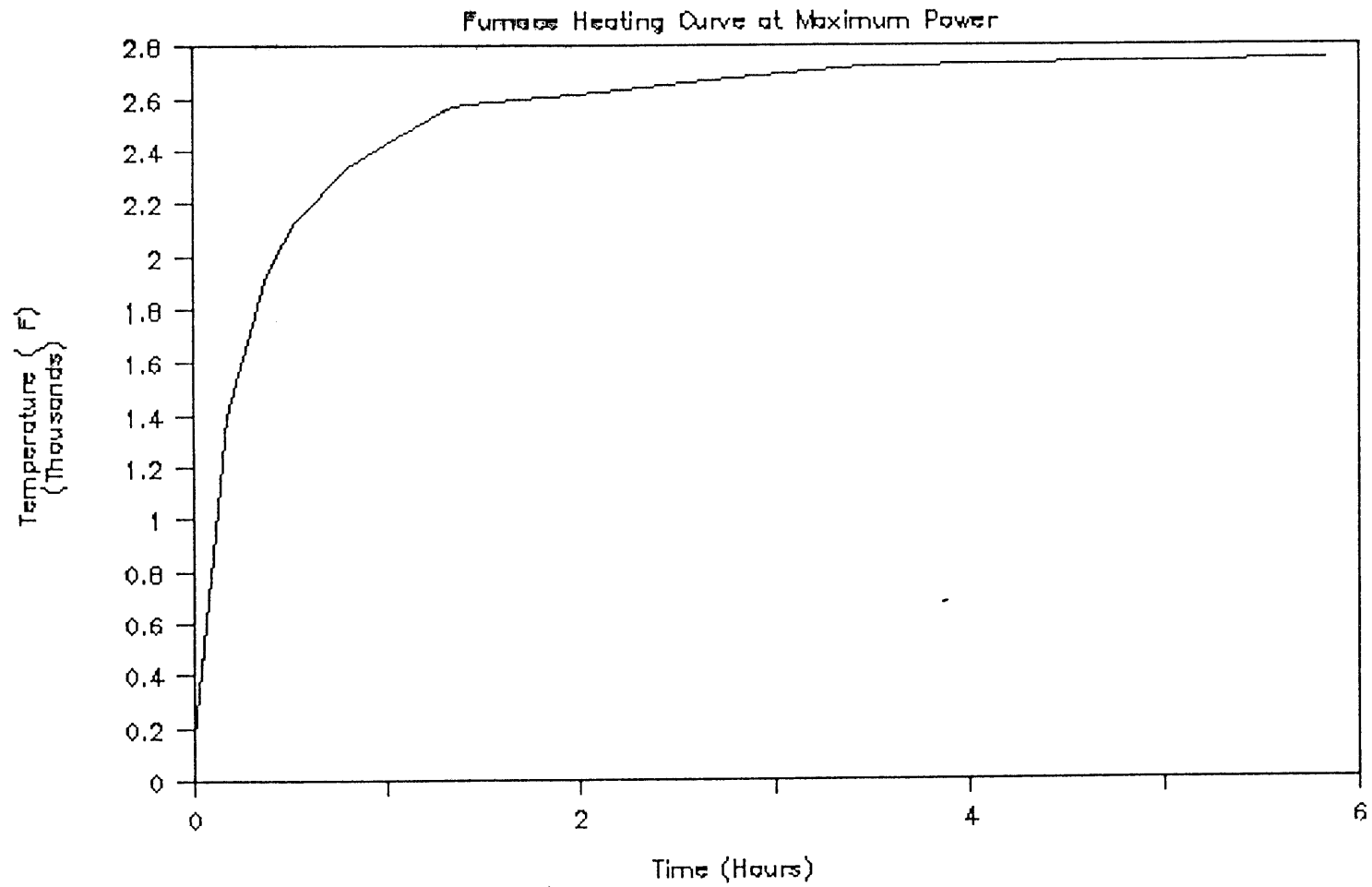Additional information on the developed testing system has been included in this Appendix.

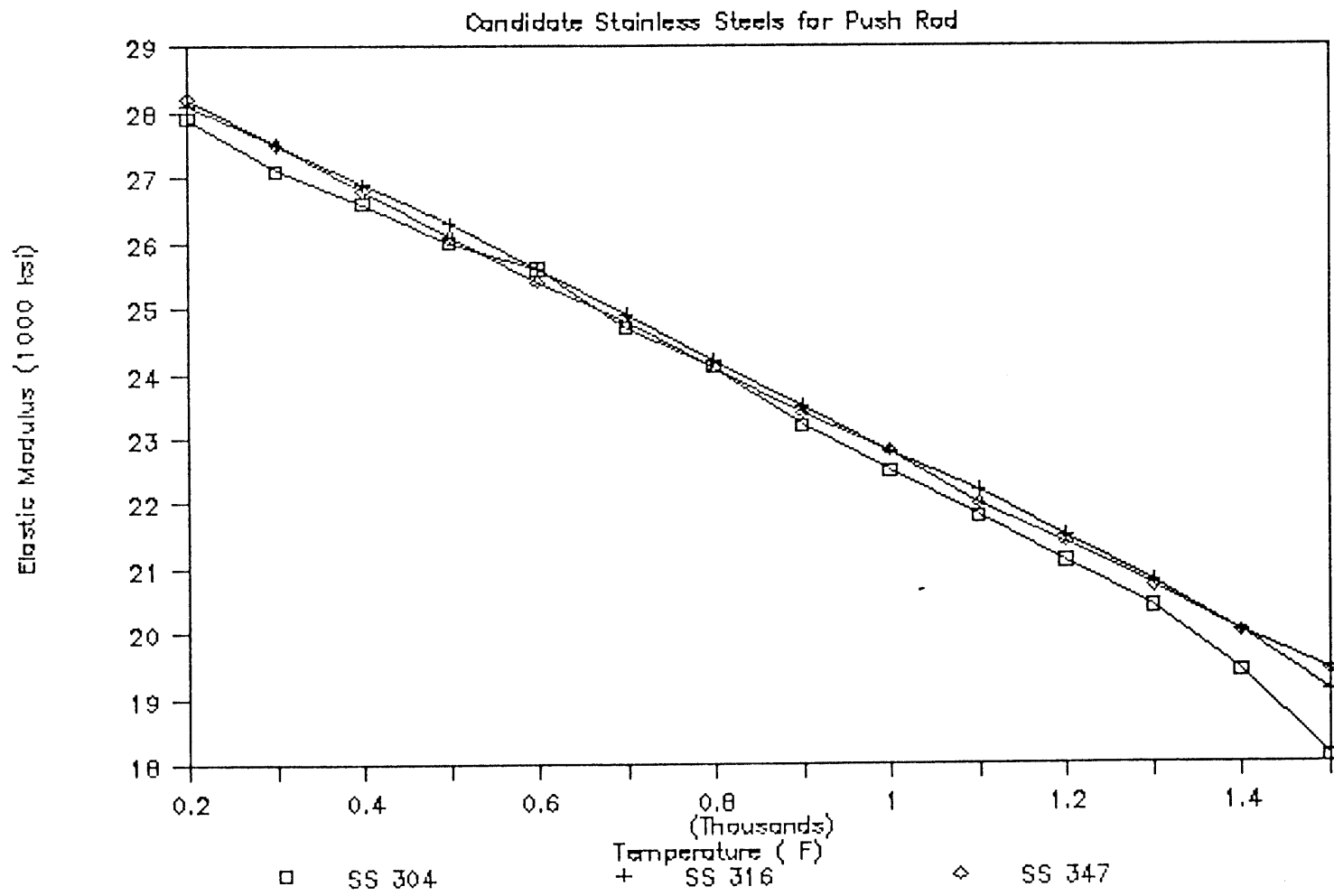Figure D.1   Furnace heating curve at maximum power

Candidate Stainless Steels for Push Rod

Elastic Modulus (1000 ksi)

Temperature (F)
(Thousands)

□　SS 304　　　+　SS 316　　　◇　SS 347

Figure D.2　　　　Variation of the elastic modulus with temperature for candidate stainless steels for push rod

Candidate Stainless Steels for Push Rod

Yield Strength (Ksi)

Temperature (F)
(Thousands)

□   SS 316   +   SS 347   ◇   SS 304
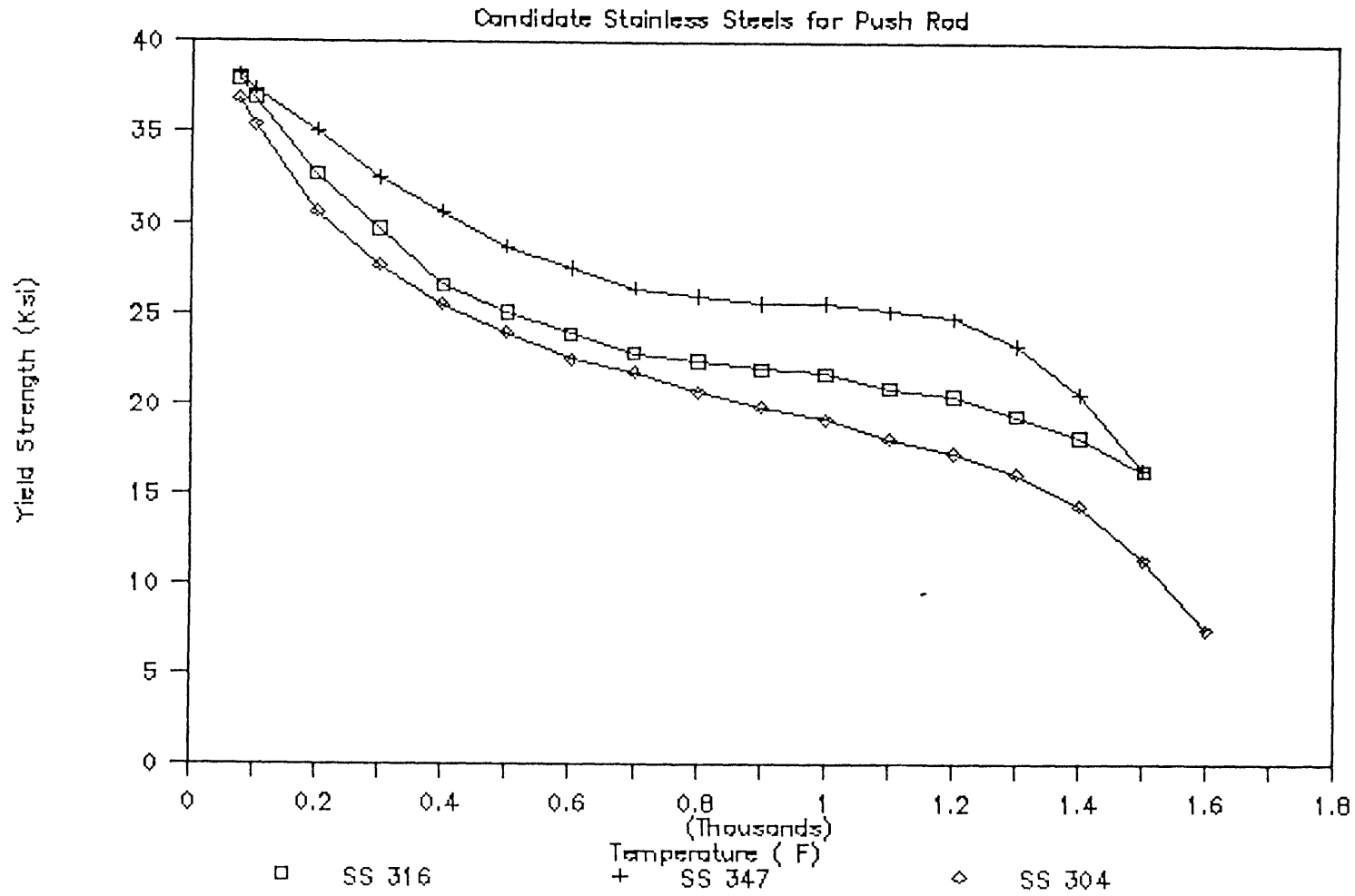
Figure D.3   Variation of the yield strength with temperature for
                      candidate stainless steels for push rod

	CLAMP #1	CLAMP #2	CLAMP #3 SHOWN	CLAMP #4
A	4⅛" DIA	3¾" DIA	5⅜" DIA	6" DIA
B	⅜" x 3"	⅜" x 3"	⅜" x 3"	⅜" x 3"
C	¾"	⅝"	1"	1⅜"
D	3¹/₁₆"	2⅞"	3¹¹/₁₆"	4"
E	2"	2"	2¾"	3"
F	6⅛"	5¾"	7⅜"	8"
G	4⅛"	3¾"	5⅛"	6"
H	1"	1"	1"	1½"

RETORT CLAMP

HALF SCALE

COLD-ROLLED STEEL

BREAK ALL SHARP EDGES
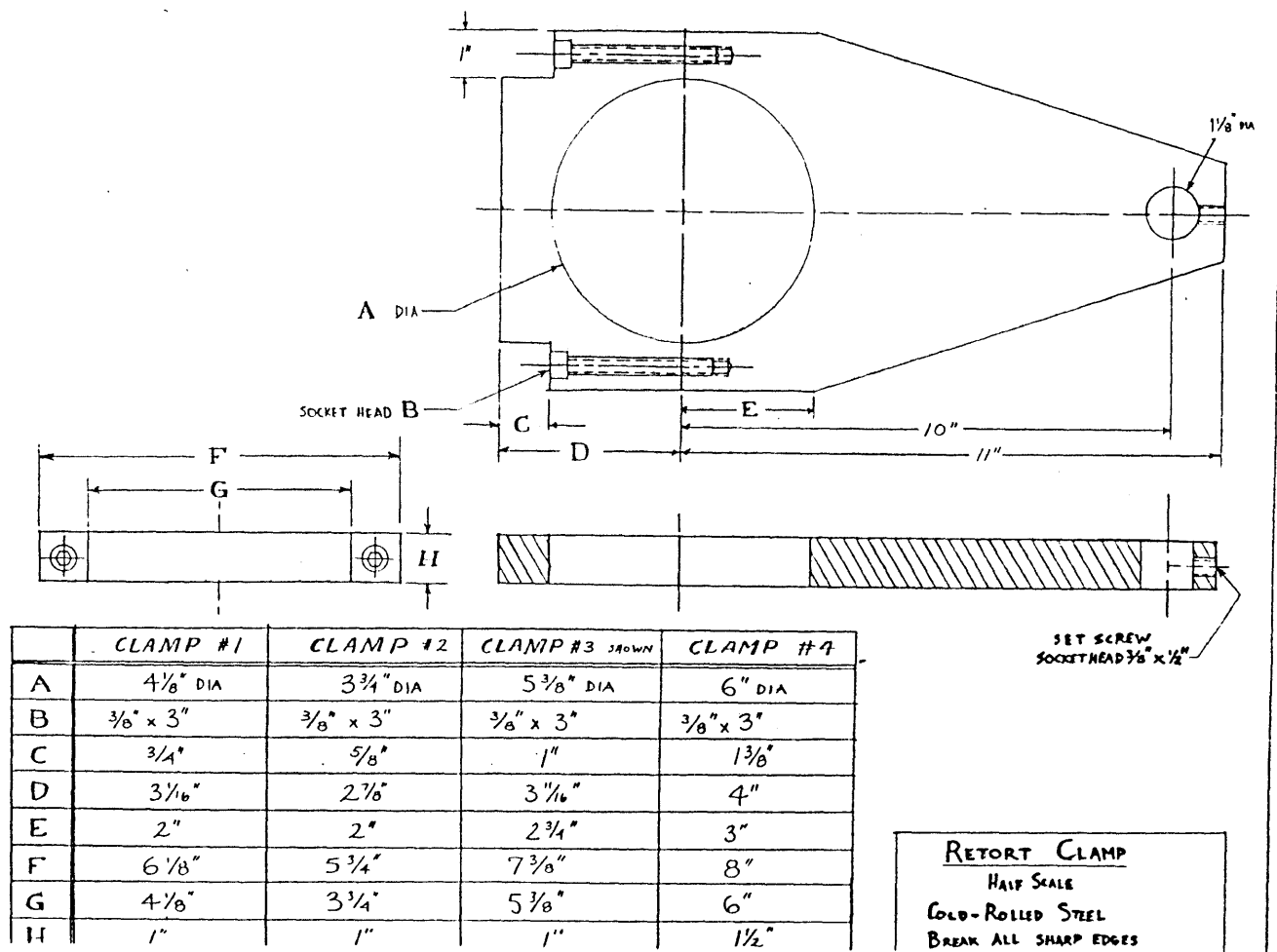
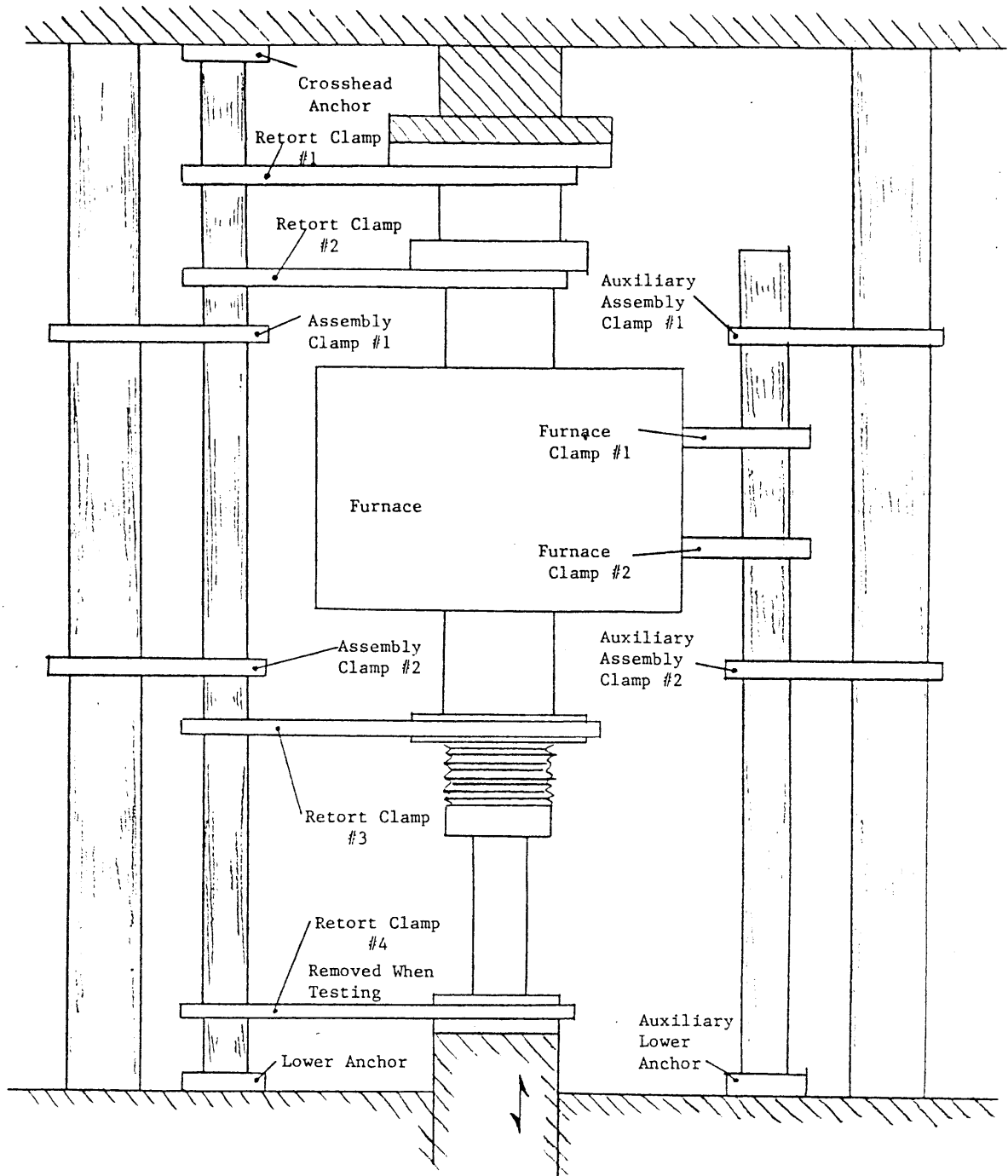Figure D.4   Dimensioning of the retort clamps

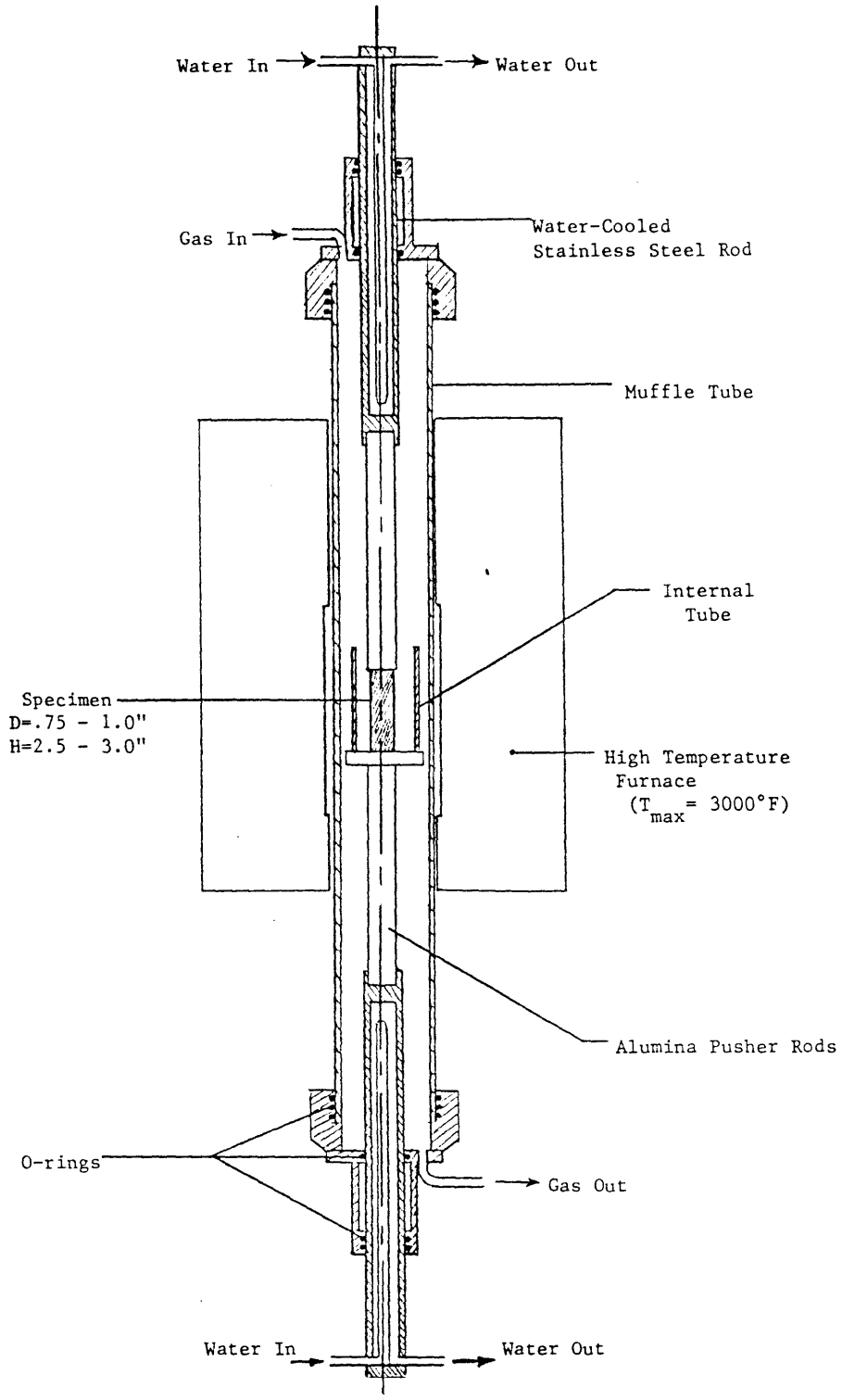**Figure D.5**   Auxiliary clamping system — side view

Figure D.6   Original conception of the retort system

APPENDIX E
SELECTED RESULTS FROM THE VARIABILITY STUDY

The production lines of various refractory materials were studied over a period of one year by taking batches of refractory blocks at random, and extracting specimens from these blocks for room temperature characterization under compressive loads. The original intent of the project was not to carry this variability study, but rather to collect data about the behavior of refractory materials. The sampling method of the bricks from the production lines was not carefully established. The quantitative conclusions arrived at by this study may or may not reflect the real variability in the production line, and thus, the results have not been published. However, the qualitative conclusions are expexted to hold, and a typical result is included in Fig. E.1 for completeness. It shows the variation of compressive strength for specimens extracted from various blocks within the same production batch and from blocks belonging to different production batches.
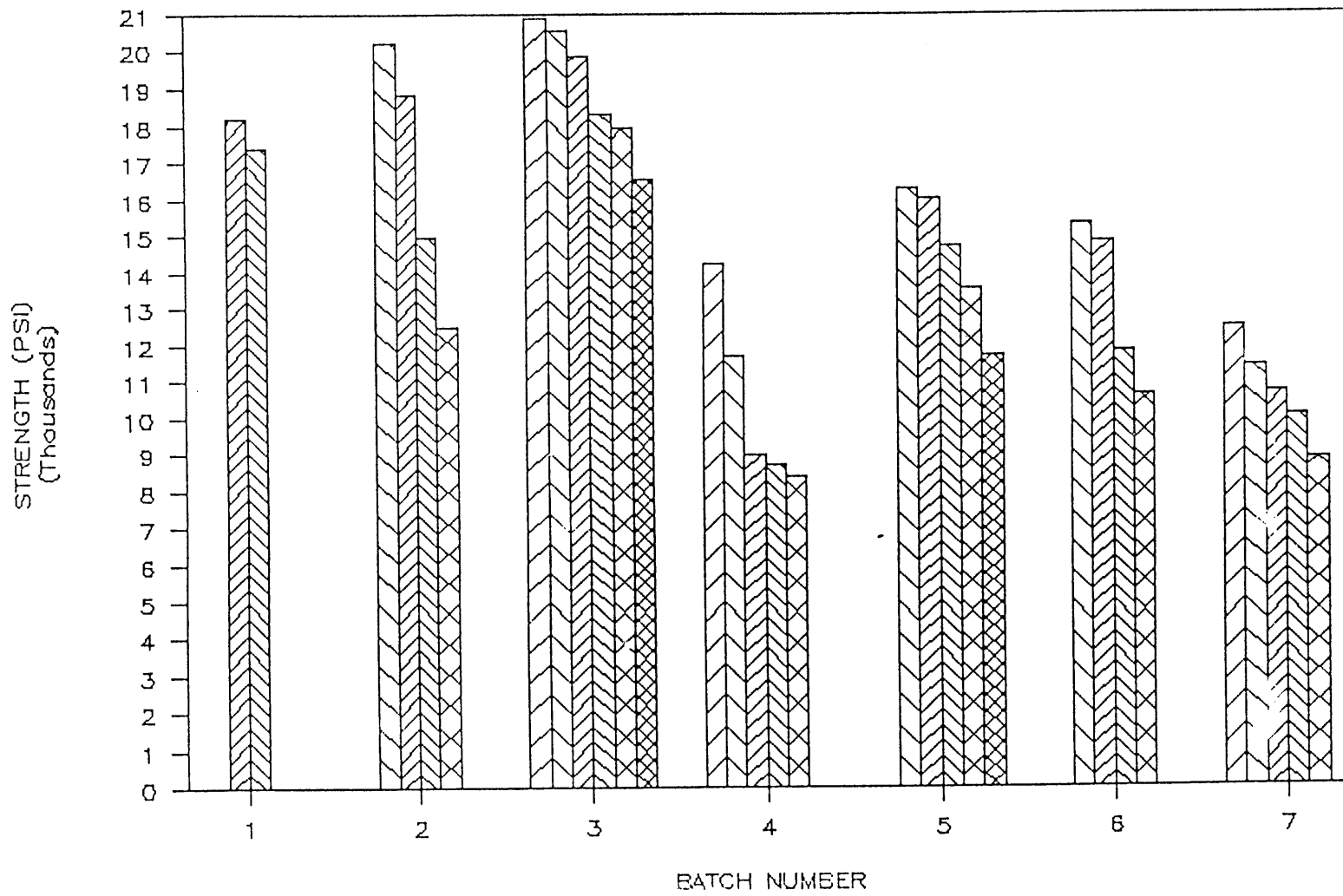
Figure E.1   Strength variability for a high—chromia refractory